

Developments in
FLUID MECHANICS
and
SPACE TECHNOLOGY

Dedicated to Satish Dhawan

Edited by

R NARASIMHA
A P J ABDUL KALAM



INDIAN ACADEMY OF SCIENCES
Bangalore 560 080

Developments in
FLUID MECHANICS
and
SPACE TECHNOLOGY

Dedicated to Satish Dhawan

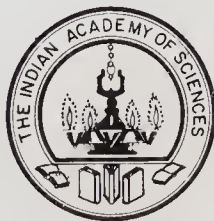
Edited by

R NARASIMHA

National Aeronautical Laboratory and
Indian Institute of Science, Bangalore

A P J ABDUL KALAM

Defence Research and Development Laboratory, Hyderabad



1 9 8 8

INDIAN ACADEMY OF SCIENCES

Bangalore 560 080

The cover shows a portion of the flow around a circular cylinder rotating in a uniform flow from the paper by Taneda

© 1988 by the Indian Academy of Sciences

The contents of this volume have appeared in various issues of *Sādhanā*

Edited by R. Narasimha and A. P. J. Abdul Kalam and printed for the
Indian Academy of Sciences by Phoenix Printing Company Pvt Ltd
Attibele Industrial Area, Bangalore 562 107, India

CONTENTS

Foreword	i
Transitional flows	
F R HAMA, U RIST, U KONZELMANN, E LAURIEN and F MEYER: Vorticity field structure associated with the 3D Tollmien-Schlichting waves	1
S TANEDA: Irregular flows	29
Turbulent flows	
D PAPAMOSCHOU and A ROSHKO: Observations on supersonic free shear layers	57
ZHANG ZHAOSHUN and WANG XILIN: Visualization and analysis of longitudinal vortices at curved walls of 2D laminar and turbulent channel flows	71
RYUJI TAKAKI and A K M FAZLE HUSSAIN: Recombination of two vortex filaments and jet noise	83
ZHOU (CHOU) PEI-YUAN and CHEN SHI-YI: On the theory of turbu- lence for incompressible fluids	97
Flow management	
R NARASIMHA and K R SREENIVASAN: Flat plate drag reduction by turbulence manipulation	113
M A BADRI NARAYANAN: The behaviour of excited plane jets	129
P R VISWANATH: Shock-wave-turbulent-boundary-layer interaction and its control: A survey of recent developments	143
Aerodynamics	
M A RAMASWAMY: Characteristics of a typical lifting symmetric super- critical airfoil	203
S M DESHPANDE and P V SUBBA RAJU: Monte Carlo simulation for molecular gas dynamics	217

T S PRAHLAD: A profile of aerodynamic research in VSSC with application to satellite launch vehicles 237

General analyses

HANS W LIEPMANN: Dimensional analysis and equilibrium radiation 295

KIRIT S YAJNIK: Limits and models in fluid mechanics 299

H S MUKUNDA: Variable property analysis – Is there anything to it? 313

Space technology

A P J ABDUL KALAM, B S SARMA and PRAHLADA: Integrated design approach for advanced aerospace vehicles 327

M R KURUP, V N KRISHNAMOORTHY and M C UTTAM: Development of solid propellant technology in India 337

S C GUPTA and B N SURESH: Development of navigation, guidance and control technology for Indian launch vehicles 343

K KASTURIRANGAN and K R SRIDHARAMURTHY: ISRO spacecraft technology evolution 359

Y S RAJAN: Management of the Indian space programme 397

Non-aerospace fluid mechanics

G N V RAO: A survey of wind engineering studies in India 415

P C SINHA: Hydrodynamic numerical modelling of storm surges – Application to the Bay of Bengal 433



Digitized by the Internet Archive
in 2018 with funding from
Public.Resource.Org

<https://archive.org/details/fluidmechanicssp00unse>



FOREWORD

IT gives us great pleasure to present this volume of papers and essays dedicated to Prof Satish Dhawan, and so to have the opportunity to honour the man who (among other things) founded fluid dynamics research in this country and led the national space programme to its present state of remarkable maturity and sophistication.

SATISH DHAWAN was born on 25 September 1920 in Srinagar, and was educated in this country and the United States. He graduated from the University of Punjab with an unusual combination of degrees: a BA in Mathematics and Physics, an MA in English Literature, and a BE in Mechanical Engineering. In 1947 he obtained an MS in Aeronautical Engineering from the University of Minnesota, and moved to the California Institute of Technology, where he was awarded the Aeronautical Engineer's Degree in 1949 and a Ph.D. in Aeronautics and Mathematics in 1951 with Prof Hans W Liepmann as adviser.

Prof Dhawan began his career in fluid dynamics research at Caltech with studies of shock reflection [1]* and shock/boundary layer interaction [6]; the definitive schlieren pictures and pressure measurements that resulted from these studies immediately illuminated the phenomena and became the point of departure for the numerous investigations that were subsequently carried out all over the world. He made the first precise direct measurements of skin friction on a flat plate [4, 5, 8], designing a special balance for the purpose that was later widely adopted and used in many laboratories (figure 1). He joined the Indian Institute of Science in 1951, becoming Professor and Head of the Department of Aeronautical Engineering there four years later. During the 11 years he spent at the Department, Prof Dhawan followed up his early interest in wind tunnels [2, 3] by setting up the high speed aerodynamics and boundary layer laboratories [7, 9, 10, 16], and in fact laid the foundations of experimental research in fluid dynamics in India. He and his students provided the first practical model for the transition zone in boundary layers [11, 13] and discovered connections with transition to turbulent flow in pipes and channels [20] and on axisymmetric bodies [27]. A series of pioneering experimental studies on the reverse transition from turbulent to laminar flow followed [21, 26]. Base flows [12], separation bubbles [22], wall jets [24], three-dimensional boundary layers [28] and transonic aerodynamics [14, 23] were other areas that received considerable attention. A pilot project carried out at the Institute under his direction [17, 18] led to the establishment of major wind tunnels at the National Aeronautical Laboratory, which was founded in 1959.

Two outstanding features of all these efforts reveal Satish Dhawan's philosophy in research [25, 32]: first, they were carried out at low cost, with ingenious

*Numbers in square brackets indicate references listed at the end.

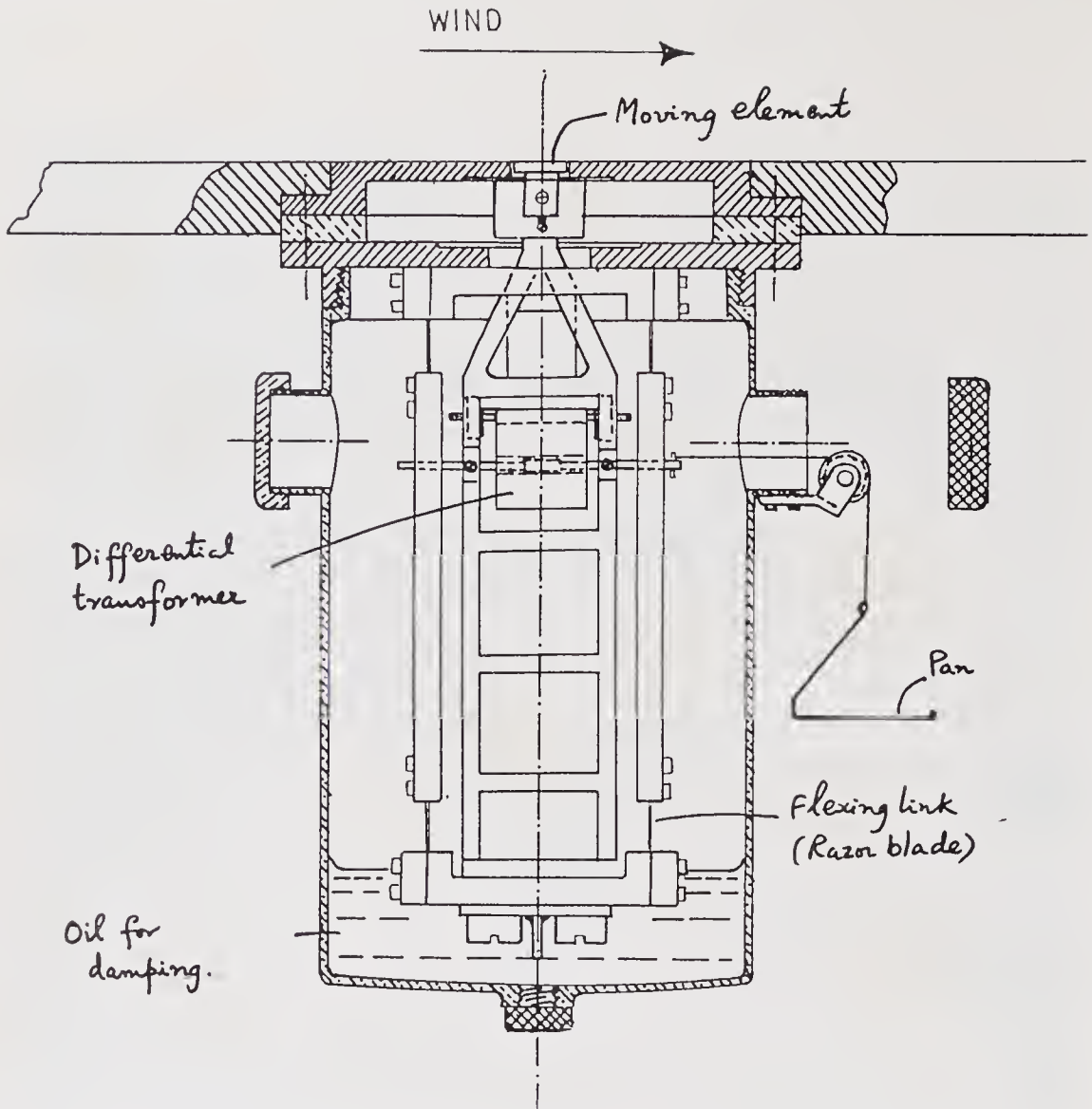


Figure 1. A skin friction balance designed and built at the Indian Institute of Science, and used for making direct measurements of skin friction in a wall jet [24].

development or adaptation of whatever materials, skills and instrumentation were available at the time; second, the basic research areas investigated in his laboratories were all inspired in some way by the problems faced by the newly-born aircraft industry of the country (in which he had spent a year before he went to the US for higher education). In later years he constantly sought to promote the development of this industry at the higher levels of policy and management.

In 1962 Prof Dhawan was appointed the Director of the Institute. During the following 18 years, he retained his interest in fluid dynamics and aeronautics (e.g. carrying out an elaborate evaluation of the airworthiness of an aircraft flying for Indian Airlines [29]), but devoted much time to the establishment of many new scientific programmes in the Institute, in such areas as automation and control theory, materials science, molecular biology and biophysics, technology for rural areas, theoretical physics, applied mathematics, solid state chemistry and atmospheric sciences. At the same time he played a key role in formulating the science

and technology policy of the country, through such bodies as the Scientific Advisory Committee to the Union Cabinet.

IN 1972 Prof Dhawan was appointed Chairman of the Space Commission and of the Indian Space Research Organisation, and Secretary to the Government of India in the Department of Space. In the following decade he directed the Indian space programme through a period of extraordinary growth and spectacular achievement [30, 31, 33]. Major programmes were carefully defined and systematically executed, including in particular the launch of Indian satellites on Indian rocket vehicles. Pioneering experiments were carried out in remote sensing and satellite communications [34], and led to operational systems that became a part of Indian life. These projects were all distinguished by their keen sensitivity to the true needs of a developing nation, a confident appreciation of the ability of its scientists and engineers [36], and the carefully planned involvement of Indian industry, both public and private [35, 38]. It is no surprise that the Indian space programme came to be seen in the 1980s as a model of technology development and application carried out within the country. One of us (Kalam) recalls a late evening in Cauvery Bhavan with Prof Dhawan, discussing space missions for the next two decades. Colleagues opened out computer printouts, data charts on launch vehicles, and plans for spacecraft launch complexes and development of connected real time software. Many mission options were debated linking launch vehicle configuration, aerodynamic design, propellant technology, and control, guidance and spacecraft systems. The long and careful consideration that Prof Dhawan had devoted to these issues were summarised by him the next morning in the form of two graphs (figures 2, 3) prepared in his own hand, bringing out a space mission profile for the next 15 years (1980–1995). These graphs have become the blueprints for the national space programme.

After his retirement from formal positions in Government, Prof Dhawan continues as a member of the Space Commission, taking time every now and then to analyse matters of public policy in science and technology [37, 38].

THIS volume is in two loosely-connected parts. The first is a collection of research papers in fluid dynamics, chiefly on subjects Prof Dhawan contributed to or was keenly interested in at one time or the other during his career. Some of the papers in this section were presented as invited lectures at the 1986 Asian Congress of Fluid Mechanics in Tokyo; these Congresses have been actively encouraged and supported by Prof Dhawan right from their inauguration in 1980. The second part highlights the advances made in space technology over the period 1972–1984 when Prof Dhawan led the national space programme.

The first part begins with a paper by Hama and coworkers on transition in the boundary layer, which was one of Prof Dhawan's first interests when he began his research in Bangalore. This paper reveals in considerable detail the dynamics of three-dimensional instability in the nonlinear stage: computer simulations, experiments, and linear, time-dependent analyses have provided much fresh insight on the problem. Hama and his colleagues offer simple explanations for the formation of the longitudinal vorticity field in the fundamental and sub-harmonic mode interactions.

S Taneda presents a pictorial survey of what he calls "irregular flows". He looks upon flows at large Reynolds numbers as consisting of many coherent structures

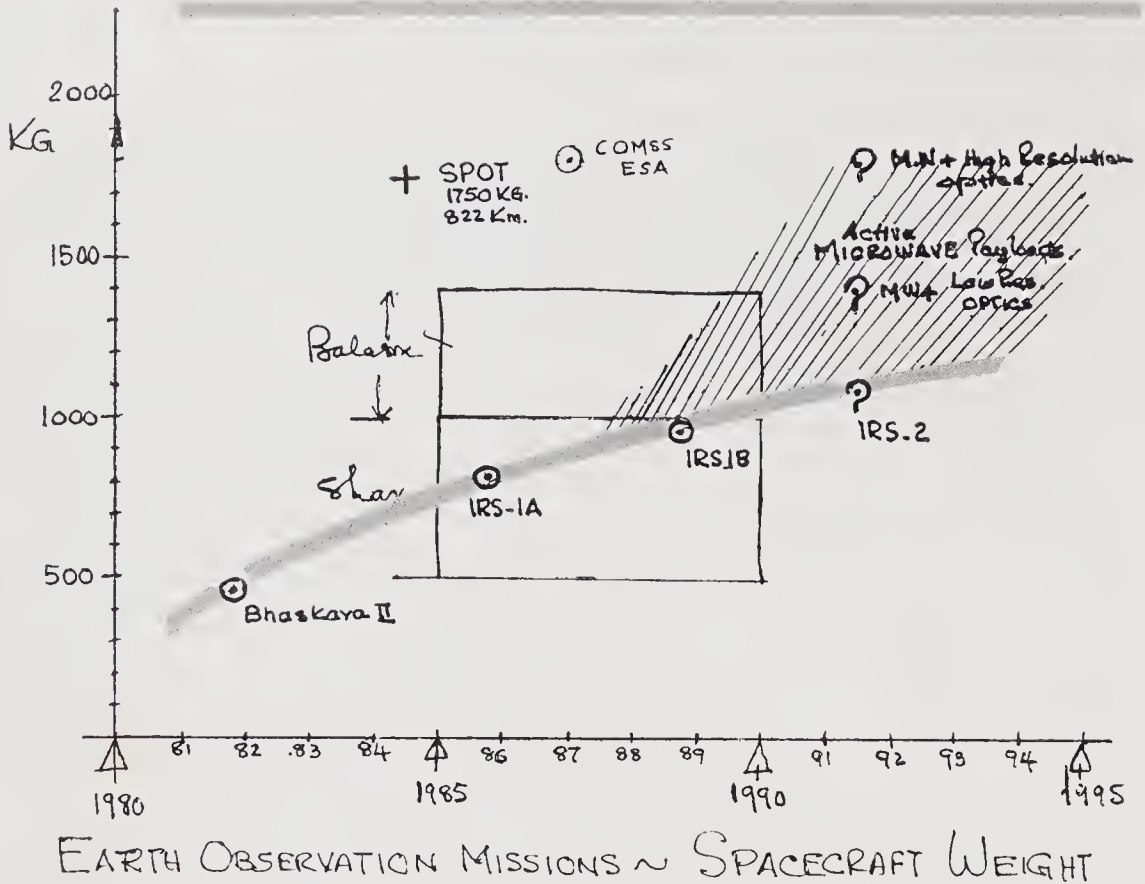


Figure 2.

fluctuating irregularly. This paper is a small album of the kind we believe is close to Prof Dhawan's heart. Papamoschou & Roshko describe some pioneering experiments on supersonic free shear layers, and show how the genuine effect of *compressibility* (as distinguished from that of *variable density*) can be accounted for through a convective Mach number. Zhang & Wang study the two-dimensional structure of longitudinal vortices on the walls of a curved channel, when the flow is laminar as well as turbulent. They combine hydrogen-bubble flow visualisation with conditional sampling and VITA analysis to describe the structure of the flow near the wall. Takaki & Hussain study numerically the recombination of two vortex filaments in a viscous compressible fluid. They apply their results in particular to predict the far-field noise of a circular jet by assuming that the main noise source is the recombination process in deformed vortex rings in the jet near-field, and show that the predicted noise intensity is consistent with the known dependence on velocity, but has an additional factor depending on the size of the vortex filament. Zhou & Chen continue with their studies of turbulent flow, and display results for triple and quadruple correlations for the plane turbulent wake.

Three papers on the control of turbulent flows attempt to assess the current position in one of Prof Dhawan's life-long interests. Efforts to reduce the skin-friction drag of a surface by introduction of manipulators in a turbulent boundary layer are reviewed by Narasimha & Sreenivasan, who provide at the end a map of manipulator parameters that might lead to lower drag. Badri Narayanan reports the results of experiments in which a plane jet is excited by periodic

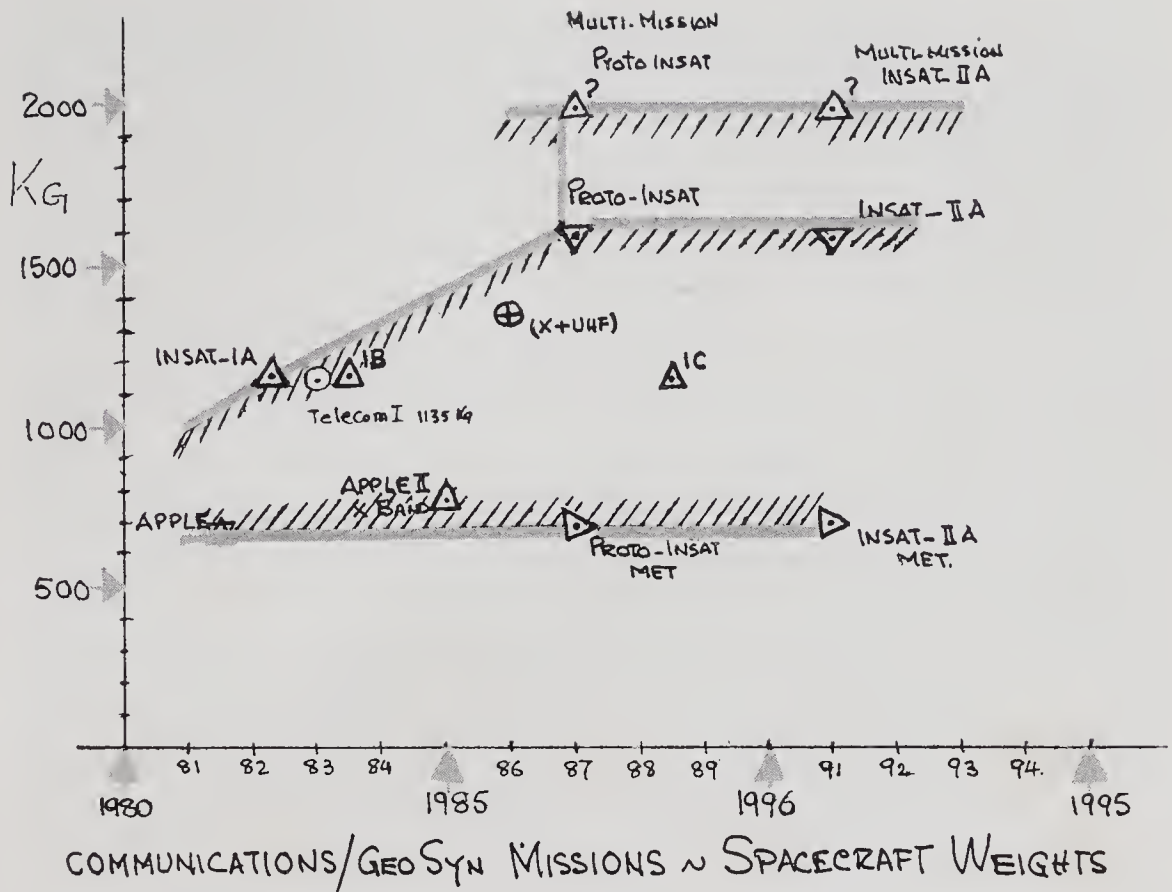


Figure 3.

oscillations into unfamiliar states of motion, involving a substantial increase in entrainment. Viswanath reviews current work on shock/boundary layer interaction and possible methods of control for applications.

There follow three papers on aerodynamics. M A Ramaswamy shows how a symmetric lifting supercritical aerofoil can be successfully designed, and presents experimental results confirming the design. The possibility that supercritical aerofoils need not have the asymmetric shapes now associated with them may have value in supersonic flight. Methods that have been developed to compute low-density flows, from an effort carried out in part for ISRO, are described in a paper by Deshpande & Subba Raju. The special aerodynamic problems posed by satellite launch vehicles are considered by T S Prahlaad, with emphasis on those encountered in the Indian space programme. Particular attention is devoted to the analysis of multi-body configurations (such as strap-on boosters) and bulbous payload shrouds.

Liepmann shows how surprisingly far one can go by dimensional analysis in understanding cavity radiation, both at rest and in motion. Yajnik makes an analysis of limiting and modelling arguments in fluid dynamics by breaking them down into a sequence of steps and examining the associated sequence of flow problems. Mukunda shows how consideration of variable thermodynamic and transport properties in analysis of combusting flows does more than merely improve the accuracy of the solutions, and in fact often leads to qualitatively different results.

In the section on space technology, the paper by Kalam, Sarma & Prahlada discusses how classical processes of aerospace vehicle system design can be integrated and automated through interface design packages using CAD/CAM work stations and parallel processors. Kurup, Krishnamoorthy & Uttam highlight the methods by which contemporary high energy propellants were developed in India, leading to the establishment of a Space Booster Rocket Propellant Plant capable of producing large rocket motors next in size only to the Space Shuttle and Titan.

The paper by Gupta & Suresh describes the upgradation of the open-loop inertial guidance technology used in the first Indian Satellite Launch Vehicle SLV3 to a closed-loop guidance system for ISRO's Augmented and Polar Satellite Launch Vehicles (ASLV, PSLV). The self-sufficiency attained in inertial guidance technology, from sensors to on-board processors, control systems and various software modules, is described. The review system developed in this programme for the design and validation of software could be a standard for application in advanced aerospace projects. Kasturirangan describes the evolution of Indian spacecraft technology in its attempt to meet the growing demand for proper utilisation of the vast natural resources of the country and for communication with the remotest regions of the land. The progress in spacecraft structural design and payload characteristics with the adoption of the modularity concept can be clearly seen. Such progress is responsible for the expectation that the Indian National Satellite INSAT-II should cost less than similar satellites made elsewhere in the world.

One of the crucial ingredients in the success of the Indian space programme has been its management system. Rajan describes the management philosophy and style of Prof Dhawan, emphasising how multiple space technologies were consolidated and oriented towards the twin space applications of remote sensing of natural resources and space communication. The space-industry network that has implemented these programmes, and the international cooperation that has marked it, are both discussed. The unique mechanisms evolved by Prof Dhawan to involve users in the management of operational space systems are also touched upon.

Finally we have two papers in areas which Prof Dhawan actively encouraged. G N V Rao surveys wind engineering studies in India, and some of the investigations carried out in the large low-speed tunnel at the Institute. P C Sinha describes the status of modelling an important geophysical problem, namely that of storm surges in the Bay of Bengal.

PROF DHAWAN has been widely honoured for his contributions to science and technology by various bodies within India and abroad. He was awarded the honorary degree of Doctor of Science by the Universities of Roorkee (1972), Punjab (1978) and Delhi (1984), the Cranfield Institute of Technology, UK (1975), and the Indian Institute of Technology, Madras (1981); and the honorary degree of Doctor of Laws by the University of Bombay (1976). He is a Distinguished Alumnus of the California Institute of Technology (1969) and of the Indian Institute of Science (1984), and an Honorary Fellow of the Aeronautical Society of India (1979), the Institution of Engineers (1983), and the Indian Institute of Science (1981). He was elected Fellow of the Royal Aeronautical Society in 1963, of the Indian Academy of Sciences in 1972, and of the Indian National Science Academy in 1978; he is a Foreign Honorary Member of the American Academy of

Arts and Sciences (1972) and a Foreign Associate of the US National Academy of Engineering (1978). He was President of the Aeronautical Society of India during 1968–69, and of the Indian Academy of Sciences during 1977–80. He has been conferred the Pandit Jawaharlal Nehru Award in Engineering and Technological Sciences of the Madhya Pradesh Government (1983), the Rajyotsava Award of Karnataka (1984), the Om Prakash Bhasin Award for Science and Technology (1985), the Parikh Memorial Award (1986) and the Watumull Foundation Medal (1987). The Government of India honoured him with Padma Shri in 1966, Padma Bhushan in 1971, and Padma Vibhushan in 1981.

PROF DHAWAN has in his professional career been engineer, teacher, research scientist, technologist, manager, leader and adviser – often all at the same time! His great human qualities, combining intense personal charm with a deep commitment to social values and an extraordinary objectivity in management, have led several generations of students, colleagues and administrators to efforts that they would otherwise not have undertaken. This volume does not pretend to reflect all the contributions to science and technology he has made: his example, counsel and philosophy have had far wider and deeper influence than the papers collected here can indicate, and will we hope be described elsewhere. Meanwhile, all the authors who have contributed to this volume take great pleasure in paying tribute to one who has distinguished himself in so many different ways, through the Academy over which he presided and the journal which he helped to found.

R NARASIMHA
A P J ABDUL KALAM
Editors

References*

- [1] Problems in shock reflection, Report, Guggenheim Aeronautical Laboratory, California Institute of Technology (1949)
- [2] Design and use of a flexible nozzle for the GALCIT 4"×10" transonic wind tunnel, Report, Guggenheim Aeronautical Laboratory, California Institute of Technology (1949)
- [3] A flexible nozzle for small supersonic wind tunnel, *J. Aeronaut. Sci.* 18: 253–258 (1951) (with A Roshko)
- [4] An instrument for the direct measurement of skin friction, Report, Guggenheim Aeronautical Laboratory, California Institute of Technology (1951)
- [5] Direct measurements of local skin friction in low-speed and high-speed flow, Proceedings of the First US National Congress of Applied Mechanics (1951) (with H W Liepmann)
- [6] On reflection of shock waves from boundary layers, Tech. Note No. 2334, National Advisory Committee for Aeronautics, Washington DC (1951) (with H W Liepmann & A Roshko)
- [7] A miniature supersonic wind tunnel, Report, Department of Aeronautics, Indian Institute of Science (1952)
- [8] Direct measurements of skin friction, Tech. Rep. No. 1121, National Advisory Committee for Aeronautics, Washington DC (1953)
- [9] Design and operation of an intermittent 1"×3" supersonic wind tunnel, *J. Aeronaut. Soc. India* 7(1):1–17 (1955)

*This list includes all publications of Prof Dhawan, and the theses submitted by his students at the Department of Aeronautical Engineering, Indian Institute of Science.

- [10] Transition from laminar to turbulent motion, Proceedings of the III Indian Congress of Theoretical and Applied Mechanics (1957)
- [11] Some properties of boundary layer flow during the transition from laminar to turbulent motion, *J. Fluid Mech.* 3:418–436 (1958) (with R Narasimha)
- [12] An experimental investigation of base flows at supersonic speed, AIISc thesis of M A Badri Narayanan (1958)
- [13] A study of transition from laminar to turbulent flow in the boundary layer on a flat plate, AIISc thesis of R Narasimha (1958)
- [14] Some problems associated with the design of transonic wind tunnels, Proceedings of the Defence Science Conference, *Def. Sci. J.* (1958)
- [15] The pitot tube displacement effect in boundary layer flows, *J. Aeronaut. Soc. India* 11(1):1–18 (1959) (with B R Vasudeva)
- [16] Studies on the pitot tube displacement effect in boundary layer measurements, AIISc thesis of B R Vasudeva (1959)
- [17] Data on peak starting loads in supersonic wind tunnels, Report, Department of Aeronautics, IISc (1960)
- [18] Equations for stress distribution in model string for the NAL trisonic wind tunnel, Tech. Note No. 4, Department of Aeronautics, IISc (1960)
- [19] Wind tunnel tests on the HF24 air intake, Report IWTR 33, Department of Aeronautics, IISc (1961) (with V Krishnamoorthy)
- [20] Studies on the transition from laminar to turbulent flow in a pipe, M Sc thesis of P V Pantulu (1963)
- [21] A study of boundary layer expansion from interactions near a sharp corner in supersonic flow, M Sc thesis of R Vivekanandar (1964)
- [22] A study of laminar boundary layers and separation bubbles near the leading edge of two-dimensional airfoils, Ph D thesis of S K Ojha (1965)
- [23] An investigation on turbulent boundary layer over ventilated walls, M Sc thesis of M A Ramayya (1965)
- [24] Two-dimensional turbulent wall jets with and without a constant outside stream, M Sc thesis of S P Parthasarathy (1965)
- [25] Twentysecond British Commonwealth Lecture: Aeronautical research in India *J. R. Aeronaut. Soc.* 71(675):149–184 (1967)
- [26] Inverse transition flow from turbulent to laminar flow in a two-dimensional channel, Ph D thesis of M A Badri Narayanan (1967)
- [27] Effect of convex transverse surface curvature on transition and other properties of incompressible boundary layers, Ph D thesis of G N Venkataramana Rao (1968)
- [28] A study of mean velocity profiles in three-dimensional incompressible turbulent boundary layers, Ph D thesis of T S Prahlad (1971)
- [29] An evaluation of the AVRO/HS 748 aircraft in India, Report of a one-man committee appointed by the Government of India in April 1973 (classified) (1975)
- [30] A glimpse of the Indian space programme, *Proc. Indian Acad. Sci.* C1:1–26 (1978)
- [31] INSAT-I: A multipurpose domestic satellite system for India, *IEEE Trans. Broadcast.* BC-25(4):121–127 (1979) (with P P Kale & S P Singh)
- [32] A glimpse of fluid mechanics research in Bangalore 25 years ago, *Proc. Indian Acad. Sci.* C4:95–109 (1981)
- [33] Space launchers for India, Sir Mokshagundam Visvesvaraya Memorial Lecture, Diamond Jubilee Celebrations of the Institution of Engineers (India), Hyderabad (1981)
- [34] The Indian space programme, Thirteenth International Symposium on Space Technology and Sciences (ISTS), Tokyo (1982)
- [35] Space and Industry, Shri Ram Memorial Lecture delivered at the P H D Chamber of Commerce & Industry, New Delhi (1983)
- [36] Application of space technology in India, Aryabhata Lecture delivered at the Indian National Science Academy, New Delhi (1985)
- [37] Star Wars: The arms race in space, Lecture to Peace Conference, Bangalore (1986)
- [38] Prospects for a space industry in India, Fifth Lala Karam Chand Thapar Memorial Lecture, Patiala Technical Education Trust, New Delhi (1988)

Vorticity field structure associated with the 3D Tollmien-Schlichting waves

F R HAMA¹, U RIST¹, U KONZELMANN¹, E LAURIEN²
and F MEYER²

¹Institut A für Mechanik, Universität Stuttgart, 7000 Stuttgart 80, West Germany

²Institut für Theoretische Strömungsmechanik, DFVLR-AVA, 3400 Göttingen, West Germany

Abstract. Details of the vorticity field structure associated with the 3D Tollmien-Schlichting waves have been examined based upon the recent numerical studies of the subject. First, a single oblique T-S wave has been found to have the velocity component parallel to the wave front playing an overall dominant role, in particular, to create the longitudinal vorticity. The so-called Benney-Lin longitudinal vortices are then demonstrated to be, in fact, a minor consequence compared with the localized longitudinal vorticity field and its periodic pumping. Finally, the formation of the longitudinal vorticity field in the fundamental- and subharmonic-mode interactions is explained.

Keywords. Vorticity field structure; 3D Tollmien-Schlichting waves; longitudinal vorticity; laminar-turbulent transition; Poiseuille flow.

1. Introduction

In the process of laminar-turbulent transition in two-dimensional (2D) boundary layers and other shear flows, such as the Poiseuille flow, the 2D Tollmien-Schlichting (T-S) waves will first appear as it is the most unstable mode. Similar but obliquely oriented linear waves are considered more stable because they are reduced to a 2D problem relative to the direction of the wave propagation for which the effective Reynolds number is always smaller than that of the 2D wave. This principle is called the Squire theorem (Squire 1933).

When the 2D T-S waves are amplified and gain a certain amount of finite amplitude, it was reported by Schubauer (1957, pp. 85–107) that the originally 2D T-S waves inherently acquire a nearly periodic spanwise modulation. This behaviour was further studied in detail by introducing artificial 3D disturbances by Klebanoff *et al* (1962).

In order to theoretically treat the early stage of such 3D developments, Benney and Lin (Benney & Lin 1960; Benney 1961) considered the first-order nonlinear interaction between the 2D T-S wave and two sets of obliquely running T-S waves

in a free-shear layer. Such a combination of T-S waves is schematically shown in figure 1a, as the fundamental-mode interaction. The most celebrated conclusion is the appearance of the mean longitudinal vortices and the resultant peak-valley splitting in qualitative agreement with experimental observations. In addition to the free-shear layer, the theory was also applied to a simplified boundary-layer type velocity profile with the same general conclusions (Benney 1964). The true Blasius boundary layer was later treated by Antar & Collins (1975). In spite of the ingenious introduction of the three-wave interaction, the significance of the mean longitudinal vortices seems to have been overemphasized. It is one of the objectives of the present paper to properly identify the more detailed and important feature of the three-wave interaction.

In addition to the fundamental-mode (sometimes called *K*-type) interaction, a staggered mode of interaction has been discovered more recently, chiefly by Russians (Kachanov & Levchenko 1984). The staggered pattern is explainable by the subharmonic-mode (sometimes called *H*-type) interaction as sketched in figure 1b, and a theoretical development has been made by Herbert (1984). As a matter of fact, similar staggered patterns have been observed many years ago (Hama 1959; Knapp & Roach 1968), but its fluid dynamic mechanism might have been different because of their axisymmetric geometry.

Before we consider the three-wave interaction, however, the flow field associated with a single oblique T-S wave system will be examined. Although this problem is known to be treated under the Squire theorem, the numerically obtained flow field is far more involved than the simple-minded application of the Squire theorem. It has been discovered that the velocity component parallel to the oblique wave front, which seems to have escaped proper attention, is in fact a dominant quantity and plays a significant role in generating the longitudinal vorticity.

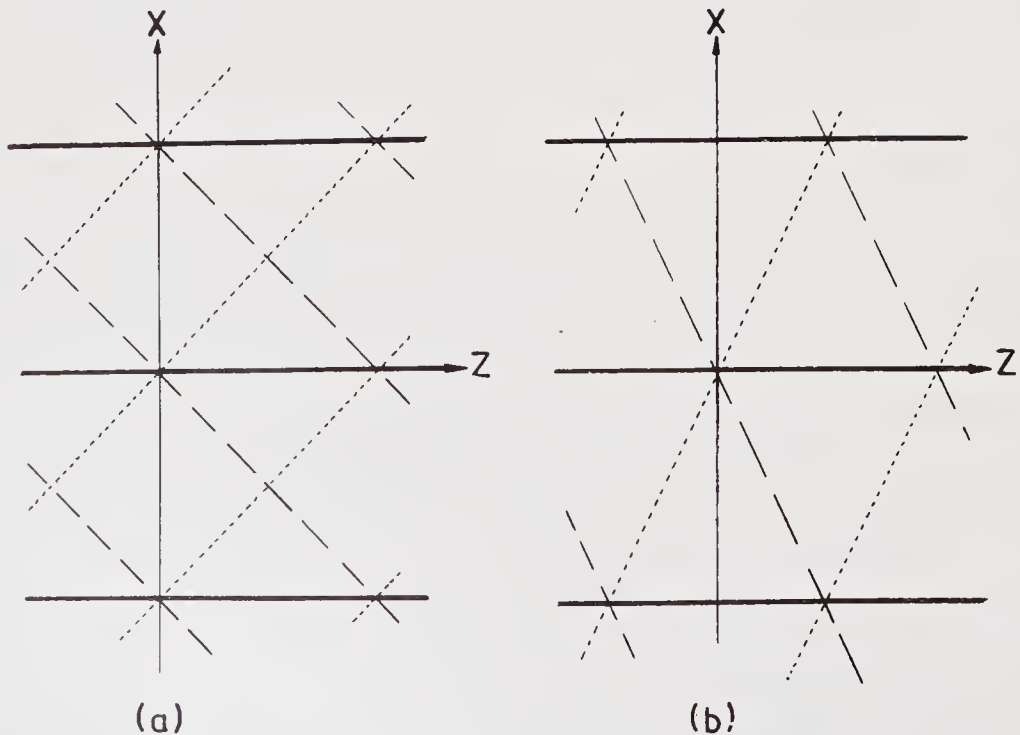


Figure 1. Three-wave interactions. (a) Fundamental mode. (b) Subharmonic mode.

Based upon the information obtained above, the formation of the longitudinal vorticity system in the fundamental- and subharmonic-mode interactions is explained. Although the aligned peak-valley splitting does not take place in the latter interaction, the creation of the local peaks and valleys is essentially the same for the two modes.

The major part of the numerical results quoted in the present paper has been obtained by U Rist and U Konzelmann under the general supervision of Prof. H Fasel and is concerned with the 2D Poiseuille flow.

First, for the linear problem, the eigenfunctions of the vertical velocity component v were obtained from the Orr-Sommerfeld equation with appropriate Reynolds number and wavenumber, for which v is invariant with the wave direction. The linearized vorticity-transport equation for the vertical vorticity component (sometimes called the Squire equation) was then solved. The other velocity and vorticity components were subsequently calculated from the continuity, the definition of vorticity and the derivatives of these equations. All derivatives involved have been treated numerically by fourth-order finite differences.

For the nonlinear problems, the complete Navier-Stokes equations in the vorticity-transport formulation were transformed by means of a Fourier-Ansatz for the longitudinal and transverse dimensions, X and Z . The resultant system of complex equations for each Fourier mode was discretized with fourth-order differences in the vertical Y direction and the second-order one-sided backward differences in time. The discretized equations were treated as fully implicit. The solution had to be obtained iteratively because of the nonlinearity in the vorticity-transport equations together with the Poisson equations for the velocities. A 2D and two oblique waves obtained from the linear problem were taken as the initial condition, and the input parameter to trigger the interaction was the amplitude of the 2D wave, which was kept constant throughout the computation. In the numerical procedure, only a few spectral modes were allowed to develop, i.e., the fundamental (and the subharmonic) and the zeroth. Therefore, the solutions are applicable to the first-order nonlinear interactions as in the Benney-Lin theory.

The computational scheme developed by Kleiser (1982) is particularly suitable to numerically simulate the progressively higher-order nonlinear developments in the transition process, as it includes many harmonics. The technique was applied by Laurien (1986) to the Blasius boundary layer. His results were not only in good agreement with the Stuttgart computation cited above in the early stage of transition, but also in excellent agreement with the experimental results of Williams *et al* (1984) in the much later stage of nonlinear, three-dimensional developments. His data have been extensively reduced by F Mayer under the guidance of Dr L Kleiser and with the support of Professor H Oertel, DFVLR-AVA, Göttingen.

2. A single oblique wave

We consider in this section a single train of the linear T-S waves running obliquely to the right with an angle φ to the free-stream direction X . Y and Z are the coordinates normal to the wall and in the spanwise direction, respectively. Basic

flow is two-dimensional throughout the paper, mostly the Poiseuille flow and in one case the boundary layer along a flat plate as remarked. The mean velocity components are U, V, W . The fluctuating velocity components u, v, w and pressure p may be expressed in a modal form (after Mack 1984)

$$[u, v, w, p]^T = [\hat{u}(Y), \hat{v}(Y), \hat{w}(Y), \hat{p}(Y)]^T \exp [i(\alpha X + \beta Z - \omega t)] \quad (1)$$

in which the quantities with circumflexes are the amplitudes, α and β are respectively the wavenumbers in the X and Z directions, and ω is the angular frequency (not to be confused with vorticity defined below). We denote the vorticity components by

$$\omega_X = \frac{\partial v}{\partial Z} - \frac{\partial w}{\partial Y}, \quad \omega_Y = \frac{\partial w}{\partial X} - \frac{\partial u}{\partial Z}, \quad \omega_Z = \frac{\partial u}{\partial Y} - \frac{\partial v}{\partial X}, \quad (2)$$

i.e.,

$$\boldsymbol{\omega} = -\text{rot } \mathbf{u}. \quad (3)$$

The velocity components u, v, w satisfy the following modal equations:

$$\left. \begin{aligned} i(\alpha U + \beta W - \omega)\hat{u} + D U \hat{v} &= -i\alpha\hat{p} + (1/R) [D^2 - (\alpha^2 + \beta^2)]\hat{u} \\ i(\alpha U + \beta W - \omega)\hat{v} &= -D\hat{p} + (1/R) [D^2 - (\alpha^2 + \beta^2)]\hat{v} \\ i(\alpha U + \beta W - \omega)\hat{w} + D W \hat{v} &= -i\beta\hat{p} + (1/R) [D^2 - (\alpha^2 + \beta^2)]\hat{w} \end{aligned} \right\}, \quad (4)$$

$$i(\alpha\hat{u} + \beta\hat{w}) + D\hat{v} = 0, \quad (5)$$

where $D = d/dY$.

The numerical solutions for the oblique waves with the propagation angles 5, 15, 30, 45 and 65° are shown in figure 2. The profiles for \hat{u} and ω_Z include also those for the exact 2D wave ($\varphi = 0^\circ$), indicating incidentally undetectably small effect of the obliqueness for $\varphi = 5^\circ$. In the calculation, the Reynolds number and the wavenumber with respect to the wave-propagation direction are taken to be constant, 2114 and 1.324, respectively. All of the quantities shown are normalized with respect to the maximum value of \bar{u} , the velocity component in the wave-propagation direction (see later). Because of the oblique orientations one may expect the presence of \hat{w} and ω_X . In addition, however, ω_Y also appears and the profiles of \hat{u} and ω_Z become increasingly more complicated with the angle.

When the coordinate system (X, Z) is transformed into (\tilde{X}, \tilde{Z}) , i.e., in the direction of the wave vector and that parallel to the wave front, and the dependent variables are adopted accordingly, cf. figure 3,

$$\begin{aligned} \tilde{\alpha}\tilde{u} &= \alpha\hat{u} + \beta\hat{w}, \quad \tilde{\alpha}\tilde{w} = \alpha\hat{w} - \beta\hat{u}, \\ \tilde{\alpha}\tilde{U} &= \alpha U + \beta W, \quad \tilde{\alpha}\tilde{W} = \alpha W - \beta U, \end{aligned} \quad (6)$$

where $\tilde{\alpha}^2 = \alpha^2 + \beta^2$, keeping \hat{v}, \hat{p}, ω and R unchanged, we have

$$i(\tilde{\alpha}\tilde{U} - \omega)\tilde{u} + D\tilde{U}\hat{v} = -i\tilde{\alpha}\hat{p} + (1/R) [D^2 - \tilde{\alpha}^2]\tilde{u}, \quad (7a)$$

$$i(\tilde{\alpha}\tilde{U} - \omega)\hat{v} = -D\hat{p} + (1/R) [D^2 - \tilde{\alpha}^2]\hat{v}, \quad (7b)$$

$$i(\tilde{\alpha}\tilde{U} - \omega)\tilde{w} + D\tilde{W}\hat{v} = (1/R) [D^2 - \tilde{\alpha}^2]\tilde{w}, \quad (7c)$$

and

$$i\tilde{\alpha}\tilde{u} + D\hat{v} = 0. \quad (8)$$

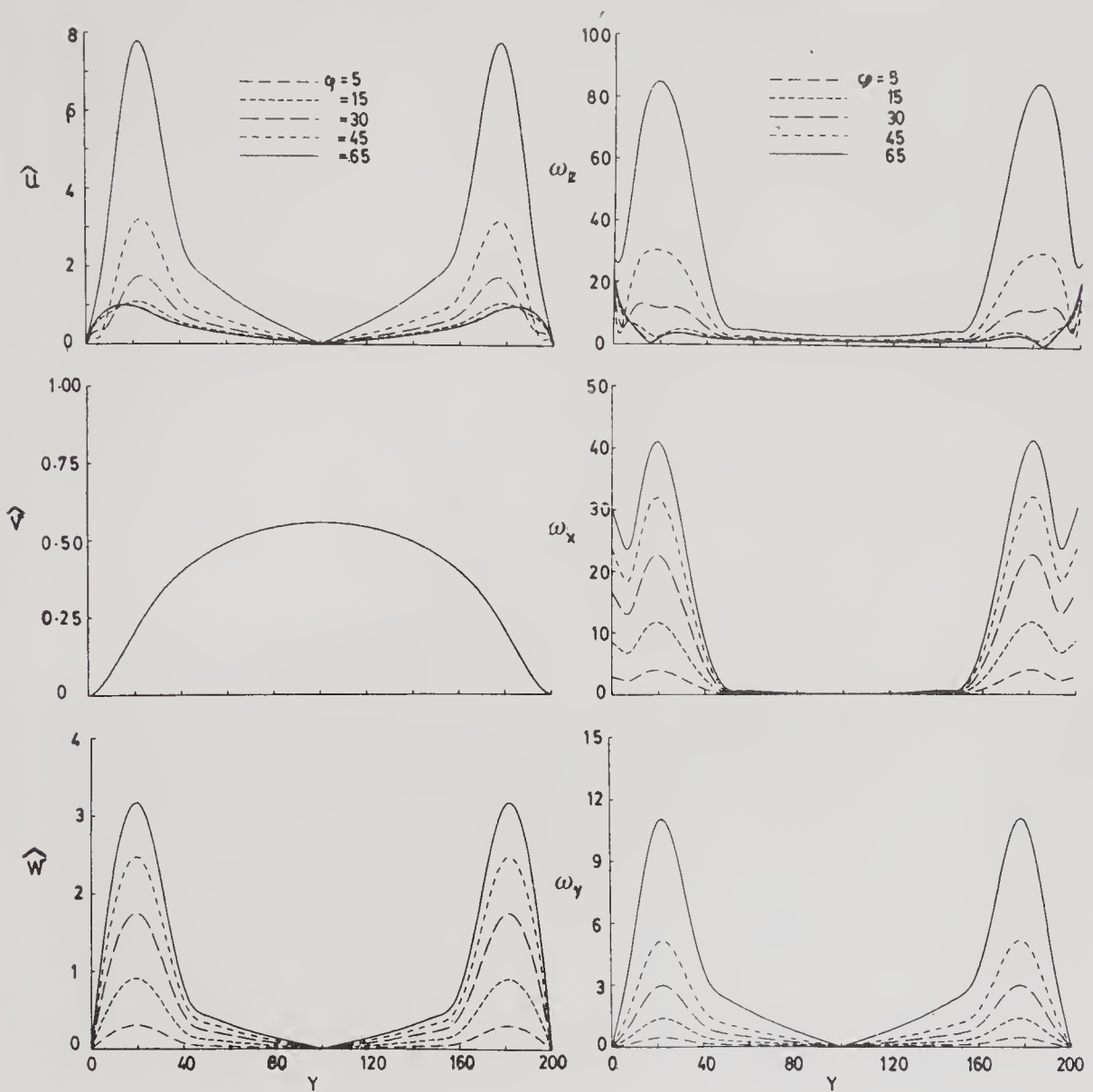


Figure 2. Amplitude distributions of oblique T-S waves.

Equations (7a) and (7b), together with (8) are exactly in the same form as in the two-dimensional case. Therefore, \hat{u} , \hat{v} , and $\hat{\omega}_z$ are exactly the same as those for the 2D solution for the Reynolds number and the wavenumber in the \bar{X} direction (the Squire theorem). It may be observed in figure 4 that the amplitude profiles of \hat{u} and $\hat{\omega}_z$ are indeed invariant with the angles. This is the reason why the maximum value of \hat{u} is taken as a reference to normalize all the quantities in figures 2 and 4. Likewise, the structures of the \hat{u} and $\hat{\omega}_z$ fields are typically two-dimensional (figures 5 and 6). In these and subsequent 'structure' figures, the lines are contour lines.

The transformation, however, does not eliminate \hat{w} , $\hat{\omega}_x$ and $\hat{\omega}_y$, none of which exists in the truly 2D waves. The amplitude profiles of \hat{w} in figure 4 indicates the large influence of the oblique wave angles. For the three-wave interactions, we will be concerned with such angles as 45° or even larger. Considering the fact that \hat{u} does not change with the angle, the dominating influence of the large magnitude of \hat{w} for those large oblique angles can be easily anticipated.

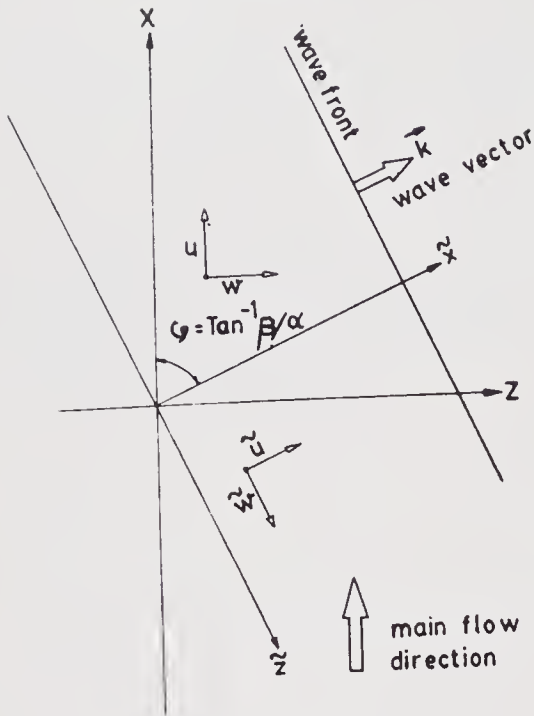


Figure 3. Oblique wave coordinates.

Instantaneous profiles of \tilde{w} for $\varphi = 65^\circ$ are shown in figure 7 and appear to be in general agreement with Hendriks' solution referred to by Usher & Craik (1975). Equation (7c) is independent of \tilde{Z} , so that \tilde{w} can only be a streaming motion parallel to the wave front. Its cross-cut structure in the manner of constant- \tilde{w} contour lines is given in figure 8, in which the solid and broken lines indicate the flows out and into the \tilde{XY} -plane, respectively. This flow field of \tilde{w} may be thought of as two (per wavelength) counter-flowing Poiseuille-like flows in two squashed tubes. In fact, the Y -coordinate is substantially enlarged in the plottings by the coordinate transformation, so that they are more squashed in reality. The vorticity vector associated with the \tilde{w} field is tangential to the contour lines, and one can easily imagine that the maximum vorticity will be located in the region where the two counter-flowing 'tubes' touch each other and neighbouring contour lines are closer together. The vector attached to the maximum vorticity is in the \tilde{XY} -plane and heavily inclined to the \tilde{X} direction, resulting in a large $\omega_{\tilde{X}}$ component with a smaller amount of ω_Y , both of which never exist in the truly 2D waves. Such observations as above concerning the interrelationship between the $\omega_{\tilde{X}}$ or ω_Y field and the \tilde{w} field can be clearly confirmed when the contour maps of the two vorticity components (figures 9 and 10) are compared with the \tilde{w} field (figure 8).

The longitudinal velocity component \hat{u} consists of the contributions from \hat{u} and \tilde{w} . Since \tilde{w} is overwhelmingly larger than \hat{u} , the \hat{u} profile (figure 2) and its structure (figure 11) are almost completely dictated by \tilde{w} , cf. figure 8. By the same token, the profiles (in figure 2) and the structures (figures 12 and 13) of the transverse as well as longitudinal vorticity components, ω_Z and ω_X , are quite similar to those of $\omega_{\tilde{X}}$ except in the near-wall region where ω is relatively small compared to the 2D wall-shear vorticity $\omega_{\tilde{Z}}$.

Overall, it is now clear that the velocity component parallel to the wave front and its resultant vorticity are indeed the dominant factors in the oblique T-S waves of those large oblique angles with which we are concerned.

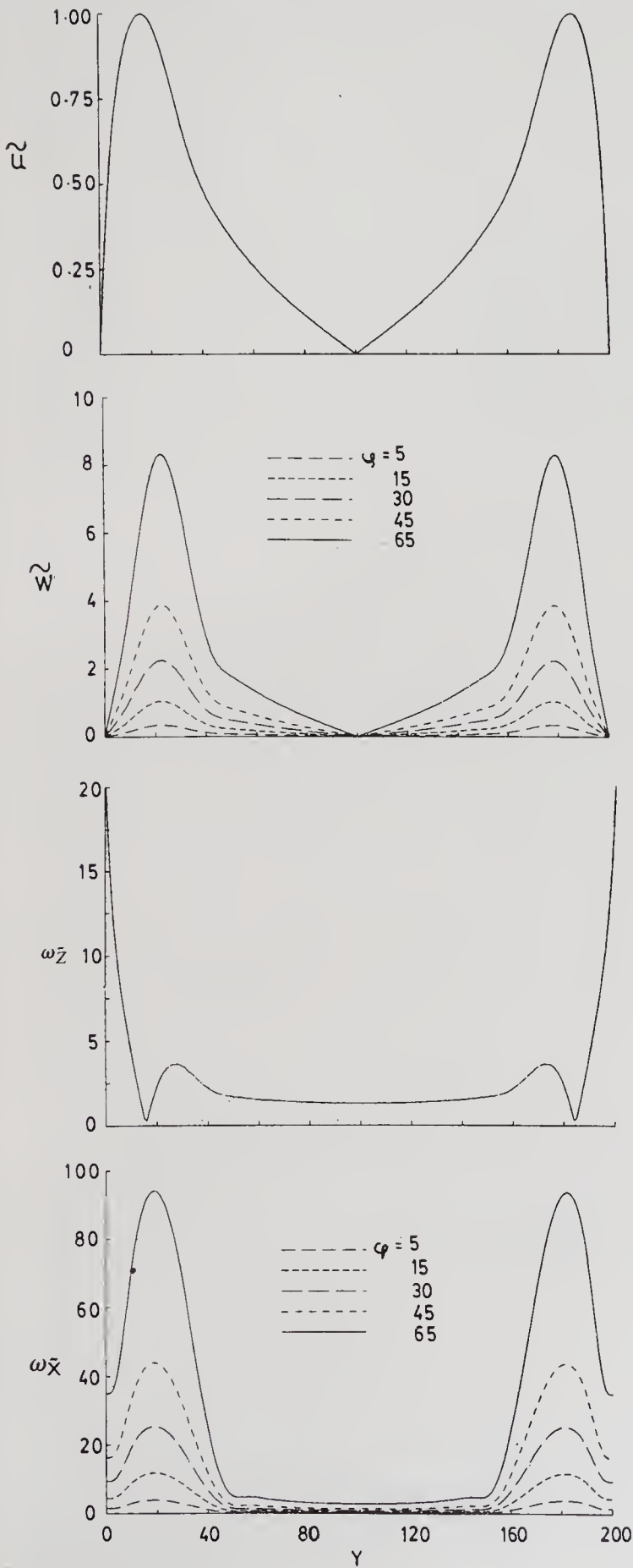
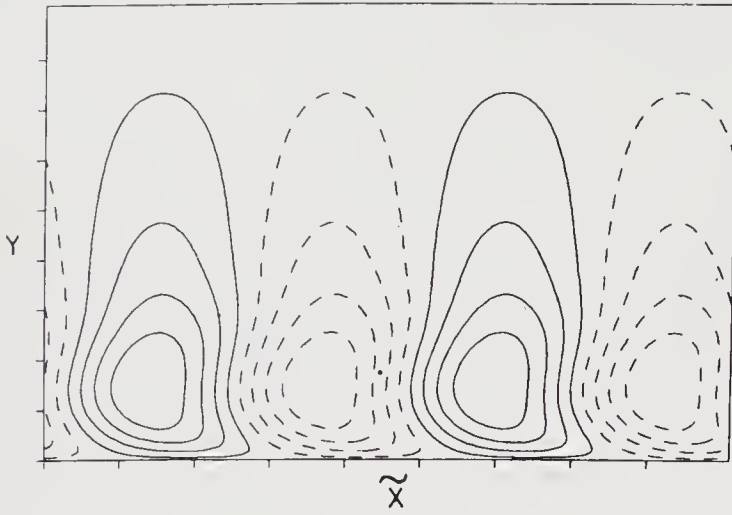
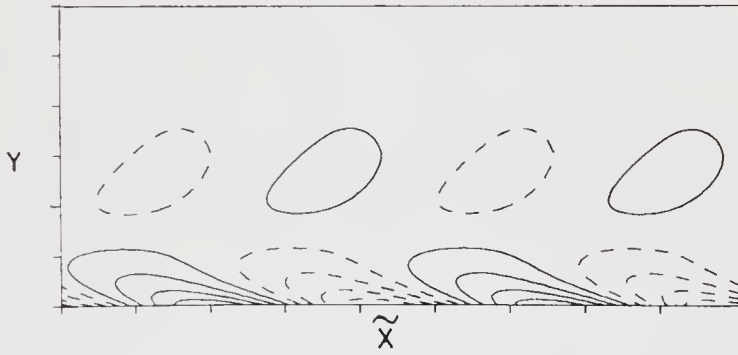
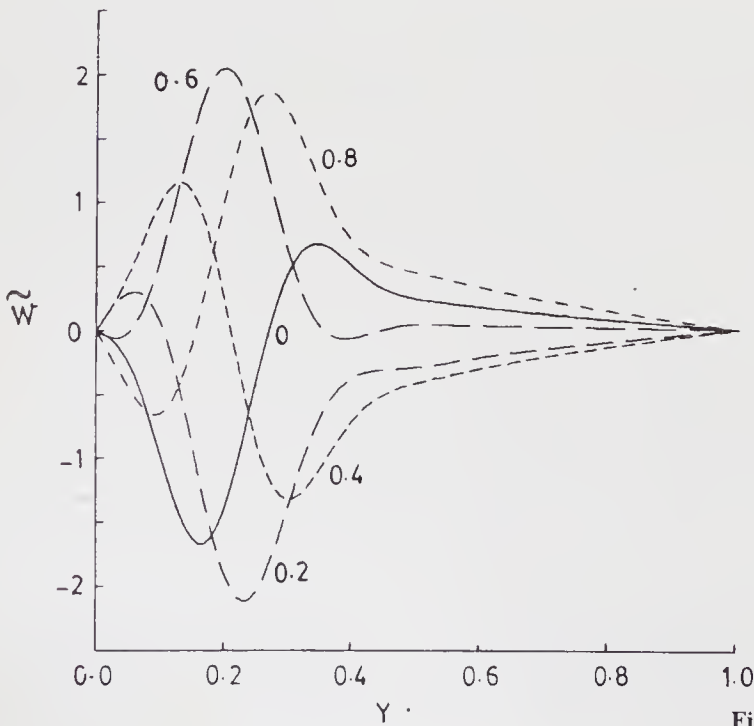
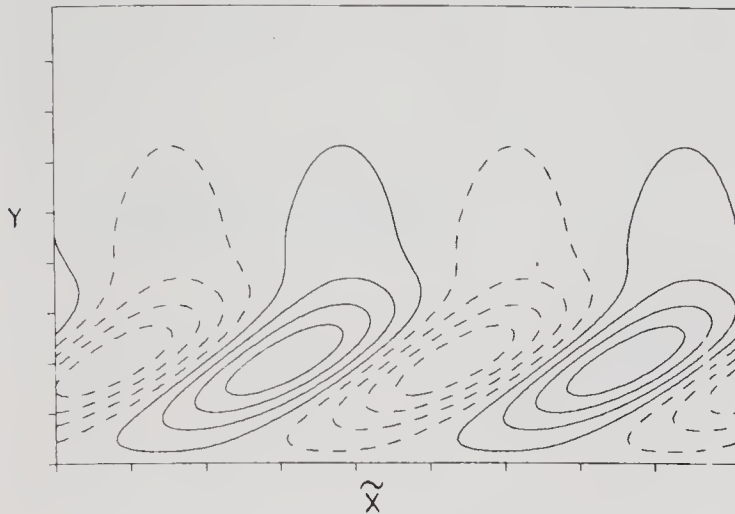
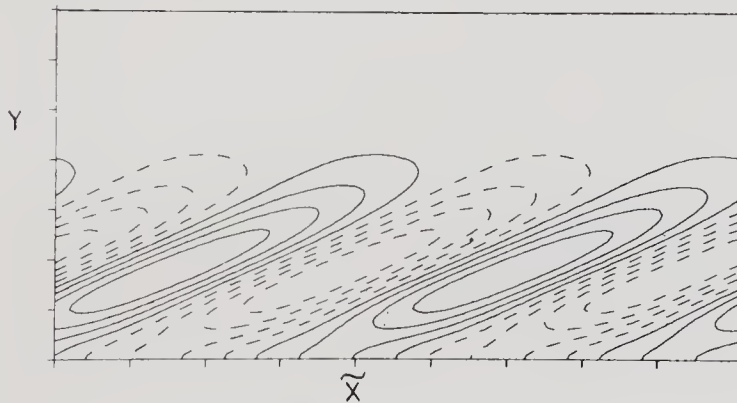
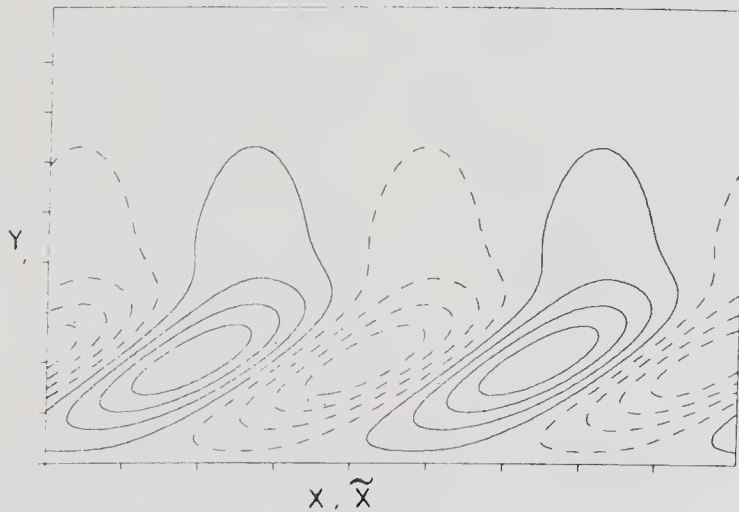


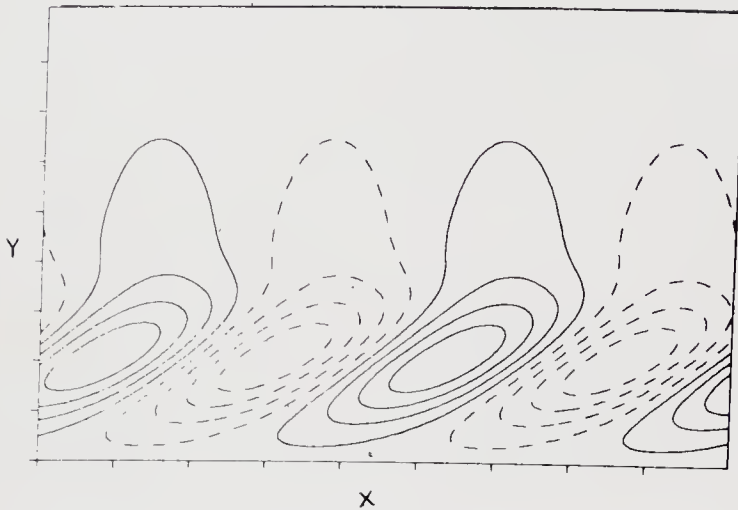
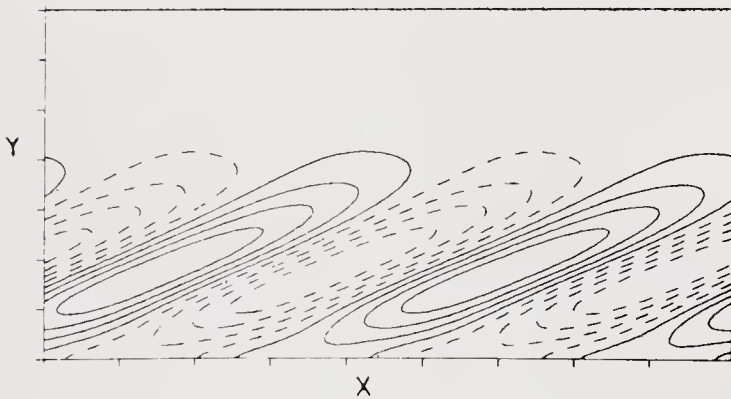
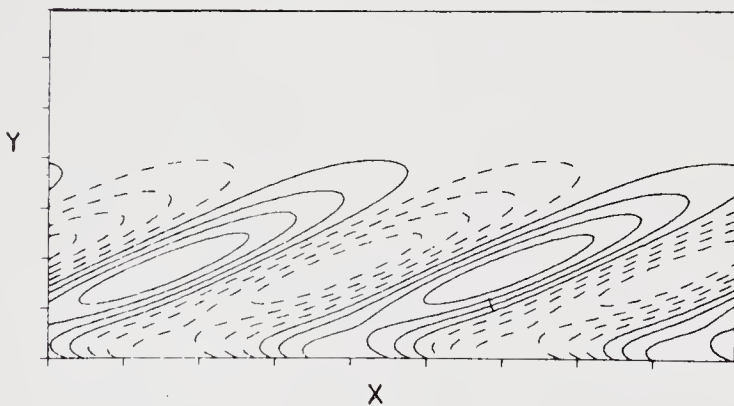
Figure 4. Amplitude distributions of oblique T-S waves in the oblique-wave coordinate system.

Figure 5. Structure of \tilde{u} field.Figure 6. Structure of ω_z field.Figure 7. Instantaneous \tilde{w} profiles.

Figure 8. Structure of \tilde{w} field.Figure 9. Structure of $\omega_{\tilde{x}}$ field.Figure 10. Structure of $\omega_{\tilde{y}}$ field.

3. On the longitudinal vortex

Benney and Lin (Benney & Lin 1960; Benney 1961, 1964) considered the first-order nonlinear interaction of the three-wave configuration, figure 1a, and obtained the celebrated mean vortex system as shown in figure 14a for a free-shear layer and a simplified boundary layer. It has offered an explanation of the so-called peak-valley splitting observed in the experiment by Klebanoff *et al* (1962). The

Figure 11. Structure of u field.Figure 12. Structure of ω_z field.Figure 13. Structure of ω_x field.

longitudinal vortices seem to imply a vortex system as sketched in figure 15. We would like to demonstrate that the mean longitudinal vortices are a rather superficial mathematical mean and that a more significant aspect is the local structure of the vorticity field. We consider here only the well-defined vorticity rather than the ill-defined vortices.

From the given streamline pattern as in (a), we can easily proceed to (b), (c) and (d) to reconstruct the corresponding vorticity field without calculations (figure 14). Such a speculative procedure has been substantiated by our own computed mean vorticity field, figure 16. In the computation $R = 5000$, $\alpha = 1.12$, $\beta = 1.2$ and the amplitude of the 2D wave is 3%. The two major counter-rotating vorticity fields are located near the critical layer with their cores at $Z = 1/4$ and $3/4$, so that the

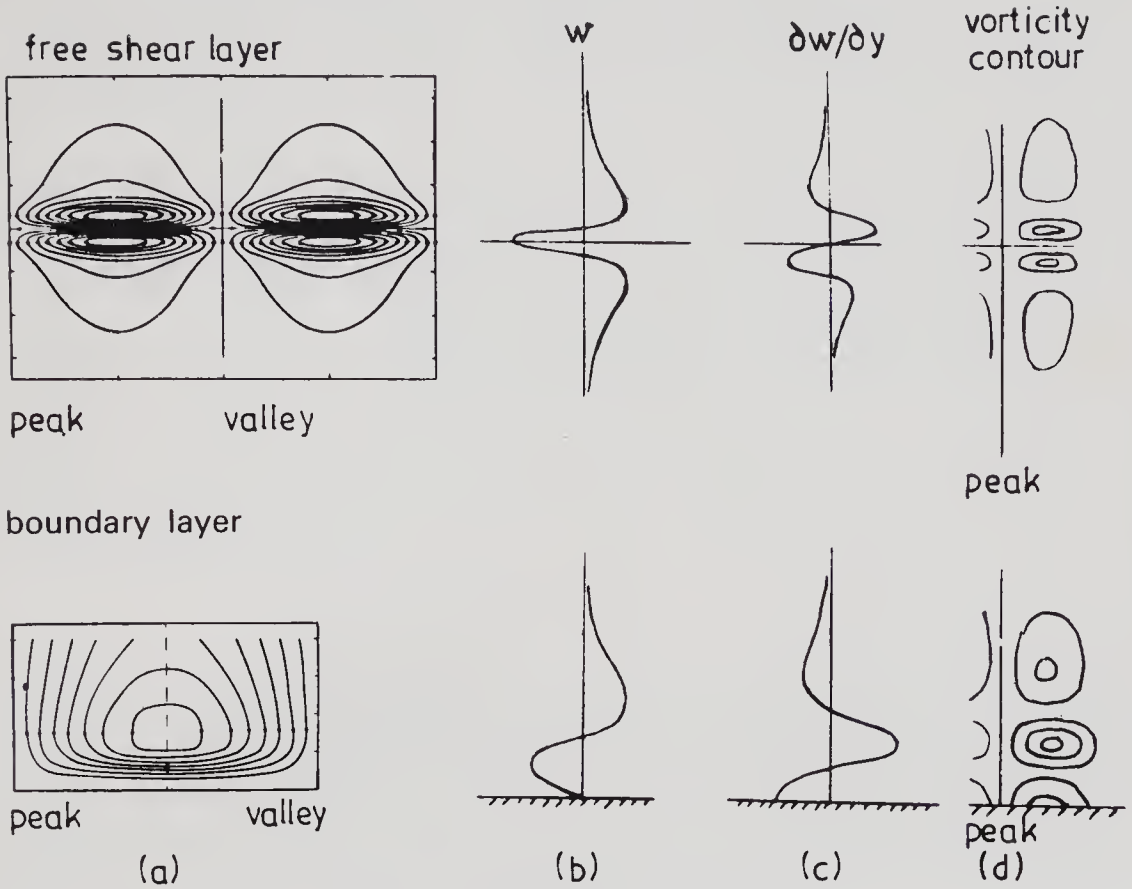


Figure 14. Benney-Lin vortex system.

peak is at $Z = 1/2$ and the valleys are at $Z = 0$ and 1 . There are additionally two vorticity fields of the opposite sign, one above and another below the main vorticity fields, to satisfy the condition at infinity and the no-slip condition on the wall.

A more detailed examination may be made first by the instantaneous vorticity field ω_X at four different X locations, $1/4$ wavelength apart, between them, figure 17. It is seen that the ω_X field is tilted nose-up, i.e., the downstream portion is located higher up relative to the lower trailing portion. The vorticity contour in the XY -plane through the core, $Z = 1/4$, is shown in figure 18, which clearly depicts

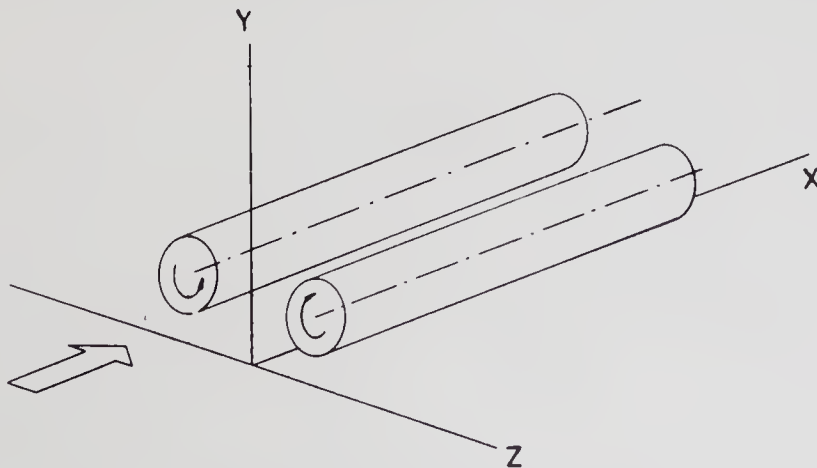


Figure 15. The longitudinal vortices?

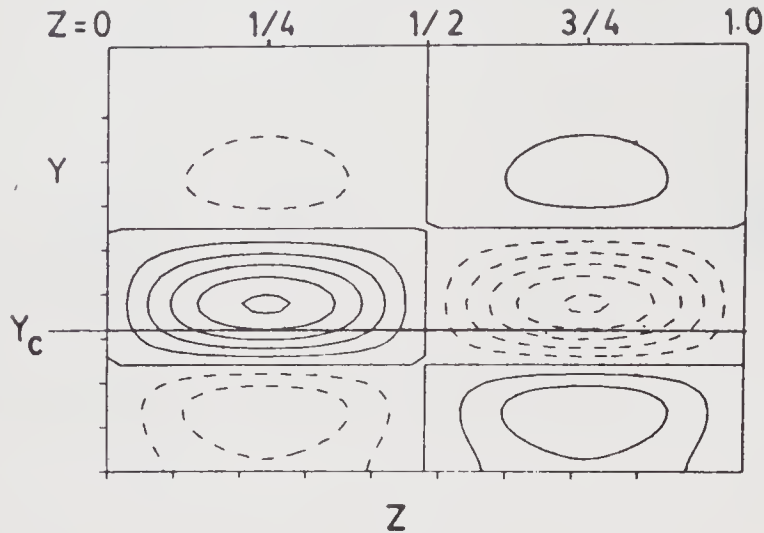


Figure 16. Mean longitudinal vorticity field $\bar{\omega}_X$.

the tilted ω_X field. More importantly, one may recognize in figure 18 that the positive ω_X region (solid lines) dominates the negative ω_X region (dotted lines), except in the region adjacent to the wall. The local magnitude of ω_X along the horizontal broken line in figure 18, corresponding to the location of the maximum $\bar{\omega}_X$, is plotted against X in figure 19. The instantaneous ω_X is seen to fluctuate sinusoidally at this stage of the nonlinear interaction but shifts to the positive side with a positive mean value $\bar{\omega}_X$, the celebrated longitudinal vortex. It is already clear, however, that the mean vorticity $\bar{\omega}_X$ is in fact a minor quantity in comparison with the maximum instantaneous ω_X , and it is rather naive to visualize the $\bar{\omega}_X$ structure as in figure 15.

The dominant importance of the local maximum of ω_X rather than the mean $\bar{\omega}_X$ manifests itself in the following observations. By the presence of the mean longitudinal vorticity, a persisting three-dimensional distortion of the mean velocity profile has been implied. The truth, however, is that such a distortion is quite small and that the major effect is the local variations of the velocity profile, as one can see at $X = 3/4$ and 1 in figure 20. If one experimentally observes a persistent 3D distortion of the mean velocity profile, it is because either the flow field is poor, very artificially manipulated or the transition process is already in the advanced stage beyond the first-order nonlinear interaction.

The same fact can also be recognized in an instantaneous mapping of the total (mean plus fluctuating) magnitude of the shear vorticity ω_Z in the peak region $Z = 1/2$, figure 21. The high shear region appears only periodically between a pair of the largest local ω_X (the positive one on the left and the negative one on the right) and slightly behind them, cf. figures 18 and 21. The periodic and local appearance of the high-shear layer, which is considered to be responsible for the secondary instability and eventual transition, is indeed in agreement with experimental observations (Klebanoff *et al* 1962; Kovaszny *et al* 1962; Hama & Nutant 1963). One may emphasize, moreover, that the appearance of the high-shear layer is a local matter and the aligned peak-valley splitting does not seem to be an essential feature toward transition.

In the first-order nonlinear three-wave interaction as seen here, the ω_X field is

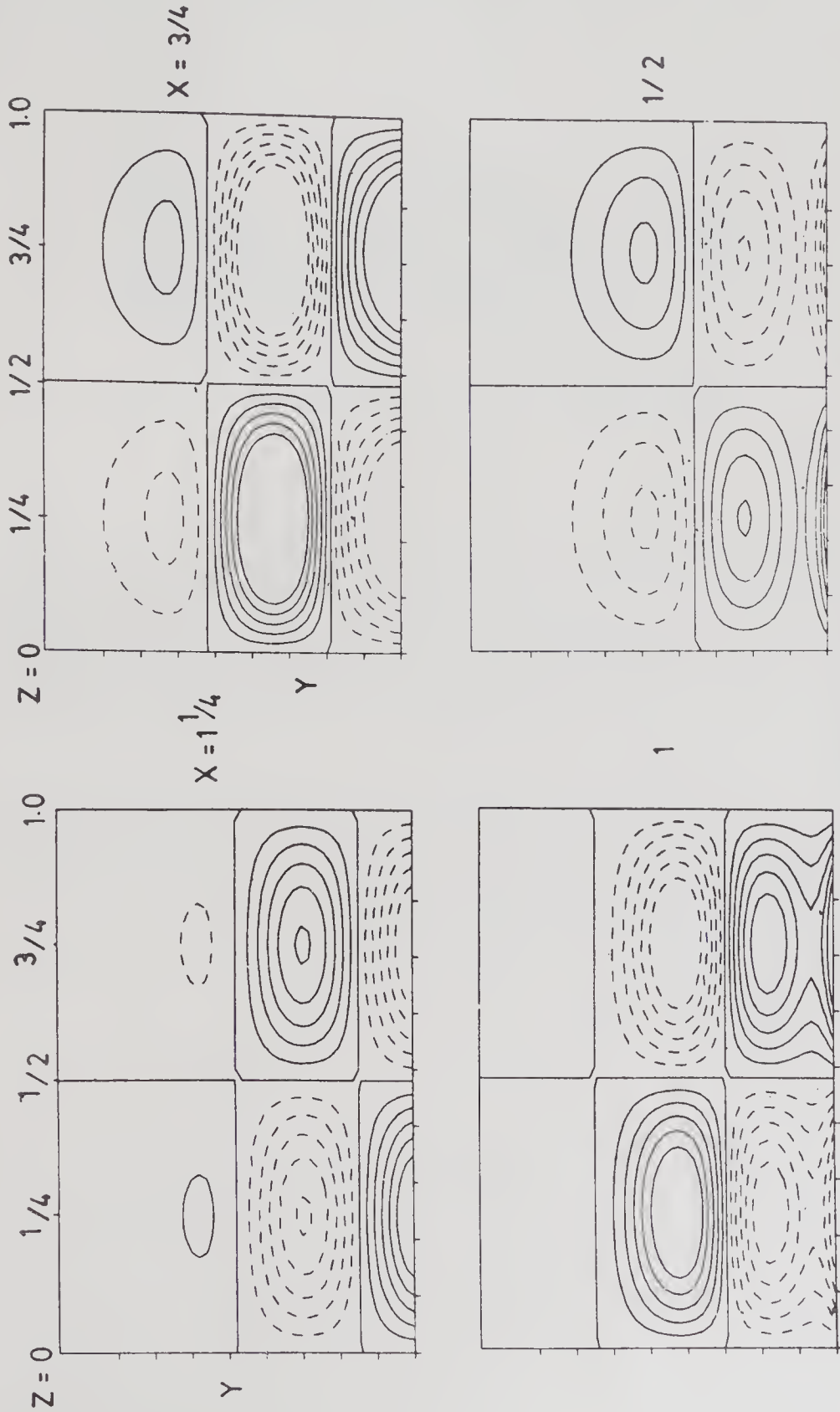


Figure 17. Instantaneous longitudinal vorticity field ω_x at $X = \frac{1}{4}, 1, 1\frac{1}{4}, 1\frac{3}{4}, 1$ and $1\frac{1}{4}$

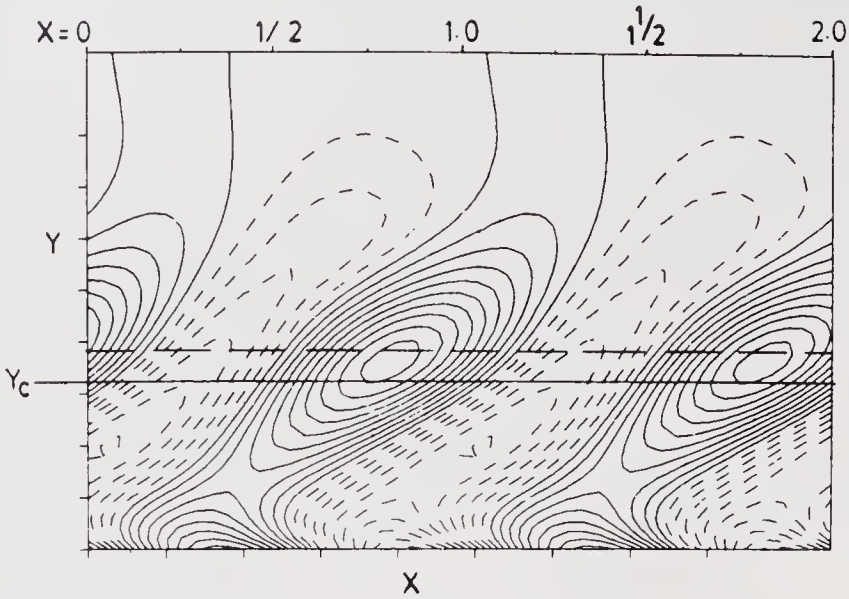


Figure 18. Longitudinal vorticity field structure in XY -plane at $Z = 1/4$.

parallel to the main flow direction and there is no converging Λ -vortex structure. Nevertheless, the computer-simulated time-line (hydrogen-bubble) pattern (figure 22) gives an impression of the Λ vortex. Therefore, such a visualized observation must be interpreted always with extreme care. On the other hand, a casual hot-wire observer may miss the three-dimensional structure, which can be detected only through an elaborate determination of the three vorticity components as performed by Williams *et al* (1984).

The relative importance of the local maximum of ω_X rather than the mean $\bar{\omega}_X$ is even more pronounced in a more developed 3D flow field. We refer here to the numerical results obtained by Laurien (1986) for a later stage of transition corresponding to the experimental work of Williams *et al* (1984). His numerical data have been replotted for the present purpose.

Figure 23 is the mapping of the mean longitudinal vorticity $\bar{\omega}_X$. In comparison

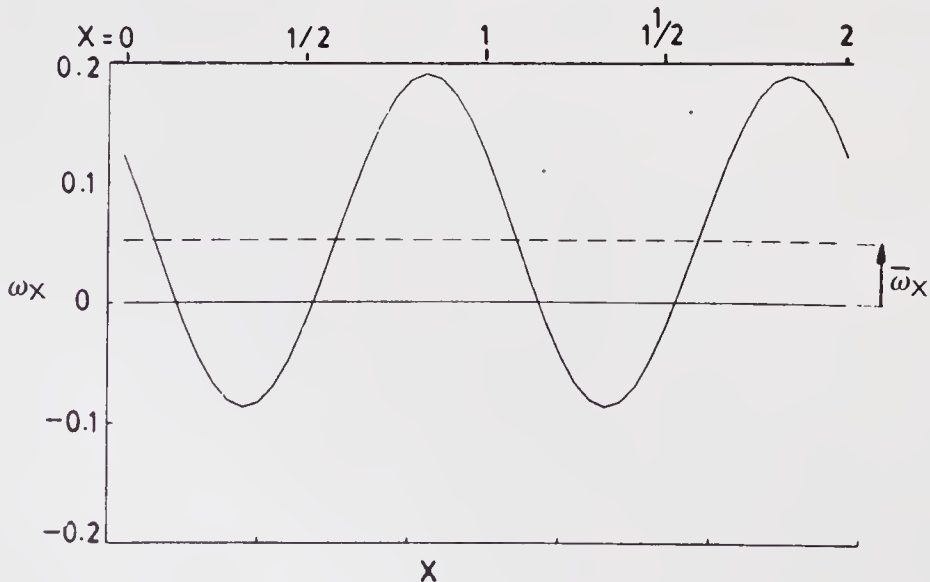


Figure 19. Local longitudinal vorticity along the broken line in figure 18.

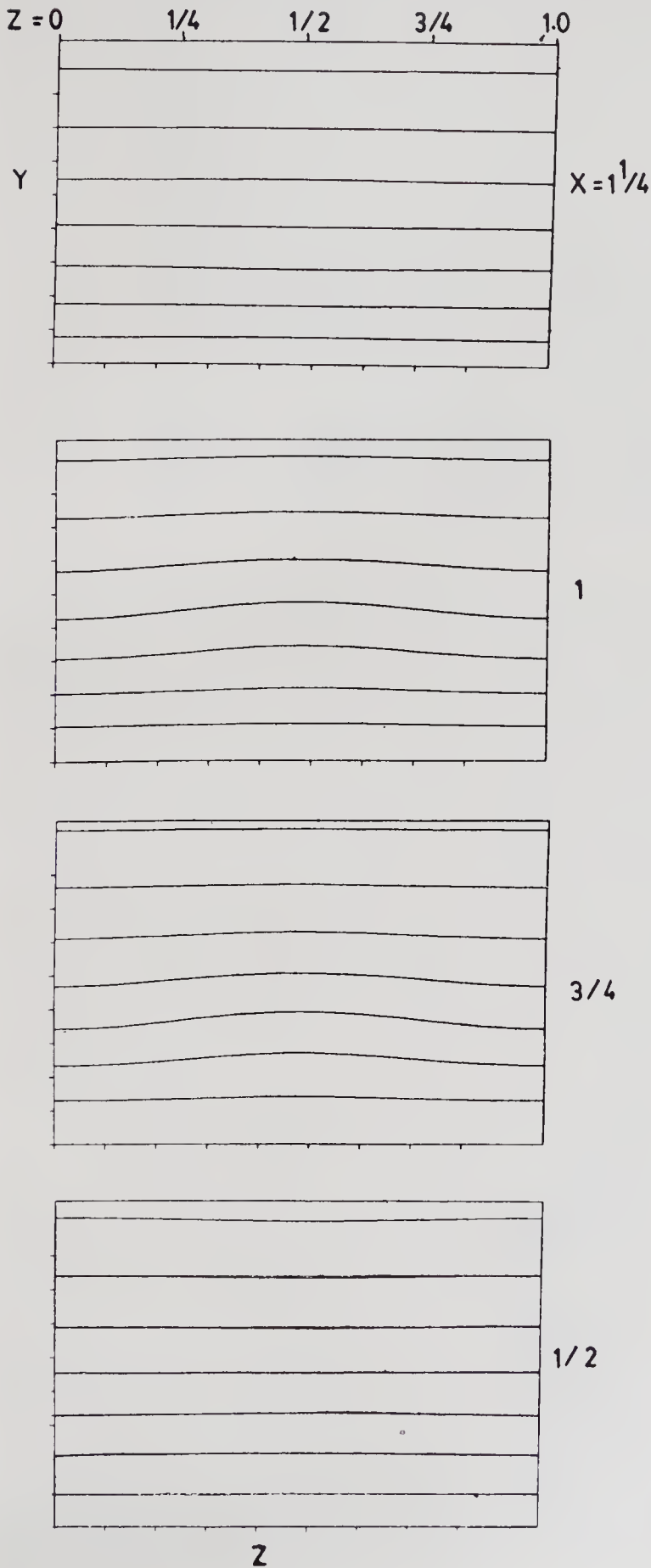


Figure 20. Transverse variation of $U = \text{constant}$ contour lines.

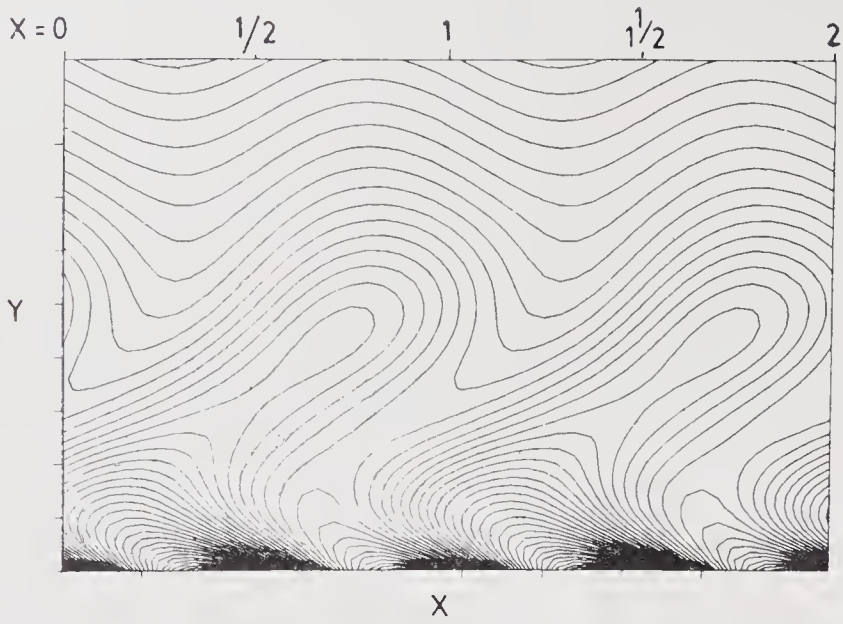


Figure 21. Instantaneous field of total transverse (shear) vorticity ω_z at $Z = 1/2$ (peak).

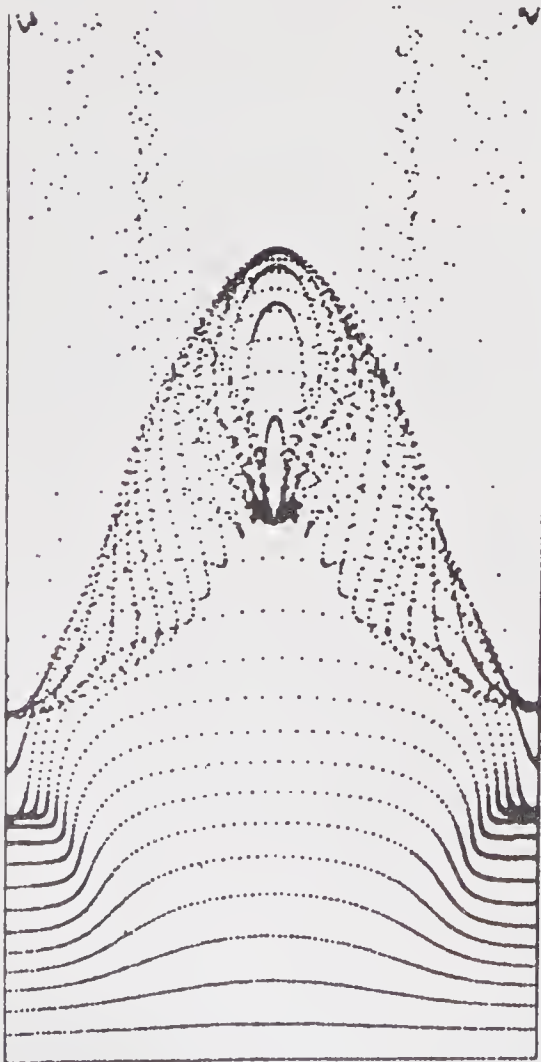


Figure 22. Time-line (hydrogen-bubble) pattern.

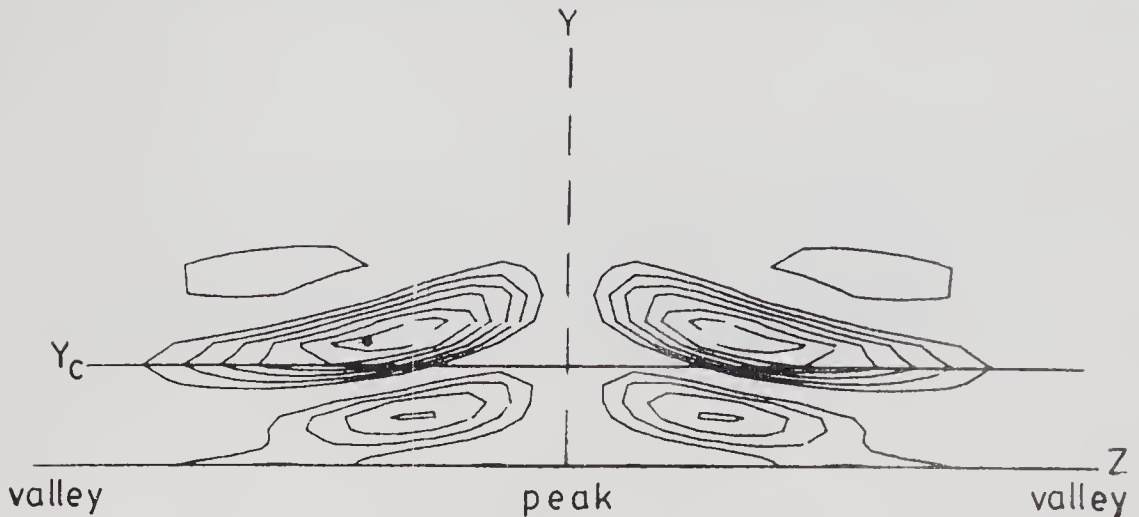


Figure 23. Mean longitudinal vorticity field in an advanced stage (DFVLR data).

with figure 16 in an early stage of development, the vorticity field is now more centred around the peak plane. The corresponding instantaneous vorticity fields at four stations are shown in figure 24, which clearly depicts a tilted (nose up) and converging Λ vorticity structure. Figure 25 is the instantaneous ω_X structure in the XY -plane through the positive maximum point in figure 23. It is again seen that there exist blobs of periodically large ω_X with intervening bands of weakly opposite sign. The local value of ω_X along the horizontal broken line in figure 25 is traced in figure 26, indicating the fact that the local value of ω_X is mostly near zero, or of mildly opposite sign, and assumes a large 'kick' when the blob of large positive ω_X passes by. Only because of the overwhelmingly large periodic pulses the mean takes a small positive value. Summarizing these observations the essential vorticity field is schematically depicted in figure 27. As a matter of fact, the proper understanding of the significance (or more properly, insignificance) of $\bar{\omega}_X$ in reference to the Λ -vortex structure has been already conceived of during our experimental determination of the 3D vorticity field in the transition process (Williams 1982).

The periodic pumping due to the localized longitudinal vorticity can be clearly observed in the instantaneous spanwise distribution of the velocity profiles (figure 28). This action results in the periodic formation of a large total shear vorticity segment in the peak region (figure 29). The high-shear layer recognized here has in fact a three-dimensional structure as shown in figure 30, which resides slightly above the Λ -type structure (figure 24) in excellent agreement with the experimental observations by Williams *et al* (1984).

4. Formation of the longitudinal vorticity field in the fundamental- and subharmonic-mode wave interactions

We have observed that the velocity component parallel to the oblique wave front is truly large and the resultant vorticity component normal to the wave front is dominating. Based upon this piece of information one can conjecture the longitudinal vorticity fields and the resultant formation of local peaks and valleys in

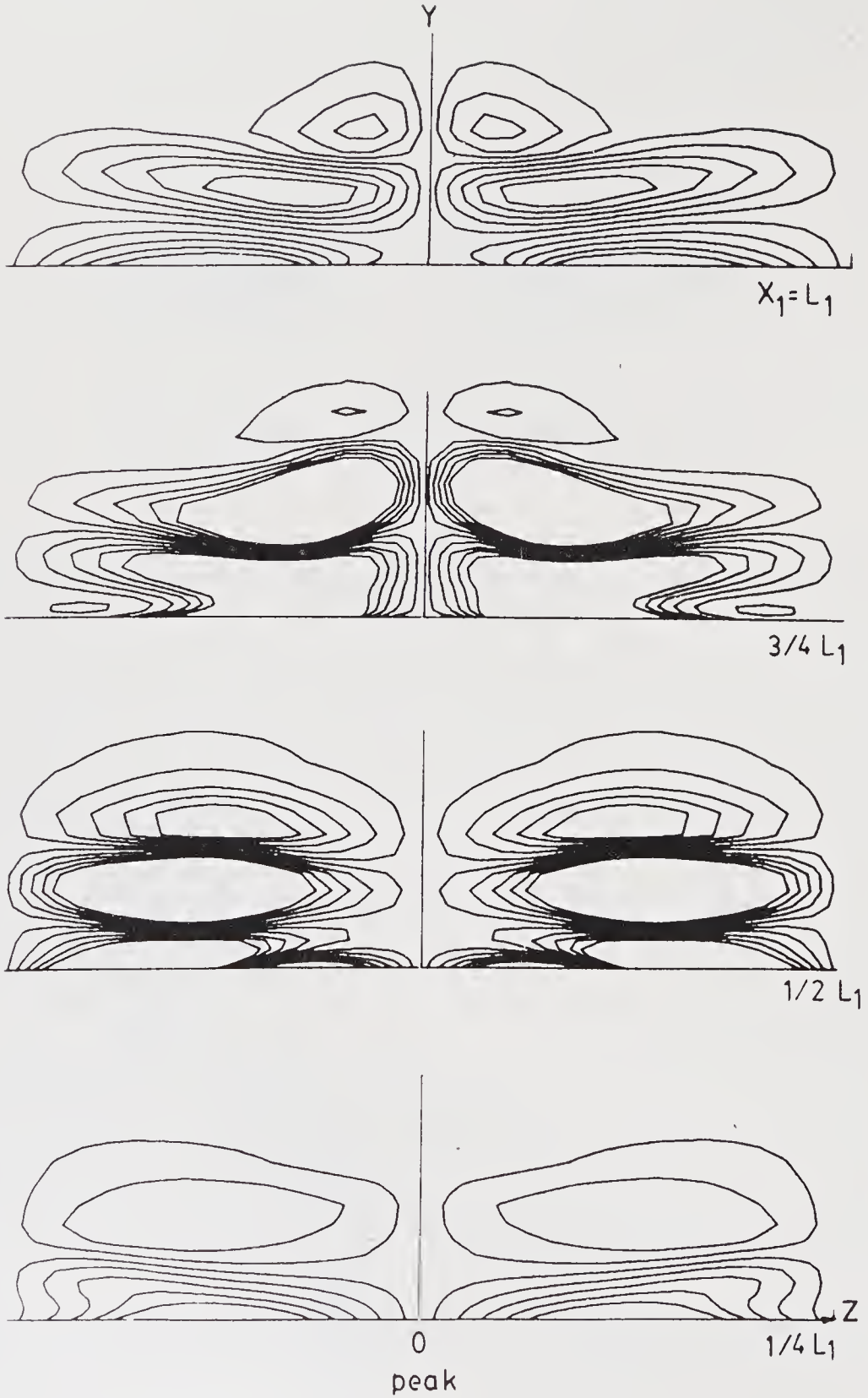


Figure 24. Instantaneous longitudinal vorticity field ω_X at $X = 1/4, 1/2, 3/4$ and 1 (DFVLR data).

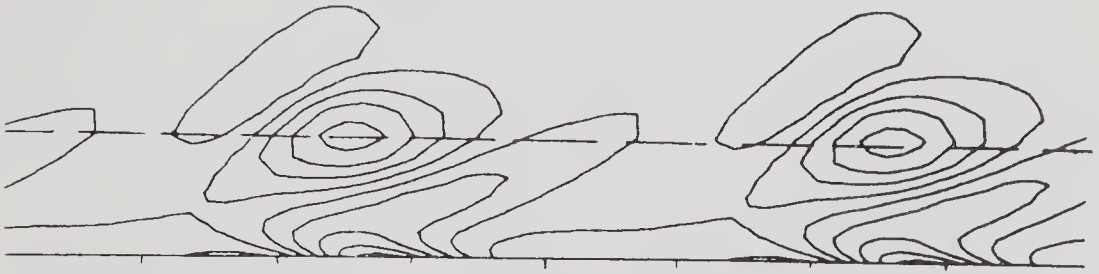


Figure 25. Longitudinal vorticity field structure ω_X in XY -plane through maximum $\bar{\omega}_X$ point (DFVLR data).

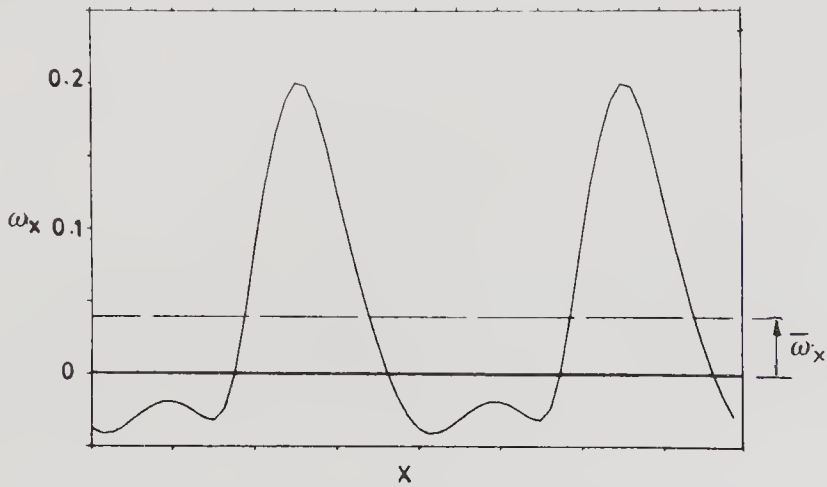


Figure 26. Local longitudinal vorticity ω_X along the broken line in figure 25 (DFVLR data).

the fundamental- and subharmonic-mode three-wave interactions, as depicted in figures 1a and 1b, respectively.

Let us first consider the essential vorticity field in a rhombus formed by a linear superposition of the two oblique waves, i.e., the right-running one RR and the left-running LL (figure 31). For each of the two waves the dominant vorticity is normal to the wave front, such as $R+$ (positive) and $R-$ (negative) or $L+$ and $L-$. The linear superposition of $R+$ plus $L+$ forms a vector A , and that of $R-$ plus $L-$ forms a vector B , both A and B being in the $X-$ direction. Likewise, $R+$ plus $L-$ superposition forms C and $R-$ plus $L+$ forms D , both of which are in the

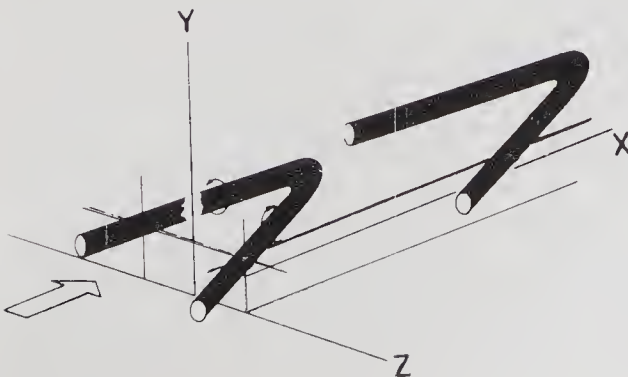


Figure 27. Schematic representation of the vorticity field.

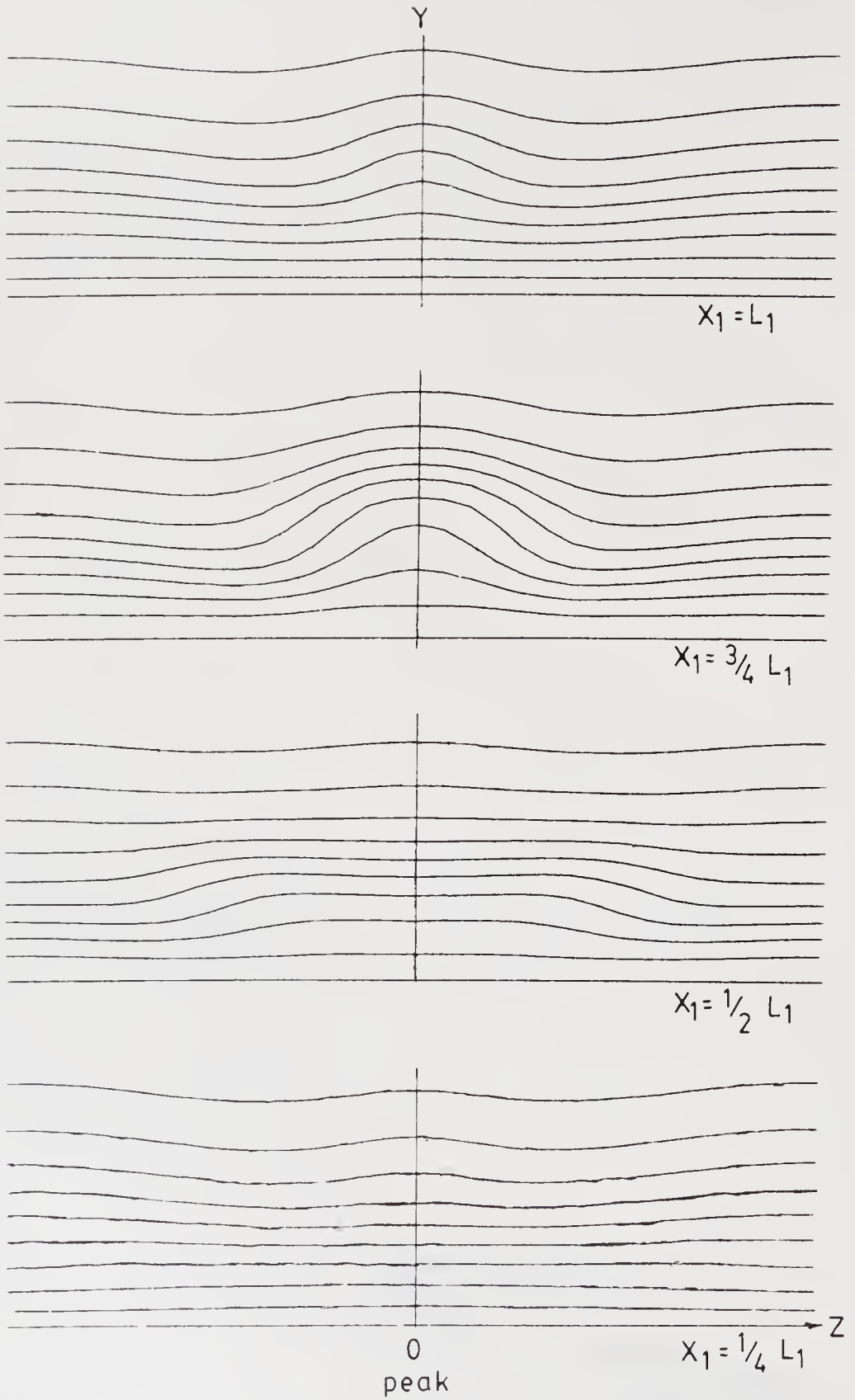


Figure 28. Transverse variation of $U = \text{constant}$ contour lines (DFVLR data).

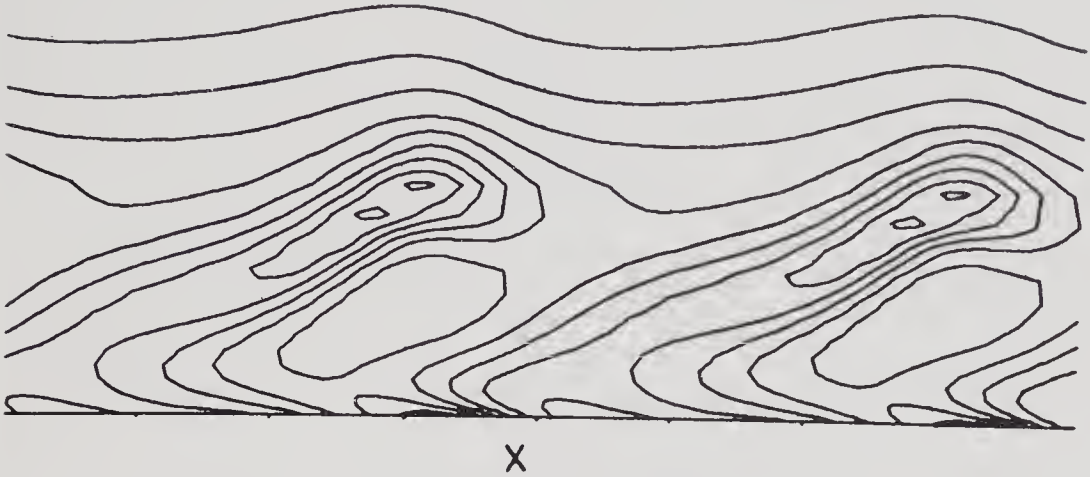


Figure 29. Instantaneous field of total transverse (shear) vorticity ω_z in peak plane (DFVLR data).

transverse direction. Such an expectation is substantiated by figure 32, where the horizontal axis represents two longitudinal wavelengths. The top figure is in the $Z = 0$ plane in which only the longitudinal vorticity vectors A and B reside whereas the transverse vorticity is identically zero due to the symmetry. On the other hand, the lower two figures show that, in the planes $Z = \pm 1/4$, the longitudinal vorticity is zero and the two transverse vorticities C and D alternately exist.

In order to consider the manner of nonlinear interaction of the two sets of the linear oblique waves with the 2D wave of a finite strength, we designate A and B in each rhombus (figure 33a). Within one longitudinal wavelength, the circled vector A is in a phase relation with respect to the 2D wave opposite to that of the circled vector B . If a nonlinear interaction is to take place between the 2D wave, which may be of a finite amplitude, and the two oblique waves, which may have only a small amplitude, it is conceivable that the circled A is intensified while the circled B is reduced, or vice versa. If this is the case, all the longitudinal vorticity vectors transversely aligned with the circled A will be intensified while those aligned with the circled B are reduced (figure 33b). This is indeed an explanation of the vorticity field (figure 18) where an intensified positive longitudinal vorticity appears successively along an X -axis once in each one wavelength of the 2D wave. As a result, in the regions between A (on the left) and B (on the right) the peaks appear locally as marked by open circles, whereas between B (on the left) and A (on the right) the local valleys appear as marked by dots. It is clear in this case that the intensified positive and negative vorticity vectors respectively line up in the main flow direction, and hence the local peaks or local valleys also line up, the so-called peak-valley splitting.

On the contrary, in the case of the subharmonic-mode interaction (figure 33c), all of the A 's as well as B 's have the identical phase relationship with respect to the 2D wave. As a result of the nonlinear interaction, therefore, all of them may be equally intensified (or reduced). As seen in figure 34, the positive and negative vorticity regions of equal strength appear along an X -axis once in every two wavelengths of the 2D wave. Consequently, the mean longitudinal vorticity is zero everywhere, i.e., no peak-valley splitting *per se*. Nevertheless, just as in the

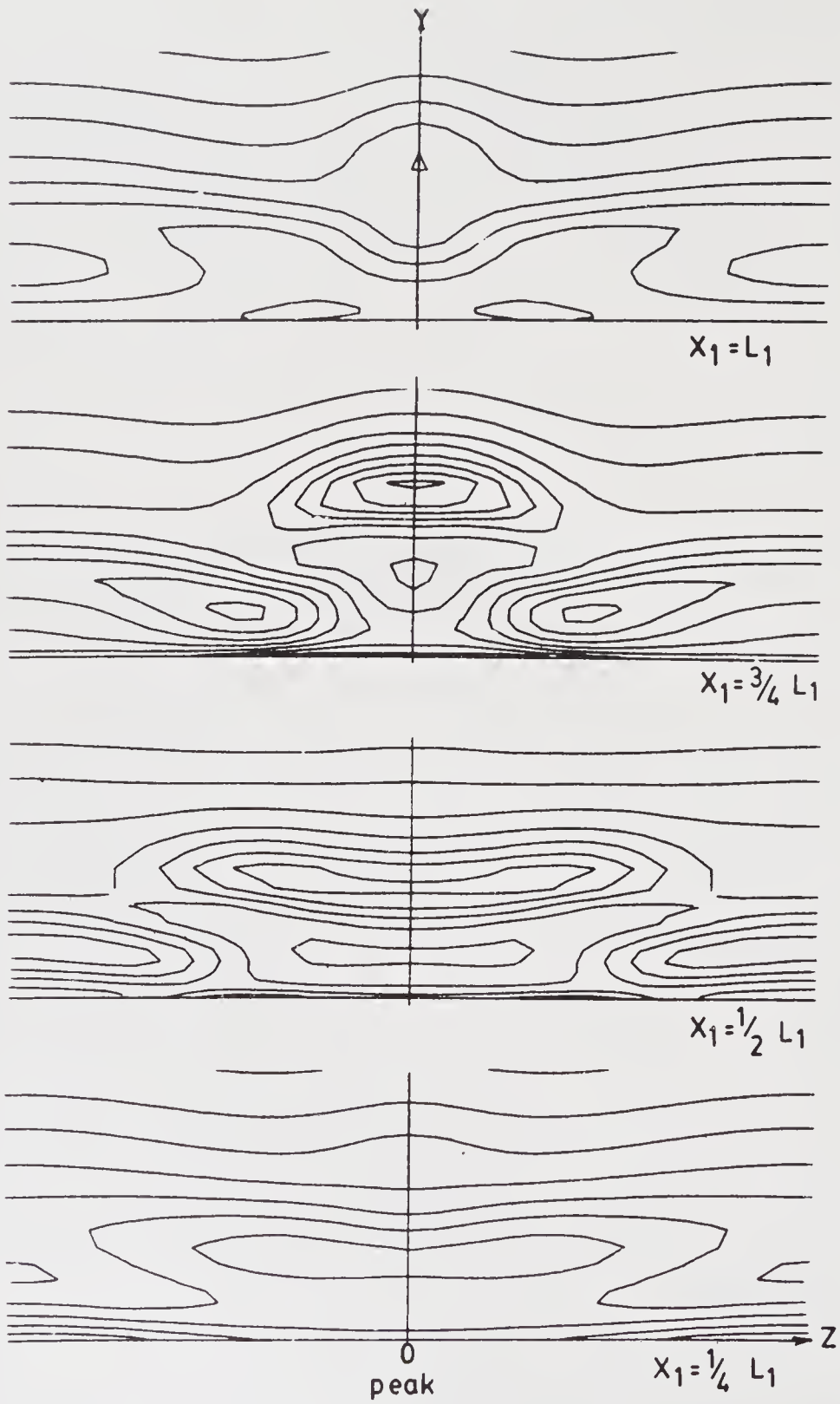


Figure 30. Three-dimensional structure of total shear vorticity ω_z (DFVLR data).

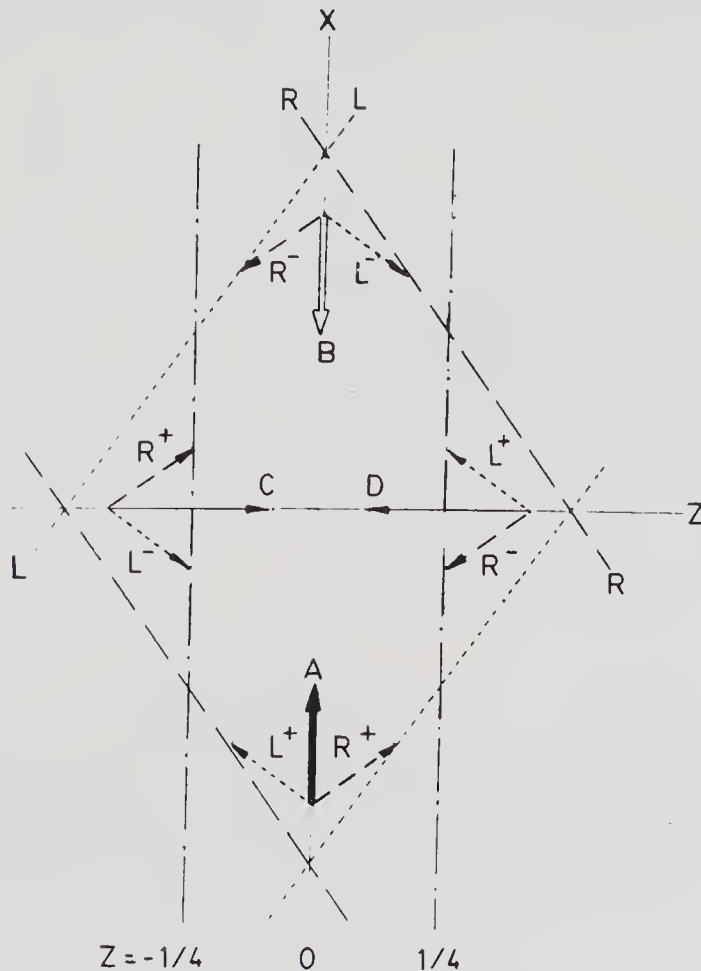


Figure 31. Essential vorticity field in the rhombus formed by two oblique-wave sets.

fundamental-mode interaction, a local peak should appear in the region between $A-B$ and a local valley between $B-A$. Figure 35 shows the appearance of a high-shear region in a very similar manner as in the fundamental-mode interaction (figure 21) but now once in two 2D wavelengths.

We have disclosed in the preceding section that the existence of the mean longitudinal vorticity is not really important and that the periodical large vorticity is the significant feature of the 3D development process. Therefore, the transition process in the present subharmonic-mode interaction must be essentially the same as in the fundamental-mode interaction, except that the local peaks and valleys appear here in a staggered pattern.

5. Concluding remarks

As the first step towards understanding the three-wave interaction, which explains certain aspects of the key turning point from the original 2D wave to the 3D development in the transition process, we have looked at the flow field of an oblique T-S wave. Frankly speaking, we used to think that the problem is reduced to an equivalent 2D problem by the Squire theorem. The computed velocity and vorticity fields, however, could not be explained by a simple-minded application of

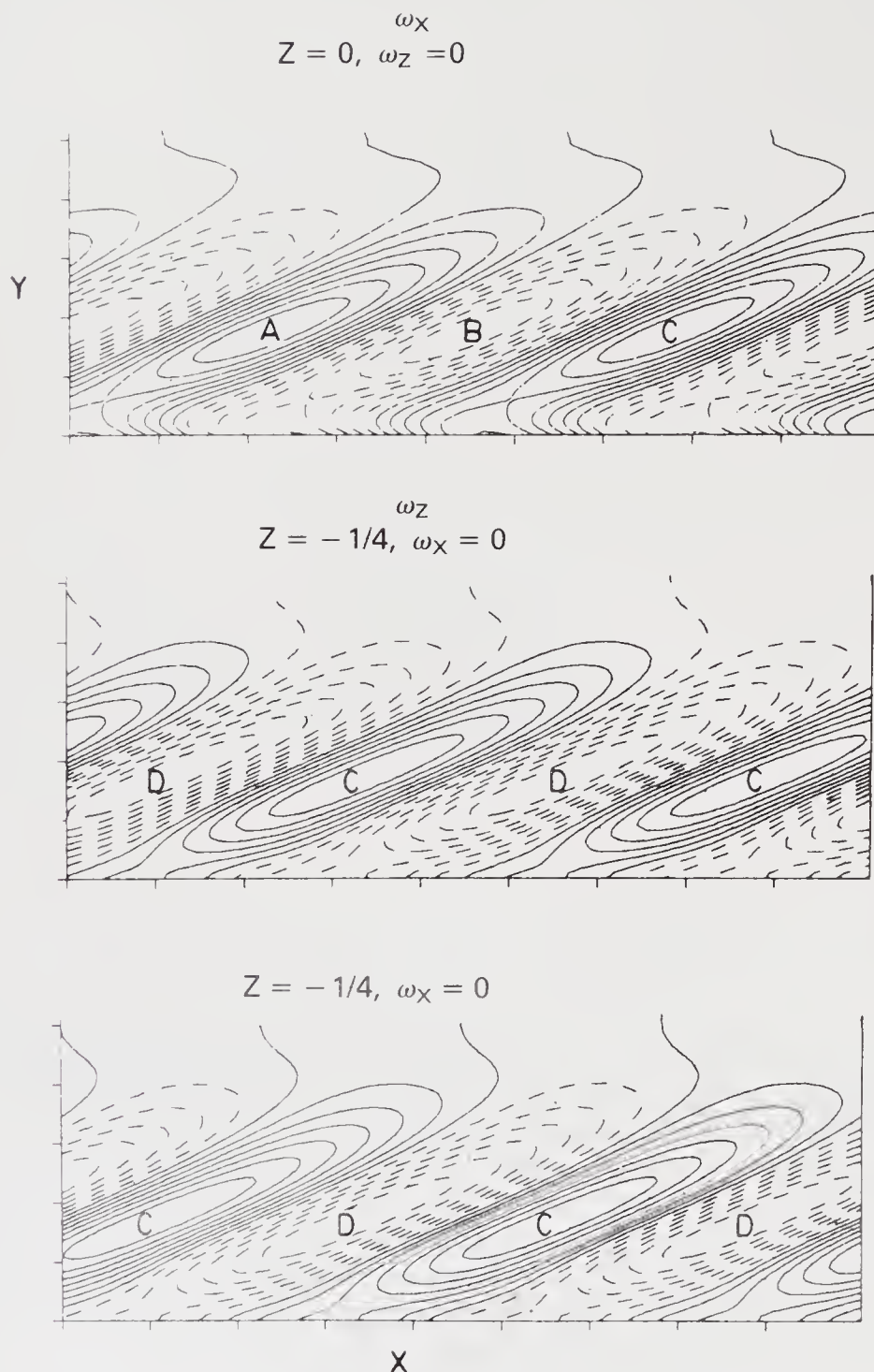


Figure 32. Vorticity field structure at $Z = 0$ and $\pm \frac{1}{4}$ in the rhombus.

the equivalent 2D field with respect to the oblique wave-vector coordinate system to the 3D field with respect to the main flow coordinates.

The fluctuating velocity component \tilde{w} parallel to the oblique wave front, which is not included in the Squire theorem, has been found to be an extremely important quantity. For those oblique-wave angles, with which we are concerned in the three-wave interaction, \tilde{w} greatly exceeds the velocity component \tilde{u} in the wave-propagation direction, so that the conventional longitudinal velocity fluctua-



Figure 33. Essential longitudinal vorticity fields in the three-wave interaction.

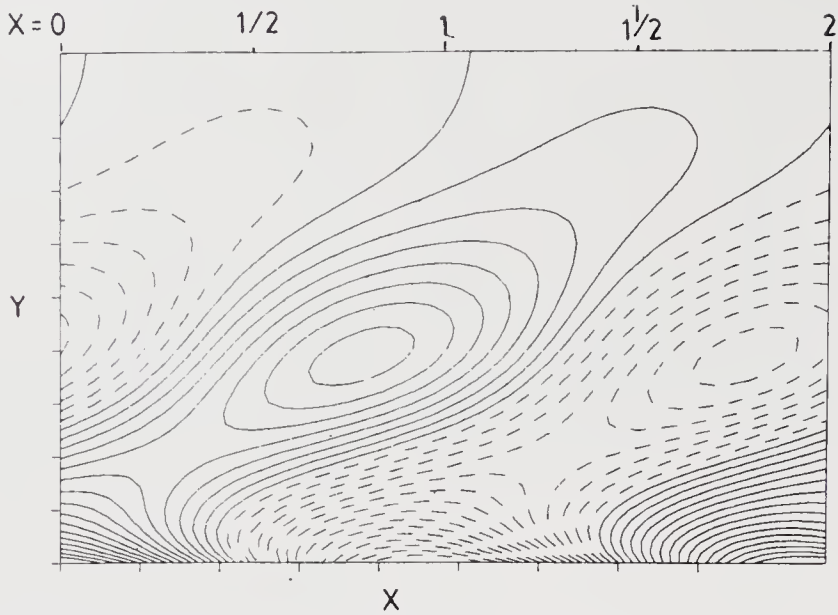


Figure 34. Longitudinal vorticity structure in the subharmonic-mode interaction (cf. figure 18).

tion \hat{u} in the main flow direction is almost totally dominated by the contribution from \bar{w} . The \bar{w} field, moreover, creates a large vorticity component $\omega_{\bar{x}}$ in the oblique wave-propagation direction, which is an overwhelming contributor not only to the longitudinal vorticity ω_X in the main flow direction but also to the shearing vorticity ω_Z except in the region very near the wall.

In fact, a simple argument could be put forward to explain the formation of a system of the longitudinal vorticity field, which is essential to the peak-valley formation in the transition process, from the $\omega_{\bar{x}}$ field. A certain aspect of the argument, however, is an intuitive conjecture only to conform with the computed

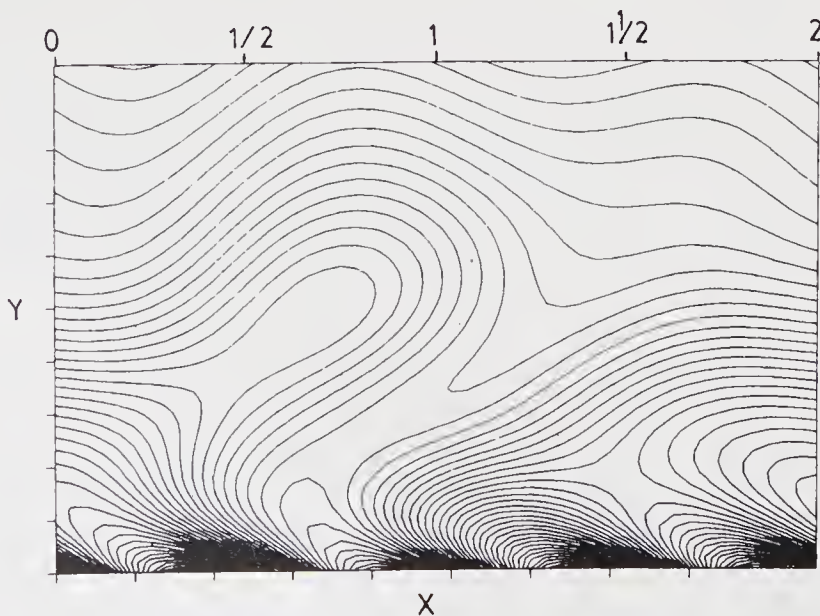


Figure 35. Instantaneous field of total shear vorticity ω_z in the subharmonic-mode interaction (cf. figure 21).

vorticity field, and a more convincing theoretical treatment must be advanced. On the other hand, the so-called Benney-Lin longitudinal vortices, or the mean longitudinal vorticity field, has been definitively demonstrated to be a rather minor consequence of the three-wave interaction. More significant is the local peak of the fluctuating longitudinal vorticity. In this respect, the aligned longitudinal vorticity field or the peak-valley splitting cannot be taken as an essential feature in the transition process. A staggered occurrence of local peaks and valleys as a result of the subharmonic-mode interaction could be equally responsible for the eventual breakdown. The question of the stability of the two types of interaction, however, is outside the scope of this paper.

It is true that the appearance of \bar{w} is derived from the equivalent 2D problem, whose stability criterion also applies to \bar{w} . Nevertheless, the magnitude of \bar{w} is so large that a certain aspect of the conventional argument concerning the oblique T-S wave may require a modification, particularly if there is any possibility of steepening oblique-wave angles. It is further conceivable that the implication of \bar{w} might be more pronounced and significant in compressible boundary layers.

The research reported in this paper has been supported in part by Bundesministerium für Forschung und Technologie and by Deutsche Forschungsgemeinschaft. The major part of the paper has been presented at the Third Asian Congress of Fluid Mechanics, 1–5 September 1986, in Tokyo, as a General Lecture by the senior author, FRH.

References

- Antar B N, Collins F G 1975 *Phys. Fluids* 12: 289–297
 Benney D J 1961 *J. Fluid Mech.* 10: 209–236
 Benney D J 1964 *Phys. Fluids* 7: 319–326
 Benney D J, Lin C C 1960 *Phys. Fluids* 3: 656–657
 Hama F R 1959 *Phys. Fluids* 2: 664–667
 Hama F R, Nutant J 1963 *Proc. Heat Transfer Fluid Mech. Inst.* 77–93
 Herbert T 1984 in ‘Special Course on Stability and Transition of Laminar Flow’, AGARD-R-709
 Kachanov Yu S, Levchenko V Ya 1984 *J. Fluid Mech.* 138: 209–247
 Klebanoff P S, Tidstrom K D, Sargent L M 1962 *J. Fluid Mech.* 12: 1–34
 Kleiser L 1982 Numerische Simulationen zum laminar-turbulenten Umchlagsprozess der ebenen Poiseuille-Strömung, Kernforschungs-zentrum Karlsruhe, KfK 3271
 Knapp C F, Roache P J 1968 *AIAA J.* 6: 29–36
 Kovasznay L S G, Komoda H, Vasudeva B R 1962 *Proc. Heat Transfer Fluid Mech. Inst.* 1–26
 Laurien E 1986 Numerische Simulation zur aktiven Beeinflussung des laminar-turbulenten Übergangs in der Plattengrenzschichtströmung, DFVLR-FB-86-05
 Mack L M 1984 in ‘Special Course on Stability and Transition of Laminar Flow’, AGARD-R-709
 Schubauer G B 1957 in *Boundary Layer Research Symposium, Freiburg* (Berlin: Springer Verlag)
 Squire H B 1933 *Proc. R. Soc. A* 142: 621–628
 Usher J R, Craik A D D 1975 *J. Fluid Mech.* 70: 437–461
 Williams D R 1982 An experimental investigation of the nonlinear disturbance development in boundary layer transition, doctoral dissertation, Princeton University
 Williams D R, Fasel H, Hama F R 1984 *J. Fluid Mech.* 149: 179–203

Irregular flows

S TANEDA

Research Institute for Applied Mechanics, Kyushu University, Kasuga 816, Japan

Abstract. Irregular flows were examined by means of flow visualization methods and hot-wire techniques. When the Reynolds number is small the flow is steady and regular. As the Reynolds number increases, however, the flow becomes irregular. It seems that at large Reynolds numbers the flow generally consists of many structures which fluctuate irregularly. As yet the mechanism by which irregularities occur is not clear.

Keywords. Irregular flows; flow visualization; hot-wire measurements; power spectra.

1. Introduction

Incompressible viscous flows depend on the Reynolds number. When the Reynolds number is small, the flow is unique and steady. As the Reynolds number increases, the flow becomes complicated and eventually chaotic. It seems that at large Reynolds numbers the flow consists of many coherent structures fluctuating irregularly. The purpose of this paper is to give a brief survey of irregular flows.

2. Examples of irregular flows

Figure 1 (plate 1) shows the wake behind a circular cylinder at Reynolds number $R = 140$ (Van Dyke 1982). When R is larger than about 40, the wake performs a progressive wave motion and forms the Karman vortex street. As will be seen, the flow pattern of the Karman vortex street appears to be very regular. But the hot-wire measurements indicate that the velocity fluctuation is irregular.

Figure 2 is the plot of Strouhal number against Reynolds number (Gerrard 1978). It can be seen that the Strouhal number scatters largely in the whole range of Reynolds numbers.

Figure 3 shows the hot-wire signal and its power spectrum of the velocity in the wake behind a circular cylinder at $R = 57.3$. The distance from the cylinder is 10 diameters. It may be seen that the velocity fluctuation has a continuous frequency spectrum.

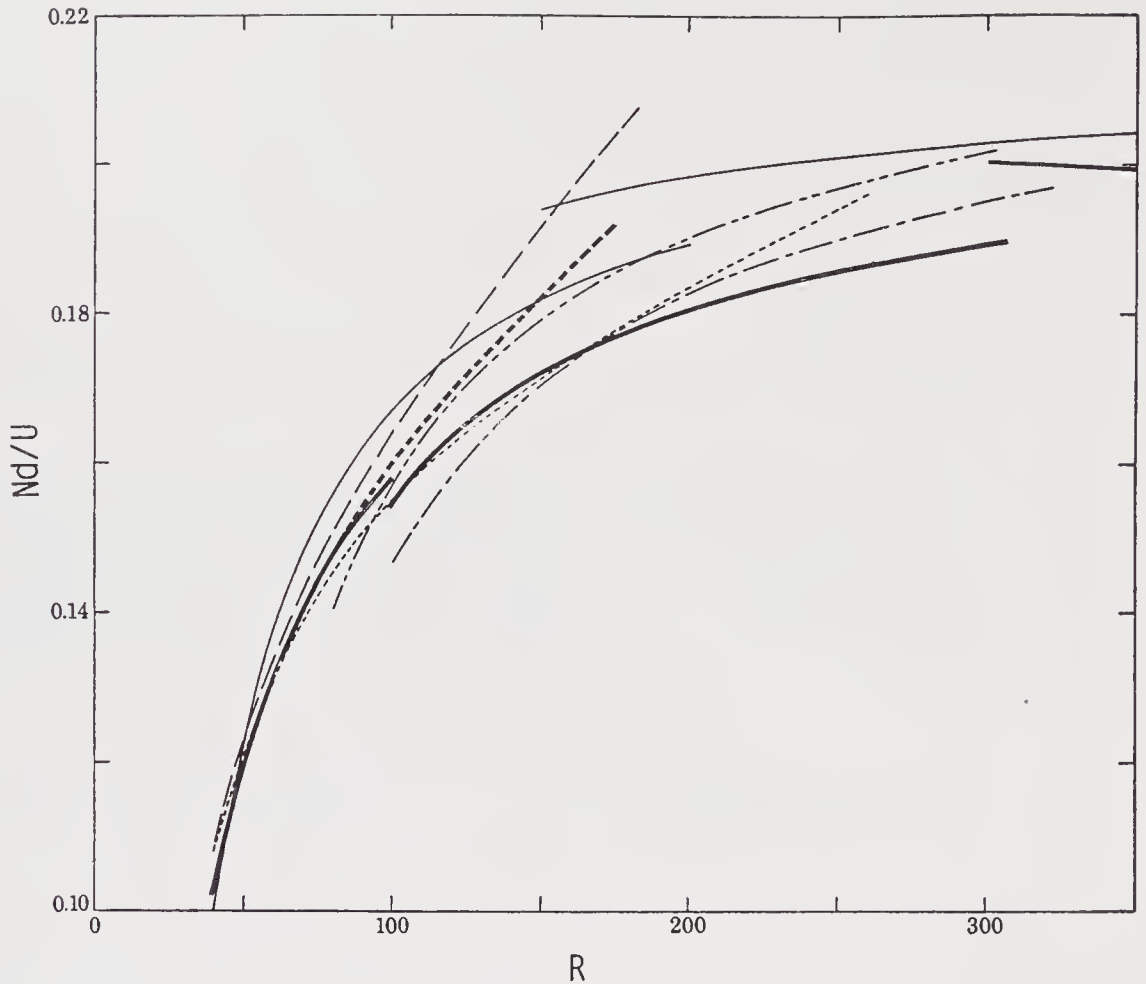


Figure 2. Strouhal number as a function of R (Gerrard 1978).

Figure 4 (plate 1) shows the integrated streaksheet pattern in the wake behind a circular cylinder at $R = 100$. The integrated streaksheets are the sheets composed of all fluid particles which come out of the whole surface of the body. As will be seen, the flow is smooth, but there exist large-scale three-dimensional irregularities.

Figure 5 (plate 2) shows the integrated streaksheet pattern in the wake behind a circular cylinder at $R = 300$ (Taneda 1985, pp. 399-410). It will be seen that there exist small-scale three-dimensional waves in the Karman vortex street. The small-scale streamwise streaks are the manifestation of the existence of three-dimensional waves.

Figure 6 (plate 2) shows the cross-stream section of the wake behind a circular cylinder at $R = 300$. The distance from the cylinder is 5 diameters. The small-scale three-dimensional structure fluctuates irregularly.

Figure 7 (plate 3) shows another example of the cross-stream section of the turbulent wake behind a circular cylinder. The Reynolds number $R = 700$ and the distance from the cylinder is 200 diameters. It will be seen that the wake contains many irregular streamwise vortices.

Figure 8 (plate 3) shows the smoke pattern of the turbulent wake behind a circular cylinder at $R = 350$ (Taneda 1985, pp. 399-410). It is clear that there exist

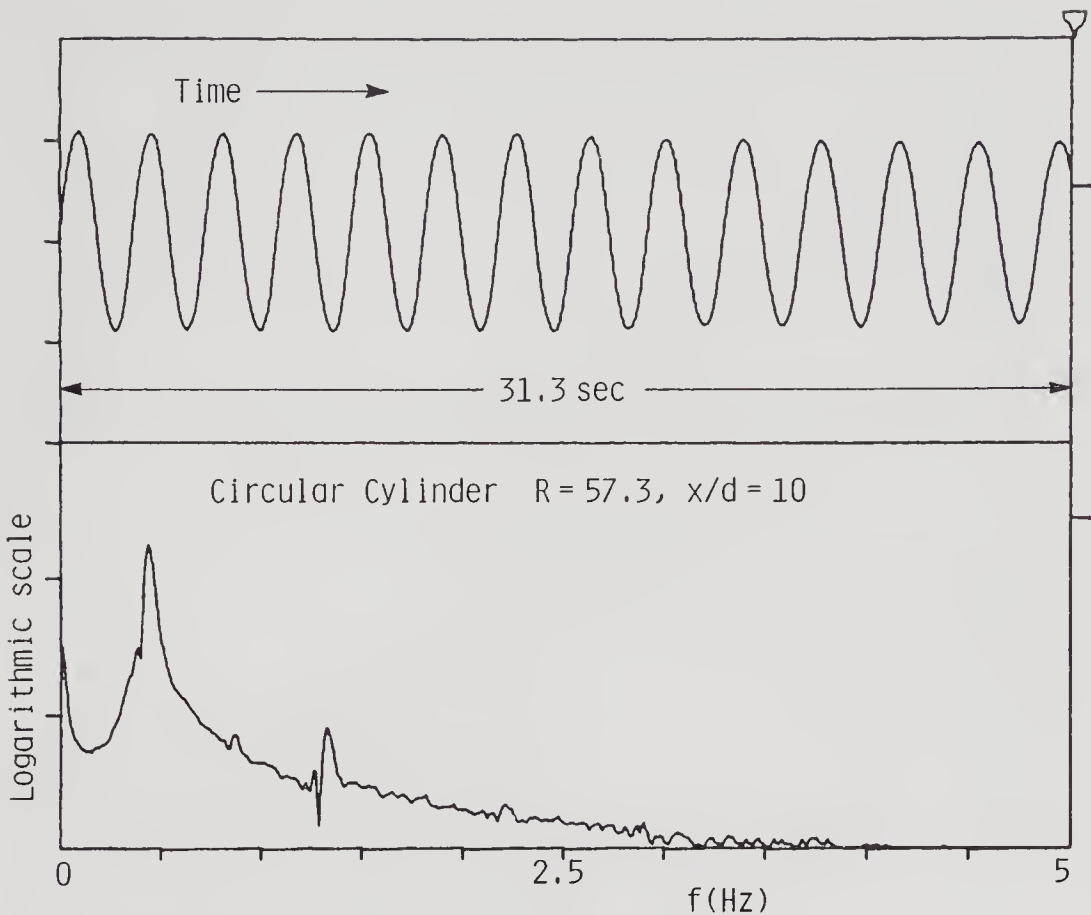


Figure 3. The hot-wire signal and power spectrum of the velocity fluctuation at $R = 57.3$.

two-dimensional instability waves in the wake. As will be seen, the primary Karman vortex street is slant, but the second vortex street is parallel to the cylinder. This indicates that the second instability wave develops independently of the first instability wave, and that the wavelength of the two-dimensional instability waves increases in the downstream direction without the vortex-pairing process.

Figure 9 shows the power spectra of the velocity fluctuation in the wake behind a circular cylinder at $R = 350$. When $x = 10d$ the wake has a continuous frequency spectrum with a peak at 44 Hz, where x is the distance from the cylinder and d the diameter of the cylinder. When $x = 100d$ and $200d$, however, there exists no peak in the power spectra, although the flow pattern clearly shows the existence of large-scale two-dimensional instability waves. This indicates that the power spectrum of the velocity fluctuation is useless for detecting large-scale instability waves.

Figure 10 (plate 4) shows the wake behind a circular cylinder at $R = 1404$. As R increases, the wake becomes more and more irregular. However, there exist some regularities in the wake, no matter how large R is.

Figure 11 shows the power spectra of the velocity fluctuations at $R = 57.3$, 350 and 1050. In all cases, the flow has a continuous frequency spectrum with small peaks. It should be noted that much difference does not exist between the three spectra.

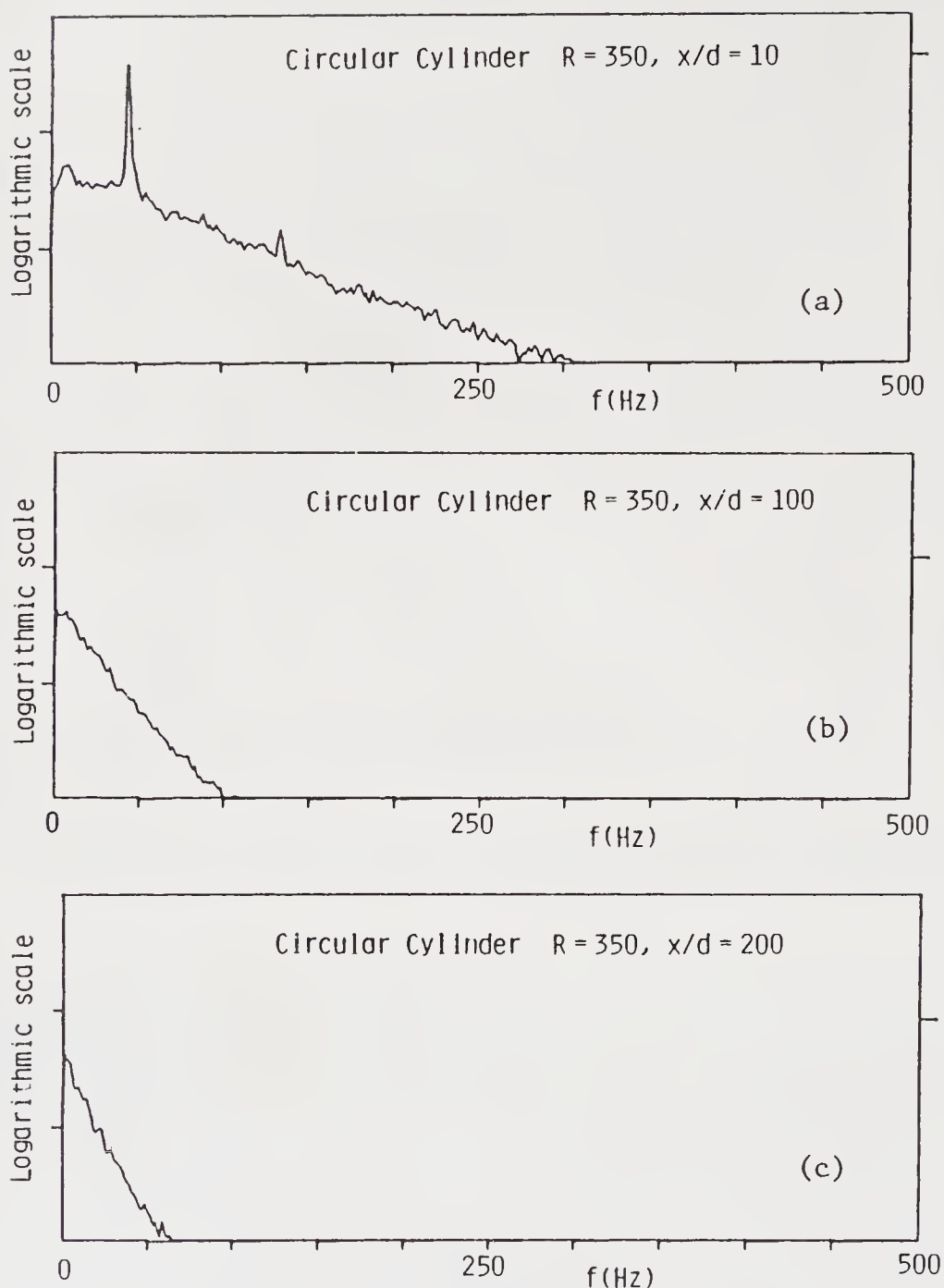


Figure 9. The hot-wire signals and power spectra of the velocity fluctuation in the wake behind a circular cylinder at $R = 350$, $x/d = 10$ (a), 100 (b), 200 (c).

Figure 12 (plate 4) shows the streamline pattern behind a flat plate parallel to the flow. The Reynolds number based on the plate length is 15,800 (Taneda 1958). It is seen that the wake begins to oscillate some distance downstream, and a beautiful Karman vortex street is formed further downstream. However, the hot-wire measurements reveal that the velocity in the wake fluctuates irregularly.

Figure 13 shows the wavelength of the oscillating wake behind a flat plate parallel to the flow (Taneda 1958). As may be seen, the wavelength λ scatters largely in the whole range of Reynolds number

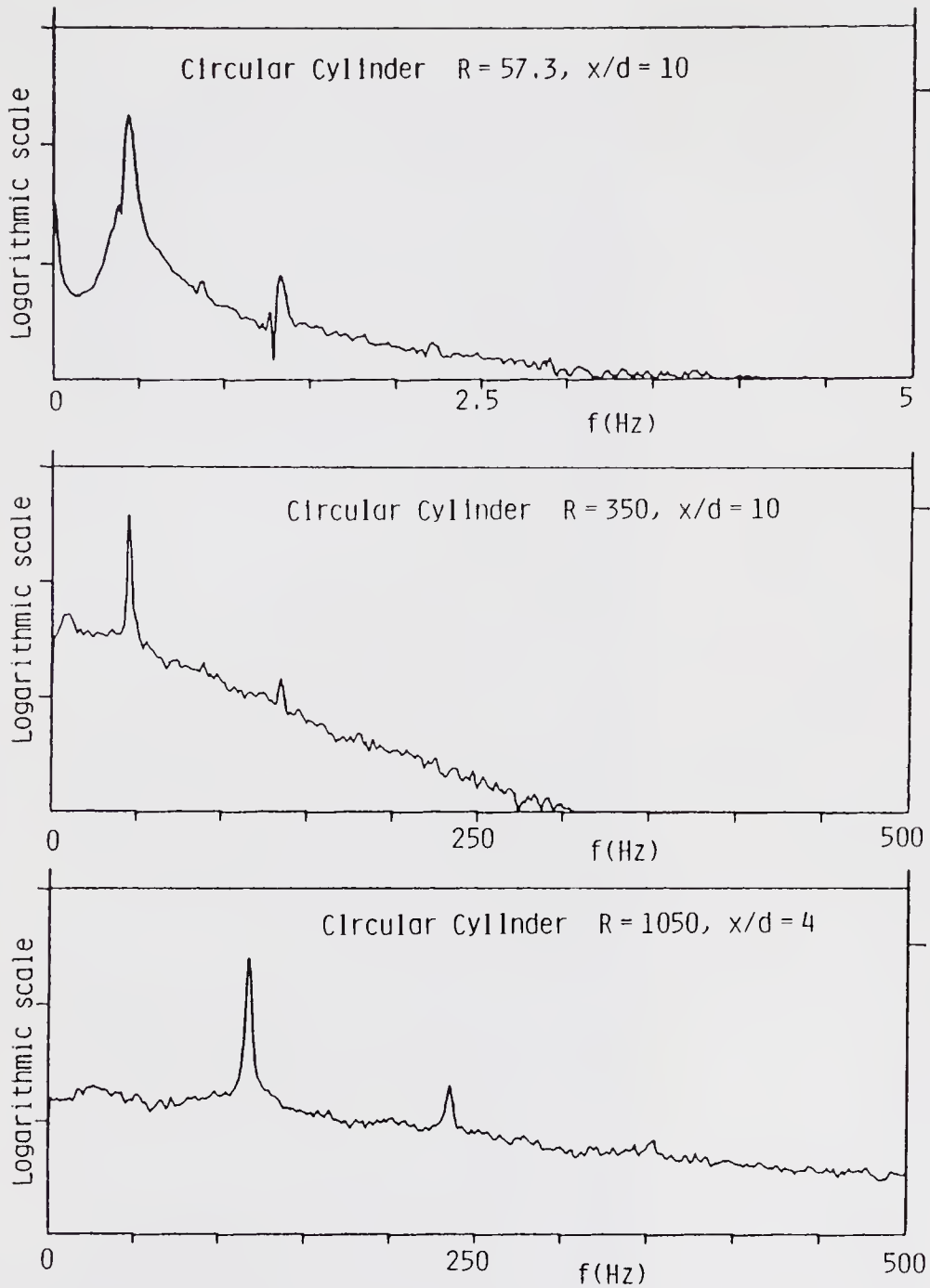


Figure 11. Power spectra of the velocity fluctuation in the wake behind a circular cylinder at $R = 57.3$, 350 and 1050.

Figure 14 (plate 5) shows the flow patterns of the wake behind an oscillating circular cylinder at $R = 100$. The cylinder diameter $d = 0.5$ cm, flow velocity $U = 2.45$ cm/s, and oscillation amplitude $a = 0.1$ cm. The oscillation of the wake is controlled by the cylinder motion in the frequency range from 0.6 Hz to 1.1 Hz. As will be seen, at the boundaries of the locking region the flow pattern becomes very irregular.

Figure 15 shows the hot-wire signals and the corresponding power spectra of the velocity fluctuation in the wake behind an oscillating circular cylinder at $R = 105$.

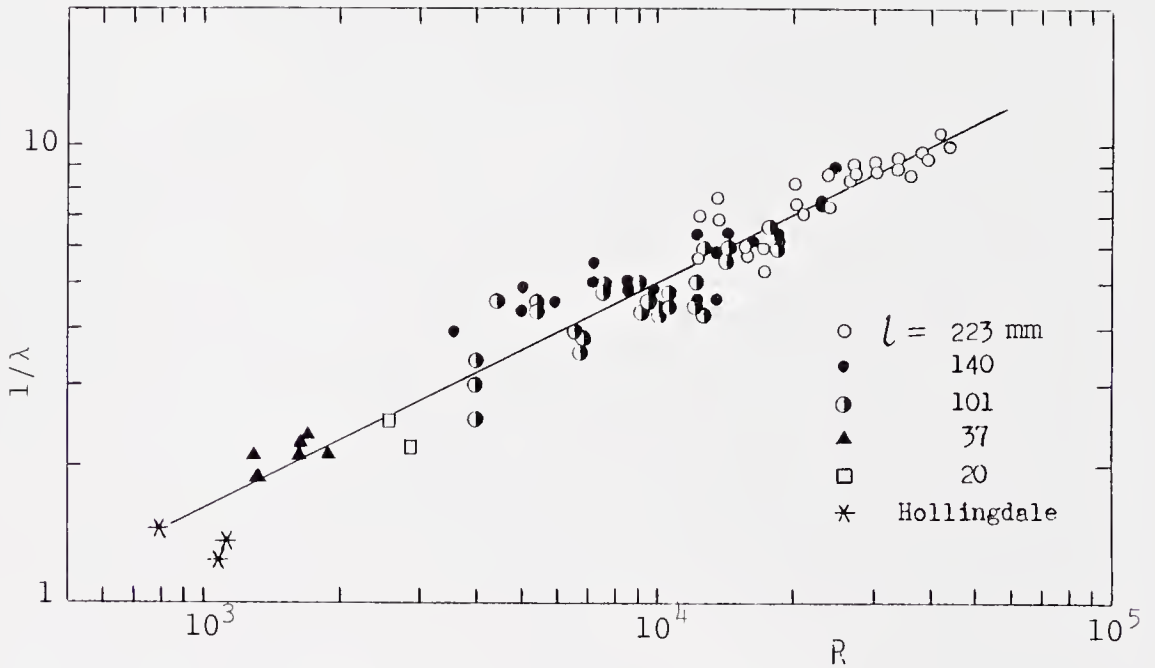


Figure 13. Wavelength as a function of R .

It should be noted that the continuous component in the power spectra is insensitive to the oscillation frequency of the cylinder, whether the wake is locked-in or not.

Figure 16 (plate 5) shows the turbulent wake behind a flat plate parallel to the flow (Taneda 1965). The Reynolds number based on the plate length is 1.3×10^6 . The wake is fully turbulent at the trailing edge of the plate. It will be seen that the turbulent wake oscillates some distance downstream. In general, the turbulent wake has a strong tendency to perform a progressive wave motion, the wavelength of which is nearly equal to the width of the wake.

Figure 17 (plate 6) shows the effect of artificial disturbances on the turbulent wake behind a circular cylinder at $R = 2200$ (Taneda 1983a). When the disturbance frequency is small the disturbance is amplified, but when the frequency is large it is damped. When the wavelength of the disturbance is nearly equal to the wake width, the disturbance is most strongly amplified.

Figure 18 (plate 6) shows the smoke pattern of the turbulent boundary layer on a flat plate (Taneda 1983b). In order to produce a thick boundary layer, a two-dimensional fence 1 cm in height is placed on the test plate 121 cm in width and 484 cm in length. The Reynolds number based on the displacement thickness $R^* = 700$. As will be seen, the turbulent boundary layer consists of large-scale two-dimensional waves and small-scale three-dimensional waves. The wavelength of the two-dimensional waves is about 20 times the displacement thickness.

Figure 19 (plate 7) shows the streamwise section of the turbulent boundary layer on a flat plate at $R^* = 400$ (Taneda 1981). It is clearly seen that there exists a large-scale two-dimensional periodic structure whose wavelength is about 20 times the displacement thickness δ^* .

Figure 20 (plate 7) is another example of the streamwise section of the turbulent boundary layer (Taneda 1983b). The Reynolds number $R^* = 1900$. The smoke

wire method was used for flow visualization. The wavelength of the two-dimensional periodic structure is about 20 times the displacement thickness, and the wave velocity determined from the cine film is about 0.8 of the free stream velocity.

Figure 21 (plate 8) shows the streak structure in the near wall region of the turbulent boundary layer at $R^* = 2100$ (Taneda 1983b). The continuous sheet of smoke issuing from the smoke wire forms a series of streamwise streaks.

Figure 22 (plate 9) shows the streak structure in the near wall region of the turbulent boundary layer at $R^* = 3600$. The smoke sheet is generated at the surface of the plate by putting titanium tetrachloride along a straight line. The smoke sheet forms an irregular array of small-scale streamwise streaks. As the streaks move downstream, they are separated from the plate surface and merge into large-scale streamwise streaks in the outer region of the boundary layer.

Figure 23 (plate 9) shows a cross-stream section of the turbulent boundary layer at $R^* = 3800$. It will be seen that there exist a series of large-scale three-dimensional structures in the outer region of the boundary layer. The large-scale three-dimensional structure fluctuates irregularly, but the average spacing between the large-scale streamwise streaks is about $5 \delta^*$.

Figure 24 (plate 10) shows the streamwise sections of the artificially disturbed turbulent boundary layer at $R^* = 5000$ (Taneda 1983). It may be seen that the disturbance whose wavelength is about $20 \delta^*$ is most strongly amplified.

Figure 25 shows the power spectra of the velocity fluctuation in the turbulent boundary layer disturbed artificially with the disturbance frequency $f_d = 2$ Hz. It is seen that the disturbance is amplified between $x = 200$ cm and 300 cm, where x is the distance from the disturbance generator.

Figure 26 shows the case when $f_d = 4$ Hz. It should be noted that the disturbance is damped in the downstream direction between $x = 200$ cm and 300 cm.

Figure 27 (plate 11) shows the flow around an impulsively started rotating circular cylinder (Van Dyke 1982). A circular cylinder 1 cm in diameter is started rotating in still water. The Reynolds number based on surface speed is 109. Immediately after the start of motion the boundary layer is uniform, but after a small time a series of ring-shaped vortices begin to grow. The ring-shaped vortices become more and more irregular with time and merge into larger vortices in an irregular manner.

Figure 28 (plate 12) shows the flow around a circular cylinder performing a rotatory oscillation in still water (Taneda 1985, pp. 399–410). The cylinder diameter is 3.18 cm, the oscillation frequency is 0.25 Hz, and the oscillation amplitude is 270 degrees. A small while after the start of motion, a series of ring-shaped vortices begin to develop. The manner of development of the vortices and the subsequent history are quite similar to those for an impulsively started rotating circular cylinder.

Figure 29 (plate 13) shows the flow around a circular cylinder rotating in a uniform flow. The Reynolds number is 33 based on the uniform flow velocity, and the circumferential velocity is 2.09 times the uniform flow velocity. It will be seen that the flow fluctuates irregularly.

Figure 30 (plate 13) shows the Taylor vortices between concentric rotating cylinders. The outer cylinder is at rest and the inner cylinder rotating. When $R = 146$, the flow is periodical in the axial direction. When $R = 644$, however, the

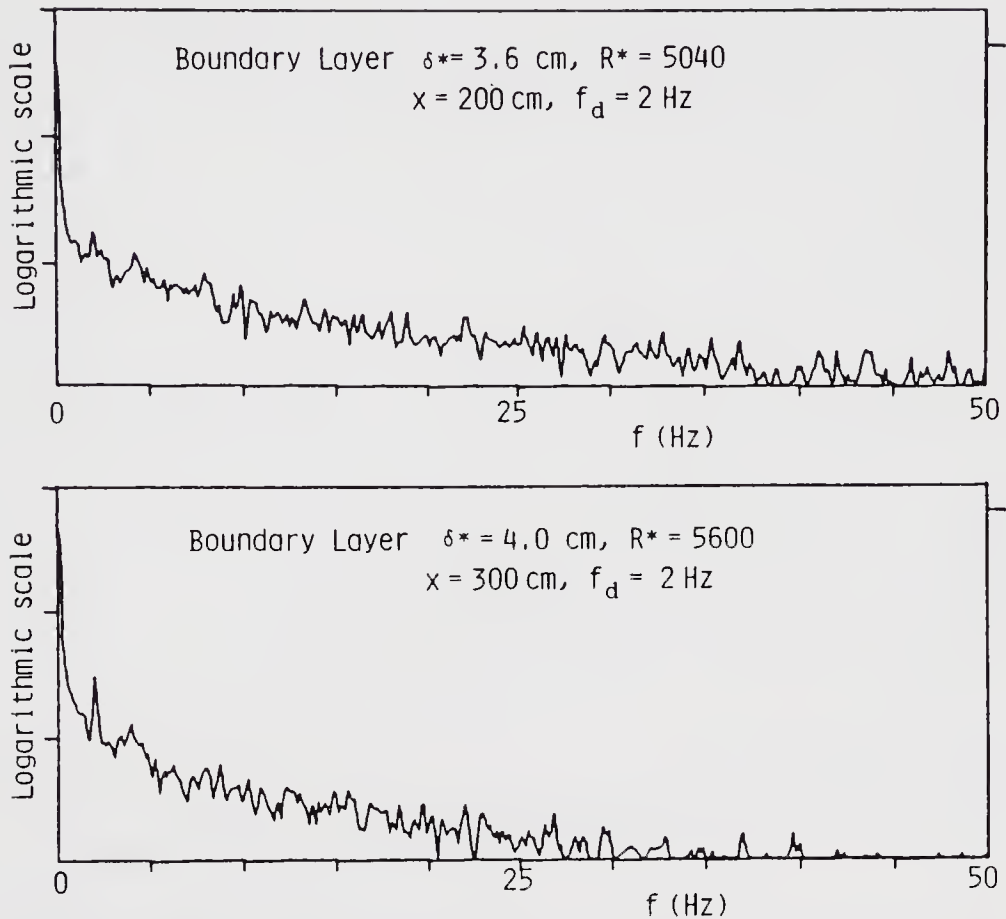


Figure 25. Variation of the power spectrum with the distance from the disturbance generator at disturbance frequency $f_d = 2$ Hz.

flow is periodical not only in the axial direction but also in the circumferential direction. As R is increased further, small-scale irregular structures develop in the whole flow field. When $R = 4184$, the flow has large-scale periodic structures and small-scale irregular structures.

Figure 31 (plate 14) shows the flow around an impulsively started flat plate at $R = 3857$. It will be seen that each of the separated shear layers forms a row of small-scale vortices which fluctuate irregularly.

Figure 32 (plate 14) shows the trailing vortex behind an airfoil. As will be seen, the integrated streaksheet rolls up to form a streamwise vortex which consists of spiral vortices. The spiral vortices fluctuate irregularly.

Figure 33 (plate 14) shows the wake behind an oil drop falling in still water at $R = 550$ (Taneda 1985). The wake forms a chain of distorted vortex loops. The vortex loops have a very complicated three-dimensional structure and fluctuate irregularly.

Figure 34 (plate 15) shows the turbulent wake behind a sphere (Taneda 1978). When R is between 7×10^3 and 3×10^5 , the turbulent wake performs a large-scale progressive motion in a plane containing the streamwise axis through the sphere centre. It should be noted that the oscillation plane rotates irregularly about that axis. When R is larger than about 4×10^5 , the turbulent wake forms a pair of streamwise vortices. The streamwise vortex-pair is offset from the wake axis through the sphere centre and rotates irregularly about that axis.

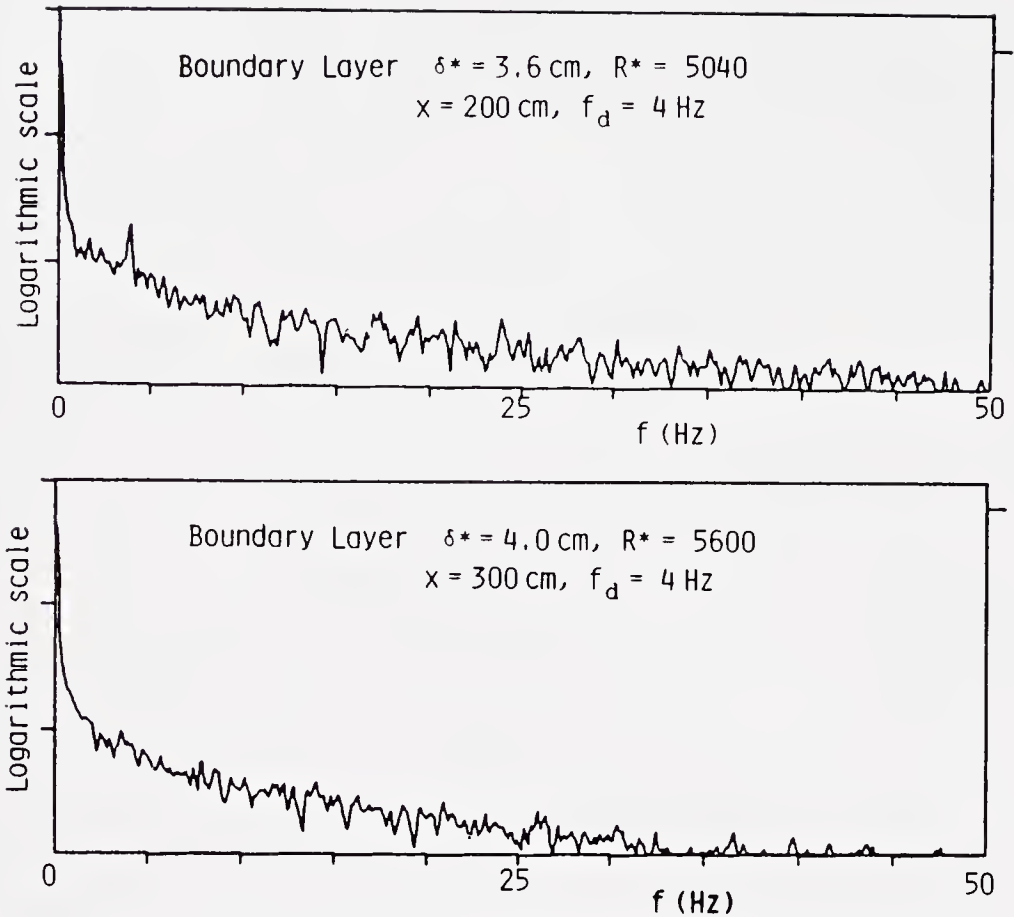


Figure 26. Variation of the power spectrum with the distance from the disturbance generator at $f_d = 4 \text{ Hz}$.

Figure 35 is the sketch of the turbulent wake behind a sphere at high Reynolds numbers.

Figure 36 (plate 15) shows the flow around a circular cylinder projecting from a plane surface (Van Dyke 1982). The Reynolds number based on the cylinder diameter is 4×10^3 . It will be seen that large-scale horse-shoe vortices are formed around the cylinder. The horse-shoe vortices are unstable and fluctuate irregularly.

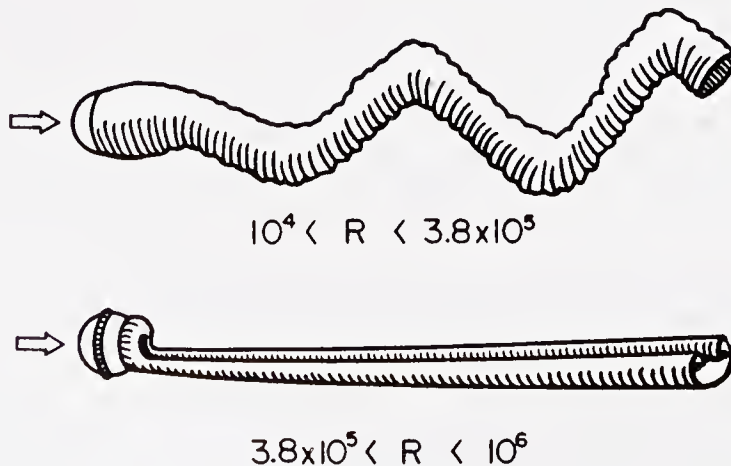


Figure 35. Sketch of the wake structure behind a sphere at high Reynolds numbers.

Figure 37 (plate 16) shows the surface wave around a sphere which is half submerged in water and forced to oscillate up and down (Taneda 1986). When the frequency or the amplitude is small, concentric circular waves are generated around the sphere. When the frequency or the amplitude exceeds a certain limit, however, the concentric waves are abruptly transfigured into the petal-shaped waves whose frequency is exactly one half of the sphere frequency. As the frequency or amplitude is increased further, the wave pattern becomes more and more irregular.

3. Conclusion

Wakes, boundary layers, surface waves, etc. were examined using flow visualization methods and hot-wire techniques. The observations demonstrate that when the Reynolds number is large the flows have coherent structures each of which fluctuates irregularly. It seems that the mean velocity profile, the transfer of momentum, the transfer of heat etc. depend mainly on the large-scale coherent structures of the flow. The investigation of the mechanism by which irregular fluctuations develop in the flow will be the subject of future research.

References

- Gerrard J H 1978 *Philos. Trans. R. Soc. London* 288: 351–382
Taneda S 1958 *J. Phys. Soc. Jpn.* 13: 418–424
Taneda S 1965 *J. Phys. Soc. Jpn.* 20: 1714–1721
Taneda S 1978 *J. Fluid Mech.* 85: 187–192
Taneda S 1981 *J. Phys. Soc. Jpn.* 50: 1398–1403
Taneda S 1983a *Phys. Fluids* 26: 2801–2806
Taneda S 1983b *J. Phys. Soc. Jpn.* 52: 4138–4144
Taneda S 1985 *Theoretical and applied mechanics* (eds) F I Niordson, N Olhoff (Amsterdam: North-Holland)
Taneda S 1986 *Fluid Dyn. Res.* 1: 1–2
Van Dyke M (ed.) 1982 *An album of fluid motion* (Stanford: Parabolic)

Plate 1.

Figure 1. The wake behind a circular cylinder at $R = 140$ (integrated streaksheet pattern, electrolytic precipitation method).

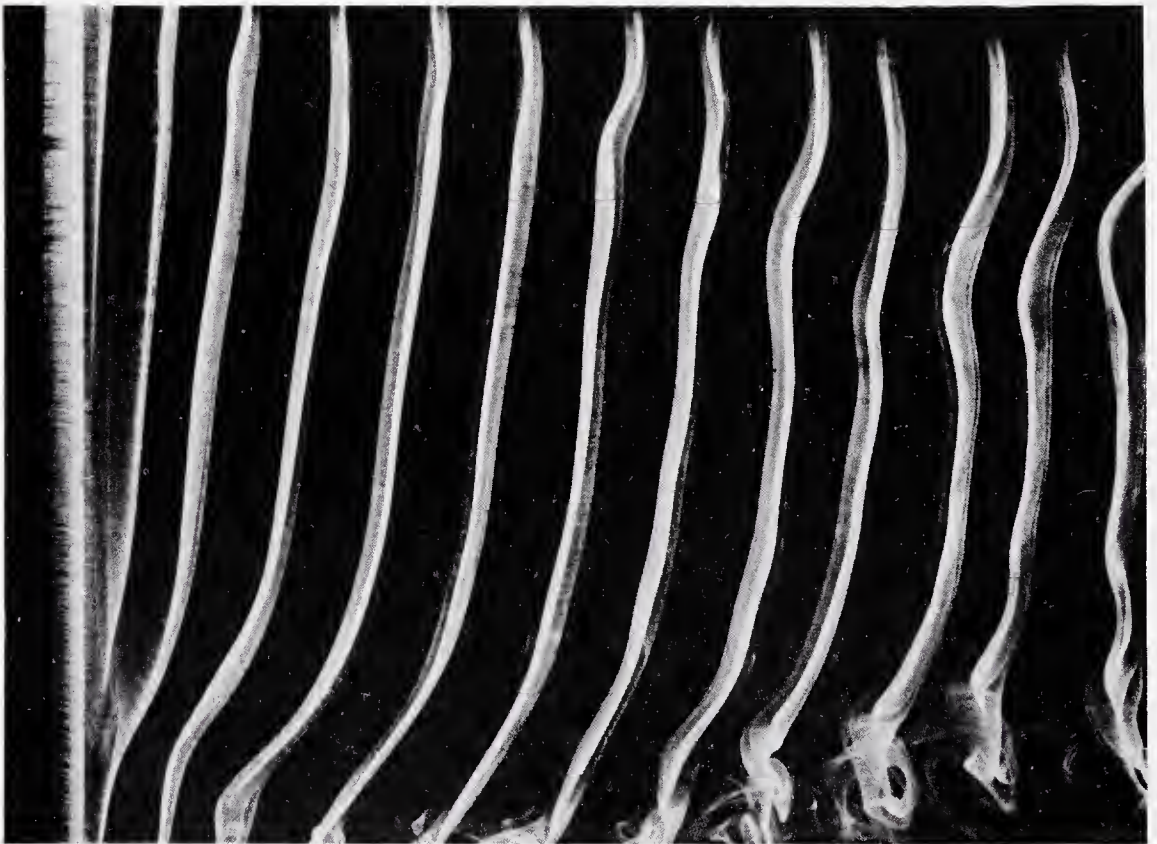


Figure 4. The wake behind a circular cylinder at $R = 100$ (integrated streaksheet pattern, electrolytic precipitation method).

Plate 2.

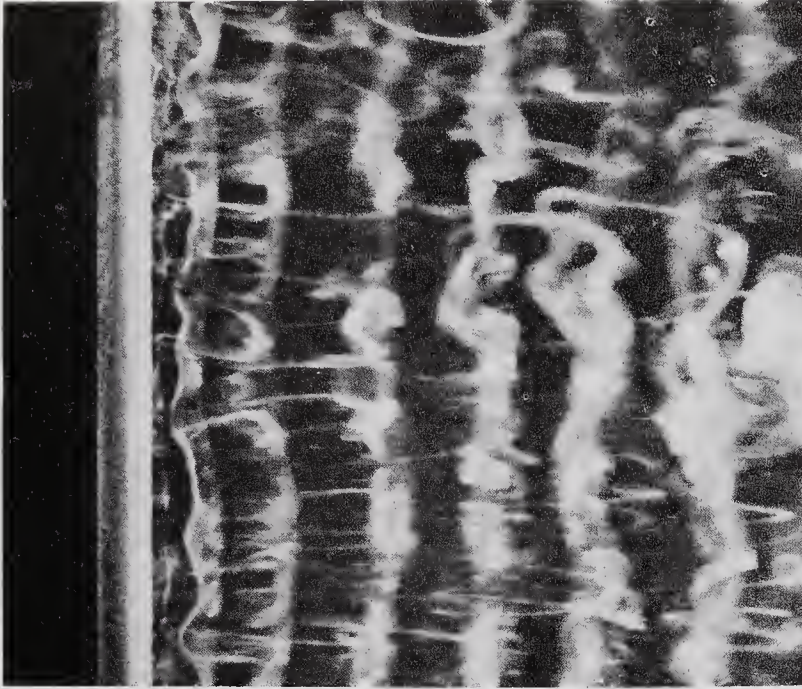


Figure 5. The wake behind a circular cylinder at $R = 300$ (integrated streaksheet pattern, electrolytic precipitation method).



Figure 6. Cross-stream section of the wake behind a circular cylinder at $R = 300$ and $x/d = 5$ (integrated streaksheet pattern, electrolytic precipitation method).



Figure 7. Cross-stream section of the wake behind a circular cylinder at $R = 700$ and $x/d = 200$ (smoke pattern, smoke-wire method).

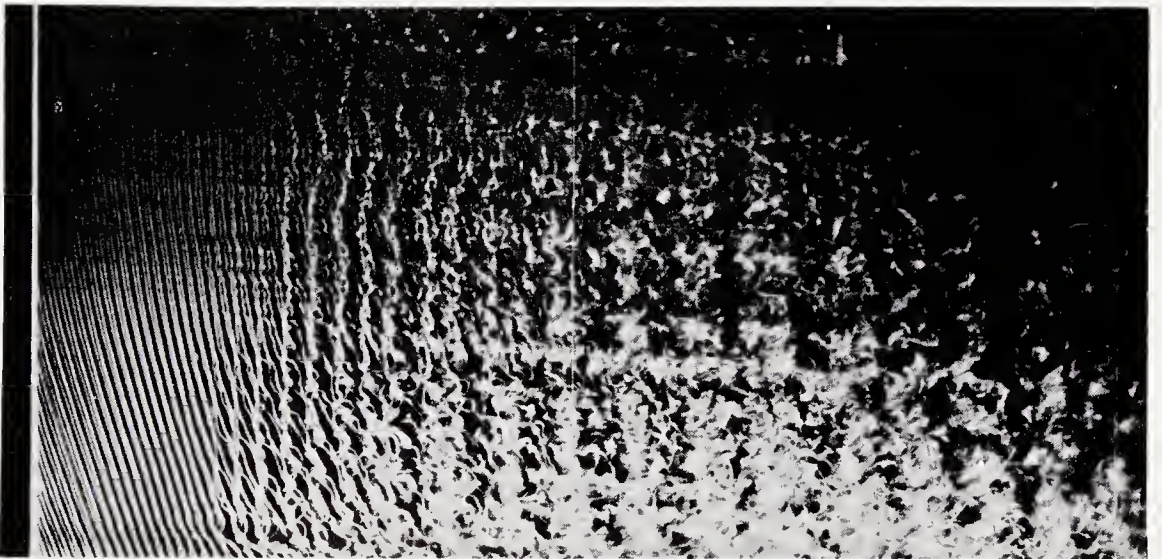


Figure 8. The wake behind a circular cylinder at $R = 350$ (smoke pattern, smoke-wire method).

Plate 4.

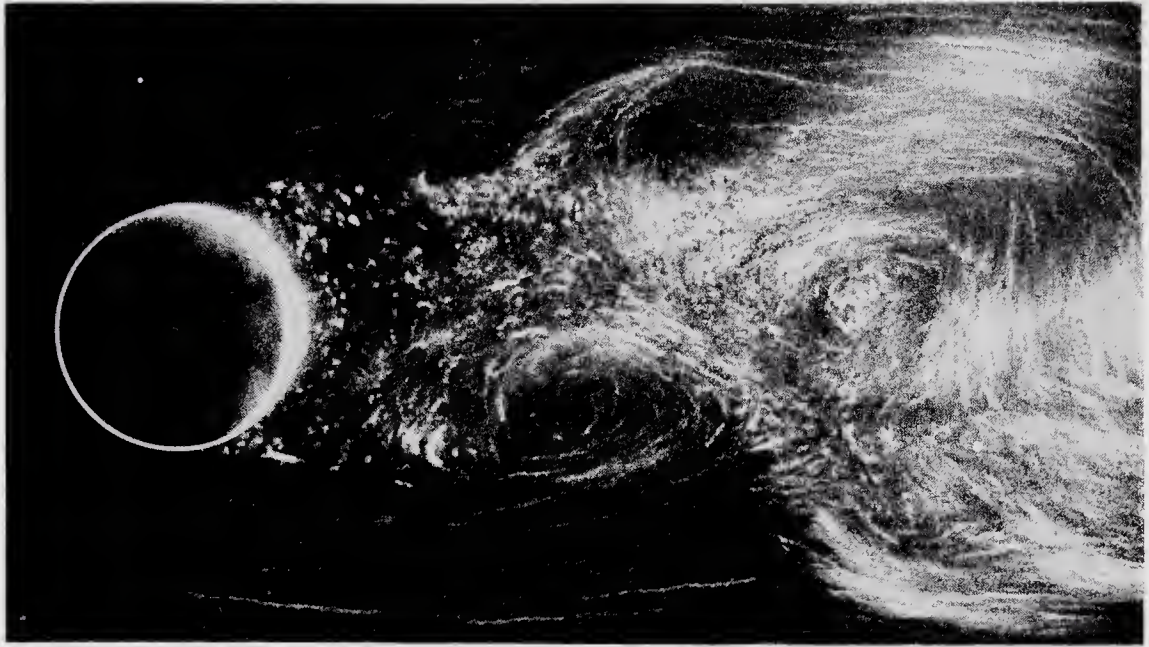


Figure 10. The wake behind a circular cylinder at $R = 1404$ (streamline pattern, aluminum dust method).

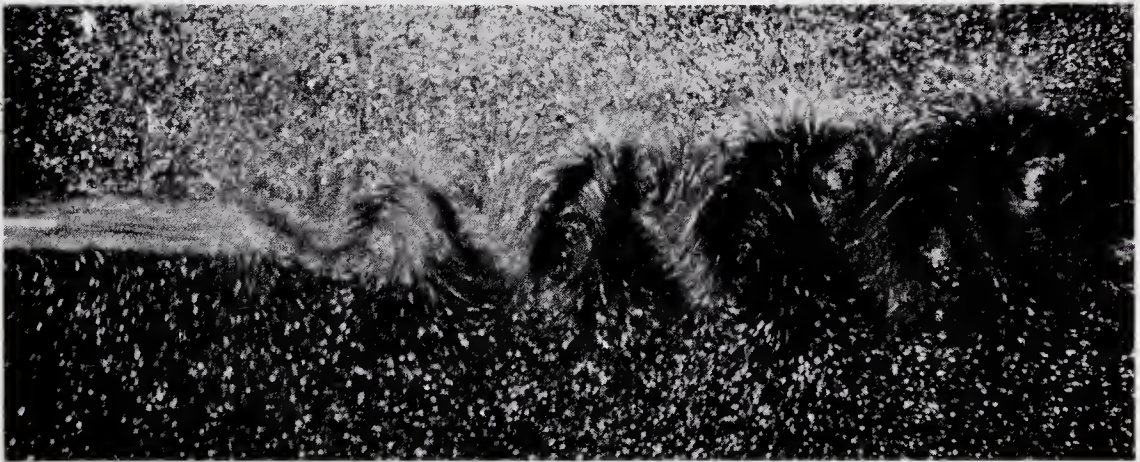


Figure 12. The flow behind a flat plate parallel to the flow at $R = 15,800$ (streamline pattern, aluminum dust method).

Plate 5.

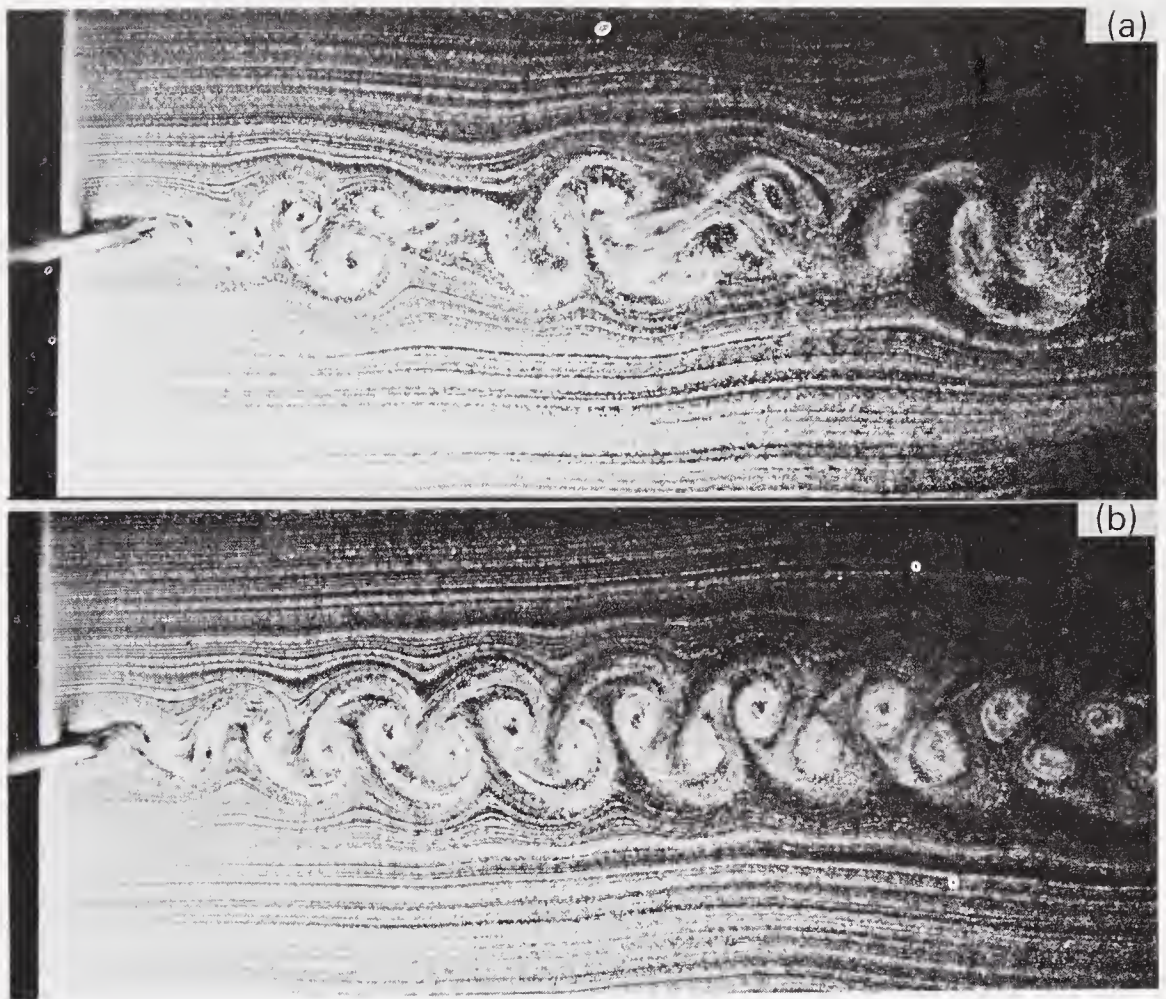


Figure 14. The wakes behind an oscillating circular cylinder at $R = 100$ cylinder frequency $f_c = 0.60$ Hz (a), 0.68 Hz (b) (streakline pattern, hydrogen bubble method).

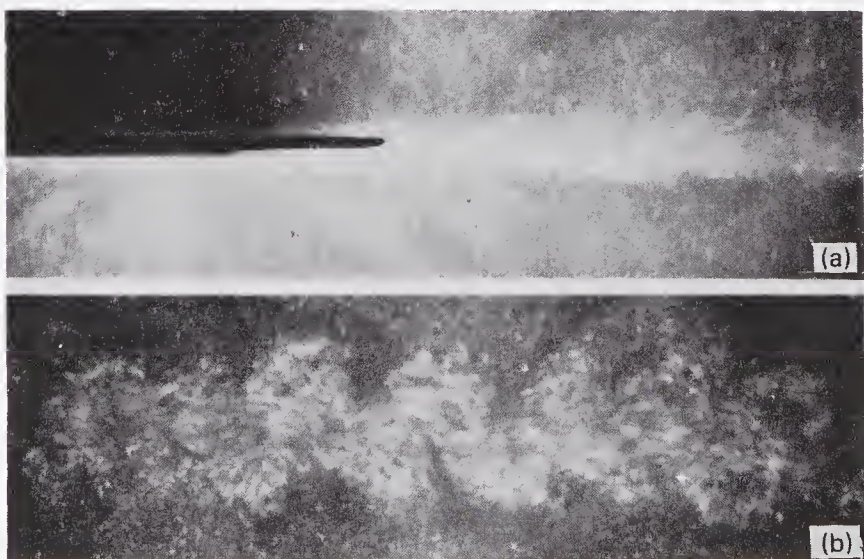


Figure 16. Turbulent wake behind a flat plate parallel to the flow at $R = 1.3 \times 10^6$ (streamline pattern, aluminum dust method).

Plate 6.

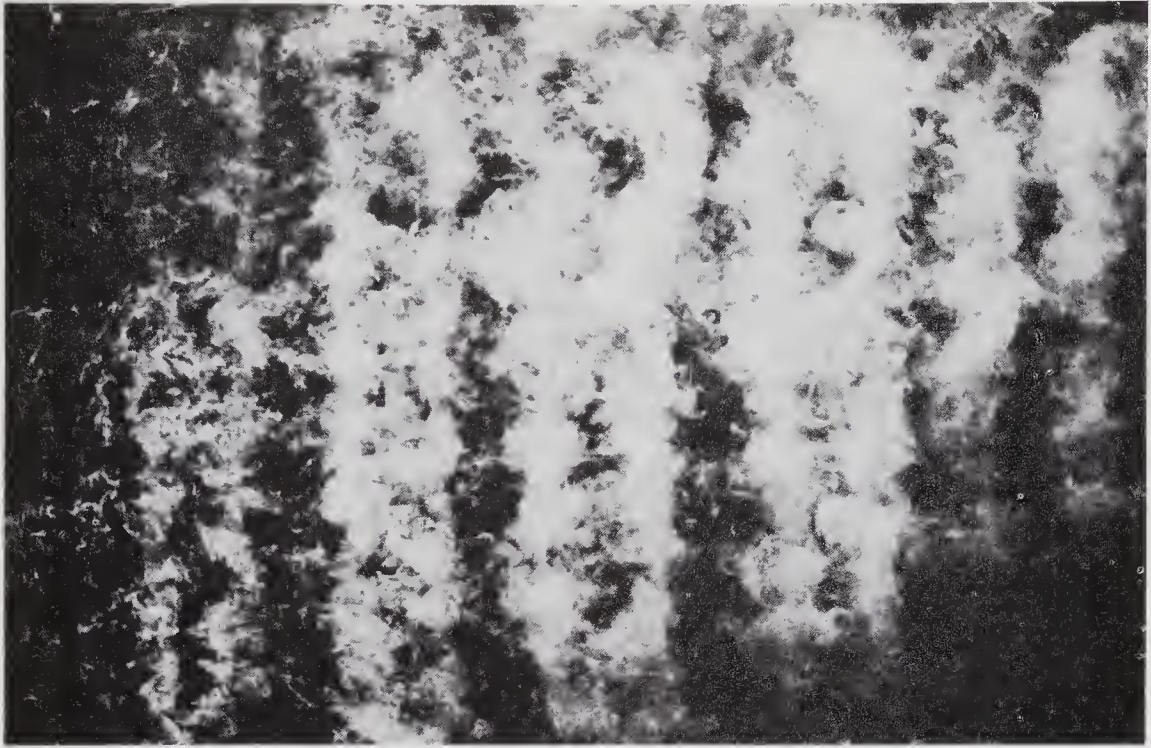


Figure 17. Artificially disturbed turbulent wake (smoke pattern, smoke-wire method).



Figure 18. The turbulent boundary layer on a flat plate at $R^* = 840$ (smoke pattern, titanium tetrachloride method).

Plate 7.



Figure 19. The turbulent boundary layer on a flat plate at $R^* = 400$ (smoke pattern, titanium tetrachloride method).

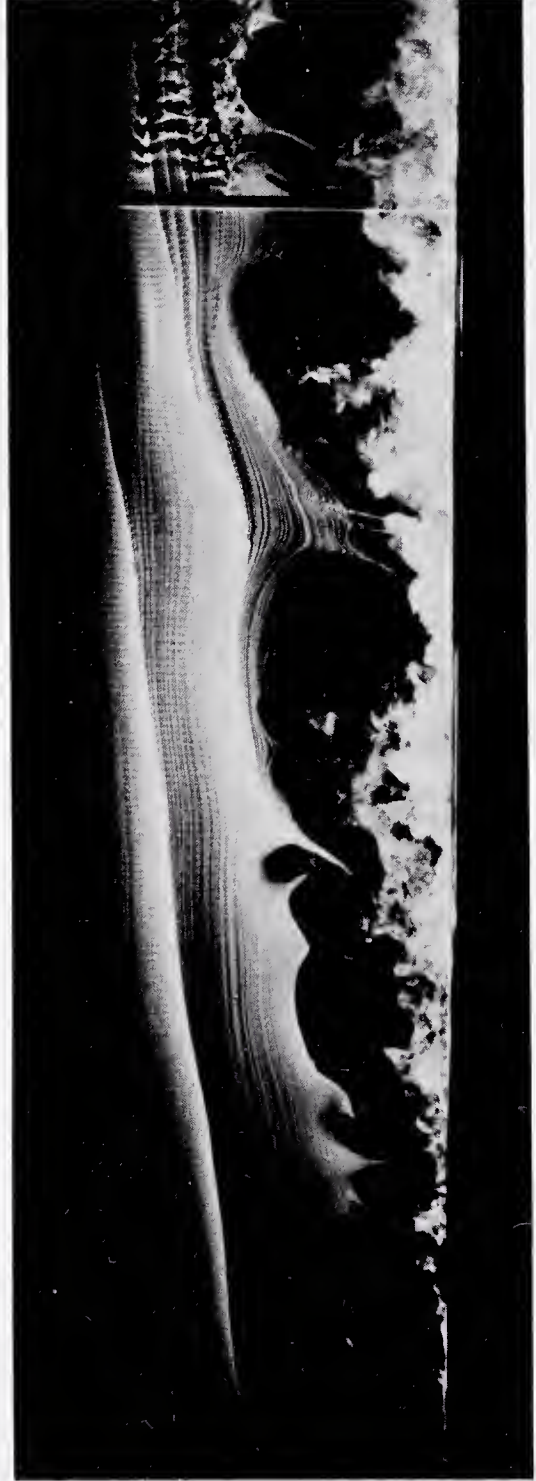


Figure 20. Streamwise section of the turbulent boundary layer at $R^* = 1900$ (smoke pattern, smoke-wire method).

Plate 8.

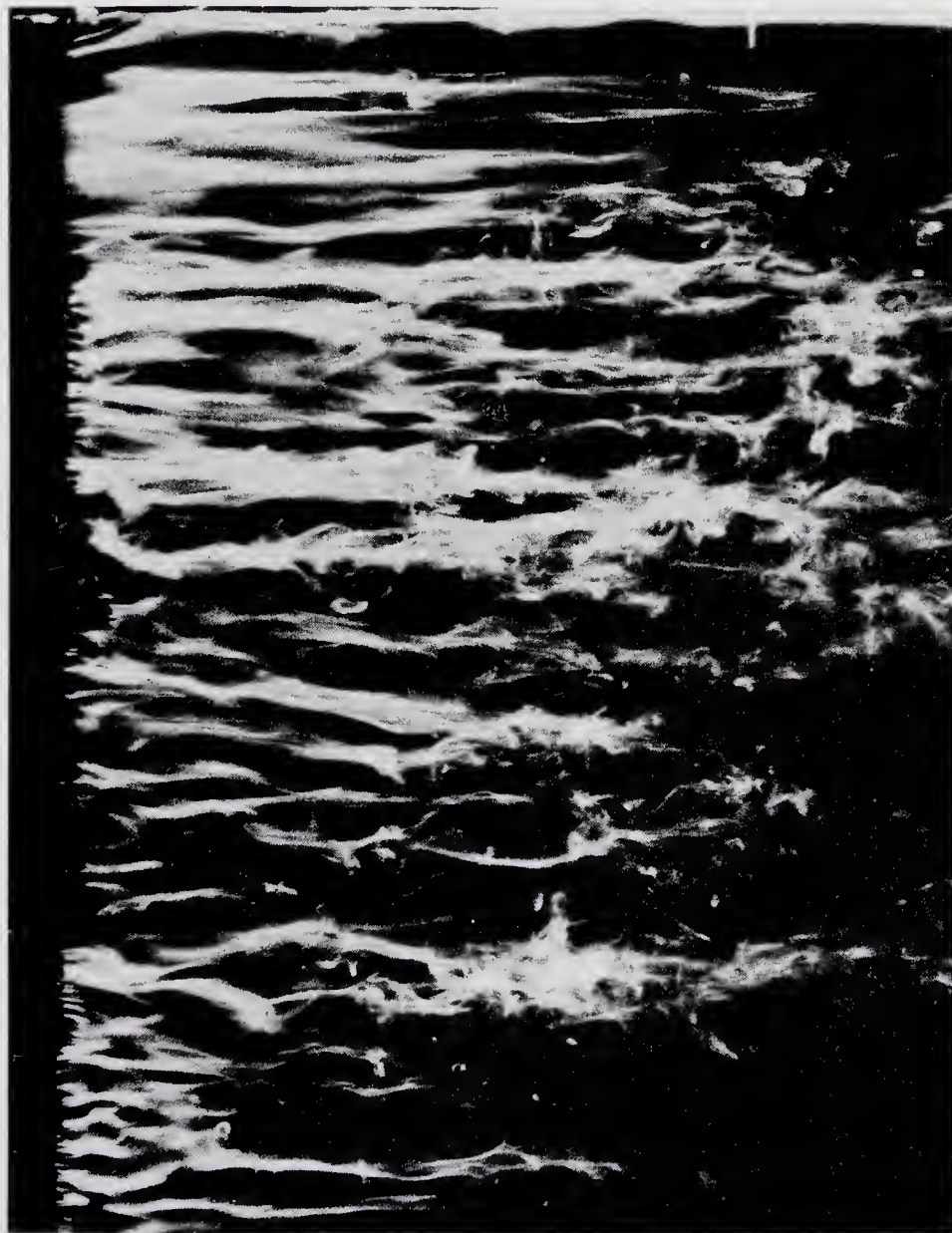


Figure 21. Streak structure in the near wall region of the turbulent boundary layer at $R^* = 2100$ (smoke pattern, smoke-wire method).

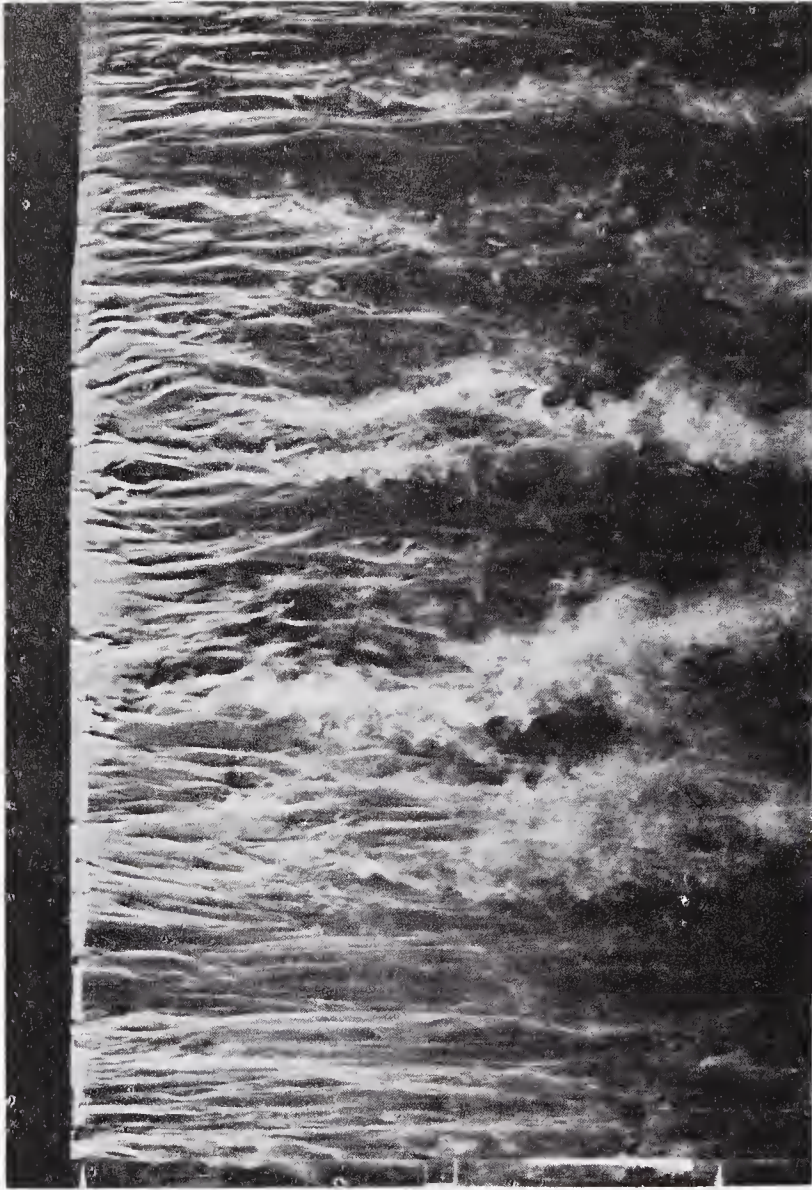
Plate 9.

Figure 22. The turbulent boundary layer on a flat plate at $R^* = 3600$ (smoke pattern, titanium tetrachloride method).



Figure 23. Cross-stream section of the turbulent boundary layer at $R^* = 3800$ (smoke pattern, smoke-wire method).

Plate 10.

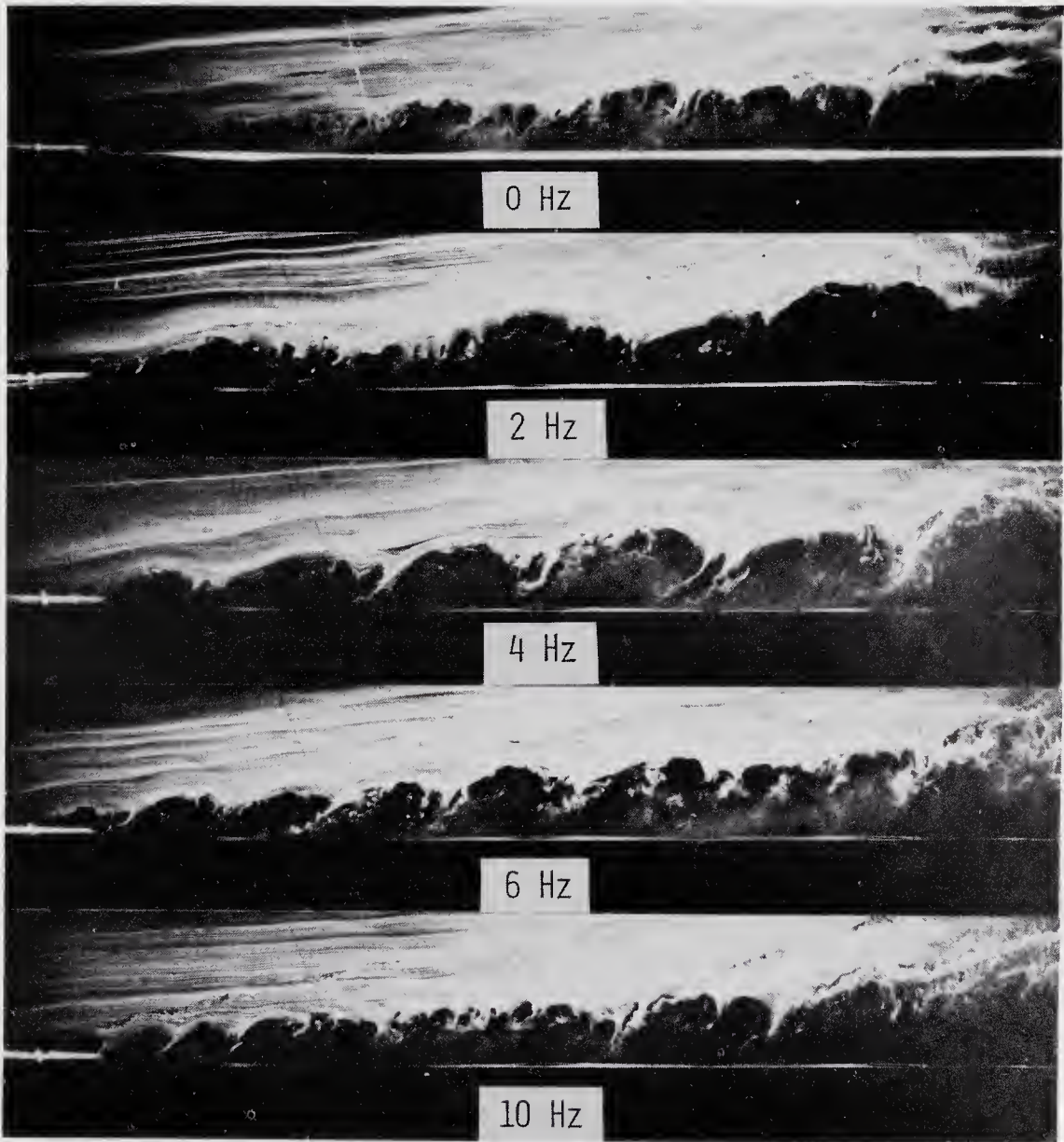


Figure 24. Artificially disturbed turbulent boundary layer at $R^* = 5000$ (smoke pattern, smoke-wire method).

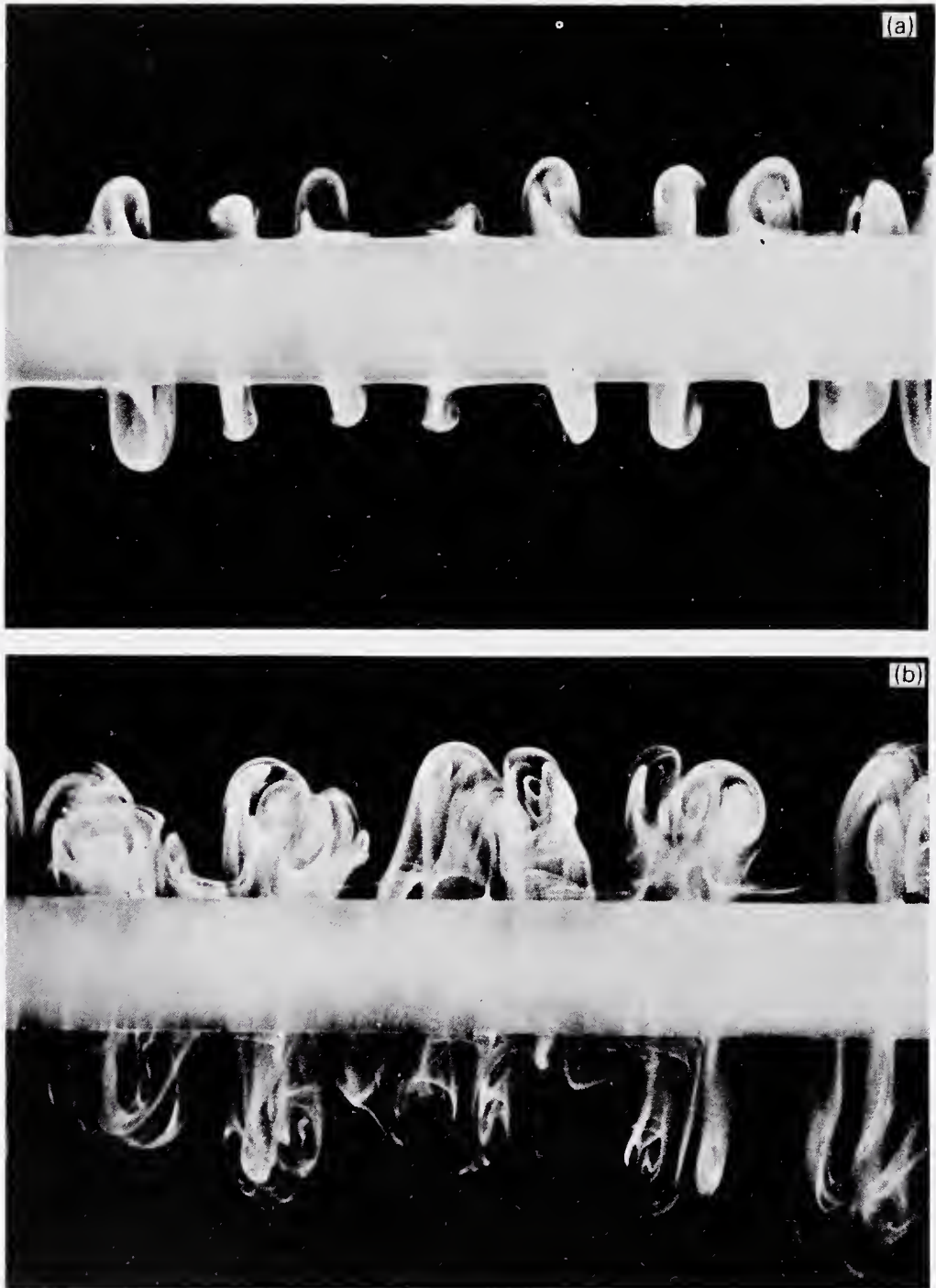
Plate 11.

Figure 27. The flow around an impulsively started rotating circular cylinder at (a) 4.7s, (b) 10s (integrated streaksheet pattern, electrolytic precipitation method).

Plate 12.

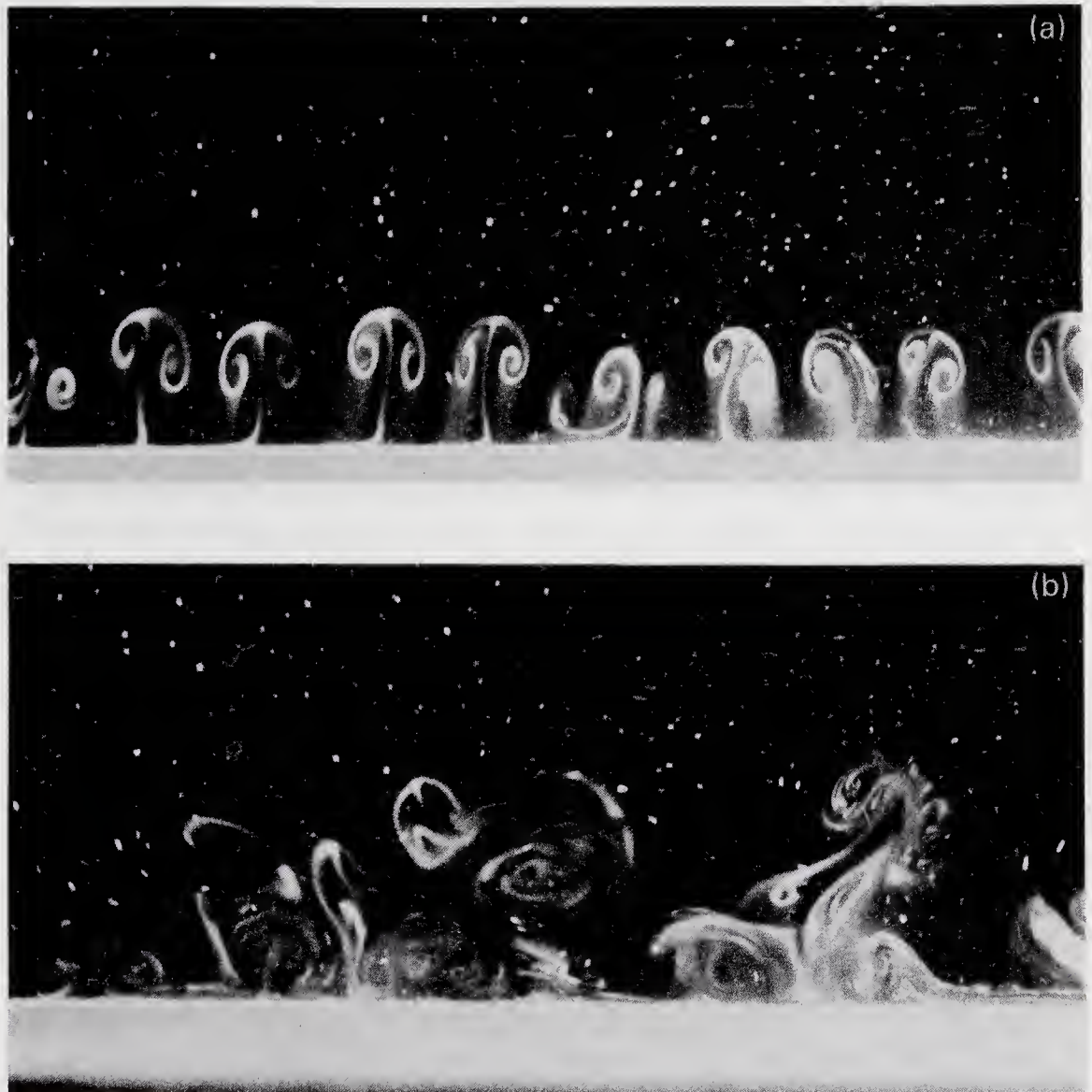


Figure 28. The flow around a circular cylinder performing a rotatory oscillation in still water at (a) 13.9s, (b) 21.8s (integrated streaksheet pattern, electrolytic precipitation method).

Plate 13.

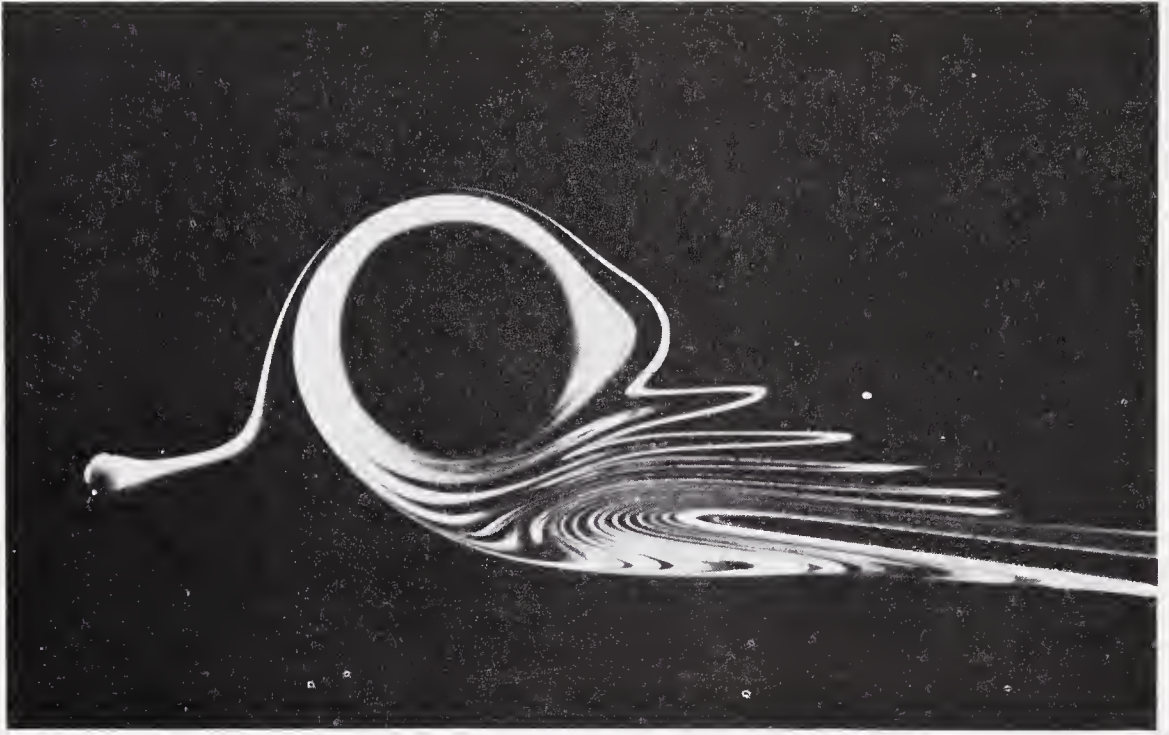


Figure 29. The flow around a circular cylinder rotating in a uniform flow (streakline pattern, electrolytic precipitation method).

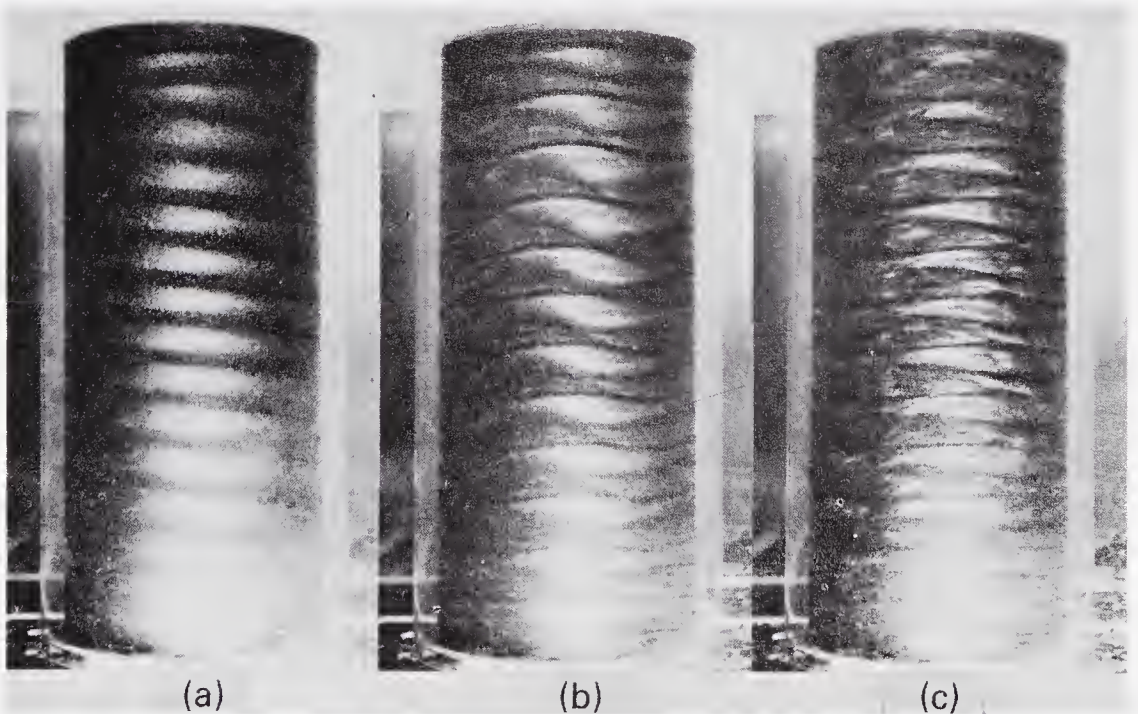


Figure 30. Taylor vortices between concentric rotating cylinders. $R = 146$ (a), 644 (b), 4184 (c).

Plate 14.

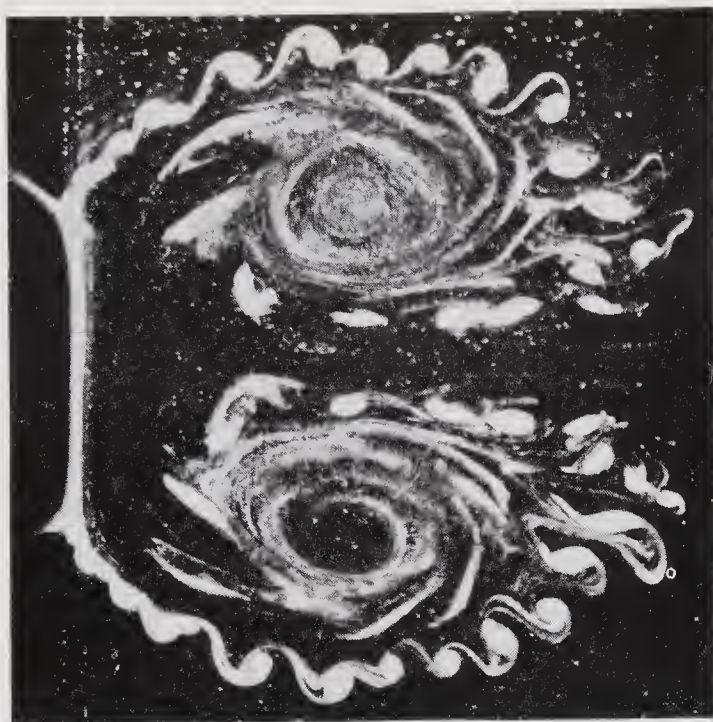


Figure 31. The flow around an impulsively started flat plate at $R = 3857$ (integrated streaksheet pattern, hydrogen bubble method).



Figure 32. The trailing vortex behind an airfoil at $R = 3070$ and attack angle 8° (integrated streaksheet pattern, condensed milk method).



Figure 33. The wake behind an oil droplet at $R = 550$ (integrated streaksheet pattern, dye method).

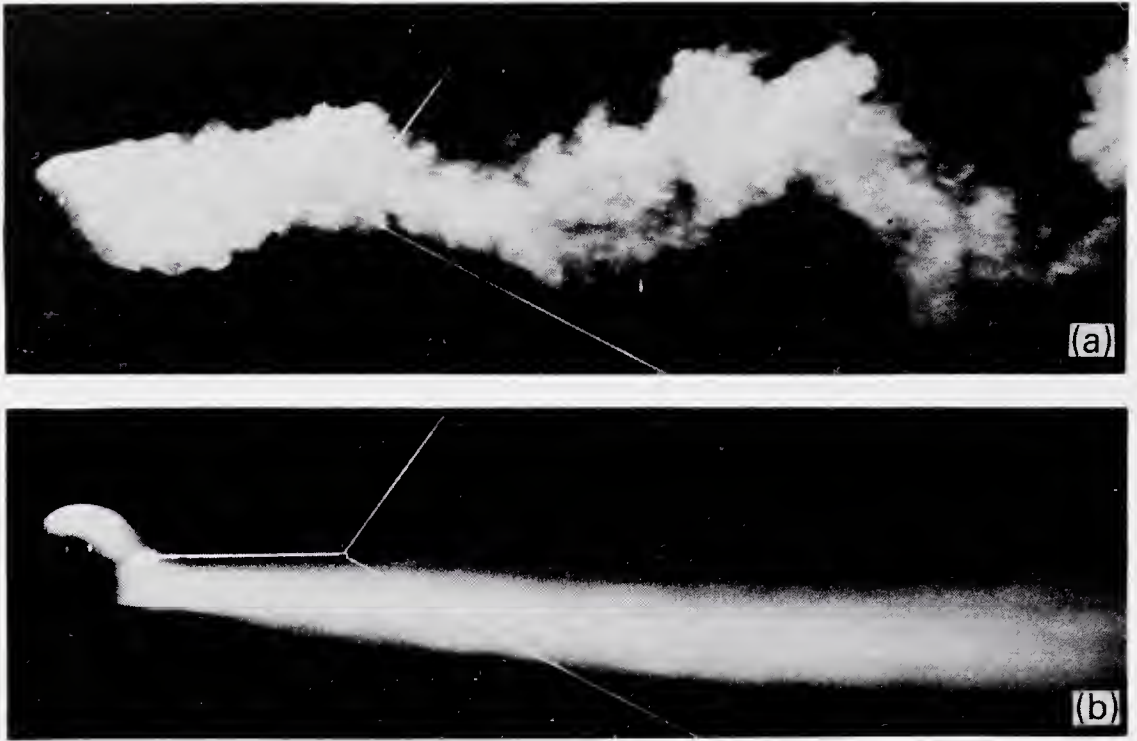
Plate 15.

Figure 34. The wake behind a sphere. $R = 2.4 \times 10^4$ (a), 6.0×10^5 (b) (smoke pattern, titanium tetrachloride method).



Figure 36. The flow around a circular cylinder put vertically on a flat plate (smoke pattern, titanium tetrachloride method).

Plate 16.

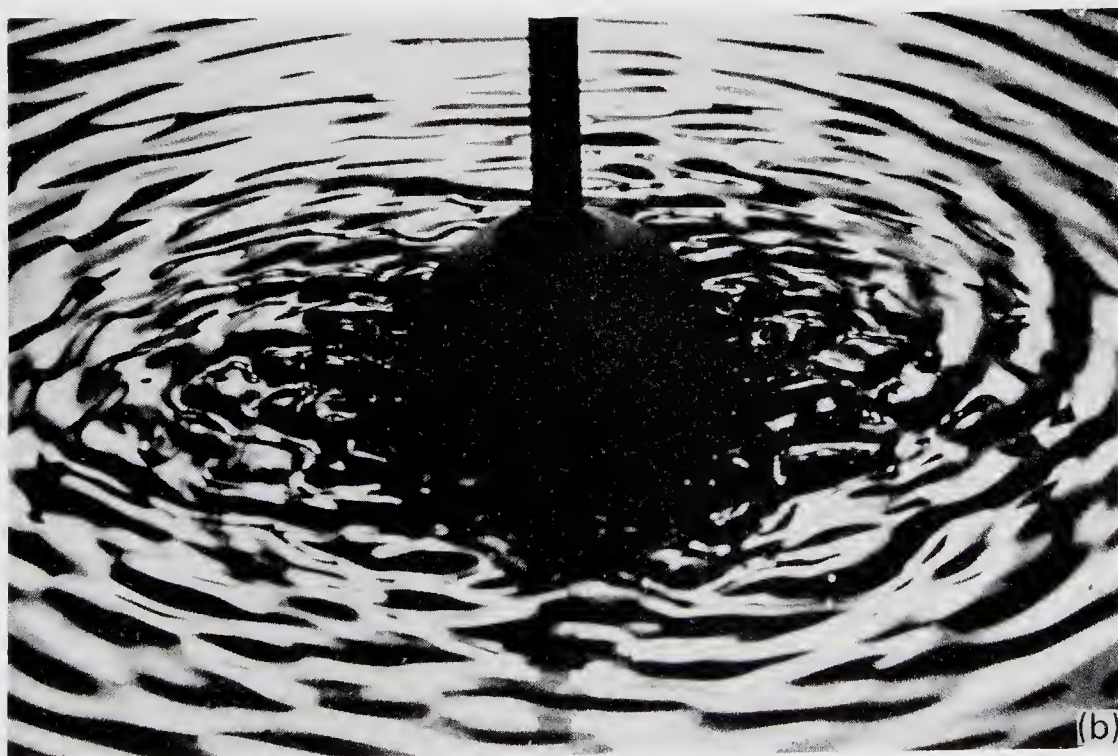
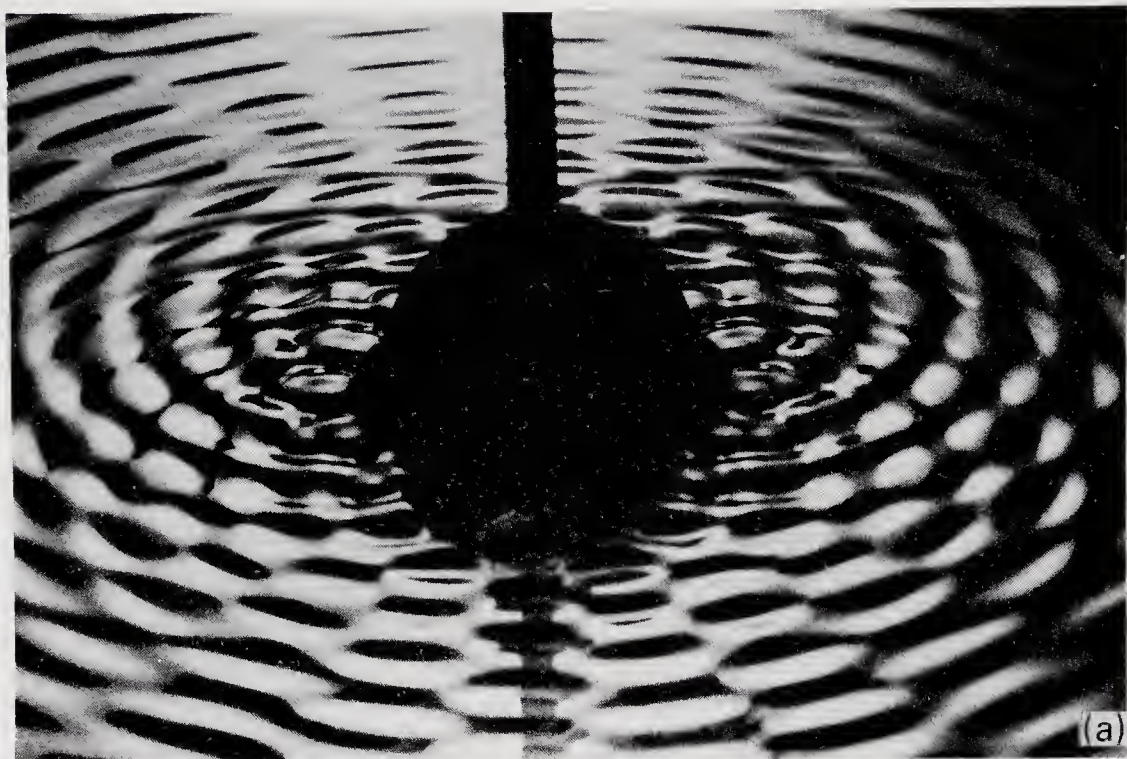


Figure 37. The waves around a sphere oscillating up and down (the sphere diameter $d = 3.75$ cm, sphere frequency $f_s = 50$ Hz) oscillation amplitude $a = 0.54$ mm (a), 1.27 mm (b).

Observations of supersonic free shear layers

D PAPAMOSCHOU and A ROSHKO

Department of Aeronautics, California Institute of Technology,
Pasadena, California 91125, USA

Abstract. Visual spreading rates of turbulent shear layers with at least one stream supersonic were measured using Schlieren photography. The experiments were done at a variety of Mach number-gas combinations. The spreading rates are correlated with a compressibility-effect parameter called the convective Mach number. It is found that for supersonic values of the convective Mach number, the spreading rate is about one quarter that of an incompressible layer at the same velocity and density ratio. The results are compared with other experimental and theoretical results.

Keywords. Supersonic free shear layers; turbulent shear layers; convective Mach number; spreading rate.

1. Introduction

The supersonic turbulent free shear layer is fashionable again. The interest which developed in the 1960s was related mainly to the near wake problem; the present, renewed interest comes largely from problems in supersonic combustion. In the earlier period it had been noted that turbulent shear layers with supersonic velocity on one side and zero velocity on the other (e.g. at the edges of jets) spread more slowly than incompressible turbulent shear layers, and it was thought that the difference was attributable to the *density* differences that were present in the supersonic cases. Thus models incorporating Howarth-Darodnitsyn transformations, density-dependent eddy viscosities etc., were invented.

Whether density effects alone could account for the differences in spreading rate was the question that motivated the experiments of Roshko & Brown (1971, 1974), who built an apparatus in which incompressible ($M = 0$) shear-layer flows with large density differences could be studied by simply using different gas combinations like nitrogen and helium, at low speeds. It was found that, while there is some effect of the density on spreading rate, it is very much smaller than is observed in the supersonic case. The relative magnitudes are summarized in figure 15 of

Roshko & Brown (1974). For example, the shear layer spreading rate at the edge of a Mach 4 jet (with uniform total temperature) is about 0.4 that of an incompressible shear layer with the same ratio of densities. It must be concluded that compressibility, *per se*, plays an important role in the supersonic case. In fact, with the observation that subsonic turbulent shear layers contain large, so-called “coherent” structures reminiscent of those in the early stages of instability, and the realization that the turbulent shear layer growth is governed largely by its instability at the corresponding large scales, it became clear that these processes must be quite different in supersonic flow. In fact, there is visual evidence that large structures also exist in supersonic turbulent mixing layers (Ortwerth & Shine 1977; Oertel 1979).

It has been found that some insights into turbulent growth rates can be obtained, at least qualitatively, from the amplification rates of instability waves in laminar shear layers (more precisely from stability calculations for typical shear-layer profiles of velocity and density). Even the simpler calculations which can be made on the instability of vortex sheets are useful. Some further discussion of the possible connection between shear-layer instability and turbulent growth rate is given below.

The discovery of organized large structure also led to the idea that the natural coordinate system in which to view the flow is one moving with those structures. In the instability analysis this coordinate system moves with the wave velocity; in turbulent flows the term “celerity” has been used by Favre *et al* (1967) to define the velocity of the moving frame in which the large structure is most nearly stationary (see Coles 1981). In this convecting frame then, the Mach number M_c , which is called the “convective” Mach number, will be different from that in the laboratory system. It may possibly be less than unity even when there is supersonic flow in the laboratory system. It would also be appropriate to call it the “intrinsic” Mach number, since it is the one that is relevant for Mach number effects.

In practically all the available data on supersonic shear layers so far the low speed side was at rest ($M_2 = 0$). Exceptions, to our knowledge, are experiments done by Demetriades & Bower (1982), Sanderson & Steel (1970) and Ortwerth & Shine (1977). Demetriades & Bower’s results apply for the laminar-transitional regime and therefore cannot be used for predicting turbulent shear layer behaviour. Sanderson & Steel’s results are hard to interpret and their shear layers are mostly wake-dominated. In Ortwerth & Shine’s experiment a stream of helium at $M = 3$ mixes with a stream of nitrogen also at $M = 3$. A spark Schlieren photograph shows a slowly growing mixing layer with large scale structure.

One of the main purposes of the experiment described here was to examine the effects of varying M_2 from subsonic to supersonic values while keeping $M_1 > 1$. This would provide a useful test of the intrinsic Mach number concept. In addition, we wanted to study the effects of a larger variation of the parameter ρ_2/ρ_1 than that afforded by the typical jet experiment of a single gas and with all total temperatures at room values. Accordingly, we designed and built an apparatus, essentially a variation of the Roshko & Brown (1974) apparatus, in which two streams of gases are allowed to mix downstream of a splitter plate.

In this work we present the mixing layer spreading rates, obtained experimentally with instantaneous Schlieren photographs, at a variety of Mach number-gas combinations. We assume that the Reynolds numbers are high enough to assure

that the mixing layers are fully developed turbulent everywhere except in a very small region near the splitter plate. Our goal is to examine the effect of compressibility on the spreading rates and to determine what are the fundamental parameters that describe this effect.

The following table lists typical experimental conditions in which the mixing layers were observed:

Mach number range	0 to 4
Density ratio range	0.2 to 10
Typical unit Reynolds number	10^5 cm^{-1}
Typical test section pressure	1 psia (7000 Pa)
Gases used	nitrogen, helium, argon

2. Experimental facility

2.1 Supersonic mixing apparatus

A schematic of the apparatus is shown in figure 1. It is essentially a two-stream blow-down supersonic wind tunnel with two independent supply sides. Each supply side is connected to pressure regulated gas cylinders. The downstream side is connected to a low pressure tank which is evacuated by a vacuum pump.

After passing through flow management devices, each gas is expanded to a design Mach number by means of an appropriately contoured centrebody, downstream of which the two gases mix. The centrebody contours, calculated by the method of characteristics, are designed to produce uniform, wavefree flows on each side. The centrebody is replaceable, allowing the use of a number of centrebodies for various Mach number combinations.

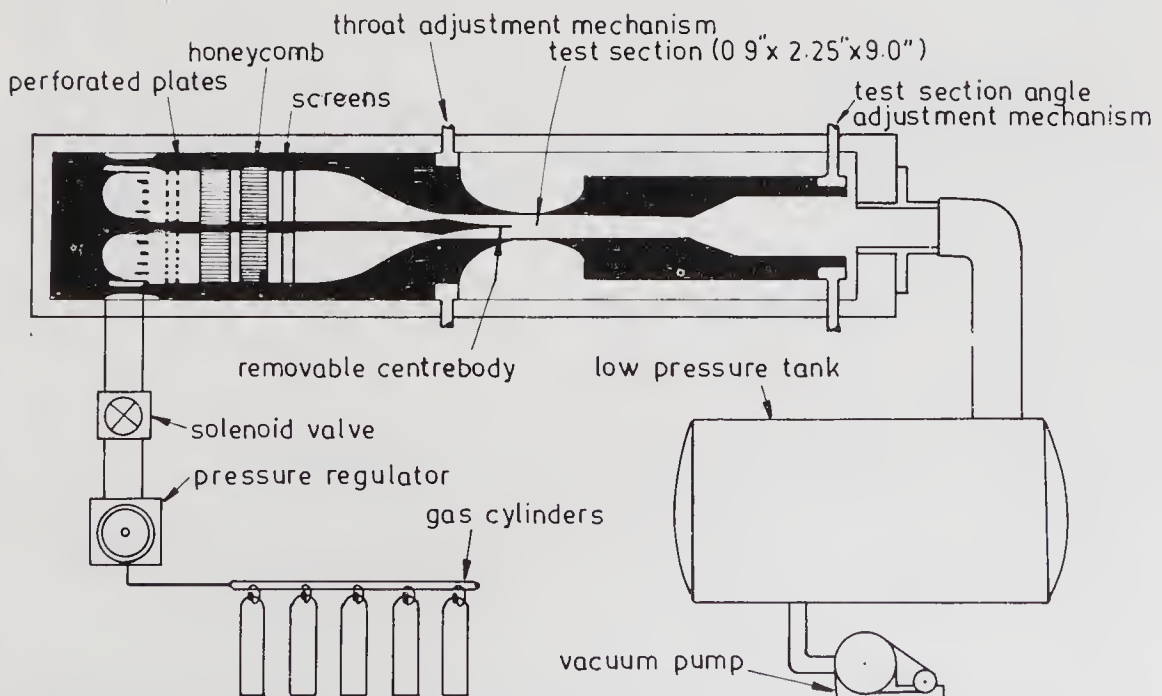


Figure 1. Experimental facility.

The test section is 2.3 cm (0.9 in.) high, 5.7 cm (2.25 in.) wide and 23 cm (9 in.) long. Optical quality glass windows extend from upstream of the centrebody tip to the end of the test section. The angle of each test section wall is adjustable within $\pm 3^\circ$ to compensate for possible displacement thickness effects. The nozzle throat heights are also adjustable to ensure proper use of each centrebody.

The operation of the facility is intermittent, each run lasting typically 1.5 to 2 s. The maximum limit on total pressures is 100 psig. The total temperatures at the beginning of each run are 300 K with a drop of 5 to 10 K occurring during each run due to expansion in the gas cylinders.

2.2 *Schlieren system*

The Schlieren system used is a conventional one with instantaneous or continuous illumination. The knife edge is horizontal and the slit in front of the light source has an adjustable opening for varying the sensitivity of the system.

The instantaneous illumination is provided by a spark source of 20 nanosecond duration (Xenon Corporation Nanolamp Model N-787B). A continuous source with a 100 Watt tungsten halogen lamp (Oriel Model 6322) is used for adjustment. The parallel beam entering the test section has a diameter of 10.1 cm (4 in.). The Schlieren system is stationary but the flow channel can be traversed on rails, to allow photography of all parts of the test section.

2.3 *Pressure and temperature measurement*

Static pressure ports along the test section and total pressure ports are connected to pressure transducers (Setra Systems Model 204) through a Scanivalve system. The output of the transducers is recorded on a Nicolet digital oscilloscope and stored on discs. Two total temperature thermocouples are connected to an electronic thermometer (Omega Model 115 TC) whose output is recorded on a plotter.

2.4 *Control of the experiment*

The starting and stopping of the flow, photography and recording are done automatically with an Intel 8085 microprocessor connected to a system of relays. Each Schlieren picture is accompanied by a record of all relevant pressures and temperatures.

3. **Concept of convective Mach number**

3.1 *Definition of convective Mach number*

In investigating the effects of Mach number on the stability and mixing of compressible shear layers (figure 2) one would like to find parameters which will correlate and unify the results for various flow conditions. In shear layers where $M_2 = 0$, M_1 itself is such a parameter (for given total conditions). However, in shear layers with $M_2 \neq 0$ and $a_2 \neq a_1$ the choice of the right parameters is not clear.

Some insight into the problem can be gained by first treating simple flows, like the unstable temporally developing vortex sheet in compressible flow. In the case of the vortex sheet it is known that the important parameters are

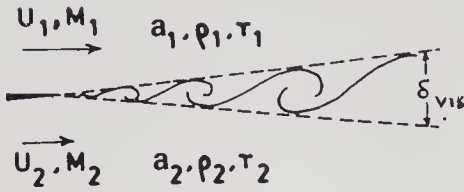


Figure 2. Shear layer nomenclature.

$$M_{c_1} = (U_1 - c_r)/a_1$$

and

$$M_{c_2} = (c_r - U_2)/a_2.$$

where c_r is the real *phase speed* corresponding to neutral ($c_i = 0$) disturbances. The requirement of continuity of pressure at the interface of the two gases is the boundary condition which determines c_r ; using Ackeret's (1927) linearized theory for the pressure perturbations this results in

$$\gamma_1 M_{c_1}^2 / (|M_{c_1}^2 - 1|)^{1/2} = \gamma_2 M_{c_2}^2 / (|M_{c_2}^2 - 1|)^{1/2}. \quad (1)$$

With the definitions of M_{c_1} and M_{c_2} , this equation implies the solution for $c_r = c_r(U_1, U_2, a_1, a_2, \gamma_1, \gamma_2)$ and thus the values of M_{c_1} and M_{c_2} . Since we are only dealing with monatomic and diatomic gases, M_{c_1} and M_{c_2} are equal or very close.

The importance of M_{c_1} as a stability determining parameter arises from the fact that when M_{c_1} exceeds a critical value only neutral disturbances exist and the vortex sheet is stable (Miles 1958).

For turbulent free shear layers a similar approach can be taken by defining

$$M_{c_1} = (U_1 - U_c)/a_1 \quad \text{and} \quad M_{c_2} = (U_c - U_2)/a_2$$

where U_c is now the *convective velocity of dominant waves or structures*. The convective velocity might again be calculated from (1), i.e. by requiring static pressure equality and calculating it in a coordinate system moving with the structures. There are two objections to this: first, we are no longer dealing with a vortex-sheet interface so there is really no way to specify static pressure equality; second, one might prefer not to use linearization as was done for (1). An alternative, related approach has been proposed by several investigators. It was first suggested to us by Dimotakis (private communication, and 1984) and is implicit in Coles (1981) sketches of streamlines in the moving coordinates of the large structures (figure 3). In this coordinate system there is a saddle point between the structures; it is a common stagnation point for both streams, thus implying equality of *total* pressures in the two streams in that system. For equal static pressures this results in

$$\{1 + [(\gamma_1 - 1)/2] M_{c_1}^2\}^{\gamma_1/(\gamma_1 - 1)} = \{1 + [(\gamma_2 - 1)/2] M_{c_2}^2\}^{\gamma_2/(\gamma_2 - 1)}. \quad (2)$$

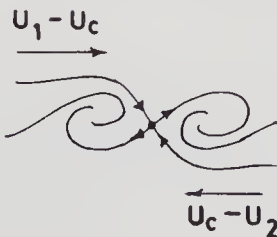


Figure 3. Shear layer structure in convecting reference (after Coles 1981).

This result has been obtained by Bogdanoff (1982) using a slightly different argument. It should also be noted that Oertel (1979, 1982) has obtained excellent experimental evidence supporting the concept of large coherent structures and associated convective velocities in supersonic mixing layers.

For M_{c_1} and M_{c_2} which are not very large, (2) can be approximated by its subsonic version:

$$\frac{1}{2}\rho_1(U_1 - U_c)^2 = \frac{1}{2}\rho_2(U_c - U_2)^2, \quad (3)$$

which gives

$$U_c/U_1 = (1 + rs^{\frac{1}{2}})/(1 + s^{\frac{1}{2}}). \quad (4)$$

Equation (4) together with the definition of convective Mach numbers gives the following relation:

$$M_{c_2} = (\gamma_1/\gamma_2)^{\frac{1}{2}} M_{c_1}, \quad (5)$$

which can also be obtained directly from (1) for small M_{c_1} and M_{c_2} . As for the vortex sheet, $M_{c_1} = M_{c_2}$ when $\gamma_1 = \gamma_2$. From the definition of convective Mach numbers we then get the following expression for U_c :

$$U_c = (a_2u_1 + a_1u_2)/(a_1 + a_2), \quad \text{for } \gamma_2 = \gamma_1, \quad (6)$$

which has the form of a speed-of-sound weighted average.

M_{c_1} and M_{c_2} are slightly different when $\gamma_1 = 7/5$ and $\gamma_2 = 5/3$ or the reverse. Figure 4 shows the dependence of M_{c_1} on M_1 and M_2 for various gas combinations. M_{c_1} has been calculated using its definition and (3) for uniform total temperature. The error that results from using (3) instead of (2) is very small for the range of M_{c_1} plotted on the figure.

3.2 Effect of M_c on stability of vortex sheet

To illustrate the effect of convective Mach number on the stability of a vortex sheet the following simplified argument is presented. In a frame of reference moving with the phase speed c_r (figure 5a) we replace the interface of the two gases with a thin flexible membrane (figures 5b,c). Then the problem reduces to that of flow past a wave-shaped boundary, first treated by Ackeret (1927). For M_{c_1} and M_{c_2} greater than 1, the pressures on both sides of the membrane balance everywhere and thus the membrane is neutrally stable (figure 5b). When at least one of the convective Mach numbers is less than 1, the pressure on both sides of the membrane cannot be balanced and thus the membrane is unstable (figure 5c).

The above argument can be used only descriptively to explain the vortex sheet stability, the analysis being quite different (Miles 1958). The basic result, however, is similar in the sense that there is a convective Mach number beyond which the vortex sheet is neutrally stable. For equal specific heat ratios and speeds of sound, the vortex sheet is stable for $M_{c_1} > 2^{1/2}$.

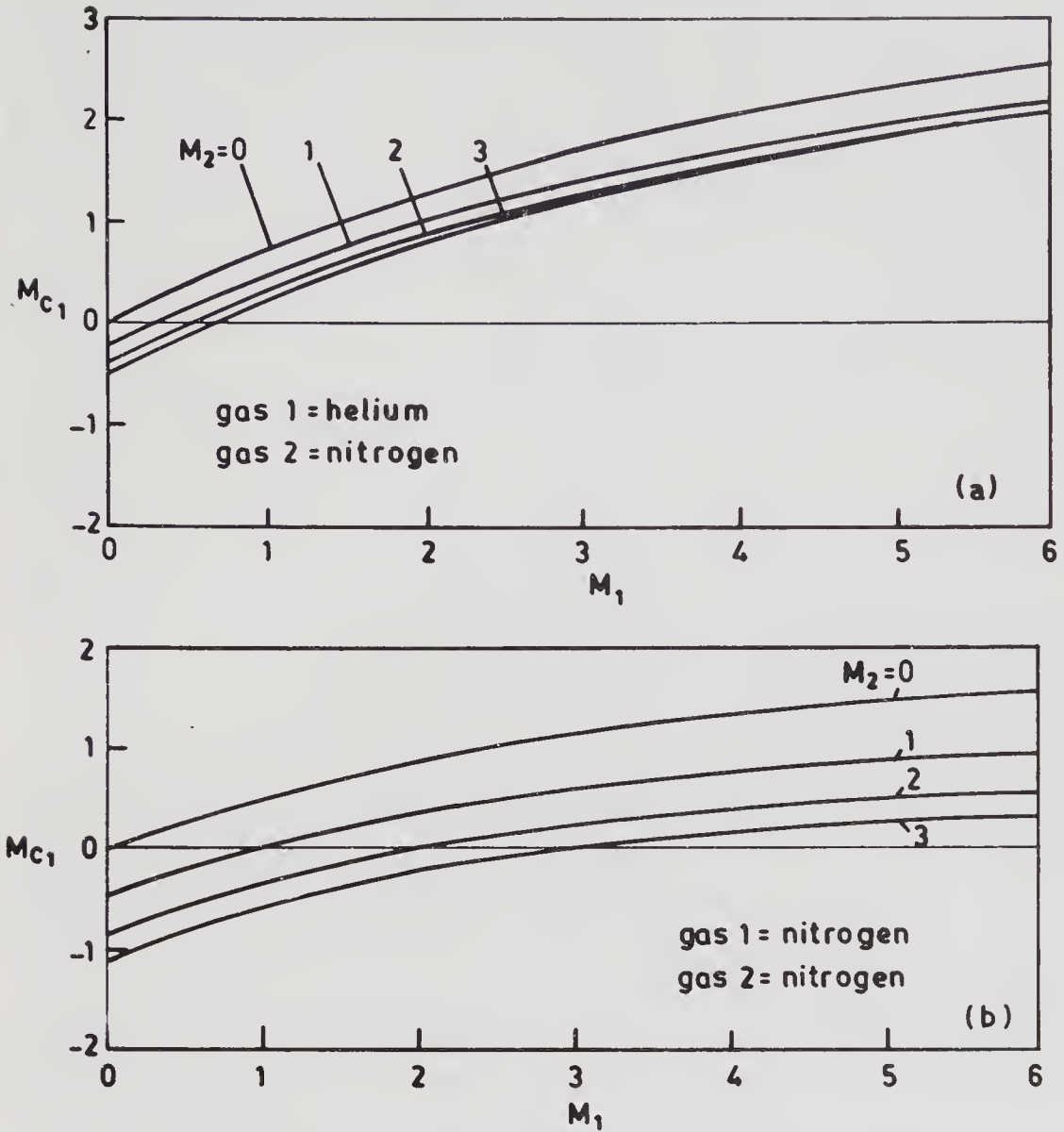


Figure 4. Convective Mach number for N_2 - N_2 and He- N_2 combinations.

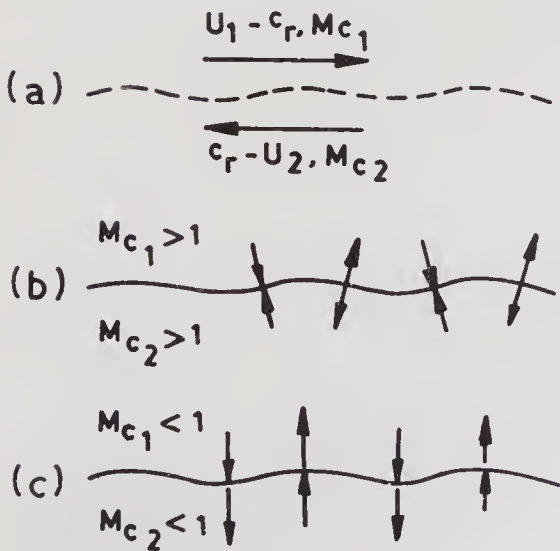


Figure 5. Vortex sheet stability argument.

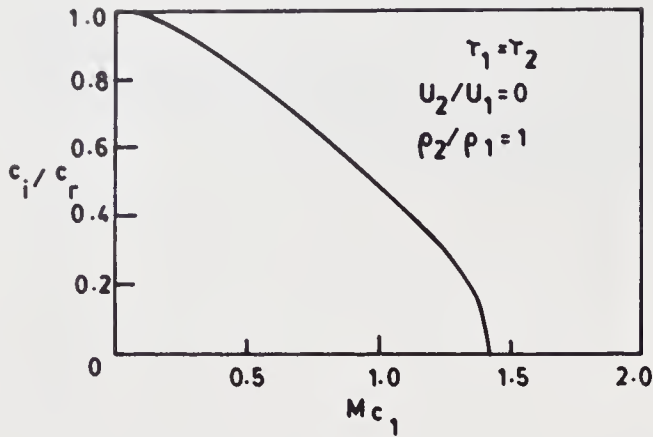


Figure 6. Vortex sheet amplification rate.

The reduction in amplification rate with $M_{c_1} = M_{c_2}$ is shown in figure 6 for $\gamma_1 = \gamma_2$, $r = 0$ and $s = 1$. This is the result of the temporal analysis that has been transformed to the spatial growth rate c_i/c_r , the wavenumber being chosen to be unity. The growth rate is normalized to be 1 at $M_{c_1} = 0$.

3.3 Effect of M_c on shear layers of finite thickness

In the case of the vortex sheet we can always find a set of conditions for which the freestream velocity is supersonic relative to the disturbance velocity. This is not true in shear layers of finite thickness where, no matter how large M_c is, there exists always a flow region where the local velocity is subsonic relative to the disturbance velocity. Disturbances in this region might amplify and lead to turbulent growth of the shear layer. This is reflected in the calculations of Blumen *et al* (1975), where it is shown that there is instability of two-dimensional disturbances at all values of M_c .

Gropengiesser (1970) has computed maximum amplification rates ($-\alpha_i$) for spatially developing compressible shear layers with a Lock velocity profile. One of his results is shown in figure 7 where $-\alpha_i$ is plotted here against M_{c_1} ($= M_{c_2}$) for $\gamma_2 = \gamma_1$, $r = 0$ and $s = 1$ and is normalized to be 1 at $M_{c_1} = 0$. Notable are the drastic decrease of $-\alpha_i$ with increasing M_{c_1} and the flattening of the $-\alpha_i$ versus M_{c_1} curve for $M_{c_1} > 1$.

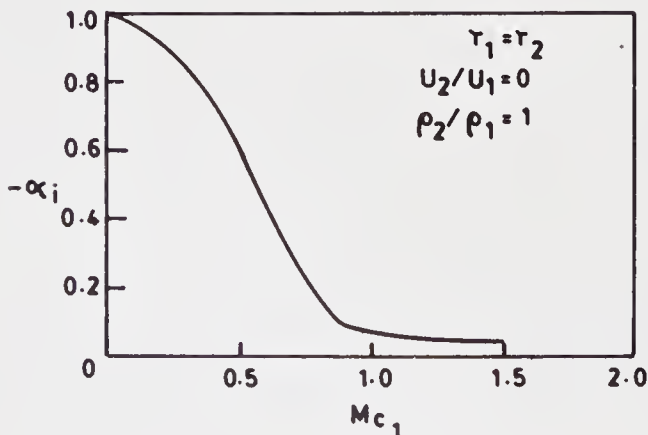


Figure 7. Shear layer amplification rate as computed by Gropengiesser (1970).

4. Results and discussion

4.1 Schlieren photography

Instantaneous Schlieren photographs for a variety of flow conditions are shown in figure 8. Each picture covers a 4-inch length of the test section. Two pictures are shown for each condition, the second one downstream of the first, with a 1/2 inch overlap unless otherwise indicated. The quality of the pictures depends on the refractive index gradients. These gradients decrease as the mixing region thickens, therefore it was usually necessary to increase the Schlieren sensitivity in order to visualize the downstream pictures. Visualization was most difficult for the case with large growth rates and small refractive index differences. It should be noted that due to the low test section pressures the refractive indices are very small and visualization was possible only with the knife edge horizontal.

4.2 Measurement of growth rates

Visual growth rate is measured by drawing straight-line mean tangents to the edges of the shear layer, as done by Roshko & Brown (1974). Considering the smallness of the growth rates and in some cases the uncertainty in defining the edges of the layer, such procedure is subjective and the error may be up to $\pm 20\%$. For each flow condition, the growth rate presented here is the average of those in several pictures at the same condition. In each case the Reynolds number is the highest possible to assure that the flow is fully developed.

4.3 Comparison with incompressible growth rates

In trying to uncouple the effects of M_c from the other flow parameters, we must compare the compressible growth rate to the incompressible one at the same velocity and density ratio. It is important then to establish a relation by which we can accurately estimate the effects of velocity and density ratio on the growth of incompressible shear layers.

In establishing such a relation, we assume that the main effect of density ratio is to determine the convective velocity U_c as given by (4). In a frame of reference moving with U_c the density ratio then drops out of the picture and we arrive at the following relation by dimensional analysis,

$$\delta/x \sim \Delta U/U_c. \quad (7)$$

For visual thickness this becomes,

$$\delta_{\text{vis}}/x = 0.17 \Delta U/U_c = (1-r)(1+s^{\frac{1}{2}})/(1+rs^{\frac{1}{2}}). \quad (8)$$

This relation has been proposed by Bogdanoff (1984) and other similar ones have been proposed by Brown (1974) and Dimotakis (1984). Figure 9 shows that (8) agrees quite well with experimental data.

The effect of M_c can now be shown by forming the ratio δ'/δ'_i , where $\delta' = d\delta/dx$ is the actual growth rate and δ'_i is the incompressible growth rate at the same values of r and s , and plotting it against M . This is done in figure 10 for the growth rates measured in the present experiments. In figure 11, the results of other experiments, in all of which $M_2 = 0$ and both gases are air, are plotted in the same manner.

4.4 Discussion

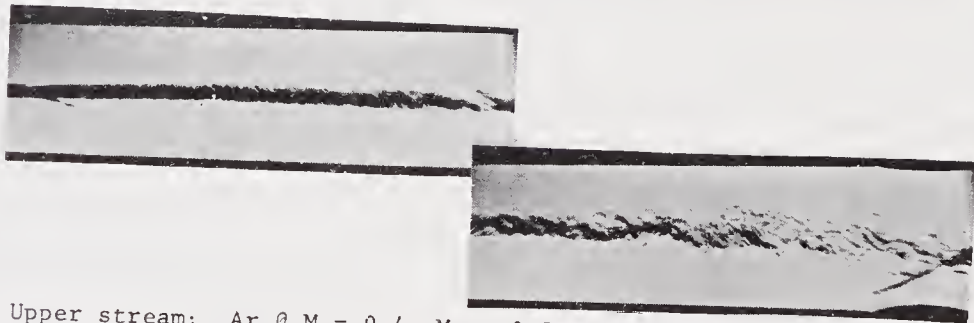
The drastic growth rate reduction with increasing M_c is evident in the experimental results presented here. It is clear that this reduction is not due to density effects, as previously believed, but to the stabilizing effect of M_c . It is worth noting that this



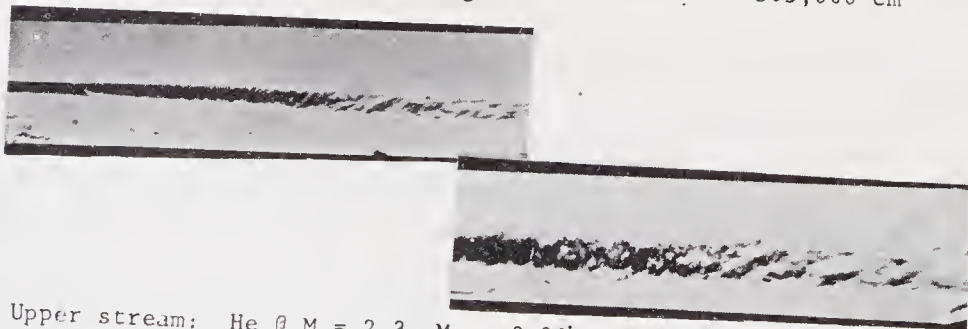
Upper stream: N_2 @ $M = 1.9$ $M_c = 0.30$ Unit $Re = 54,000 \text{ cm}^{-1}$
 Lower stream: N_2 @ $M = 3.3$ $M_c = 0.30$ Unit $Re = 184,000 \text{ cm}^{-1}$



Upper stream: He @ $M = 2.0$ $M_c = 0.77$ Unit $Re = 32,000 \text{ cm}^{-1}$
 Lower stream: N_2 @ $M = 3.3$ $M_c = 0.84$ Unit $Re = 145,000 \text{ cm}^{-1}$



Upper stream: Ar @ $M = 0.4$ $M_c = 0.80$ Unit $Re = 5,000 \text{ cm}^{-1}$
 Lower stream: Ar @ $M = 4.0$ $M_c = 0.80$ Unit $Re = 305,000 \text{ cm}^{-1}$



Upper stream: He @ $M = 2.3$ $M_c = 0.90$ Unit $Re = 33,000 \text{ cm}^{-1}$
 Lower stream: N_2 @ $M = 3.5$ $M_c = 0.99$ Unit $Re = 135,000 \text{ cm}^{-1}$

Figure 8 (For caption see facing page.)

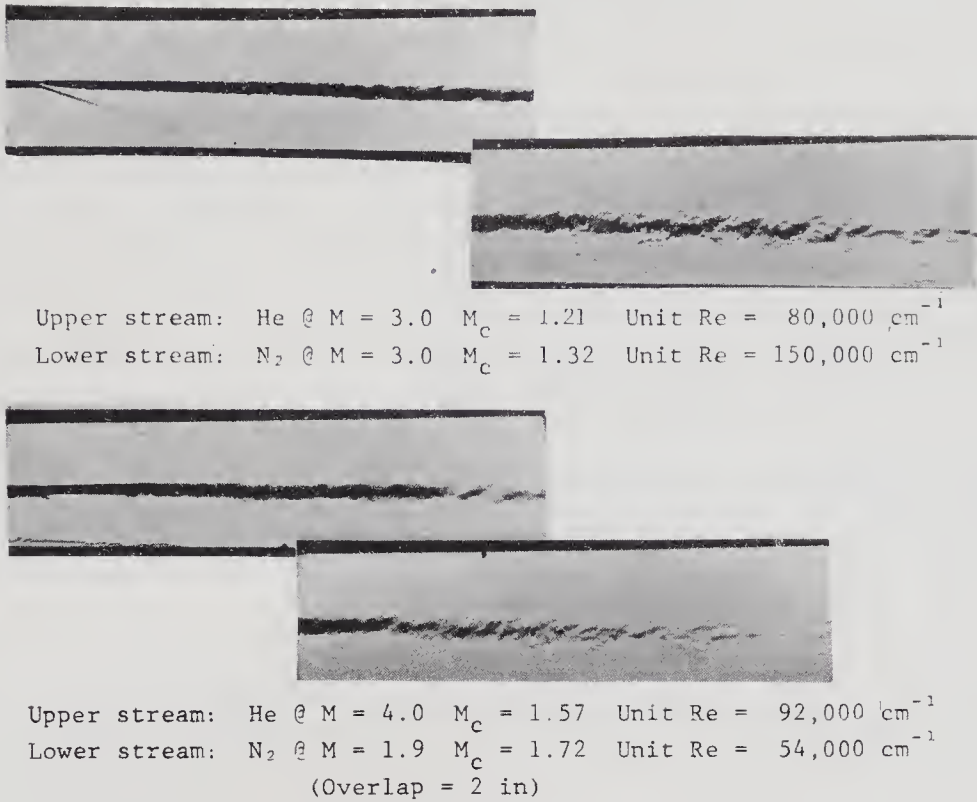


Figure 8. Schlieren photographs for a variety of flow conditions.

reduction levels off as M_c exceeds 1, something that appears in the present results and in those of other experiments. The amplification rates computed by Gropengiesser (1970) have the same trends as the experimental results for growth rates.

In the present experiments, the growth rate reduction for $M_c > 1$ ($\approx 75\%$) is considerably larger than that in the other experiments ($\approx 50\%$). One explanation for this difference may be the fact that in the other experiments with $M_2 = 0$ upstream propagation of disturbances is possible. Such upstream coupling might enhance the growth rate; it would also tend to be facility dependent. More likely, the difference may also arise from the fact that in the present experiment the

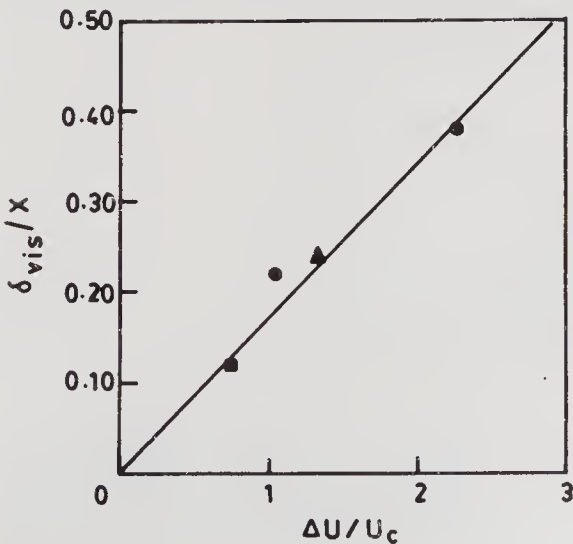


Figure 9. Visual thickness of incompressible shear layer. ● and ■ data points from Roshko & Brown (1974) for $s = 7$ and $s = 1/7$, respectively; ▲ from Dimotakis & Brown (1976) ($s = 1$).

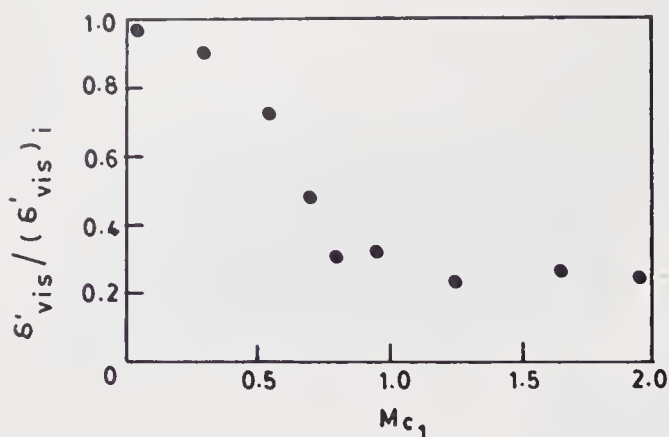


Figure 10. Present experimental values of visual thickness.

comparison is based on *visual* thickness measured from photographs, while in the other experiments it is the *vorticity* thickness, δ_ω , based on mean velocity profiles, which is compared. The ratio $\delta_{vis}/\delta_\omega$ may be a function of M_c ; the above results would then suggest that this ratio decreases for $M_c > 1$.

In forming the ratio δ'/δ'_i we hope to have uncoupled the effects of M_c from those of r and s . While this may be true to first order, the effectiveness of M_c in reducing the growth rate may still depend on r and s . Furthermore, all the above discussion of shear layer instability has been limited to two-dimensional disturbances. It has been pointed out by several investigators (Lessen *et al* 1965, for example) that three-dimensional (oblique) disturbances can exist in supersonic shear layers. The effect of oblique waves on the vortex sheet stability can be accounted for by replacing M_c by an effective convective Mach number $M_c \cos \theta$ where θ is the angle between wave propagation and flow direction. Bogdanoff (1982) suggests that the above transformation can be used to determine an effective M_c in shear layers of finite thickness. We therefore expect the shear layer to become more unstable with increased obliquity of the disturbances. The current experimental set-up was not suitable for observing the possible presence of oblique waves in the flow, so nothing definite can be said about their effect on the present results. The consistent inhibition of growth rate for $M_c > 1$ may indicate that if there exist three-dimensional waves, their obliquity is small.

With our present limited measurements the results are suggestive rather than definitive. To improve this, we are planning to measure Pitot-pressure and total-temperature profiles across the shear layer.

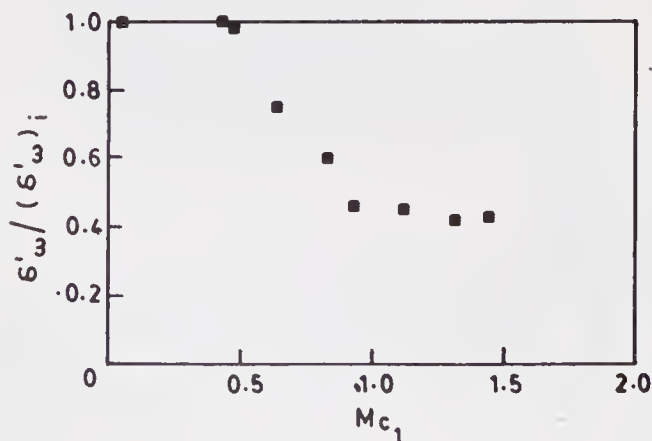


Figure 11. Experimental values of vorticity thickness obtained by other investigators as compiled in figure 1 of Bogdanoff (1982).

5. Concluding remarks

The good correlation of experimentally obtained growth rates with M_c at a variety of Mach numbers, density ratios and velocity ratios supports the idea that the convective Mach number is useful as a compressibility-effect parameter. It is found that the compressibility effect becomes significant at about $M_c = 0.5$, increasing rapidly, then tending to level off for $M_c > 1$. The compressibility effect on turbulent growth rate is mainly an effect on the stability of the flow, rather than a density effect, as indicated by the corresponding effect on amplification rates of waves in vortex sheets or laminar free shear layers. The overall reduction in growth rate for $M_c > 1$ is by a factor of about 2 for vorticity thickness and about 4 for visual thickness. Thus the ratio of visual thickness/vorticity thickness appears to decrease by about a factor of 2. More work is needed to refine these results and, especially, to establish quantitatively how mixing rates (molecular, chemical) decrease with increasing M_c .

This work is being supported by a research grant from the Rockwell International Corporation Trust.

List of symbols

a	speed of sound;
$c = c_r + ic_i$	complex disturbance wave speed;
M	Mach number;
M_c	convective Mach number;
r	velocity ratio U_2/U_1 ;
s	density ratio ρ_2/ρ_1 ;
Re	Reynolds number;
U, U_c	freestream and convective velocities, respectively;
x	streamwise distance from shear layer origin;
$\alpha = \alpha_r + i\alpha_i$	complex disturbance wave numbers;
γ	ratio of specific heats;
δ	shear layer thickness (unspecified);
δ'	$d\delta/dx$;
$\delta_{vis}, \delta_\omega$	shear layer visual and vorticity thicknesses, respectively;
θ	oblique wave angle;
ρ	density;
$()_1$	fast-stream properties;
$()_2$	slow-stream properties;
$()_i$	incompressible value at same r and s .

References

- Blumen W, Drazin P G, Billings D F 1975 *J. Fluid Mech.* 71: 305–316
 Bogdanoff D W 1982 *AIAA J.* 21: 926–927

- Bogdanoff D W 1984 *AIAA J.* 22: 1550–1555
- Brown G L 1974 *Fifth Australasian conference on hydraulics and fluid mechanics* (New Zealand: Christchurch) pp. 352–359
- Coles D 1981 *Proc. Indian Acad. Sci. (Eng. Sci.)* 4: 111–127
- Demetriades A, Bower T L 1982 Experimental study of transition in a compressible free shear layer, AFOSR-TR No. 83-0144
- Dimotakis P E 1984 Entrainment into a fully developed, two-dimensional shear layer, AIAA-84-0368
- Dimotakis P E, Brown G L 1976 *J. Fluid Mech.* 78: 535–560
- Gropengiesser H 1970 Study of the stability of boundary layers and compressible fluids, NASA TT-F-12,786
- Lessen M, Fox J A, Zien H M 1965 *J. Fluid Mech.* 23: 355–367
- Miles J W 1958 *J. Fluid Mech.* 4: 538–552
- Oertel H 1979 *Proc. 12th Int. Symp. of Shock Tubes and Waves, Jerusalem* pp. 266–275
- Oertel H 1982 Structure of complex turbulent shear flow, *IUTAM Symp. Marseille*
- Ortwerth P J, Shine A J 1977 On the scaling of plane turbulent shear layers, AFWL-TR-77-118
- Roshko A, Brown G L 1971 The effect of density difference on the turbulent mixing layer, AGARD CP-93
- Roshko A, Brown G L 1974 *J. Fluid Mech.* 64: 775–781
- Sanderson R J, Steel P C 1970 Results of experimental and analytical investigations in compressible turbulent mixing, Martin Marietta, R-70-48638-003

Visualization and analysis of longitudinal vortices at curved walls of 2D laminar and turbulent channel flows

ZHANG ZHAOSHUN and WANG XILIN

Department of Engineering Mechanics, Tsinghua University, Beijing, China

Abstract. The three-dimensional structure of longitudinal vortices at the curved walls of both laminar and turbulent channel flows is visualized by the hydrogen bubble technique. Together with the conditional sampling of the turbulent characteristics at the wall processed by the VITA method the dynamics of the near-wall structure is discussed.

Keywords. Turbulent shear flow; turbulent structure; vortex; flow visualization.

1. Introduction

The longitudinal vortices at the wall of a plate boundary layer flow are regarded as a crucial event leading to production of turbulence in both transitional and turbulent regimes (Wortmann 1977; Cantwell 1981). The near-wall structure in curved wall shear flows has been emphasized recently (Johnston 1982; Winoto 1983; Zhang & Wang 1985). However, it is necessary to combine the three-dimensional view of the flow patterns with the conditional sampling of the turbulent properties in order to understand the structure in detail. In addition, to explore the coherency and the dynamics of the longitudinal vortices it is worthwhile investigating the phenomena in a wide range of Reynolds numbers from 170 to 10,000, i.e., in both transitional and fully turbulent regimes.

2. Apparatus and tests

The experiments were carried out in a closed plexiglass rectangular duct composed of a ten-metre long straight channel and a curved part with a cross-section of $400 \times 30 \text{ mm}^2$. Pure water was used as working medium, and the flow patterns were visualized by the hydrogen bubble technique with a laser light sheet. The distribution of the bubble wires and the lighting planes are illustrated in figure 1. The two-dimensionality of the flows in the channel with high aspect ratio was satisfactorily checked by bubble line at the entrance of the curved channel, as shown in figure 2.

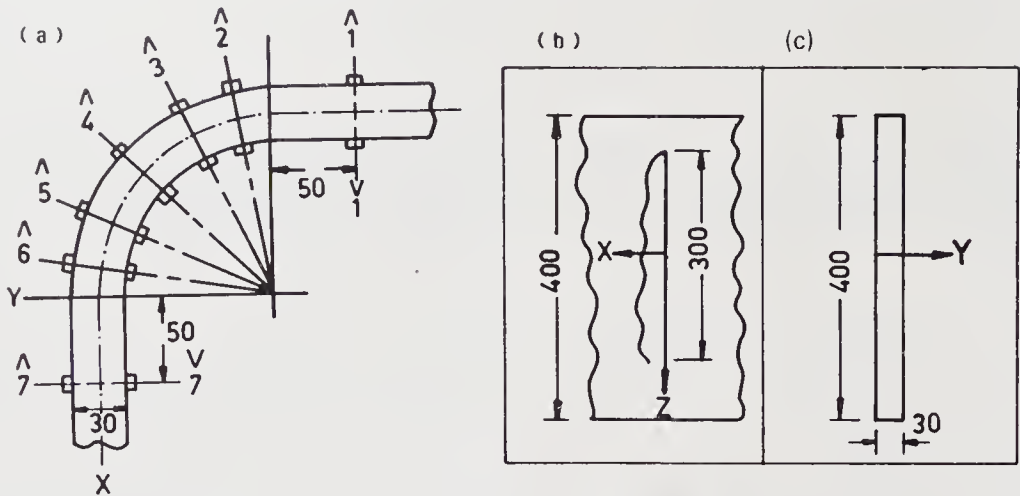


Figure 1. Distribution of the bubble wires, (a) top view, (b) side view, (c) cross view.

The flow velocity in the channel was measured by LDV and checked by hot film anemometer. The logarithm profiles were obtained at Reynolds numbers higher than 2300, defined by Uh/ν , where U is the averaged velocity over the channel section, h its half width and ν the kinetic viscosity of pure water. The friction velocity of the fully developed turbulent flows were then evaluated from the logarithm profiles. Some results are listed in table 1.

The turbulent properties near the wall were measured by the hot film anemometer with a boundary layer type probe, which was calibrated every ten minutes at a fixed location in the channel. The output signals of the CTA were digitized and collected by an Apple II plus mini-computer through an AD/DA converter and then processed by the VITA method.

3. Visualized results

Figure 3 shows the three-dimensional view of the streak structure at both concave and convex walls of the turbulent channel flows at $Re = 5,000$.

Figures 4 and 5 illustrate similar flow patterns on $Y-Z$ and $X-Y$ planes at Reynolds numbers 2,300 and 10,000 respectively.

The development of the spanwise disturbances to longitudinal vortices in laminar curved channel flows at $Re = 170,660$ is shown in figure 6 in side view, which clearly demonstrates the features of the vortices, so that the views on other planes are omitted.

These pictures in figure 6 show that the longitudinal vortices are regular in laminar cases but irregular, much stronger and break up quickly in turbulent cases.

Table 1. The friction velocity u^+ (cm/s).

Re	flat wall	concave wall 45°	convex wall 45°
2300	0.83	0.76	0.96
5000	1.72	1.61	1.90

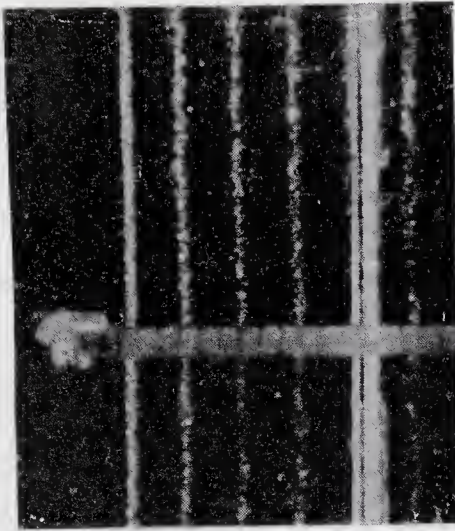


Figure 2. Bubble lines at the entrance.

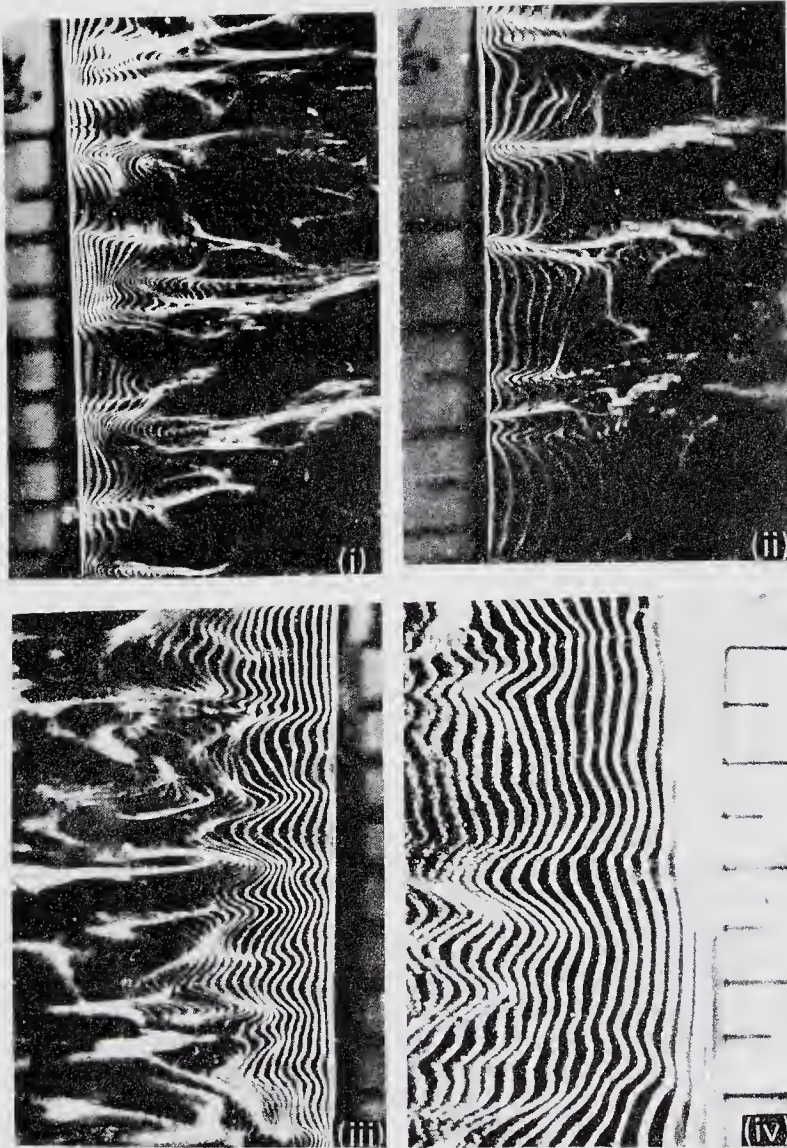


Figure 3 (a). Side view, i.e., on X - Z plane, $Y^+ = 5$, $Re = 5000$ (i) wire 2, concave; (ii) wire 5, concave; (iii) wire 2, convex; (iv) wire 5, convex.



Figure 3(b). Cross view, i.e., on Y - Z plane, $Y^+ = 5$, $Re = 5000$ (i) wire 2, concave; (ii) wire 5, concave; (iii) wire 2, convex; (iv) wire 5, convex.



Figure 3(c). (Below) Development of the spanwise vortices on X - Y plane. (i) top view, $Re = 5000$; (ii) top view, downstream of (i)



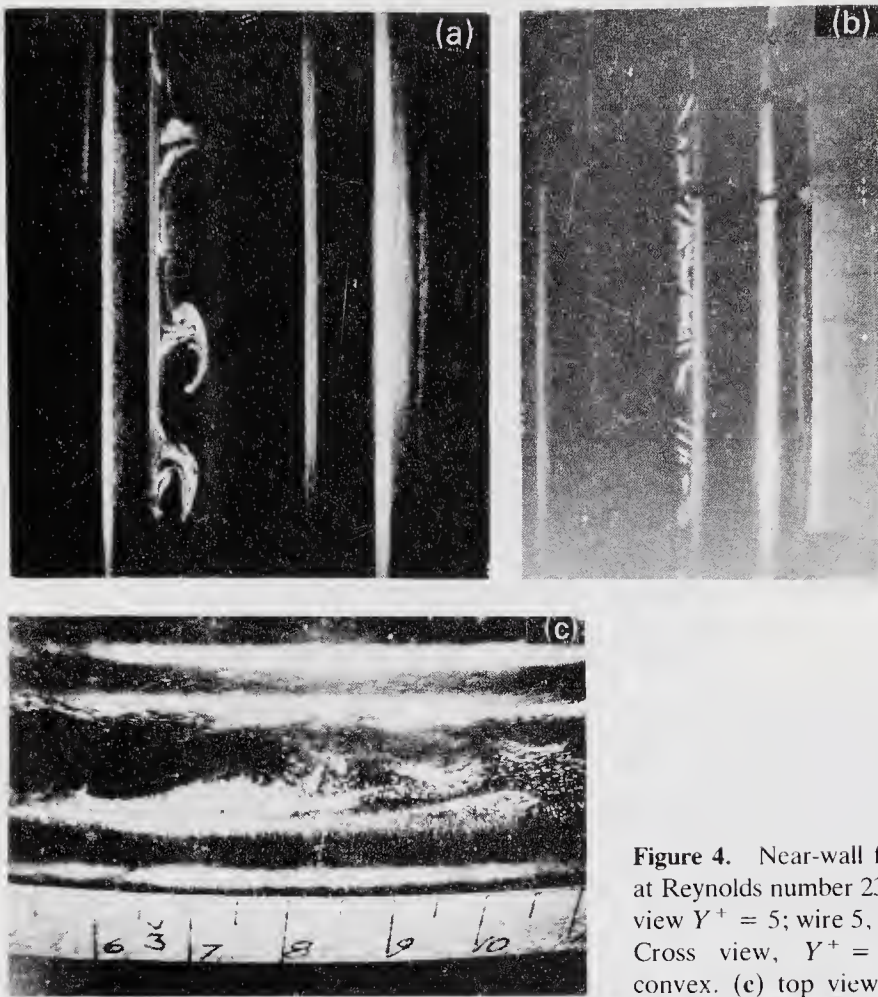


Figure 4. Near-wall flow patterns at Reynolds number 2300. (a) cross view $Y^+ = 5$; wire 5, concave. (b) Cross view, $Y^+ = 5$; wire 5, convex. (c) top view.

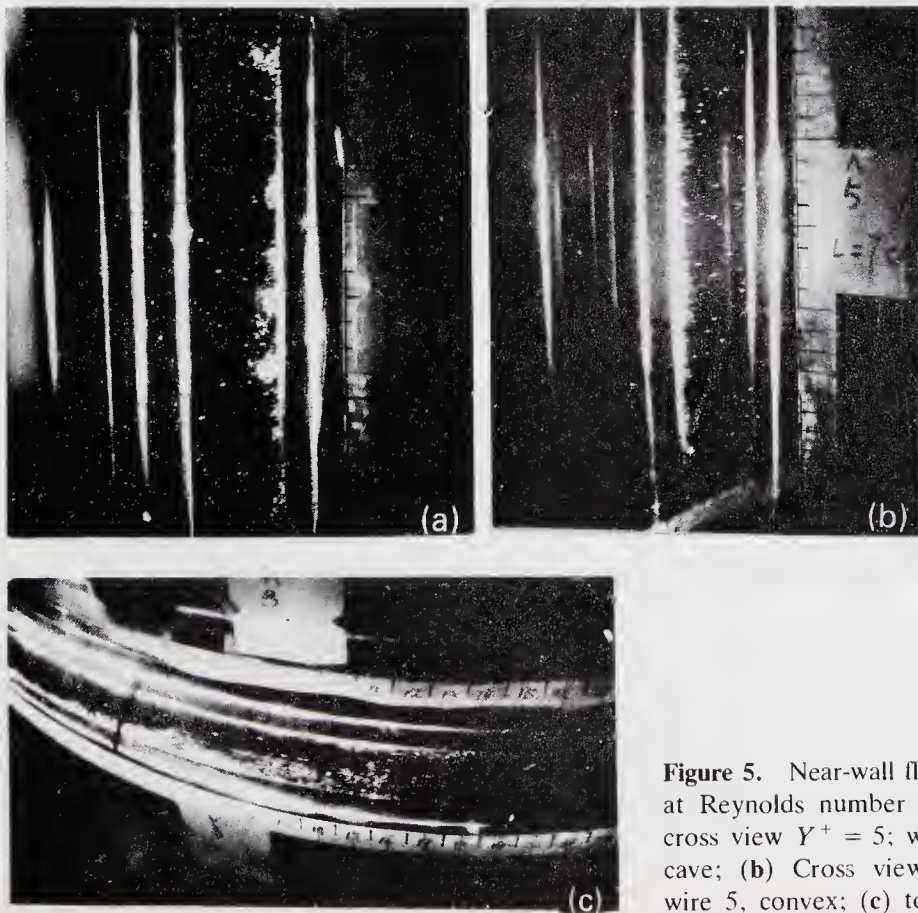


Figure 5. Near-wall flow patterns at Reynolds number 10,000. (a) cross view $Y^+ = 5$; wire 5, concave; (b) Cross view, $Y^+ = 5$, wire 5, convex; (c) top view.

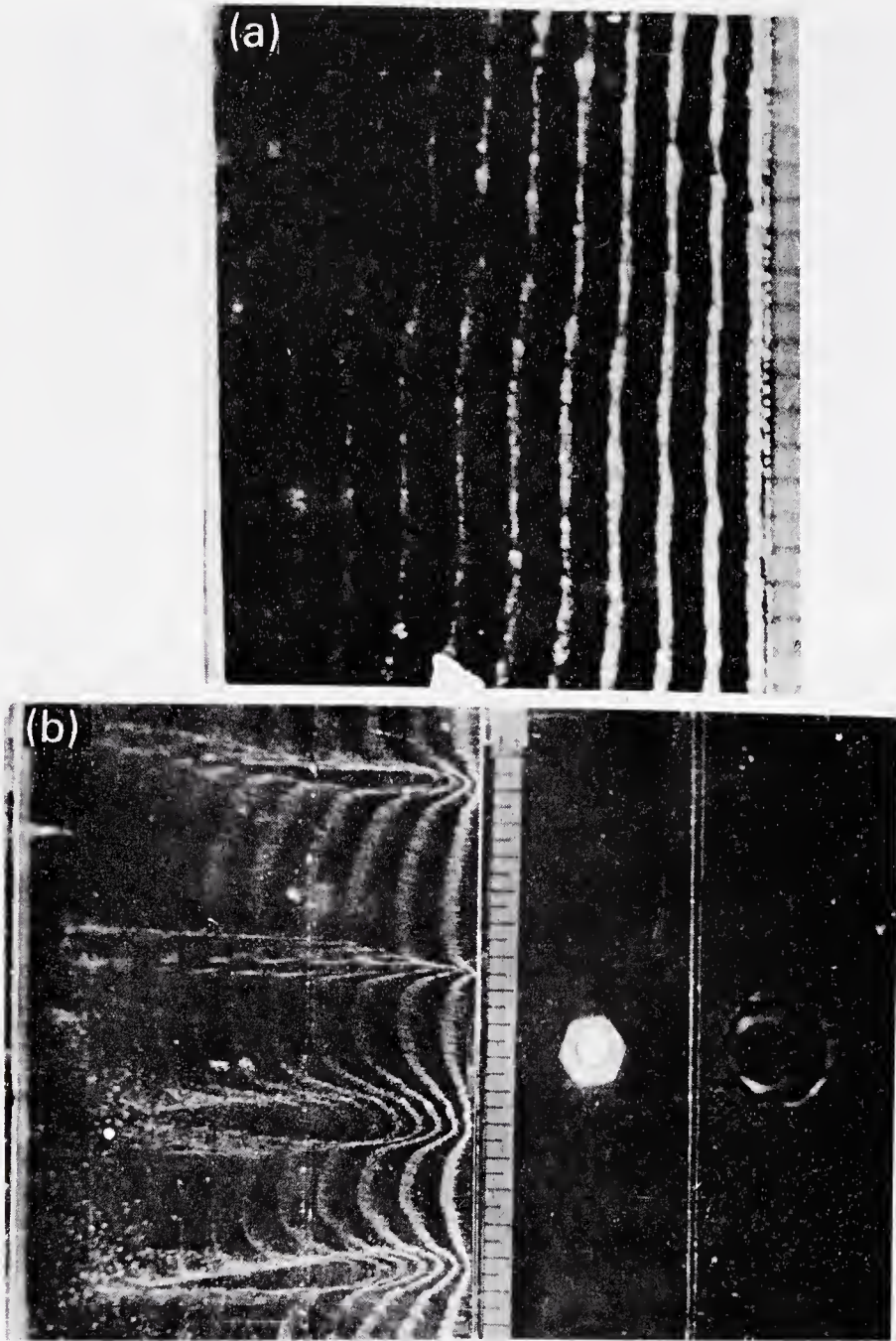


Figure 6. Development of the longitudinal vortices at a concave wall, (a) wire 3, $Re = 170$, $Y = 2$ mm; (b) wire 3, $Re = 660$, $Y = 2$ mm.

4. Conditional sampling

The conditional average of the longitudinal velocity was obtained by the VITA method from three thousand sets of data sampled in 27 seconds for each test run. Figure 7 shows the apparent rapid acceleration following a deceleration, which is considered an ejection and sweep cycle and a signal for the breakdown, or a burst. Figure 7a shows the comparison of the conditional averages at different threshold levels, it indicates that $k = 1.0$ is satisfactory as suggested by Blackwelder & Haritonidis (1983). Figure 7b shows that the burst feature is independent of the

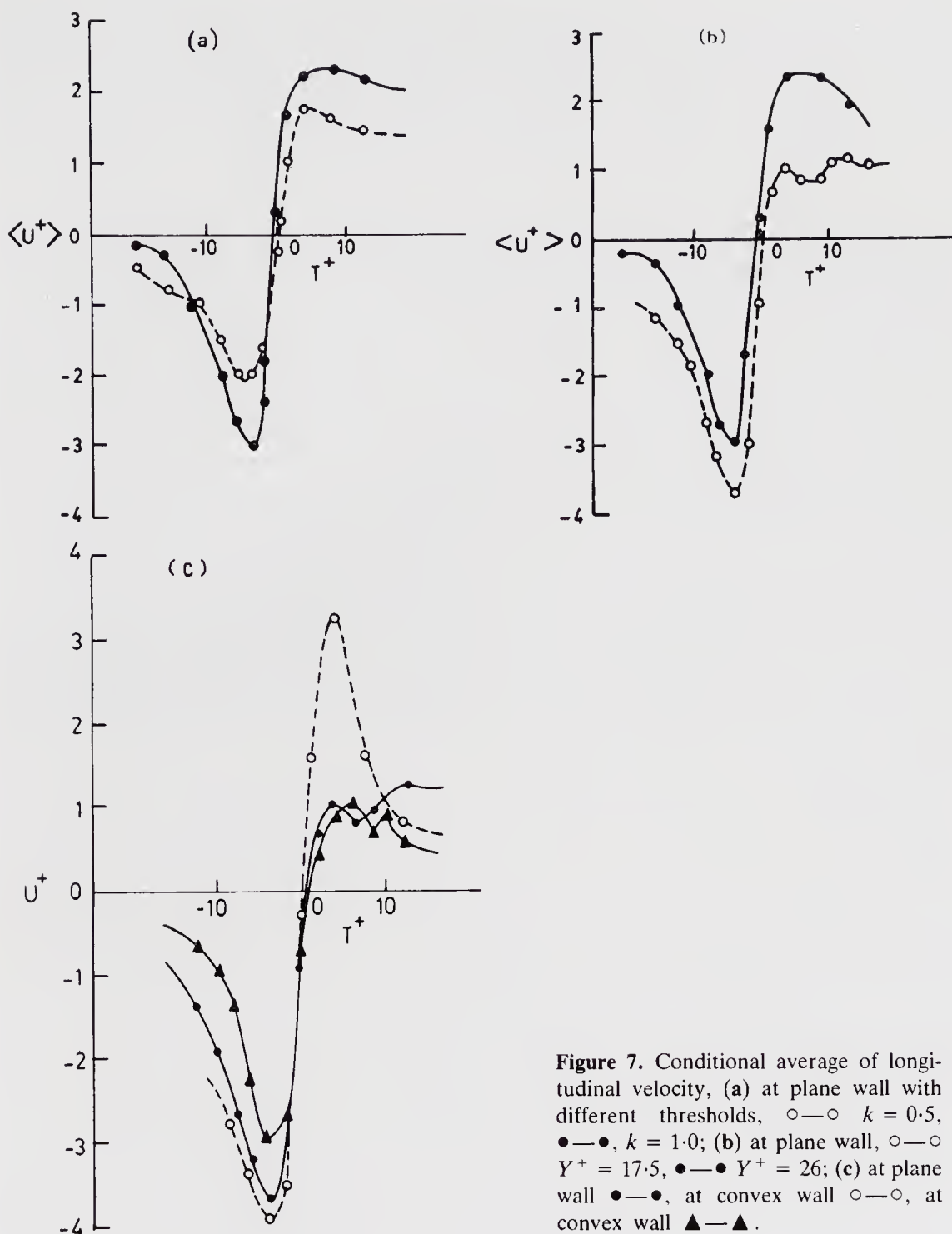


Figure 7. Conditional average of longitudinal velocity, (a) at plane wall with different thresholds, $\circ-\circ$ $k = 0.5$, $\bullet-\bullet$, $k = 1.0$; (b) at plane wall, $\circ-\circ$ $Y^+ = 17.5$, $\bullet-\bullet$ $Y^+ = 26$; (c) at plane wall $\bullet-\bullet$, at convex wall $\circ-\circ$, at convex wall $\blacktriangle-\blacktriangle$.

distance from the wall in the inner layer. Figure 5c compares the bursting behaviour between curved and plane walls. We can see the most rapid acceleration occurring at the concave wall and the lowest at the convex wall. This is consistent with the visualized results and previous measurements (So & Mellor 1972).

Counting the number of peaks exceeding an appropriate threshold level in the sampling interval we have obtained the average period between two successive bursts. Table 2 shows that the bursts occur most frequently at the concave wall and seldom at the convex wall. The results at the plane wall are in good agreement with

Table 2. Average periods between bursts $T^+ = T(u^+)^2/\nu$.

Re	Plane	Concave	Convex	Plane (empirical)
2300	220–287	140–150	280–430	300
5000	287	182	399	300

the empirical formulae proposed by Blackwelder & Haritonidis (1983), thus confirming the reliability of our measurements.

5. Analysis and discussion

5.1 The evolution of the longitudinal vortices

In laminar regime the longitudinal vortices originate from the spanwise disturbances when the Reynolds number exceeds the linear critical value. We have made a linear analysis of the spatial growth of the spanwise disturbances, and the predicted dominant streamwise wavelength is in good agreement with the visualized results as shown in figure 8. While the Reynolds numbers are increasing the regular vortices move about, and there appears unsteadiness of the disturbances, which was explained by some authors as the environmental influence (e.g. Winoto 1983, p. 767). However, we believe that the unsteadiness is an inherent property of the

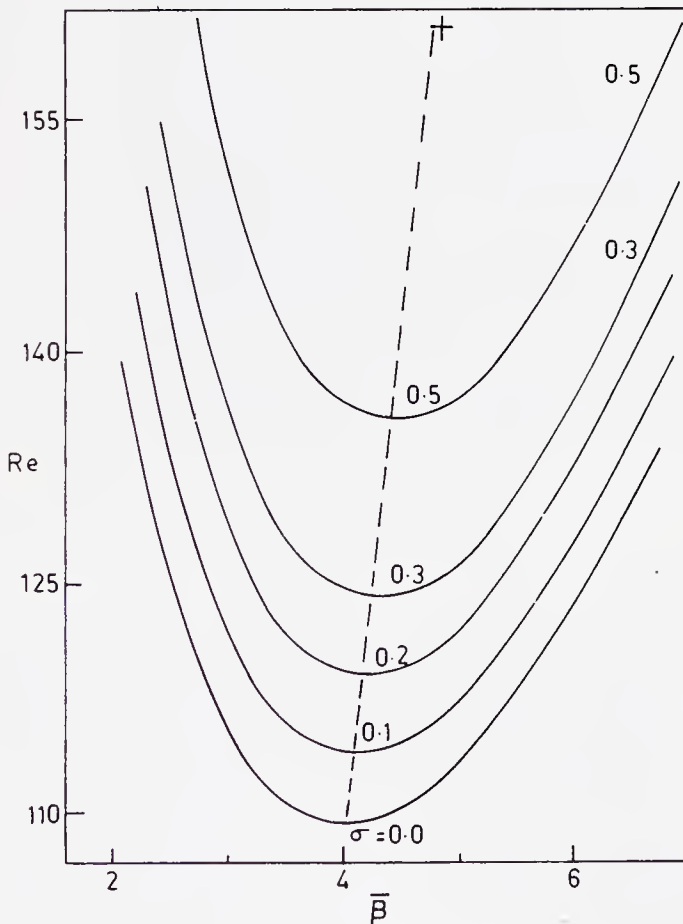


Figure 8. ---- Most unstable modes; + visualized spacing of vortices.

non-linear development of finite disturbances, for instance, the secondary instability might lead to an aperiodic time-dependent disturbance. Finally the longitudinal vortices emerge randomly, presumably as a result of a series of non-linear interactions, meanwhile the vortices are confined at the wall region with narrower spacing and feature as streaks.

5.2 *The Reynolds number effects*

The mean velocity and the channel width are the characteristic quantities for the laminar disturbances, whereas the nondimensional parameters of the turbulent streaks are scaled on the wall units. This implies that the laminar disturbances are initiated by centrifugal instability, but the turbulent streaks are generated by the secondary instability of the wall layer with high shear rates (Zhang & Lilley 1982, p. 60). The nondimensional spacing of turbulent streaks and the frequency of the bursts are almost independent of the Reynolds numbers, therefore the turbulence intensity and Reynolds stress are greater at higher Reynolds number.

5.3 *The curvature effects*

The turbulent flow structure at the concave walls has great resemblance to that at the plate wall except for the smaller spacing and higher bursting frequencies. For instance, the spanwise spacing of streaks is about 80 wall units on the average at the concave walls from Reynolds numbers 2300 to 10,000 and it is 88 at the wall of the straight channel in the same Reynolds number range. The mean period between bursts equals 287 wall units at the plate wall but is 181 at the concave wall at $Re = 5000$. It is expected that the positive curvature of the wall, i.e., the concave wall, has a destabilization effect and thus intensifies turbulence. In contrast, the spanwise disturbances are suppressed usually at the convex wall in both laminar and turbulent cases. Nevertheless the bursts still occur at the convex wall with one half of frequency in the turbulent curved channel, see table 2. We believe that the bursts at the convex wall are induced by the influence of the opposite concave wall, as we can see the lump-like bursts embedded in a nearly undisturbed wall flow in side view, e.g. figure 3a (iii), (iv). Moreover the mean spacing of these lump-like bursts is the same as that of streaks at the concave wall. The half frequency of the bursts at the convex wall seems to contradict the direct influence from the bursts at the concave wall. It may be explained as follows, that the parts of the upstream bursts at the concave walls have a strong enough influence on the convex wall layer to initiate a new burst there. The influence of the concave wall on the convex wall makes great difference between curved channel and boundary layer flows, for instance, the relaminarization at the convex boundary layer flows may not be true at the convex wall of a turbulent channel flow, in particular with small relative curvature, $2h/R$, where R is the radius of the channel central line.

6. Concluding remarks

Our experiment is limited to the Reynolds numbers below 10,000 and at moderate curvature ($2h/r_1 = 0.161$), where r_1 is the radius of the convex wall. However a number of points can be summed up which might be helpful in understanding the

nature of the complex wall shear flows and in casting a reasonable model.

1. The near-wall turbulent structure at the concave wall is similar to but stronger than that at the plane wall, and the mechanism of generating turbulence in the wall region presumably has the same dynamics for both.
2. The centrifugal instability analysis is valid for predicting the wave characteristics of the spanwise disturbances and the regular longitudinal vortices in laminar curved channel flows not very far from the critical Reynolds number, and it is unacceptable to the streak structure of turbulent curved flows.
3. There are neither longitudinal vortices nor streaks at the convex wall, but there still exist bursts, so that the generation mechanism of turbulence has to be reconsidered. In channel flows the turbulence at the convex wall is induced by the opposite wall turbulent flows.

Our results indicate that the longitudinal vortices are the governing structure leading to the production of turbulence in the near-wall region at both plate and concave surfaces, however, further exploration of the vortex structure in detail is necessary for rational modelling of the curved wall shear flow. Some authors have suggested a closure scheme based on the quasi-ordered longitudinal vortices at the plate wall turbulent flows with encouraging satisfaction (e.g. Bernard 1982), and we are also making progress in this direction.

The authors are very grateful to the Science Fund of the Chinese Academy of Science for financial support to the research project. Many thanks to the staff and students at the fluid dynamics laboratory of Tsinghua University for their helpful cooperation.

List of symbols

R	radius of the channel central line;
Re	Reynolds number defined by Uh/ν ;
T	mean period between two successive bursts;
T^+	nondimensional T scaled on wall units;
U	mean longitudinal velocity over the channel;
U^+	nondimensional U scaled on the wall units;
$\langle U^+ \rangle$	conditional average of U^+ ;
X	streamwise direction;
Y	transverse direction and normal distance to the wall;
Y^+	nondimensional distance to the wall scaled on the wall units;
Z	spanwise direction;
h	half width of the channel;
k	threshold level;
r_1	radius of the convex wall;
u^+	friction velocity;
β	spanwise wave number;
$\bar{\beta}$	nondimensional spanwise wave number based on h ;
ν	kinetic viscosity of pure water;
σ	spatial growth rate of linear unstable modes.

References

- Bernard P S 1982 *SIAM J. Appl. Math.* 42: 453-467
Blackwelder R F, Haritonidis J H 1983 *J. Fluid Mech.* 132: 87-103
Blackwelder R F, Kaplan, R. E. 1976 *J. Fluid Mech.* 76: 89-112
Cantwell, B. J. 1981 *Annu. Rev. Fluid Mech.* 13: 457-515
Johnston J P, 1982 Rep. MD-40 Thermosciences Div. Stanford Univ.
So R M C, Mellor G L 1972 NASA CR-1940
Winoto S H 1983 *Proc. of 2nd Asian Congress of Fluid Mech.* (Beijing: Science Press) p. 767
Wortmann F X 1977 AGARD CP244
Zhang Z, Lilley G M 1982 *Turbulent shear flows* (Berlin: Springer-Verlag) vol. 3
Zhang Z, Wang X 1985 Proc. of Int. Symp. on Refined Modeling of Turbulence and Measurements.
Iowa, USA, I-12

Recombination of two vortex filaments and jet noise

RYUJI TAKAKI¹ and A K M FAZLE HUSSAIN²

¹Tokyo University of Agriculture and Technology, Fuchu, Tokyo 183, Japan

²Department of Mechanical Engineering, University of Houston, Houston, Texas 77004, USA

Abstract. The recombination of two vortex filaments in a viscous incompressible fluid is analysed by the use of the vorticity equation. The analysis is confined to a local flow field, where the recombination process occurs, and is based on several assumptions, such as the conservation of the fluid impulse, spatial symmetry of the flow field etc. The flow field is expanded as polynomials of coordinates, and variations of their coefficients are obtained by the use of the vorticity equation. It is proved that the process is completed within a short time of $O(\sigma^2/\Gamma)$ and the viscous effect is essential; σ and Γ are the size and the circulation of the vortex filaments, respectively. This result is applied to predict the far-field noise of a circular jet by assuming that the main noise source is the recombination process in deformed vortex rings in the jet near field. The predicted noise intensity shows the U dependence and has an additional new factor $(d/\sigma)^6$; U is the jet velocity and d is the average spacing between vortex rings.

Keywords. Vortex filament; recombination; viscous effect; jet noise.

1. Introduction

There are certain types of vortex interactions, where vortices approach each other and undergo strong interactions. In the two-dimensional case, the vortex merger is the well-known example and has been studied both experimentally and theoretically (see Aref 1983). In this case the vorticity field is approximated by a cloud of point vortices, and the viscous effect is to cause vorticity diffusion; this effect, however, is not strong compared with that due to mutual induction.

A strong interaction in the three-dimensional case is the recombination of two vortex filaments as observed by several authors: Hama (1960), Crow (1970), Kambe & Takao (1971), Fohl & Turner (1975) and Oshima & Asaka (1977). This occurs in the following way. When local parts of two filaments approach each other, they are cut and then connected in a very short time after being switched,

i.e., the vortex filaments are cross-linked. The term “cut-and-connect” is also used in this paper to indicate this process. Except for an analysis of MHD flow by Yeh & Axford (1970), the cut-and-connect mechanism has not been studied theoretically and remains a major challenge for theoretists as Saffman (1981) points out. Very little progress has been made in analysing this process theoretically because of inherent complexities. First, both the inertia and the viscous effect play equally important roles. Second, the fluid motion varies rapidly in essentially three-dimensional manner.

The purpose of the present paper is to analyse this flow field with an idealized model. The analytical approach is motivated by our claim that this process is one of the main aspects of the development of three-dimensional turbulence during transition, and that the mixing and noise production in the near field of a jet results primarily from the breakdown of initial toroidal structures (Hussain 1983), where the cut-and-connect is considered to be a key mechanism. Although the vortex merger is suggested by Ffowcs Williams & Kempton (1978) and Kibens (1980) as a key mechanism for jet noise, there are also several experimental facts contradicting this assumption (see Hussain 1983).

In this paper an approximate solution of a vortex motion representing the cut-and-connect process is developed based upon the vorticity equation with the viscous term retained. Since no established method of solution is available, we proceed in a heuristic way, with several guiding principles, viz., conservation of fluid impulse, symmetry properties of flow field and polynomial expansion of velocity and vorticity fields. The result is then applied to prediction of jet noise.

2. Analysis of the flow field

2.1 Basic assumptions

Consider that two vortex filaments with the same strength but with opposite senses of rotation approach each other. Then, parts of the filaments close to each other will deform strongly and are pushed upwards as shown in figure 1a. After a recombination process the new filaments are arranged as shown in figure 1b, and the adjacent parts move downwards. It is reasonable to assume that this cut-and-connect process is confined to a local part of the filaments and that the

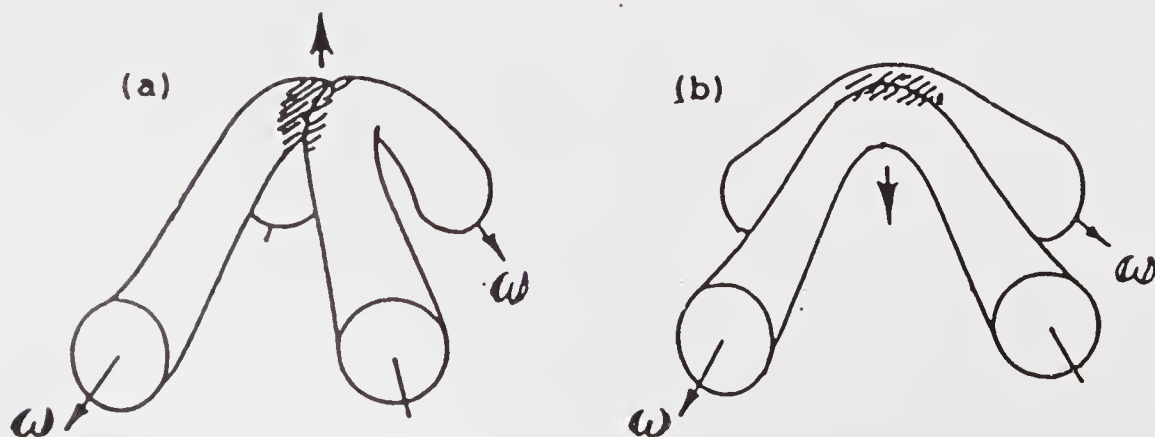


Figure 1. Vortex configurations (a) before, and (b) after, the cut-and-connect process.

distant parts remain unaffected for a short time during the interaction. This local fluid region is called an interaction region.

Now, we consider the change of the fluid impulse between the initial and the final states. The impulse is defined as

$$P = \frac{1}{2} \rho \int \mathbf{r} \times \boldsymbol{\omega} dV, \quad (1)$$

where ρ is the fluid density, \mathbf{r} is the position vector, $\boldsymbol{\omega}$ is the vorticity, and the volume integral is taken over the whole fluid region (Batchelor 1967). From the above assumption the change in P comes only from the integral in the interaction region.

Contributions from the interaction regions give upward- and downward-directed impulses for the initial and the final states, respectively, hence violating impulse conservation. To compensate for this difference, we need to superpose another fluid motion, i.e., a recoil motion of a small-size fluid element ejected upwards.

The cut-and-connect process then is considered to proceed as follows. The vortex filaments in the interaction region are strongly deformed until some adjoining fluid forms a recoil. The remaining parts of the vortices are reconnected and the process is completed. This complicated process can be also looked upon as superposing a pair of colinear, small ring vortices on the initial vortex filaments as shown in figure 2. These rings have equal size and opposite senses of rotation and are of equal circulations, which are also equal to that of either of the initial vortex filaments. They are centred at a position above that of the interaction region, so that the lower ring overlaps with the interaction region and produces a new vortex configuration, while the upper ring plays a role of recoil vortex (see figure 2b). This abrupt appearance of a ring pair may seem puzzling, but is an idealized model for the real and complex dynamics.

This process is expressed quantitatively by asymptotic conditions of the velocity (\mathbf{u}) and the vorticity ($\boldsymbol{\omega}$) fields. Let these fields in the initial state, final state and the ring pair be denoted by $\mathbf{u}_i, \boldsymbol{\omega}_i, \mathbf{u}_f, \boldsymbol{\omega}_f, \mathbf{u}_r, \boldsymbol{\omega}_r$, respectively. The origin of t is chosen so that the process occurs at $t \cong 0$. The suffixes i, f and r refer to the initial, the final and the ring throughout this paper. Since the process is a very rapid one, the

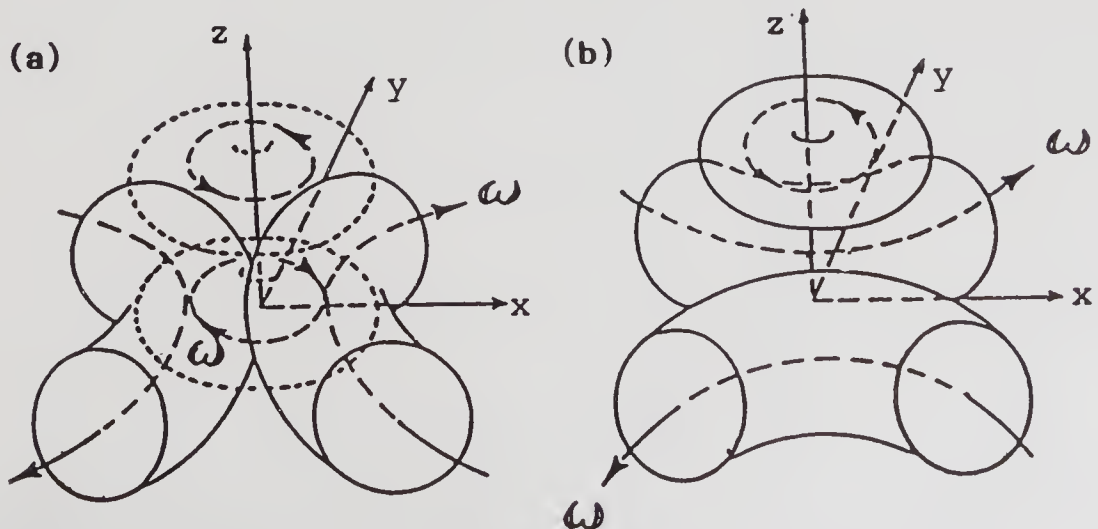


Figure 2. Assumed mechanism of the process. Definition of coordinates is also given.

instants before and after the process, to which the asymptotic conditions of the intermediate flow functions should refer, correspond to $t = 0-$ and $0+$ on the time scales of the initial and the final states, respectively. Then, the asymptotic conditions are

$$\mathbf{u}_r(-\infty) = 0 \text{ and } \mathbf{u}_i(0-) + \mathbf{u}_r(t) \rightarrow \mathbf{u}_f(0+), \text{ for } t \rightarrow \infty, \quad (2a)$$

$$\boldsymbol{\omega}_r(-\infty) = 0 \text{ and } \boldsymbol{\omega}_i(0-) + \boldsymbol{\omega}_r(t) \rightarrow \boldsymbol{\omega}_f(0+), \text{ for } t \rightarrow \infty. \quad (2b)$$

2.2 Functional forms of initial and final flow fields

The coordinate system is introduced as shown in figure 2. It is assumed that the two filaments have a configuration with two planes of inversion symmetry: the xz - and yz -planes. Then, velocity and vorticity components in the initial and the final states can be inferred (see table 1). Although the initial and final states have the same symmetry properties, they differ in dependence on x and y . This is because the vortex filaments are nearly aligned with the y - and the x -axes and the velocity vectors are nearly confined in the xz - and yz - planes in these states, respectively (see figure 1).

Next, the velocity and the vorticity fields are expanded by polynomials of coordinates up to $O(r^2)$, where $O(r^m)$ denotes the m th order polynomial. From the symmetry and the x - and y -dependences mentioned above, the components v , ω_x and ω_z vanish in the initial state and non-zero components do not depend on y , in the lowest terms, i.e., up to $O(r^2)$. In the same way, the components u , ω_y and ω_z are zero and the other components do not depend on x up to $O(r^2)$. In table 1 the quantities $\Delta\boldsymbol{\omega}_i$ and $\Delta\boldsymbol{\omega}_f$ are expanded as if they are independent from $\boldsymbol{\omega}_i$ and $\boldsymbol{\omega}_f$,

Table 1. Symmetries and leading terms in polynomial expansions for the initial and final states.

	Symmetry		Polynomials		
	x	y	$O(1)$	$O(r)$	$O(r^2)$
u_i	odd	even	–	x	$x(z - z_0)$
v_i	even	odd	–	–	–
w_i	even	even	1	$z - z_0$	$x^2, (z - z_0)^2$
ω_{ix}	even	odd	–	–	–
ω_{iy}	odd	even	–	x	$x(z - z_0)$
ω_{iz}	odd	odd	–	–	xy
$\Delta\omega_{ix}$	even	odd	–	y	–
$\Delta\omega_{iy}$	odd	even	–	x	–
$\Delta\omega_{iz}$	odd	odd	–	–	–
u_f	odd	even	–	–	–
v_f	even	odd	–	y	$y(z - z_0)$
w_f	even	even	1	$z - z_0$	$y^2, (z - z_0)^2$
ω_{fx}	even	odd	–	y	$y(z - z_0)$
ω_{fy}	odd	even	–	–	–
ω_{fz}	odd	odd	–	–	xy
$\Delta\omega_{fx}$	even	odd	–	y	–
$\Delta\omega_{fy}$	odd	even	–	x	–
$\Delta\omega_{fz}$	odd	odd	–	–	–

The symbol (–) means that the term is absent. z_0 refers to the centre of the interaction region.

respectively. However, if the vorticity is expanded up to $O(r^3)$ and substituted into $\Delta\boldsymbol{\omega}$, we obtain equivalent expressions as listed in this table.

Since the centre (denoted by $z = z_0$) of the interaction region moves in the z -direction, say with a velocity $w_0(t)$, during the process, the variable z in the polynomial expansion should be replaced by $z - z_0$, where

$$z_0(t) = \int w_0(t) dt. \quad (3)$$

The origin of the z -axis is chosen so that $z_0(0) = 0$. The velocity $w_0(t)$ constitutes the $O(r^0)$ terms for w_i and w_f .

Now, the flow fields with polynomial expansion are obtained as

$$\left. \begin{aligned} u_i &= -m_i x + k_i x(z - z_0), \\ v_i &= 0, \\ w_i &= w_0(t) + m_i(z - z_0) - k_i(z - z_0)^2/2 - l_i x^2/2, \end{aligned} \right\} \quad (4)$$

$$\omega_{ix} = 0, \omega_{iy} = (k_i + l_i)x + n_i x(z - z_0), \omega_{iz} = 0. \quad (5a)$$

$$\Delta\omega_{ix} = g_{ix}y, \Delta\omega_{iy} = g_{iy}x, \Delta\omega_{iz} = 0. \quad (5b)$$

In the same way for the final state we have

$$\left. \begin{aligned} u_f &= 0, \\ v_f &= m_f y - k_f y(z - z_0), \\ w_f &= w_0(t) - m_f(z - z_0) + k_f(z - z_0)^2/2 + l_f y^2/2, \end{aligned} \right\} \quad (6)$$

$$\omega_{fx} = (k_f + l_f)y + n_f y(z - z_0), \omega_{fy} = 0, \omega_{fz} = 0. \quad (7a)$$

$$\Delta\omega_{fx} = g_{fx}y, \Delta\omega_{fy} = g_{fy}x, \Delta\omega_{fz} = 0. \quad (7b)$$

In these expansions the coefficients $m_i, m_f, k_i, k_f, l_i, l_f, n_i, n_f, g_{ix}, g_{iy}, g_{fx}, g_{fy}$ are functions of time.

Physical meanings of terms in the velocity fields are easily understood. The term $-m_i x$ or $m_f y$ is a flow which presses or separates the two filaments before or after the interaction. They are relatively weak because these flow fields are contributed by far parts of filaments. Terms with coefficients $k_i, k_f, l_i, l_f, n_i, n_f$ come from the vorticity located close-by, and are relatively strong.

Order estimations of these coefficients are possible. Characteristic quantities are the core size σ , the circulation Γ and a scale L corresponding to the curvature of the filament. Since coefficients $k_i, k_f, l_i, l_f, n_i, n_f$ and $w_0(t)$ are considered to be related to σ and Γ , while m_i and m_f to L and Γ , we have

$$\begin{aligned} k_i, k_f, l_i, l_f &= O(\Gamma/\sigma^3); \quad n_i, n_f = O(\Gamma/\sigma^4); \quad w_0(t) = O(\Gamma/\sigma), \\ m_i, m_f &= O(\Gamma/L^2). \end{aligned} \quad (8)$$

The equation which governs variations of these coefficients is derived from the vorticity equation

$$\partial\boldsymbol{\omega}/\partial t + (\mathbf{u}\nabla)\boldsymbol{\omega} - (\boldsymbol{\omega}\nabla)\mathbf{u} - \nu\Delta\boldsymbol{\omega} = 0, \quad (9)$$

where ν is the kinematic viscosity. Substitution of (4) and (5a, b) into this equation yields equations for $k_i + l_i$ and $k_f + l_f$, which prove the slow variation of these quantities.

Table 2. Symmetries and leading terms in polynomial expansions for vortex rings superposed on the initial state.

	Symmetries		Polynomials		
	x	y	$O(1)$	$O(r)$	$O(r^2)$
u_r	odd	even	–	x	xz
v_r	even	odd	–	y	yz
w_r	even	even	1	z	$z, (x+y)$
ω_{rx}	even	odd	–	y	yz
ω_{ry}	odd	even	–	x	xz
ω_{rz}	odd	odd	–	–	
$\Delta\omega_{rx}$	even	odd	–	y	yz
$\Delta\omega_{ry}$	odd	even	–	x	xz
$\Delta\omega_{rz}$	odd	odd	–	–	

(–) means that the term is absent. The axisymmetry around the z -axis is also assumed.

2.3 Functional form of the intermediate flow field

The pair of vortex rings superposed on the initial state has the same symmetry as the initial and final states with respect to the x - and y -axes. It is assumed also to have an axisymmetry around the z -axis. The symmetry properties and possible polynomials for the intermediate flow field are listed in table 2. Expansions of the velocity and the vorticity components up to $O(r^2)$ are

$$u_r = (c_1 - c_2 z)x, \quad v_r = (c_1 - c_2 z)y, \\ w_r = -c_0 - 2c_1 z + c_2 z^2 + c_2^r (x^2 + y^2), \quad (10)$$

$$\omega_{rx} = (c_2 + c_2^r - c_3 z)y, \quad \omega_{ry} = -(c_2 + c_2^r - c_3 z)x, \quad \omega_{rz} = 0, \quad (11a)$$

$$\Delta\omega_{rx} = g_{rx}y, \quad \Delta\omega_{ry} = -g_{ry}x, \quad \Delta\omega_{rz} = 0, \quad (11b)$$

where the coefficients in these expansions are functions of t . Note that these expressions satisfy the continuity equation, the relation $\boldsymbol{\omega} = \text{rot } \mathbf{u}$ and the required symmetry. Since the intermediate flow field grows with the cut-and-connect process and leads to the final state, the coefficients in (10) and (11) should vanish for $t = -\infty$ and approach finite values for $t = \infty$.

Here, it is assumed for the sake of simplicity that these coefficients contain only one function $T(t)$ in common, so that

$$c_0(t) = \delta T(t), \quad c_1(t) = mT(t), \quad c_2(t) = kT(t), \quad c_2^r(t) = lT(t), \\ c_3(t) = nT(t), \quad g_{rx}(t) = g_x T(t), \quad g_{ry}(t) = g_y T(t), \quad (12)$$

where coefficients in front of $T(t)$ are constants and $T(t)$ satisfies

$$T(-\infty) = 0, \quad T(\infty) = 1. \quad (13)$$

2.4 Flow field throughout the cut-and-connect process

Expansion coefficients in the initial, final and intermediate flow fields are related to each other via (2a, b). Then, after reducing the number of independent coefficients, we obtain the following expressions for the flow field during the cut-and-connect process:

$$\begin{aligned}
u &= -m(1-T)x + k(1-T)xz, \\
v &= mTy - kTyz, \\
w &= w_0(0-) - \delta T + m(1-2T)z \\
&\quad - l(1-T)x^2/2 + lTy^2/2 - k(1-2T)z^2/2,
\end{aligned} \tag{14}$$

$$\begin{aligned}
\omega_x &= (k+l)Ty - nTyz, \\
\omega_y &= (k+l)(1-T)x - n(1-T)xz,
\end{aligned} \tag{15a}$$

$$\begin{aligned}
\omega_z &= 0, \\
\Delta\omega_x &= g_x Ty, \quad \Delta\omega_y = g_y(1-T)x, \quad \Delta\omega_z = 0.
\end{aligned} \tag{15b}$$

The parameters m , k , l , δ and $w_0(0-)$ are treated as given. Parameters g_x and g_y will be related to the other parameters, while solving the vorticity equation (9) to obtain $T(t)$.

3. Solution of the vorticity equation

By substituting the final expressions (14) and (15) into the x - and y -components of the vorticity equation (9), we have, up to $O(r)$,

$$\begin{aligned}
x: & (k+l)dT/dt + m(k+l)T - (w_0(0-) - \delta T)nT + (k+l)Tm(1-T) \\
& = \nu g_x T,
\end{aligned} \tag{16a}$$

$$\begin{aligned}
y: & -(k+l)dT/dt - m(1-T)(k+l)(1-T) - (w_0(0-) - \delta T)n(1-T) \\
& - (k+l)(1-T)mT = \nu g_y(1-T).
\end{aligned} \tag{16b}$$

From these equations and condition (13), values of g_x and g_y are determined as

$$g_x = m(k+l) - [w_0(-0) - \delta]n, \quad g_y = -m(k+l) - w_0(-0)n, \tag{17}$$

and the two equations (16a, b) are reduced to a single equation of the same simple form

$$dT/dt - t^{*-1}T + t^{*-1}T^2 = 0, \tag{18}$$

where

$$t^* = \delta n / (k+l) = O(\Gamma/\sigma^2). \tag{19}$$

This equation does not contain the viscosity explicitly, but, since the parameter t^* is related to the viscosity through (17) and (19), the viscous effects play an essential role. The two components of the vorticity equation (16a, b) contradict each other even in the lowest order, i.e. $O(r)$, if the viscous terms are neglected.

The solution of the differential equation (18) satisfying (13) is

$$T = e^\tau / (1 + e^\tau); \quad \tau = t/t^*. \tag{20}$$

This solution shows expected behaviour, because it varies from 0 to 1 during a time of $O(t^*)$.

The present results, though derived on the model shown in figure 2, do not necessarily require the existence of the ring pair. What is essential in this model is that the intermediate flow field has an axisymmetry expressed as (10), but no

inversion symmetry with respect to the xy -plane. There may be another model for the cut-and-connect process leading to the same result. However, production of a recoil motion may be the simplest picture of this complicated process.

4. Sound production from the cut-and-connect event

The pair of rings superposed abruptly on the initial state may be a strong source of noise. Therefore, noise production in shear flows where cut-and-connect interactions are occurring will also be understood by this mechanism. In this section characteristics of the sound from a cut-and-connect process are obtained, and its relation to jet noise is discussed.

4.1 Sound from a single event

Estimation of a far-field sound from a compact source of inviscid flow can be made by Lighthill's formula (1952, 1954):

$$p(x, t+r/a) = (4\pi a^2 r) x_i y_j / r^2 \cdot \partial^2 / \partial t^2 \int T_{ij}(x', t) dx', \tag{21}$$

where $T_{ij} = \rho u_i u_j$, a is the speed of sound, ρ is the density of the static fluid, $r^2 = x^2 + y^2 + z^2$, and (x', y', z') is the source coordinate. Although the viscosity is essential for occurrence of the cut-and-connect process, it is reasonable to assume that prediction of sound from a given flow field can be made without viscous effect.

Since the analysis in the preceding section is based on the polynomial expansion up to $O(r^2)$, it gives no conclusion on the spatial extent of the interaction region except that it is $O(\sigma)$. However, the integrals in (21) can be estimated, except for a common constant factor, based on the symmetry of the flow field and on the three-pressure theorem derived by Powell (1962). This theorem states that the pressures $P(a, t)$, $P(b, t)$, $P(c, t)$ at equal distances from the source to the x -, y -, z -directions, respectively, satisfy

$$P(a, t) + P(b, t) + P(c, t) = 0. \tag{22}$$

Now, since the flow is symmetric with respect to the xz - and yz -planes, the integrals in (21) vanish except those of u^2 , v^2 , w^2 . Then, the formula (21) is written as

$$p(x, t+r/a) = \rho/4\pi a^2 r \cdot (x^2 A_x / r^2 + y^2 A_y / r^2 + z^2 A_z / r^2), \tag{23}$$

where A_x , A_y and A_z are functions of time expressed as

$$\left. \begin{aligned} A_x &= d^2/dt^2 \int u^2 dx' = (m^2 \mathcal{J}_1 + k^2 \mathcal{J}_2) d^2/dt^2 (1-T)^2, \\ A_y &= d^2/dt^2 \int v^2 dx' = (m^2 \mathcal{J}_1 + k^2 \mathcal{J}_2) d^2/dt^2 T^2, \\ A_z &= d^2/dt^2 \int w^2 dx' = d^2/dt^2 [a_1(1-\alpha T)^2 + a_2(1-\alpha T)(1-2T) \\ &\quad + a_3(1-2T)^2] \end{aligned} \right\} \tag{24}$$

where

$$\mathcal{J}_1 = \int (x')^2 dx' = O(\sigma^5), \quad \mathcal{J}_2 = \int (x')^2 (y')^2 dx' = O(\sigma^7),$$

and a_1 , a_2 and a_3 are constants. Next, the three-pressure theorem requires that $A_x + A_y + A_z = 0$ at any time, hence we must have $\alpha = 2$ and $a_1 + a_2 + a_3 = -(m^2 \mathcal{F}_1 + k^2 \mathcal{F}_2)/2$. Thus, we obtain the pressure fluctuation without specifying unknown parameters except for the factor $(m^2 \mathcal{F}_1 + k^2 \mathcal{F}_2)$. It should be noted here that the integrals in (21) must converge in order to have this result; it will not be assured by flow field with polynomial expansion. Actual flow field, however, is confined to a finite region, so that the integrations should be cut off within this region. As is seen from the above analysis, the uncertainty of the integration region is excluded as a common unknown factor, which we do not need to specify for the following analysis.

Power intensity of sound is given by $|p|^2/\rho a$. Since the sound from the cut-and-connect process is considered to propagate as a single pulse, its time integral, i.e.

$$I(x, y, z) = \int_{-\infty}^{\infty} |p|^2/\rho a dt, \quad (25)$$

gives a good measure for a sound strength from a cut-and-connect event. Then, substituting (23) into (25) and after some manipulations, we have

$$I(x, y, z) = \rho/(16\pi^2 r^2 a^5 t^{*3}) (m^2 \mathcal{F}_1 + k^2 \mathcal{F}_2)^2 P(x, y, z), \quad (26)$$

where P stands for the directional distribution and is expressed as

$$P = B_{xx}x^4/r^4 - B_{yy}y^4/r^4 + B_{zz}z^4/r^4 + 2B_{xy}x^2y^2/r^4 + 2B_{yz}y^2z^2/r^4 + 2B_{zx}z^2x^2/r^4, \quad (27)$$

and $B_{xx} = B_{yy} = 2/35$, $B_{zz} = 2/21$, $B_{xy} = -1/105$, $B_{yz} = -1/21$.

Directional distribution of the integrated intensity in the xz - and xy -planes obtained from (27) is shown in figure 3. The intensity has a relatively strong direct-

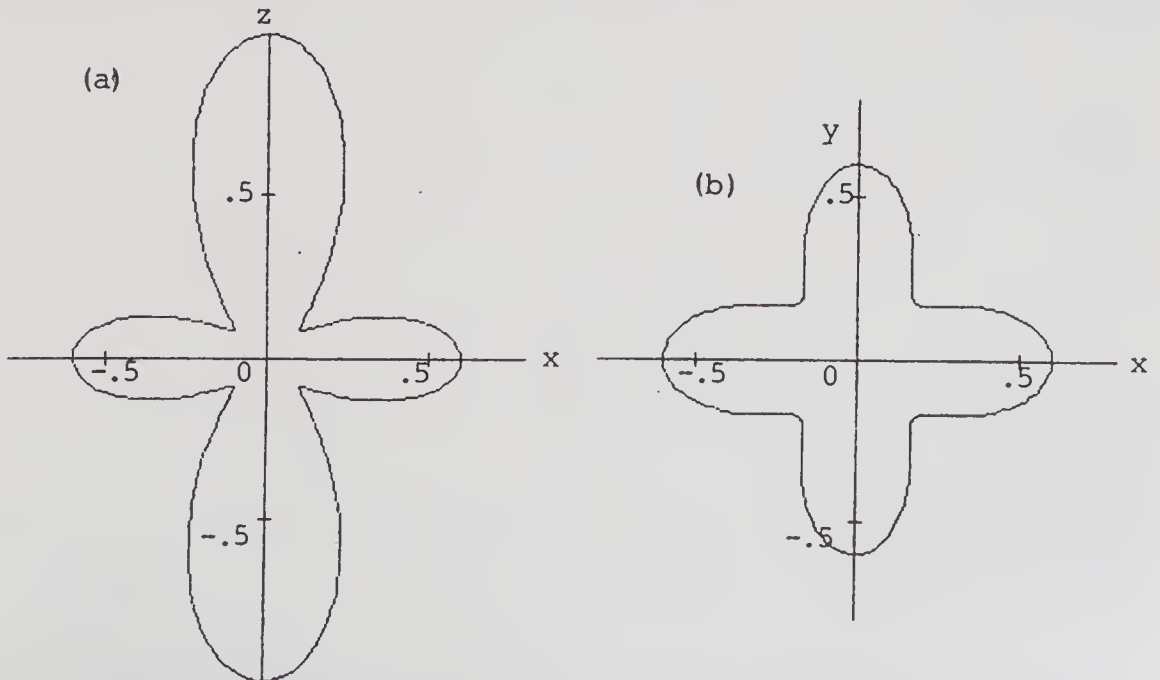


Figure 3. Directional distribution of the far-field sound intensity from a single cut-and-connect process.

ivity in the z -direction, which has come from the fact that the sound source is essentially an appearance of a vortex pair arranged along the z -direction.

Order estimate of the integrated intensity by the use of (8) and (26) is

$$I \sim \rho \Gamma^7 / a^5 r^2 \sigma^4. \quad (28)$$

Thus, I depends strongly on the vortex strength and on the core size σ .

4.2 Jet noise

We examine intensity, spectrum and directional distribution of the noise from a round jet. It is assumed that the jet noise originates in superposition of sounds emitted from many cut-and-connect events on distorted vortex rings, which are produced at the nozzle exit. Let the jet speed, the nozzle diameter and the mutual distance between rings be denoted by U , D and d , respectively. The rings are expected to move with speed $U/2$ and the number of rings crossing a fixed station per unit time is $U/2d$, while the circulation of each ring is Ud . It is reasonable to assume $D \gg \sigma$ and $d \gg \sigma$. The number N of cut-and-connect events on one ring is considered to be the same as that of azimuthal lobes of the ring filament, which was observed by Widnall *et al* (1975) and is analysed by Saffman (1978). Both of these works suggest that $N = O(D/\sigma)$.

It is assumed also that each cut-and-connect event occurs incoherently with each other, and a far point perceives an irregular train of separated sound pulses. Noise level at a fixed far point, then, is obtained simply by multiplying the intensity, (28), by the number N and the frequency of passage of rings $U/2d$, i.e.

$$I \sim (\rho \Gamma^7 / a^5 r^2 \sigma^4) (D/\sigma) (U/2d) = (\sigma D^2 / a^5 r^2) U^8 (d/\sigma)^6 \sigma / D. \quad (29)$$

The power law $I \propto U^8$ and the factor before this power are already known while the factor $(d/\sigma)^6 (\sigma/D)$ is a new result and shows critical dependence of the noise level on the degree of vorticity concentration.

The power spectrum of the sound is obtained by making Fourier transformation of coefficients, (24). Let the Fourier transforms of A_x , A_y and A_z be denoted by J_x , J_y and J_z , respectively. Then, after some manipulations, we have

$$\begin{aligned} J_x &= J_y \propto (2\pi ft^*)^2 (2\pi^2 ift^* + 1) / [\exp(2\pi^2 ft^*) - \exp(-2\pi^2 ft^*)], \\ J_z &\propto (2\pi ft^*)^3 / [\exp(2\pi^2 ft^*) - \exp(-2\pi^2 ft^*)], \end{aligned} \quad (30)$$

where f is the frequency. Power spectrum from J_x and J_y has a single peak and behaves as $(ft^*)^2$ for $ft^* \rightarrow 0$ and as $(ft^*)^6 \exp(-2\pi^2 ft^*)$ for $ft^* \rightarrow \infty$. That from J_z has a similar form except that $|J_z|^2 \sim (ft^*)^4$ for $ft^* \rightarrow 0$. Since the jet noise is a random superposition of sounds from many cut-and-connect events, the power spectrum of jet noise is expected to be a certain average of two expressions in (30).

Directional distribution of the jet noise is obtained by averaging the distribution for a single cut-and-connect event (figure 3). For that purpose we need an assumption on the orientation of the axis of the cut-and-connect process (the z -axis in figure 2) in the turbulent jet. Suppose the large scale vortex rings in the jet are

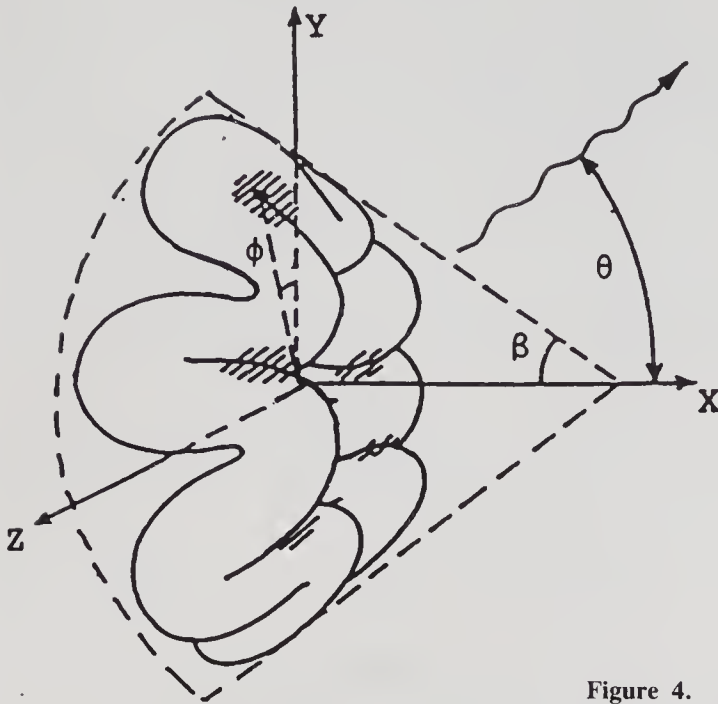


Figure 4. Distorted vortex ring in a round jet.

distorted as shown in figure 4, where the xy -plane in each cut-and-connect process is inclined from the jet axis (the X -axis) by an angle β . The cut-and-connect events are assumed to distribute uniformly along the large scale vortex ring. For the angle β , the most probable value is $\pi/4$, because the large scale vortex filament receives a shear strain of the jet whose principal axis is inclined from the jet axis by $\pi/4$; this is also supported by observation of a bursting vortex ring by Maxworthy (1977). Now, including this case, we examine the following three cases for distribution $Pr(\beta)$:

$$\left. \begin{array}{l} \text{I. } Pr(\beta) = \delta(\beta - \pi/4), \text{ Dirac's delta function,} \\ \text{II. } Pr(\beta) = \sin 2\beta, \quad 0 \leq \beta \leq \pi/2, \text{ peak at } \pi/4, \\ \text{III. } Pr(\beta) = 2/\pi, \quad 0 \leq \beta \leq \pi/2, \text{ uniform distribution.} \end{array} \right\} \quad (31)$$

Now, the directional distribution of the sound from a distorted vortex ring is obtained by superposing intensities (26) from many sources on the ring and by averaging it with the weight $Pr(\beta)$. Figure 5a shows results for the above three cases with arbitrary scales (relative strengths among these cases are correct). The large intensity in the oblique direction in case I results from the sharp distribution in (31). On the other hand, case III yields strong forward and backward intensities.

In the jet noise problem, effects of convection and refraction of sound by the jet mean flow cannot be ignored. Among theories for these effects, that of Goldstein (1984) is useful for the present purpose, which gives a far field pressure fluctuation in the direction out of the zone of silence, i.e. $\cos \theta < (1 + M)^{-1}$, where M is the Mach number of source convection. Application of this theory leads to modified directional distributions for the three cases of $Pr(\beta)$, as shown in figure 5b. The distribution in case I shows a weak forward intensity as in figure 5a. It is noted here that this effect coming from the source orientation may provide another explanation for the appearance of a zone of silence.

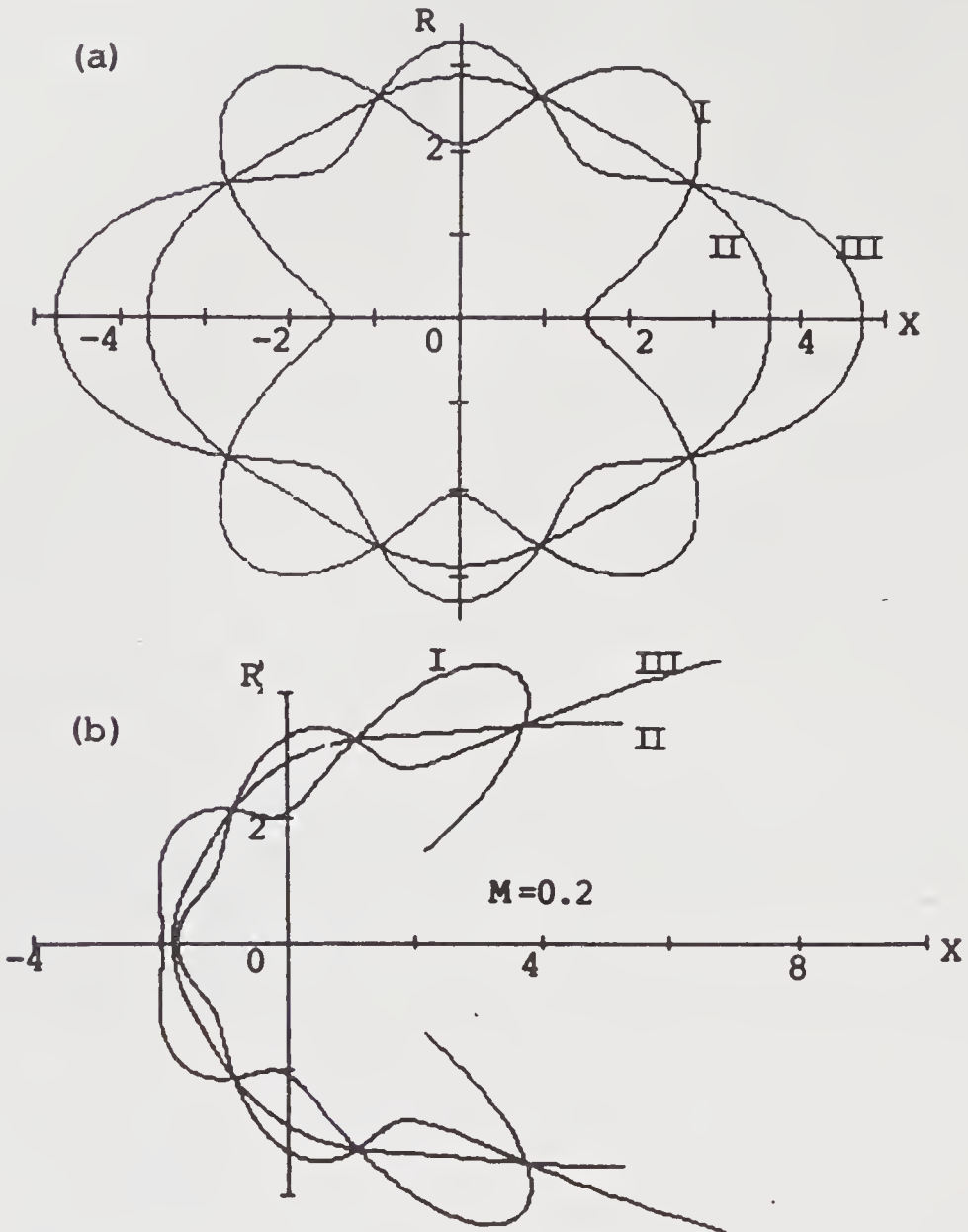


Figure 5. Directional distributions of sound intensities emitted from (a) a single ring, and (b) a round jet, for $M = 0.2$. The x -axis is the ring or the jet axis. I, II and III in the figure indicate three cases for distributions $Pr(\beta)$.

5. Concluding remarks

The approximate solution obtained here for the cut-and-connect process explains well this rapid fluid motion observed by flow visualization. The method of solution shows that the viscous term in the governing equation is essential. The superposition of the ring pair on the initial state may give us an impression that the kinetic energy is not conserved. But, this problem is solved by assuming a growth of core size after the interaction or by assuming that the ejected recoil stays near the interaction region.

Application to prediction of the jet noise shows that the U^8 law is valid for any angle θ and any Mach number. The former is supported by Lush (1971). The

present result shows a strong dependence of the noise intensity on the ratio d/σ . It seems to be related to the experimental fact that the broad-band spectra of turbulence and noise in a round jet were suppressed considerably by exciting it with a frequency of the shear layer mode (Zaman & Hussain 1981; Kibens 1980). It is suggested that the excitation of shear layer mode makes d/σ smaller at the noise producing region. Theories to predict directional distribution of the jet noise, such as that by Mani (1976), are based on the assumption of the isotropy of sources. But, the isotropy is not supported by real vortex dynamics. Then, the present analysis provides a method to take the source orientation into account.

The authors would like to express their cordial thanks to Dr J Bridges for his interest in this work and valuable suggestions.

List of symbols

$A_x, A_y, A_z,$	coefficients in the far-field pressure fluctuation;	
a	sound speed;	
B_{xy} etc.	coefficients in the far-field sound intensity;	
$c_0, c_1, c_2,$ $c_2', c_3,$	coefficients in the flow field for the ring pair	
D		diameter of jet nozzle;
d	distance between successive vortex rings in the jet;	
f	frequency in the power spectrum;	
g_{ix} etc.	coefficients of Taylor expansions of $\Delta\omega_i$ etc.;	
I	intensity of sound;	
$\mathcal{I}_1, \mathcal{I}_2$	integrals of polynomials within interaction region;	
$J_x, J_y, J_z,$	Fourier transforms of pressure fluctuations;	
$m_i, m_f, m,$ $k_i, k_f, k,$ $l_i, l_f, l,$ $n_i, n_f, n,$ $w_0 (-0), \delta$	coefficients of Taylor expansions of flow fields in the initial(i), final(f) and the intermediate states;	
M		Mach number;
N		number of cut-and-connect events on a large scale vortex ring;
$P(x, y, z)$		directional part in the sound intensity;
p		pressure;
$Pr(\beta)$	probability density of angle of source orientation;	
r	distance from the origin (sound source);	
$T(t)$	function standing for the cut-and-connect process;	
t	time;	
t^*	time scale of cut-and-connect process;	
U	jet velocity;	
u_i	velocity components;	
$u_i, u_f, u,$ $v_i, v_f, v,$ w_i, w_f, w	velocity components in the initial(i), final(f) and intermediate states;	

$w_0(t)$	velocity of the centre of the interaction region;
X	coordinate in the jet axis;
x, y, z	coordinates referring to a single cut-and-connect;
x', y', z'	source coordinates;
$z_0(t)$	height of the centre of the interaction region;
$\alpha = \delta/w_0(-0)$	parameter characterizing the flow field;
Γ	circulation of vortex filament;
ρ	fluid density;
β	angle of inclination of the interaction region in jet;
ν	kinematical viscosity;
σ	core size of the vortex filament;
θ	angle measured from the jet axis;
τ	normalized time;
$\omega_i, \omega_f, \omega$	vorticities in the initial(<i>i</i>), final(<i>f</i>) and intermediate states.

References

- Aref H 1983 *Annu. Rev. Fluid Mech.* 15: 345–389
 Batchelor G K 1967 *An introduction to fluid dynamics* (Cambridge: Univ. Press) chap. 7
 Crow S C 1970 *AIAA J.* 8: 2172–2179
 Ffowes Williams J E, Kempton A J 1978 *J. Fluid Mech.* 84: 673–694
 Fohl T, Turner J S 1975 *Phys. Fluids.* 18: 433–436
 Goldstein M E 1984 *Annu. Rev. Fluid Mech.* 16: 263–285
 Hama F R 1960 *Proc. Heat Transfer Fluid Mech. Inst.* 92–105
 Hussain A K M F 1983 *Phys. Fluids* 26: 2816–2850
 Kambe T, Takao T 1971 *J. Phys. Soc. Jpn.* 31: 591–599
 Kibens V 1980 *AIAA J.* 18: 434–441
 Lighthill M J 1952 *Proc. R. Soc.* A211: 564–587
 Lighthill M J 1954 *Proc. R. Soc.* A222: 1–32
 Lush P A 1971 *J. Fluid Mech.* 46: 477–500
 Mani R 1976 *J. Fluid Mech.* 73: 753–778
 Maxworthy T 1977 *J. Fluid Mech.* 81: 465–495
 Oshima Y, Asaka S 1977 *J. Phys. Soc. Jpn.* 42: 708–713
 Powell A 1962 *J. Acoust. Soc. Am.* 34: 902–906
 Saffman P G 1978 *J. Fluid Mech.* 84: 625–639
 Saffman P G 1981 *J. Fluid Mech.* 106: 49–58
 Widnall S E 1975 *Annu. Rev. Fluid. Mech.* 7: 141–165
 Yeh T, Axford W I 1970 *J. Plasma Phys.* 4: 207–229
 Zaman K B M Q, Hussain A K M F 1981 *J. Fluid Mech.* 103: 133–160

On the theory of turbulence for incompressible fluids*

ZHOU (CHOU) PEI-YUAN and CHEN SHI-YI

Department of Mechanics, Peking University, Beijing, China

Abstract. The theory of turbulence, based upon the Reynolds equations of mean motion and the dynamical equations of the velocity correlations of successive orders derived from the equations of the turbulent velocity fluctuation by using the condition of pseudo-similarity and the hypotheses on the viscous dissipation terms in the correlation equations, is developed by a method of successive approximation. As examples in the first order approximation, we have solved the turbulent flows through a channel, in a plane wake and in jets by using the equations of mean motion and of double correlation, while the terms in the triple correlation have been neglected. The agreements between the calculated values and the experiments are satisfactory.

In the present paper, the equations of the triple and quadruple correlations in addition to those used in the first order approximation are solved for the plane turbulent wake in the second order approximation by the method of substitution, starting from the solution of the first order approximation. Agreements between theory and existing experiments for the triple velocity correlation are also satisfactory. The theory has also yielded the components of the quadruple correlation which can be tested by experiment.

Keywords. Reynolds equations; turbulent velocity fluctuation; pseudo-similarity; viscous dissipation; successive approximation.

1. Introduction

The theory of turbulence for incompressible fluids, based upon the Navier-Stokes equations of motion, was first put forward by Reynolds in 1895. His important contribution consists of pointing out that a fully developed turbulent flow is composed of two parts, the mean motion and the turbulent fluctuation, and the derivation of the equations of mean motion by taking the average of the Navier-Stokes equations of motion. Due to the non-linearity of these latter equations, there appears the apparent stress, known as the Reynolds stress, in the equations of mean motion. On account of the Reynolds stress being unknown, the dynamical equations of mean motion thus derived are not closed. The subsequent

* Presented at the Third Asian Congress of Fluid Mechanics on September 1, 1986, in Tokyo, Japan.

mixture length theories of the momentum or vorticity transport proposed by Prandtl, Taylor and von Kármán in the early part of this century had the objective of relating the turbulent velocity fluctuations to the derivatives of the mean motion in order to make the set of equations of mean motion closed, while the equations of turbulent fluctuation, which are the differences of the Navier-Stokes equations of motion and the Reynolds equations of mean motion, were ignored since Reynolds' time.

The theory of turbulence, based upon the solutions of the dynamical equations of the velocity correlations of the double and triple orders derived from the equations of turbulent velocity fluctuation, and the equations of mean motion was first put forward in 1940 (Chou 1940) and then further developed in 1945 (Chou 1945). In the 1945 paper it was also pointed out that the direct approach to the solution of the general turbulence problem is to solve simultaneously the equations of mean motion and of turbulent fluctuation together with their corresponding equations of continuity. But this is a set of non-linear integro-partial differential equations and to seek their solutions for general shear turbulent motions of fluids is very difficult.

However, for simpler problems like the homogeneous isotropic turbulence and the homogeneous shear turbulent flow, simultaneous solutions of the equations of mean motion and of turbulent fluctuation can be carried out. For homogeneous isotropic turbulence we introduce the condition of pseudo-similarity into the solution in order to choose the right kind of vortex to be the turbulence element. From the solutions of the turbulent velocity fluctuation we can then build the velocity correlations of any order to be compared with experimental measurements. For homogeneous turbulent shear flows special types of flow also satisfy this condition of pseudo-similarity.

For general turbulent shear flows, two methods of tackling the problem have been developed without resorting to a direct solution of the equations of mean motion and turbulent fluctuation. The first method follows the line initiated in the 1940 paper (Chou 1940). Due to the non-linearity of the equations of turbulent fluctuation, the dynamical equations of the correlations thus built are not closed, similar to the equations of mean motion containing the unknown Reynolds stress which is a turbulent velocity correlation of the second order mentioned before. To overcome this difficulty in this method a relation between the velocity correlation of a given order with that of a lower one is assumed. Further hypotheses upon the pressure gradient and velocity fluctuation correlations and the terms in viscous decay have to be assumed in order to obtain definite solutions of the given turbulence problem. This line of approach was subsequently developed by Rotta (1951) and a number of investigators in the sixties and seventies, especially after the computer was invented (Launder 1979, pp. 259–266 and references therein).

The second method of approach is to consider the derivation of the equations of mean motion, the building of the turbulent velocity correlations of successive orders and seeking the solutions of their corresponding dynamical equations as a method of successive approximation. This point of view was first brought out in 1945 (Chou 1945) and further developed in a recent paper (Zhou 1985). Here we must point out that the condition of pseudo-similarity for the homogeneous isotropic turbulence has to be generalized for the general shear turbulent flows. The turbulent pressure gradient and velocity correlations and the dissipation terms in the dynamical equations of the double correlation have been treated before

(Chou 1945), while those for the equations of the triple and quadruple correlations can be treated in a similar way.

This second method of solution theoretically has an advantage over the first by being able to obtain velocity correlations of higher orders if we carry out the process of successive approximation further.

As the first order approximation we have used the equations of mean motion and the equations of the double velocity correlation to solve the problems of the flow in a channel, the plane wake (Zhou 1985), the plane and axial jets (Wu 1986), while terms involving triple velocity correlations have been neglected. Agreements between the theoretical values of the mean velocities and double velocity correlations calculated from experiments are more satisfactory for free turbulence, the plane wake and jets, than the channel flow (Zhou 1985).

In the present paper we give the solution of the plane wake problem to the next order of approximation by using the dynamical equations for the velocity correlations of the triple and quadruple orders, while neglecting the fifth order correlation. Agreements between the calculations and the existing experimental data for the components of the triple velocity correlation are satisfactory. Since the present theory has given the values of those of the quadruple correlations which are not yet known, experiments can be carried out to test their validity.

2. Equations of motion

We first put down the equations of motion and start with the Navier-Stokes equations and the equation of continuity for incompressible fluids:

$$\begin{aligned} (\partial u_i / \partial t) + u^j u_{i,j} &= -(1/\rho) p_{,i} + \nu \nabla^2 u_i, \\ u^j_{,j} &= 0, \end{aligned} \quad (1)$$

in which u_i is the velocity vector, p , the pressure, and ν , the kinematic coefficient of viscosity. Since we are using the rectangular system of coordinates x^i , the contravariant vector u^i is the same as its covariant form u_i and the comma sign followed by the coordinate x^j under u_i like $u_{i,j}$ denotes the covariant partial differentiation of u_i with respect to the coordinate x^j .

Following Reynolds, the vector u_i and pressure p in a fully developed turbulent flow can be separated into the mean motion and the turbulent fluctuation:

$$u_i = U_i + w_i, \quad p = \bar{p} + \varpi, \quad (2)$$

in which U_i and \bar{p} are the mean values of the velocity u_i and pressure p , respectively, while w_i and ϖ are their turbulent fluctuations of which the mean values are both zero:

$$\bar{w}_i = 0, \quad \bar{\varpi} = 0.$$

By introducing (2) into (1) and taking the average, we obtain the Reynolds equations and the equation of continuity for the mean motion,

$$\begin{aligned} (\partial U_i / \partial t) + U^j U_{i,j} &= -(1/\rho) \bar{p}_{,i} + (1/\rho) \tau^j_{i,j} + \nu \nabla^2 U_i, \\ U^j_{,j} &= 0, \end{aligned} \quad (3)$$

with the Reynolds stress,

$$\tau_i^j = -\rho \overline{w_i w^j}.$$

By subtracting the Reynolds equations and the equations of continuity from the Navier-Stokes equations (1), we obtain the dynamical equations and the equation of continuity for the turbulent velocity fluctuation:

$$\begin{aligned} (\partial w_i / \partial t) + U^j w_{i,j} + w^j w_{i,j} + w^j U_{i,j} \\ = -(1/\rho) \varpi_{,i} - (1/\rho) \tau_{i,j}^j + \nu \nabla^2 w_i, \\ w_{,j}^j = 0. \end{aligned} \quad (4)$$

From the equations of turbulent velocity fluctuation we can derive the dynamical equations of the double, triple and quadruple velocity correlations as follows:

$$\begin{aligned} \frac{\partial}{\partial t} \overline{w_i w_k} + U_{i,j} \overline{w^j w_k} + U_{k,j} \overline{w^j w_i} + U^j (\overline{w_i w_k})_{,j} + (\overline{w^j w_i w_k})_{,j} \\ = -\frac{1}{\rho} (\overline{\varpi_{,i} w_k} + \overline{\varpi_{,k} w_i}) + \nu \nabla^2 \overline{w_i w_k} - 2\nu g^{mn} \overline{w_{i,m} w_{k,n}}, \end{aligned} \quad (5)$$

$$\begin{aligned} \frac{\partial}{\partial t} \overline{w_i w_k w_l} + U_{i,j} \overline{w^j w_k w_l} + U_{k,j} \overline{w^j w_l w_i} + U_{l,j} \overline{w^j w_i w_k} \\ + U^j (\overline{w_i w_k w_l})_{,j} + (\overline{w^j w_i w_k w_l})_{,j} \\ = -\frac{1}{\rho} (\overline{\varpi_{,i} w_k w_l} + \overline{\varpi_{,k} w_l w_i} + \overline{\varpi_{,l} w_i w_k}) + (\overline{w^j w_i})_{,j} \overline{w_k w_l} \\ + (\overline{w^j w_k})_{,j} \overline{w_l w_i} + (\overline{w^j w_l})_{,j} \overline{w_i w_k} + \nu g^{mn} (\overline{w_i w_k w_l})_{,mn} \\ - 2\nu g^{mn} (\overline{w_{i,m} w_{k,n} w_l} + \overline{w_{k,m} w_{l,n} w_i} + \overline{w_{l,m} w_{i,n} w_k}), \end{aligned} \quad (6)$$

$$\begin{aligned} \frac{\partial}{\partial t} \overline{w_i w_k w_l w_p} + U_{i,j} \overline{w^j w_k w_l w_p} + U_{k,j} \overline{w^j w_l w_p w_i} + U_{l,j} \overline{w^j w_p w_i w_k} \\ + U_{p,j} \overline{w^j w_i w_k w_l} + U^j (\overline{w_i w_k w_l w_p})_{,j} + (\overline{w^j w_i w_k w_l w_p})_{,j} \\ = -\frac{1}{\rho} (\overline{\varpi_{,i} w_k w_l w_p} + \overline{\varpi_{,k} w_l w_p w_i} + \overline{\varpi_{,l} w_p w_i w_k} + \overline{\varpi_{,p} w_i w_k w_l}) \\ + (\overline{w^j w_i})_{,j} \overline{w_k w_l w_p} + (\overline{w^j w_k})_{,j} \overline{w_l w_p w_i} + (\overline{w^j w_l})_{,j} \overline{w_p w_i w_k} \\ + (\overline{w^j w_p})_{,j} \overline{w_i w_k w_l} + \nu g^{mn} (\overline{w_i w_k w_l w_p})_{,mn} \\ - 2\nu g^{mn} (\overline{w_{i,m} w_{k,n} w_l w_p} + \overline{w_{k,m} w_{l,n} w_i w_p} + \overline{w_{l,m} w_{p,n} w_i w_k} \\ + \overline{w_{i,m} w_{l,n} w_k w_p} + \overline{w_{k,m} w_{p,n} w_i w_l} + \overline{w_{i,m} w_{p,n} w_k w_l}). \end{aligned} \quad (7)$$

In the above differential equations $\varpi_{,i}$ is the solution of the Poisson equation obtained earlier (Chou 1945) and g_{ik} is the metric tensor. In the rectangular system of coordinates $g_{ik} = 1$, for $i = k$, and $g_{ik} = 0$, for $i \neq k$.

For the wall-bound and free turbulent flows like the channel, wakes and jets, we choose the solution of the equation of velocity turbulent fluctuation (4) of the type (Zhou 1985):

$$w_i = q\phi_i[(x/\lambda), t]$$

$$\text{with } q^2 = \overline{w_j w_j} = q^2(x, t), \quad \lambda = \lambda(x, t). \quad (8)$$

Here q is the magnitude of the velocity fluctuation and λ is the generalized Taylor's microscale of turbulence.

The velocity correlations of the second, third, and quadruple orders between two distinct points P and P' from (8) can be written as:

$$\begin{aligned} \overline{w'^n w_i} &= \overline{w^n w_i} + q^2 \phi_i^n(\eta, x, t), \\ \overline{w'^m w'^n w_i} &= \overline{w^m w^n w_i} + q^3 \psi_i^{mn}(\eta, x, t), \\ \overline{w'^n w_i w_k} &= \overline{w^n w_i w_k} + q^3 \phi_{ik}^n(\eta, x, t), \\ \overline{w'^m w'^n w_i w_k} &= \overline{w^m w^n w_i w_k} + q^4 \psi_{ik}^{mn}(\eta, x, t), \\ \overline{w'^n w_i w_k w_l} &= \overline{w^n w_i w_k w_l} + q^4 \phi_{ikl}^n(\eta, x, t). \end{aligned} \quad (9)$$

In the above equations we have

$$\xi^i = x'^i - x^i, \quad \eta^i = \xi^i / \lambda. \quad (10)$$

The functions ϕ_i^n , ψ_i^{mn} , ϕ_{ik}^n , ψ_{ik}^{mn} and ϕ_{ikl}^n all vary rapidly with ξ^i , the coordinate difference between the two points P and P' , and vary slowly with x^i . Hence partial derivatives of the functions defined in (9) with respect to ξ^i are much greater than those with respect to x^i .

The turbulent pressure gradient and velocity fluctuation correlations, and the dissipation terms in the dynamical equations of correlations in (5), (6) and (7) are written below. Their calculations are explained in the appendix.

For the pressure gradient and velocity fluctuation correlation we have

$$(1/\rho)(\overline{\varpi_{,i} w_k} + \overline{\varpi_{,k} w_i}) = q^2 a_{mik}' U_{,n}^m + q^2 \lambda a_{mik}'' U_{,nr}^m + (q^3/\lambda) b'_{ik}, \quad (11)$$

in which

$$\begin{aligned} a_{mik}' &= \frac{1}{2\pi} \int \int \int [\phi_{i,mk}^n + \phi_{k,mi}^n] \frac{1}{r} dV', \\ a_{mik}'' &= \frac{1}{2\pi\lambda} \int \int \int \{ \phi_{i,m}^n \delta_k^r + \phi_{k,m}^n \delta_i^r + \xi^r [\phi_{i,mk}^n + \phi_{k,mi}^n] \} \frac{1}{r} dV', \\ b'_{ik} &= \frac{\lambda}{4\pi} \int \int \int [\psi_{i,mnk}^{mn} + \psi_{k,mni}^{mn}] \frac{1}{r} dV'; \end{aligned} \quad (12)$$

$$\begin{aligned} \frac{1}{\rho} (\overline{\varpi_{,i} w_k w_l} + \overline{\varpi_{,k} w_l w_i} + \overline{\varpi_{,l} w_i w_k}) &= \\ &= q^3 b_{mikl}' U_{,n}^m + q^3 \lambda b_{mikl}'' U_{,nr}^m + \frac{q^4}{\lambda} c'_{ikl}, \end{aligned} \quad (13)$$

in which

$$b'_{mikl} = \frac{1}{2\pi} \iiint [\phi'_{ik,ml} + \phi'_{kl,mi} + \phi'_{li,mk}] \frac{1}{r} dV',$$

$$b'_{mikl}{}^{nr} = \frac{1}{2\pi\lambda} \iiint \{ \phi'_{ik,m} \delta_l^r + \phi'_{kl,m} \delta_i^r + \phi'_{li,m} \delta_k^r$$

$$+ \xi^r [\phi'_{ik,ml} + \phi'_{kl,mi} + \phi'_{li,mk}] \} \frac{1}{r} dV',$$

$$c'_{ikl} = \frac{\lambda}{4\pi} \iiint [\psi'_{kl,mni} + \psi'_{li,mnk} + \psi'_{ik,mnl}] \frac{1}{r} dV'; \quad (14)$$

$$\frac{1}{\rho} (\overline{\varpi_{,i} w_k w_l w_p} + \overline{\varpi_{,k} w_l w_p w_i} + \overline{\varpi_{,l} w_p w_i w_k} + \overline{\varpi_{,p} w_i w_k w_l})$$

$$= q^4 c'_{miklp} U_{,n}^m + q^4 \lambda c'_{miklp}{}^{nr} U_{,nr}^m + \frac{q^5}{\lambda} d'_{iklp}, \quad (15)$$

in which

$$c'_{miklp} = \frac{1}{2\pi} \iiint [\phi'_{ikl,mp} + \phi'_{klp,mi} + \phi'_{lpi,mk} + \phi'_{pik,ml}] \frac{1}{r} dV',$$

$$c'_{miklp}{}^{nr} = \frac{1}{2\pi\lambda} \iiint \{ \phi'_{ikl,m} \delta_p^r + \phi'_{klp,m} \delta_i^r + \phi'_{lpi,m} \delta_k^r + \phi'_{pik,m} \delta_l^r$$

$$+ \xi^r [\phi'_{ikl,mp} + \phi'_{klp,mi} + \phi'_{lpi,mk} + \phi'_{pik,ml}] \} \frac{1}{r} dV',$$

$$d'_{iklp} = 0. \quad (16)$$

All the partial differentiations under the above integrals are taken with respect to the coordinate ξ^i and all the tensors a' , b' , c' , d' with various ranks defined integrals (12)–(16) are approximately constants proved earlier (Chou 1945).

The viscous dissipation terms in (5), (6) and (7) are given by (cp. appendix).

$$2\nu g^{mn} \overline{w_{i,m} w_{k,n}} = -(2\nu/3\lambda^2)(k-5)q^2 \delta_{ik} + (2\nu k/\lambda^2) \overline{w_i w_k}, \quad (17)$$

$$2\nu g^{mn} (\overline{w_{i,m} w_{k,n} w_l} + \overline{w_{k,m} w_{l,n} w_i} + \overline{w_{l,m} w_{i,n} w_k})$$

$$= (2\nu/\lambda^2) [c_1 (\overline{w_i w_j w^j} \delta_{kl} + \overline{w_k w_j w^j} \delta_{li} + \overline{w_l w_j w^j} \delta_{ik}) + c_2 \overline{w_i w_k w_l}], \quad (18)$$

$$2\nu g^{mn} (\overline{w_{i,m} w_{k,n} w_l w_p} + \overline{w_{k,m} w_{l,n} w_i w_p} + \overline{w_{l,m} w_{p,n} w_i w_k}$$

$$+ \overline{w_{i,m} w_{l,n} w_k w_p} + \overline{w_{k,m} w_{p,n} w_i w_l} + \overline{w_{i,m} w_{p,n} w_k w_l})$$

$$= (2\nu/\lambda^2) [d_1 (\overline{w_i w_k w_m w^n} \delta_{lp} + \overline{w_k w_l w_m w^n} \delta_{ip} + \overline{w_l w_p w_m w^n} \delta_{ik}$$

$$+ \overline{w_i w_l w_m w^n} \delta_{kp} + \overline{w_k w_p w_m w^n} \delta_{il} + \overline{w_i w_p w_m w^n} \delta_{kl}) + d_2 \overline{w_i w_k w_l w_p}]. \quad (19)$$

3. Theory of homogeneous isotropic turbulence and the condition of pseudo-similarity

In a wind-tunnel the mean velocity of the air-stream behind the grid is constant. For an observer moving with this mean velocity, the equations of motion for the turbulent fluctuation (4) are the same as the Navier-Stokes equations of motion. The theory of homogeneous isotropic turbulence is based upon the vortex solution of the Navier-Stokes equations which forms the element of turbulence. This vortex is axially symmetrical and is randomly distributed as regards to its position and orientation of its axis of symmetry in the turbulent fluid. Then the turbulent velocity correlation of any order at one point or between two distinct points can be calculated by averaging the products of the velocity components at two points within the vortex over its position and the orientation of its axis in the fluid.

But the Navier-Stokes equations are non-linear partial differential equations of the second order and have different kinds of solutions. The theory was first applied to the case in the final period of decay in which the non-linear terms in the Navier-Stokes equations can be neglected (Chou & Tsai 1957), and a similarity condition was assumed to select the right kind of vortex to represent the turbulence element. The already well-known double velocity correlation could be thus explained. Furthermore, the theory predicted the triple velocity correlation (Huang 1965) which was verified experimentally by Bennett & Corrsin (1978).

For very high Reynolds number flows in the initial period of decay near the grid in the wind-tunnel, there are solutions of the Navier-Stokes equations. By using another condition of similarity a different vortex solution was obtained, yielding the law of decay of turbulence and the spread of Taylor's scale of micro-turbulence λ in agreement with experiments. The double and triple velocity correlations thus calculated have also qualitative agreements with measurements (Chou *et al* 1965).

The condition of pseudo-similarity was proposed to correlate the two kinds of similarity in the initial and final periods of decay for isotropic homogeneous turbulence (Chou & Huang 1975; Huang & Chou 1981). A large number of theoretical calculations of the decay of turbulent energy, the spread of Taylor's scale of micro-turbulence λ , the double and triple velocity correlations from the initial to the final period of decay, together with the three-dimensional and one-dimensional energy spectrum functions and the energy transfer spectrum function etc., all agree very well with experimental measurements.

This condition of pseudo-similarity for homogeneous isotropic turbulence can be written in terms of λ and R_λ , the turbulence Reynolds number, as follows (Zhou 1985):

$$(\lambda/\nu)(d\lambda/dt) = (1/R_0)R_\lambda^2 + 2, \quad (20)$$

with

$$R_\lambda = q\lambda/\nu, \quad (21)$$

in which R_0 , a Reynolds number, is a constant. In this relation when R_λ is large, namely, in the initial period of decay, the number 2 in (20) can be ignored. Then we have λ^2 and q^2 satisfying,

$$\lambda^2 = 10\nu t, \quad q^2 \sim 1/t. \quad (22)$$

In the final period of decay, R_λ in (20) can be neglected and we have

$$\lambda^2 = 4\nu t, \quad q^2 \sim (1/t^{5/2}). \quad (23)$$

The experimental proof of the condition (20) from the initial to the final period of decay has been carried out in the turbulence wind-tunnel of Peking University (to be published).

For general shear turbulent flows the condition of pseudo-similarity (20) can be put in the following form,

$$\begin{aligned} (\lambda/\nu)[(\partial\lambda/\partial t) + U^j\lambda_{,j}] &= (1/R_0)\{R_\lambda^2 - [R_1 + (\kappa_1/\nu)\lambda^2(g^{kl}U^j_{,k}U_{j,l})^{1/2} \\ &+ (\kappa_2/\nu)\lambda^3(g^{ij}g^{kl}g^{mn}\Omega_{ik,m}\Omega_{jl,n})^{1/2}]^2 + 2R_0\}, \end{aligned} \quad (24)$$

where $\Omega_{ik} = U_{i,k} - U_{k,i}$, and κ_1, κ_2, R_0 , and R_1 are constants, and q and R_λ are defined by (8) and (21), respectively.

In the first order approximation for the channel flow, the wake and jets, the equations of mean motion (3), the double velocity correlation (5) and the condition of pseudo-similarity (24) have been used, while terms in the triple correlation have been ignored (Zhou 1985).

4. The plane turbulent wake

Now we consider the problem of the plane turbulent wake in which there are already measurements of the triple velocity correlation. For the second order approximation, besides the equations of mean motion and of the double velocity correlation, and the condition of pseudo-similarity, we have in addition to use the dynamical equations of the triple and quadruple orders (6) and (7). The rigorous method of solution is to solve simultaneously for the mean velocity U_i , the double, triple and quadruple velocity correlations and the turbulence scale λ from all the equations, (3), (5), (6), (7), and (24) with (11)–(19), while neglecting the terms in the quintuple correlation. But this method of solution is complicated.

A simpler method of approach is to find the solution by successive substitution. This method was used in the first order approximation of the solution for the plane wake (Chen 1984). To start with in the first step we find the approximate expression of the Reynolds shear τ_{xy} to be proportional to the gradient of the mean velocity $\partial U/\partial y$, a result which was obtained earlier (Chou 1959). This gives us $\overline{w_1 w_2}^{(0)}$. Then the mean velocity denoted by $U_i^{(0)}$ is solved and the other components of the double velocity correlation, $\overline{w_i w_k}^{(0)}$, and the scale of turbulence $\lambda^{(0)}$ can be obtained from the equations of the double velocity correlation and the condition of pseudo-similarity, the terms in the triple correlation being ignored. The theoretical values of the above functions $U_i^{(0)}$, and $\overline{w_i w_k}^{(0)}$ thus calculated agree very well with experimental measurements.

The next step in this first order approximation is to use the above values of $\overline{w_i w_k}^{(0)}$ and $\lambda^{(0)}$ to solve for $U_i^{(1)}$, $\overline{w_i w_k}^{(1)}$ and $\lambda^{(1)}$. The new functions $U_i^{(1)}$, $\overline{w_i w_k}^{(1)}$ and $\lambda^{(1)}$ obtained by this substitution differ very little from those obtained in the first step and this process can be repeated.

In this first order approximation for the solution of the plane wake, one of us, Chen Shi-yi, who carried out this investigation, has also solved simultaneously the equations of mean motion (3) and of the double correlation (5), neglecting the terms in triple correlation, under the condition of pseudo-similarity (24), by using a computer. The results thus obtained also agree quite well with those obtained in the above method of successive substitution.

The rigorous method of finding the solution of the plane wake in the second order approximation, as mentioned before, is to solve simultaneously the equations of mean motion, of the double, triple and quadruple correlations together with the condition of pseudo-similarity. To avoid this, we use again the method of successive substitution. Since in the first order approximation we have already obtained values of the mean velocity and double correlation which agree with experiment quite well, we can use them as known values and put them into the equations of $\overline{w_i w_k w_l}$ and $\overline{w_i w_k w_l w_p}$ and look for their solutions.

But to solve the equations for the triple and quadruple correlations together is still complicated. Hence we can separate their solutions by assuming an often used relation between the quadruple correlation with the double correlation in homogeneous isotropic turbulence based upon the quasi-normal distribution condition, which is given by

$$\overline{w_i w_k w_l w_p} = \overline{w_i w_k} \overline{w_l w_p} + \overline{w_i w_l} \overline{w_p w_k} + \overline{w_i w_p} \overline{w_k w_l}, \quad (25)$$

and solve the equations of triple correlation first. All of the six non-vanishing components of the triple correlation for the plane wake thus computed agree very well with experiment (cp. figures 1–6) (Fabris 1983).

The next step is to put the known triple correlation obtained above into the equation of quadruple correlation, neglect the quintuple correlation and seek its solution which can then be compared with the relation (25). Their agreement is comparatively satisfactory [cf. figures 7–9, agreeing well or not so well with (25), e.g., out of its total nine non-vanishing components]. Since the solution of

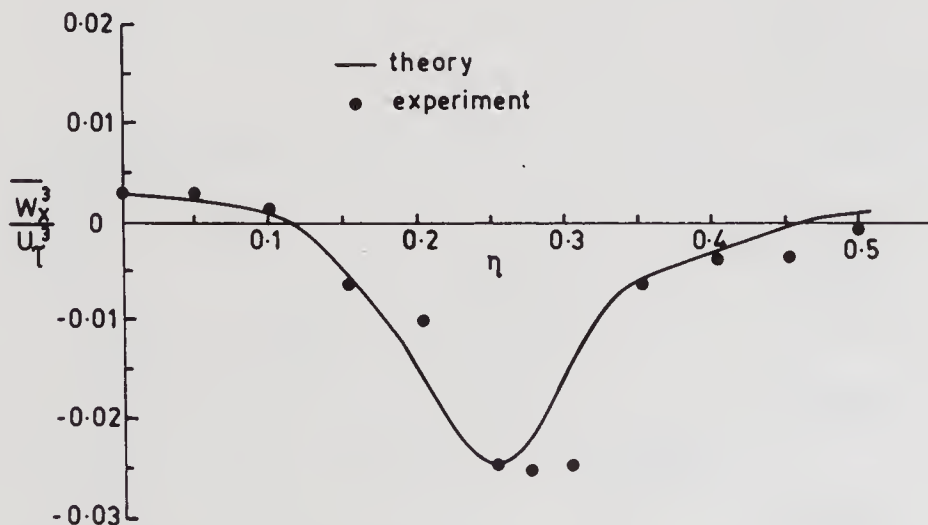


Figure 1. Comparison of experimental data with present theory for components of the triple correlation in a plane wake.

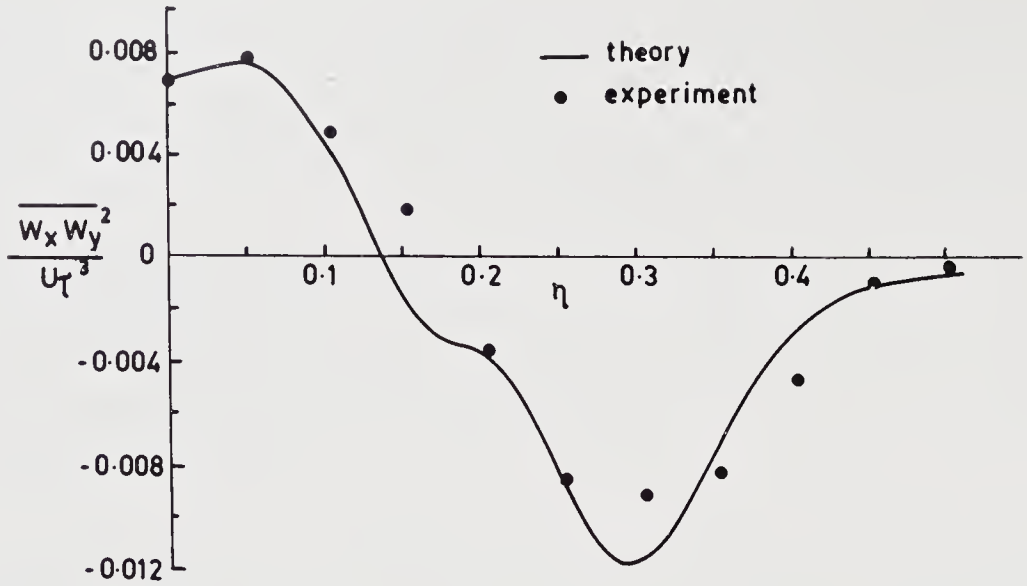


Figure 2. Comparison of experimental data with present theory for components of the triple correlation in a plane wake.

$\overline{w_i w_k w_l w_p}$ from its dynamical equations agrees fairly well with (25), there is no need to put this solution of $\overline{w_i w_k w_l w_p}$ into the equations of triple correlation and find its solution again.

On the other hand, if we want to have more accurate values of U_i , $\overline{w_i w_k}$ and λ , we can put the third order velocity correlation obtained into the equations for $\overline{w_i w_k}$ and solve for U_i , $\overline{w_i w_k}$ and λ from (3), (5) and (24). This method of substitution can obviously be extended to get higher order approximations.

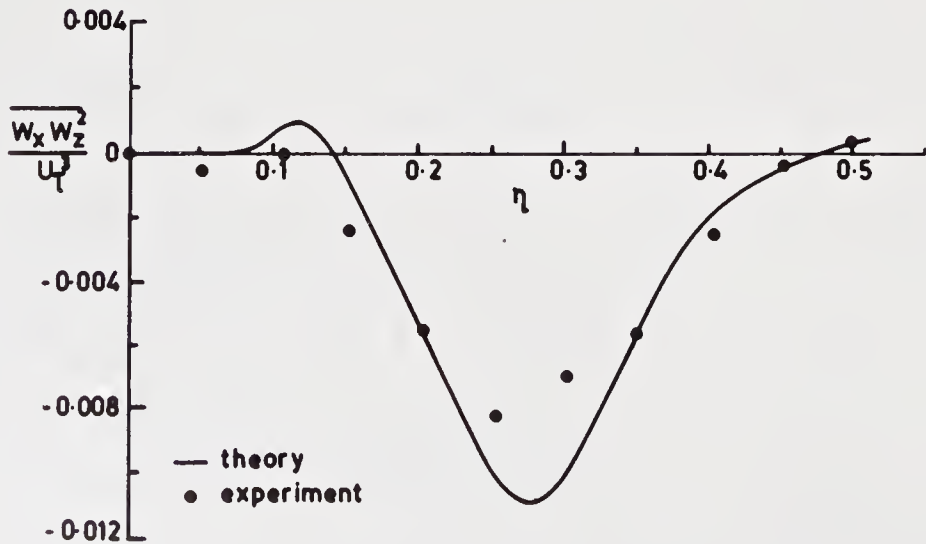


Figure 3. Comparison of experimental data with present theory for components of the triple correlation in a plane wake.

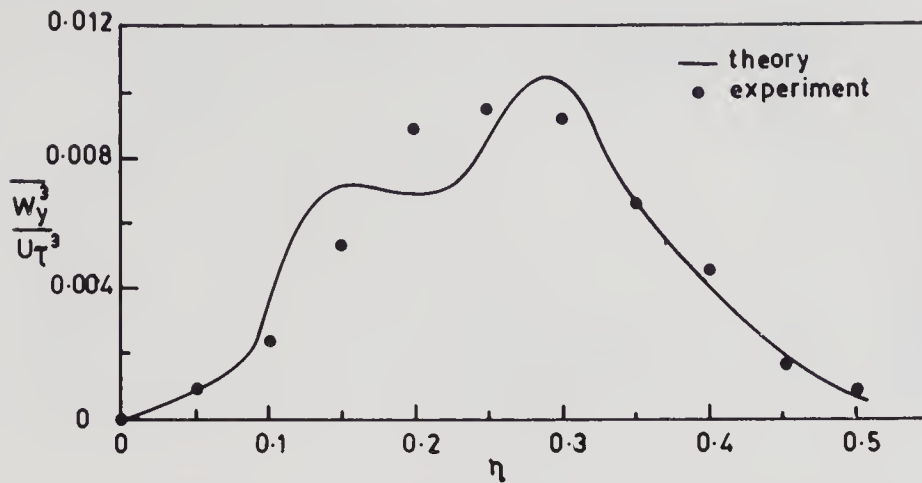


Figure 4. Comparison of experimental data with present theory for components of the triple correlation in a plane wake.

5. Discussion

In the above methods of successive approximation in treating the general shear turbulence problem there are some points which need further discussion. The solution of the turbulent velocity fluctuation given in the form (8) is a special form of solution which has the property of pseudo-similarity. This is analogous to the kind of similarity discovered by Prandtl in the steady viscous incompressible laminar flows along a semi-infinite plane, through a channel and a pipe, and in wakes and jets. But it is well-known that there are also other different kinds of solutions for laminar viscous flows. We have a similar situation in incompressible turbulent flows. For example, for homogeneous shear flows, there are types of flow

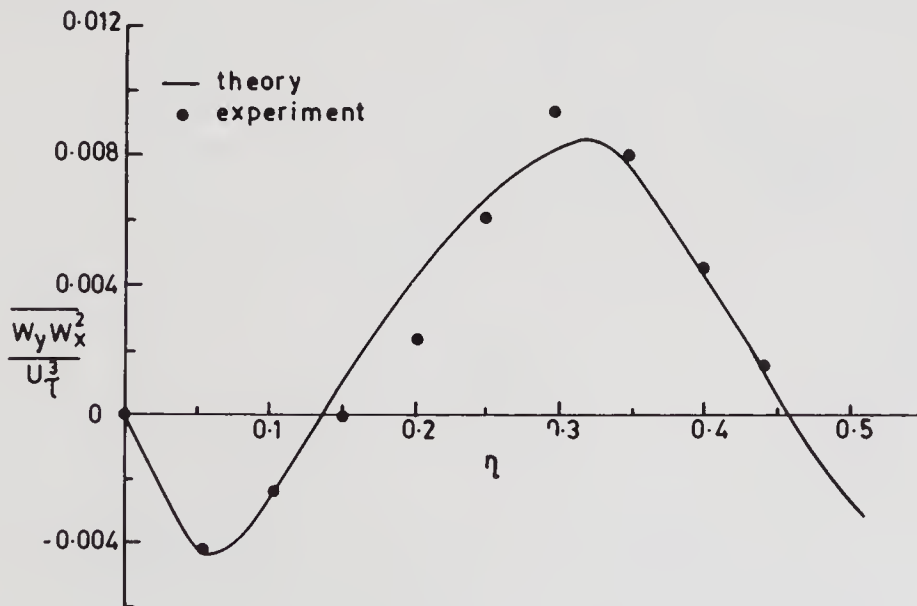


Figure 5. Comparison of experimental data with present theory for components of the triple correlation in a plane wake.

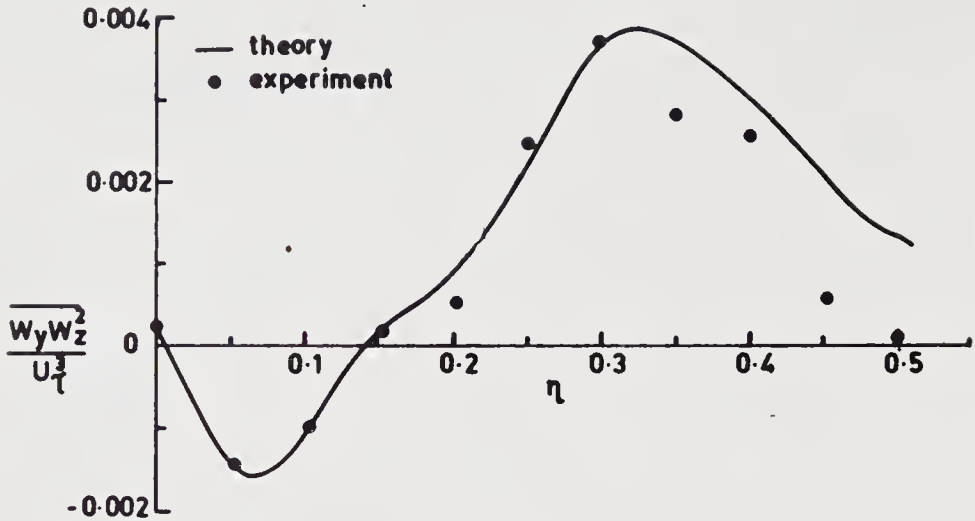


Figure 6. Comparison of experimental data with present theory for components of the triple correlation in a plane wake.

which satisfy the pseudo-similarity condition while there are other flows which have different properties (Huang 1982, pp. 137–159, 1984, pp. 357–364).

In the first order approximation in solving the plane wake problem, we earlier considered the mean velocity and the double velocity correlation together, neglecting the terms in the triple correlation, and found their solutions from their dynamical equations under the condition of pseudo-similarity. Likewise, in the second order approximation we now consider the correlations of the triple and quadruple orders together, add their dynamical equations to the first set and find

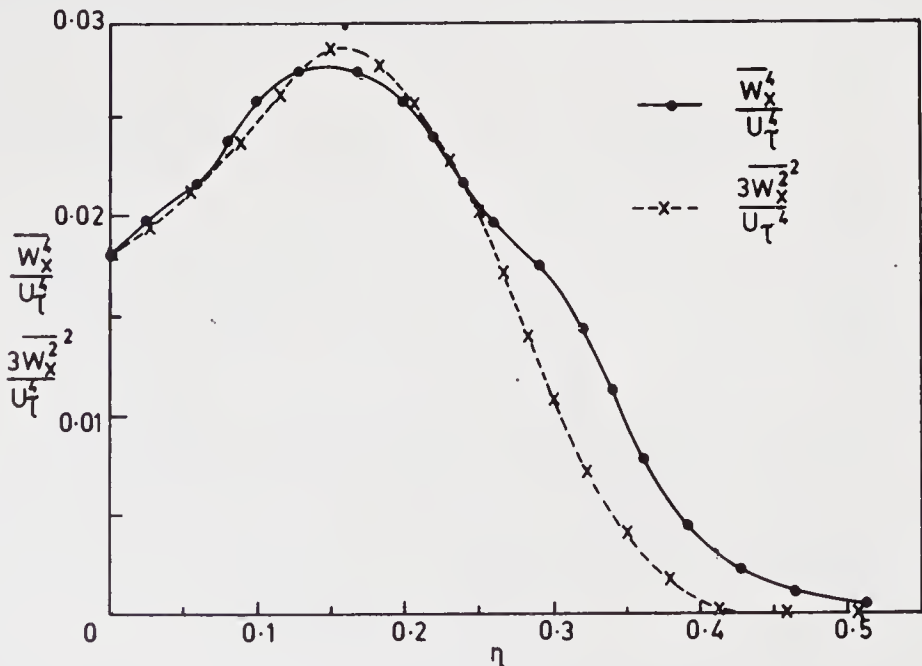


Figure 7. Comparison of experimental data with present theory for components of the quadruple correlation in a plane wake.

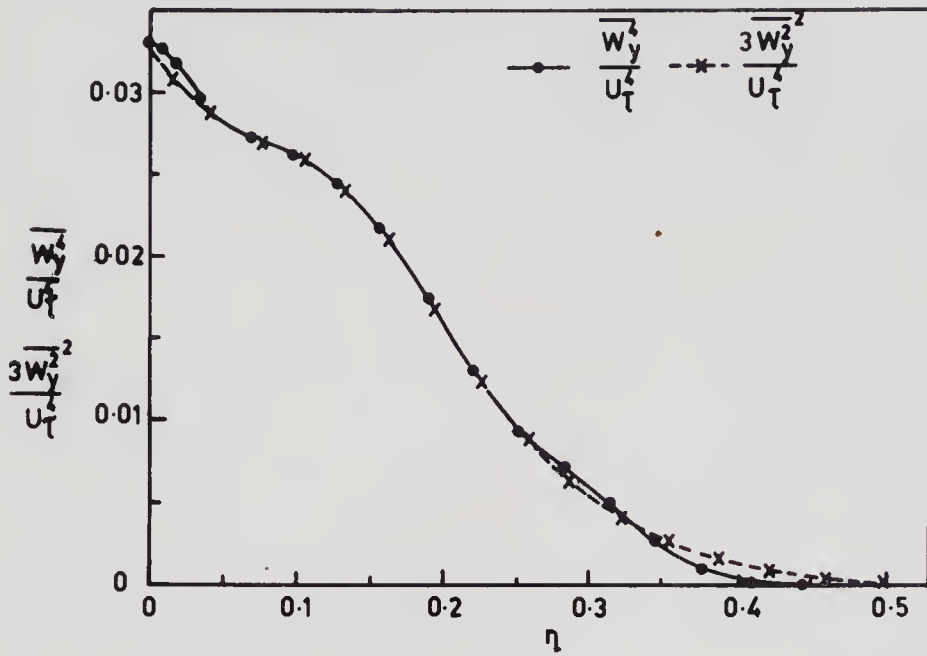


Figure 8. Comparison of experimental data with present theory for components of the quadruple correlation in a plane wake.

their solutions, while neglecting correlation terms of the fifth order. This method of solving correlation equations of an odd order and of the following even order together gives better approximation of the former and can be extended to find approximate solutions of still higher orders.

In the appendix we have obtained the three viscous dissipation terms in (5), (6), (7) based upon the hypotheses introduced. Their justification also depends upon experiments.

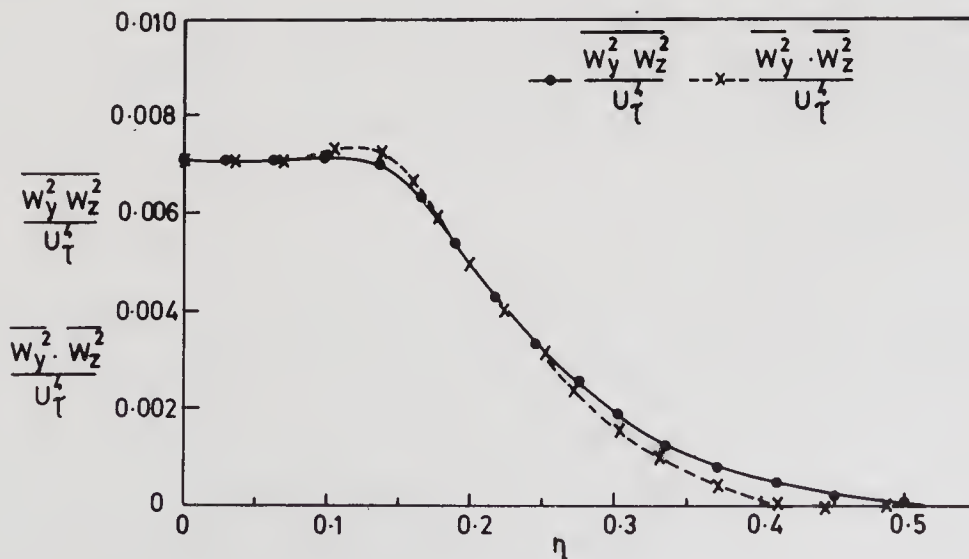


Figure 9. Comparison of experimental data with present theory for components of the quadruple correlation in a plane wake.

Appendix

In the computations of the integrals in the turbulent pressure gradient and velocity fluctuation correlations we used the first term in the series expansion of $U'_{,n}$ as an approximation in the 1945 paper (Chou 1945). This expansion has been improved to consider the second term (Zhou 1985) as follows:

$$U'_{,n}{}^m = U_{,n}^m + \xi^r U'_{,nr}{}^m. \quad (\text{A1})$$

Then in (5) we have

$$[U'_{,n}{}^m (\overline{w'^n w_i})'_{,m}]'_{,k} = U_{,n}^m (\overline{w'^n w_i})'_{,mk} + U'_{,nr}{}^m [(\overline{w'^n w_i})'_{,m} \delta_k^r + \xi^r (\overline{w'^n w_i})'_{,mk}]. \quad (\text{A2})$$

Similarly in (6) and (7), we have

$$\begin{aligned} [U'_{,n}{}^m (\overline{w'^n w_k w_l})'_{,m}]'_{,i} &= \\ &= U_{,n}^m (\overline{w'^n w_k w_l})'_{,mi} + U'_{,nr}{}^m [(\overline{w'^n w_k w_l})'_{,m} \delta_i^r + \xi^r (\overline{w'^n w_k w_l})'_{,mi}]. \end{aligned} \quad (\text{A3})$$

$$\begin{aligned} [U'_{,n}{}^m (\overline{w'^n w_k w_l w_p})'_{,m}]'_{,i} &= \\ &= U_{,n}^m (\overline{w'^n w_k w_l w_p})'_{,mi} + U'_{,nr}{}^m [(\overline{w'^n w_k w_l w_p})'_{,m} \delta_i^r + \xi^r (\overline{w'^n w_k w_l w_p})'_{,mi}], \end{aligned} \quad (\text{A4})$$

respectively.

Putting the above relations into the integrals of (5), (6) and (7), respectively, and considering the functions defined in (9), we then obtain (11), (12), (13), (14), (15) and (16). Here we note that the constant d'_{iklp} in (16) involves differentiations leading to macro-lengths in the denominator and quintuple correlations under its integral. Therefore d'_{iklp} can be set equal to zero.

We found earlier (Chou 1945) the viscous dissipation terms in the equations of double correlation (5) by assuming that the double velocity correlation between two points P and P' , $\overline{w_i w'_k}$, could be expanded in powers of ξ_j and the coefficients of $\xi_l \xi_m$ in the expansion should be linear functions of $\overline{w_n w_p}$, δ_{rs} and their products. The double correlation $\overline{w_i w'_k}$ should furthermore satisfy the equation of continuity

$$(\overline{w_i w'^j})'_{,j} = 0. \quad (\text{A5})$$

From $\overline{w_i w'_k}$ the dissipation term in (17) was obtained by partial differentiations of $\overline{w_i w'_k}$ with respect to x^m and x'^n , setting x'^n equal to x^n and then contracting by g^{mn} .

The viscous dissipation terms in (18) and (19) can be obtained in the same way. For the term in (18) we assume that in the expansion of $\overline{w_i w_k w'_l}$ in powers of ξ^j , the coefficients of $\xi_m \xi_n$ should be linear combination of $\overline{w_p w_q w_r}$, δ_{st} and their products. Likewise $\overline{w_i w_k w'_l}$ should satisfy the equation of continuity.

$$(\overline{w_i w_k w'^l})'_{,l} = 0. \quad (\text{A6})$$

By the method used to obtain (17), we can get (18).

Equation (19) can be obtained by the same method and similar assumptions explained for getting the dissipation terms in the equations of the double and triple correlations in (17) and (18), respectively. This method can be extended to find similar viscous dissipation terms for still higher approximations.

References

- Bennett J C, Corrsin S 1978 *Phys. Fluids* 21: 2129–2140
- Chen Shi-yi 1984 *The solution of the turbulent plane wake under the condition of pseudo-similarity* M S thesis, Peking University, Beijing
- Chou P Y 1940 *Chin. J. Phys.* 4: 1–33
- Chou P Y 1945 *Q. J. Appl. Math.* 3: 38–54
- Chou Pei-yuan 1959 *Sci. Sin.* 8: 1095–1119
- Chou Pei-yuan, Huang Yong-nian 1975 *Sci. Sin.* 18: 199–222
- Chou Pei-yuan, Shih Hsun-kang, Li Sung-nian 1965 *Acta Sci. Nat. Univ. Pekinensis* 10: 39–52
- Chou Pei-yuan, Tsai Shu-tang 1957 *Acta Mech. Sin.* 1: 3–14
- Chou Pei-yuan, Tsai Shu-tang 1957 *Acta Mech. Sin. Chin. J. Mech.* 1: 3–14
- Fabris G 1983 *Phys. Fluids* 26: 422–427
- Huang Yong-nian 1965 *Acta Mech. Sin.* 8: 122–132
- Huang Yong-nian 1982 Papers on theoretical physics and mechanics in commemoration of Professor Zhou (Chou) Pei-yuan's eightieth birthday (Beijing: Science Press)
- Huang Yong-nian 1984 *Turbulence and chaotic phenomena in fluids* (ed.) T Tatsumi (Amsterdam: North-Holland)
- Huang Yong-nian, Zhou (Chou) Pei-yuan 1981a *Sci. Sin.* 24: 1207–1230
- Huang Yong-nian, Zhou (Chou) Pei-yuan 1981b *Proc. Indian Acad. Sci. (Eng. Sci.)* 4: 177–197
- Launder B E 1979 *Turbulent shear flows* (Berlin: Springer-Verlag)
- Rotta J C 1951a *Z. Phys.* 129: 547–572
- Rotta J C 1951b *Z. Phys.* 131: 51–77
- Wu Zhong 1986 *The solutions of the turbulent plane and axial jets under the condition of pseudo-similarity* M S thesis, Peking University, Beijing
- Zhou (Chou) Pei-yuan 1985 *Sci. Sin.* A28: 405–421

Flat plate drag reduction by turbulence manipulation

R NARASIMHA¹ and K R SREENIVASAN²

¹National Aeronautical Laboratory and Indian Institute of Science, Bangalore 560 017, India

²Mason Laboratory, Yale University, New Haven, CT 06520, USA

Abstract. The major objective of the present paper is to delineate the conditions under which a turbulent boundary layer manipulated by the insertion of a passive object may lead to a lower overall drag than in the unmanipulated flow. It is pointed out that almost any device inserted in the boundary layer will lead to a lower *skin friction* drag. Experimental evidence is presented to support this conclusion, which is most easily thought of as characterizing “wall wakes”. However when the stream-wise extent of the manipulator is not small, the no-slip condition forced on the manipulator boundary modifies the flow through what is here described as the “blade” effect. The presence of this effect may be inferred from experimental data which unambiguously show that a flat plate with a chord c of the order of the boundary layer thickness δ produces the same order of skin friction reduction as a cylindrical rod with a higher wake momentum thickness θ_w . As in general both blade and wake effects are operating simultaneously, available data are analysed in the plane formed by the two variables c/δ and θ_w/δ . This analysis shows that the net drag reduction, if it occurs at all, is quite small, and that its realization demands a blade chord (at zero incidence) larger than about $40 \theta_w$.

Finally, it is pointed out that if, as often claimed, such manipulators effect a permanent decrease in boundary layer momentum thickness, then sufficiently far downstream where the boundary layer may be expected to have returned to equilibrium, the local skin friction coefficient at any station must be higher than in the unmanipulated flow at the same station because of the lower momentum thickness Reynolds number. It therefore follows that any possible reduction in drag due to the manipulator can only be achieved for certain limited downstream lengths behind the manipulator.

Keywords. Drag reduction; turbulence manipulation; skin friction; wall wakes; blades.

1. Introduction

The extraordinary increases in the price of fossil fuels that have occurred in the last 15 years have directed attention once again to problems connected with the control of turbulent flows. A large part of the resistance offered to the flow of fluids in a variety of technological applications can be traced to the high skin friction drag associated with flow turbulence. Although there are cases where *enhancing* the turbulence levels in a flow may produce beneficial effects, even for the drag, as in the classic experiment of Wieselsberger (in which a ring trip placed on the front of a sphere was shown to reduce the drag of the sphere significantly over a certain Reynolds number range), the subject which has attracted most attention in recent years is the possibility of modifying or manipulating turbulence to reduce the skin friction drag of bodies.

Turbulence may be controlled in many different ways. To begin with, it may be totally *prevented* from occurring. This has been a subject of long-standing interest; work done in the 1950s showed in particular how boundary layer suction could maintain laminar flow on aerodynamic surfaces. For a variety of operational and technical reasons, however, development along these lines was abandoned in the 1960s, but perhaps oil was at that time too cheap for sophisticated fluid-dynamical technologies of drag reduction to be worthwhile on aircraft. More recent work has demonstrated the scientific feasibility of active control of transition (Liepmann & Nosenchuck 1982; Thomas 1983; Strykowski 1986). We are certain that the wave-cancellation ideas that inspire this approach, and other more familiar preventive methods, will be pursued with vigour in coming years.

Another concept is to relaminarize an initially turbulent flow: this is essentially *curative*. It has become clear here that there is a vast number of agencies that can force a turbulent flow back to a laminar or quasi-laminar state. The present authors have in recent years considered these problems at great length (Narasimha & Sreenivasan 1979; Sreenivasan 1981; Narasimha 1983), and if only for this reason we feel that it is unnecessary to discuss the possibilities here once again.

The third concept involves modifying turbulence in some beneficial way; and it is indeed this possibility that is going to be the major concern of the present analysis. An early demonstration of this possibility was perhaps contained in Roshko's (1955) study of the effect of a splitter plate in the wake of a circular cylinder: he found that the base pressure coefficient could be raised approximately from -1.1 to -0.5 , implying a substantial reduction in the *pressure* drag of the cylinder. The question is whether similar manipulation is likely to reduce *skin friction* drag on streamlined bodies. The expectation that such reduction might be feasible rests, we believe, on certain basic characteristics of turbulent flows that have emerged from various fundamental studies carried out during the last fifteen years. Among these characteristics are (i) the presence of a considerable degree of order or structure in turbulent shear flows [reviewed in recent years by Cantwell (1981) and Coles (1985) among others], (ii) the production of turbulent energy in "bursts" (Kline *et al* 1967), which show a strong coupling between the outer and inner flows in the boundary layer (Rao *et al* 1971; Narasimha & Kailas 1987, pp. 188–222), and (iii) the long memory of turbulent flows (Clauser 1956; Narasimha & Prabhu 1972). These facts support the tantalizing possibility that appropriate interference with the organized motion in a turbulent boundary layer, active or passive, could lead to

favourable effects that will persist for long times or flow distances. Numerous schemes based on this concept have been tried (Bushnell 1983), but few have yet travelled the long road to practical application. The current status of such ideas for turbulence modification has been examined in previous AIAA meetings (Bushnell 1983; Corke *et al* 1982). We will therefore not go over the ground that has already been covered by our predecessors but concentrate on what seems still to be the most intriguing possibility in all of these, namely that of being able to modify turbulence favourably by the use of so-called manipulators. (These have also been called large eddy break-up devices, but this name presumes a mechanism that does not yet seem to have been conclusively established.) The notation for such manipulators is shown in figure 1.

2. General approach

One of the major objectives of the present analysis is to delineate the conditions under which a turbulent boundary layer manipulated by the insertion of a passive object may lead to a lower overall drag than in the unmanipulated flow.

First of all, it must be remarked that almost any object or device inserted in the boundary layer will lead to lower *friction* drag (– we shall present the evidence for this shortly): the question is whether the lower friction is not more than lost by the ‘parasite’ drag of the device itself. Let us consider the data available on such flows (often not studied in the context of drag reduction at all). We may begin with the experiments of Klebanoff & Diehl (1951), who measured boundary layer development with a rod placed on the surface. Figure 2 shows the growth of the momentum thickness θ with and without the rod. It is seen that with the rod θ is always higher (implying higher total drag) but that there is a short region downstream of the rod where θ goes down. It is possible that the friction here is not only reduced but is actually negative due to local separation. It is convenient to think of such flows as representing *wall-wakes* (as we shall call them), in which momentum is extracted from a wall-bounded flow; this is in contrast to *wall-jets* where momentum is injected into the flow, usually through a nozzle at or below the surface.

Wall-wake flows need not necessarily result only from the placement of objects *on* the surface. Marumo *et al* (1978) have reported studies with an 8 mm dia rod at heights of 0.222, 0.556 and 1.24 times the undisturbed boundary layer thickness δ_m (≈ 27 mm). Their results, shown in figure 3, once again demonstrate how in general the skin friction coefficient drops when the rod is inserted.

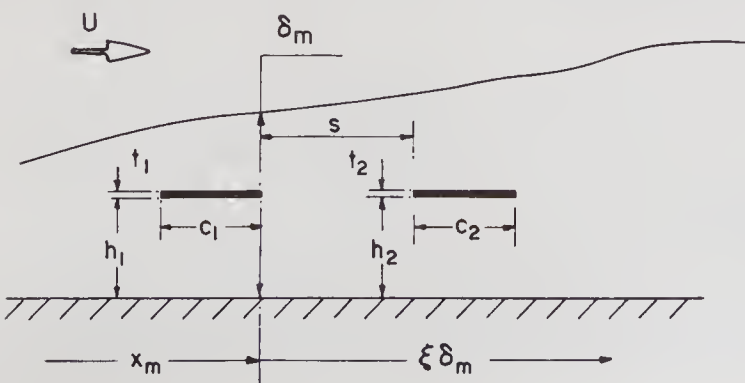


Figure 1. Sketch of a tandem blade manipulator, showing notation adopted here. One or both the blades of the manipulator could be at some small angle of attack.

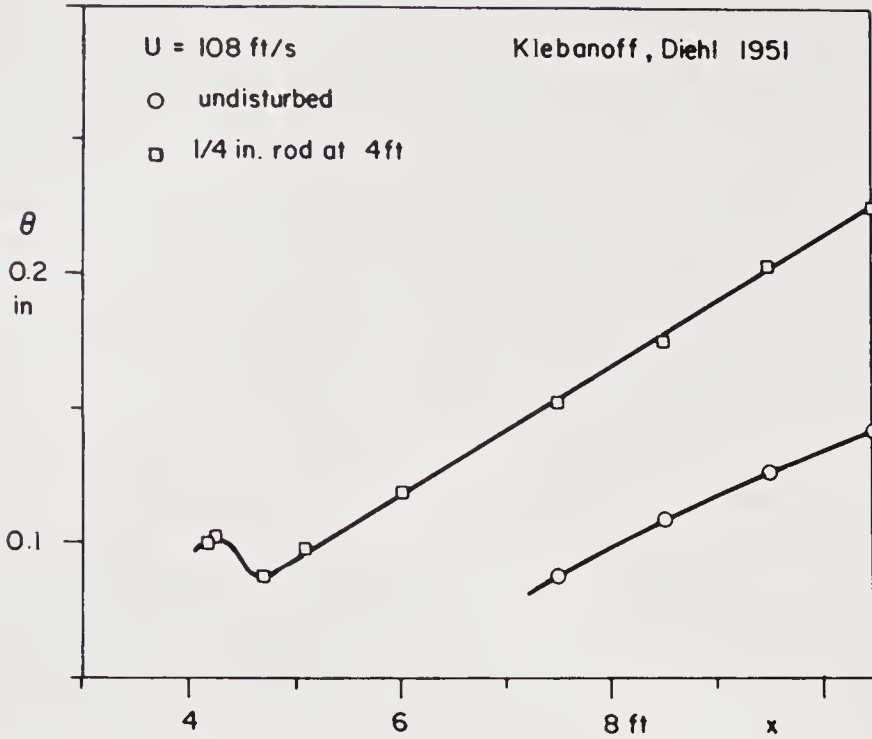


Figure 2. Effect of a rod placed on the wall on the growth of the boundary layer momentum thickness: data from Klebanoff & Diehl (1951).

We conclude by citing just one more example, from the work of Kacker & Whitelaw (1971). Actually the flow studied by them was a wall-jet, but the lip of the nozzle, which rested above the surface, acted like a wake generator: when the jet was slower than the free stream (a situation that they also describe as a wall-wake), the skin friction coefficient showed a substantial drop (figure 4).

Now the insertion of any object in the flow is bound to produce a wake of some kind, and a corresponding *increment* in drag. However, especially if the streamwise extent of the body is not small, the new surface introduces an additional boundary

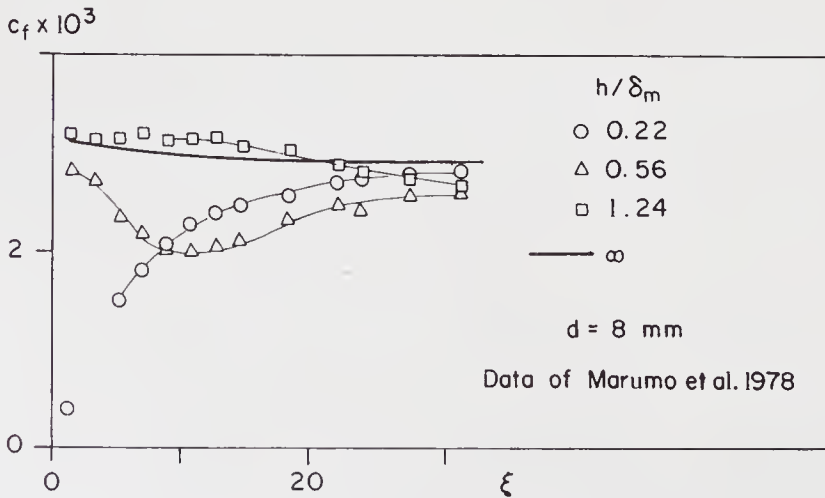


Figure 3. Streamwise variation of skin friction coefficient with a rod placed in a turbulent boundary layer at different heights above the surface: data from Marumo *et al* (1978). Full line indicates undisturbed boundary layer.

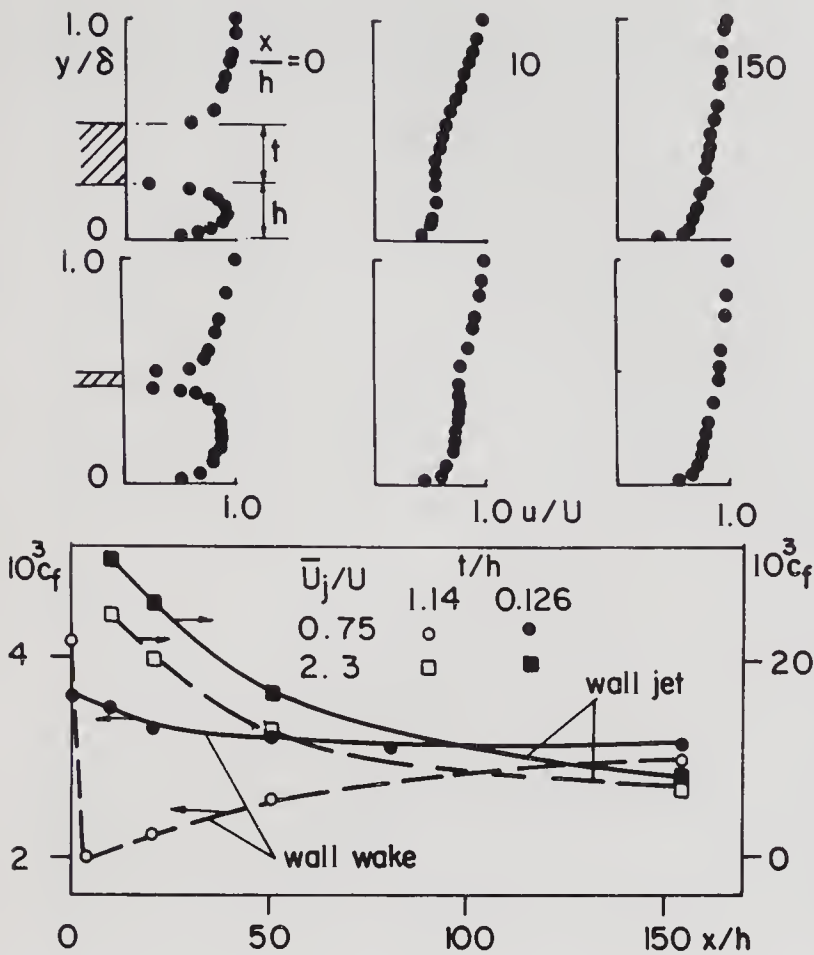


Figure 4. Data from Kacker & Whitelaw (1971) on velocity profiles and skin friction coefficient in a wall-jet and a wall-wake, the latter being defined by the condition that $\bar{U}_j/U < 1$ where \bar{U}_j is the average jet velocity and U is the velocity at the edge of the boundary layer. The velocity profiles in two wall-wake cases are shown in the upper part of the figure. Note the large drop in skin friction in the thick-plate case.

in the flow; all flow velocities are forced to vanish over this boundary, and (if the object is impervious) a discontinuity in the instantaneous pressure can be sustained across the surface. The intriguing question is whether the enforcement of such boundary conditions can have a sufficiently large beneficial effect on the turbulent flow so that the drag penalty of the device itself can be overcome.

In the light of these observations, it is convenient to distinguish between what we shall call here the *wake* effect (loss of momentum in the main flow) and the *blade* effect (establishment of new boundary conditions in the main flow) – fully realizing, of course, that the two will generally coexist (to different degrees) with any particular device.

3. The wake effect

All experiments with wakes interacting with boundary layers show that even the strong disturbances introduced by sizeable bodies eventually die down, at rates that increase as the body approaches the surface. Clauser (1956) reported decay distances (the precise definition he used is not clear) of $2 \delta_m$ and $8 \delta_m$ for the mean velocity perturbation produced by a 1/2 in. rod when placed at heights of $0.16\delta_m$ and $0.59\delta_m$ respectively from the surface.

A wake in uniform flow is characterized largely by its momentum thickness θ_w ; although initial conditions, including in particular the geometry of the body

producing the wake, can exert a long influence on flow development, there is much evidence that, sufficiently far downstream, it is useful to adopt θ_w as a basic length scale in the flow (Sreenivasan 1982). In this spirit we examine the wake effect of boundary layer manipulators.

Figure 5 shows the variation of the velocity defect with streamwise distance for a rod immersed in the boundary layer. It is seen that for distances of order $200\theta_w$, the variation follows the inverse square root law characteristic of equilibrium wakes. At larger distances, however, the velocity deficit seems to fall off more rapidly – an effect that was noted by Eskinazi (1959), who also suggested the explanation that energy transport is helped considerably by the prevailing velocity gradients outside the wake, especially on its wallward edge. (Actually Eskinazi suggested an average variation of the maximum defect velocity like $x^{-4/5}$, but his data are not inconsistent with the view we would take that it is only for $x/\theta_w \geq 200$ that the decay is faster: closer to the body the wake is thin enough that mean flow shear does not have a significant effect.)

Figure 6 shows Eskinazi's data on wake thickness; this again grows at first like $x^{1/2}$ as in the equilibrium solution, and much faster downstream – a trend that is consistent with the observed variation of the velocity deficit.

The most extensive study of such wall-wakes to-date is due to Marumo *et al* (1978), whose work we have already cited in §2 (see figure 3). Their skin friction coefficient, estimated using a Preston tube (in reasonable agreement with the Ludwig-Tillmann formula) shows that with the rod close to the wall, there is a substantial reduction in skin friction, almost certainly associated with a separation bubble just downstream of the cylinder. At the highest rod position ($1.24 \delta_m$) c_f starts dropping only at $400 \text{ mm} = 15 \delta_m$ downstream of the rod. At the intermediate position ($0.556 \delta_m$) c_f reaches a minimum around $11 \delta_m$, and has relaxed half-way to the asymptotic value far downstream at about $7 \delta_m$ further downstream. Interestingly, the recovery distance at the lowest cylinder position is seen to be about the same, measured in this case from around where $c_f = 0$.

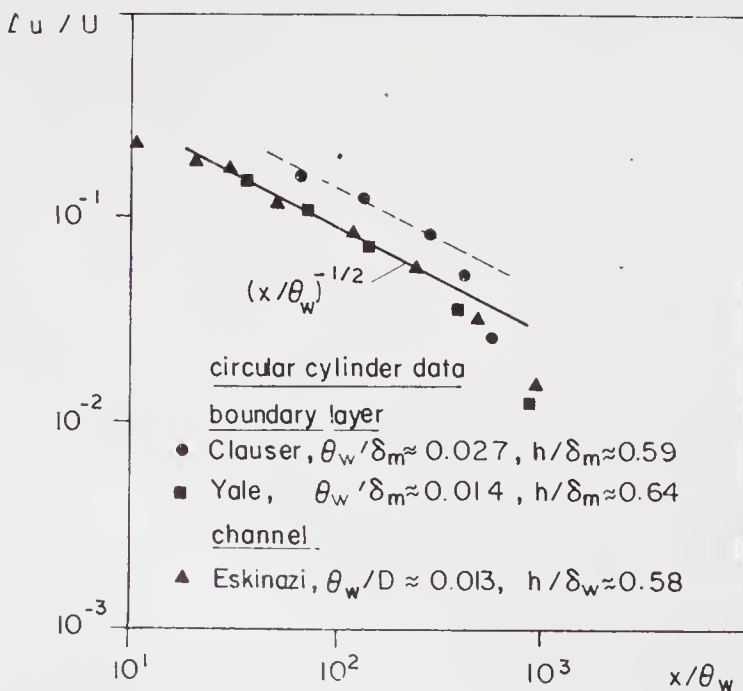


Figure 5. Velocity deficit due to insertion of circular cylinder in a turbulent boundary layer. The Yale data are from Lynn & Sreenivasan (1984, unpublished).

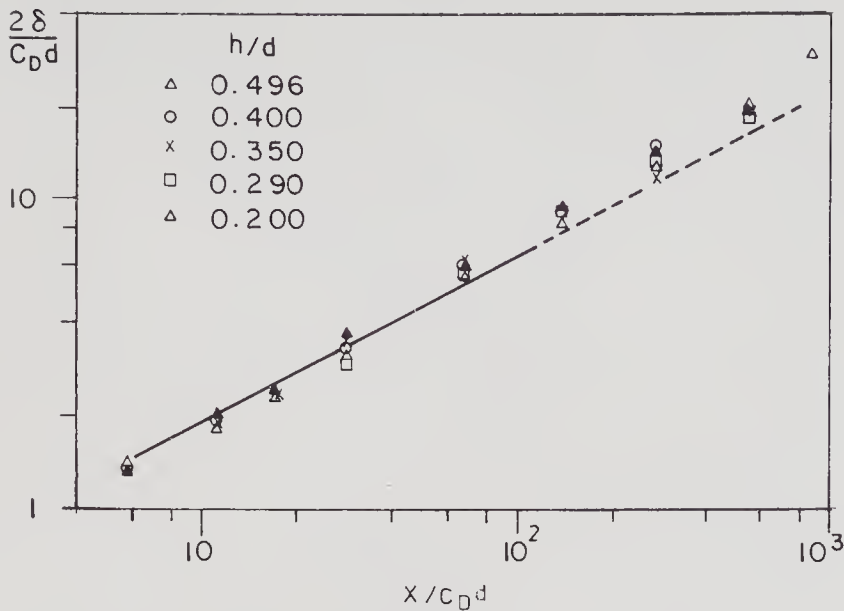


Figure 6. Half-defect thickness of wake generated by cylinder in a turbulent boundary layer, $\eta = h$ (data from Eskinazi 1959).

Greater insight into the structure of this flow is perhaps gained by examining the measured turbulence length scales, which are summarized in figure 7. The cylinder introduces smaller scales into the flow, in part through Karman vortices (for which there was independent evidence in the measured periodicity of the correlation coefficients), albeit with an altered shedding frequency when the cylinder is close to the wall. The data for the intermediate cylinder position show that at $\xi = 6.9$ the scales are still rather low, like those in a wake; but at $\xi = 14.3$ they have recovered to boundary-layer-like values. For the high position, the scales are hardly affected by the wake up to $y = 10$ mm, but are clearly lowered further away. At the low position, the scales at $\xi = 1.4$ are almost the same as in the wake.

A key length scale in these phenomena seems to be provided by the distance, say x_w , to the station around which the wake begins to impinge directly on the plate. Although no precise value for this length can be determined from the experimental data, it seems plausible (from an examination of the measured skin friction) that c_f begins to recover downstream of that point. For example, in the intermediate position, c_f recovery starts around $\xi = 10$; the scales at the wall are wake-like at $\xi = 6.9$, and boundary-layer-like at $\xi = 14.3$. The other two sets of data are also consistent with the proposal that wake-impingement signals c_f recovery. More recent data of Lynn (1987) on half-defect trajectories confirm this general expectation.

Recovery distances from minimum c_f are slightly less than $10 \delta_m$. Taking the wake thickness δ_w to be proportional to $(\xi \delta_m \theta_w)^{1/2}$, it is seen that δ_w becomes comparable to h in a distance

$$x_w = \text{const.}(h^2/\theta_w)$$

from the manipulator.

The early work of Yajnik & Acharya (1977) showed skin friction reduction when a screen was introduced in the boundary layer; from the general discussion above,

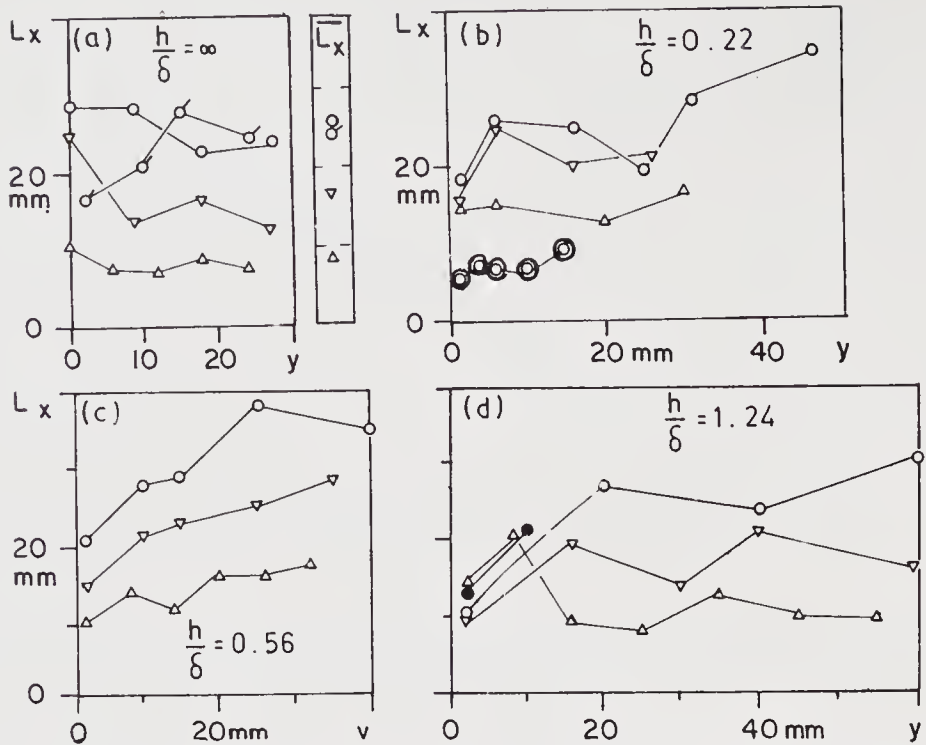


Figure 7. Distribution of integral length scales in a turbulent boundary layer with cylinder placed at different heights (after Marumo *et al* 1978). (a) shows the scales in a free wake and in the undisturbed boundary layer (flagged circles). \bar{L}_x is the length scale averaged over the outer region of the boundary layer. The double circles in (b) are points that we infer from the test to correspond to $\xi = 1.4$ (they appear to have been wrongly marked in the original).

Symbols: $\xi = \bullet$ 1.4, \triangle 6.9, ∇ 14.3, \circ 31.

we believe that the flow in these experiments was in the nature of a wall-wake, but because the wake generator is wide and dispersed the length x_w is not easily defined in this case; the long recovery distances (of order $45\delta_m$) reported here may be due to the wide range of h characterizing the wake generator.

4. The blade effect

Considerable evidence has accumulated during the last five years that even without a strong wake effect there can be a substantial reduction in the skin friction co-efficient when an aerofoil-like body (we shall call them “blades”, hacking away at the eddies if you wish: also often called ribbons and plates) is immersed in the turbulent boundary layer. We may consider, for example, the data of Mumford & Savill (1984), shown in figure 8, based on wall stress measurements using a direct skin friction balance. What is interesting here is that the reduction in skin friction coefficient, at the station $\xi = 12.5$, is of the same order with a flat plate aerofoil whose chord is of order δ_m , as with a rod of diameter $0.08\delta_m$. It is clear therefore that a body which has a much smaller momentum thickness can for other reasons induce the same kind of skin friction reduction as a wall-wake.

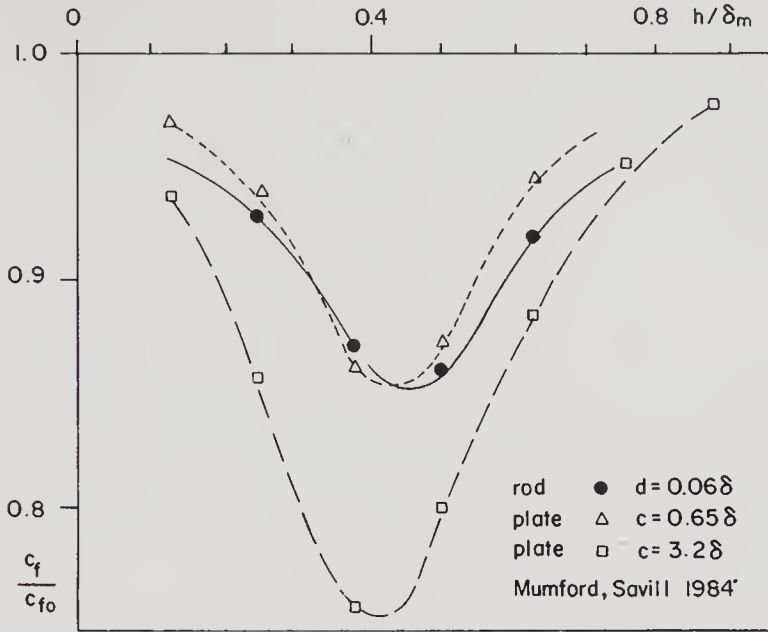


Figure 8. Skin friction at a fixed station ($\xi = 12.5$), as a fraction of undisturbed value, with rod and blade placed at different heights above the surface (Mumford & Savill 1984).

The question here is the relative magnitude of the drag of the two kinds of bodies we are discussing. This has generally been sought to be resolved by making measurements of the momentum thickness. Typical results from the work of Nagib and co-workers (Corke *et al* 1979) are shown in figure 9; it is seen that just downstream of the blade there is a jump in the momentum thickness (attributable to blade drag), but further downstream the growth in thickness is slower than it would have been in the absence of the blade, implying lower skin friction. In particular, there is a station downstream beyond which the momentum thickness of the boundary layer is actually less than it would have otherwise been, implying favourable interference and a corresponding reduction in the *total* drag of the surface-blade combination. Although such data tend to be slightly marred by the difficulty of ensuring strict two-dimensionality, evidence from a variety of measurements in different laboratories tend to show that beyond a certain point there could be a small net reduction in the drag experienced by the surface. Figure 10 summarizes these data, in terms of a drag index, showing that beyond 50 boundary layer thicknesses, if not earlier in certain cases, the drag is marginally lower.

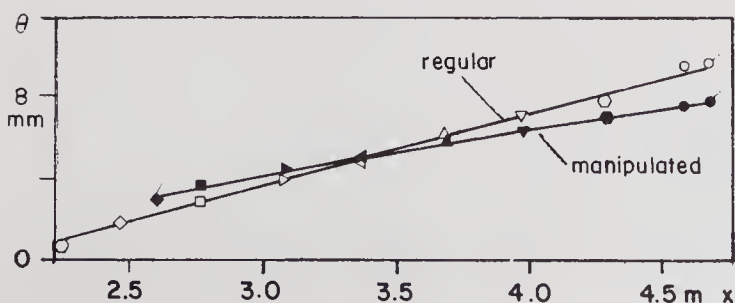


Figure 9. Variation of momentum thickness in manipulated boundary layer.

If we note that drag reduction estimates based solely on two-dimensional momentum balance are often unreliable (because of the invariably present small three-dimensionalities in small-to-moderate aspect ratio wind tunnels), the drag balance required to arrive at the conclusion of the sort shown in figure 10 requires an accurate estimate of both the surface friction of the flat plate and the device drag. From a detailed assessment of the accuracy of these various measurements (Lynn 1987), it appears that the net drag reduction, if it occurs, is quite small (no more than a few per cent), and that its realization in practice is somewhat uncertain. We may also note the recent experiments on the effect of blade manipulators in turbulent channel flow, reported by Prabhu *et al* (1987). In these experiments all combinations of manipulators tried, including tandems and stacks, showed no reduction in the pressure loss for a given mass flow through the channel. Although it may be questioned whether channel flow results are directly applicable to boundary layers, the great similarity in the turbulent structure of the two flows suggests that the negative result in the channels would be very hard to reconcile with a large effect in boundary layers.

It must be emphasized that we cannot assert, on the basis of the measurements reported as they stand, that the wake effect of the blade makes no contribution to skin friction reduction. To illustrate this point, we plot in figure 11 the velocity defect as a function of distance from the manipulator in the case of tandem blade manipulators. Once again, a variety of measurements here show that up to about a couple of hundred momentum thicknesses the observed velocity defect in the blade manipulator wakes scales the same way as in a cylinder wake in a uniform stream. However, the wake of a blade manipulator does not spread in quite the same way as that of a cylinder. Figure 12 shows data on the edge of the wake, both wallward and outward, from some measurements made at Yale (T B Lynn & K R Sreenivasan 1984, unpublished) using a blade manipulator located half-way across the boundary layer. The striking result here, in comparison with the wall wakes discussed in § 3, is that the wallward edge of the wake appears to impinge on the wall much sooner. It also appears that the manipulated boundary layer is slightly *thicker* very close to the manipulator, followed by a reduction in thickness almost immediately further downstream. Figure 13 shows the measured position of both edges of the wake when the manipulator is at negative incidence compared with the

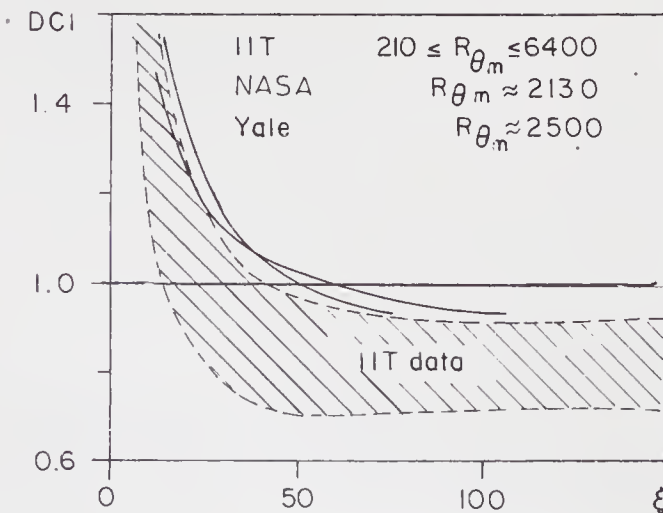


Figure 10. Summary of data on a drag change index, defined as the ratio of the drag measured from a reference station in the manipulated boundary layer to that in the unmanipulated boundary layer. The IIT (Illinois Inst. Technol.) data are from Corke *et al* (1982), the NASA data from Hefner *et al* (1983), and the Yale data from Lynn & Sreenivasan (1985).

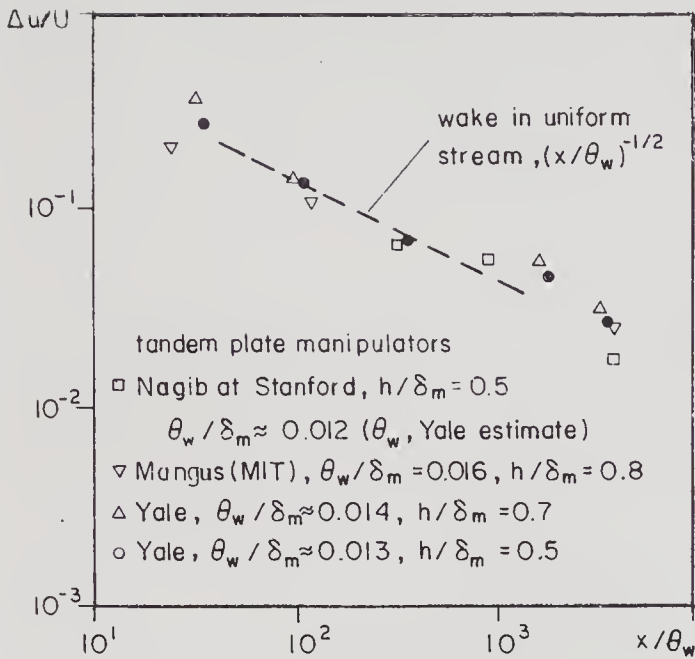


Figure 11. Wake defect velocity in manipulated boundary layers. The Yale data are from the unpublished measurements of Lynn & Sreenivasan (1984); the MIT data from Mangus (1984).

same parameters at zero incidence. It is seen that the outward edge of the boundary layer is further lifted at the negative incidence; however, the wallward edge of the wake does not show any significant change.

We finally look at the evidence on the velocity defect in the wake of a tandem plate manipulator, deduced from measurements reported by Nagib (Appendix B of Corke *et al* 1979). These data, shown in figure 14, indicate that the character of the wake quickly undergoes a change in this case, let us say around 10 boundary layer thicknesses downstream of the second manipulator. Beyond this point, for example at $\xi = 45$, no wakelike profile or defect is evident. A small positive angle of attack on the manipulator appears to produce an appreciable increase in the drag reduction (figure 15), as is made clear from the measurements of Plesniak & Nagib (1985).

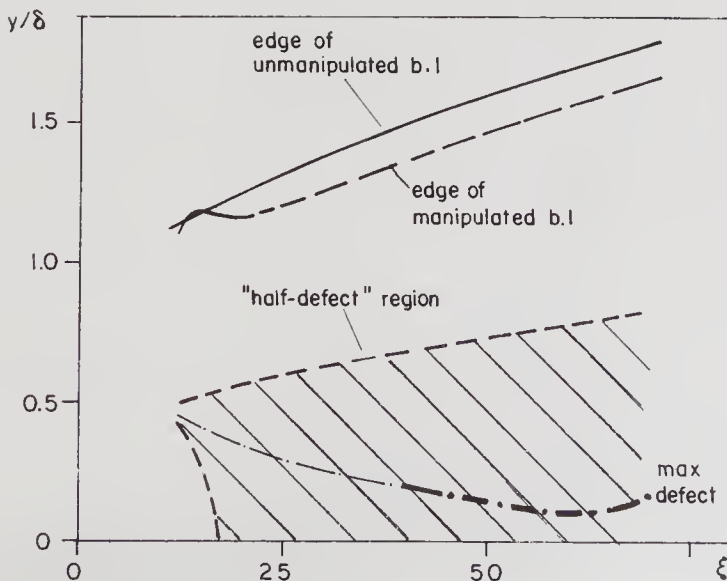


Figure 12. Spread of manipulator wake in boundary layer, from the measurements of Lynn & Sreenivasan (1984, unpublished).

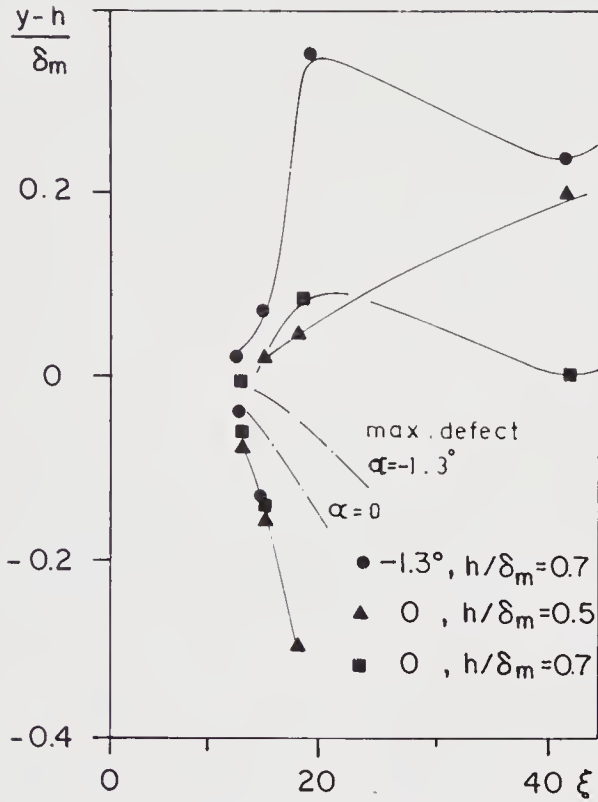


Figure 13. Effect of manipulator incidence on wake edges in manipulated boundary layer.

These observations, taken together, suggest that there is a separate effect, which we shall call the blade effect, that is responsible for the different behaviour characteristic of blade manipulators as distinct from the wall-wake results of § 3.

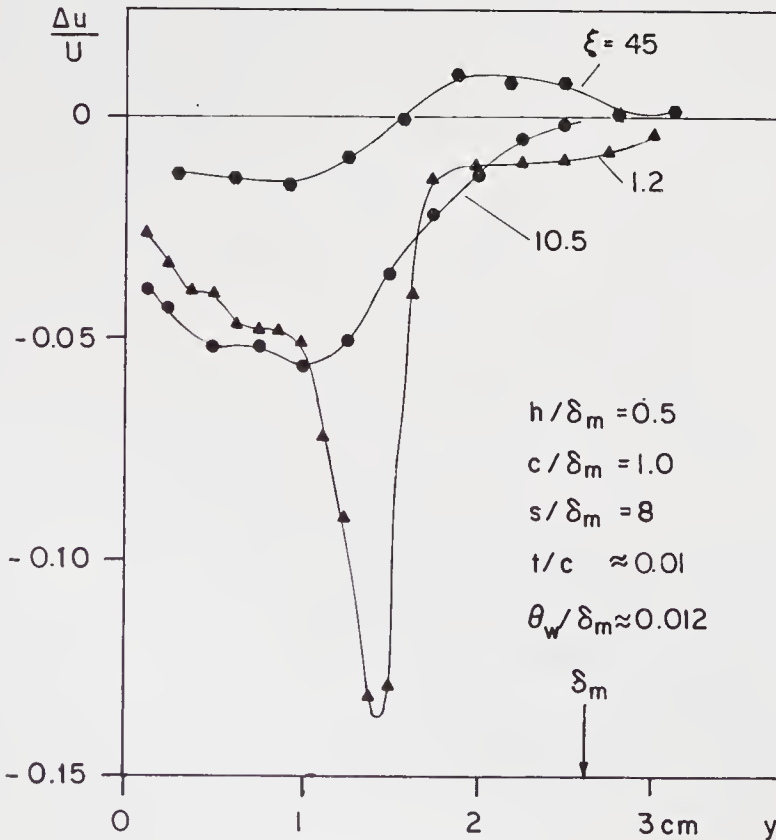


Figure 14. Defect profiles in manipulated boundary layer.

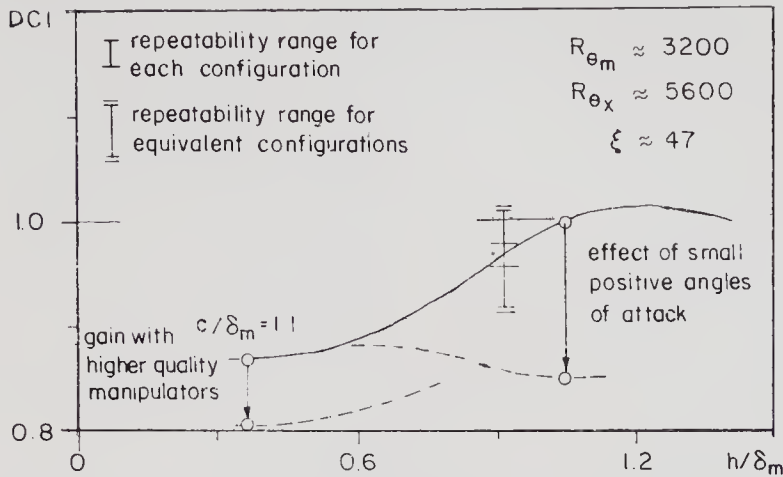


Figure 15. Effect of blade incidence on drag change (from Plesniak & Nagib 1985).

This is particularly shown up in figure 16 where the inclination of the stream just behind the manipulator, as measured by Plesniak & Nagib (1985), is seen to be appreciably different from values further downstream.

5. Discussion

Table 1 makes a broad comparison of the wake and blade effects discussed above. We now make the hypothesis that while the wake effect may be expected on general grounds to scale on the momentum thickness of the wake, the blade effect is more likely to scale on the chord c of the blade (at zero incidence: otherwise the incidence would be an additional parameter). It is attractive to speculate that while the wake effect is due to the drag of the body the blade effect is primarily due to the lift on it. An analysis of the lift on aerofoils immersed in boundary layers, made by Kumar & Narasimha (1986), shows that the major contribution to the lift at zero incidence comes from the presence of shear in the approaching stream. We conjecture that the lift so experienced by the body leads to an induced velocity downstream of the blade which is such that the coherent structure in the boundary layer is favourably modified from the point of view of the drag experienced by the surface. We have earlier remarked (Narasimha & Sreenivasan 1979) that the turbulent boundary layer appears to be particularly sensitive to manipulation with the normal velocity component in the flow. It would not be surprising therefore if

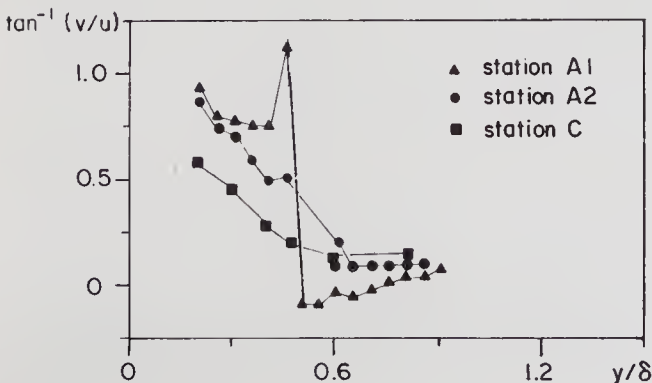


Figure 16. Mean streamline inclination in manipulated boundary layer (Guezennec & Nagib 1985).

Table 1. Blade and wake effects compared.

Wake effect	Manipulation	Blade effect
* Alters turbulent energy production		* Suppresses normal velocity over blade
* Introduces smaller scales		* Generates Kutta-Joukowski-type vortices
* Generates Karman-type vortices		* Alters structure of turbulence
Scales on θ_w, h		Scales on c, h
Limit: $c/\delta \rightarrow 0$		Limit: $\theta_w/\delta \rightarrow 0$
θ_w/δ finite		c/δ finite

the downward velocity field induced by the lift on the blade (i.e. by the vortex responsible for it) so alters the normal velocity component in the turbulent flow that the balance maintained in an equilibrium turbulent boundary layer is upset, resulting in a reduction in the skin friction as well as the net drag. We know from experience in other situations that such effects can persist for long distances, because of flow-memory.

These arguments suggest that a useful map of the effect of a manipulator in a boundary layer would be in the plane of the two non-dimensional variables θ_w/δ_m and c/δ_m . All available results on drag coefficient are plotted on this map in figure 17. If the chord of the body is negligible, as it would be in the case of a circular cylinder immersed in the flow, we have the wake effect, characterized by the ordinate in this plane. An ideal manipulator would have zero drag and so would be represented by the abscissa. Of course such ideal manipulators do not exist (although it is interesting to speculate on the possibility of reducing the drag of the manipulator, for example by setting it in motion), but it is clear that there is a certain region in figure 17 where we may expect a drag reduction. This boundary corresponds to the line $c/\theta_w \approx 40$. The fact that most measurements are not too far from this boundary may explain why experimental work in this area is so hard and also why the reported drag reductions have not always been beyond the likely bands of uncertainty in the measurement technique. Looking at this diagram, the scatter in the different results reported so far is no longer very surprising.

The reason for the fairly large manipulator chord (in terms of θ_w) necessary for favourable interference is not hard to see from another point of view. Lynn (1987) concluded from a detailed study of iso-correlation maps of the velocity field that one effect of the blades (as already pointed out at the beginning of § 4) appears to be to cut the hairpin eddies present in the boundary layer into two parts, the efficiency of this operation being directly dependent on the chordwise extent of the blades. The remnants of the hairpin eddies on the top of the blade are now inclined to the flow direction at much shallower angles than 45° , thus making them inefficient at entraining the outside flow. Because the rate of strain is very small in the outer region of the turbulent boundary layer, it takes a large distance for the equilibrium structure to be restored. This accounts for the relatively large relaxation distances observed behind blades.

We end by noting one paradoxical feature that *ought* to be observed in manipulated flows but is not supported by any strong direct evidence yet. This is as

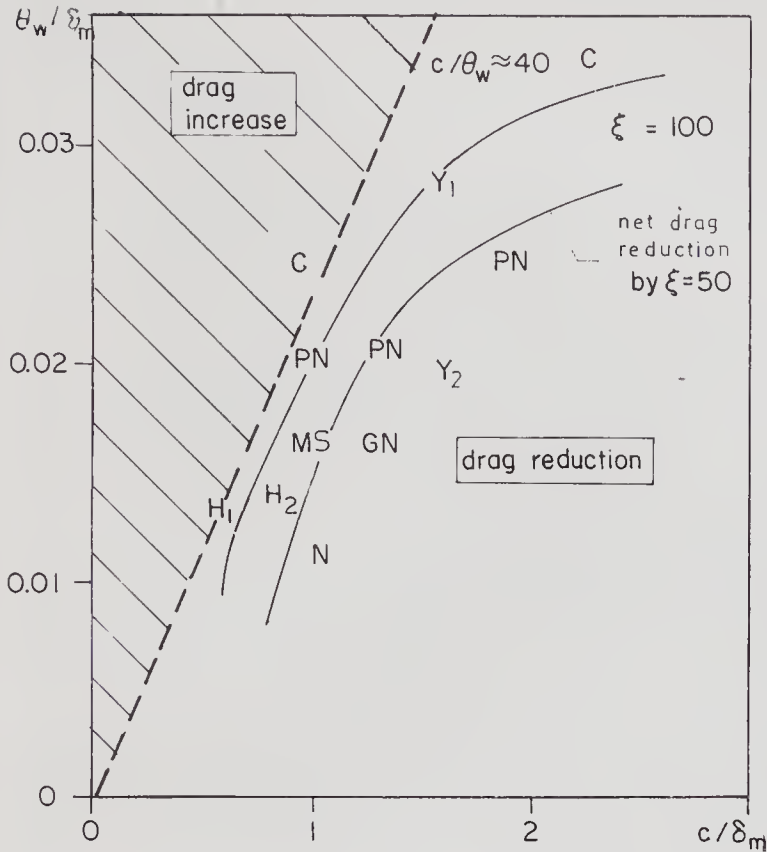


Figure 17. Tentative map of drag reduction regime in variables characterizing respectively the wake and blade effects. A blunt body like a circular cylinder would plot very close to the y -axis.

C: Corke *et al* (1979); H_1 , H_2 : Hefner *et al* (1983); MS: Mumford & Savill (1984); PN: Plesniak & Nagib (1985); Y_1 , Y_2 : Lynn & Sreenivasan (1985); N: Corke *et al* (1982); GN: Guzevnenec & Nagib (1985). MS, H_1 , and the two C's do not report any net reduction in drag at one last station of measurement. Y_1 reports no drag reduction at $\xi = 70$, but extrapolated to $\xi = 100$, a small reduction seems possible.

follows. Suppose the manipulator is effective and does lead to a net decrease in the boundary-layer momentum thickness downstream as shown in figure 9. Now we expect on general grounds (see e.g. Working Rule No. 4, Narasimha 1984) that, sufficiently far downstream, the manipulated boundary layer asymptotically returns to "maturity" or "equilibrium" in some sense. If now in this state the momentum thickness Reynolds number is lower than it would have been at the same station in the unmanipulated boundary layer – as it must be for net drag reduction – the skin friction coefficient should be higher at that station. Thus the traditional wisdom on the behaviour of the boundary layers – namely that irrespective of the perturbation made there will be a tendency for the boundary layer to return to the usual equilibrium sufficiently far downstream of the perturbation – implies that an *increase* in skin friction coefficient far downstream is inevitable. If this is true it further follows that any possible reduction of drag due to the insertion of a manipulator will be achieved only for limited downstream lengths behind the manipulator where the blade effect has temporarily won over the wake effect. Precisely what this distance is we still do not know, and we find it difficult to estimate it from currently available measurements. We believe however that the resolution of this paradox will go far towards elucidating the effect of manipulators on boundary layers.

This paper is largely based on an invited lecture given by the authors at the AIAA Shear Flow Control Conference held at Boulder, CO, in 1985. RN acknowledges the support received from the Council of Scientific & Industrial Research for attending the conference, and from the Department of Science and Technology for the research carried out at the Indian Institute of Science.

References

- Bushnell D M 1983 Turbulent drag reduction for external flows, AIAA Paper 83-0227
- Cantwell B J 1981 *Annu. Rev. Fluid Mech.* 13:457–515
- Clauser F H 1956 *Adv. Appl. Mech.* 4:2–51
- Coles D 1985 Uses of coherent structure, AIAA Paper 85-506
- Corke T C, Guezennec Y, Nagib H M 1979 In *Viscous flow drag reduction*, *Prog. Astronaut. Aeronaut.* 72:128–143
- Corke T C, Nagib H M, Guezennec Y G 1982 A new view on origin, role and manipulation of large scales in turbulent boundary layers, NASA CR 165861
- Eskinazi S 1959 Mixing of wakes in a turbulent shear flow, NASA Tech. Note D-83
- Guezennec Y G, Nagib H M 1985 Documentation of mechanisms leading to net drag reduction in manipulated boundary layers, AIAA Shear Flow Control Conference, Boulder, CO
- Hefner J N, Anders J B, Bushnell D M 1983 Alteration of outer flow structures for turbulent drag reduction, AIAA-83-0293
- Kaeker S C, Whitelaw J H 1971 *J. Appl. Mech.* E38: 239–252
- Klebanoff P S, Diehl Z W 1951 Some features of artificially thickened fully developed turbulent boundary layers with zero pressure gradient, NASA Tech. Note 2475
- Kline S J, Reynolds W C, Schraub F A, Rundstadler P W 1967 *J. Fluid Mech.* 30:741–73
- Kumar S K, Narasimha R 1986 The lift on an aerofoil in a turbulent boundary layer, Report TM DU 8601 & TM DU 8605, NAL, Bangalore
- Liepmann H W, Noschueck D M 1982 *J. Fluid Mech.* 118:201–204
- Lynn T B 1987 *Manipulation of the structure of a turbulent boundary layer*, Ph D thesis, Yale University
- Lynn T B, Sreenivasan K R 1985 Measurements in manipulated turbulent boundary layers, Report No. IFM-85, Yale University
- Mangus J S 1984 Preliminary measurements of drag and bursting frequency in a manipulated turbulent boundary layer, Report 84-2, Aeronaut. Astronaut. Dept., Mass. Inst. Technol.
- Marumo E, Suzuki K, Sato T 1978 *J. Fluid Mech.* 87:121–141
- Mumford J C, Savill A M 1984 In *Laminar/turbulent boundary layers* (eds) E M Uram, H E Weber (New York: ASME, Fluids Eng. Div.)
- Rao K N, Narasimha R, Badri Narayanan M A 1971 *J. Fluid Mech.* 48: 339–352
- Narasimha R 1983 In *Liquid metal flows and magnetohydrodynamics*, *Prog. Astronaut. Aeronaut.* (eds) H Branover, P S Lykoudis, A Yakhov 84:30–52
- Narasimha R 1984 The turbulence problem – A survey of simple turbulent flows, GALCIT Report FM 8401
- Narasimha R, Kailas S 1987 In *Perspectives in turbulence studies* (eds) H U Meier, P Bradshaw (Berlin: Springer-Verlag)
- Narasimha R, Prabhu A 1972 *J. Fluid Mech.* 54:1–17
- Narasimha R, Sreenivasan K R 1979 *Adv. Appl. Mech.* 19:221–301
- Plesniak M W, Nagib H M 1985 Net drag reduction in turbulent boundary layers resulting from optimised manipulation, AIAA Paper 85-0518
- Prabhu A, Vasudevan B, Kailas Nath P, Kulkarni R S, Narasimha R 1987 In *Turbulence management and relaminarisation* (eds) H W Liepmann, R Narasimha (Berlin: Springer-Verlag)
- Roshko A 1955 *J. Aeronaut. Sci.* 22:124–132
- Sreenivasan K R 1981 *AIAA J.* 19:1365–1367
- Sreenivasan K R 1982 *Acta Mech.* 44: 1–48
- Strykowski 1986 *The control of absolutely and convectively unstable shear flows*, Ph D thesis, Yale University
- Thomas A S W 1983 *J. Fluid Mech.* 137:233–250
- Yajnik K S, Acharya M 1977 In *Lecture notes in physics* (eds) H Fiedler (Berlin: Springer-Verlag), 75:249-260

Note added in proof: KRS acknowledges his indebtedness to Dr T B Lynn, some of whose data are reported here, and to AFOSR for financial assistance.

The behaviour of excited plane jets

M A BADRI NARAYANAN

Department of Aerospace Engineering, Indian Institute of Science,
Bangalore 560 012, India

Abstract. A plane subsonic jet can be excited to entrain more fluid from its surroundings by subjecting it to antisymmetric periodic disturbances. The essential feature in this phenomenon is the rolling-up motion of an initially flapping jet to form large vortices which are responsible for greater entrainment. Several methods developed to impart oscillations to the flow at the nozzle, such as the acoustic pressure oscillator, the vibration of a single vane in the potential core region, the reciprocating lip system and the twin vane exciter, are described in this article. A minimum threshold in amplitude is necessary for exciting the flow. However, the frequency of oscillation is much less than that predicted by stability considerations.

Keywords. Jet; unsteady flows; vortex dynamics; jet excitation.

1. Introduction

The fluid dynamics of steady jets, plane as well as axisymmetric, has been the subject of intense study for the past few decades on account of its direct influence in the aerospace industry (Hinze 1981; Wygnanski & Fiedler 1969; Crow & Champagne 1971; Hussain & Clark 1977). One of the significant characteristics of a turbulent jet is its ability to entrain more fluid from its surroundings due to the shear inherently present in the flow. The induced flow even in the case of a steady jet is not smooth and continuous but is indented with large turbulence structures (figure 1) which exhibit a wavy motion along the outer edge of the flow (Townsend 1976). Though these large eddies are formed in a random fashion, they do follow a well-defined statistical pattern which enables us to describe the overall characteristics of the flow using a minimum number of parameters such as a velocity and a length scale for a given nozzle flow.

Crow & Champagne (1971) observed that the large eddies in a round jet could be energized in a selective manner by imposing disturbances at some definite frequencies. Their pioneering work initiated further activity in jet excitation. Since the eddies play a major role in the production of noise, selective modification of the large-scale turbulence structures can be usefully employed for altering the radiating noise pattern. Recently, this subject has evoked further interest due to its

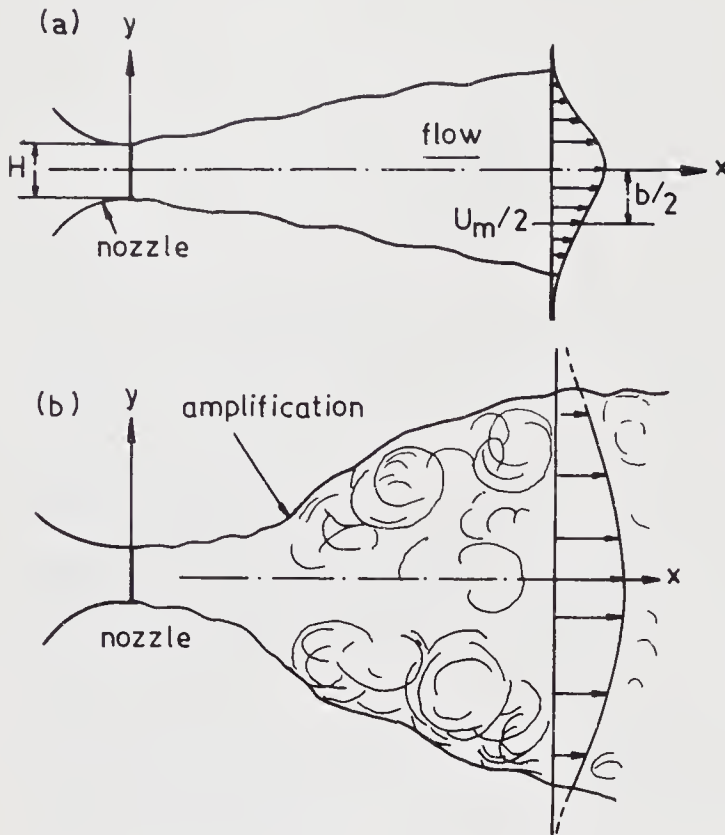


Figure 1. (a) Steady, and (b) excited jet.

application to V/STOL aircraft propulsion, which requires efficient thrust augmenting ejectors (Bevilaqua 1984; Braden *et al* 1982). In this system, the induced flow plays a major role. An excited jet which has a higher mixing capability could satisfy the above requirement.

The oscillations for exciting the jet can be categorized as: (a) pulsating the flow which produces periodic fluctuations in mass flow, and (b) the flapping of the jet. It is not always necessary that the application of such disturbances should induce excitation. The criterion for excitation is still under exploration and the available information on this subject indicates that the configuration of the jet, the strength of the imposed disturbance, and the mode of applying it, influence the process in a selective manner. For instance, a plane jet and a round jet exhibit entirely different behaviour when subjected to the same disturbance. The former can be excited only by antisymmetric oscillations whereas a round jet is sensitive to many modes (Rockwell & Nicolls 1985; Bernal & Sarohia 1984). A round jet gets excited through the dynamics of vortex rings, but the process involved in a plane jet is still under speculation. This article is mainly concerned with the excitation of a plane jet, a field in which the author has been actively engaged for the past few years.

2. Plane jet excitation

It is now well-established that a plane jet cannot be excited by mass fluctuations in the nozzle flow or by any other symmetric disturbances. Only antisymmetric oscillations are effective. The early experiment on plane jet excitation was

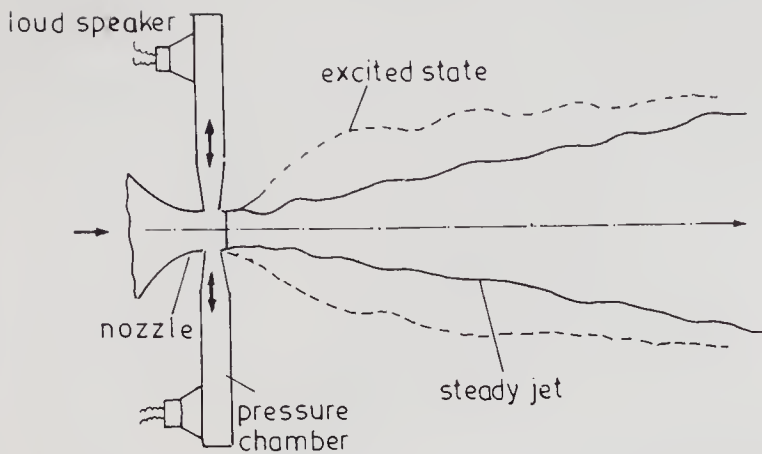


Figure 2. Pressure driven exciter.

performed by Fiedler & Korschelt (1979) using periodic pressure pulses generated by a pair of loud speakers at the exit of the nozzle (figure 2). Only when the two speakers were operating in an out-of-phase mode did the jet exhibit a tendency to a greater spread. It was observed that a perceptible amplification set in only after a threshold of driving amplitude; beyond a certain level of excitation, there was little effect on the overall flow condition. At low frequencies, the jet was only flapping from one side to another, without any increase in the overall entrainment. With an increase in frequency, the flapping mode ceased and the flow generated alternate vortices spanning the entire width of the jet. At higher frequencies, the vortices could not be distinctly identified. The entrainment enhanced only when the flapping mode changed to the vortex mode. Fiedler & Korschelt (1979) also noticed that the onset of amplification occurred only at some distance downstream of the nozzle, and this (distance) depended on the imposed frequency. Since the disturbances in their experiments were generated by loud speakers, the intensity of the pressure fluctuations was small and restricted the amplification to only a short distance downstream of the nozzle. The possibility that there might be a critical Strouhal number associated with the excitation process was also suggested by them.

For industrial applications, more practical methods are required to excite the jet. To achieve this, simple mechanical devices were tried (Lai & Simmons 1985; Badri Narayanan & Platzer 1986; Badri Narayanan 1987) to increase the strength of the imposed oscillations. The first attempt was the introduction of a tiny vane placed across the jet in the potential core region and subjected to periodic pitching oscillations by an external mechanism (figure 3). This technique was quite successful and the entrainment ratio of the jet could be increased significantly. The stationary vane kept at a zero angle of attack had negligible effect on the flow. Several investigators have examined this flow under different conditions (Lai & Simmons 1985; Badri Narayanan & Raghu 1983; Collins *et al* 1984). All the experiments carried out on this vane system were mainly confined to mean and turbulent velocity measurements by varying the amplitude and frequency of the vane oscillations. No attempts were made to examine the flow patterns. However it was speculated that the entrainment could be associated with the formation of vortices. The major conclusion arrived at was that, for a given exit velocity, the amplitude as well as the frequency influence entrainment. Some typical experimental results obtained by Badri Narayanan & Raghu (1983) are shown in

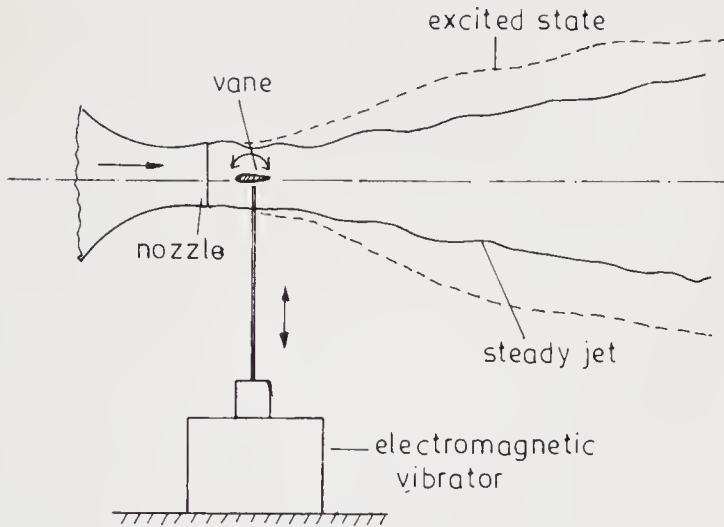


Figure 3. Single vane exciter.

figure 4. None of the investigators established a Strouhal number for excitation for this arrangement.

The single vane system described above has its own drawbacks when considered for aircraft applications. Since the vane is placed in the centre of a high speed jet, aeroelastic problems do arise and the penalty is more severe if the jet is hot. Hence better techniques were sought, as a result of which, a reciprocating lip device was developed (Badri Narayanan & Platzer 1986, 1987). The novel feature of this oscillating mechanism is the incorporation of two small segments in the exit region of the jet, spanning the entire length of the nozzle (figure 5). These segments, which form the lips of the nozzle, reciprocate in opposite directions at the required frequency by a gear-cam arrangement coupled to a variable speed motor. The maximum movement of the segments (L) was controlled by the eccentricity of the cam. Some experiments were conducted with this system at an exit velocity of 120 m/s. Using cams with different eccentricities, the movement of the segments was varied in steps of 0.25, 0.50, 0.75 and 1.0 cm. Mean velocity profiles were measured in this investigation using a hot-wire anemometer. Flow patterns were observed with smoke filaments. Initial experiments indicated that at low frequencies, the jet was flapping up and down for all values of L . As the frequency was increased, formation of vortices could be clearly seen only for $L = 0.75$ and 1.0 cm. For $L = 0.50$ cm, vortices could be observed only at a considerable distance away from the nozzle but not distinctly. There was no rolling-up motion at all for $L = 0.25$ cm, a trend clearly suggesting that a minimum disturbance is essential for excitation of the jet. Detailed velocity measurements were therefore carried out only for $L = 0.75$ cm, for which the entrainment was enhanced. Entrainment higher than that of the single vane system was achieved by this oscillator. The spread of the jet and the entrainment ratio with and without excitation are shown in figure 6.

Flow visualisation clearly indicated that the initial vortex formation occurred at a certain distance downstream of the nozzle exit and this distance was influenced by the exit velocity as well as by the frequency. For a given exit velocity, the vortex moved towards the nozzle as frequency was increased, while for a fixed frequency, the distance increased with the exit velocity. Since flow visualisation using smoke

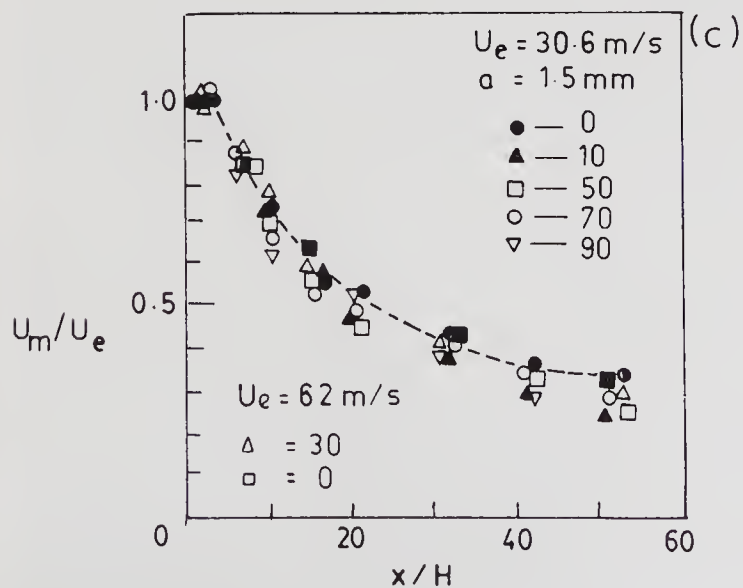
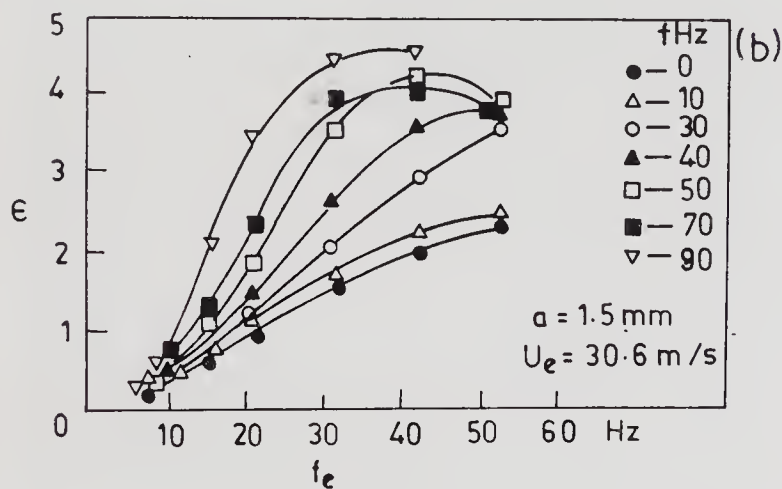
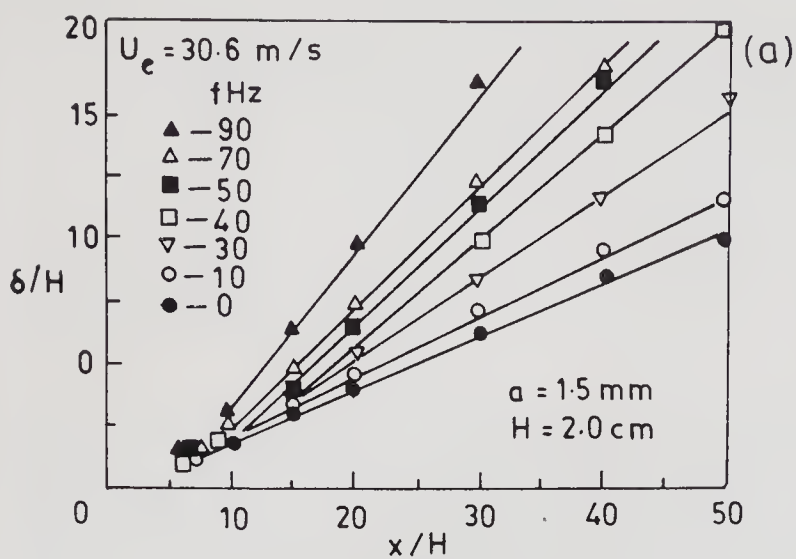


Figure 4. The effect of single vane excitation on the jet. (a) Growth of the jet due to excitation, (b) entrainment ratio, (c) variation of mean velocity along the centre line.

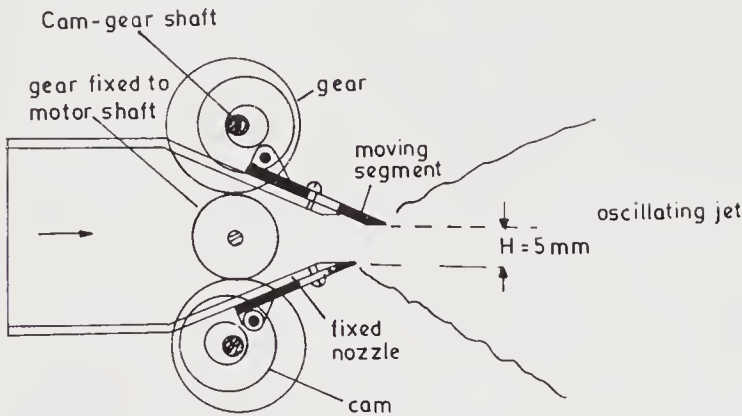


Figure 5. Reciprocating lip mechanism.

filaments could not be successfully used beyond an exit velocity of 20 m/s, attempts were made to identify the change-over from the flapping motion of the jet into the excited state using hot-wire traces. Near the vicinity of the nozzle, the velocity fluctuations exhibited a large swing reaching zero value for a considerable period at every stroke of the moving lip, clearly indicating flapping motion. As the hot-wire was shifted downstream, the velocity, though fluctuating periodically, did not reach zero value but was found to ride over a non-zero base velocity. This modification in the flow pattern was rapid and clearly distinguishable in the hot-wire traces especially in the outer part of the jet. The criterion for the above condition was examined for different values of exit velocity and excitation frequency, and the results suggested a critical Strouhal number ($St_c = f\delta/U_m$) associated with this process. St_c was about 0.067, based on the excitation frequency, the width, and the centre-line velocity of the steady jet. Overall, the reciprocating lip jet did clearly reveal that the excitation is associated with the formation of large periodic vortices which are responsible for inducing additional mass flow into the jet.

Very recently another technique was developed (Badri Narayanan 1987) for imparting oscillations to the jet, which seems to be superior in many respects to the earlier methods. It is a twin-vane system. A pair of vanes is employed (instead of a single one), located in the outer edges of the jet as shown in figure 7. The vanes are rigidly attached to each other so that their movements are in phase. Preliminary experiments were carried out with the vanes oscillating in the transverse push-pull mode (Badri Narayanan 1987). The oscillations generated vortices on both sides of

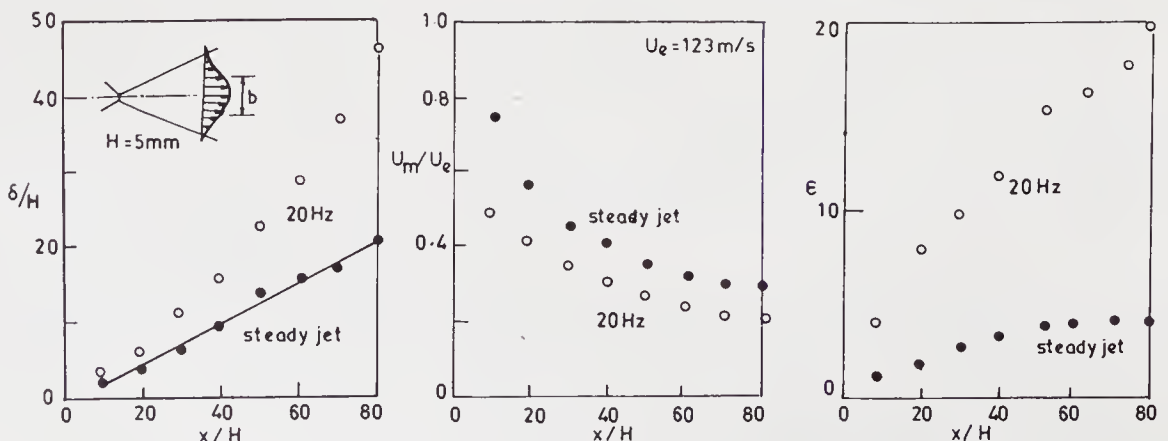


Figure 6. Characteristics of the jet excited by reciprocating lips.

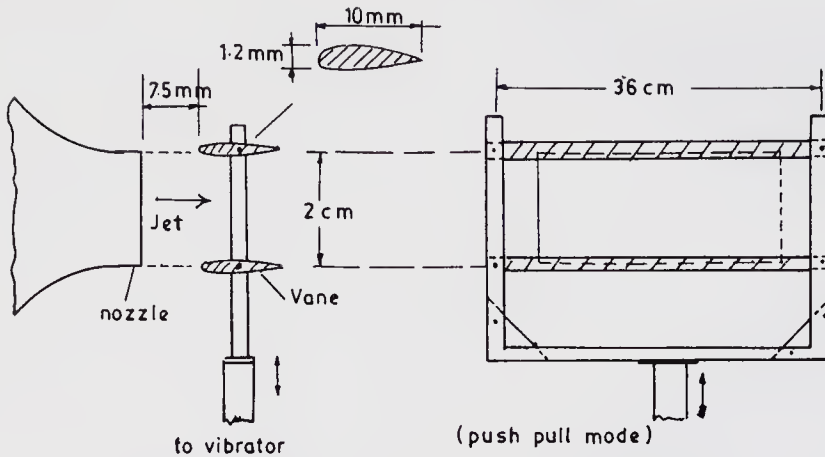


Figure 7. Twin vane exciter in the push-pull mode.

the jet some distance downstream of the nozzle and they grew rapidly in size giving a bloom-like appearance when observed with smoke filaments (figure 8). As in the case of the reciprocating lip system, the amplification distance (x_c) depended on the exit velocity and the frequency of oscillation. In this mode of operation, the jet did not exhibit a tendency to flap. On the other hand, vortices were formed at the edges of the jet in the same fashion as observed in the case of free shear layers (Wyganski *et al* 1979). They grew rapidly in an individual manner and at some distance downstream (x_c) the vortices from both sides interacted with each other. The distance x_c moved towards the nozzle as the frequency was increased and reached a minimum close to the potential core region. x_c was insensitive to the amplitude of excitation beyond a minimum threshold level. Since the vortices formed in this technique are different in nature from those formed by the reciprocating lip method, the possibility that two separate mechanisms are involved in the formation of the vortices cannot be ruled out.

When the twin vanes were oscillated with a rotary motion around a pivot as illustrated in figure 9, which is termed as pitching mode in this report hereafter, the vortex formation was different from that of the push-pull mode, but similar to that of the reciprocating lip oscillator described earlier (Badri Narayanan & Platzer 1987). The jet initially exhibited a flapping motion which rolled up as the frequency was increased (figure 10). As in the case of other techniques, the movement of the amplification region varied with the imposed frequency and exit velocity. Mixing in this case was more predominant than in the push-pull mode. For low exit velocity and frequency operations, a critical Strouhal number around 0.05 could be identified for this system. Since the detailed velocity measurements in the pitching mode were carried out at high blowing pressures for an ejector application, the entrainment ratio and the spread of the jet cannot be directly compared with those of other systems which were operated at low exit velocities.

The twin-vane system oscillating in the pitching mode seems to be more suitable for practical applications. The thrust of the jet measured with and without the vanes showed a loss of about 3% even when the vanes were oscillating. In addition, the vanes, being placed at the edges of the jet, will not bear the burnt of the gas temperature if the issuing jet is hot. It is the opinion of the author that the two-vane oscillator operating in the pitching mode is a more practical system for exciting a plane jet when compared to other systems described earlier.

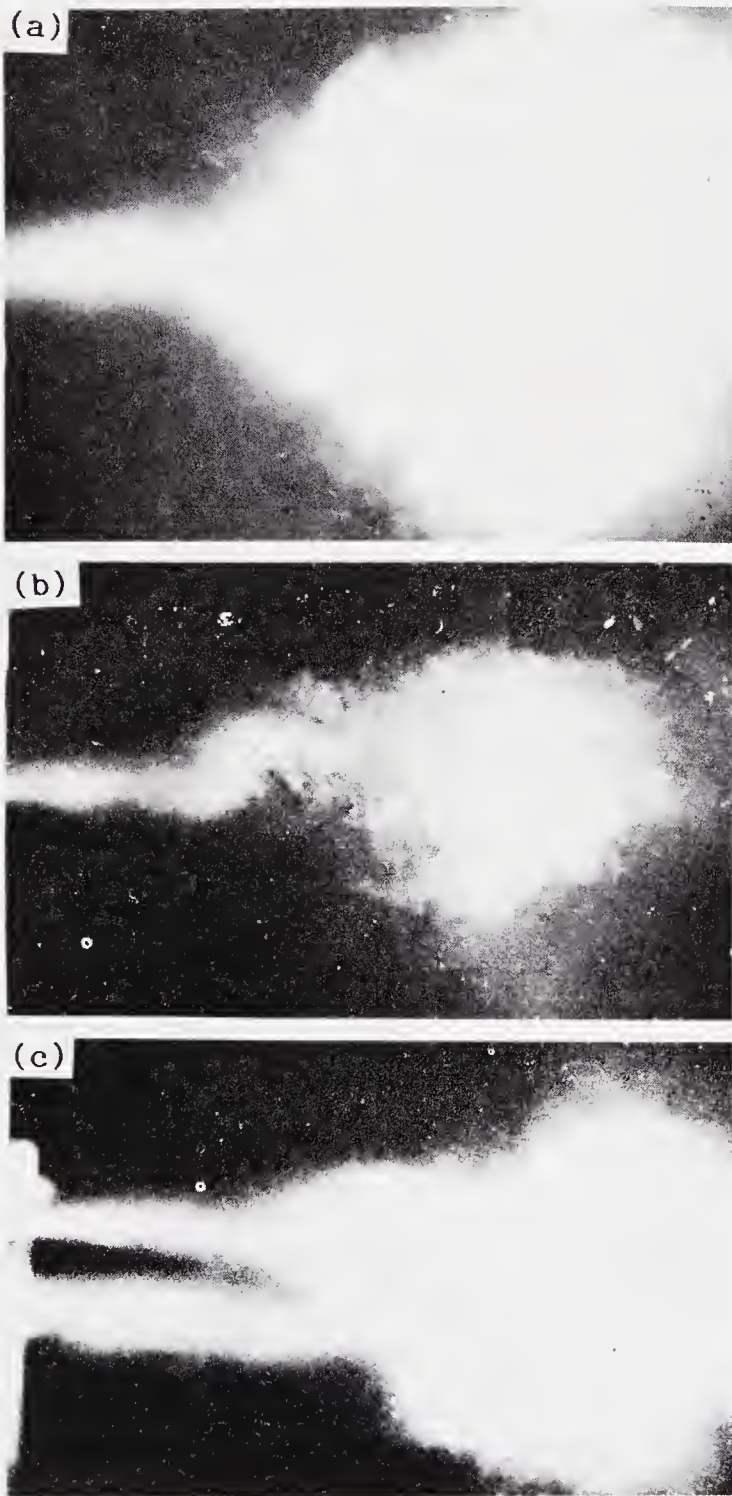


Figure 8. Flow patterns observed with twin vane exciter in the push-pull mode. (a) Excited jet, long exposure without strobe. (b) and (c) with strobe light, smoke injected on one vane and on both vanes, respectively.

3. Discussions

All the investigations on excited turbulent plane jets converge to the conclusion that the initially present flapping motion produces large vortices on either side of the flow which are primarily responsible for entrainment of additional mass into the system. The amplitude of the imposed oscillations do not affect the location of the amplification; however, it has an influence on the size of the vortex. It was also

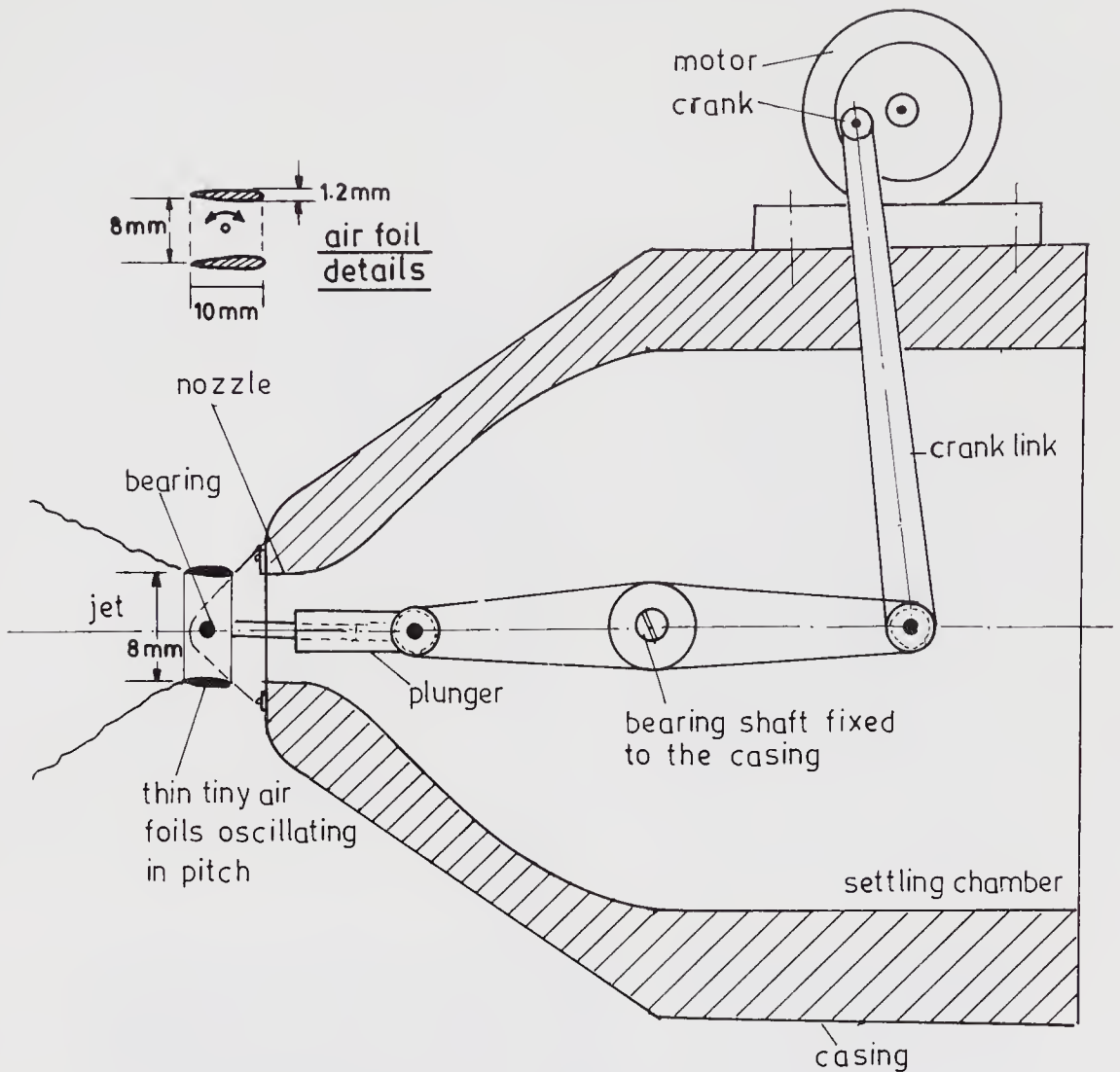


Figure 9. Twin vane oscillator in the pitching mode.

noticed that the extent of amplification is restricted to a certain distance depending on the strength of excitation. Since the amplification distance depends only on the frequency and the exit velocity and not on the amplitude of oscillation, it is possible to construct a critical Strouhal number for amplification. This could be considered as the criterion for the conversion of the flapping mode to the rolling motion. At low exit velocities and low frequencies, the vortex formation can be distinctly observed by flow visualisation, which enables the location of the excitation distance (x_c). For this condition, the estimated critical Strouhal number is around 0.05 ± 0.01 .

A steady turbulent jet is also known to be associated with a reasonably well-defined Strouhal number equal to 0.22 for its self-generated large eddies for which the frequency was obtained from auto correlation of the velocity fluctuations (Cervantes & Goldschmidt 1980). The frequency varies along the jet in such a manner that the Strouhal number is constant at all longitudinal stations, a result which gave rise to the speculation that the jet has an inherent flapping tendency in a stochastic sense. Whether flapping or not, the steady jet does generate smaller

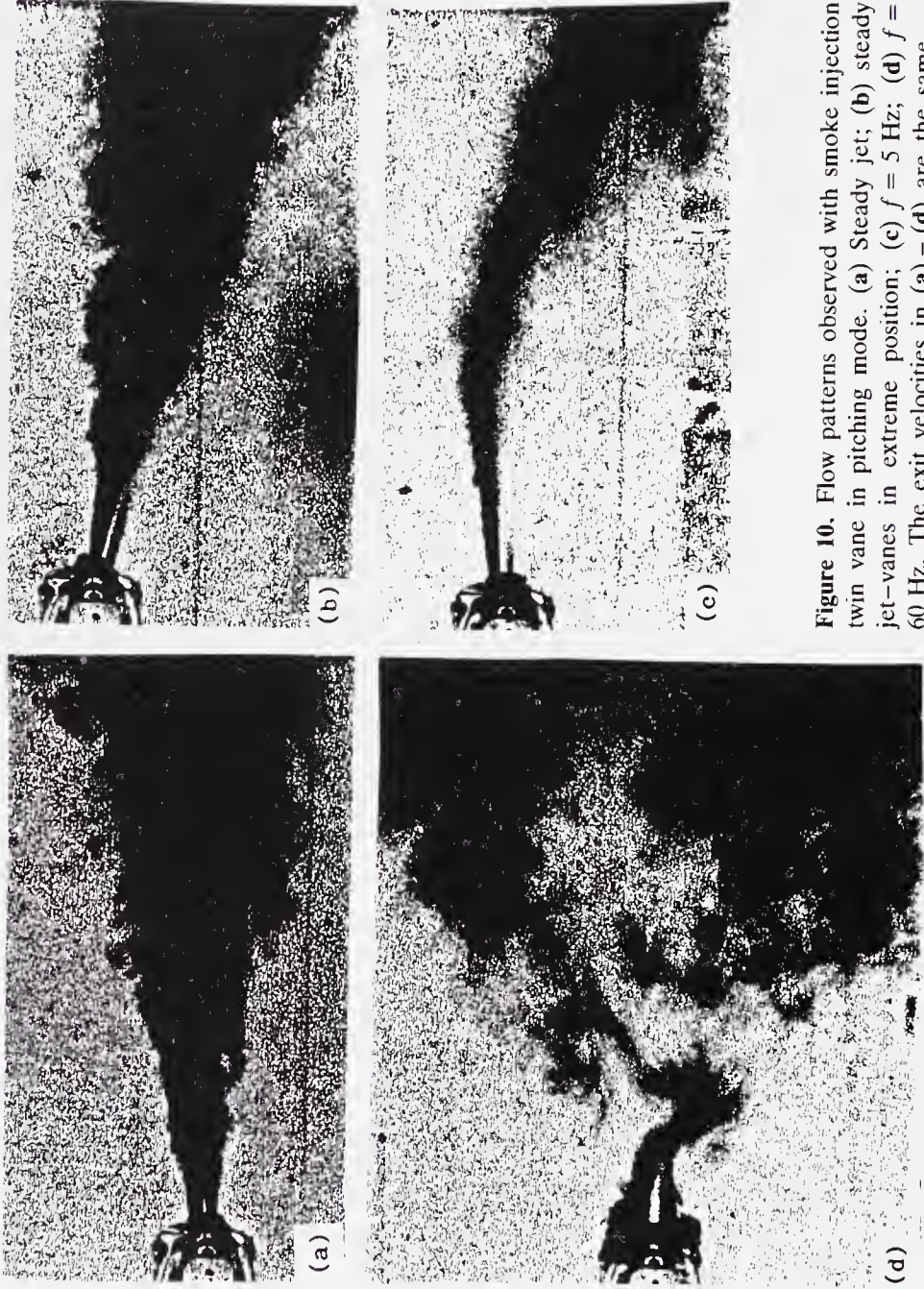


Figure 10. Flow patterns observed with smoke injection twin vane in pitching mode. (a) Steady jet; (b) steady jet-vanes in extreme position; (c) $f = 5$ Hz; (d) $f = 60$ Hz. The exit velocities in (a) - (d) are the same.

vortices which grow in size as they are convected downstream. These vortices are entirely different from the large periodic ones generated by the flapping motion.

The significant process in the excited jet is the conversion of the flapping motion into rolling motion. This could be due to a simple mechanical process, without involving viscosity, an analogy of rotation due to a crank and wheel mechanism. A flapping motion does produce a transverse flow, periodically changing its direction in tune with the imposed oscillations. When the longitudinal and the transverse velocities become comparable, a circular motion is possible which is one of the preferred modes of a vortex. This hypothesis supports the dependence on the location of amplification by the excitation frequency and the exit velocity. Further experiments on the instantaneous velocity components are required to verify this suggestion. Of course, the viscous forces will eventually play a role in breaking up of the large eddies into smaller ones.

The mechanism involved in the entrainment process is also not clear. Measurements do indicate large entrainment, which does not increase suddenly in one step but continuously, the jet engulfing more fluid as the flow moves downstream. Flow visualisation reveals large turbulence-free potential flow from outside ingested into the jet. This pattern suggests the possibility of some other mechanism being involved in the entrainment process. It has been noticed that the flapping jet generates large pressure fluctuations on either side of the flow (Badri Narayanan & Platzer 1987). They are out of phase during flapping motion but seem to become in-phase (Badri Narayanan 1987) at the onset of amplification. Therefore, the possibility that pressure fluctuations may play a significant role in the entrainment of fluid into the system requires consideration.

4. Practical applications

The main characteristic of an excited jet is to entrain more mass flow by mixing. An ejector system whose efficiency depends on jet mixing can take advantage of excitation. Another possible use is to accelerate convective cooling. The possibility that excitation could be employed to improve combustion efficiency is yet to be explored. So far, investigation on plane jet excitation is mainly confined to the development of a suitable oscillating mechanism which is practical and suitable for the aircraft industry.

The installation of ejectors in a wing to produce lift for vertical take-off is under consideration by the aircraft industry (Braden *et al* 1982). However, the designers are looking for higher ejector thrust. In practice, a thrust augmentation ratio (ϕ) of nearly 1.4 could be achieved with a diffuser duct ejector shroud even though higher values are theoretically possible. The main limitation is due to separation of the flow in the diffuser especially at higher blowing pressures. In an aircraft system, short wide angle diffusers are required to satisfy the design conditions. An excited jet seems to suppress diffuser stall on account of its additional mixing characteristics. Laboratory experiments indicate that an excited jet can increase the ejector thrust by nearly 20% even at high blowing pressures (Badri Narayanan & Platzer 1987). These tests are preliminary in nature and it is envisaged that the shape of the duct could be optimized to increase the ejector thrust further.

5. Concluding remarks

A plane turbulent jet can be excited only by subjecting it to antisymmetric oscillations. The jet which is initially in the flapping mode rolls up forming vortices, initiating amplification. During excitation, the entrainment increases appreciably from that of the steady counterpart, due to enhanced mixing. A critical Strouhal number seems to be associated with amplification. The conversion of flapping motion into a vortex mode seems to be a fundamental phenomenon of unsteady flows and further investigations are necessary to understand this process. Similarly, the mechanism involved in the ingestion of fluid into the jet is not clear. The role played by the large pressure fluctuations during excitation needs further study.

List of symbols

a	maximum amplitude of vane oscillation;
f_e	oscillating frequency;
H	height of the nozzle;
Q_0	mass flow at the nozzle exit;
Q	mass flow in the jet at any x station;
St	Strouhal number = $f_e \delta / U_m$;
T_1, T_2	thrust of the jet and ejector, respectively;
U	mean velocity;
U_e	exit velocity;
U_m	mean velocity along the centre line of the jet;
x_c	distance between the nozzle exit and the region of amplification;
x	coordinate along the longitudinal axis;
y	coordinate along the width of the jet;
δ	width of the jet based on half the centre velocity ($U_m/2$);
ε	entrainment ratio = $(Q - Q_0) / Q_0$;
ϕ	thrust augmentation ratio = $(T_1 + T_2) / T_1$.

References

- Badri Narayanan M A 1987 Excitation of plane jet by twin vane oscillator; A preliminary investigation, Report No. AE 87 FM 1, Department of Aerospace Engineering, Indian Institute of Science, Bangalore
- Badri Narayanan M A, Platzer M F 1986 Excitation of a two-dimensional turbulent jet by a novel method and its application to ejector system, Report No. NPS 67-86-005 CR (1986) Naval Postgraduate School, Monterey, California
- Badri Narayanan M A, Platzer M F 1987a The mixing mechanism by organised turbulence structures in a plane jet excited by a novel method, *Proceedings of the IUTAM symposium on turbulence management and relaminarisation, January, Bangalore* (Berlin: Springer-Verlag) (in press)
- Badri Narayanan M A, Platzer M F 1987b Jet excitation by a bivane system and its application to an ejector for thrust augmentation, Report No. NPS-67-87-004, Naval Postgraduate School, Monterey, California (under print)
- Badri Narayanan M A, Raghu S 1983 *Indian Inst. Sci. J.* A64 : 83-98
- Bernal L, Sarohia V 1984 Large amplitude forcing of a high speed two-dimensional jet, JPL publication 84-91, Jet Propulsion Laboratory, California

- Bevilaqua P M 1984 Advances in ejector thrust augmentation, AIAA report No. AIAA 84-2425, Aircraft design systems and operations Meeting, San Diego, California
- Braden R P, Nagaraja K S, Von Ohain H J F 1982 Proceedings: Ejector workshop for aerospace applications, June, University of Dayton Research Institute, AFWAL-TR-82-3059
- Cervantes de Gortari, Goldschmidt V M 1980 The apparent flapping motion of a turbulent plane jet—further experimental results, November ASME paper 80-WA/FE-13
- Collins D J, Harch W H, Platzer M F 1984 Measurements of vane-excited jets, Laser anemometry in fluid mechanics, Ladoan, Instituto Superior Tecnico 1096, Lisboa, Coden, Portugal, pp. 215–236
- Crow S C, Champagne F H 1971 *J. Fluid Mech* 48: 547–591
- Fiedler H, Korschelt D 1979 The two-dimensional jet with periodic initial condition, 2nd symposium in turbulent shear flows, Imperial College, London
- Hinze J O 1981 *Turbulence* (New York: McGraw-Hill)
- Hussain A K M F, Clark A R 1977 *Phys. Fluids* 20: 1416–1426
- Lai J C S, Simmons J M 1985 *AIAA J* 23: 1157–1164
- Rockwell D O, Niccolls W O 1985 *Trans. ASME J. Fluid Eng.* 108: 380–382
- Townsend A A 1976 *The structure of turbulent shear flows* (Cambridge: University Press)
- Wynanski I, Fiedler H 1969 *J. Fluid Mech.* 38: 577–612
- Wynanski I, Oster D, Fiedler H, Dziomba B 1979 *J. Fluid Mech.* 93: 325–335

Shock-wave-turbulent-boundary-layer interaction and its control: A survey of recent developments

P R VISWANATH

Aerodynamics Division, National Aeronautical Laboratory, Wind Tunnel Centre, Bangalore 560 017, India

Abstract. This paper presents an overview of some of the recent developments that have taken place in the understanding, prediction and control of two-dimensional shock-wave-turbulent-boundary-layer interaction at high speeds. Following a brief description of the upstream influence phenomena, detailed discussions of incipient and fully separated flows at supersonic and transonic speeds are presented. A brief account of certain gross unsteady features of shock-separated flows is given next. Typical examples demonstrating the current ability to predict these complex flows are also included. Finally, a review of techniques using suction and tangential blowing for controlling shock-separated flows is presented.

Keywords. Shock-wave-boundary-layer interaction; boundary layer control; viscous-inviscid interaction.

1. Introduction

The subject of shock-wave-boundary-layer interaction continues to be an important area of research in view of its many applications in both external and internal aerodynamics. Shock-wave-boundary-layer interactions occur on airfoils and in turbo-machinery blades in transonic flow, in supersonic intakes, and ahead of control surfaces and flares in supersonic flow, to cite just a few of the applications. Flow separation, often associated with these interactions, generally leads to increased energy losses in the system and degrades the performance of the aerodynamic device; flow unsteadiness, often a result of separation, can cause additional problems (e.g. wing buffeting, air intake buzz etc.) which are undesirable in practice. Separation control by some active or passive means, in general, is beneficial for improving the performance of the device under consideration.

It is now over three decades since the early investigations on shock-boundary layer interaction were reported. These include the studies of Liepmann (1946), Ackeret *et al* (1946), and Liepmann *et al* (1951) from which emerged many important observations on the nature of these interactions with laminar and turbulent boundary layers at transonic speeds. Pearcey (1961, pp. 1164–1344) provided an excellent summary of earlier work on the subject of transonic interactions on

airfoils and their control. Following these, research shifted to the supersonic/hypersonic regimes as a result of increasing speeds of aircraft and developments in space flight. In the last two decades, considerable experimental and theoretical research has been carried out on the many aspects of this complex fluid dynamical problem. This has led to some degree of understanding on the nature of these interactions, and in identifying some of the important parameters affecting the phenomena in the different speed regimes. While there has been significant progress made in the understanding and analysis of laminar interactions, in general, the structure of turbulent interactions is still poorly understood; progress is hampered by our inadequate understanding of the dynamics of turbulence, particularly in the presence of adverse pressure gradients. In spite of these limitations, several engineering calculation methods, of varying degrees of complexity and sophistication, have emerged for predicting these flows even when there are small regions of separation.

This paper presents an overview of some of the important developments that have taken place in the understanding, prediction and control of these complex interactions. This article is not intended to be a critical review of all aspects or an exhaustive survey of relevant papers in the published literature. Following Green's (1970, pp. 235–340) review paper, quite a few survey papers covering various aspects of the problem have appeared (Charwat 1970, pp. 1–132; Stanewsky 1973; Sirieix 1975; Brusseeleers 1980; Adamson & Messiter 1980), the most recent being that of Delery (1985); these publications may be referred to for more details. The emphasis in this paper is on turbulent interactions because of their importance in practical applications. Since most of the investigations have been carried out on two-dimensional flows, the discussions to follow are limited primarily to two-dimensional interactions, and without heat transfer at the wall (the adiabatic case). In reality, shock-wave-boundary-layer interactions occur under rather complex circumstances, for example, involving surface curvature, heat transfer at the wall, nonuniform approaching flow and three-dimensionality. With the idea of understanding some of the basic features of these interactions, most investigations have been carried out on relatively simple model geometries with the boundary layer developing on a flat plate ahead of the interaction. These interactions have often been referred to as 'basic interactions' and will form the major part of the material in this paper.

The paper begins with a brief discussion of the upstream influence phenomena which is followed by detailed discussion of incipient and fully separated flows at supersonic speeds. Features of certain transonic shock-wave-boundary-layer interactions are discussed next. A brief account of certain gross unsteady features of shock-induced separated flows is given, although the data available is still very meagre. Typical examples, demonstrating the current state of calculation methods, are included. Finally, a discussion of techniques employing suction and injection (or blowing) for controlling these separated flows are presented.

2. The mechanism of upstream influence in shock-boundary layer interaction

In inviscid supersonic flow, it is well-known that when a shock wave meets (or is generated at) the surface, the surface pressure changes discontinuously through the

shock (figure 1). However, with a boundary layer developing on the wall, such a discontinuous pressure rise cannot occur because of the presence of the subsonic part of the boundary layer close to the wall, which cannot support an abrupt pressure rise. As a result, the pressure disturbances imposed by the shock are propagated partly upstream and partly downstream on the surface. The thickening of the subsonic stream tubes, in reaction to the adverse pressure gradients imposed by the shock, generate compression waves in the supersonic part of the boundary layer. These waves cause additional pressure rise and lead to further readjustment in the subsonic part of the boundary layer. This process continues and an equilibrium is reached so that the gradual pressure rise in the subsonic part of the boundary layer is compatible with the rather discontinuous pressure rise in the outer inviscid flow.

If the overall pressure rise across is not large, the boundary layer may not separate. Under these conditions, the interaction is termed 'weak' implying that the outer inviscid flow and the resulting shock pattern are only weakly altered (figure 1). On the other hand, if the total pressure rise associated with the shock system is large, boundary layer separation occurs causing significant perturbations in the outer flow as well as in the wave system (figure 1). These interactions are termed 'strong' implying strong coupling between the inviscid and the viscous part of the flow-field.

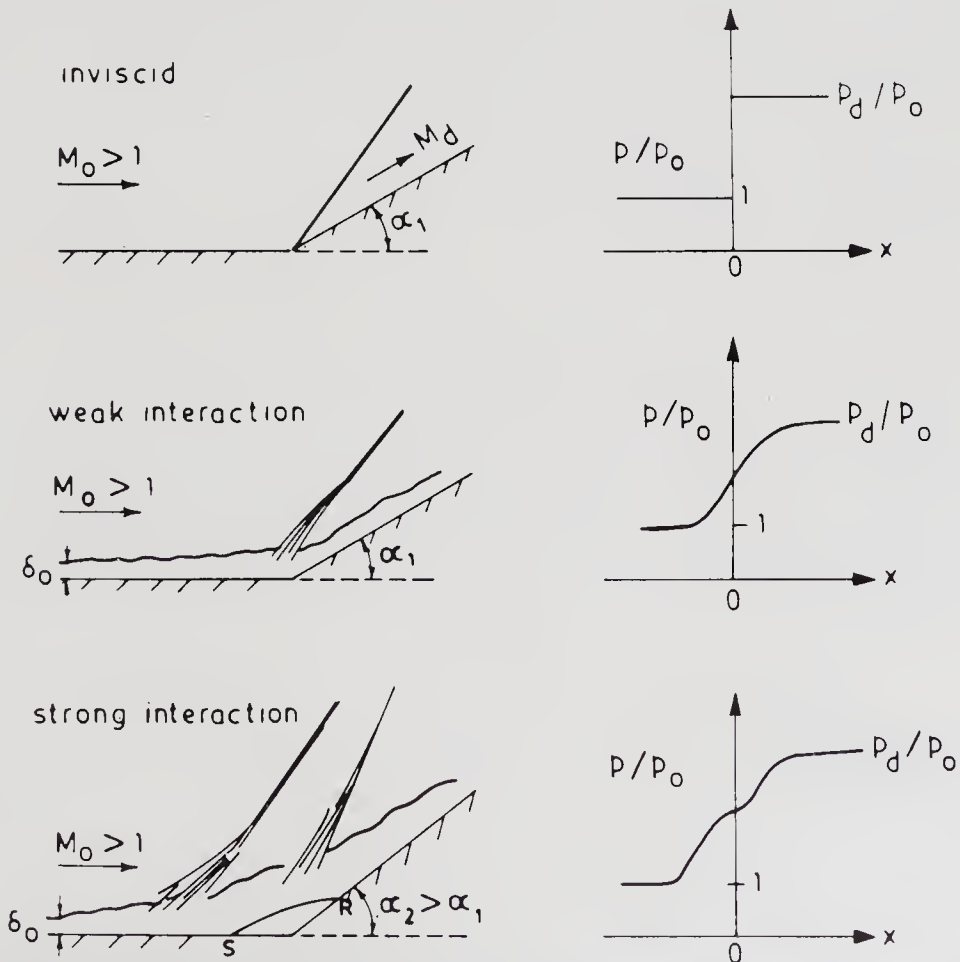


Figure 1. Schematic of wave pattern and wall pressure distributions at a compression corner.

The shock-wave-boundary-layer interaction zone, which in general depends on the nature of the boundary layer, the flow conditions upstream of the shock and the overall shock pressure rise, can extend over several boundary-layer thicknesses. With a laminar boundary layer, the interaction zone can be several times longer than the corresponding turbulent case for the same overall pressure rise.

3. Supersonic interactions without extended separation

3.1 Interaction without separation

If the total pressure rise associated with the shock system is either small or moderate, the boundary layer can negotiate the pressure gradients without separating. Typical examples of weak interactions for the cases of a compression corner and an impinging shock wave are shown in figure 2. The pressure rise occurs typically over a distance of 2–3 boundary layer thicknesses for the turbulent case. In the inner subsonic region of the boundary layer, shear stress gradients normal to the wall are important, while in the outer supersonic part the flow is largely inviscid. A (weak) secondary wave system is generally formed as a result of the interaction (shown dotted in figure 2). In the case of the compression corner, the secondary wave system results partly from the streamline curvature arising from thickening of the subsonic stream tubes and partly by the refraction of the outgoing compressive waves which generate waves that get reflected at the sonic line. For the case of the impinging shock wave, a second (secondary) wave system is formed due to the refraction of the incident shock. The wave pattern in the outer supersonic part of the boundary layer is essentially due to its vorticity or rotationality. This process is described in detail by Henderson (1967). The boundary layer thickness decreases across the interaction since a large fraction of the boundary layer flow is supersonic.

3.2 Nature of turbulent separation

Before addressing the problem of incipient separation, it is important and instructive to include a brief discussion of a fundamental feature of the turbulent separation process. Unlike in the case of steady laminar flows, turbulent boundary layer separation involves a gradual process before becoming separated in a time-averaged sense. Fully developed (or time-averaged) separation occurs where the mean wall shear stress is zero and flow downstream involves regions of back or reversed flow ($u < 0$).

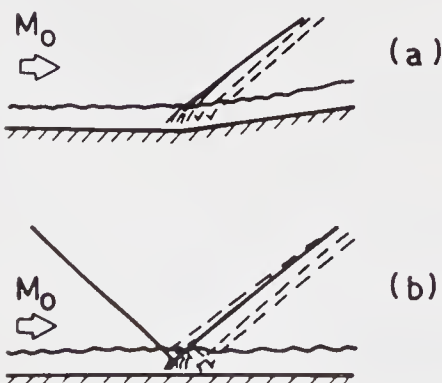


Figure 2. Schematic of wave pattern without separation (from Green 1970), (a) compression corner, (b) incident shock.

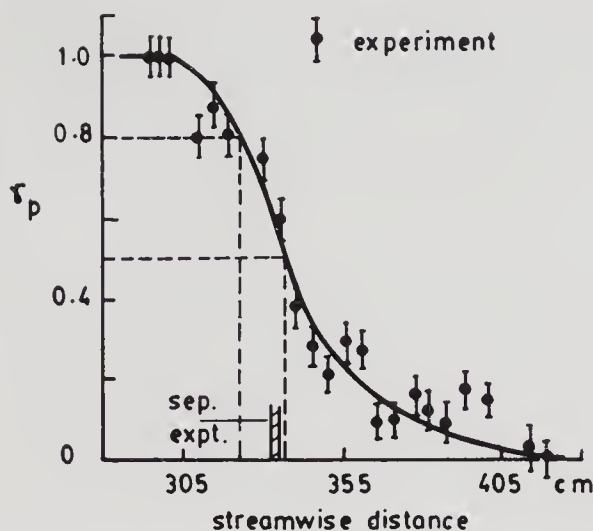


Figure 3. Velocity intermittency near the wall (from Simpson *et al* 1977).

It is now well-established (Sandborn & Kline 1961; Simpson *et al* 1977) that turbulent boundary layer separation exhibits intermittent reversed flow near the wall much ahead of the time-averaged separation point; this upstream zone has been termed the intermittent separation region. Measurements (Simpson *et al* 1977) related to this unsteady behaviour of separation in the case of a low speed separated flow on a flat plate is illustrated in figure 3, along with the associated boundary layer edge velocity distribution in figure 4. Laser velocimeter measurements of intermittency, γ_p (defined as the fraction of the time the flow is in the downstream direction, $\dot{U} > 0$), at a location near the wall, is plotted against streamwise distance. After a careful examination of low speed data, values of γ_p near the wall of about 0.8 and 0.5, for the onset of intermittent separation and fully developed separation, respectively, have been suggested (e.g. Simpson *et al* 1977); the pressure gradient relief appears to follow the beginning of intermittent separation. Measurements of γ_p in transonic separated flows have also revealed features qualitatively similar to low speed flows (Delery 1981; Viswanath & Brown 1983); a further discussion of this aspect is contained in § 5.

3.3 Incipient separation

As the overall pressure rise across the shock system is increased, a situation is reached which marks the beginning of a tiny separated region or a bubble. In the

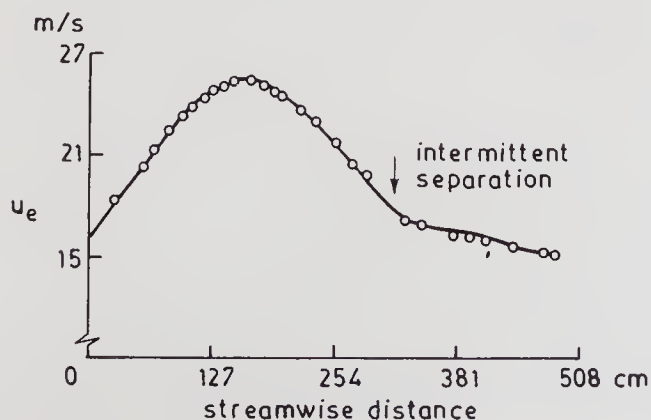


Figure 4. Boundary layer edge velocity distribution (from Simpson *et al* 1977).

literature, considerable emphasis has been given to a rather (hypothetical) condition in which the mean wall shear stress is positive everywhere except at one location (or a narrow region), where it is vanishingly small. This flow condition has been referred to as incipient separation (IS). From a practical or design view point, it is important to know what conditions lead to incipient separation, since it marks, in some sense, the onset of adverse effects.

Experimental determination of IS has not been easy because of the difficulties in accurately measuring rather small values of wall shear stress in a region of strong adverse pressure gradient. As a result, investigators in the past have proposed and employed several indirect techniques to identify IS. The emphasis has been to identify the onset of a small bubble or some marked change in the flow pattern. As we shall see in the next section, the use of different techniques have partly contributed to a somewhat confusing picture in the understanding of the IS phenomena, and the Reynolds number effects, in particular.

Kuehn (1959) proposed the appearance of a kink or a triple inflection point in the surface pressure distributions as a condition for IS. Another common method involves extrapolation of a measure of the bubble size to zero value from a series of experimental surface pressure distributions, which range from fully attached to fully separated conditions. The bubble size (in the streamwise direction) can be obtained, for example, from a surface oil flow technique. The first appearance of a 'separation' or an 'induced shock wave' as seen in a Schlieren/shadowgraph has often been adopted to identify IS. The orifice dam technique, which is intrusive, has been employed to detect surface flow direction. The various methods that have been used, their merits and shortcomings are discussed by Settles *et al* (1976a).

3.4 Pressure rise to incipient separation

Determination of the pressure rise associated with IS has been the subject of several investigations. The relevant parameters of the problem include the Mach number ahead of the interaction, M_o , a characteristic Reynolds number of the boundary layer flow and the geometry of the shock generator. For boundary layers developing in a zero pressure gradient upstream of the interaction, shape factor effects are related through the Reynolds number; also, the boundary layer thickness δ_o has been found to be a useful length scale. Although incipient separation data exist from many different sources involving different shock generators, reliable data covering a wide range of Reynolds number are only available for a compression corner (or ramp) geometry around $M_o = 3.0$. Figure 5 shows these results (Settles *et al* 1976a) in a plot of α_{is} , the ramp angle at which a tiny bubble is formed, as a function of Re_{δ_o} ; the pressure rise at IS can be calculated from M_o and α_{is} .

In the lower Reynolds number range ($10^4 < Re_{\delta_o} < 10^5$), α_{is} shows a decreasing trend, which is consistent with the free interaction principle (to be discussed in § 4). For $Re_{\delta_o} > 10^5$, mixed trends are seen; the data of Roshko & Thomke (1969, pp. 109–138) and Law (1974) show an increasing trend, while the data of Settles *et al* (1976) show little or no variation with increased Re_{δ_o} . The data of Settles and coworkers cover a wide range of Re_{δ_o} and the near constancy of α_{is} is observed for all the different techniques employed by them. For the data shown in figure 5 no systematic variation of H with Re_{δ_o} is observed (figure 6) suggesting weaker effects, if any, of H on α_{is} in the range of Re_{δ_o} considered.

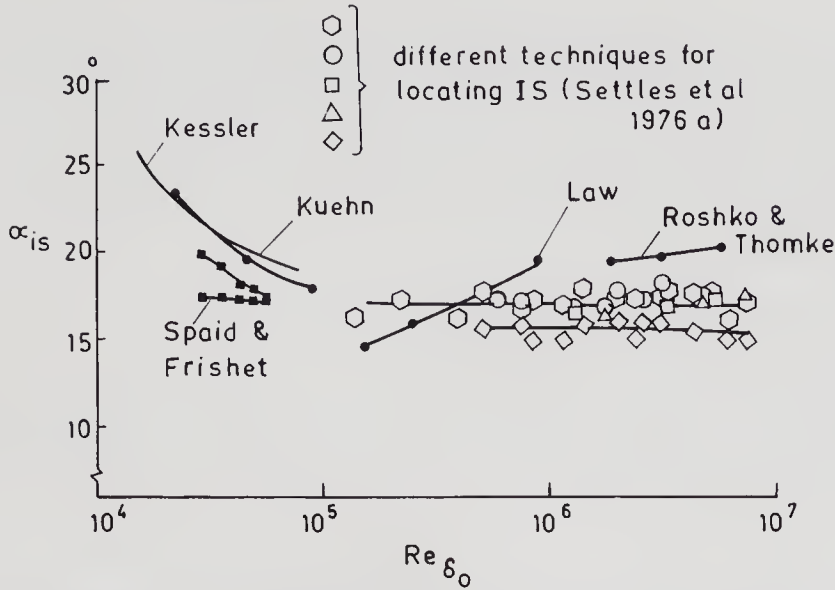


Figure 5. Reynolds number effect on incipient separation at a compression corner: $M_o = 2.9$ (from Settles *et al* 1976a).

Satisfactory explanation for the observed reversal in the trend of α_{is} vs. Re_{δ_0} , seen at the higher Reynolds number (for some of the data in figure 5), still does not exist, although certain speculations have been made (Elfstrom 1972; Roshko & Thomke 1969, pp. 109–138). Settles *et al* (1976a) have provided some explanation in favour of their observations. They suggest that the IS phenomenon is a gradual transition between attached and fully separated flow and does not involve an abrupt change; therefore a small spread in α_{is} values (about 3° , depending on the technique used, figure 5) is understandable. They further point out that the use of a single technique over a limited range of Reynolds numbers could give misleading results.

There is insufficient data in the literature concerning Reynolds number effects at other Mach numbers. Regarding the effect of Mach number available data show an increase in the pressure rise to IS (or equivalently α_{is}) with M_o which is to be expected on general grounds and is consistent with the free interaction principle.

The turbulent separation process being intermittent in character, the difficulties associated with locating IS experimentally can be reconciled with since different techniques would average the unsteady nature of the flow in a different manner.

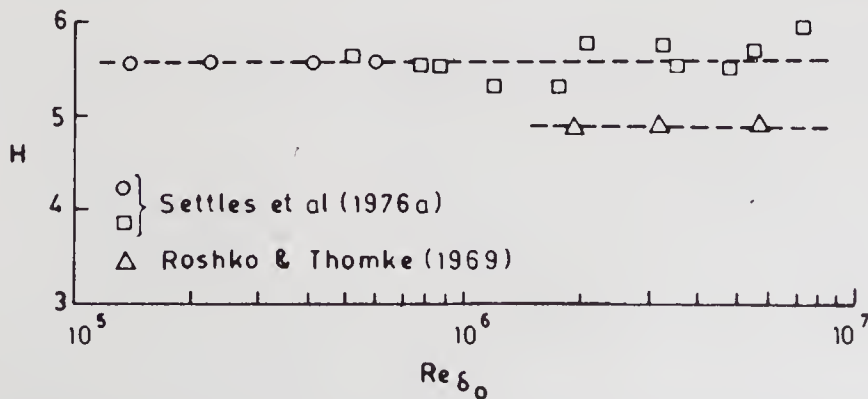


Figure 6. Shape factor variation with Reynolds number at $M_o = 3.0$.

Although information on mean properties is sufficient from an engineering or practical view point, further understanding of the IS process and the effects of Reynolds number may require deeper understanding and modelling of the unsteady character of the turbulent separation process described earlier (§ 3.2). Perhaps there is need to reexamine the concept of IS in view of the unsteady nature of the turbulent separation phenomena.

4. Supersonic interactions: Fully separated flows

Progressive increase in the shock strength or overall pressure rise beyond incipient separation leads to rapid thickening of the subsonic stream tubes and a corresponding increased deflection of the supersonic part of the boundary layer. As a result, the adverse pressure gradient in the interaction region increases leading to significant deceleration of the flow near the wall. The boundary layer near the wall eventually separates when it can no longer negotiate the pressure gradients imposed by the outer inviscid flow. Boundary layer separation leads to a bubble of reversed flow followed by reattachment. Further increase in the overall pressure rise following separation generally causes a further increase in the separated zone.

4.1 Some general features

In figure 7 are shown some schematic representations of the wave pattern and surface pressure distributions, for three different interactions, due to impingement of a shock on a flat wall, in front of a compression corner and a forward facing step. Wall pressures are shown for both laminar and turbulent cases to bring out qualitatively some of the major differences. The separation and reattachment of the boundary layer are indicated by *S* and *R* respectively. The pressure distributions for the compression corner and the incident shock have much in

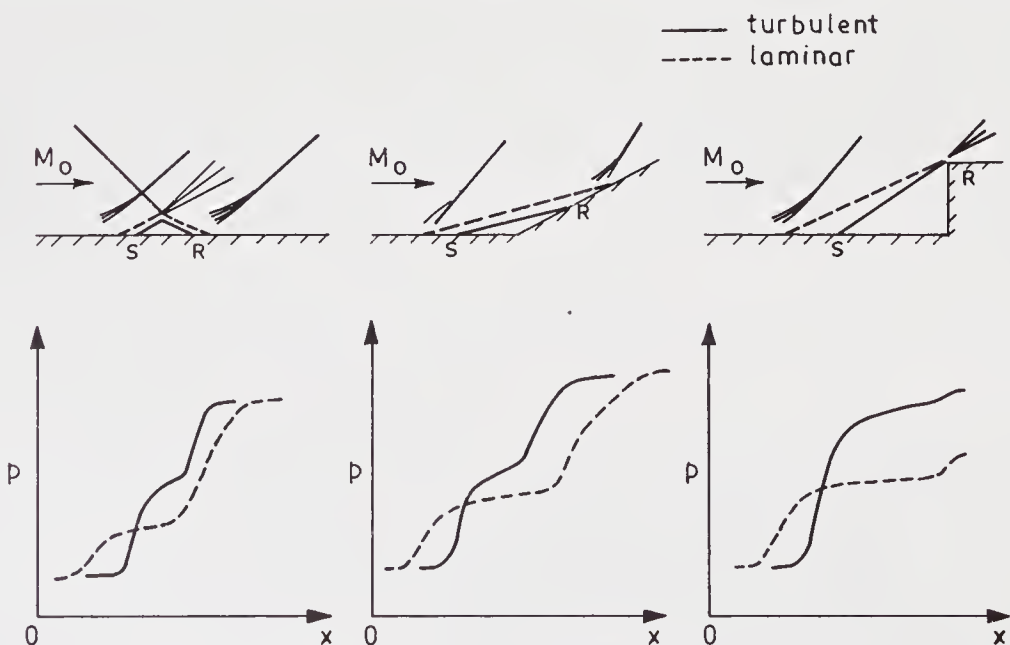


Figure 7. Schematic of wave pattern and wall pressure distributions in supersonic separated flows.

common; three distinct regions, pressure rise due to separation, a reduced or zero pressure gradient in the bubble region and pressure rise following reattachment may be observed. The separated boundary layer grows as a free shear layer which acquires kinetic energy as a result of mixing and is able to overcome the pressure gradient at reattachment. For the interactions at a forward facing step, the reattachment occurs on the step face and the separation location is free to move. In the vicinity of separation the pressure distribution is similar to the two cases just described earlier, while downstream, it looks somewhat different.

For laminar separated flows the pressure rise to separation and the pressure gradients, in general, are relatively smaller than for the corresponding turbulent case; furthermore, the interaction spreads over a longer streamwise distance for the same overall pressure rise.

4.2 Free interaction concept

The basic mechanism that causes boundary layer separation involves a two-way localized interaction between the boundary layer flow and the inviscid outer supersonic flow. Based on an extensive series of experiments on various experimental configurations, Chapman *et al* (1957) postulated the concept of "free interaction." They suggested that, if the separated region is large enough, the interaction in the vicinity of separation is localized, free of downstream influences (or geometry) and independent of the agency provoking separation. In essence, the separation process would depend only on the Mach number and the boundary layer characteristics ahead of the interaction.

Chapman *et al* (1957) used simple order of magnitude analysis to derive expressions for similarity in pressure distributions in the separation region. For supersonic flow under small rate of boundary layer growth, the local pressure coefficient may be related to the growth of the displacement thickness:

$$c_p = (p - p_o)/q_o = [2/(M^2 - 1)^{1/2}] (d\delta^*/dx), \quad (1)$$

where o refers to conditions at the beginning of the interaction. For viscous flow, boundary layer approximations are assumed valid; the momentum equation applied at the wall gives

$$dp/dx = (\partial\tau/\partial y)_w. \quad (2)$$

Equation (2) emphasizes the importance of the flow near the wall for analysing separation.

Applying order of magnitude considerations and introducing a length scale l_f (characteristic of the free interaction region), (1) & (2) can be written as

$$(p - p_o)/q_o \sim [1/(M^2 - 1)^{1/2}] (\delta^*/l_f), \quad (3)$$

$$(p - p_o)/l_f \sim \tau_{wo}/\delta^*. \quad (4)$$

Algebraic manipulation of (3) and (4) leads to

$$(p - p_o)/q_o \sim (c_{fo})^{1/2}/(M_o^2 - 1)^{1/4}, \quad (5)$$

$$l_f/\delta_o^* \sim 1/[(c_{fo})^{1/2}(M_o^2 - 1)^{1/4}]. \quad (6)$$

These expressions are valid for both laminar and turbulent interactions provided

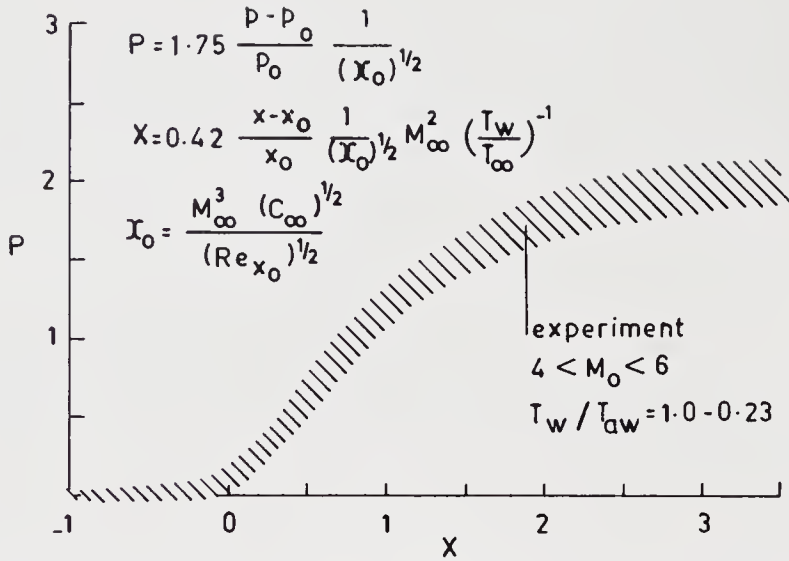


Figure 8. Free interaction similarity in laminar flow (from Lewis 1967).

appropriate $c_f \sim Re_x$ relationships are chosen. Good correlation of experimental data at moderate Reynolds numbers were seen (Chapman *et al* 1957) in the expressions suggested above.

Extensions and refinements of the free interaction concept have been reported in the literature; two such examples are shown in figures 8 and 9. Pressure

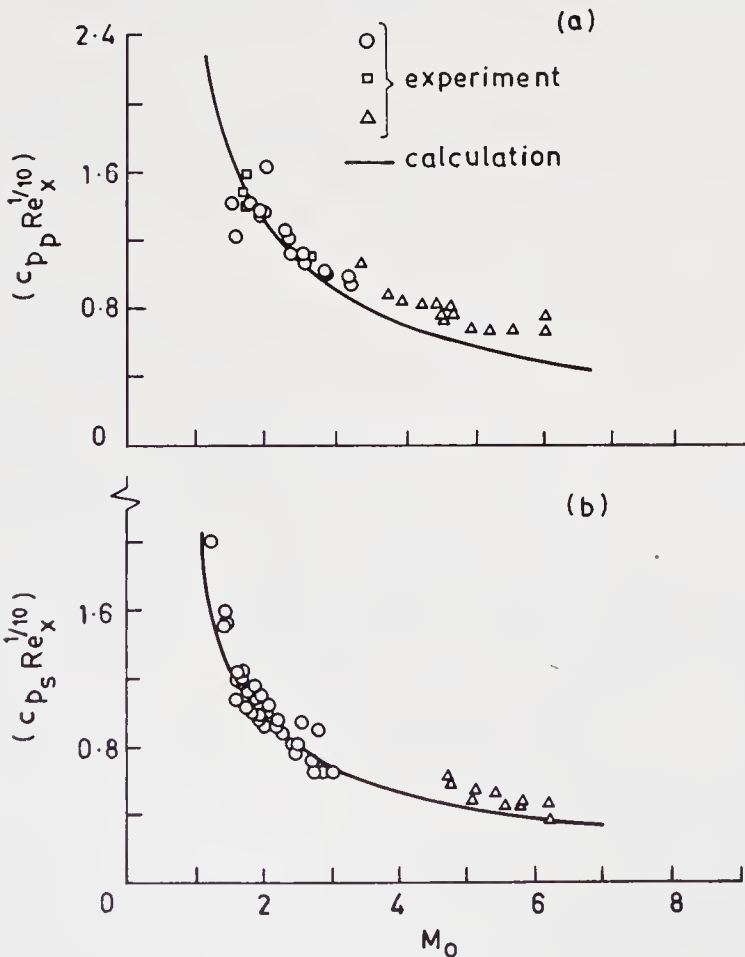


Figure 9. Free interaction similarity in turbulent flow (from Erdos & Pallone 1962), (a) plateau pressure rise, (b) separation pressure rise.

distributions, in the variables suggested (Lewis 1967), are shown in figure 8 for laminar-separated flow at a compression corner at different values of M_o and Re including effects of surface heat transfer. Good correlation may be seen for the separation including the plateau region although the similarity parameters are expected to be valid only for the free interaction region in the vicinity of separation. For the turbulent case, results of separation and plateau pressure rise are shown in figure 9 from the semi-empirical theory of Erdos & Pallone (1962, pp. 239–254). Reasonably good agreement may be seen except for some departure at the higher M_o for the plateau pressure rise, which has been attributed to the linearized expression used in describing the inviscid flow. With turbulent interactions, unlike the laminar counterpart, similarity in pressure distributions (for different geometries) are not clearly observed (Chapman *et al* 1957) beyond the separation point, indicating relatively stronger influence of the downstream geometry.

4.3 Flow development through the interaction

Although a large number of experimental investigations with separated flows have been reported, the flow-field has been explored only in very few of these. Certain broad features of separated flows were discussed in the previous sections. Both surface and flow-field data are now discussed based on the measurements of Settles *et al* (1976b) on a 24° compression corner at a Mach number of 2.85 and at high Reynolds number.

Distributions of surface pressure and skin friction (obtained using a Preston tube) distributions are displayed in figure 10. The pressure distribution shown is

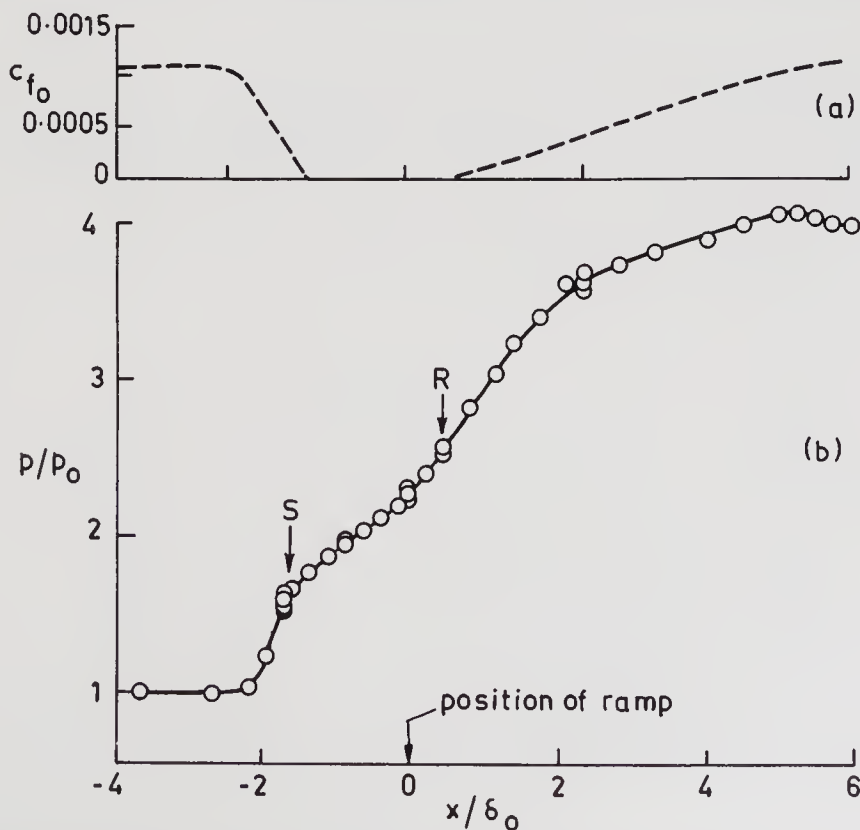


Figure 10. Experimental data for a compression corner flow: $M_o = 2.9$ (from Settles *et al* 1976b), (a) skin friction distribution (b) wall pressure distribution.

typical of compression-corner-separated flows. The c_f distributions show a rapid decrease towards separation and a more gradual recovery following reattachment. Both surface oil flow technique and c_f data reveal a bubble length of about $2 \delta_o$. The pressure gradients in the bubble region suggests that they are apparently balanced by the Reynolds stress gradients, since the velocities in the reversed flow are small. The maximum reversed flow velocity was only about 15% of the boundary layer edge velocity in these experiments.

Development of streamwise mean velocity profiles through the interaction is shown in figure 11. Significant retardation of the flow, particularly near the wall in the separated zone, is evident. Static pressure measurements in this flow have revealed significant normal pressure gradients near separation and reattachment, arising out of streamline curvature. Gross features of the flow-field determined from detailed measurements are shown in figure 12. The separation shock-wave originates at a distance of about $2 \delta_o$ upstream of the corner turning the outer flow by 10° . The sonic line is displaced outwards considerably as a result of flow separation. A system of compression waves is generated in the reattachment zone which coalesce with the separation shock.

With flow separation, turbulence quantities in general undergo significant variations through the interaction. At supersonic speeds, detailed information on turbulence quantities like kinetic energy and shear stress does not exist as yet for shock separated flows. There are, however, some data available in the absence of separation (Rose 1973; Rose & Johnson 1975) which show effects which are typical of adverse pressure gradient flows. A discussion of turbulence behaviour for a shock separated flow at transonic speeds is included in § 5.4.

4.4 Scaling of upstream influence interaction length

It is of considerable interest to determine scaling laws for different characteristic lengths associated with the separated flow. Figure 13 shows suitably defined lengths characterizing separation, reattachment and bubble size for fully separated flows;

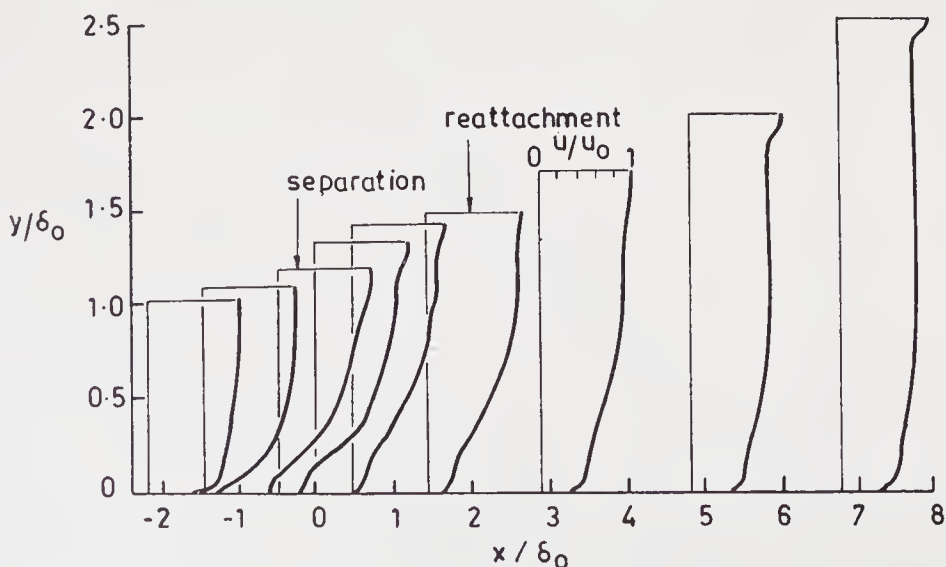


Figure 11. Mean velocity profiles in the interaction region: $M_o = 2.9$ (from Settles *et al* 1976b).

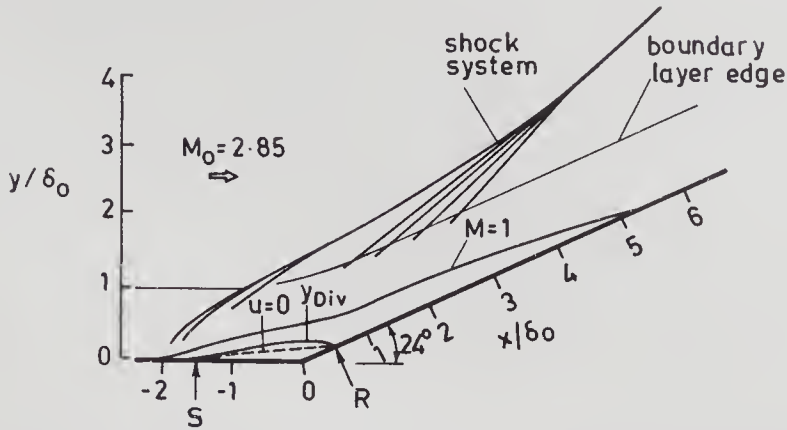


Figure 12. Features of separated flow at a compression corner: $M_o = 2.9$ (from Settles *et al* 1976b).

these lengths can be determined without much difficulty from experimental pressure distributions. In the literature, however, several attempts have been made to determine the scaling for the interaction length, l_o , associated with the upstream influence phenomena (figure 13). The boundary layer thickness, δ_o , at the beginning of the interaction has been used for normalising l_o in most earlier studies. We shall now present two correlations that have been proposed in the context of compression corner flows.

The free interaction principle provides a frame work for analysing and correlating experimental data, in particular, to characterize certain gross features of the separated flow as they depend on important variables like M_o , Re etc. Doubts have often been raised as to the validity of these arguments at higher Reynolds numbers, an example of which was seen in connection with the experimentally determined pressure rise to incipient separation (figure 5).

For boundary layers developing on a flat plate ahead of interaction, in general, we may expect l_o/δ_o , to depend on M_o , Re_{δ_o} , and the ramp angle α . Results l_o/δ_o from different experiments at relatively higher Reynolds numbers show (e.g. Roshko & Thomke 1969, pp. 109–138) the following general trend; it decreases with increase in M_o (for fixed values of Re_{δ_o} and α) and Re_{δ_o} (for fixed values of M_o

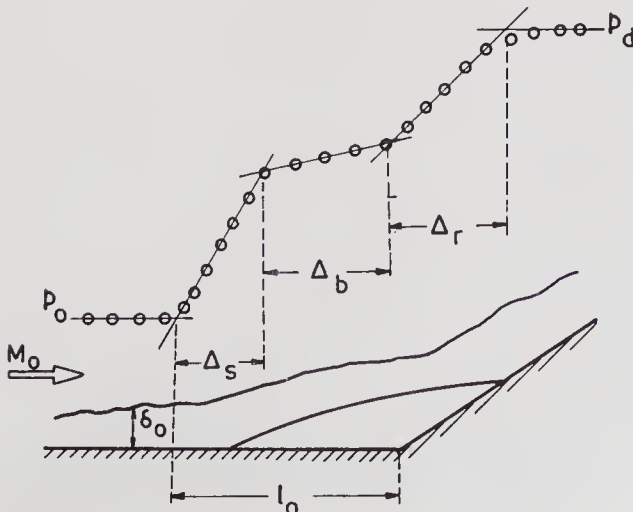


Figure 13. Sketch defining characteristic lengths in separated flow.

and α); it increases with α for given values of M_o and Re_{δ_o} . These results may imply an increased resistance to separation with increase in Re_{δ_o} and M_o .

Roshko & Thomke (1976), based on an extensive series of tests in the range $2 < M_o < 4.5$ and $10^5 < Re_{\delta_o} < 10^6$, found that, for $M_o > 2$, their data l_o/δ_o correlated with c_{f_o} at each ramp angle independent of both M_o and Re_{δ_o} (figure 14). Other data from the experiments of Law (1974) and Settles *et al* (1976a), at relatively high Reynolds numbers, were found to be in good agreement with the above correlation. The physical reasoning behind this correlation is not known; the trend of these results with Reynolds number is in clear contradiction with the free interaction principle.

The second correlation is due to Settles & Bogdonoff (1982) and is based on simple dimensional arguments; for a compression corner, one can write

$$l_o/\delta_o = f(M_o, Re_{\delta_o}, \alpha).$$

Figure 15 shows their data at $M_o = 3$ as well as those of Law (1974) and Roshko & Thomke (1969, pp. 109–138); at each α , l_o/δ_o decreases with Re_{δ_o} . They obtain, after choosing an average value of $-1/3$ for the slope,

$$(l_o/\delta_o)(Re_{\delta_o})^{1/3} = 0.9 \exp(0.23\alpha), \text{ at } M_o = 3.0.$$

To throw further light on these observations, Settles & Bogdonoff (1982), based on their measurements at $M_o = 3$, examined the variation of other relevant boundary layer length scales (e.g. displacement, and momentum thicknesses, distance to sonic line, sub-layer thickness) with Re_{δ_o} ; none of these exhibited the $Re_{\delta_o}^{-1/3}$ variation suggested by the correlation.

In conclusion, while engineering correlations for an interaction length associated with separation are now available for compression corner flows over limited M_o and Re_{δ_o} ranges, our understanding of the influence of the Reynolds number, particularly at the higher range of practical interest is rather poor. A similar

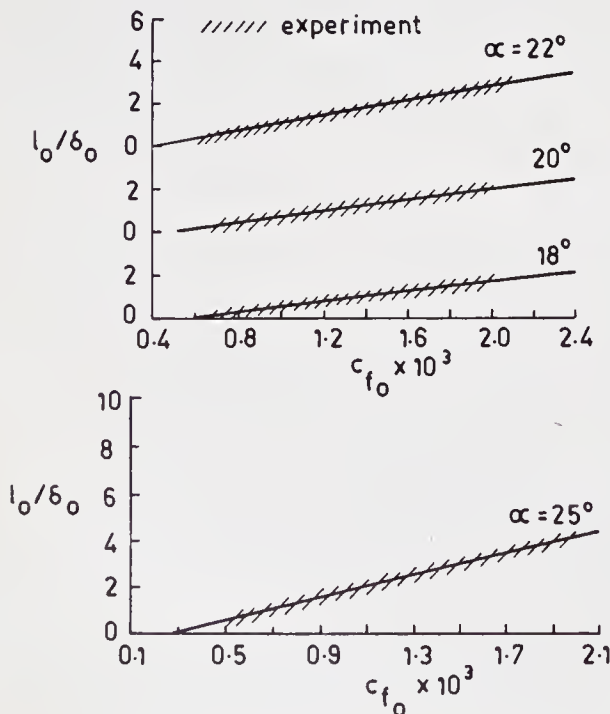


Figure 14. Correlation of interaction length at a compression corner (from Roshko & Thomke 1976).

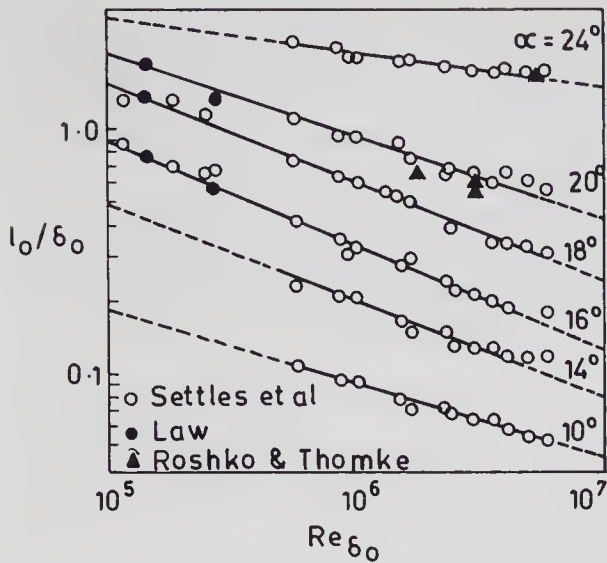


Figure 15. Variation of interaction length with Reynolds number at a compression corner: $M_o = 2.9$ (from Settles *et al* 1982).

situation can be expected with other interactions also (e.g. impinging shock wave, forward facing step etc); sufficient data covering a wide range of Re does not even exist for these cases to attempt such a correlation. It is therefore not surprising that little information exists for the scale of the separation bubble or the reattachment region (figure 13); even identifying relevant parameters for these cases may not be easy.

4.5 Certain experimental aspects

Experimental research has provided the most valuable information on the subject of shock-wave-boundary-layer interaction. Two aspects of experimental testing which have proved to be very important are now discussed.

4.5a Three-dimensional effects in nominally two-dimensional interactions: To realize nominally 2D interaction in experiments is a difficult task, particularly in the presence of strong adverse pressure gradients. Differences in the experimental results amongst experiments conducted in different tunnels on similar geometrical configurations and in similar flow conditions, have often been due to varying degrees of three-dimensional (3D) effects. It is very important to make as many checks as possible to assess departure from two-dimensionality or the degree of 3D effects in any experiment. 3D effects arise largely from shock-boundary layer interactions on the side wall when the model spans the wind tunnel side walls. Isolating the central part of the model flow by some means or use of side fences are known to minimize 3D effects (Settles *et al* 1976b). Use of axisymmetric geometry is a good remedy, but would require a model of a larger size so that the transverse curvature effects are reduced to a minimum; furthermore, large size of the model would imply a larger size for the wind tunnel. Another source of error could arise if the scale of separation (e.g. extent of separated zone) becomes comparable to the span of the tunnel, which is in essence an aspect ratio effect.

Various methods are available for assessing the degree of two-dimensionality. The surface oil flow technique is widely employed to assess the spanwise uniformity of the surface flow and to locate the separation-reattachment points; it has been a

very valuable tool in separated flow experiments. An assessment of spanwise variation of flow or surface parameters would be very useful. The 2D boundary layer momentum balance through the interaction region should be assessed; this exercise would involve measurements of streamwise mean velocity profiles and surface parameters like skin friction and pressures.

Every attempt should be made to keep the 3D effects to a minimum in experiments. This is important from the point of view of understanding the true behaviour of the flow, for providing quality data for validating calculation methods and for providing the necessary feedback to the modeller.

4.5b Tripping device and occurrence of transition: An assessment of the state of the boundary layer ahead of the interaction is an important requirement since the interaction, in general, is strongly dependent on the nature of the boundary layer. Most experiments reported in the literature have been conducted in relatively small tunnels which imply smaller models; this combined with the stagnation pressure supply generally available have lead to insufficiently high Reynolds numbers in which natural transition can occur well ahead of the interaction. Therefore the boundary layer is often tripped downstream of the leading edge of the model to ensure a turbulent boundary layer ahead of the interaction; the presence of the trip also avoids varying transition locations at different Reynolds numbers. Having tripped, checks have rarely been made to assess the state of the boundary layer. It is well-known that tripping becomes more difficult at relatively lower Reynolds numbers and higher Mach numbers because of the increased stability of the laminar boundary layers.

It has often been argued (e.g. Green 1970, pp. 235–340) that, in experiments conducted in tunnels at relatively low Reynolds numbers with a tripping device, the boundary layer upstream of the interaction may not have been fully developed or close to equilibrium. This effect may have contributed to another source of error while comparing different sets of data on similar configurations and flow conditions. Realizing their importance, boundary layer velocity profile measurements have been made ahead of the interaction in many recent studies. In some of the experiments (e.g. Settles *et al* 1976b) care has been taken to ensure that the boundary layer exhibits the well-known law of the wall and wake regions.

5. Transonic interactions

5.1 Some general features

Normal shock-wave-boundary-layer interactions occur in a variety of flow situations; on airfoils at transonic speeds, in supersonic intakes, in supersonic nozzles/diffusers etc. Interactions at transonic Mach numbers, in general, have not received much attention; the renewed interest in transonics after 1970 has triggered many new investigations in the last decade. Transonic-shock-boundary-layer interactions exhibit certain features distinct from those at supersonic speeds, as illustrated by the following two examples.

The first is the interaction between a normal shock wave and a flat plate boundary layer, studied by several investigators (Seddon 1960; Kooi 1975; Sawyer *et*

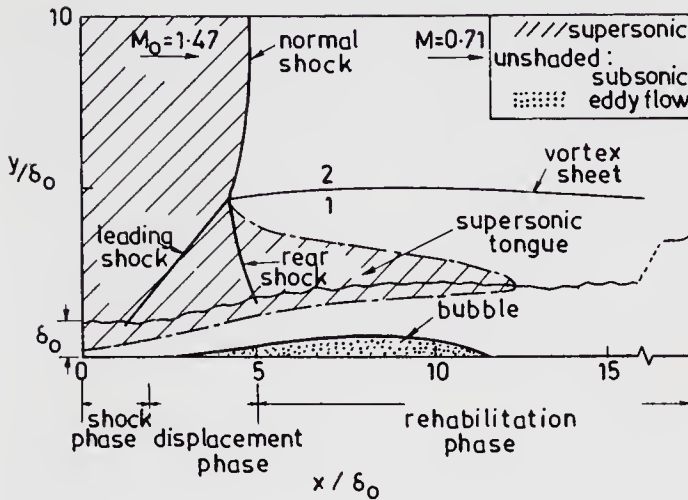


Figure 16. Interaction of normal shock with a turbulent boundary layer: $M_0 = 1.47$ (from Seddon 1960).

al 1977). Figures 16 and 17 show some of the important features of the separated flow and the surface pressure distributions as observed by Seddon (1960). The strong normal shock wave bifurcates near the wall (leading to what is often called lambda shock) as a result of flow separation; the leading shock results from free interaction between the boundary layer flow and the outer inviscid flow. Behind the rear shock there is a supersonic region, often referred to as a supersonic tongue, which generally occurs for $M_0 \geq 1.40$. Because of the differences in the static pressures and flow directions in regions 1 and 2 of figure 16 a vortex sheet or slip line originates at the lambda intersection. The downstream flow is subsonic, hence, downstream conditions can exert significant effects on the entire interaction. The surface pressure increases continuously in the interaction zone towards the inviscid value and the distribution in general does not exhibit a plateau region like in supersonic interactions at relatively higher Mach numbers. The overall total pressure rise through the interaction is, in general, decided by the strong interaction between the viscous flow and the outer inviscid flow and is not known a priori. In view of the fairly extensive region of separation, and because of the influence of the downstream subsonic flow, interactions at transonic speeds are relatively less localized, adding further to the difficulty in prediction of these flows.

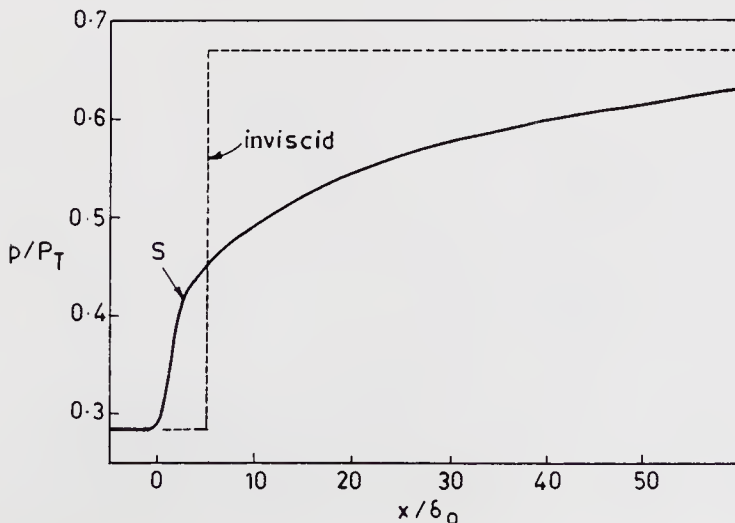


Figure 17. Surface pressure distribution due to normal-shock-turbulent-boundary layer interaction: $M_0 = 1.47$ (from Seddon 1960).

The second example illustrates additional complexity that can arise if the separated shear layer does not reattach to a surface, as often happens on an airfoil (figure 18). The flow is seen to separate at the foot of the shock wave and leaves downstream a massive separated flow. Two main differences relative to flat plate interactions may be observed here. The boundary layer upstream of the shock interaction develops in a region of continuous favourable pressure gradient caused by the airfoil contour; depending on the shock strength and the airfoil geometry, the separated shear layer may close only in the wake downstream of the airfoil trailing edge (figure 18), adding further complexity to the modelling of the reattachment process.

5.2 Unseparated flows

Figure 19 shows a sketch of a normal shock wave interaction for which the boundary layer does not separate ($M_o \approx 1.30$). The flow downstream of the shock

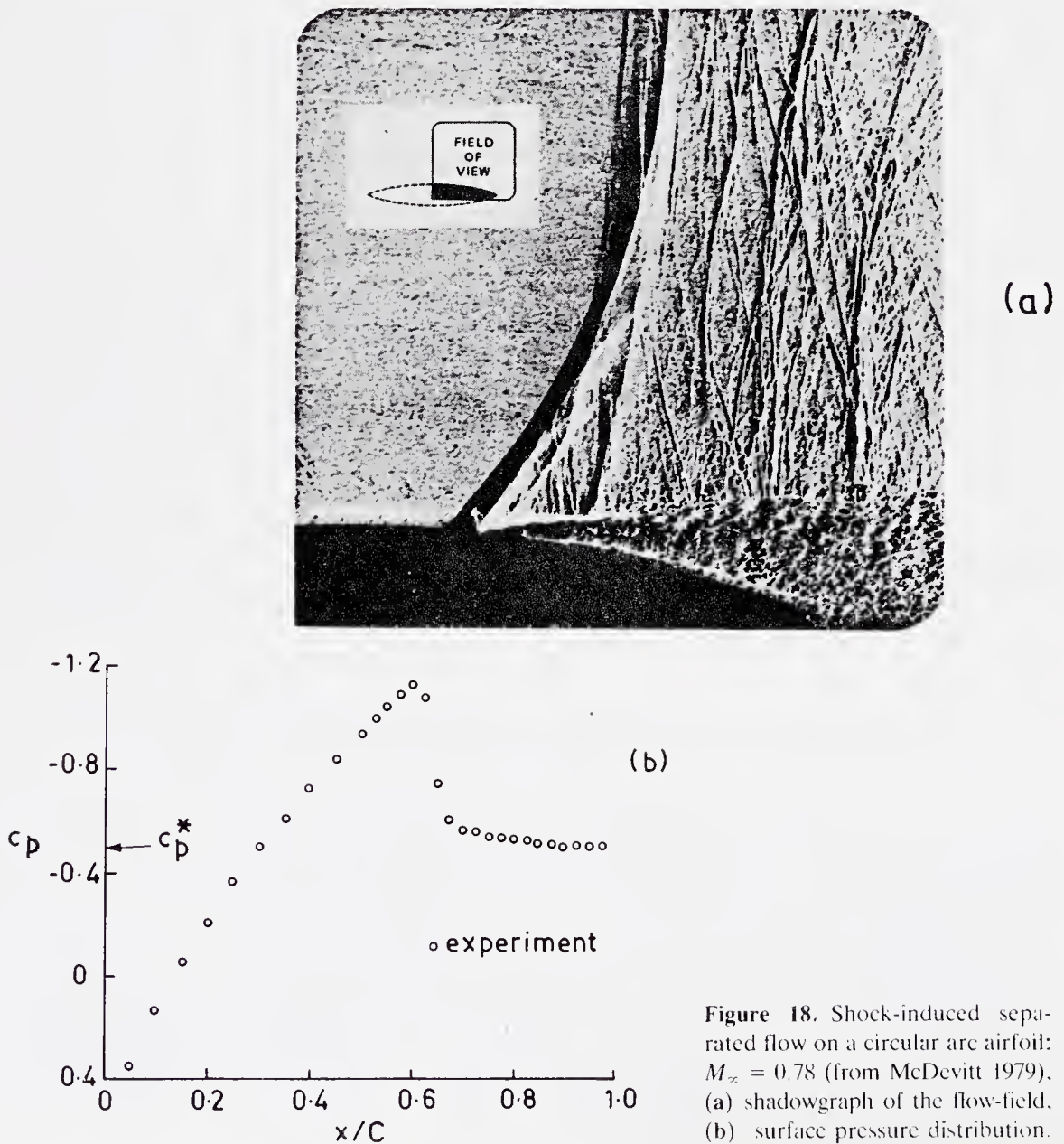


Figure 18. Shock-induced separated flow on a circular arc airfoil: $M_\infty = 0.78$ (from McDevitt 1979), (a) shadowgraph of the flow-field, (b) surface pressure distribution.

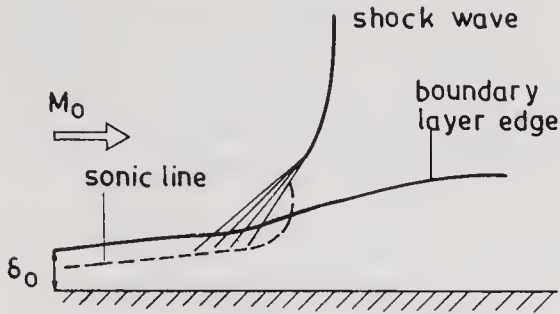


Figure 19. Schematic of wave pattern due to normal shock-turbulent boundary layer interaction (from Melnik & Grossman 1974).

is subsonic and the interaction is not localized in contrast to the supersonic case. Thickening of the subsonic stream tubes, as a result of upstream influence, generates compression waves at the foot of the shock wave. The subsonic part of the boundary layer, having a large fraction of the boundary layer thickness, plays an important role in the generation of the wave system. The boundary layer thickness increases across the interaction.

5.3 Incipient separation

Very few investigations have dealt with the problem of incipient separation at transonic Mach numbers. The difficulties in experimentally determining incipient separation discussed in connection with supersonic interactions are present in the transonic case also. Experimental results (Delery 1985) obtained by different techniques are shown in a plot of M_0 vs. Re_{δ_0} (or H_{i0}) in figure 20. The shape factor has only a weak influence in determining incipient separation; a slight rise in M_0 at low values of H_{i0} is indicated, which is consistent with fuller velocity profiles associated with low values of the shape parameter. Inger's (1981) result based on a triple deck analysis shows (figure 20) fair agreement with the data.

Certain important features of the flow just following incipient separation, taken from the experiments of Delery (1983), are shown in figures 21 and 22. Measurements were made in the interaction zone at the diverging end of a symmetric nozzle at $M_t = 1.30$. The mean velocity profiles, as a result of the adverse pressure gradients imposed by the shock, go through a significant deceleration particularly near the wall (stations 2, 3); following the pressure gradient relief beyond station 4, the velocity profiles recover again near the wall.

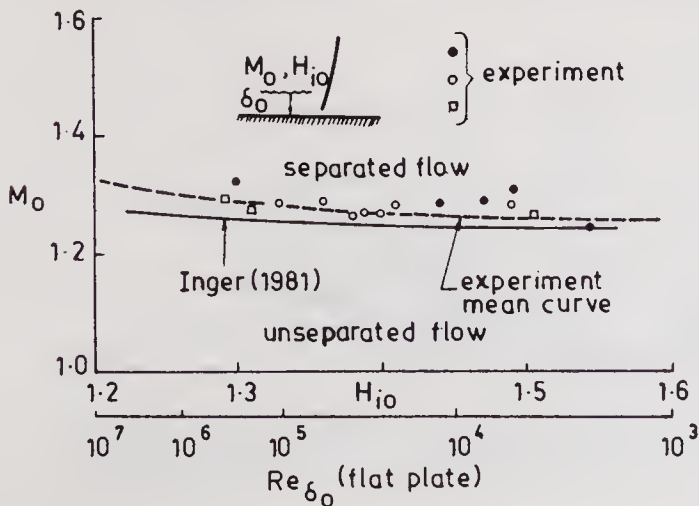


Figure 20. Experimental data of shock-induced incipient separation in transonic flow (from Delery 1985).

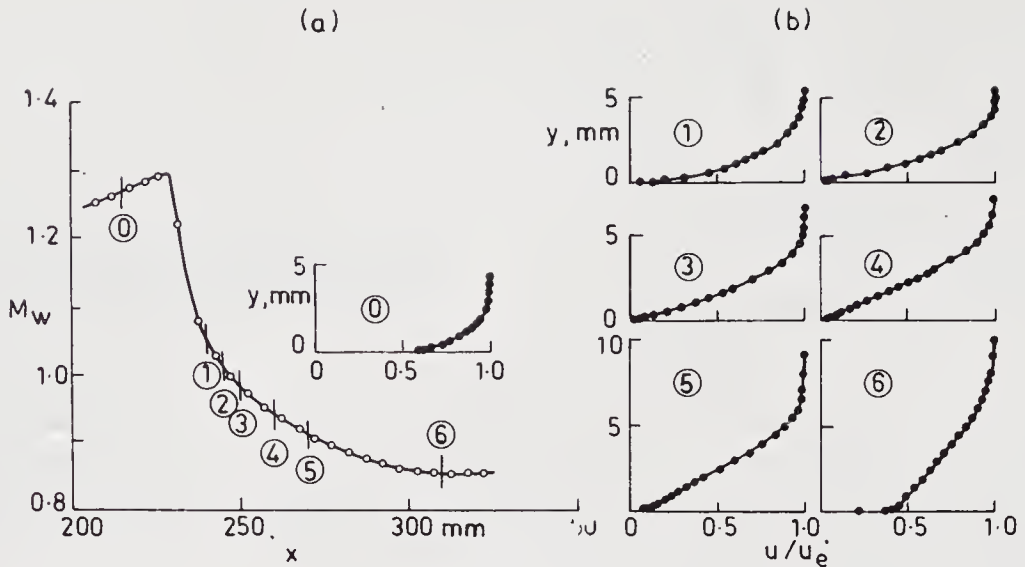


Figure 21. Experimental data at nearly incipient separation condition (from Delery 1983). (a) wall Mach number distribution, (b) mean velocity profiles.

The boundary layer shape factor (figure 22) is seen to reach a maximum value of about 2.6, which is close to the value of 2.5 generally expected at the separation location; following the relief in the pressure gradients, H_i decreases and returns to the flat plate value downstream. The streamwise velocity intermittency data (described in § 3.2), measured using a laser velocimeter, are shown in figure 22, in terms of the probability for the instantaneous value of U , to be negative, i.e. $P(U \leq 0)$, which corresponds to $(1 - \gamma_p)$. These measurements reveal a tiny bubble about $2 \delta_o$ in streamwise length. The intermittent flow reversal near the wall is spread over a distance of about $2 \delta_o$, upstream of the mean separation point.

5.4 Fully separated flows

Experimental results indicate (figure 20) that the turbulent boundary layer at transonic speeds separates for $M_t \geq 1.30$; with a fully separated flow, dissipative phenomena play a major role in determining the dynamics of the mean flow. There

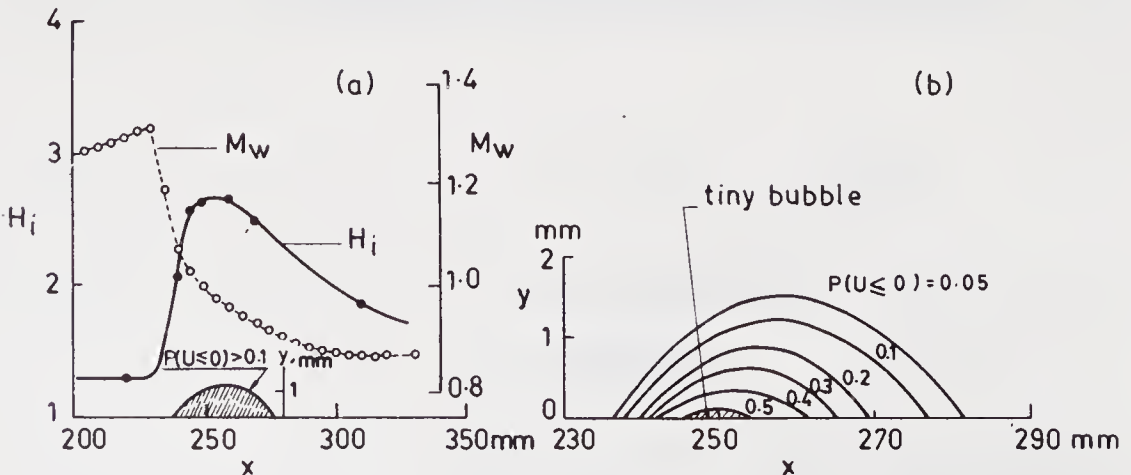


Figure 22. Experimental data at nearly incipient separation condition (from Delery 1983). (a) shape factor and wall Mach number distributions, (b) lines of constant value for $P(U \leq 0)$.

have been, in recent years, quite a few experimental investigations (Delery 1981; Bachalo & Johnson 1979) wherein the flow-field with separation has been explored. The flow development through such an interaction will be discussed based on results obtained by Delery (1983) on a bump in a transonic channel.

Figure 23 shows the wall Mach number distributions and an interferogram of the flow-field. The shock interaction occurs at $M_I = 1.37$; a well-defined separated flow results and reattachment occurs on the flat wall downstream of the bump trailing-edge. The Mach number distributions suggest a pressure plateau in the bubble zone followed by a pressure rise associated with the shear layer reattachment.

Results of mean velocity and turbulent quantities measured with a laser anemometer are shown in figures 24 to 26. The mean velocities are shown normalized with respect to boundary layer edge values; the turbulent kinetic energy and shear stress data are normalized by the stagnation speed of sound so that absolute changes across the interaction can be clearly seen. In the separated zone, maximum reverse flow velocities reach about 20% of local boundary layer edge

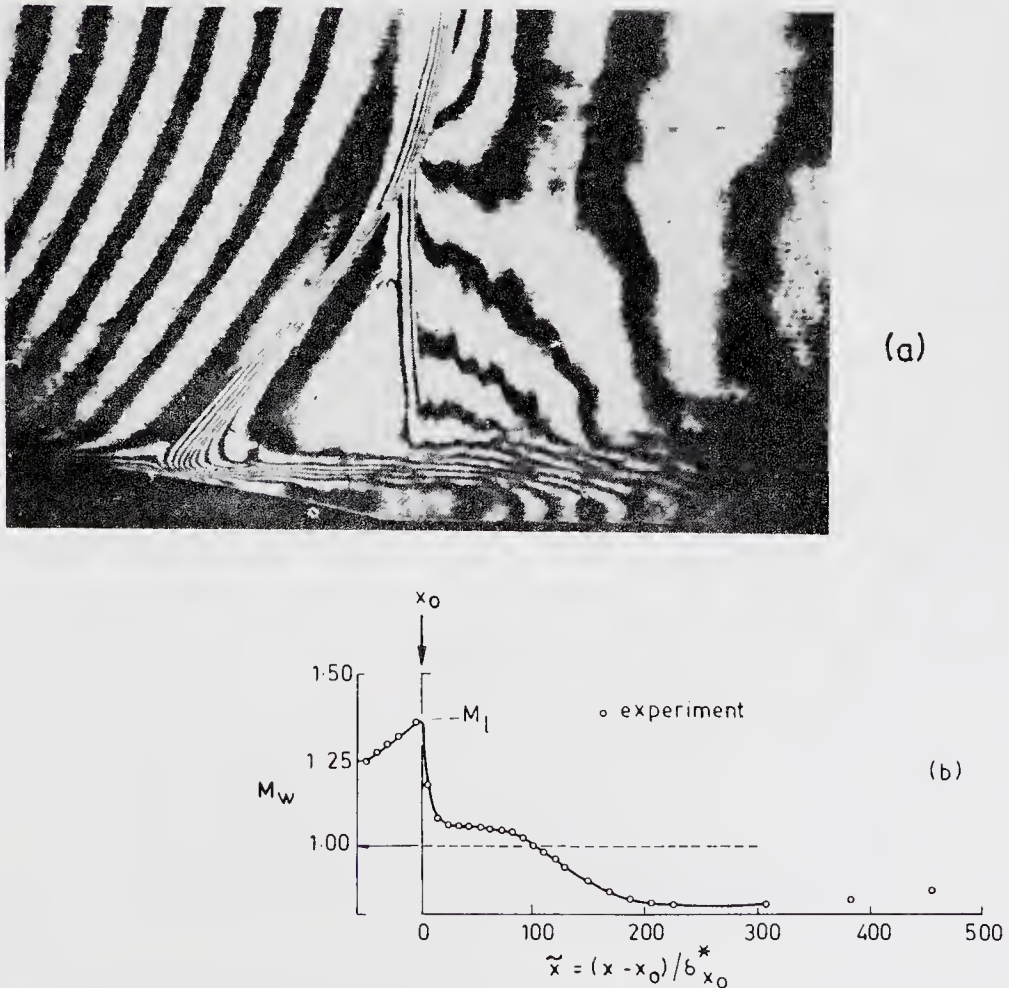


Figure 23. Shock-induced separated flow on a bump: $M_I = 1.37$ (from Delery 1981). (a) interferogram of the flow-field, (b) wall Mach number distribution.

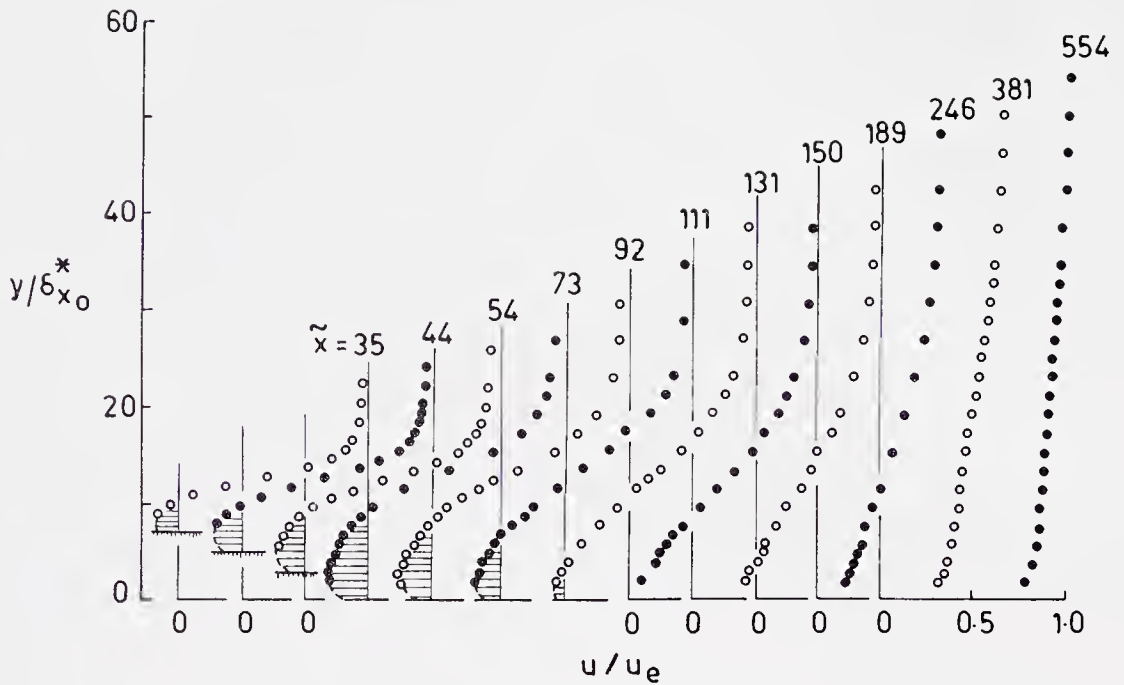


Figure 24. Mean velocity profiles in the interaction region: $M_I = 1.37$ (from Delery 1983).

velocities and the vertical extent of the bubble is as large as about 10 times the value of δ^* at the beginning of interaction. The velocity profiles, otherwise, are qualitatively similar to what one would find in low speed separated flow.

The turbulent kinetic energy and shear stress profiles show streamwise variations which are qualitatively similar. Following the start of the separation process, both kinetic energy and shear stress levels increase rapidly with streamwise distance. These profiles, in the separated region, exhibit clear maxima in the neighbourhood

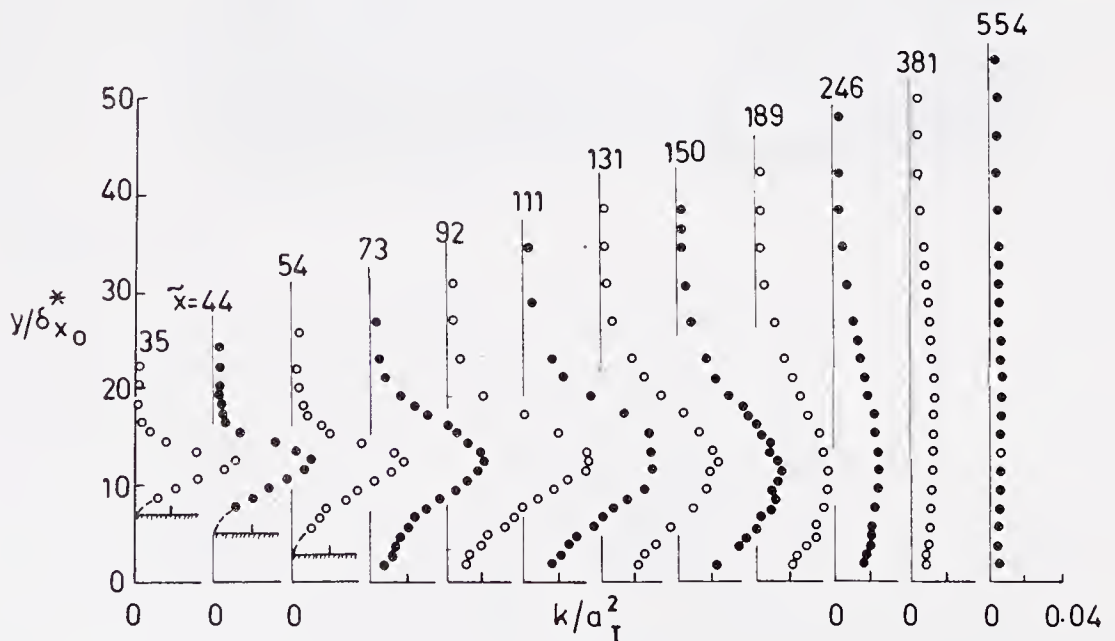


Figure 25. Turbulent kinetic energy profiles in the interaction region: $M_I = 1.37$ (from Delery 1983).

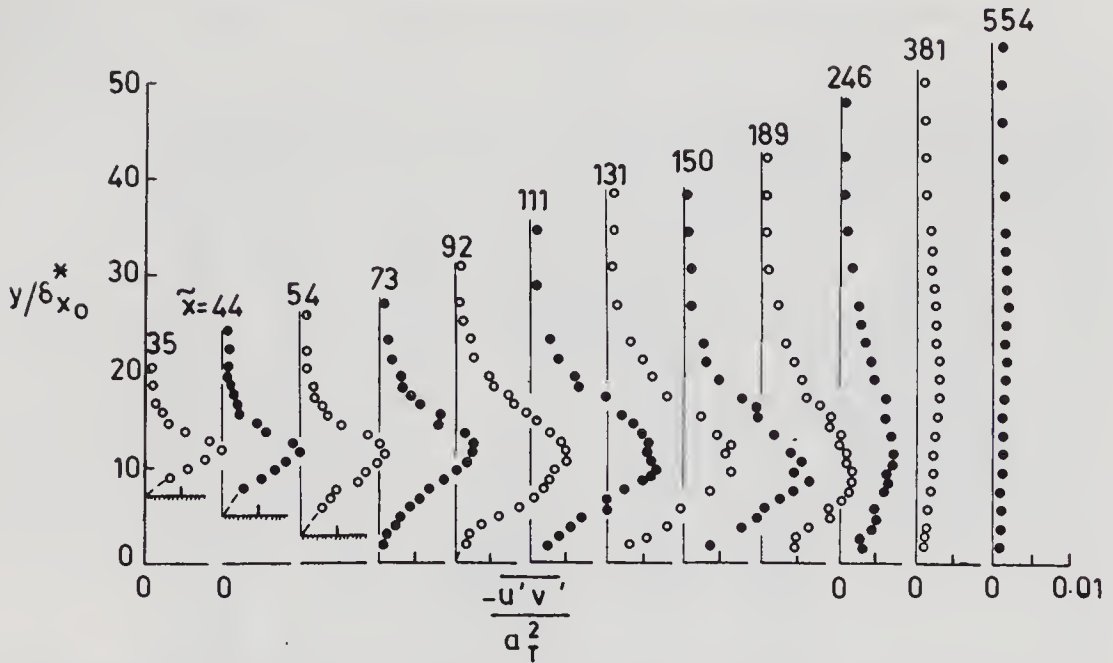


Figure 26. Turbulent shear stress profiles in the interaction region: $M_t = 1.37$ (from Delery 1983).

of the maximum mean velocity gradient, $\partial u/\partial y$ (well away from the wall). Data on streamwise evolution of the maximum kinetic energy and shear stress (figure 27) show that they reach peak values well downstream of separation and rather close to the reattachment location. Following reattachment, these peak values diminish gradually as the flow develops into a new equilibrium state.

Analysis of turbulence data has revealed (Delery 1983) that (i) the turbulent normal stress term assumes importance in the vicinity of separation, both from the point of view of mean flow dynamics as well as in the production of turbulence energy; and (ii) that the turbulent shear flow, as a result of flow separation, undergoes significant departures from equilibrium (see figure 42 on p. 181). Following separation, there is a significant lag in the turbulent shear stress. Downstream of reattachment, the relaxation towards a new equilibrium state is a rather long process due to the memory of the large scale structures. These results suggest the strong need for one or more transport equations for modelling turbulence in these complex interactions.

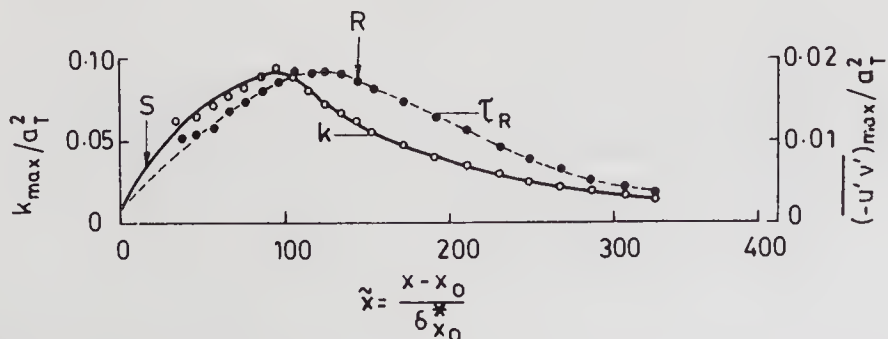


Figure 27. Maximum turbulent shear stress and kinetic energy variation in the streamwise direction: $M_t = 1.37$ (from Delery 1983).

In addition to modelling history effects, there appears to be a need to account for the direct effects of shock waves on turbulence. The analysis of Anyiwo & Bushnell (1982) combined with available experimental information has shown that shock waves can amplify turbulence in the shear layer through three major mechanisms: (i) direct amplification of incident turbulence across a shock region, (ii) generation of turbulence from incident acoustic and entropy fluctuations, and (iii) conversion of mean flow energy into turbulence by shock oscillations. Their results, based on linear analysis, show that amplifications by as much as 100% of the incident turbulence intensity are possible across shocked regions. They suggest that these effects could be a significant factor in the observed large increase in the turbulent shear stress and kinetic energy across the shock in regions of separation. In the absence of a shock wave, for example, at low speeds one would normally expect a frozen or nearly frozen Reynolds stress behaviour along streamlines in regions of rapidly varying pressure gradients as a result of rapid distortion of turbulence (e.g. Narasimha & Sreenivasan 1973; Narasimha & Prabhu 1972).

5.5 Interaction length

Since, in general, transonic shock-boundary layer interactions involve both supersonic and subsonic regions in the outer inviscid part of the flow, one can expect more difficulty in trying to correlate experimental data. The attempts, therefore, have been to look for a correlation for a suitably defined ‘interaction length’ for the supersonic domain of the interaction, and in the absence of separation (Sirieix *et al* 1981, pp. 149–214).

Figure 28 shows a typical interferogram and wall Mach number distribution at $M_o = 1.3$ (Sirieix *et al* 1981, pp. 149–214). Domain I is characterized by rapid supersonic compression to a local Mach number of 1.0 and domain II primarily involves gradual subsonic diffusion depending on downstream conditions, shape of the wall etc.

As in supersonic interactions, the primary variables include the Mach number M_o ahead of the shock, a characteristic Reynolds number Re , the overall shock pressure rise and a boundary layer shape parameter to take into account (in a gross manner) the pressure gradient effects, if any, upstream of the interaction. However the pressure rise itself depends on M_o , Re and model geometry. For domain I, M_o can be taken to represent the pressure rise.

In figure 29 is shown l^*/δ_o^* vs. M_o with Re_{δ_o} as a parameter for a fixed value of H_{io} , the incompressible shape parameter; figure 29 shows significant effects of H_{io} for fixed M_o . The boundary layer displacement thickness δ_o^* appears to be a useful normalizing factor, which takes into account the effect of Re . The correlation suggests that the extent of interaction decreases with increase in Re_{δ_o} . The weak dependence of M_o (for a fixed value of H_{io}) seems surprising (figure 29) since an increase in l^* with M_o (or equivalently shock pressure rise) is to be expected; perhaps this increase is compensated by the decreased upstream influence arising out of the thinning of the sonic layer for a fixed value of H_{io} . A correlation for the transonic ‘supersonic interaction length’, based on data obtained from different facilities and different states of the boundary layer ahead of interaction, has been suggested by Sirieix *et al* (1981, pp. 149–214); the empirical law is of the form

$$l^*/\delta_o^* \approx 70 (H_{io} - 1).$$

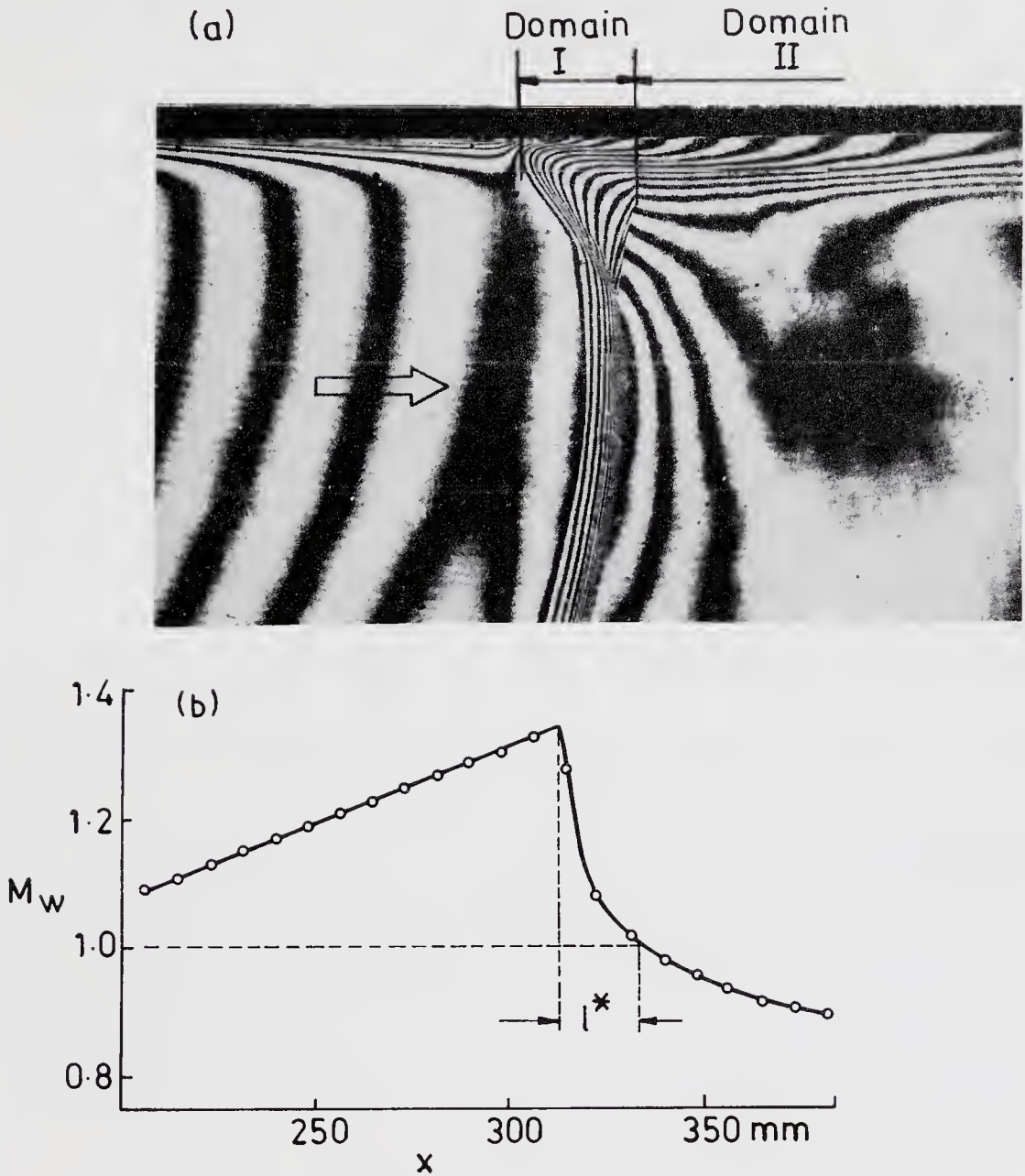


Figure 28. Definition of interaction length in transonic interaction (from Sireix *et al* 1981), (a) interferogram of the flow-field, (b) wall Mach number distribution.

With flow separation, a simple picture is unlikely to result for reasons indicated earlier. Results presented by Kooi (1980) for the length of the separation bubble as a function of Re_{δ_0} , with M_0 as a parameter are shown in figure 30; these data refer to boundary layer interactions on a flat plate obtained in different facilities. Although there is some scatter in the data (which may be due to effects of three-dimensionality, different techniques used for defining separation bubble etc), a strong dependence on both M_0 and Re_{δ_0} is quite evident as in the case of supersonic interactions. There appears to be insufficient data to examine if there is any systematic effect of the shape parameter on the non-dimensional bubble length.

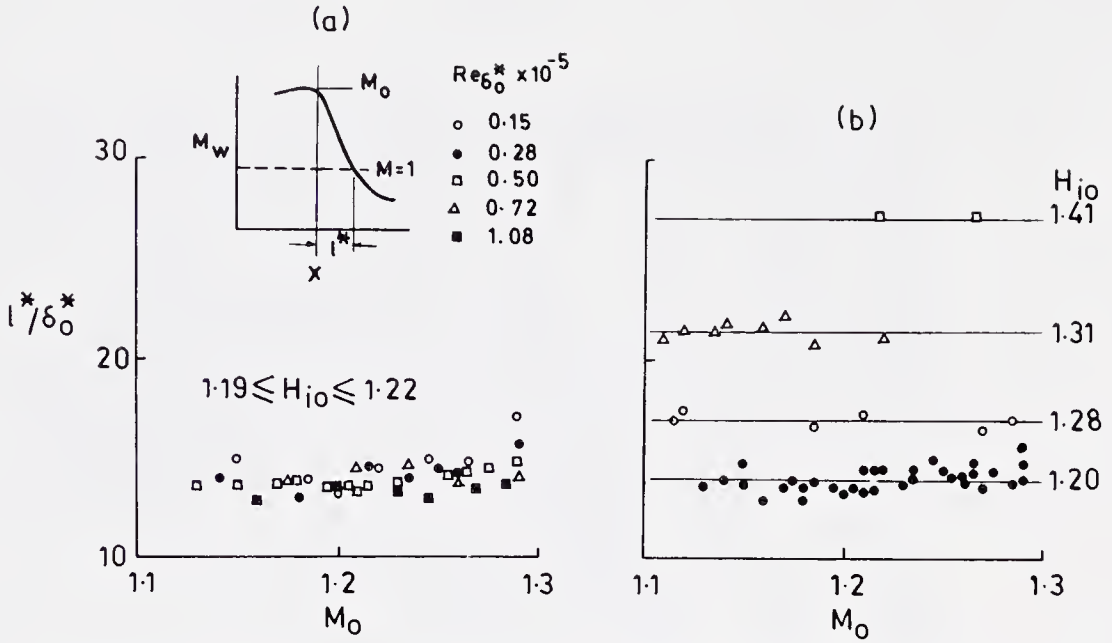


Figure 29. Data of interaction length in transonic interaction (from Sirieix *et al* 1981), (a) effect of Reynolds number (b) effect of incompressible shape factor.

6. Certain unsteady features of shock wave-turbulent boundary layer interactions

An important unsteady feature of a turbulent separating flow, namely its intermittent character of separation, was briefly touched upon in § 3.2. There are several examples in the literature (Kistler 1964; Eaton & Johnston 1982, pp. 162–170; Dolling & Murphy 1983; Driver *et al* 1983) indicating that, even when the mean flow approaching separation is nominally steady, turbulent separated flows often have in them some gross or large scale unsteadiness (e.g. oscillation of the bubble, oscillations of separation and reattachment points, excursion of a shock wave). A basic question is whether such low frequency unsteadiness is an inseparable

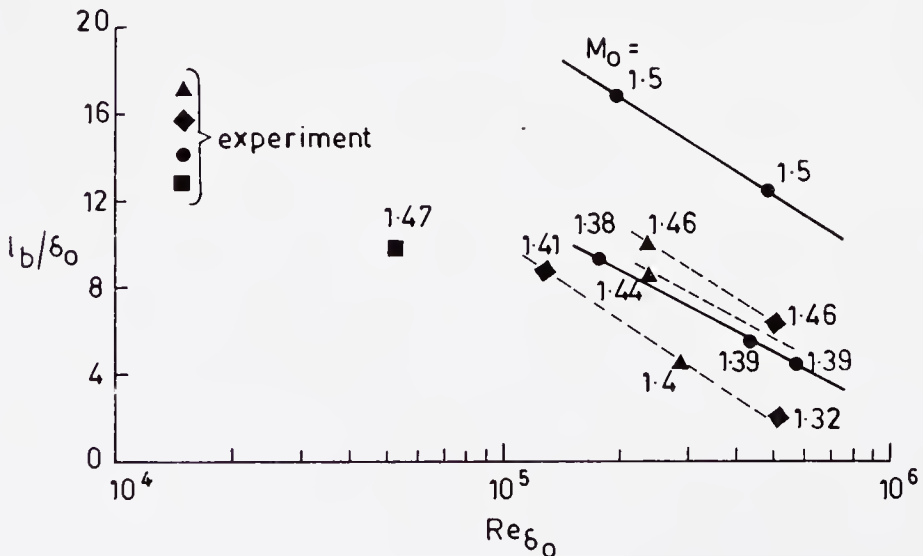


Figure 30. Variation of bubble length with Reynolds number (from Kooi 1980).

ingredient of all turbulent separated flows, and if so, how important it is in modelling mean flow dynamics. In the literature, not much attention has been paid to this modelling aspect.

There is now growing evidence (e.g. Dolling & Or 1983) that the shock wave, when it interacts with a turbulent boundary layer, is generally unsteady even in the absence of separation; the shock oscillations or excursions appear to be driven by turbulence in the shear flow (Plotkin 1975; Grande & Oates 1973). These oscillations can amplify turbulence (Anyiwo & Bushnell 1982) in the flow thereby adding another element of complexity in the turbulence modelling of these interactions. Two examples of the unsteady character of shock-separated flows at supersonic speeds, as revealed by surface measurements, are briefly discussed.

Unsteady surface pressure fluctuations obtained by Dolling & Murphy (1983) for a separated compression corner flow at $M_o = 2.9$ (discussed in § 4.3) are displayed in figure 31. A large peak upstream of separation and a second (weak) peak close to reattachment in the r.m.s. values may be seen; these are presumably a result of the unsteady shock wave structure in the vicinity of separation and reattachment. Pressure-time history of the signals just upstream of separation displayed in figure 32 shows strong intermittent character of the wall pressure – jumping back and forth in a random fashion between a low level characteristic of the undisturbed boundary layer to a higher level that varies with the instantaneous shock position and strength. Similar features have also been observed by Kistler (1964) in a separated flow induced by a forward facing step at $M_o = 4.0$. Presumably the mean wall pressure is generated by the superposition of these relatively low frequency large amplitude fluctuations on the undisturbed wall pressure. An intermittency factor, suitably defined to represent the fraction of the time the wall pressure is disturbed (upstream of separation) from its undisturbed value, shows (Dolling & Murphy 1983) that it reaches a value of 1.0 near the location of the peak r.m.s. value (figure 31); shock excursion is assessed to be of the order of δ_o based on these measurements. These measurements also show that the extent of upstream influence continuously varies with time. Power spectral measurements in the intermittent and in the separated zone show (e.g. Dolling & Or 1983; Coe *et al* 1973) show that there is an enormous increase (at least a factor of 100) in the power

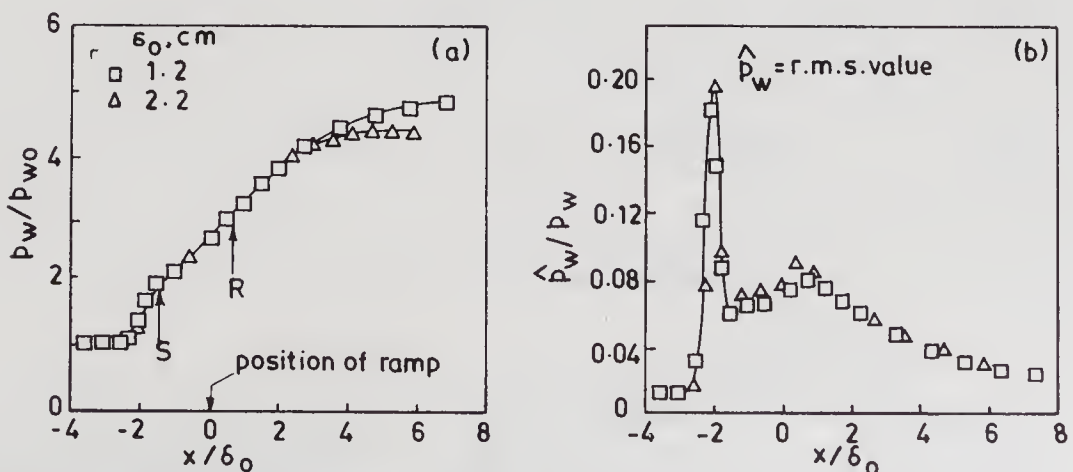


Figure 31. Wall pressure distributions in a compression corner separated flow (from Dolling & Murphy 1983), (a) mean value, (b) r.m.s. value.

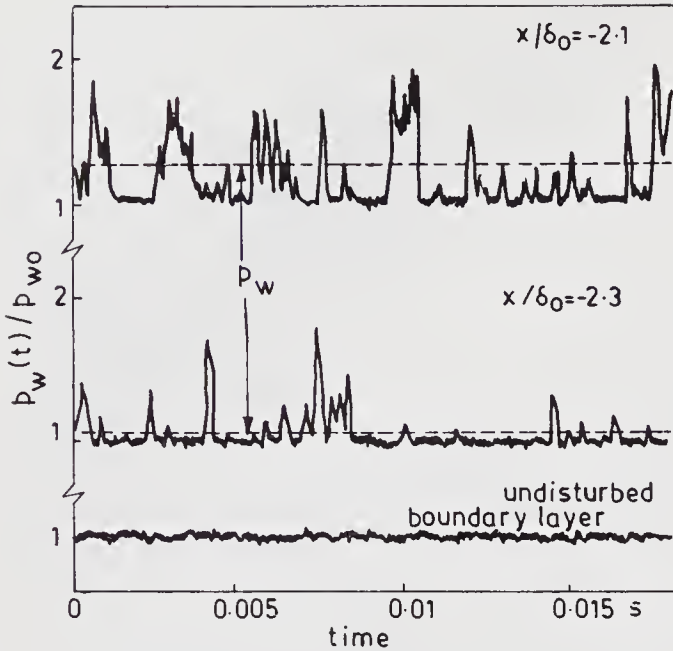


Figure 32. Pressure-time histories near separation (from Dolling & Murphy 1983).

levels at relatively low reduced frequencies in comparison with the attached boundary layer flow upstream.

Observations of separated flow unsteadiness in hypersonic (impinging) shock-wave-turbulent-boundary layer interactions (Horstman & Owen 1974) on an

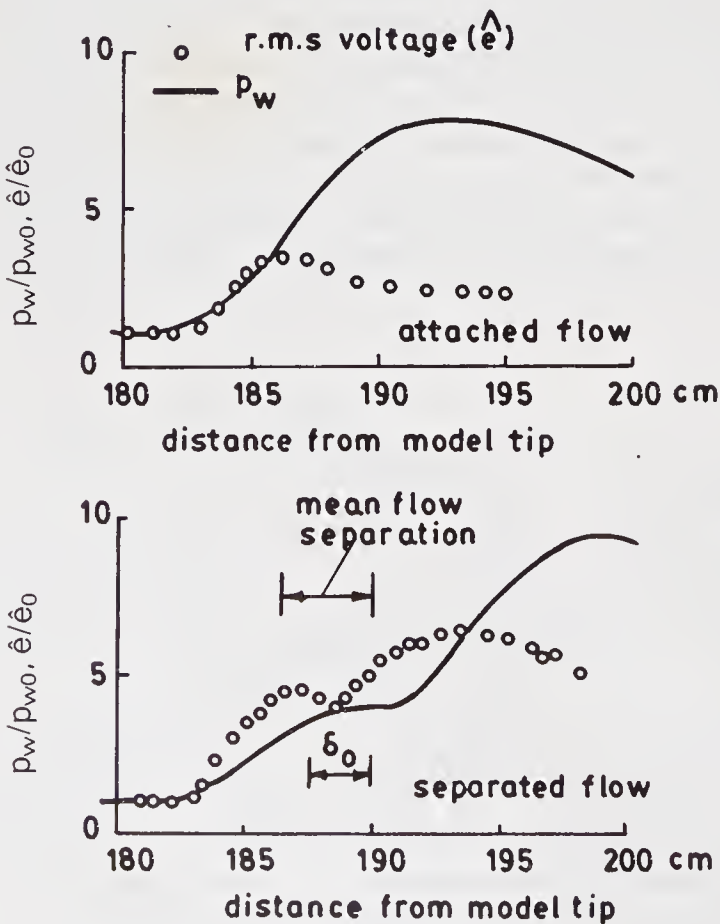


Figure 33. Distribution of mean surface pressure and r.m.s. voltage from thin-film gauge (from Horstman & Owen 1974).

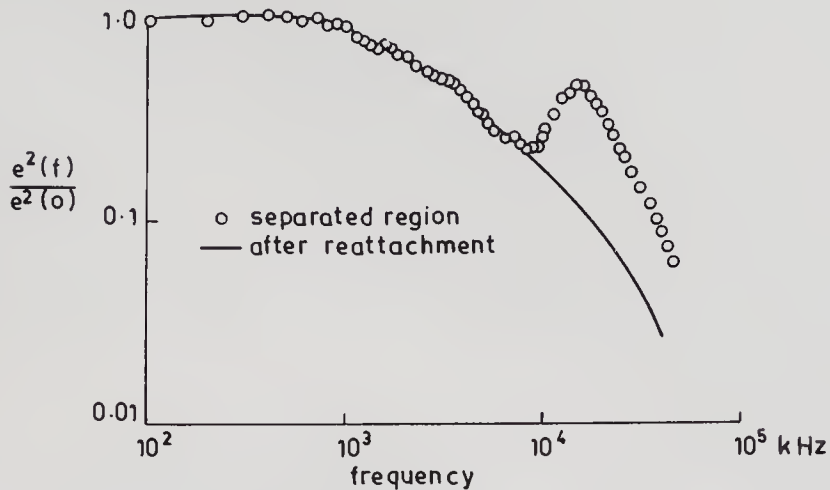


Figure 34. Normalised energy spectra in the interaction zone (from Horstman & Owen 1974).

axisymmetric model are shown in figures 33 and 34. Normalized r.m.s. voltages measured by a surface mounted heated thin film gauge (figure 33) indicate significant increases in r.m.s. values upstream of separation and just downstream of reattachment, which are broadly similar to those of the compression corner flows discussed earlier (figure 31). The normalized power spectra in the separated region reveal (figure 34) a pronounced periodicity around a frequency of 15 kHz ($f\delta_o/u_o \approx 0.5$); such a peak was not observed either in the upstream attached turbulent boundary layer or in laminar separated flow on the same model at lower Reynolds numbers. These suggest an oscillatory nature of the separated flow which is confirmed by correlation measurements as well. What causes this observed periodicity is not known; there is insufficient information in literature to judge if the periodicity is peculiar to separated flows caused by impinging shock waves. The length scale of unsteadiness for this flow was found to be of the order of the streamwise extent of the separated zone (figure 33).

In transonic flows, although the frequent occurrence of such unsteadiness has been known for a long time [for example, in wind tunnels (Liepmann 1947; Meier 1975), on airfoils (Finke 1975) and in supersonic intakes (Seddon & Goldsmith 1985)], detailed information on the unsteady aspect of shock interactions even for simple geometries (e.g. on a flat plate) seems absent. Since normal shock-boundary layer interactions often involve massive separation, unsteady effects in transonic interactions may be even more severe and important than at higher speeds. Investigations of unsteady features in connection with normal shock-boundary layer interactions would be of considerable interest, both from the point of view of basic fluid mechanics as well as in practical applications.

7. Calculation methods for shock wave-boundary layer interaction

The last fifteen years have seen considerable development in the ability to calculate both laminar and turbulent separated flows. This has been made possible by the rapid developments in computer speed and memory and parallel advances in the

development of efficient numerical algorithms for solving the equations governing fluid motion. Progress has also been made in the asymptotic description of laminar supersonic free interactions and turbulent interactions in the transonic regime in the absence of separation. In this section, following a brief presentation of results obtained from asymptotic methods, we shall highlight features of viscous-inviscid interaction methods and Navier-Stokes methods, and then show results from state-of-art calculations and comparison with experiments. Approximate/semi-empirical calculation methods, which are useful for design purposes, are omitted from the discussion here; examples of these may be found in the publications by Green (1970) and Stanewsky (1973).

7.1 Asymptotic theories

Results from asymptotic theories provide considerable insight with regard to the dominant physical mechanisms operating in the different regions of flow, and provide appropriate scaling laws. In general, they can also be very useful for assessing the accuracy of numerical schemes since they become more reliable at higher Reynolds numbers where numerical computations become more difficult.

Asymptotic theories, valid for $Re \rightarrow \infty$, are now fairly well developed for the analysis of laminar free interactions in supersonic/hypersonic flows. These are based on the original ideas of Lighthill (1953) and have been developed further in detail by Neiland (1969), Messiter (1970) and Stewartson & Williams (1969). These theories indicate that as $Re \rightarrow \infty$, solutions of the Navier-Stokes equations develop a multi-layered structure widely referred to as the "triple-deck". Applications of the asymptotic theory to various problems have been summarized by Stewartson (1974). Adamson & Messiter (1980) have presented a comprehensive survey of the investigations employing asymptotic techniques to shock wave-boundary layer interaction problems. Asymptotic flow structures for two problems are described in the following paragraphs.

7.1a Laminar flow past a compression corner: An example of triple-deck structure that develops in front of a compression corner in supersonic laminar flow (Burggraf *et al* 1979) is shown in figure 35. If the ramp angle α^* is of order $Re^{-1/4}$, separation first occurs and a triple-deck structure develops with a longitudinal length scale of the disturbed region of order $Re^{-3/8}$ centred about the plate compression corner junction; with further increase in α , separation moves upstream and a well-defined plateau region forms between separation and reattachment (Burggraf 1975).

In the interaction region, there are three distinct scalings in which different physical mechanisms dominate. The middle (or main) deck has a transverse scale of

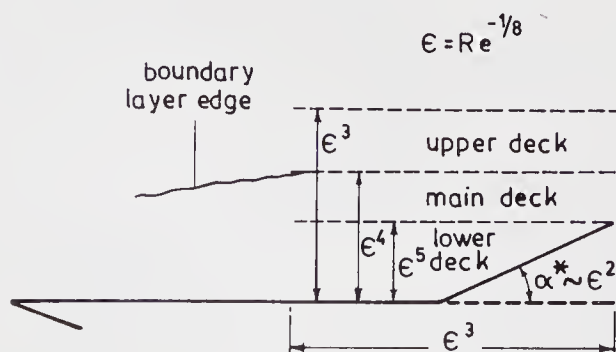


Figure 35. Asymptotic flow structure at a compression corner (from Burggraf *et al* 1979).

$Re^{-1/2}$ and is simply the streamwise continuation of the upstream boundary layer. Since the interaction region is short, the dominant mechanism is an inviscid turning of streamlines in the upstream boundary layer. The lower deck is characterized by viscous flow essentially to satisfy the no-slip condition at the wall; this deck has a traverse length scale of order $Re^{-5/8}$ and is governed by classical boundary layer equations. Because the wall layer is very thin, flow here is essentially incompressible. The boundary conditions involve the no-slip condition at the wall and a new edge condition which results from the matching of the inviscid rotational middle deck. The flow in the lower deck responds strongly to the compressive disturbances producing large vertical motions which displace the main deck outwards, which in turn displaces the upper deck. The upper deck has a transverse length scale of order $Re^{-3/8}$ and consists of fluid which is disturbed by the flow in the interaction region through the outward propagation of Mach waves. The flow in the upper deck is inviscid and irrotational.

The mathematical problem has been dealt with in detail by Stewartson (1974) and by Rizetta *et al* (1978). Approximate analytical as well as numerical solutions have been obtained for the shock interaction problems (e.g. Stewartson 1974, Rizetta *et al* 1978, Burggraf *et al* 1979). Comparisons of pressure distribution predicted from triple-deck analysis (Rizetta *et al* 1978) and experiments (Lewis *et al* 1968) are shown in figure 36 for a 10° ramp at $M_o = 4.0$ and $Re_L = 68,000$. The triple-deck result, while giving a good qualitative trend, is seen to overpredict the upstream pressure rise. It is of course to be remembered that the triple-deck solution is only valid in the limit $Re \rightarrow \infty$.

7.1b Normal-shock-turbulent-boundary-layer interactions at transonic speeds:

Weak shock interactions with a turbulent boundary layer developing on a flat plate have been analysed by several investigators (e.g. Melnik & Grossman 1974; Adamson & Feo 1975); all these analyses correspond to interactions without separation. Basic features of these interactions, as revealed by the studies of Melnik & Grossman (1974, 1975, pp. 262–272, 1977, pp. 415–433) are described next.

In the transonic case, two basic parameters appear in the problem, namely, the Mach number ahead of the interaction and the Reynolds number. The analysis involves asymptotic expansion of the Reynolds-averaged Navier-Stokes equations in the double limit $M_\infty \rightarrow 1$ and $Re \rightarrow \infty$. The Reynolds number parameter is expressed in terms of a non-dimensional frictional velocity, $E = u_* / U_\infty$, so that the solution is obtained in the double limit $M_\infty \rightarrow 1$ and $E \rightarrow 0$. Melnik & Grossman

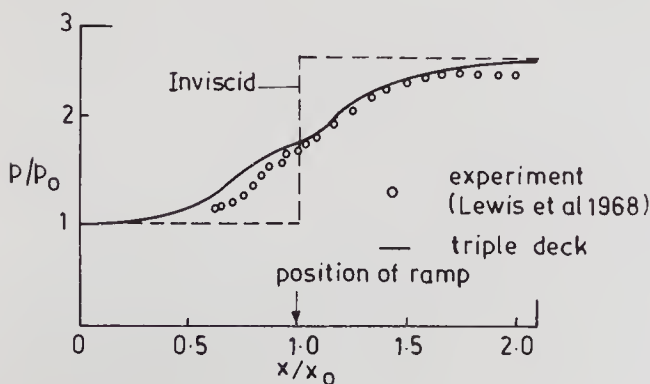


Figure 36. Comparison of predicted surface pressure distribution with experiment (from Rizetta *et al* 1978).

(1974) define a parameter $X_r = (M_\infty^2 - 1)/E$ which controls the relative rates at which the two parameters M_∞ and E approach their respective limits. Two distinguished limits, corresponding to weak and strong shocks, respectively, were considered.

The main features of the interaction problem and the asymptotic flow structure corresponding to the weak shock limit, $X_r = 0(1)$, are shown in figure 37. In the regions upstream and downstream of the interaction zone, the flow exhibits the conventional turbulent-boundary-layer-inviscid-flow structure, with the former having the well-known law of the wall/law of the wake structure. In the shock-interaction zone, the boundary layer develops a three-layer structure: (1) an outer layer (or main deck) extending over most of the boundary layer which is inviscid but rotational, (2) a wall layer which is a continuation of the upstream wall layer in which the total shear stress (laminar plus turbulent) is constant across it; and (3) a blending (or Reynolds stress) layer coupling the inner and outer layers. In the outer layer the Reynolds stresses are nearly frozen because of the short streamwise scale of the interaction zone. In the inner layer, on the other hand, Reynolds stresses are in equilibrium with the local skin friction, which varies in the streamwise direction. The mismatch in the Reynolds stresses across the outer and inner layers is resolved by the blending layer solution; in this layer there is a balance between the inertia, the pressure gradient and the Reynolds stress terms. The derivation of the governing equations and the boundary and matching conditions are contained in the papers cited above. Fairly good agreement of

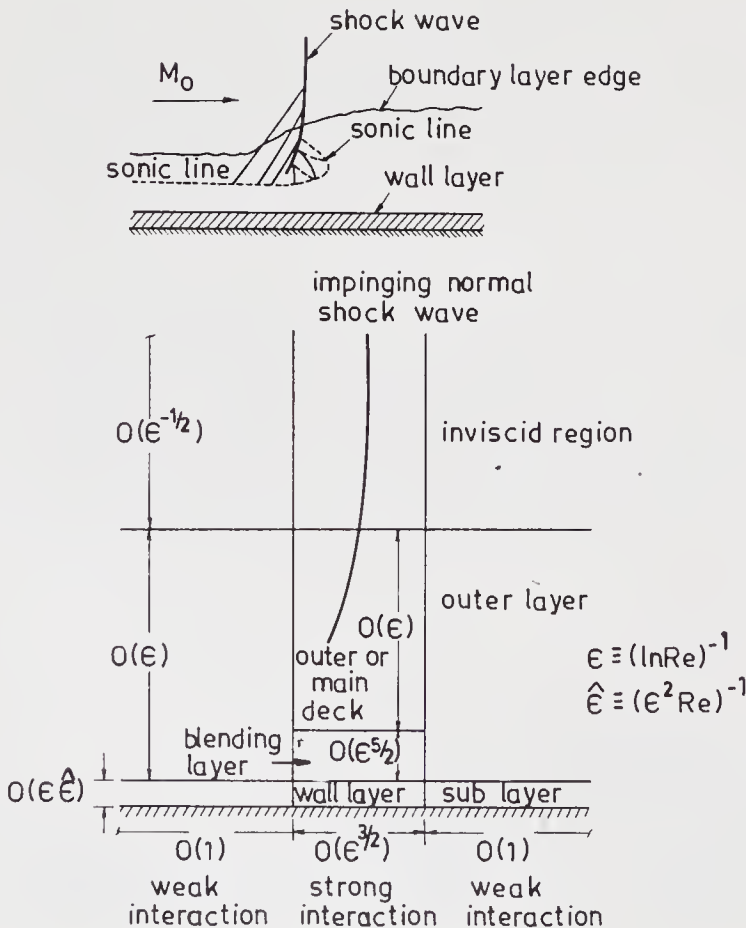


Figure 37. Asymptotic flow structure for a weak normal shock wave-boundary layer interaction (from Melnik & Grossman 1974, 1975).

theoretical wall pressure distributions was obtained with Gadd's (1961) experimental data obtained in an axisymmetric internal flow.

It is of interest to note some of the similarities and differences between the laminar and turbulent interactions. In both, the major part of the boundary layer flow is governed by inviscid equations. A four-layer structure in the interaction zone appears for a turbulent boundary layer, in contrast with a three-layer structure for laminar flows; this is because the former has a two layer structure as opposed to a single layer structure in laminar flows. For laminar flows, the growth of the viscous layer has strong effects on the main deck and the outer flow, and solutions for all three layers have to be determined simultaneously. This is in contrast to a turbulent weak interaction, wherein, to a first approximation, the wall layer does not influence the outer layer and the inviscid flow. This is because the wall layer in which flow deceleration takes place is much thinner (a fraction of δ_o) than in the corresponding laminar flow. This feature allows calculation of wall pressure distributions without taking into account the wall layer in turbulent interactions. These results would of course become inaccurate once separation sets in. There are examples in the literature (Roshko & Thomke 1969, pp. 109–138; Elfstrom 1972) to show that, for unseparated turbulent interactions at supersonic/hypersonic speeds, the surface pressure distributions calculated ignoring the sub-layer are in good agreement with experimental data. The results from the asymptotic analyses also suggest that the choice of a turbulence model could influence the wall skin friction distributions, but may only have a weak effect on prediction of surface pressures. Numerical calculations of Viegas & Horstman (1978) for shock interactions in an axisymmetric internal flow support these findings.

To summarize, for turbulent interactions with a shock wave, asymptotic methods have been applied to steady, two-dimensional attached flow situations at transonic speeds; approximate theories based on the two-layer hypothesis of Lighthill (1953) have also been reported (Inger & Mason 1976); an example of such a calculation was seen in figure 20. With boundary layer separation, complications arise from reversed flow zones, normal pressure gradients and turbulence closure problems.

7.2 *Viscous-inviscid interaction methods*

The term "viscous-inviscid interaction" refers to all flow situations wherein the viscous flow in the boundary layer has noticeable influence on the pressure distribution. In 'weak' interactions the viscous effects on the potential flow pressure distributions are generally small; viscous effects on an airfoil in subcritical flow without separation is an example. On the other hand, for example, in the vicinity of unseparated shock-boundary layer interaction and in the separation-reattachment regions of a separated flow, viscous effects are significant and the interaction is generally termed 'strong' because of the strong coupling between the viscous and inviscid parts of the flow field. Calculations of turbulent interactions therefore involve modelling both strong viscous-inviscid interactions as well as turbulence in the shear layers.

Considerable progress has been made in the development of very sophisticated viscous-inviscid interactive methods. Although there are many differences in the details of these methods, the three main elements of such a method are:

- (i) a technique for obtaining a solution of the inviscid part of the flow-field; in principle, any inviscid flow "solver" can be used;

- (ii) a method for obtaining a solution for the viscous boundary layer flow (with flow separation, special treatment is necessary);
- (iii) a coupling equation to link the inviscid and viscous flow solutions at a suitable location in the flow, and an efficient iterative scheme providing convergence of the interactive calculations.

A variety of procedures is now available for solving both potential as well as Euler equations. With regard to items (ii) and (iii) mentioned above, some further discussion seems appropriate.

7.2a *Viscous flow solution*: There is now growing evidence (Cebeci *et al* 1984, pp. 1–40; McDonald & Briley 1984, pp. 141–162) that boundary layer approximations are useful and adequate for analysing flows with small separated zones. Favourable comparisons of boundary layer solutions (used in an interactive calculation) with triple-deck and Navier-Stokes results for laminar flow problems are now available (e.g. Rizetta *et al* 1978; Burggarf *et al* 1979). However, in the solution of the boundary layer equations, two problems arise when applied to flows involving separation. The first is the classical Goldstein singularity at separation which arises when the pressure distribution $p(x)$ is prescribed; the second involves difficulties associated with the appearance of reverse flow velocities following separation. The singularity can be avoided by specifying not $p(x)$ but rather an interaction law between the viscous and inviscid flows, as suggested by Crocco & Lees (1952). Solving the boundary layer equations in an “inverse mode” also eliminates the separation singularity. In the inverse mode, the classical outer boundary condition, $\lim_{y \rightarrow \infty} u(x, y) = u_e(x)$, is replaced by prescribing a displacement thickness distribution $\delta^*(x)$, or a wall skin friction distribution $c_f(x)$, which must be satisfied by the solution; the pressure gradient $p(x)$ [or $u_e(x)$] comes out as part of the solution. The problem associated with the reversed flow arises because of the forward marching along the flow into the separated region. Several numerical schemes have been devised to overcome this difficulty (e.g. Klineberg & Steger 1974, Carter 1975). Interesting discussions on the use of boundary layer equations in interactive calculations may be seen in the paper by McDonald & Briley (1984, pp. 141–162).

Integral methods have been favoured in most interactive methods primarily because of their simplicity and ability to give good engineering predictions when properly tailored. It seems much easier to incorporate empirical information into such methods than into finite difference calculations. First-order boundary layer equations are generally adopted in the derivation of the momentum integral equations, although some of the recent methods (e.g. La Balleur & Blaise 1985) include an allowance for non-zero pressure variation across the boundary layer. In addition to the momentum integral equation, additional auxiliary equations, for example the mean kinetic energy equation or an equation for entrainment, are used.

Certain closure relationships including modelling turbulent shear stresses are generally necessary before the complete set of equations can be solved. These involve specification of (i) relationships among boundary layer integral thicknesses and shape parameters, (ii) a skin friction law, and (iii) information required to evaluate the entrainment equation or dissipation integral etc. For the calculation of

separated flows, it is also important to model the nonequilibrium or history effects, which is done through the use of a lag equation in calculating the entrainment or the dissipative integral. Simplified turbulent transport integral equations may also be employed for determining the lag effects.

More details on some of the integral techniques currently used in connection with interactive methods may be seen in the publications by La Balleur (1981), Lock (1981) and Whitfield *et al* (1981).

7.2b Viscous-inviscid coupling: The coupling algorithm relating the viscous and inviscid parts of the flow-field plays a crucial role in the successful calculation of these complex flows. Considerable attention has been paid to the mathematical and numerical aspects of these coupling techniques (e.g. La Balleur 1984, pp. 259–284, Carter 1985, Veldman 1984, pp. 343–363). Three schemes which have been frequently employed are shown in figure 38.

7.3 Navier-Stokes calculation methods

In this approach, mean flow solutions of the “Reynolds-averaged” Navier-Stokes equations (RANS) are obtained numerically. The approach has an inherent advantage since the viscous-inviscid interactions are naturally built into the equations, so that the potential exists for assessing turbulence modelling aspects in a systematic manner.

Rapid advances have been made in the development of efficient algorithms for solving RANS. Notable amongst these are the methods of McCormack (1976, 1982) and Beam & Warming (1978). The equations are parabolic in time and elliptic in space, and are solved numerically in time until steady-state solutions are reached. Surveys of various methods in use have been presented by McCormack & Lomax (1979) and Mehta & Lomax (1982).

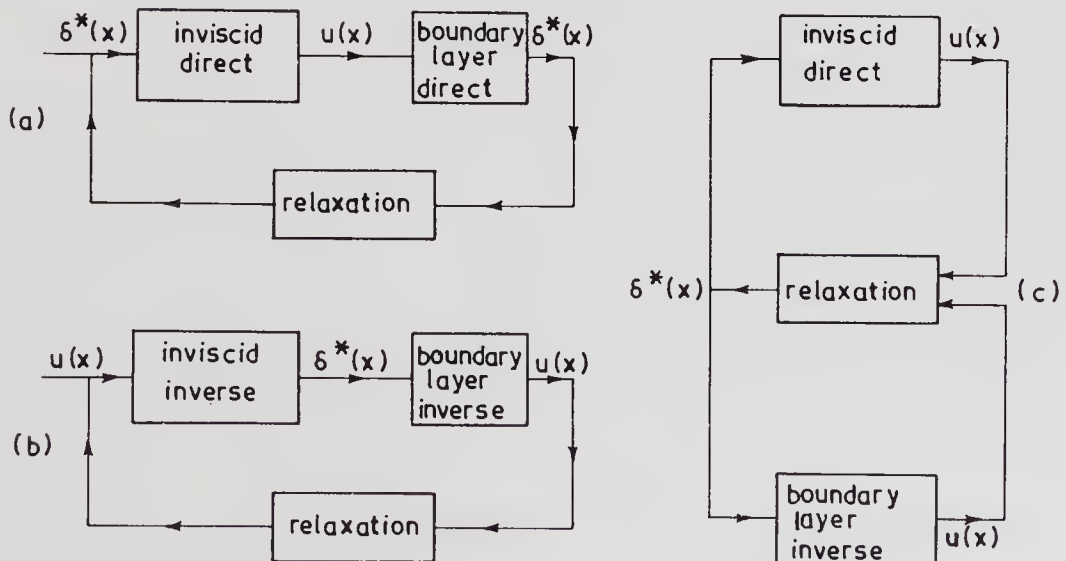


Figure 38. Calculation schemes used in viscous-inviscid interactive methods: (a) direct, (b) inverse, and (c) semi-inverse.

7.3a Turbulence modelling aspects: In the RANS, the turbulent stresses have to be modelled to close the system of equations governing the fluid motion. Furthermore, in compressible flow applications, the product of density and velocity fluctuations that appears in the equations of mean motion also needs to be modelled. To overcome this difficulty, mass-averaging (or Favre-averaging) of the governing equations is employed which reduces the equations to the incompressible form. For a further discussion of compressibility effects in turbulence modelling, the reader is referred to the paper by Rubesin (1982).

The models that have been used may be classified as either eddy viscosity or Reynolds stress models. In the former the Reynolds stresses are assumed proportional to the mean strain rate or velocity gradient. The resulting eddy viscosity is a property of the flow-field and can be looked upon as being proportional to the product of a velocity and the length scale of turbulence. These models may be further classified under zero-, one-, and two-equation models which refer to the additional partial differential equations employed to define the eddy viscosity.

The zero equation model represents an equilibrium model in which the eddy viscosity is related algebraically to the mean-flow variables. The Cebeci-Smith model is a typical example of this type. The one-equation model uses an additional partial differential equation for the turbulent kinetic energy which defines the velocity scale for determining the eddy viscosity; the length scale is prescribed by an algebraic equation. Glushko's (1965) model is a typical example of this type. In the two-equation models, two partial differential equations, one for the turbulent kinetic energy and the other for obtaining a length scale, are solved to define the eddy viscosity function. The Jones-Launder (1971) and Wilcox-Rubesin (1980) two-equation models have been used with RANS for shock separated flows. The one- and two-equation models do account for history effects to some degree since turbulent transport equations are utilized in arriving at the eddy viscosity. The specification of boundary conditions for turbulent properties is an added requirement with these models; the studies of Cebeci & Meier (1979) suggest that the uncertainties introduced by the boundary conditions may not be small. Finally, it may also be noted that all these models have been primarily developed for incompressible unseparated boundary layer flows.

In Reynolds stress models, all the equations for the relevant Reynolds stresses are modelled and are free of the assumption that the stresses respond immediately to change in mean strain rate. The difficulties in modelling at this level have led to approximate methods (e.g. Bradshaw *et al* 1967). These models may also utilize additional differential equations for either the length scale or rate of dissipation. There appears to be hardly any attempt in which stress modelling is used for computing shock-boundary layer interactions.

Excellent discussions of turbulence modelling aspects for high speed separated flows may be seen in the papers by Marvin (1982, 1983) and Viegas & Horstman (1978).

7.4 Computations and comparisons with experiments

In this section, examples of state-of-art calculations from both interactive methods and RANS are compared with experimental data. Wherever possible, comparison

from more than one calculation is shown. For more details on the computations or experiments, the original references cited may be seen.

7.4a *Transonic interactions*: Viscous effects on airfoils, even under attached flow conditions, can be significant at transonic speeds. An example of such effects on a supercritical airfoil is shown in figure 39; also included are comparisons from interactive calculations due to Stanewsky *et al* (1981). The calculations employ a potential flow modelling for the outer flow, an integral method due to Rotta (1968) for the boundary layer flow, and a triple-deck analysis (Inger & Mason 1976) to model shock-boundary-layer interactions. Results of calculations, with and without the triple deck analysis, are also included in figure 39. The observed double-shock system is fairly well-predicted when the local effects of shock-boundary-layer interaction are included in the calculation.

The two experimental flows in a transonic channel discussed in §§ 5.3 and 5.4 have recently been computed by La Balleur & Blaise (1985). Their calculations are based on an Euler solver for the outer inviscid flow and an integral type method for the viscous flow with an allowance for normal pressure gradients. Approximate transport equations for turbulent shear stress and turbulent kinetic energy are employed for modelling turbulence.

Results for surface pressure distributions for the case of weak separation at $M_l = 1.3$ show (figure 40) reasonably good agreement (in figures 40 and 41, the streamwise distance is normalized by channel height, B). Detailed comparisons indicate (La Balleur & Blaise 1985) that both δ^* and H are somewhat overpredicted in the calculation. For the asymmetric channel flow at $M_l = 1.37$ involving massive separation, comparisons are shown in figures 41 and 42. There is an overshoot of surface pressure near separation, and the pressure plateau is less well-defined; for $x/B \geq 3$, δ^* prediction is considerably lower than the data. The nonequilibrium effects in this flow, mentioned briefly in § 5.4, are shown in figure 42. The transport

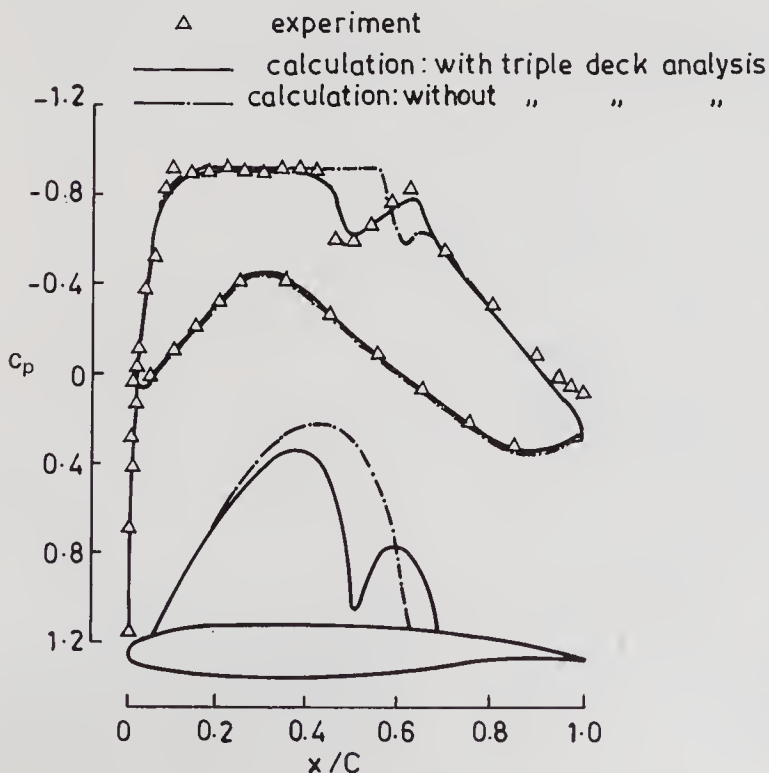


Figure 39. Experimental and computed surface pressure distributions: $M_\infty = 0.76$ (from Stanewsky *et al* 1981).

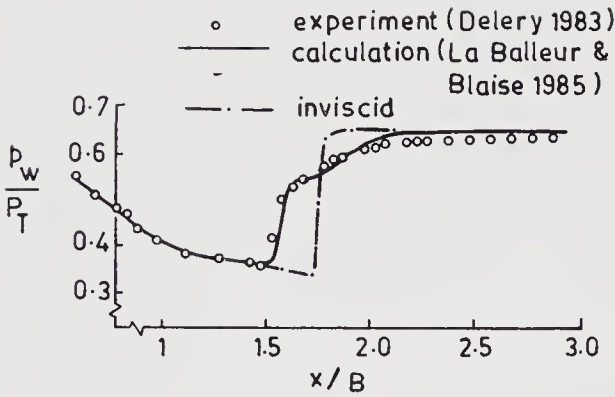


Figure 40. Experimental and computed surface pressure distributions: $M_1 = 1.30$ (from La Balleur & Blaise 1985).

models used seem to reflect the experimentally observed behaviour in the separation region but are deficient in the reattachment and relaxation zones.

In the numerical calculations of flows involving strong normal shock waves, it is often very important to simulate precisely the downstream boundary condition. The back pressure in the subsonic flow can play a significant role in defining the gross features of the interactions. In the calculations presented in figures 40 to 42, the back pressure was so selected for each flow that the beginning of the compression at the foot of the shock wave matched the experimental data.

The turbulent separated flow on a flat plate (discussed in § 5.1) at $M_o = 1.47$ have been computed using RANS (Viegas & Horstman 1978) employing zero-, one-, and two-equation models. All three models appear to predict the pressure rise upto

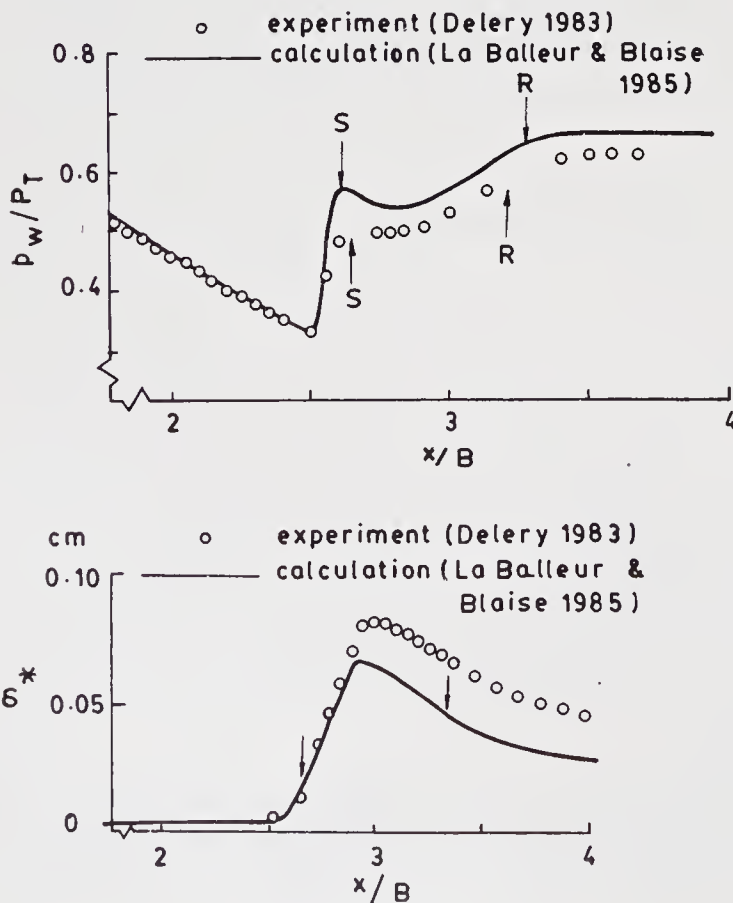


Figure 41. Experimental and computed surface pressure and displacement thickness distributions: $M_1 = 1.37$ (from La Balleur & Blaise 1985).

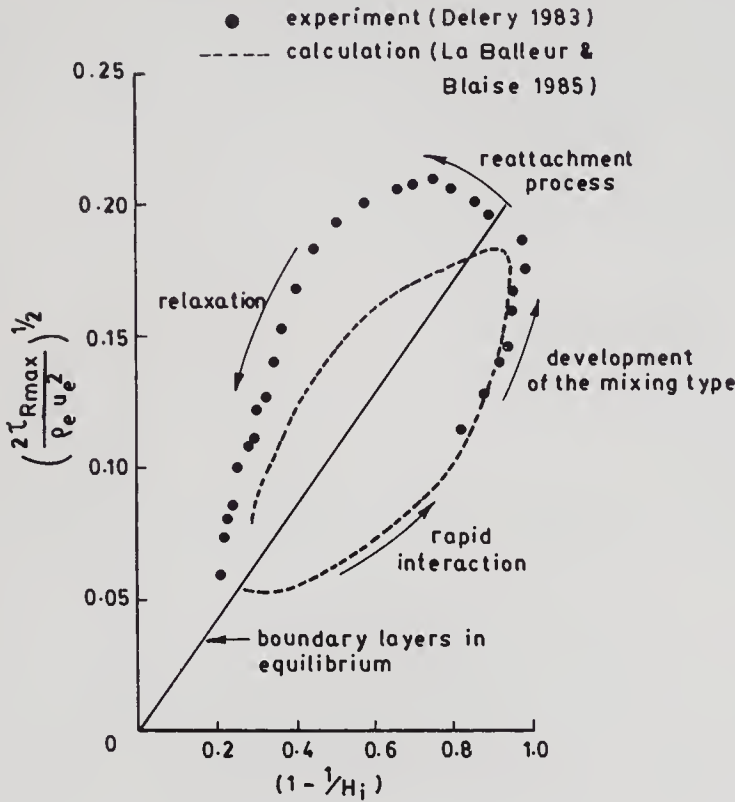


Figure 42. Evolution of maximum shear stress with equilibrium shape parameter for shock separated flow: $M_I = 1.37$ (from La Balleur & Blaise 1985).

separation reasonably well, but they all depart from the measurements downstream (figure 43). The velocity profile comparisons (Viegas & Horstman 1978) did not reveal any consistent picture amongst the three models; considerable disagreement was evident for different models in different regions of the flow. As in the previous case of massive separation, comparisons demonstrate again the inadequacy in modelling turbulence.

An example of a successful RANS calculation for a periodic separated flow at transonic speeds is shown in figures 44 and 45. Experiments on a thick circular arc airfoil in a high Reynolds number channel (with contoured top and bottom walls)

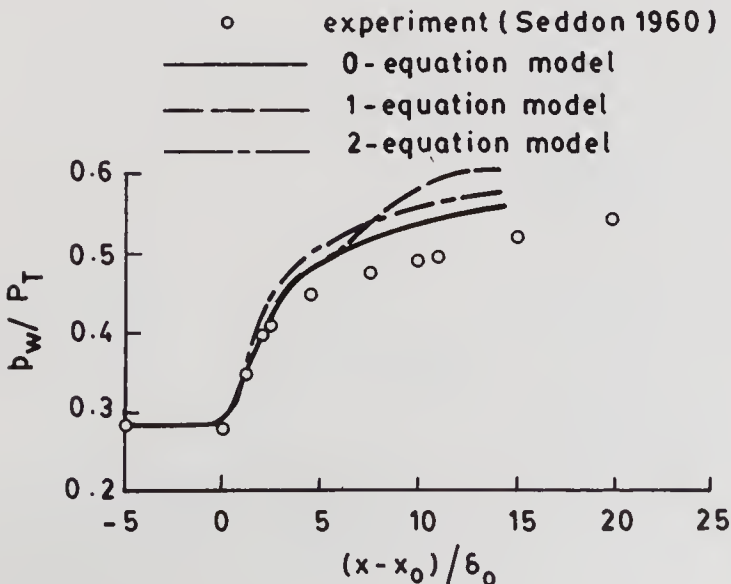


Figure 43. Comparison of experimental and computed surface pressure distributions: $M_o = 1.47$, $Re_{\delta_o} = 5.3 \times 10^4$ (from Viegas & Horstman 1978).

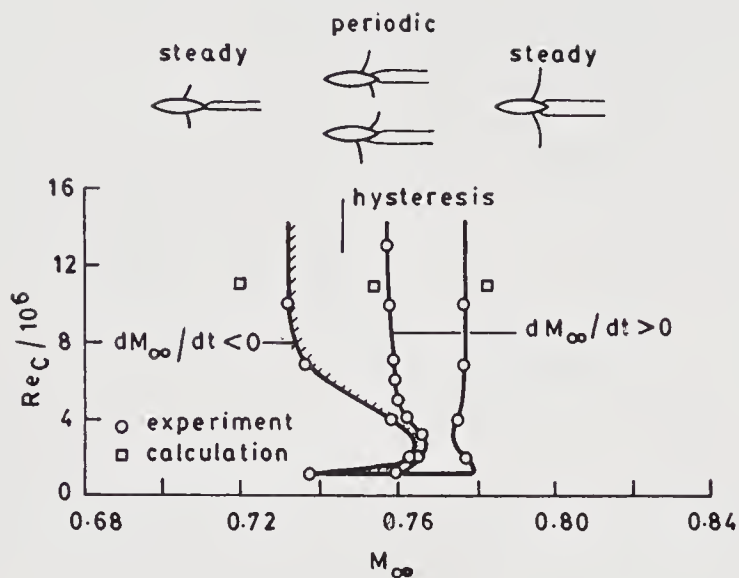


Figure 44. Experimental flow domains for a 18% thick circular arc airfoil (from McDevitt *et al* 1976).

revealed oscillatory flow, switching between shock-induced separation and trailing-edge flow separation in a narrow Mach number range (figure 44). On either side of the unsteady zone, the flow was relatively steady. Levy (1978) made calculations at three values of M_∞ of 0.720, 0.754 and 0.783 (figure 44), using an algebraic eddy viscosity model. These calculations revealed the observed steady flow at $M_\infty = 0.72$ and 0.783 and periodic flow at $M_\infty = 0.754$. Figure 45 shows comparisons of surface pressure variations with time at four locations on the airfoil for the unsteady case. Excellent reproduction of the unsteady pressure, including the phase difference between the upper and lower surfaces of the airfoil, may be seen in the calculations. The frequency of oscillations from predictions agreed within about 20% of the measured value.

The success of the calculation with a simple turbulence model described above may seem surprising since the evidence to-date suggests that none of the turbulence models available can satisfactorily predict flow with significant separation. A possible explanation is that, in the unsteady regime, the oscillations are sustained

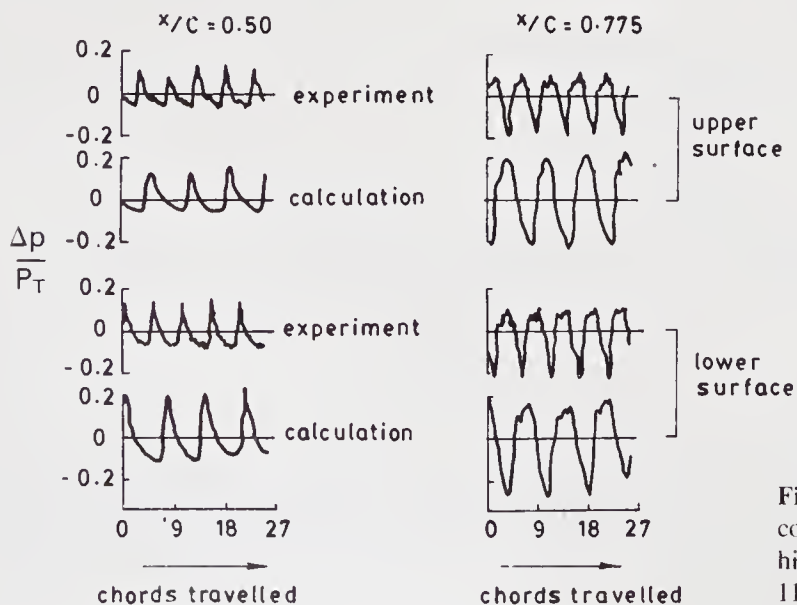


Figure 45. Experimental and computed surface pressure-time histories: $M_\infty = 0.754$, $Re_c = 11 \times 10^6$ (from Levy 1978).

by the outer flow (inviscid mechanisms), and the turbulence modelling is only important to the extent that the separation which is necessary for triggering the large scale unsteadiness is induced in the calculation.

Recently Purohit (1987a) has computed levels of surface pressure fluctuations (at $M_\infty = 0.8$) arising from shock oscillations on a bulbous payload shroud using RANS and an algebraic turbulence model. Although the paper does not contain comparison of calculated unsteady properties with experiments, the computations have revealed interesting unsteady flow features on such a configuration.

7.4b Supersonic interactions: Turbulent separated flows induced by compression corners or ramps have been investigated by several authors at supersonic speeds. Experimental results for two ramp angles of 20 and 24° at $M_o = 2.8$ are compared with calculations in figures 46 and 47. RANS computations, employing a version of McCormack's algorithm, have been made (Viegas & Horstman 1978) for both cases, while the 24° case has been computed recently using the interactive method of La Balleur & Blaise (1985) discussed previously. The turbulence models used with the RANS are indicated in the figures.

For the 20° ramp, pressure distributions are reasonably well-predicted by the two-equation models, while the skin friction predictions seem deficient downstream of reattachment. For the flow with large separation (24° case), again, the predictions with two-equation models are relatively better than the zero- and one-equation models, but are still deficient in an overall sense. The results from the interactive method are comparable to those obtained using the two-equation

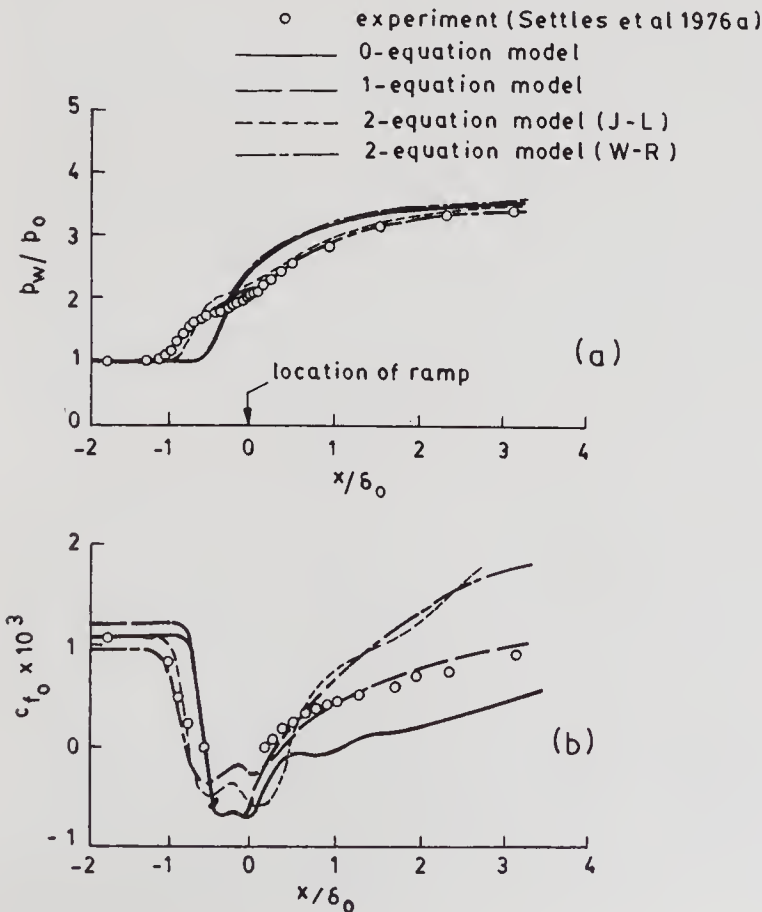


Figure 46. Comparison of experimental and computed surface data: $M_o = 2.8$, $Re_{\delta_o} = 1.65 \times 10^6$, $\alpha = 20^\circ$ (from Viegas & Horstman 1978), (a) surface pressure, (b) skin friction.

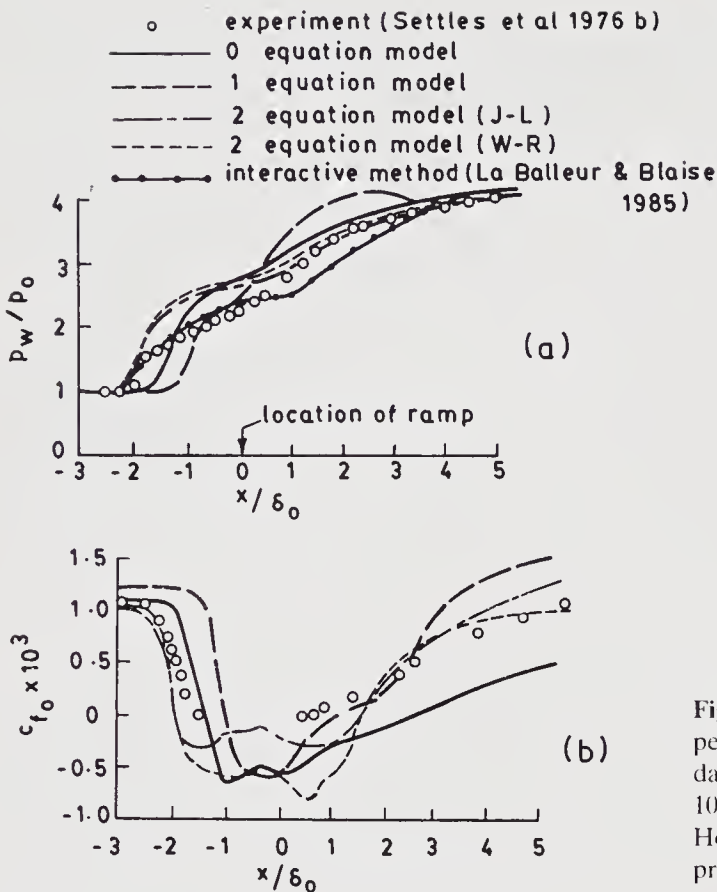


Figure 47. Comparison of experimental and computed surface data: $M_\infty = 2.8$, $Re_{\delta_0} = 1.33 \times 10^6$, $\alpha = 24^\circ$ (from Viegas & Horstman 1978), (a) surface pressure, (b) skin friction.

models. Surface pressure fluctuation measurements made recently (Dolling & Or 1983) for the two flows have revealed a certain unsteady character of these flows; to what degree this might influence the mean flow field is still an important question to be answered.

The importance of accounting for the history effects of turbulence in flows undergoing rapid pressure gradients hardly needs to be stressed. Attempts have also been made to modify, for example, the zero-equation eddy viscosity model to reflect history effects in an approximate sense. Figure 48 shows comparisons of measured surface pressure distributions with RANS calculations (Shang & Hankey 1975) for a 25° ramp at $M_\infty = 2.96$. Predictions have been made with three versions of the zero-equation model; (i) the Cebeci-Smith equilibrium model, (ii) a frozen model, and (iii) a relaxation model. The frozen model concept is relevant in flows undergoing rapid pressure gradients (e.g. Narasimha & Srinivasan 1973). In the relaxation model, the Reynolds stress relaxation phenomena are described by a simple algebraic equation for the eddy viscosity coefficient, which involves a relaxation length scale λ to be described empirically; a value of $\lambda = 10 \delta_0$ based on available information has been chosen in these calculations (Shang & Hankey 1975).

The equilibrium and frozen models predict small and large separated regions, respectively. The relaxation model, on the other hand, shows significant improvement in a relative sense; the need for further refinements is also clear. Similar success with an algebraic relaxation model is also seen in the calculations of separated flows caused by impinging shock waves (Shang *et al* 1976).

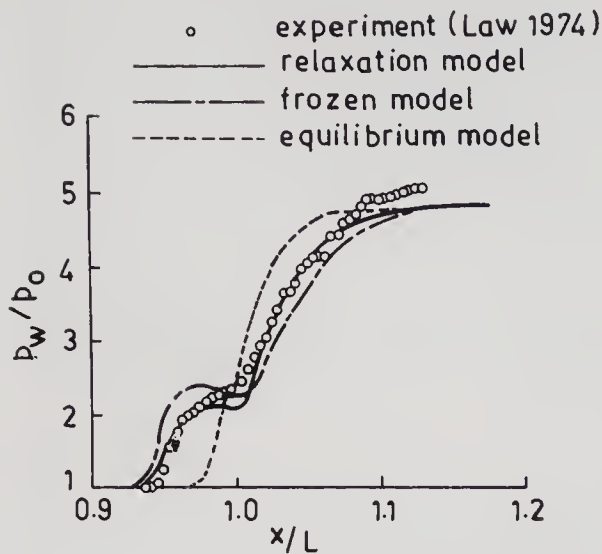


Figure 48. Comparison of experimental and computed surface pressure distribution: $M_o = 2.96$, $Re_L = 10^7$, $\alpha = 25^\circ$ (from Shang & Hankey 1975).

The current state-of-the-art in computing two-dimensional shock-boundary layer interactions may be summarized as follows. As long as the separated region is small [$0(\delta_o)$], both interactive and RANS seem to perform equally well in an engineering sense. The wall pressure distributions can be predicted by any model, while the two-equation models give better predictions of the skin friction distributions. For flows involving large scale separation, significant improvements in modelling the dynamics of turbulence are necessary, and in general, calculations based on RANS equations may be preferable; significant pressure variations normal to the flow which arise in these flows are well-handled by RANS.

Although certain broad conclusions are drawn above based on the examples discussed, some caution is required in the assessment of the calculation methods in general. To perform a clean experiment with massive separation is not an easy task. As discussed in § 4.5, unless sufficient care is taken, some degree of three-dimensionality is present even in nominally two-dimensional flows; an assessment of the departure from two-dimensionality is essential before conclusions about the prediction method can be drawn. The experimentally observed large-scale unsteadiness in the separated flows involving shock waves, which is not accounted for in the methods of calculation, could lead to differences between calculation and experiments.

8. Control of shock-wave-boundary-layer interaction

Separation control by active or passive means is often desirable and some times necessary for improving aerodynamic performance. The use of suction and tangential blowing for separated-flow-control is known for several decades. Suction removes low momentum fluid in the boundary layer near the wall thereby providing sufficient energy in the fluid close to the surface to overcome adverse pressure gradients. Tangential blowing through a narrow slot, as commonly used, energizes the boundary layer near the wall providing sufficient kinetic energy to negotiate adverse pressure gradients. It may be useful to incorporate suction and tangential blowing in a single device (or system) to exploit the benefit from both schemes.

In the context of shock-boundary-layer interaction control, there have been several studies dealing with suction and tangential blowing in the different speed regimes; a brief account of some of these may be found in the book by Chang (1976). Most of the investigations even to-date have been either exploratory in nature or focussed towards some design application. Systematic studies of these control techniques with regard to "basic interactions" are rather few. Many questions remain both from the point of view of general understanding and of applications.

In this section, a brief overview of the developments in control techniques using suction and blowing is presented. A more detailed review of the subject may be found in the recent article by Delery (1985).

8.1 Applications of tangential blowing

Tangential blowing for control of shock-boundary layer interaction has been studied by several investigators (e.g. Chinneck *et al* 1955; Peake 1966; Wong & Hall 1975; Wong 1977; Viswanath *et al* 1977, 1983; Schwendemann & Sanders 1982). These studies have revealed that blowing is generally effective in controlling shock-induced separation in both two-dimensional and axisymmetric flows. Since very few systematic studies on simpler geometries exist in the literature, our understanding of some of the general features of the flow field and of the parameters that may influence the effectiveness of blowing are still somewhat unclear.

8.1a *Parameters governing blowing performance:* Since blowing involves injection of additional mass and momentum into the boundary layer, the parameters affecting its performance include the jet velocity, its density and the slot width b in two-dimensional flows (figure 49). The most widely used parameter is the blowing momentum coefficient, C_μ defined by

$$C_\mu = \dot{m}_j u_j / \rho_o u_o^2 \theta_o,$$

where \dot{m}_j is the jet mass flow rate, u_j is the jet velocity, ρ_o is the free stream density, u_o is the free stream velocity and θ_o is the boundary layer momentum thickness ahead of the interaction. Some investigators in the past have also used an excess blowing momentum coefficient, defined in figure 49.

Figure 50 shows an example (Wong & Hall 1975) of the effectiveness of a tangential blowing system consisting of discrete jets in controlling separation in a supersonic inlet at $M_\infty = 2.0$. A significant reduction in the separated region may be inferred from the surface pressure distributions even for a value of $C'_\mu = 0.9$; their results also showed an appreciable improvement in the total pressure recovery and a low flow distortion for $C'_\mu = 1.5$.

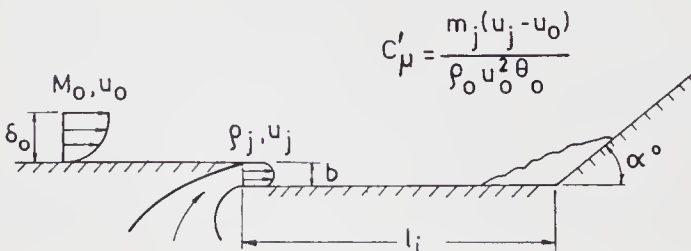


Figure 49. Sketch defining notation used with tangential blowing.

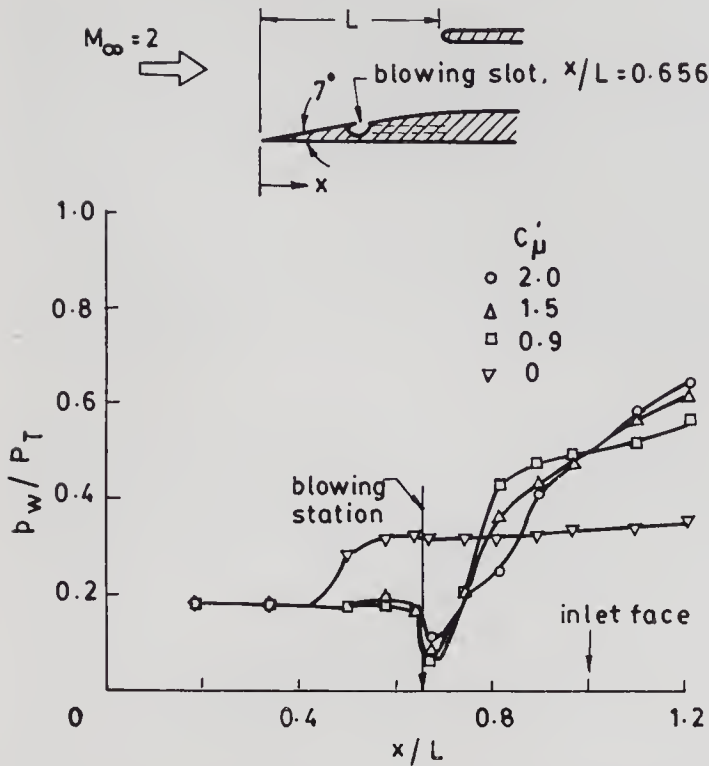


Figure 50. Ramp centreline pressure distributions: $M_\infty = 2.0$ (from Wong & Hall 1975).

There have been some attempts (Grin 1967; Lakshminantha *et al* 1969) to suggest correlations for blowing effectiveness based on their own limited data. It is interesting to touch upon the correlation presented by Lakshminantha *et al* (1969). Based on a series of experiments involving impinging shock waves at $M_\infty = 2.2$ and 2.6, they presented a correlation for the minimum blowing pressure (\hat{P}_i) required to suppress separation which is of the form (figure 51),

$$\hat{P}_i = 1.25 \Delta p (l_i/\delta_o)^{0.70},$$

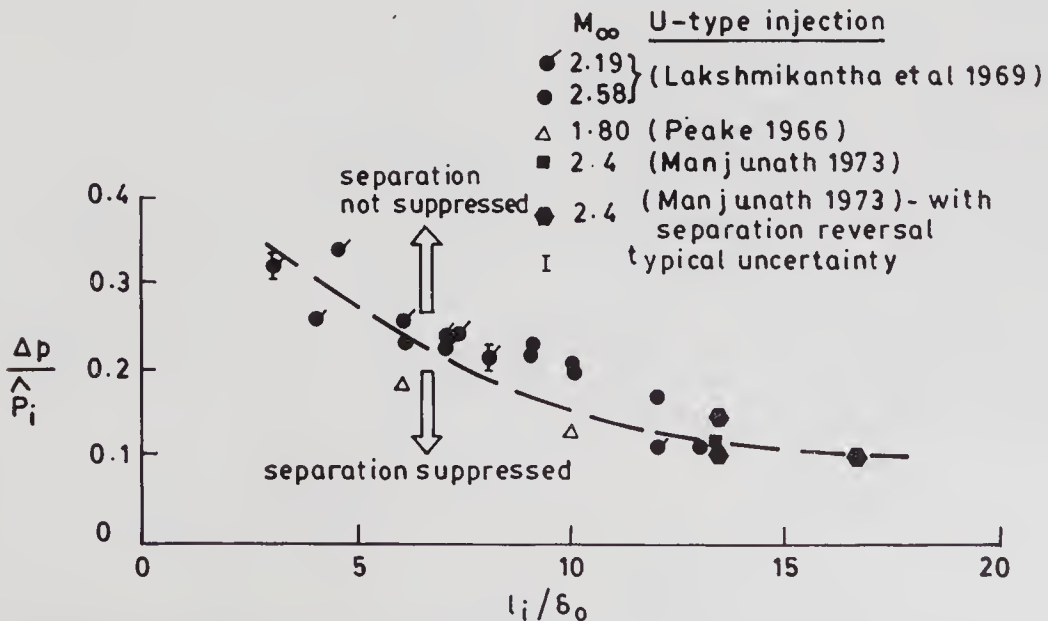


Figure 51. Correlation of minimum injection pressure required to suppress separation (from Lakshminantha *et al* 1969).

where Δp is the observed pressure rise across the shock wave, l_i is the distance between the injection slot and shock intersection point on the wall in inviscid flow and δ_o is the boundary layer thickness ahead of interaction. It is interesting to note that, unlike the mass or momentum coefficient, the above correlation does not involve the slot width b ; in these tests, b/δ_o was varied between 0.1 and 0.4. Although the data shown in figure 51 are suspected to have some interference effects (Viswanath *et al* 1977, 1983), the trend indicates that the total mass or momentum injected may not be an important factor at least for improving the surface pressures in the separated flow; it is likely that the excess velocity injected is the dominant factor.

8.1b *Location of blowing slot:* Among the various factors that may determine the effectiveness of injection, several studies (Peake 1966; Krishnamurthy 1973; Manjunath 1973), have revealed that the injection slot location is a critical parameter. We shall examine this aspect in some detail.

At the outset it is convenient to distinguish between two types of injection depending on the location of the injection slot (figure 52):

1. *U-type:* injection is upstream of where the separation point would have been in the absence of injection (i.e., the conventional location adopted for boundary-layer control).
2. *D-type:* injection is downstream of the same point, but within the recirculating (or “dead air”) zone.

Based on detailed experiments at a free stream Mach number of 1.8 with *U-type* injection, Peake (1966) made an important distinction between wall flow reversal and wake (or outer flow) reversal, and found that there was an optimum slot location at which both wall and wake flow reversals were avoided. For his experimental conditions, this optimum was at $l_i \approx 6\delta_o$.

The experiments of Krishnamurthy (1973) and Manjunath (1973) with *U-type* supersonic injection to control separation at a compression corner revealed some interesting and unexpected features. The first is what may be called “separation reversal”; with increase in injection total pressure P_i , the extent of separation first decreases and then increases (as inferred from wall static pressure distributions) after a certain value of P_i , which seems to depend on l_i and on the compression corner angle (all other conditions remaining the same). This puts a serious limitation on the range of P_i that can be usefully employed to suppress separation. The second feature is that the upstream influence or the extent of separation in the absence of injection was much larger than would be expected from earlier observations with similar flow conditions and ramp angles. It was demonstrated (Sagdeev 1974) that this abnormal upstream influence was due to the effects of the injection slot geometry on the oncoming boundary layer, which acts as a backward-facing step in the absence of injection.

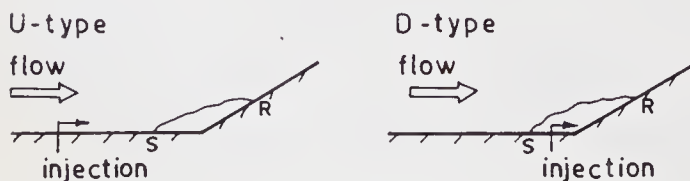


Figure 52. Sketch showing *U-* and *D-type* tangential injection.

8.1c. *Experiments with D-type blowing*: Although there was some indirect evidence (Chinneck *et al* 1955; Wong 1977) that *D*-type injection could be useful, a quantitative assessment of its effectiveness resulted from the investigations of Viswanath *et al* (1977, 1983). They studied *D*-type injection (by design) for two values of l_i namely, $0.77 \delta_o$ and $1.54 \delta_o$ at a ramp induced turbulent separated flow at $M_o = 2.5$.

Figure 53 shows surface pressure distributions with and without injection for $l_i = 1.54 \delta_o$. A monotonic increase in the maximum slope of the pressure distributions with increasing P_i is evident and suggests a progressive reduction of the length of the separation bubble. Similar results were seen at $l_i = 0.77 \delta_o$. Measured Mach number profiles in the interaction region for the case $l_i = 1.54 \delta_o$ (figure 54) shows conclusively the absence of wake flow reversal as well, suggesting complete suppression of boundary layer separation.

Effectiveness of *D*-type injection for the above experiments was assessed using two measures; (i) a suitably defined "reattachment length", Δ_r (figure 55), which is related to the bubble size Δ_b (Manjunath 1973) and (ii) the pressure recovery coefficient c_{p_r} defined as

$$c_{p_r} = (p_{\text{ref}(i)} - p_{\text{ref}(o)}) / (p_d - p_{\text{ref}(o)}),$$

where $p_{\text{ref}(i)}$ and $p_{\text{ref}(o)}$ denote the static pressures at a reference location on the ramp with and without injection, respectively.

Figures 55 and 56 show the variation of normalized reattachment length and the pressure recovery coefficient with injection pressure ratio (for both values of l_i) with *D*-type injection. These results are compared with those of Krishnamurthy (1973) and Manjunath (1973) who used *U*-type injection under essentially the same conditions as those in the experiments of Viswanath *et al* (1977, 1983). These

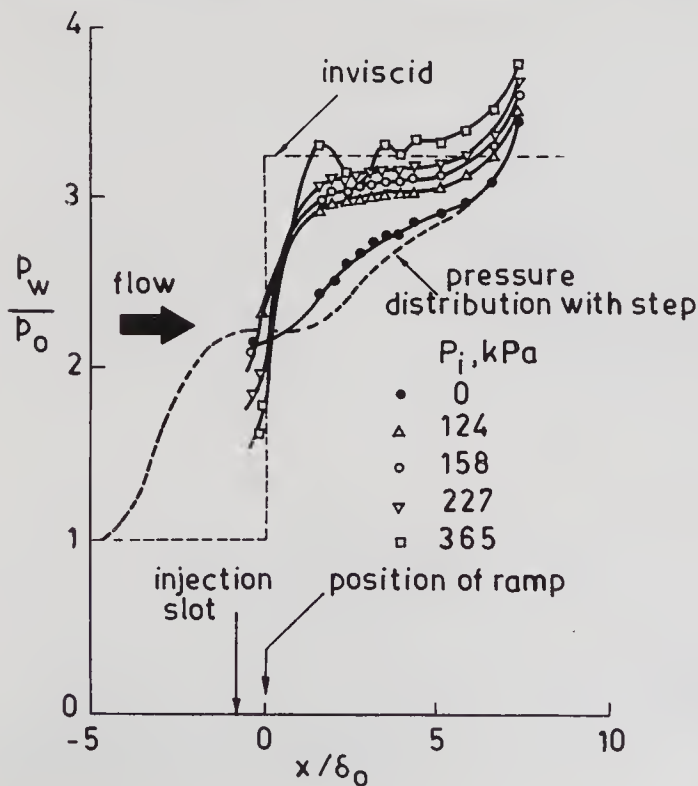


Figure 53. Wall static pressure distributions with injection: $M_o = 2.5$, $l_i = 1.54 \delta_o$ (from Viswanath *et al* 1983).

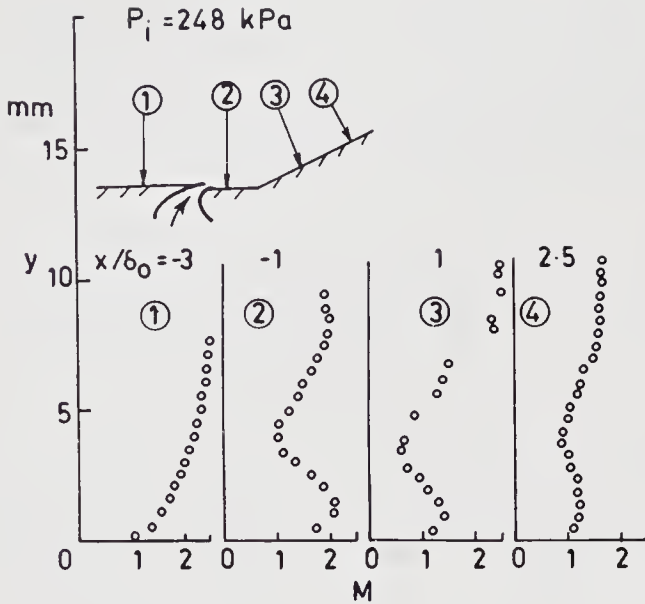


Figure 54. Mach number profiles in the interaction region with injection: $M_o = 2.5$, $l_i = 1.54 \delta_o$ (from Viswanath *et al* 1983).

comparisons show clearly the superiority of *D*-type over the *U*-type injection. In these experiments, the mass and momentum flux in the jet needed to suppress separation is estimated to be only about 18 and 14% of that in the oncoming boundary layer.

The success of the *D*- over the *U*-type injection suggests that mechanisms, other than energizing the boundary layer near the wall upstream of the beginning of adverse pressure gradients (as in the conventional *U*-type), exist for effective separation control. It has been speculated (Viswanath *et al* 1983) that an important factor in the *D*-type injection is the interaction of the jet injected at high total

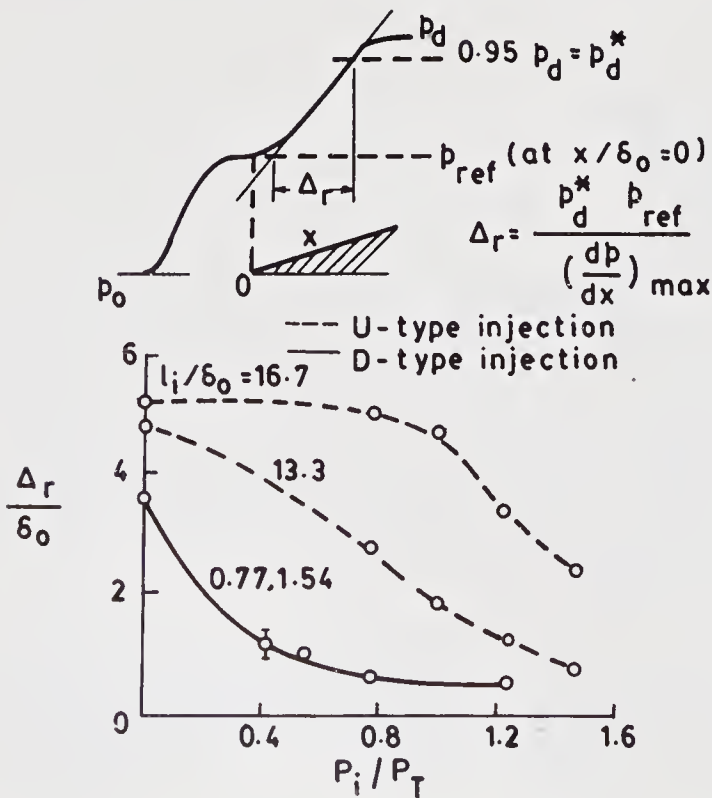


Figure 55. Variation of reattachment length with injection (from Viswanath *et al* 1983).

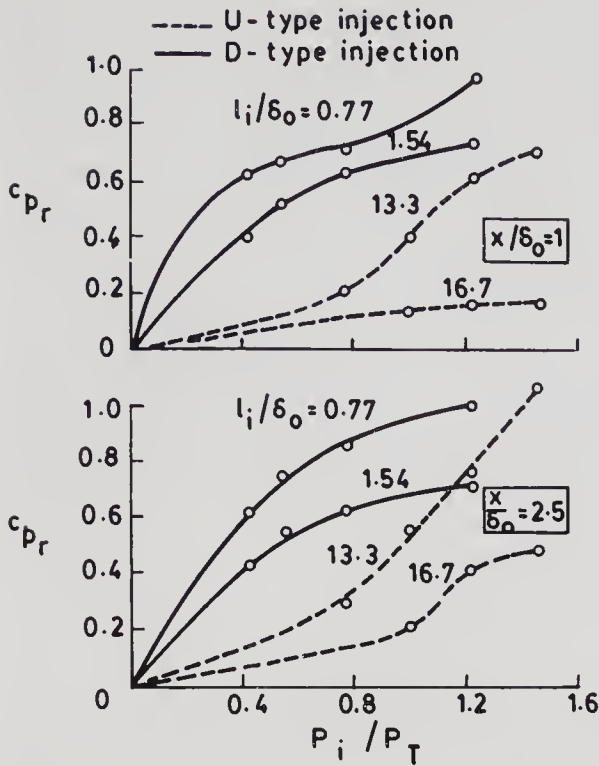


Figure 56. Static pressure recovery in the reattachment region with injection (from Viswanath *et al* 1983).

pressures with the (otherwise reverse flow) boundary layer, leading to eventual removal of the reattachment point. It is likely that the entrainment of the recirculating flow by the jet may play a role in the mechanisms involved.

8.1d Calculation methods: The problem discussed here certainly presents complexity in flow modelling and in calculation methods. There has been hardly any attempt to calculate these interacting turbulent flows with tangential fluid injection at high speeds. From an engineering viewpoint, a viscous-inviscid interactive type of calculation, with the viscous flow represented by an integral method, may be adequate. Even with *U*-type injection, there is insufficient mean flow data at high speeds covering a range of flow and geometrical parameters to enable construction of a reliable integral method. Experience gained in calculating low speed wall jet flow fields in adverse pressure gradients (Gartshore & Newman 1969; Hubbard & Bangert 1970; Yegna Narayan & Narasimha 1973) could be utilized as a first step in predicting these viscous flows at high speeds. With *D*-type injection, the complexity may be even greater, and further understanding of the physical mechanisms at play is essential before any modelling or calculation method can be formulated.

8.2 Application of suction

Boundary layer suction is a powerful tool (useful in many different speed regimes) for controlling flow separation, apart from the other engineering applications it has. Fluid near the wall is removed through slots or perforations, so that the new boundary layer which is formed downstream of the suction zone can withstand the imposed adverse pressure gradients. Suction generally leads to a fuller velocity profile and a consequent reduction of the boundary layer thickness. As with blowing, suction involves energy investment, and it is important in applications to

determine the “minimum suction volume” or the power required to drive the suction pump.

Several exploratory studies dealing with suction for control of shock-boundary layer interactions have been reported (e.g. Pate 1969; Seebaugh & Childs 1970; Tanner & Gai 1970; Mathews 1970; Wong 1974; Fukuda *et al* 1977). These studies, while showing the general effectiveness of suction in the various situations studied, contain little information on flow-field behaviour. Even engineering correlations for suction effectiveness do not seem to have been attempted; this situation is perhaps undesirable, since suction adds several new geometrical parameters to the problem, which even otherwise is complex enough. In this section, we shall present examples of application of suction and bleed (the distinction between the two being that bleed does not require energy input but could still drain energy) for the control of shock-boundary-layer interactions, and include an assessment of the state of the calculation methods.

8.2a *Parameters governing suction-performance*: It is common practice to define a suction quantity coefficient given by

$$C_Q = Q/Au_o,$$

where Q is the total volume rate of fluid removed, A denotes the wetted area and u_o is the free stream velocity. For the case of uniform suction (with a suction velocity of $-v_w$).

$$C_Q = -v_w/u_o$$

As with tangential blowing, for a given shock pressure rise and upstream flow conditions, the suction performance would, in general, depend on where the fluid is sucked in relation to the interaction zone, the total mass flow removed and the suction arrangement. At least three different arrangements have been employed in the various investigations; they include porous (or perforated) wall suction, slot suction and scoop suction. Several geometrical parameters are associated with each of the above suction configurations. For example, perforated wall arrangement (which is widely used) is defined by the number of bleed holes, their shape, diameter and distribution; with slot suction, the width and number of slots, and their orientation and distribution, are relevant parameters. For each of the configurations, the plenum or bleed chamber geometry could have an added influence. In view of the fairly large number of parameters associated with a suction device, perhaps it may not be worthwhile to attempt generalized engineering correlations for effectiveness even in the context of basic interactions.

8.2b *Location of suction system*: As may be expected, the location of suction in relation to the interaction zone is an important factor governing suction effectiveness. Since suction is often applied over a finite distance (in the range of several δ_o), the definitions U - and D -type (described in § 8.1b) may not be strictly applicable; we shall therefore use a much broader concept for suction location in the examples to follow.

Mathews (1970) investigated the effects of suction in an (internal) axisymmetric conical shock-wave-boundary-layer interaction at $M_\infty = 2.0$. The suction geometry consisted of one row of perforated holes located around the circumference and

suction was applied “within” the interaction region. Both the shock strength and the mass flow sucked were varied in his experiments. Figure 57 shows a schematic of the wave pattern, measured wall static pressures and c_f distributions in the interaction region, both with and without suction, for a separated flow generated by a 30° (total apex angle) cone. With a bleed mass flow of 7.5% of the approaching boundary layer mass flow, separation was nearly suppressed; the skin friction distributions show much higher values as a result of suction.

In a similar test set-up (Seebaugh & Childs 1970) at $M_\infty = 3.8$, a separated zone (of length approximately $2\delta_o$) could be controlled with a bleed mass flow rate of 3% of the boundary layer mass flow rate with suction applied “within” the interaction zone (figure 58). In this experiment, the suction geometry was similar to that used by Mathews (1970), but had four rows of perforated holes around the circumference and distributed over a length of about $1.5\delta_o$. It was also found that a similar suction performed “upstream” of the interaction region was less effective.

Detailed experiments to determine the effects of bleed geometry and bleed rate on the boundary layer development following shock-boundary-layer interaction in an axisymmetric mixed compression inlet at $M_\infty = 2.5$ revealed (Fukuda *et al* 1977) that suction performed “upstream or downstream” of the interaction zone was more beneficial than “within”; this assessment was made by examining the shape factor following the interaction. This observation, which is in contrast with those of Mathews (1970) and of Seebaugh & Childs (1970), might be a result of several differences in the bleed geometries used in the three experiments. Furthermore, the flow studied by Fukuda *et al* (1977) was more complex, involving multiple shock reflections between the centre body and the inlet cowl.

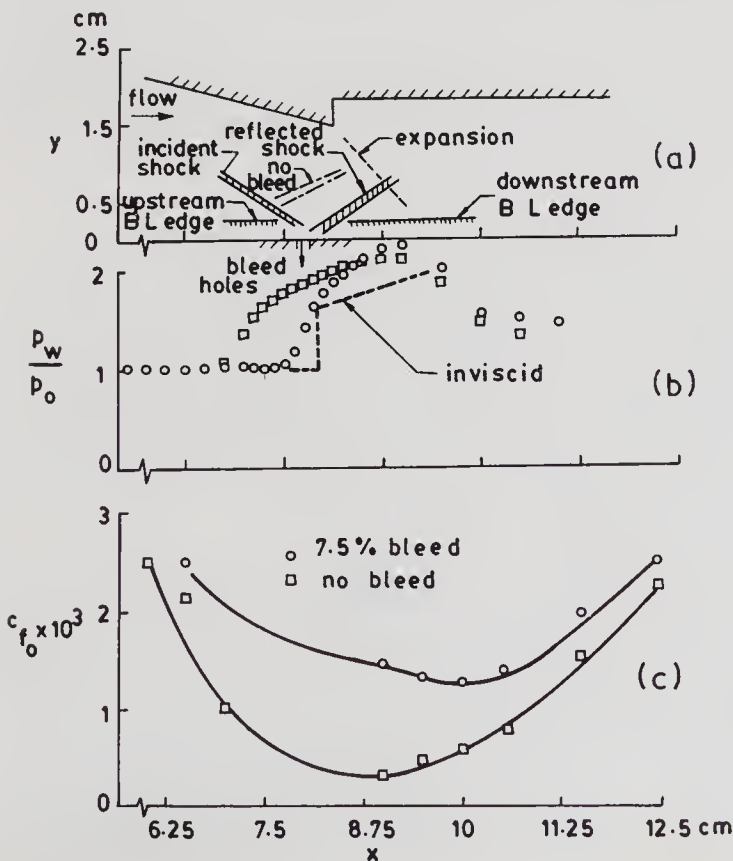


Figure 57. Effect of suction in an axisymmetric shock-boundary layer interaction: $M_\infty = 2.0$ (from Mathews 1970), (a) wave pattern, (b) wall pressure distribution, (c) skin friction distribution.

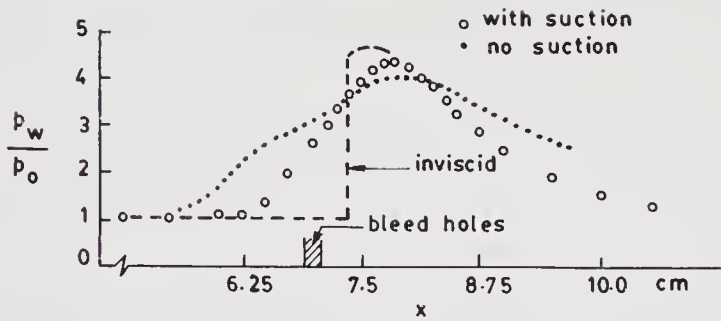


Figure 58. Effect of suction on wall static pressure distribution: $M_\infty = 3.78$ (from Seebaugh & Childs 1970).

The experiments of Wong (1974) in an axisymmetric external compression inlet at $M_\infty = 2.0$ also showed the effectiveness of suction performed both “upstream” and “within” the interaction region; suction was applied in a (nearly) continuous fashion in these tests.

The results discussed above suggest that suction “within” the interaction zone can be quite effective; there is very little information in the literature at comparable conditions to make a better judgement on the best location for suction. The bleed system arrangement can be expected to influence the overall performance associated with suction.

Effects of slot suction, with the slot located “within” a separated flow, have been studied by Tanner & Gai (1970) at $M_o = 1.93$. The suction slot, formed between the flat plate and the ramp under surface, was varied in the tests; there was also provision for varying suction mass flow independently. An example of the effectiveness of *D*-type suction for a 16° ramp is shown in figure 59 for different values of suction coefficient (defined in figure 59). Progressive increase in the surface pressure recovery and reduction in the upstream influence with increasing suction rate is evident. For a value of suction coefficient of 1.5 (for which the inviscid pressure level is reached), the mass flow removed corresponds to about 20% of the mass flow in the approaching boundary layer. Qualitatively similar effects of suction were seen at other ramp angles.

8.2c Examples of natural bleed: Natural bleed has many similarities with suction and does not involve any power input. The high pressure in the (separated) dead air zone, if vented to a low pressure region, causes natural bleed or suction of the mass flow from the dead air region, leading to an effective suppression of the separated flow. This is a case of *D*-type suction or bleed in the sense defined in § 8.1b. Several studies employing *D*-type bleed have been conducted (e.g. Crawford 1961; Ball & Korkegi 1968; Ball 1970). Results from Ball & Korkegi (1968) and Ball (1970) are shown to illustrate the suction effectiveness in such cases.

Ball & Korkegi (1968) studied effects of suction through a 2D slot at a compression corner, formed by a flat-plate-flap combination (figure 60) at a hypersonic Mach number of 12.3 and with laminar boundary layer conditions. The slot formed at the intersection of the flat plate and flap could be varied in width providing a variation of bleed mass flow. The effects of suction for various ramp angles were examined. Static pressure distributions for a 20° flap deflection angle (shown in figure 60) indicate a progressive decrease in the extent of the separated region with increasing values of slot width d^* (or bleed mass flow); the pressure distribution corresponding to $d^* = 0.22$ cm resembles the inviscid case. In a later

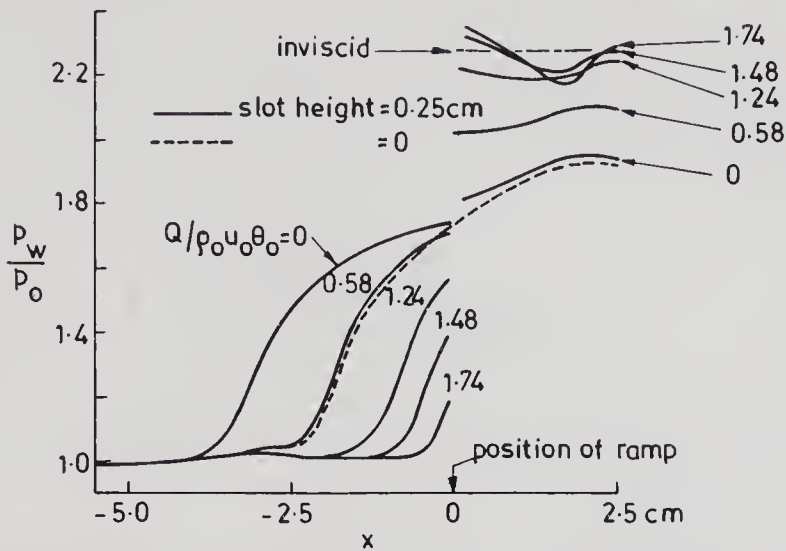


Figure 59. Wall static pressure distributions with slot suction: $M_o = 1.93$, $\alpha = 16^\circ$ (from Tanner & Gai 1970).

study, Ball (1970) showed the effectiveness of the *D*-type bleed (discussed above) at other values of M_o in the range 5 to 8. A simple correlation (figure 60) for the minimum mass flow to be removed for complete suppression of separation was given by Delery (1985).

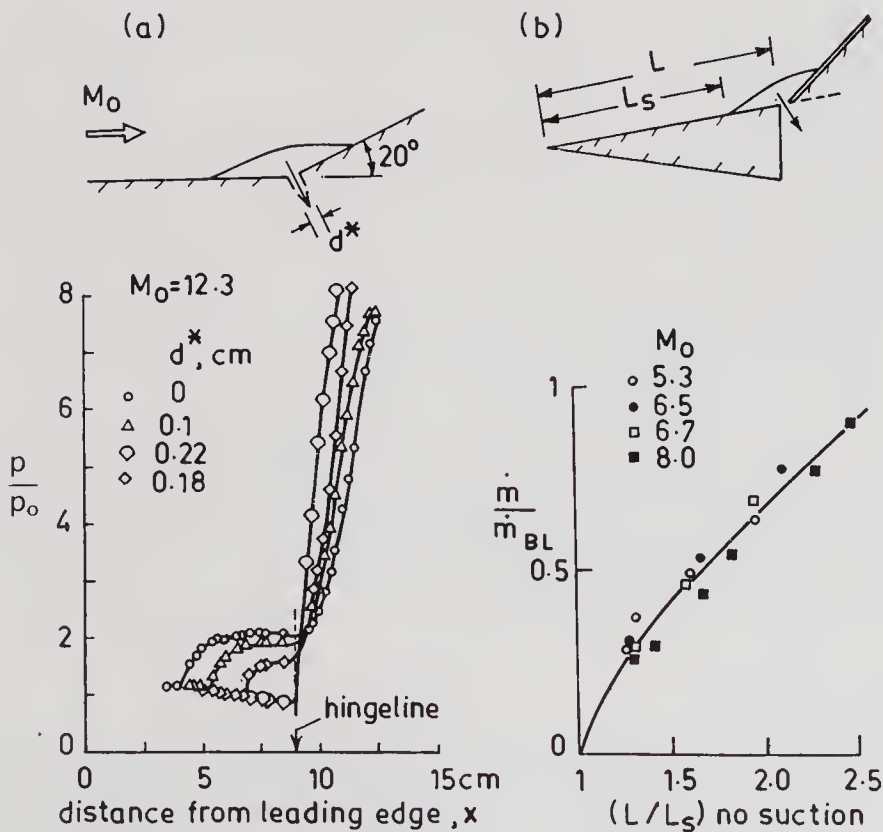


Figure 60. Effect of natural bleed on ramp-induced shock boundary layer interaction: (a) surface pressure distributions (from Ball & Korkegi 1968), (b) correlation of suction mass flow for suppression of separation (from Delery 1985).

8.2d *Calculation methods*: Methods for the calculation of boundary layer development with distributed or porous suction are fairly well-developed (Schlichting 1968). Porous suction, which can be realized in practice without much difficulty, offers the simplest boundary condition at the wall; it is common practice to prescribe the transpiration velocity ($-v_w$) as a function of the streamwise distance. In experiments, the suction velocity is often estimated from certain gross measurements (mass flow, pressure etc) in the bleed chamber. For other suction arrangements involving either slots or perforations, the flow through these devices is sufficiently complex such that an estimation of appropriate suction velocities at the wall becomes very difficult. There are very few experimental investigations wherein attempts have been made to get some idea of the flow development through the devices. So, the central problem in the calculation of effects of mass transfer at the wall is concerned with the estimation of the true boundary condition appropriate to the device.

For turbulent-shock-boundary-layer interactions with suction, there has been no attempt to calculate the flow using RANS to the author's knowledge. Effects of porous suction on laminar shock-induced separated flows have been studied using RANS by Tassa & Sankar (1979) and Purohit (1987b). The calculations made by Purohit (1987b) show that vectored porous suction can be more beneficial than normal suction. Don Gray & Maus (1981) have extended the Lees & Reeves (1964) interaction method to the calculation of slot suction at a ramp-induced laminar separated flow at $M_\infty = 6.7$. Their calculations, assuming uniform flow through the slot, indicate moderate agreement with the data of Ball (1970).

Engineering methods to calculate the variations of certain gross parameters of the flow through the interaction have been attempted. Seebaugh *et al* (1968), using a control volume approach and an integral method of analysis, present results for the changes in boundary layer thickness, velocity profile shape and other thickness parameters across the interaction; they consider porous, single slot as well as scoop suction configurations. Their paper, however, contains very limited comparisons with experiments, perhaps because of paucity of reliable data. The approach is further extended by Sun & Childs (1974) to treat successive shock reflections between an axisymmetric centre body and an outer circular cowl, including small amounts of suction at the location of the second shock-boundary layer interaction zone. Their results show fair agreement with experimental data for small bleed rates of about 3% of the boundary layer mass flow.

To summarize, considerable difficulty exists in dealing with the problem of the shock-turbulent boundary layer interaction with mass transfer at the wall. The problems include formulation of the wall boundary condition for different suction configurations, and modelling turbulence as affected by the mass transfer at the wall.

9. Concluding remarks

Although considerable amount of research has been carried out on the problem of shock-wave-boundary-layer interaction, our general understanding of turbulent interactions and Reynolds number effects in particular still remains poor. The progress is hampered primarily by our inadequate knowledge of turbulence dynamics in these complex flows. In the author's opinion, the principle of "free

interaction" (now known for over three decades) still remains a significant step in the understanding of high speed separated flows, despite the progress that has been made on the various fronts. There is now growing evidence that fully separated turbulent flows in reality are inherently unsteady and 3D to some degree; the idealization that the mean flow is 2D and steady may be an over-simplification.

Use of modern diagnostic techniques like laser velocimetry has provided valuable information on the complex behaviour of turbulence in these interactions. Similarly, sophisticated computer codes are now available for predicting these flows including regions of small separation which are of value to an engineer. Regarding turbulence modelling, accounting rationally for history or nonequilibrium effects and shock effects on turbulence appear to be important to achieve any success in computing separated flows; systematic research at high speeds of the kind reported by Narasimha & Prabhu (1972) investigating memory effects of large scale structures should prove valuable. Both surface and flow-field measurements investigating the unsteady character of shock-separated flows are necessary before modelling of large scale unsteadiness associated with shock waves can even be attempted.

Shear layer reattachment, being a key element in the dynamics of separated flows, has received very little attention in the literature. The role played by viscosity in the reattachment process is still an open question. It would be informative to examine if the general ideas of free interactions can be extended to the reattachment process; in particular, to see if the pressure rise to reattachment and the pressure distribution in the reattachment region can be related to the properties of the shear layer approaching reattachment for different shock-separated flows at supersonic/hypersonic Mach numbers.

On control techniques employing tangential blowing and suction, the available evidence suggests that interference with the flow in the separated zone or bubble can lead to effective separation control. With D -type injection, further research, both from the point of view of understanding the phenomena and assessing its effectiveness in other separating flows, is needed. Several interesting issues with regard to tangential blowing, including a suggestion for "intermittent blowing or blowing in puffs" have been discussed by Narasimha (1978). As regards suction "within" the interaction zone (or D -type suction), the mass imbalance created in the separated zone as a result of suction is likely to be a prime factor causing suppression of separation. Base-bleed causing base-drag reduction is a clear example of such a mechanism.

On the applications front, the situation is rather unclear regarding the best mode (or technique) for separation control. Such an assessment or judgement will have to be made on a case to case basis, giving due consideration to the energy input. For example, in applications where shock excursions are large, perforated wall suction spread over the required length is probably a good choice; on the other hand, if the location of the separated zone is in some sense stationary, D -type injection is an obvious choice. It would be rewarding to examine the usefulness of passive control techniques of the kind being investigated on transonic airfoils (e.g. Bahi *et al* 1983; Krogmann *et al* 1984) for shock-wave-boundary-layer interaction control in general.

Three-dimensional shock-boundary layer interactions are of greater interest in practical applications. Attempts to understand certain basic features of relatively simpler 3D interactions have begun in recent years (e.g. Oskam *et al* 1975; Settles *et*

al 1980; Dolling 1982). Since, in general, 3D separated flows are vortex-dominated, there is hope that turbulence modelling may not be as critical as in 2D flows, at least for certain 3D interactions (Horstmann & Hung 1979; Hung & Kordulla 1983). There is a definite need for systematic and focussed research in the area of 3D shock-wave-turbulent-boundary-layer interaction.

List of symbols

a_T	stagnation speed of sound;
b	slot width;
C	airfoil chord;
c_f, c_p	skin friction and pressure coefficients, respectively;
e	mean voltage;
H	boundary layer shape factor;
H_i	incompressible shape factor;
k	turbulent kinetic energy;
L	model length;
l_o	upstream influence interaction length (defined in figure 13);
l_b	separation bubble length;
l^*	interaction length (defined in figure 28);
l_i	injection distance (defined in figure 49);
\dot{m}	mass flow rate;
M	Mach number;
p	static pressure;
P_i	injection total pressure;
P_T	tunnel stagnation pressure;
q	dynamic pressure;
Re	unit Reynolds number;
R	reattachment point;
S	separation point;
T	temperature;
U, V	instantaneous velocity components;
u, v	mean velocity components;
u', v'	fluctuating velocity components;
x, y	coordinates along and normal to the wall;
α	ramp or compression corner angle;
γ_p	velocity intermittency;
δ	boundary layer thickness;
δ^*	boundary layer displacement thickness;
θ	boundary layer momentum thickness;
ρ	density;
τ_R	turbulent shear stress;
τ_w	wall shear stress;

Subscripts

BL	oncoming boundary layer;
d	conditions downstream of the interaction;

<i>e</i>	conditions at the edge of the boundary layer;
<i>i</i>	conditions of injected fluid;
<i>is</i>	conditions at incipient separation;
<i>l</i>	local conditions;
<i>o</i>	conditions at the edge of the flat plate boundary layer just ahead of the interaction;
<i>p</i>	conditions at the beginning of plateau region;
<i>r</i>	conditions at reattachment;
<i>s</i>	conditions at separation;
<i>w</i>	conditions at the wall;
<i>aw</i>	adiabatic wall;
∞	conditions at upstream infinity.

References

- Ackeret J, Feldman F, Rott N 1946 Investigations of compression shocks and boundary layers in gases moving at high speed, NACA TM 1113
- Adamson T C, Feo A 1975 *SIAM J. Appl. Math.* 29: 121–145
- Adamson T C, Messiter A F 1980 *Annu. Rev. Fluid Mech.* 12: 103–138
- Anyiwo J C, Bushnell D M 1982 *AIAA J.* 20: 893–899
- Bachalo W D, Johnson D A 1979 An investigation of transonic turbulent boundary layer separation generated on an axisymmetric flow model, AIAA Paper 79-1479
- Bahi L, Ross J M, Nagamatsu H T 1983 Passive shock-wave/boundary layer interaction control for transonic airfoil drag reduction, AIAA Paper 83-037
- Ball K O W 1970 *AIAA J.* 8: 374–375
- Ball K O W, Korkegi R H 1968 *AIAA J.* 6: 239–243
- Beam R M, Warming R F 1978 *AIAA J.* 16: 393–402
- Bradshaw P, Ferris D H, Atwell N P 1967 *J. Fluid Mech.* 28: 593–616
- Brusseleers M 1980 *Shock-boundary layer interactions in turbomachines*, Von Karman Inst. (Belgium), Lecture Series 1980-8
- Burggraf O R 1975 Flow separation, AGARD-CP-168, Paper no 10
- Burggraf O R, Rizetta D, Werle M J, Vatsa V N 1979 *AIAA J.* 17: 336–343
- Carter J E 1975 Inverse solutions for laminar boundary layer flows with separation and reattachment, NASA TR-R-447
- Cebeci T, Meier H U 1979 Turbulent boundary layers, experiments, theory and modelling, AGARD-CP-271
- Cebeci T, Stewartson K, Whitelaw J H 1984 *Numerical and physical aspects of aerodynamic flows II* (Berlin: Springer Verlag)
- Chang P K 1976 *Control of flow separation* (New York: Hemisphere)
- Chapman D R, Kuehn D M, Larson H K 1957 Investigation of separated flows in supersonic and subsonic streams with emphasis on the effect of transition, NACA TN 3869
- Charwat A F 1970 *Advances in heat transfer* (eds) J P Hartnett, T F Irvine (New York: Academic Press) 6: 1–132
- Chinneck A, Jones G C A, Tracey C M 1955 An interim report on the use of blowing to reduce fall in control effectiveness associated with shock-induced separation at transonic speeds, ARC 1756 FM 2231
- Coe C F, Chyu W J, Dods J B 1973 Pressure fluctuations underlying attached and separated supersonic turbulent boundary layers and shock waves, AIAA Paper 73-996
- Crawford D H 1961 The effect of air bleed on heat transfer and pressure distribution on 30° flares at a Mach number of 6.8, NASA TMX-439
- Crocco L, Lees L 1952 *J. Aero. Sci.* 19: 649–676
- Delery J M 1981 Investigation of strong shock-turbulent boundary layer interaction in 2-D transonic flows with emphasis on turbulence phenomena, AIAA Paper 81-1245
- Delery J M 1983 *AIAA J.* 21: 180–185

- Delery J M 1985 *Prog. Aerosp. Sci.* 22: 209–280
- Dolling D S 1982 *AIAA J.* 20: 1385–1391
- Dolling D S, Murphy M T 1983 *AIAA J.* 21: 1628–1634
- Dolling D S, Or C T 1983 Unsteadiness of shock-wave structure in attached and separated compression corner ramp flow fields, AIAA Paper 83-1715
- Don Gray J, Maus J R 1981 *AIAA J.* 19: 948–950
- Driver D M, Lee Seegmiller H, Marvin J G 1983 Unsteady behaviour of a reattaching shear layer, AIAA Paper 83-1712
- Eaton J K, Johnston J P 1982 *Turbulent shear flows*, 3. (eds) L J S Bradbury, F Durst, B E Launder, F W Schmidt, J H Whitelaw (Berlin: Springer Verlag)
- Elfstrom G M 1972 *J. Fluid Mech.* 53: 113–127
- Erdos J, Pallone A 1962 *Proc. Heat Transfer & Fluid Mech. Inst.* (Stanford: University Press)
- Finke K 1975 Flow separation, AGARD-CP-168, Paper no. 28
- Fukuda M K, Hingst W R, Roshko E 1977 *AIAA J.* 14: 151–156
- Gadd G E 1961 Interactions between normal shock waves and turbulent boundary layers, ARC R&M 3262
- Gartshore J S, Newman B G 1969 *Aeronaut. Q.* 20: 25–56
- Glusko G S 1965 *Bull. Acad. Sci. USSR Mech. Ser.* (no. 4): 13–23
- Grande E, Oates G C 1973 Unsteady flow generated by shock-turbulent boundary layer interactions, AIAA Paper 73-168
- Green J E 1970 *Prog. Aerosp. Sci.* 11: 235–340
- Grin V T 1967 *Mech. Fluids Gases* 6: 115–117 (in Russian)
- Henderson L F 1967 *J. Fluid Mech.* 30: 699–722
- Horstmann C C, Hung C M 1979 Computation of three-dimensional turbulent separated flows at supersonic speeds, AIAA Paper 79-002
- Horstmann C C, Owen F K 1974 *AIAA J.* 12: 1436–1438
- Hubbart J E, Bangert L H Turbulent boundary layer control by a wall jet, AIAA Paper 70-107
- Hung C M, Kordulla W 1983 A time split finite volume algorithm for three-dimensional flow field simulations, AIAA Paper 83-1957
- Inger G R 1981 Transonic shock/turbulent boundary layer interaction and incipient separation on curved surfaces, AIAA Paper 81-1244
- Inger G R, Mason W H 1976 *AIAA J.* 14: 1266–1272
- Jones W P, Launder B E 1971 *Int. J. Heat Mass Transfer* 15: 301–314
- Kistler A L 1964 *J. Acoust. Soc. Am.* 36: 543–550
- Klineberg J M, Steger J L 1974 On laminar boundary layer separation, AIAA Paper 74-94
- Kooi J W 1975 Flow separation, AGARD-CP-168, Paper no. 30
- Kooi J W 1980 *Shock-boundary layer interaction in turbomachines*, Von Karman Inst. (Belgium), Lecture Series 1980-8
- Krishnamurthy V 1973 *Suppression of shock-induced separation using tangential fluid injection: Part I*, M E Project Report, Dept. Aerosp. Eng., Indian Inst. Sci. Bangalore
- Krogmann P, Stanewsky E, Thiede P 1984 Effect of local boundary layer suction on shock-boundary layer interaction and shock-induced separation, AIAA Paper 84-0098
- Kuehn D M 1959 Experimental investigation of the pressure rise required for the incipient separation of turbulent boundary layers in two-dimensional supersonic flow, NASA Memo 1-21-59A
- La Ballleur J C 1981 Computation of viscous-inviscid interactions, AGARD CP 291, Paper No. 1
- La Balleur J C 1984 *Numerical and physical aspects of aerodynamic flows II* (Berlin: Springer Verlag)
- La Balleur J C, Blaise D 1985 *Rech. Aerosp.* (no. 4): 1–17
- Lakshmikantha H, Yegna Narayan K, Srinivasan G 1969 Effect of fluid injection on shock-wave boundary layer interaction, Report 69 FM 7, Dept. Aerosp. Eng., Indian Inst. Sci., Bangalore
- Law C H 1974 *AIAA J.* 12: 794–797
- Lees L, Reeves B L 1964 *AIAA J.* 2: 1907–1920
- Levy L L 1978 *AIAA J.* 14: 564–572
- Lewis J E 1967 *Experimental investigation of supersonic laminar two-dimensional boundary layer separation in a compression corner with and without cooling*, Ph D thesis, Cal. Inst. Technol.
- Lewis J E, Kubota T, Lees L 1968 *AIAA J.* 6: 7–14
- Liepmann H W 1946 *J. Aeronaut. Sci.* 13: 623–637
- Liepmann H W 1947 *J. Aeronaut. Sci.* 14: 295–302

- Liepmann H W, Roshko A, Dhawan S 1951 On reflection of shock waves from boundary layers, NACA TN 2334
- Lighthill M J 1953 *Proc R. Soc. London* A217: 478–507
- Lock R C 1981 Computation of viscous-inviscid interactions, AGARD CP 291, Paper no. 2
- Manjunath A R 1973 *Suppression of shock-induced separation using tangential fluid injection: Part II*, M. E. Project Report, Dept. Aerosp. Eng., Indian Inst. Sci., Bangalore
- Marvin J G 1982 Turbulence modelling for computational aerodynamics, AIAA Paper 82-0164
- Marvin J G 1983 Modelling of turbulent separated flows for aerodynamic applications, NASA TM 84392
- Mathews D C 1970 *Shock-wave boundary layer interactions in two-dimensional and axially-symmetric flows*, Ph D thesis, University of Washington
- McCormack R W 1976 An efficient numerical method for solving the time-dependent compressible Navier-Stokes equations at high Reynolds number, NASA TM X-73129
- McCormack R W 1982 *AIAA J.* 20: 1275–1281
- McCormack R W, Lomax H 1979 *Annu. Rev. Fluid Mech.* 11: 289–316
- McDevitt J B 1979 Supercritical flow about a thick circular-arc airfoil, NASA TM 78549
- McDevitt J B, Levy L L, Deiwert G S 1976 *AIAA J.* 14: 606–613
- McDonald H, Briley W R 1984 *Numerical and physical aspects of aerodynamic flows II* (Berlin: Springer Verlag)
- Mehta U, Lomax H 1982 *Prog. Astronaut. Aeronaut.* 82: 297–375.
- Meier G E A 1975 Flow separation, AGARD-CP-168, Paper no. 29
- Melnik R E, Grossman B 1974 Analysis of interaction of a weak normal shock wave with a turbulent boundary layer, AIAA Paper 74-598
- Melnik R E, Grossman B 1975 *Symp. Transonicum II* (Berlin: Springer Verlag)
- Melnik R E, Grossman B 1977 *Transonic problems in turbomachinery* (New York: Hemisphere)
- Messiter A F 1970 *SIAM J. Appl. Math.* 18: 241–257
- Narasimha R 1978 Turbulent flow separation: Two problems in application oriented research, Report 78 FM 11, Dept. Aerosp. Eng., Indian Inst. Sci., Bangalore
- Narasimha R, Prabhu A 1972 *J. Fluid Mech.* 54: 1–17
- Narasimha R, Sreenivasan K R 1973 *J. Fluid Mech.* 61: 417–447
- Neiland V 1969 *Fluid Dyn. (Engl. Transl.)* 4: 33–35
- Oskam B, Vas I E, Bogdonoff S M 1975 Flow separation, AGARD-CP-168, Paper no. 41
- Pate S R 1969 *AIAA J.* 7: 847–851
- Peake D J 1966 The use of air injection to prevent separation of turbulent boundary layer in supersonic flow, ARC CP 890
- Pearcey H H 1961 *Boundary layer and flow control* (ed.) G V Lachmann (New York: Pergamon) vol. 2
- Plotkin K J 1975 *AIAA J.* 13: 1036–1040
- Purohit S C 1987a *J. Spacecraft Rockets* 23: 590–596
- Purohit S C 1987b *AIAA J.* 25: 759–760
- Rizetta D P, Burggraf O R, Jenson R 1978 *J. Fluid Mech.* 89: 535–552
- Rose W C 1973 The behaviour of a compressible turbulent boundary layer in a shock-wave induced adverse pressure gradient, NASA TN D-7092
- Rose W C, Johnson D A 1975 *AIAA J.* 13: 884–889
- Roshko A, Thomke G J 1969 *Proc. Symp. on viscous interaction phenomena in supersonic and hypersonic flow* (Univ. of Dayton Press) pp. 109–138
- Roshko A, Thomke G J 1976 *AIAA J.* 14: 873–879
- Rotta J C 1968 Computation of turbulent boundary layers – 1968 AFOSR-IFP, Stanford Conference, vol I, pp 177–181
- Rubesin M W 1982 The 1980–81 AFOSR-HTTM-Stanford Conference on Complex Turbulent Flows: Comparison of Computation and Experiment, vol II, pp 713–719
- Sagdeo P M 1974 *Suppression of shock-induced separation using tangential fluid injection, Part III: Effect of injection slot*, M E Project Report, Dept. Aerosp. Eng., Indian Inst. Sci., Bangalore
- Sandborn V A, Kline S J 1961 *J. Basic Eng. Trans. ASME* 83: 317–327
- Sawyer W G, East L F, Nash C R 1977 A preliminary study of normal shock wave turbulent boundary layer interaction, RAE Tech. Memo Aero. 1714
- Schlichting H 1968 *Boundary-layer theory* (New York: McGraw-Hill)
- Schwendemann M F, Sanders B W 1982 Tangential blowing for control of strong normal shock-boundary layer interactions on inlet ramps, AIAA Paper 82-1082

- Seddon J 1960 The flow produced by interaction of a turbulent boundary layer with a normal shock wave of strength sufficient to cause separation, ARC R&M 3502
- Seddon J, Goldsmith E L 1985 *Intake aerodynamics* (New York: Collins)
- Seebaugh W R, Childs M E 1970 *J. Aircraft* 7: 334–339
- Seebaugh W R, Paynter G C, Childs M E 1968 *J. Aircraft* 5: 461–467
- Settles G S, Bogdonoff S M 1982 *AIAA J.* 20: 782–789
- Settles G S, Bogdonoff S M, Vas I E 1976a *AIAA J.* 14: 50–56
- Settles G S, Perkins J J, Bogdonoff S M 1980 *AIAA J.* 18: 779–785
- Settles G S, Vas I E, Bogdonoff S M 1976b *AIAA J.* 14: 1709–1715
- Shang J S, Hankey W L 1975 *AIAA J.* 13: 1368–1374
- Shang J S, Hankey W L, Law C H 1976 *AIAA J.* 10: 1451–1457
- Simpson R L, Strickland J H, Barr P W 1977 *J. Fluid Mech.* 79: 553–594
- Sirieux M 1975 Flow separation, AGARD-CP-168, Paper no. 12
- Sirieux M, Dclery J, Stanewsky E 1981 *Advances in fluid mechanics* (New York: Springer Verlag)
- Stanewsky E 1973 *Transonic flows in turbomachinery*, Von Karman Institute (Belgium), Lecture Series 59
- Stanewsky E, Nandanam M, Inger G R 1981 Computation of viscous-inviscid interactions, AGARD CP 291, Paper no. 4
- Stewartson K 1974 *Adv. Appl. Mech.* 14: 145–239
- Stewartson K, Williams P G 1969 *Proc. R. Soc. London* A312: 181–206
- Sun C C, Childs M E 1974 *J. Aircraft* 11: 54–59
- Tanner L H, Gai S L 1970 Effects of suction on the interaction between shock wave and boundary layer at a compression corner, ARC CP 1087
- Tassa Y, Sankar N L 1979 *AIAA J.* 17: 1268–1270
- Viegas J R, Horstmann C C 1978 Comparison of multi-equation turbulence models for several shock separated boundary layer interaction flows, AIAA Paper 78-1165
- Veldman A E P 1984 *Computational methods in viscous flows* (ed.) W G Habashi (Gedney, NY: Pineridge) vol. 3
- Viswanath P R, Brown J L 1983 *AIAA J.* 21: 801–807
- Viswanath P R, Sankaran L, Sagdeo P M, Narasimha R 1977 Tangential blowing for control of shock-induced boundary layer separation: Review of recent IISc work, Report 77 FM 11, Dept. Aerosp. Eng., Indian Inst. Sci., Bangalore
- Viswanath P R, Sankaran L, Sagdeo P M, Narasimha R, Prabhu A 1983 *J. Aircraft* 20: 726–732
- Whitfield D L, Swafford T W, Jacocks J L 1981 *AIAA J.* 19: 1315–1322
- Wilcox D C, Rubesin M W 1980 Progress in turbulence modelling for complex flow fields including compressibility effects, NASA TP-1517
- Wong W F 1974 The application of boundary layer suction to suppress strong shock-induced separation in supersonic inlets, AIAA Paper 74-1063
- Wong W F 1977 Application of boundary layer blowing to suppress strong shock-induced separation in supersonic inlets, AIAA Paper 77-147
- Wong W F, Hall G R 1975 Suppression of strong shock boundary layer interaction in supersonic inlets by boundary layer blowing, AIAA Paper 75-1209
- Yegna Narayan K, Narasimha R 1973 *Aeronaut. Q.* 24: 207–218

Characteristics of a typical lifting symmetric supercritical airfoil[†]

M A RAMASWAMY

Aerospace Department, Indian Institute of Science, Bangalore 560 012, India (On deputation from National Aeronautical Laboratory, Bangalore 560 037, India)

Abstract. The theoretical aerodynamic characteristics of a typical lifting symmetric supercritical airfoil demonstrating its superiority over the NACA 0012 airfoil from which it was derived are presented in this paper. Further, limited experimental results confirming the theoretical inference are also presented.

Keywords. Transonic flow; supercritical airfoil; aerodynamic characteristics.

1. Introduction

All lifting supercritical airfoils, to the best knowledge of the author, have camber which gives wave drag at supersonic speeds. Hence these supercritical airfoils are unsuitable for use in supersonic aircraft. It has been reported that supercritical airfoils were considered for Y.F. 16 and Y.F. 17, but were discarded for the above reason. Also camber gives excessive pitching moment, an undesirable characteristic for helicopter rotor blades. Ramaswamy (1976) suggested that it should be possible to design symmetric airfoils which under design lift and incidence conditions are nearly shock-free. Such lifting symmetric supercritical airfoils would eliminate the disadvantages mentioned earlier. The feasibility of designing such lifting symmetric supercritical airfoils has been demonstrated by Nandan & Ramaswamy (1985).

In this paper, a brief outline of the method used in designing such airfoils is illustrated. Then the theoretical results for the aerodynamic characteristics of a typical airfoil derived from modifying the NACA 0012 are presented to demonstrate the superiority of the modified airfoil over the original one. Finally, limited experimental data obtained on NACA 0012 and the modified airfoil are presented to confirm the theoretical conclusions.

[†]Invited Lecture given at the 3rd Asian Congress on Fluid Mechanics, held in Tokyo during 1–5 September, 1986

2. Outline of the method

The method used is essentially the design method of Sobieczky *et al* (1979), called the fictitious gas method. This method is used for modifying a given profile to make it shock-free. The method needs a reliable potential code for computing the transonic flow past the profile to be modified. The code used by Sobieczky is the one developed by Bauer *et al* (1975, the BGKJ code) and the same with the non-conservative option is adopted here. The code solves the potential equation

$$(a^2 - U^2)\phi_{xx} - 2UV\phi_{xy} + (a^2 - V^2)\phi_{yy} = 0, \quad (1)$$

with the relation for density

$$\rho/\rho_\infty = \{1 + [(\gamma - 1)/2] M_\infty^2 (1 - U^2 - V^2)\}, \quad (2)$$

where U and V are the velocity components in x and y directions, ϕ is the potential function, M_∞ , the free stream Mach number, a is the local speed of sound. Without loss of generality, U_∞ is taken to be unity.

Consider a profile to be modified to make it shock-free at a particular M_∞ and incidence α . Then analyse this profile using the potential code with the modification that when the total velocity q in the flow field exceeds a^* , the critical speed of sound, replace (2) by a fictitious gas law,

$$\rho/\rho^* = (a^*/q)^p; \quad p < 1 \dots \text{for } q > a^*, \quad (3)$$

which makes the differential equation elliptic even in the supersonic region $q > a^*$. For instance, when $p = 0$, $\rho = \rho^*$ and this incompressible flow in the region $q > a^*$. Therefore as shown in figure 1, the flow pattern over the airfoil profile will have no shocks and the flow in the region between the sonic line and the airfoil boundary is fictitious. But the flow on the sonic boundary and everywhere else outside it is correct.

In order to make the flow in this region also correct corresponding to real gases, the flow angle and the sonic velocity on the sonic boundary are taken as initial conditions, and this region is solved for a real gas using the characteristic method. This solution to the real flow field would generate a new surface on the airfoil between the sonic points so as to be compatible with the real gas flow and would also generate the real pressure distribution on this modified contour. The modified airfoil is re-analysed using the potential code, with real gas law everywhere, to confirm shock-free flow. If wiggles in the pressure distribution are noticed near the sonic points, then the contours are locally smoothed in those regions to remove the wiggles. Complete details of this method are given by Sobieczky *et al* (1979). As pointed out by him, there is no guarantee that the characteristic solution does not end up with limit lines. However, it has been found in practice that with a suitable choice of p , this problem can be overcome in most of the cases.

To design a symmetric lifting supercritical airfoil, we take a baseline airfoil which is symmetric. We choose an M_∞ and α such that there is moderate shock on the top surface and no shock on the lower surface. Using the method described above, the top surface is modified to make it shock-free. Then the bottom surface is made symmetrical with the top surface to get a symmetrical airfoil. This airfoil is analysed to confirm that the shock-free characteristic is preserved. Thus a lifting symmetric supercritical airfoil is obtained.

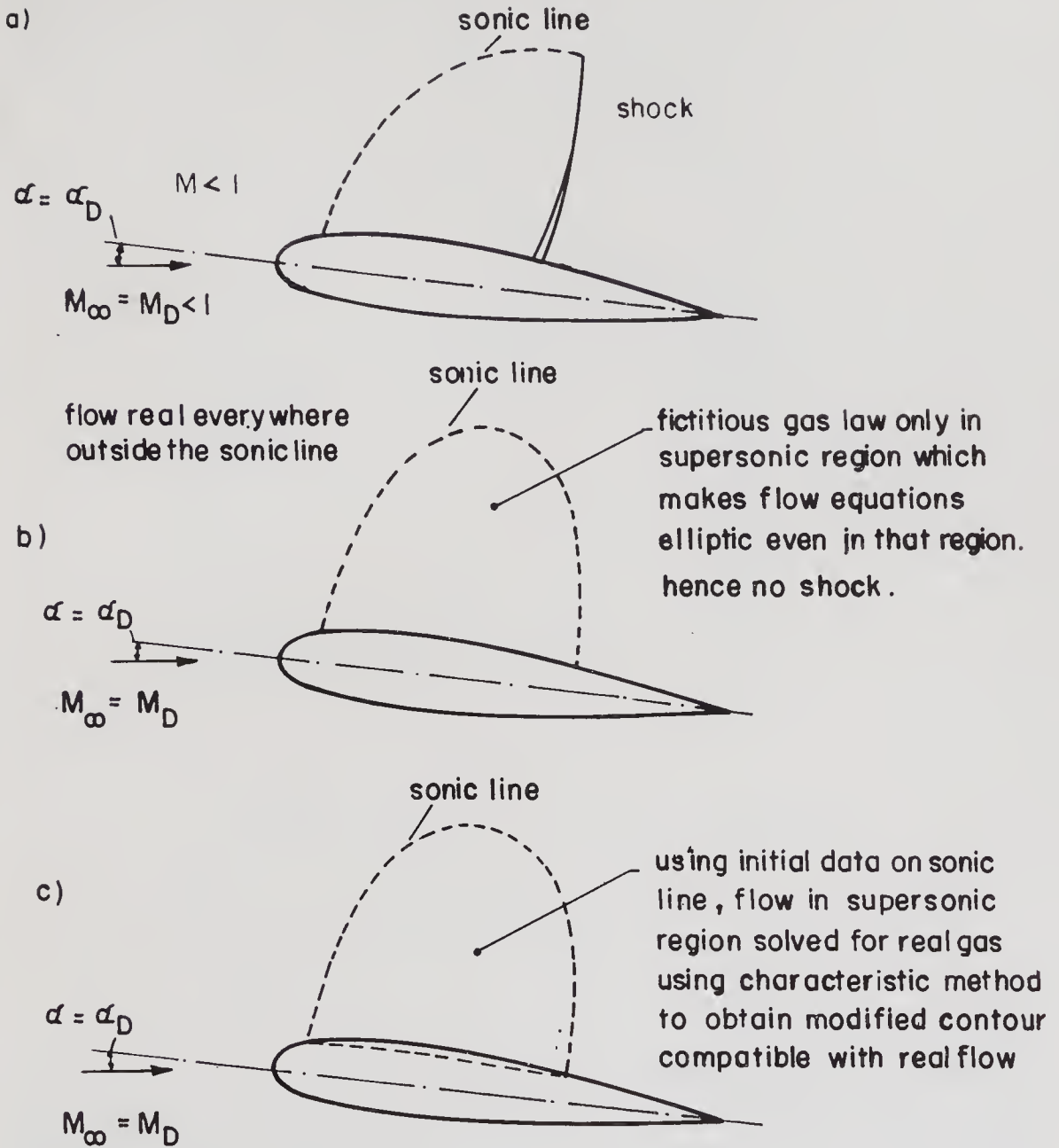


Figure 1. Principle of shock-free airfoil design by fictitious gas method. (a) Flow over basic airfoil with real gas flow; (b) flow over basic airfoil at same M and α but with fictitious gas law in supersonic region; (c) modification to contour to maintain shock-free flow.

The basis of our thinking that the shock-free characteristic of the flow on the upper surface would be maintained even after the bottom surface was modified to make it symmetrical was the following. There was evidence that when supercritical airfoils for transport aircraft were modified as shown in figure 2 to provide increased lift through aft camber, the pressure distribution on the upper surface was hardly affected. Our experience has also shown that shock-free characteristic on the upper surface was maintained even after the bottom surface was modified to make it symmetrical with the top surface.

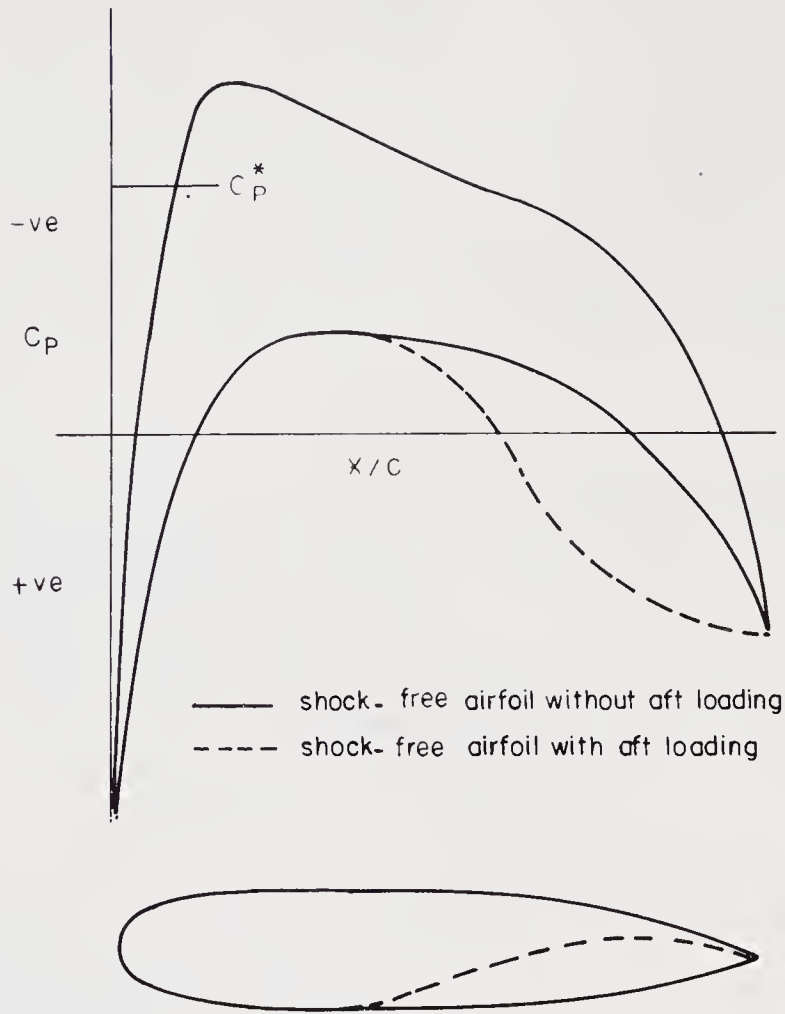


Figure 2. Example illustrating modification to lower contour without affecting shock-free flow on top surface.

3. Theoretical characteristics of NAL-114-36-00 airfoil

This airfoil has been obtained by modifying the NACA 0012 airfoil. It is 11.4% thick, with maximum thickness at 36% chord; and zero camber. To arrive at this airfoil, the flow past NACA 0012 airfoil at $M_\infty = 0.752$ and incidence equal to 1.1 degrees was considered. The pressure distribution obtained using the BGKJ code is shown in figure 3. Reasonably strong shock can be noted. As described in the previous section, the top surface of this airfoil was modified to make it shock-free and the bottom surface was made symmetrical with the top one to make the airfoil as a whole symmetrical. Comparison of the contour of NAL-114-36-00 with that of NACA 0012 is shown in figure 4. The pressure distribution obtained on the NAL 114-36-00 airfoil at the same M_∞ and α condition is shown in figure 5. The shock-free nature of the pressure distribution may be noted. The corresponding pressure distribution on NACA 0012 is also shown for comparison. Figure 6 shows the pressure distributions under slightly off design incidence conditions, whereas figure 7 shows the pressure distributions under slightly off design Mach number conditions. From these figures, it may be seen that no abrupt changes take place

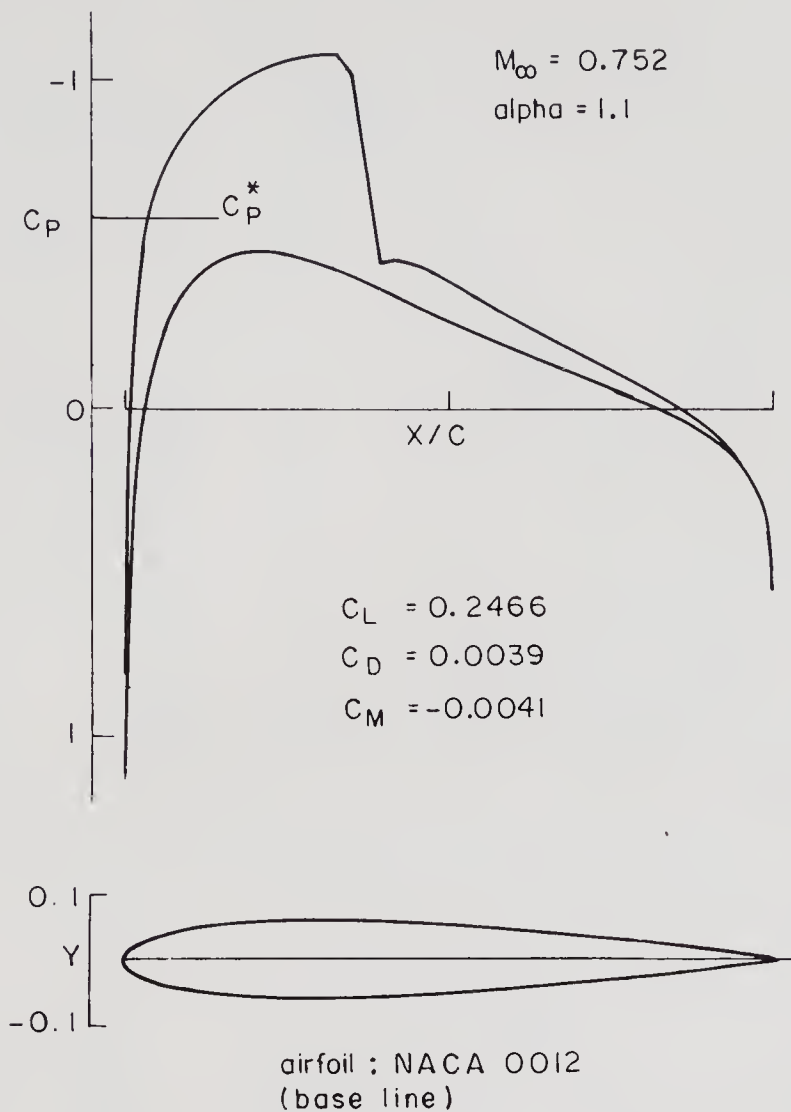


Figure 3. Pressure distribution on NACA 0012 airfoil.

under slightly off design conditions. Figures 8 and 9 show the variation of drag with Mach number for different C_L values for the NACA 0012 and the NAL 114-36-00 airfoils, respectively. Being a potential code, only the wave drag component is obtained from these computations. Drag rise Mach number is taken as that M_∞ at which C_D is 0.002 more than C_D at $M_\infty = 0.6$ and these points are also indicated on the figures. Figure 10 shows a comparison of the drag rise boundaries for the two airfoils. It is clear from this figure that the modified lifting symmetric supercritical airfoil NAL 114-36-00 is superior to the original NACA 0012 airfoil from which it was derived, even under considerably off design conditions.

4. Experimental results on NAL 114-36-00 airfoil

Some experimental data on a 150 mm chord NACA 0012 airfoil at a Reynolds number of 4 million (based on chord) had been obtained earlier in the 0.3 m transonic wind tunnel at the National Aeronautical Laboratory (NAL). Therefore tests were conducted on a 150 mm chord NAL 114-36-00 aerofoil in the same tunnel

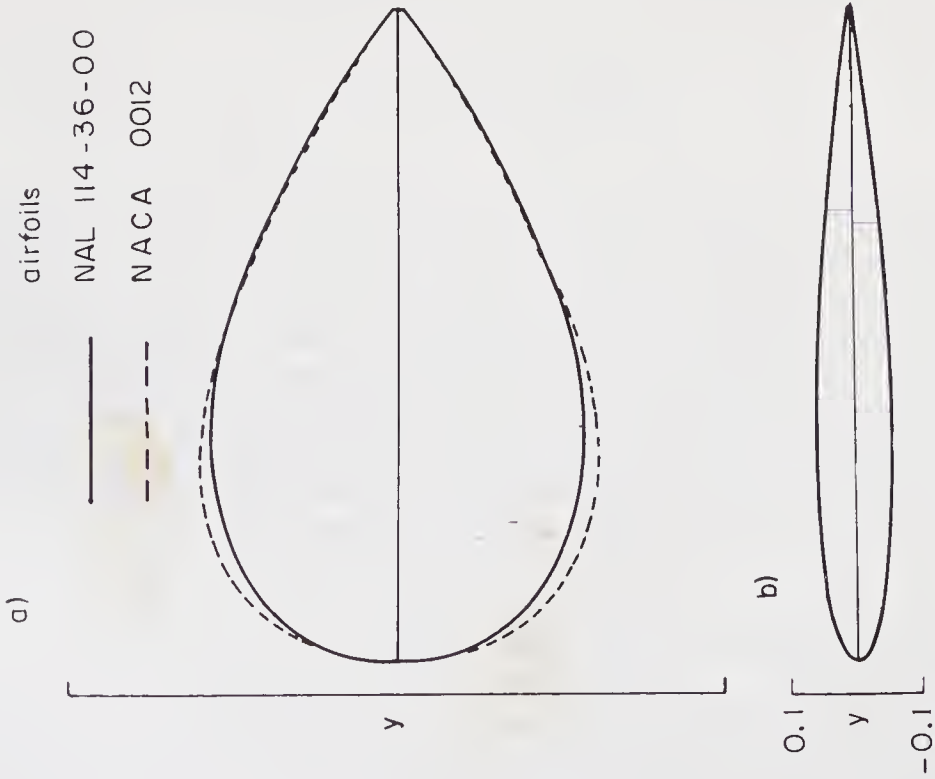


Figure 4. Comparison of the airfoil contours (a) Ordinates enlarged by a factor of 5; (b) actual contour of the airfoil NAL-114-36-00.

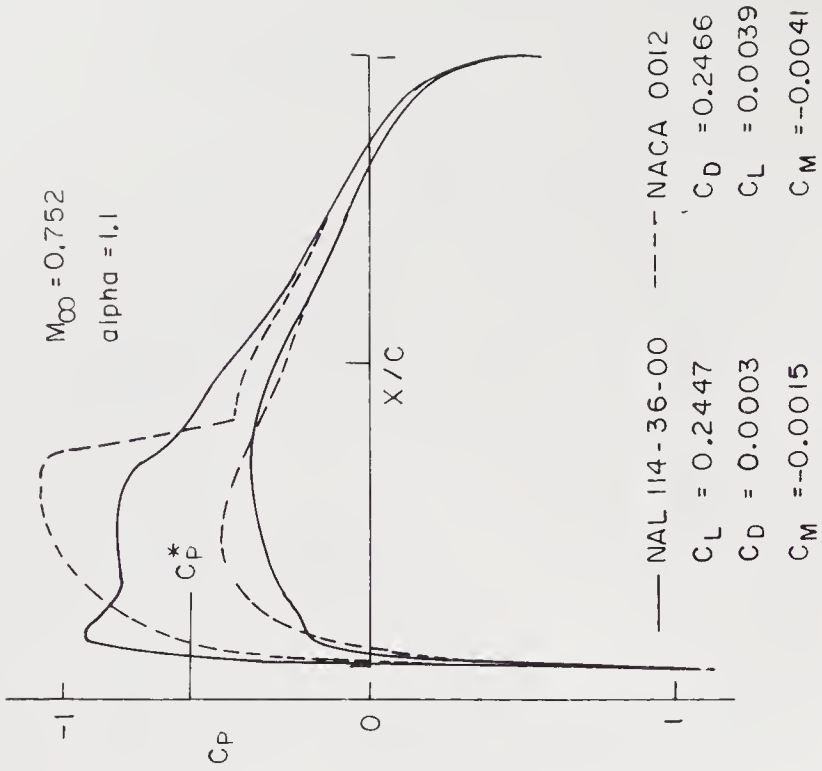


Figure 5. Pressure distribution on NAL-114-36-00 airfoil under design conditions.

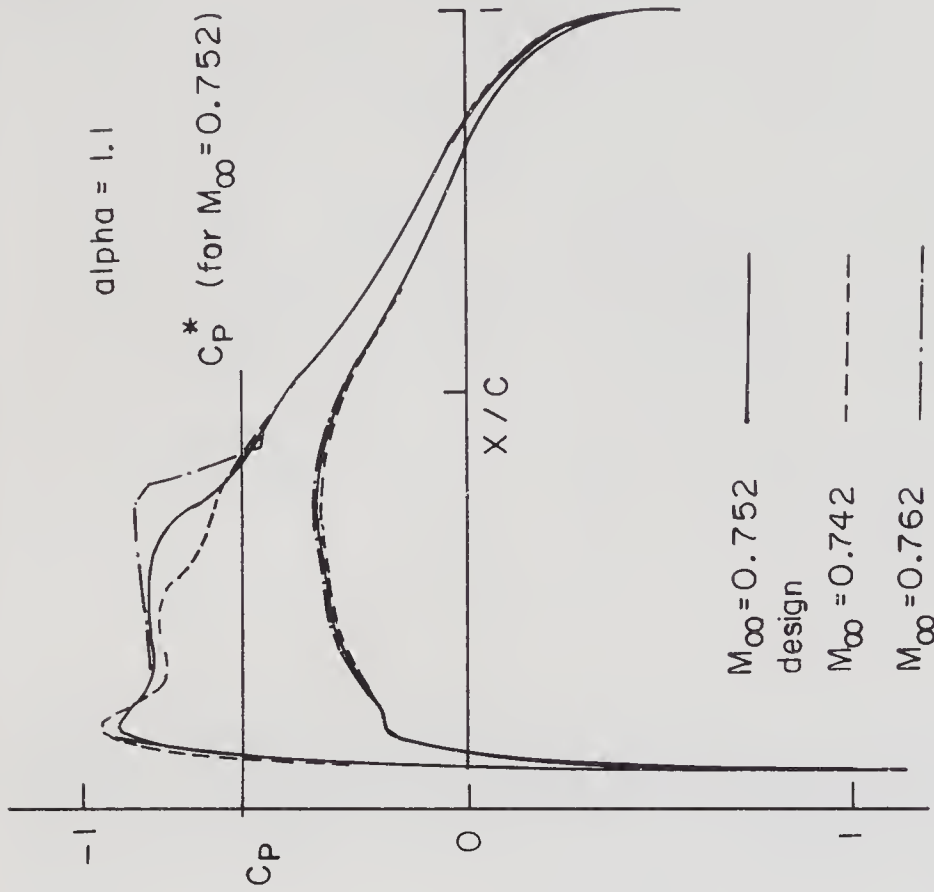


Figure 7. Pressure distribution on NAL airfoil under slightly off design M_∞ values (same design incidence).

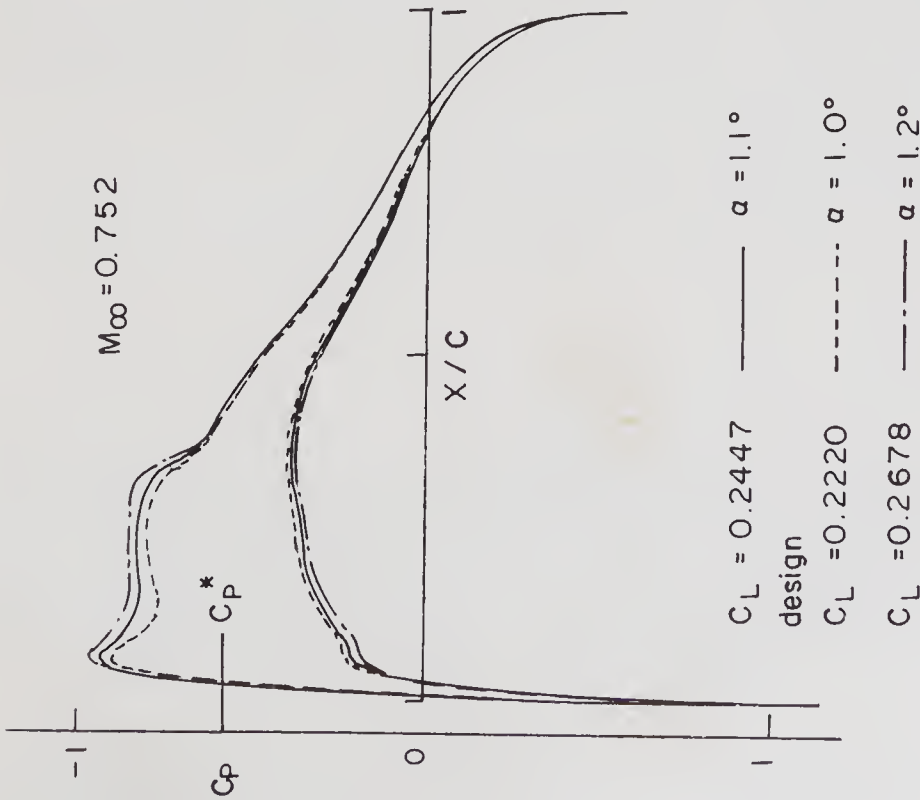


Figure 6. Pressure distribution on NAL airfoil under slightly off design C_L values (same design M_∞).

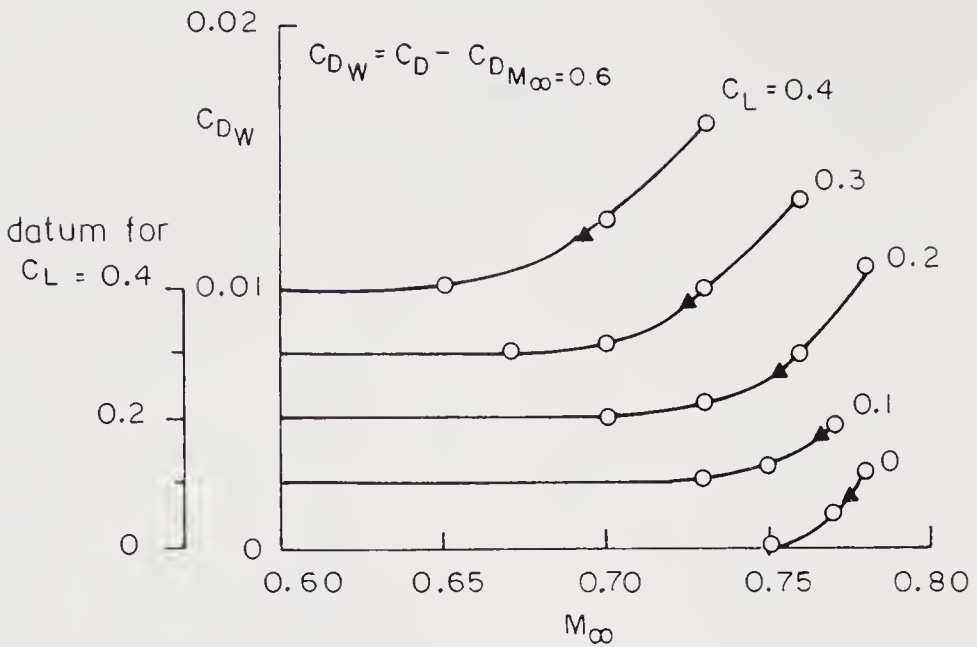


Figure 8. Drag coefficient C_D vs. M_{∞} for constant C_L ; AIRFOIL: NACA 0012.

at the same Reynolds number so that comparison gives the relative performance positively. The NAL 114-36-00 airfoil model was fabricated to an accuracy of ± 0.05 mm in the ordinates.

Figure 11 shows the details of the transonic test section of the 0.3 m wind tunnel. Figure 12 shows the airfoil mounting details.

Figures 13 to 15 show the comparison of the pressure distributions for NAL 114-36-00 and NACA 0012 airfoils at (a) near design conditions of NAL airfoil, (b) at $\alpha = 2.0^\circ$ and near design Mach number, and (c) at higher Mach number but

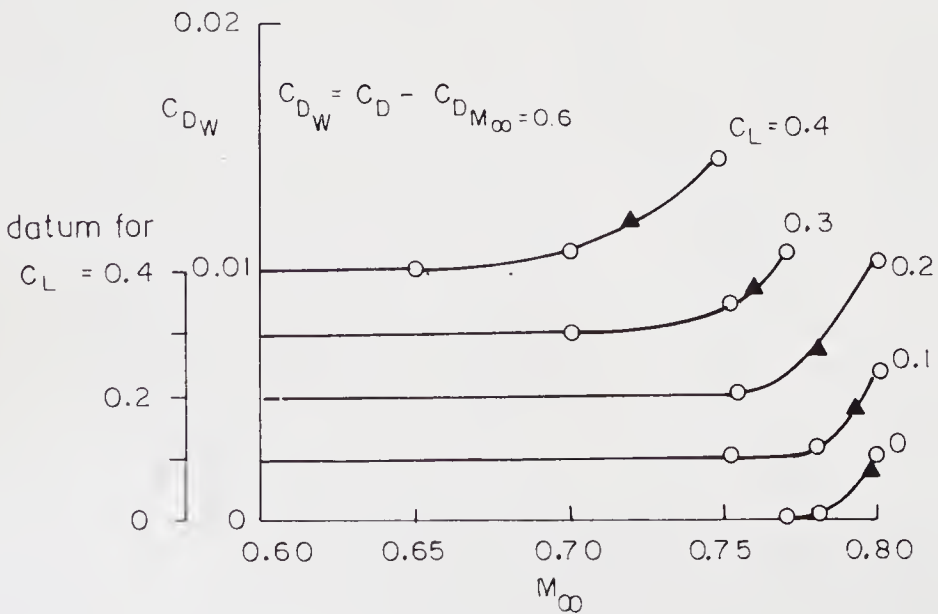


Figure 9. Drag coefficient C_D vs. M_{∞} for constant C_L ; AIRFOIL: NAL-114-36-00.

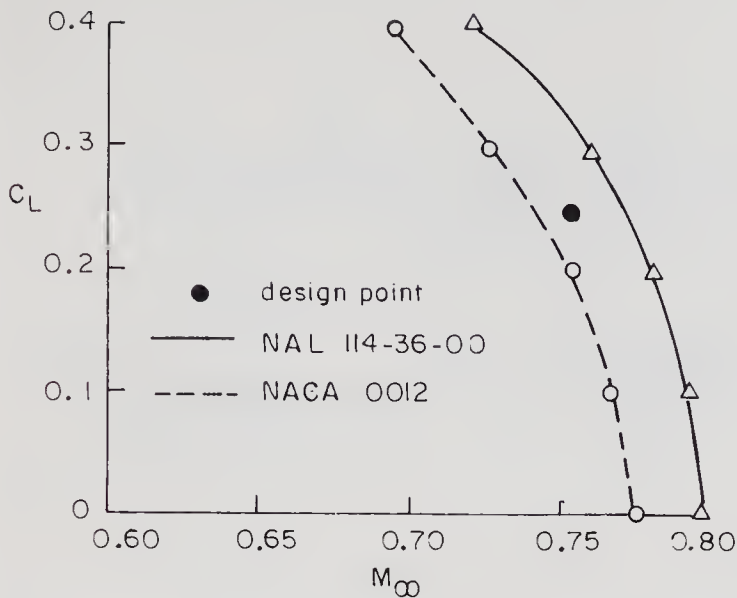


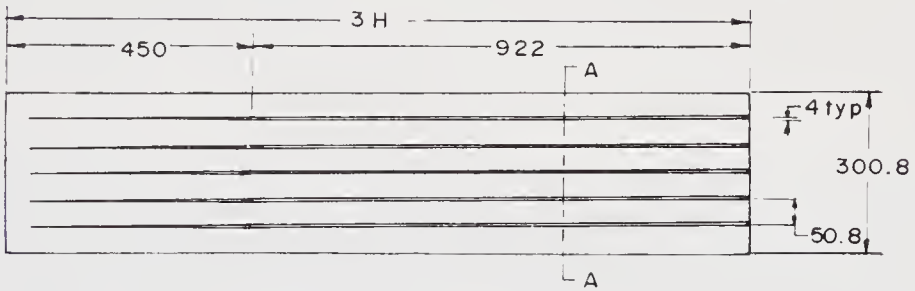
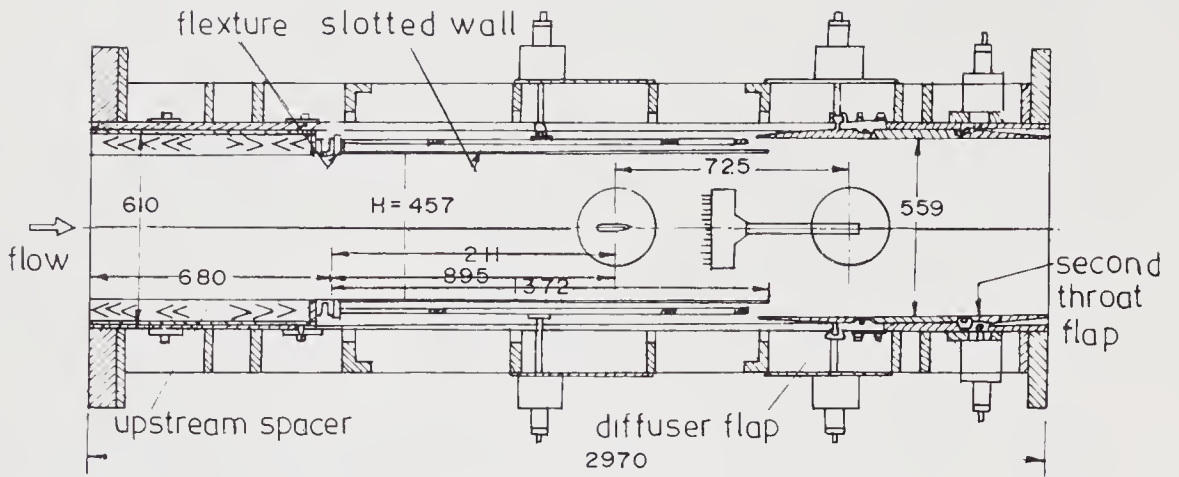
Figure 10. Comparison of drag rise boundaries for the airfoils.

$\alpha = 0^\circ$, respectively. In all these cases, it is clearly seen that the shock strength on the NAL airfoil is much less than that on the NACA 0012 indicating the superiority of the NAL 114-36-00 airfoil over the NACA 0012 airfoil from which it was derived. Unfortunately, because of some problems encountered in the Scani valve system used in the measurements of the wake profiles, the drag data could not be obtained.

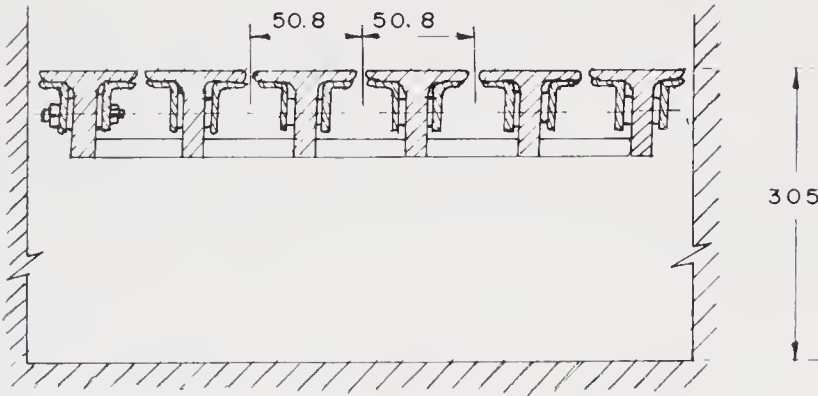
5. Conclusions

Feasibility of designing symmetric supercritical airfoils has been demonstrated. The superiority of the designed airfoil over the conventional airfoil from which it was derived has been demonstrated even under off design conditions, both from computations and experiments.

Dr M Nandan was the co-investigator in the computational studies and Mr K Krishnamurthy was the co-investigator in the experimental studies. Their participation in these studies is gratefully acknowledged. For these studies, the computer and tunnel facilities at the National Aeronautical Laboratory were used. The author thanks Prof. R Narasimha, Director, NAL, Bangalore for them.



details of slotted wall



size : 0.3x0.457x1.37 m
 5 full slots + 2 half slots
 OAR: 0 to 8 %

Figure 11. Details of transonic test-section.

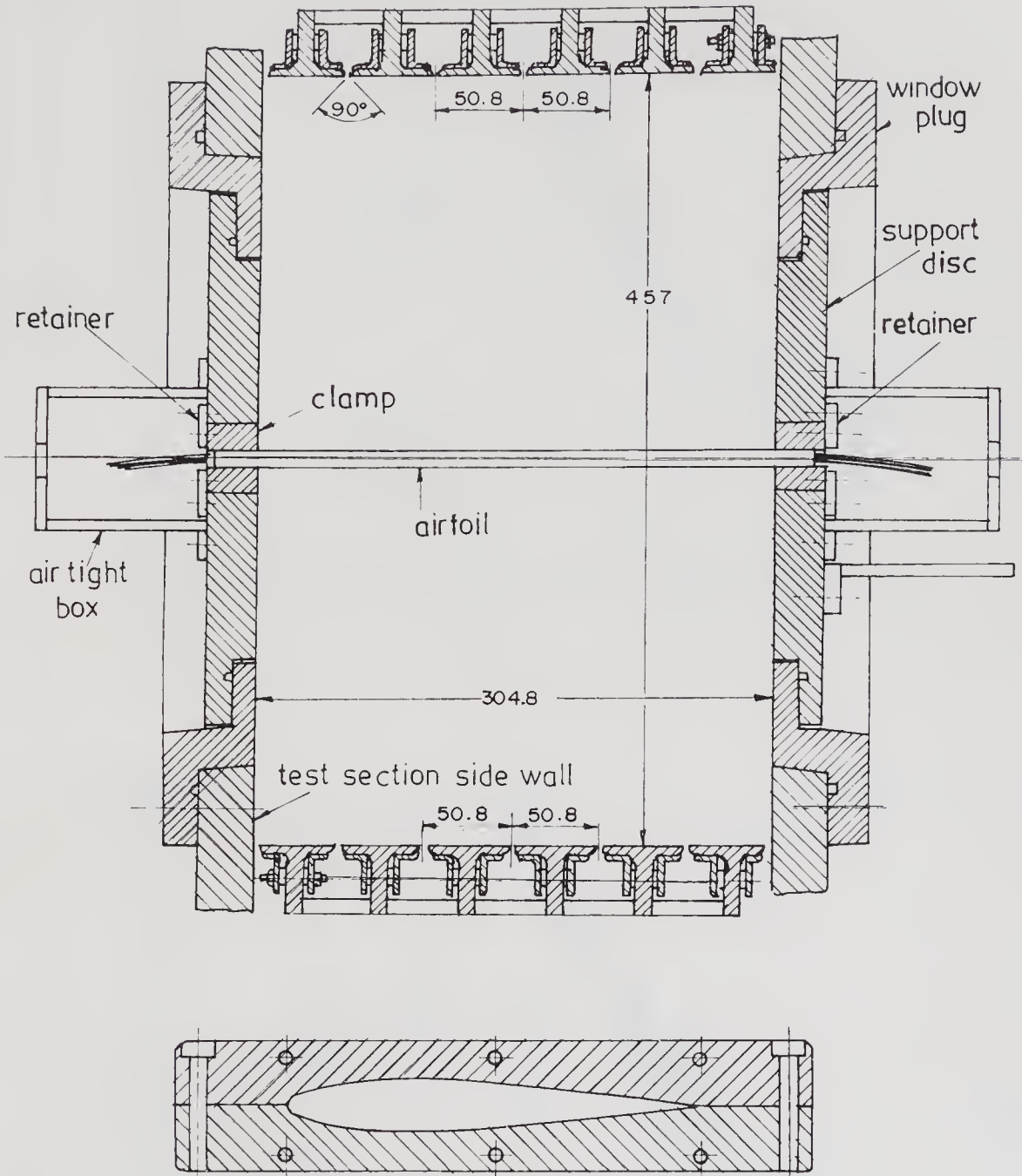


Figure 12. Airfoil mounting details.

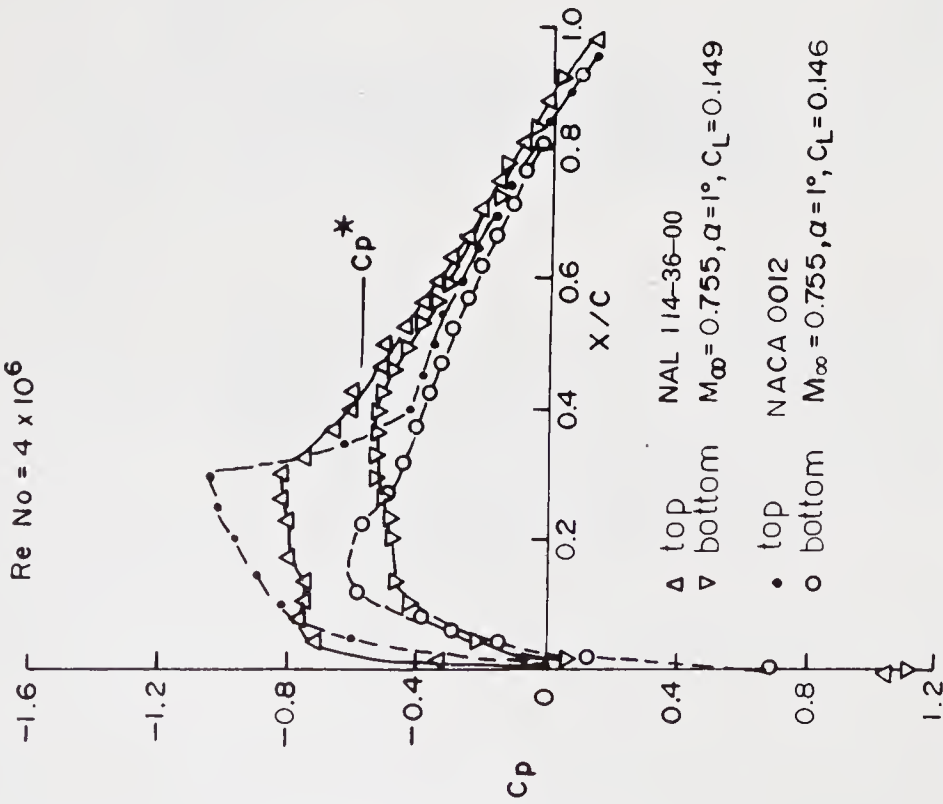


Figure 13. Comparison of experimental pressure distribution between NACA 0012 and modified supercritical airfoil (near design conditions).

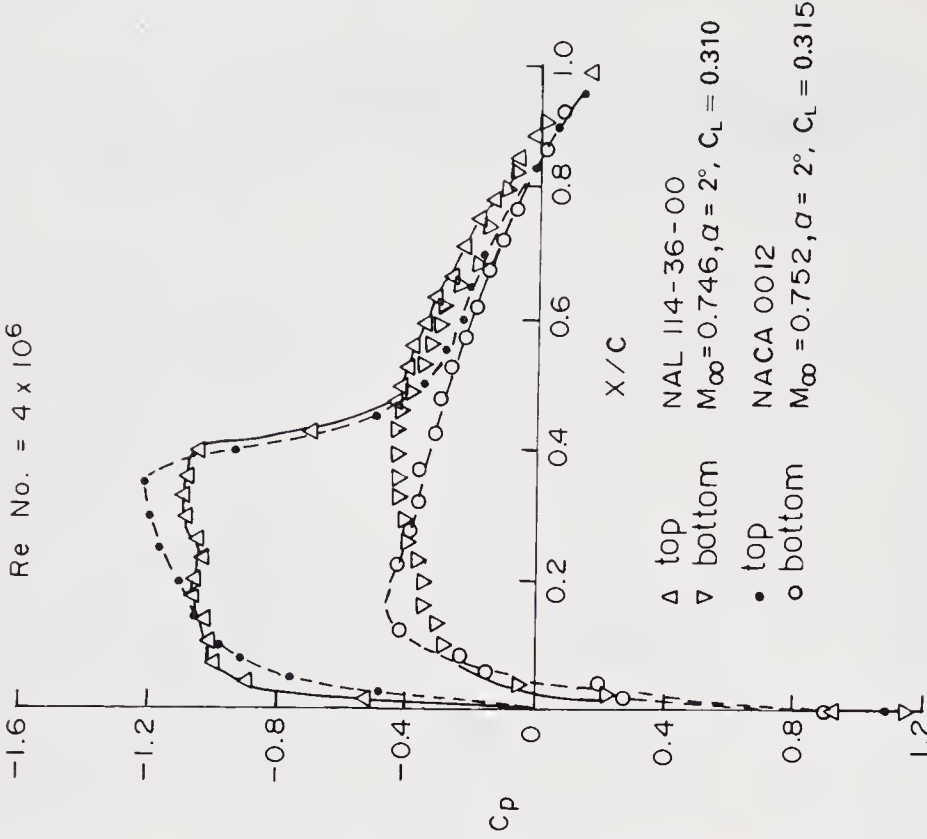


Figure 14. Comparison of experimental pressure distribution between NACA 0012 and modified supercritical airfoil (near design M_∞ and $\alpha = 2^\circ$).

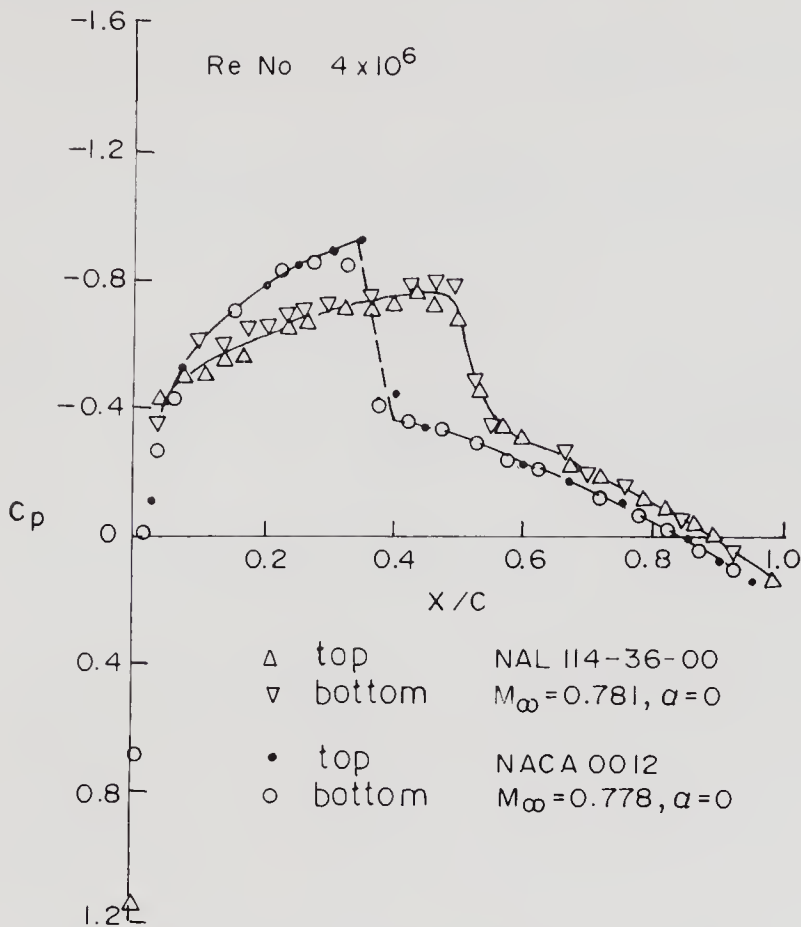


Figure 15. Comparison of experimental pressure distribution between NACA 0012 and modified supercritical airfoil (near design α ; $M_\infty = 0.780$).

List of symbols.

- a local speed of sound;
- C_D drag coefficient;
- C_L lift coefficient;
- C_M pitching moment coefficient;
- C_P pressure coefficient;
- M Mach number;
- q total velocity; $u^2 + v^2$;
- U velocity in the x direction;
- V velocity in the y direction;
- X coordinate direction along the free stream;
- Y coordinate direction perpendicular to the x direction;
- α angle of incidence;
- γ ratio of specific heats;
- ϕ velocity potential;
- ρ density.

Subscripts

∞ free stream conditions.

Superscripts

* critical conditions corresponding to local sonic speed.

References

- Bauer F, Garabedian P, Korn D, Jameson A 1975 *Supercritical wing sections II* (Berlin, Heidelberg, New York: Springer-Verlag)
- Nandan M, Ramaswamy M A 1985 *J. Aeronaut. Soc. India* 36: 15–21
- Ramaswamy M A 1976 Revival of transonic aerodynamic research, Prelude on Workshop in Transonic Aerodynamics, Bangalore
- Sobieczky H, Yu N J, Fung K Y, Seebass A R 1979 *AIAA J.* 17: 722–729

Monte Carlo simulation for molecular gas dynamics

S M DESHPANDE and P V SUBBA RAJU[†]

Department of Acrospace Engineering, Indian Institute of Science,
Bangalore 560 012, India

[†] Aerodynamics Division, Vikram Sarabhai Space Center, Trivandrum
695 022, India

Abstract. The dynamics of low-density flows is governed by the Boltzmann equation of the kinetic theory of gases. This is a nonlinear integro-differential equation and, in general, numerical methods must be used to obtain its solution. The present paper, after a brief review of Direct Simulation Monte Carlo (DSMC) methods due to Bird, and Belotserkovskii and Yanitskii, studies the details of the DSMC method of Deshpande for mono as well as multicomponent gases. The present method is a statistical particle-in-cell method and is based upon the Kac-Prigogine master equation which reduces to the Boltzmann equation under the hypothesis of molecular chaos. The proposed Markoff model simulating the collisions uses a Poisson distribution for the number of collisions allowed in cells into which the physical space is divided. The model is then extended to a binary mixture of gases and it is shown that it is necessary to perform the collisions in a certain sequence to obtain unbiased simulation.

Keywords. Low density flow; Boltzmann equation; Kac-Prigogine master equation; collision dynamics; Monte Carlo method; unbiased and consistent estimator.

1. Introduction

With the advent of space vehicles flying at altitudes of several hundred kilometers or more, it has become necessary to study aerodynamics at low densities. The chief parameter that governs such flows is the Knudsen number Kn , which is the ratio of the mean free path of molecules between collisions (say λ) to a characteristic linear dimension of the body in flight (say L). Figure 1 shows the variation of λ with altitude in the International Tropical Reference Atmosphere (ITRA) (Ananthasayanam & Narasimha 1986). It is seen that for $L \approx 1$ m, the Knudsen number $Kn \approx 1$ at an altitude of 110 km. At much lower altitudes, Kn is small and by

A part of the material in this paper was presented at the Minisymposium 2 of the ICIAM 87 held in Paris during June 29–July 3, 1987

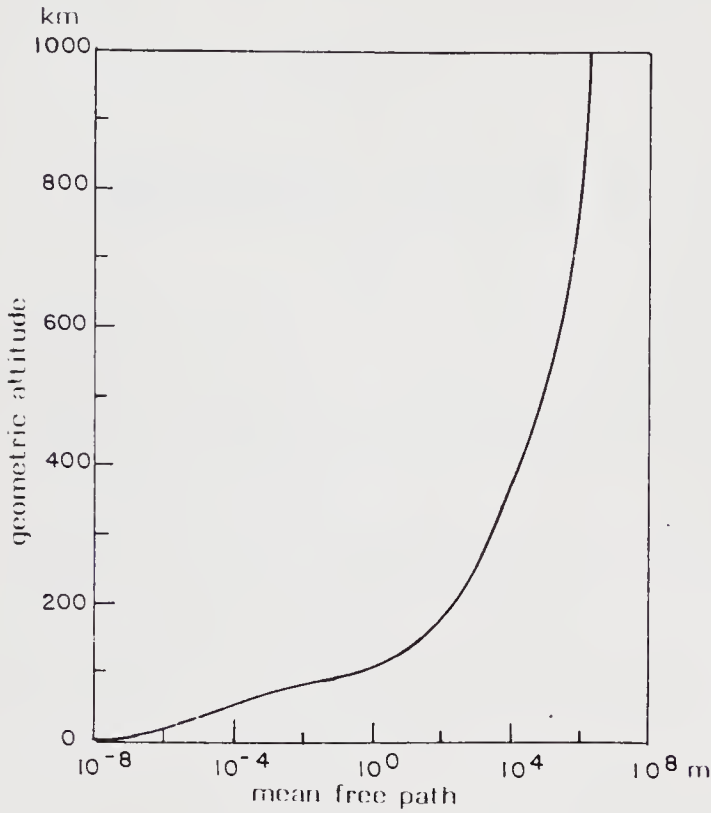


Figure 1. Variation of mean free path with altitude in the International Tropical Reference Atmosphere (1986).

implication the number of intermolecular collisions (in volume L^3) is much larger than the molecular impacts with the body. Consequently, the gas is very nearly in thermodynamic equilibrium everywhere and may be treated as obeying the laws of classical gas dynamics to a good approximation. In the opposite limit of a large Knudsen number, the molecules hardly collide among themselves; the 'free molecule' flow that results is then dominated by molecular impacts with the body and the gas is everywhere far from thermodynamic equilibrium. The molecular gas dynamics regime starts roughly when $\text{Kn} = O(1)$ and continues all the way upto $\text{Kn} \rightarrow \infty$. In this regime the governing equation is the well-known Boltzmann equation of the kinetic theory of gases. This is a nonlinear integro-differential equation governing the spatio-temporal evolution of the one-particle velocity distribution function $f(t, \mathbf{x}, \mathbf{v})$, and is given by

$$(\partial f / \partial t) + \mathbf{v} \cdot (\partial f / \partial \mathbf{x}) + \mathbf{F} \cdot (\partial f / \partial \mathbf{v}) = \int [f(\mathbf{v}')f(\mathbf{w}') - f(\mathbf{v})f(\mathbf{w})] g b \, db \, d\varepsilon \, D\mathbf{w}, \quad (1)$$

where \mathbf{v} is the molecular velocity, \mathbf{x} is the position vector, \mathbf{F} is the external force per unit mass; \mathbf{v} , \mathbf{w} are the precollision velocities of a colliding pair; b is the impact parameter; ε is the angle between the plane of motion and a reference plane (see figure 2), and $D\mathbf{w}$ is an infinitesimal volume in velocity space. Further, in (1) we have written $f(\mathbf{v})$ in place of $f(t, \mathbf{x}, \mathbf{v})$ and shown only one integration symbol for brevity. The velocities \mathbf{v}' , \mathbf{w}' are functions of \mathbf{v} , \mathbf{w} , ε and the scattering angle θ (see figure 2) and are given by

$$\mathbf{v}' = \mathbf{v} + \mathbf{k}(\mathbf{k}, \mathbf{g}), \quad \mathbf{w}' = \mathbf{w} - \mathbf{k}(\mathbf{k}, \mathbf{g}), \quad (2)$$

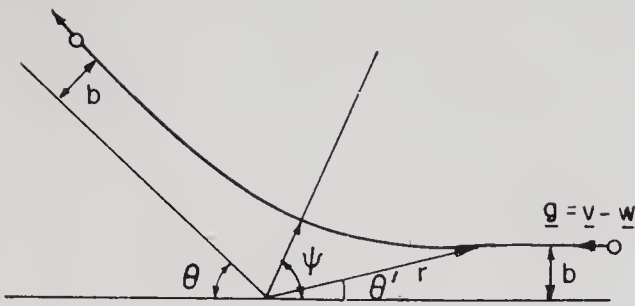


Figure 2. Trajectory of a particle in a central force field.

where $\mathbf{g} =$ relative velocity of colliding pair $= \mathbf{v} - \mathbf{w}$ (3)

and \mathbf{k} is the unit vector given by

$$\mathbf{k} = [\cos(\theta/2) \cos \varepsilon, \cos(\theta/2) \sin \varepsilon, \sin(\theta/2)]. \quad (4)$$

The scattering angle θ has to be determined by the two-body collision dynamics and, in general, depends on the impact parameter b , relative speed g and the intermolecular force law.

It is clear that obtaining a solution of (1) for bodies in low density flows is a formidable task and no exact solution to (1) is known except when the gas is everywhere in thermodynamic equilibrium. Over the last several years the statistical-particle-in-cell method or the Monte Carlo method for obtaining the numerical solution of the Boltzmann equation has been developed and successfully applied to a variety of low density flows, some of the most recent examples being hypersonic transitional flows by Moss (1986) and Advanced Orbital Transfer Vehicle (AOTV) entry flows by Bird (1986). We will consider in the following sections of the paper the basics of DSMC (Direct Simulation Monte Carlo) and some aspects of its application to free molecule as well as transitional flows. The development of various computer codes and the Kac-Prigogine equation based DSMC were undertaken under various ISRO*-sponsored research contracts spanning the period from 1970 to 1983.

2. Free molecule drag calculation by Monte Carlo

In free molecule flows the intermolecular collision term in (1) is zero, and the flow field changes because of molecular impacts with the body. It is then possible to calculate the drag and lift coefficients as well as the Stanton number by simply calculating the momentum and energy transferred to the body by the impacts. In fact, assuming diffuse reflection at the body surface the free molecule drag coefficient C_{Dfm} for an arbitrary body is given by

$$C_{Dfm} = 1/(\frac{1}{2}\rho_{\infty} U_{\infty}^2 A_{ref}) \int \hat{dS}(p) \int_{v_n > 0} D\mathbf{v} [v_n^2 + v_n(\pi R T_w/2)^{\frac{1}{2}} \cdot n_x(p) + v_{t1} v_n t_{1x}(p) + v_{t2} v_n t_{2x}(p)] F_{\infty}, \quad (5)$$

* Indian Space Research Organisation

where ρ_∞ = density in the free stream,

A_{ref} = reference area,

F_∞ = the free-stream Maxwellian distribution

$$= n_\infty (\beta_\infty / \pi)^{3/2} \exp [-\beta_\infty (\mathbf{v} - \mathbf{U}_\infty)^2], \quad (6)$$

n_∞ = free stream number density,

$\beta_\infty = 1/(2RT_\infty)$, T_∞ = free stream temperature,

R = gas constant per unit mass,

\mathbf{U}_∞ = mean velocity in the free stream,

∂B = body surface,

$dS(p)$ = elementary area on ∂B around point P ,

$D\mathbf{v} = dv_1 dv_2 dv_3$ = infinitesimal volume in velocity space (v_1, v_2, v_3) ,

$n_x(p)$, $t_{1x}(p)$, $t_{2x}(p)$ are respectively the x -components of normal vector \mathbf{n} and \mathbf{t}_1 , \mathbf{t}_2 are two tangent vectors to the body surface ∂B at the point P , and v_n, v_{t1}, v_{t2} are the corresponding components of velocity \mathbf{v} .

The limits of integration with respect to \mathbf{v} in (5) are defined by $v_n > 0$. By defining the characteristic function $X(v_n) = 1$, if $v_n > 0$, $= 0$ otherwise, the integral in (1) can be written in the compressed form

$$C_{Dfm} = \int_{\partial B} dS(p) \iiint_{-\infty}^{+\infty} D_F(\mathbf{v}, p) X(v_n) D\mathbf{v}, \quad (7)$$

where

$$D_F(\mathbf{v}, p) = [v_n^2 + v_n(\pi RT_w/2)^{1/2} n_x(p) + v_{t1} v_n t_{1x}(p) + v_{t2} v_n t_{2x}(p)] F_\infty / (\frac{1}{2} \rho_\infty U_\infty^2 A_{\text{ref}}).$$

The sample mean Monte Carlo estimator for C_{Dfm} can now be constructed as follows. First, we choose a finite volume Ω in velocity space in such a way that the contribution to C_{Dfm} due to velocities falling outside Ω is negligibly small. For example, Ω can be taken as a cube centred around \mathbf{U}_∞ and having sides equal to several times the mean thermal speed $1/\beta_\infty^{1/2}$. The body surface is then divided into several elemental surfaces $A_1, A_2 \dots A_N$ as shown in figures 3 and 4 where the SLV-3 surface is paneled. Then the sample mean Monte Carlo estimator for C_{Dfm} is given by

$$C_{Dfm} = (\Omega_A/N) \sum_{i=1}^N D_F(v_i, p_i) X(v_{ni}) (A_i/A) \quad (8)$$

where P_i is a point uniformly distributed on the SLV-3 surface, \mathbf{v}_i is a random velocity vector uniformly distributed within the volume Ω , and A is the total area of all the panels on the body. Figure 5 shows the free molecule drag coefficient of SLV-3 with zero angle of attack and diffuse reflection using the above sample mean Monte Carlo estimator at various speed ratios. Also shown in the same figure is the scatter of the estimator. The statistical scatter is always present in any Monte Carlo estimator and is a very characteristic feature of the Monte Carlo method. The details of surface paneling, drawing of random numbers, estimation of variance,

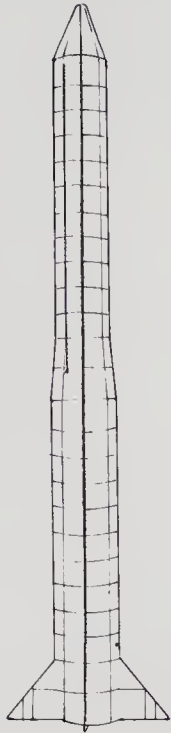


Figure 3. Paneling of SLV-3 surface (side view).

use of variance reduction techniques and calculation of drag coefficients for various bodies including SLV-3 are given in Deshpande & Subba Raju (1973).

3. DSMC method for the Boltzmann equation

3.1 Introduction

For the purpose of Monte Carlo simulation of (1) we drop the $\mathbf{F} \cdot (\partial f / \partial \mathbf{v})$ term and the equation becomes

$$\begin{aligned}
 (\partial f / \partial t) + \mathbf{v} \cdot (\partial f / \partial \mathbf{x}) &= J(f, f) \\
 &= \int [f(t, \mathbf{x}, \mathbf{v}') f(t, \mathbf{x}, \mathbf{w}') - f(t, \mathbf{x}, \mathbf{v}) f(t, \mathbf{x}, \mathbf{w})] g \sigma(\Omega, g) D\mathbf{w} d\Omega,
 \end{aligned}
 \tag{9}$$

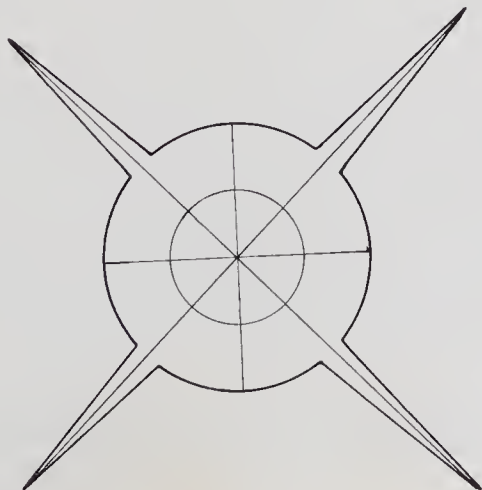


Figure 4. Approximate representation of SLV-3 base (enlarged).

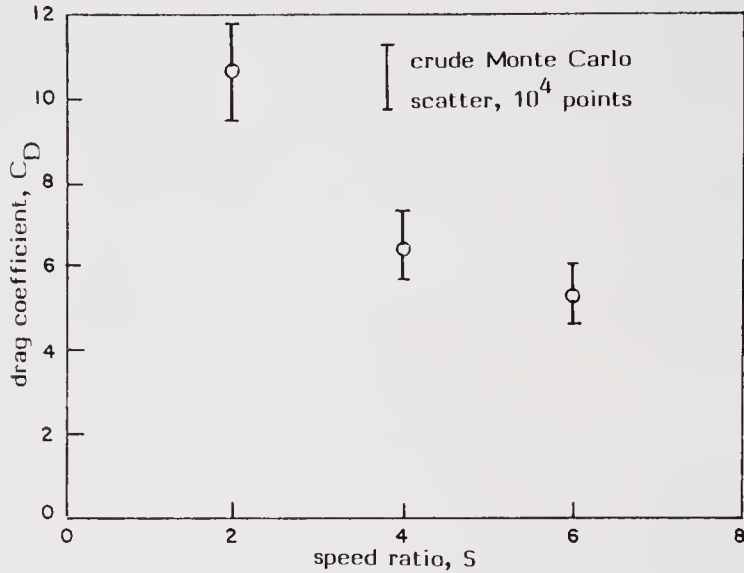


Figure 5. Drag coefficient for SLV-3 at zero angle of attack in free molecule flow, diffuse reflection.

where $\sigma d\Omega$ is the differential scattering cross section, $d\Omega = \sin \theta d\theta d\epsilon$ is the infinitesimal solid angle, and θ is the scattering angle. In terms of impact parameter b introduced in §1 we have $\sigma d\Omega = b db d\epsilon$. The most difficult problem in seeking a solution of (9) has been the tackling of the quadratic nonlinear collision term $J(f, f)$. Among different numerical methods used the DSMC of Bird (1970, 1976) has been very successful in handling a variety of multidimensional flows in aerospace engineering. The faithfulness of the Time Counter (TC) strategy of Bird has always been doubted (Deshpande 1978; Pullin 1974; Yanitskii 1973). For example, Yanitskii (1973) has shown that the collision-relaxation model of Bird is not satisfactory in the sense that Bird's method distorts the actual distribution of the number of collisions q and further that the method gives a biased value of the mathematical expectation of q . This bias becomes vanishingly small as the number of molecules per cell tends to infinity. Further, Deshpande (1976) has pointed out that while trying to simulate the collision term Bird (1970) suggests that a time counter be kept for each class of molecules whose velocity vectors fall within \mathbf{v} and $\mathbf{v} + d\mathbf{v}$. On the other hand, in all applications of this method to specific flow problems, a time counter is kept for each cell in physical space, that is, for all molecules in a physical cell. No analysis is made regarding the possible approximation involved. Bird (1970) has observed that the Monte Carlo would be more directly comparable to the Boltzmann equation if a time counter is kept for each molecule and suitably advanced. We will show that for faithful simulation it is *not* necessary to keep a time counter for each cell[†].

The motivation for the Kac-Prigogine based DSMC arose from the above doubts concerning the faithfulness of the TC strategy of Bird. The connection between the master equation and the Boltzmann equation was exploited by Deshpande (1976) to develop an RCN (random collision number) strategy. The theoretical basis of the unbiasedness and consistency of the RCN method was studied in considerable detail

[†] In a private communication with the author in 1976 Bird stated that he no longer speculates on the possibility of using a separate time counter for each molecule.

by Deshpande (1978). A modified RCN (MRCN) method was developed by Deshpande *et al* (1979) to keep the computing task proportional to the number of particles by using the sampling technique to determine the expected number of collisions per cell. A considerably simpler and transparent proof of the Kac-Prigogine-equation-based DSMC method of Deshpande was given by Deshpande (1982) in a paper at a workshop on Monte Carlo methods. This method was later extended to multicomponent mixtures by Deshpande (1983). Further, the above DSMC method was made computationally more efficient by Deshpande & Subba Raju (1981) by using operator splitting.

It may be noted here that Belotserkovskii & Yanitskii (1975) were the first to use the master equation to develop the statistical particle in cell method, termed the tracer method by Yen (1985). Their method is different from that of Deshpande (1976) in that Belotserkovskii & Yanitskii (1975) use a time counter while Deshpande uses the Poisson distribution to draw the allowed number of collisions in a cell. A review of different DSMC methods is given by Yen (1985) and by Nanbu (1986). As we shall see later some comments of Nanbu (1986) about Deshpande's method are not entirely correct. We shall study here the theoretical basis of the Kac-Prigogine equation-based DSMC of Deshpande for mono and multicomponent gases.

3.2 Kac-Prigogine master-equation-based DSMC

We write the Boltzmann equation (9) as

$$(\partial f / \partial t) = (\partial f / \partial t)_{\text{con}} + (\partial f / \partial t)_{\text{col}} \quad (10)$$

where

$$(\partial f / \partial t)_{\text{con}} = \text{streaming term} = -\mathbf{v} \cdot (\partial f / \partial \mathbf{x}), \quad (11)$$

$$(\partial f / \partial t)_{\text{col}} = \text{collision term} = J(f, f). \quad (12)$$

Using the operator splitting theory of Yanenko (1971) we construct the solution of (9) in two steps as:

$$(\partial f / \partial t) = (\partial f / \partial t)_{\text{con}}, \quad \overline{f^{n+1}} = O_{\text{con}}(\Delta t) f^n = f^n + \Delta t (\partial f / \partial t)_{\text{con}}^n, \quad (13)$$

$$\begin{aligned} (\partial f / \partial t) &= (\partial f / \partial t)_{\text{col}}, \quad f^{n+1} = O_{\text{col}}(\Delta t) \overline{f^{n+1}} \\ &= \overline{f^{n+1}} + \Delta t J(\overline{f^{n+1}}, \overline{f^{n+1}}), \end{aligned} \quad (14)$$

where f^n = velocity distribution at the time level n , and $\overline{f^{n+1}}$ is the solution at the intermediate time level. The solution $\overline{f^{n+1}}$ given by (13) is the solution when the collision term is dropped and hence will represent the free molecule flow, while (14) is the solution with only the collision term present and thus represents the solution of the homogeneous Boltzmann equation. The decoupling between the collision and streaming is possible due to the splitting and the resultant solution

$$\begin{aligned} f^{n+1} &= O_{\text{con}}(\Delta t) O_{\text{col}}(\Delta t) f^n + O(\Delta t^2) \\ &= O_{\text{col}}(\Delta t) O_{\text{con}}(\Delta t) f^n + O(\Delta t^2), \end{aligned} \quad (14a)$$

is only first-order accurate in time. It is now necessary to develop methods for solving the split equations or equivalently for constructing the solution operators O_{con} and O_{col} .

The solution operator O_{con} can be easily constructed as follows. We choose a sufficiently large box (see figure 6) around a body to approximate the infinite flow field. The computational domain is then divided into a network of cells (or finite volumes), the molecules outside the box are assumed to obey the free stream velocity distribution which in many cases is the Maxwellian distribution defined by (6). Several thousands of molecules are distributed initially in the box with their positions distributed in space and their velocities are uniformly drawn from the free stream Maxwellian distribution. Once the initialization is over the simulation of $(\partial f/\partial t) + \mathbf{v} \cdot (\partial f/\partial \mathbf{x}) = 0$ is done by moving along the characteristics

$$\begin{aligned} (df/ds) &= (\partial f/\partial t)(dt/ds) + (\partial f/\partial \mathbf{x}) \cdot (d\mathbf{x}/ds), \\ (dt/ds) &= 1, \quad (d\mathbf{x}/ds) = \mathbf{v}, \end{aligned} \quad (15)$$

that is, we just move the molecules with their velocities over the time interval Δt . During this movement the molecules may quit the box, may hit the body and get reflected, and thus transfer momentum and energy to the body. The various possibilities are taken care of by developing (1) a subroutine for influx of molecules into the box through the boundaries, (2) a subroutine for determining the intersection of the molecular trajectory with the body surface, (3) a subroutine for obtaining reflected velocities after impact with the body, and (4) a subroutine for arranging a molecular list according to the cell numbers they occupy. Subroutines CONV and ARANG were developed by Deshpande *et al* (1977) and validated against available results for a cone and cone-cylinder in a free molecule flow.

3.3 Simulation of collisions

The Markoff process for the simulation of the homogeneous Boltzmann equation (12) is based on the Kac-Prigogine model

$$\begin{aligned} \frac{\partial P_0}{\partial t} &= \frac{1}{\text{Vol}} \sum_{1 < j < k < N} \int d\Omega_{jk} \sigma(\Omega_{jk}, g_{jk}) g_{jk} \\ &\times [P_0(t, V'_{jk}) - P_0(t, V)], \end{aligned} \quad (16)$$

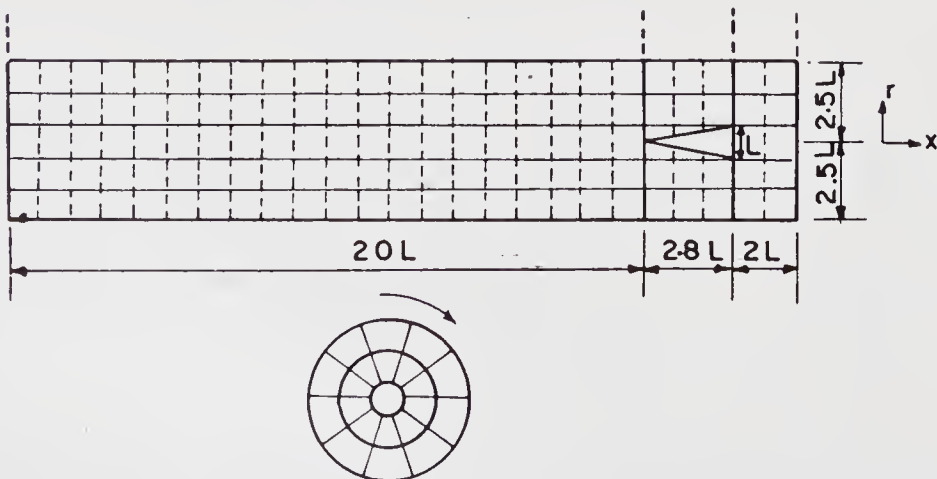


Figure 6. Division of flow field for computing flow past a cone.

where P_0 is the N -particle velocity distribution function,

$$V = \{\mathbf{v}_1, \mathbf{v}_2, \dots, \mathbf{v}_N\}, \quad V'_{jk} = \{\mathbf{v}_1, \mathbf{v}_2, \dots, \mathbf{v}'_j, \dots, \mathbf{v}'_k, \dots, \mathbf{v}_N\},$$

$$\mathbf{g}_{jk} = \mathbf{v}_j - \mathbf{v}_k. \quad (17)$$

The master equation (16) governs the time evolution of the N -particle distribution due to collisions among N molecules in the cell whose volume is denoted by "Vol". One of the very important properties of the Kac-Prigogine equation (16) is that under the hypothesis of molecular chaos

$$P_0(t, V) = \Phi(t, \mathbf{v}_1) \Phi(t, \mathbf{v}_2) \dots \Phi(t, \mathbf{v}_N), \quad (18)$$

where $\Phi(t, \mathbf{v})$ is the one-particle velocity distribution function, the master equation reduces to the Boltzmann equation. Further, the molecular chaos once established perpetuates in time provided N is very large, and the initial validity of the chaos is ensured by taking

$$P_0(t_0, V) \propto F_\infty(\mathbf{v}_1) F_\infty(\mathbf{v}_2) \dots F_\infty(\mathbf{v}_N). \quad (19)$$

F_∞ is the free stream Maxwellian defined by (6).

The relationship between the simulation method and the master equation becomes transparent if we write (16) in the form

$$(\partial P_0 / \partial t) = B(O - I)P_0(t, V), \quad (20)$$

where

$$B = \text{number of binary interactions per unit volume per unit time} = \text{SUM}/\text{Vol},$$

$$\text{SUM} = \sum_{1 \leq i < r \leq N} \int g_{ir} \sigma(\Omega_{ir}, g_{ir}) d\Omega_{ir}, \quad (21)$$

$$OP_0 = \sum_{1 \leq j < k \leq N} \int p_{jk}(\sigma_{jk}, g_{jk}) P_0(V'_{jk}) d\Omega_{jk}, \quad (22)$$

$$p_{jk}(\Omega_{jk}, g_{jk}) = [g_{jk} \sigma(\Omega_{jk}, g_{jk})] / \text{SUM}, \quad (23)$$

I = identity operator.

The operator O gives OP_0 which is the new N -particle velocity distribution after one collision. Everytime there is a collision the N -particle velocity distribution undergoes a change $(O - I)P_0(t, V)$. As there are B binary interactions per unit time per unit volume the total change due to them will be $B(O - I)P_0$. Equation (20) is obtained by equating this change per unit time to $\partial P_0 / \partial t$. A formal solution of (20) for a small time interval Δt is

$$P_0(t + \Delta t, V) = \exp(-B\Delta t) \exp(\Delta t B O) P_0$$

$$= \exp(-B\Delta t) \sum_{r=0}^{\infty} [(\Delta t B)^r / r!] O^r P_0(t, V). \quad (24)$$

Recognizing that

$$[(\Delta t B)^r / r!] \exp(-B\Delta t), \quad (25)$$

is a Poisson distribution, it follows from (24) that $P_0(t + \Delta t, V)$ is the mathematical expectation of $O^r P_0(t, V)$ with r obeying a Poisson distribution having a mean equal to $B\Delta t$.

The Monte Carlo simulation of the homogeneous Boltzmann equation (12) can thus be performed by the following algorithm:

- (a) Calculate the binary interaction rate B by using (21), which requires relative velocity for every possible colliding pair, and the differential scattering cross-section $\sigma(\Omega, g)$.
- (b) Draw a random variable r from the Poisson distribution $\exp(-B\Delta t)(B\Delta t)^r/r!$
- (c) Select a pair of molecules $\mathbf{v}_j, \mathbf{v}_k$ and solid angle Ω_{jk} from the probability distribution $p_{jk}(\Omega_{jk}, g_{jk})$.
- (d) For the collision partners drawn in step (c) determine the post-collision velocities $\mathbf{v}'_j, \mathbf{v}'_k$ from collision dynamics and replace \mathbf{v}_j and \mathbf{v}_k by \mathbf{v}'_j and \mathbf{v}'_k . The determination of the post-collision velocities requires the use of (2) which in turn requires the values of the azimuthal angle ε and the scattering angle θ . The latter can be determined from the dynamics of two-body collision.
- (e) Repeat the steps (c) and (d) r times.

Several comments are in order about the Kac-Prigogine-equation-based DSMC method. First, step (a) requires the calculation of $N_c = N(N-1)/2$ pairs of relative velocities g_{jk} as j and k run from 1 to N . Hence, the collision strategy described above will require an operation count that goes like N^2 . It is preferable to have an operation count that goes like N especially when N is large. However, whenever the number of molecules per cell is very large (as happens when the flow is collision-dominated) it is possible to estimate the SUM given by (21) by a sampling procedure. In order to determine SUM in such a case all that is required is to randomly draw N pairs g_1, g_2, \dots, g_N corresponding to partners $(i_1, r_1), (i_2, r_2), \dots, (i_N, r_N)$, and then determine SUM by the sample mean Monte Carlo estimator

$$\text{SUM} = \sum_{j=1}^N \int g_j \sigma(\Omega, g_j) d\Omega. \quad (26)$$

Further, several variance reduction techniques can be employed (importance sampling, stratified sampling etc.) to construct an estimator for SUM having smaller variance than for the sample mean estimator (26). The sample mean estimator (26) is the basis of the MRCN method of Deshpande *et al* (1979). In summary, the present DSMC can be easily designed to have an operation count that is linearly related to the number of molecules in a cell. This point has not been recognised by Nanbu (1986) in his recent article on "Theoretical basis of the DSMC method" where he claims that unless the molecular model is Maxwellian, only Bird's method and Nanbu's method modified by Babovsky are of practical use as the computing task is proportional to the number of particles. This claim as we have seen is not entirely correct because in the present DSMC method also the computing task is proportional to the number of particles. Further Nanbu (1986) has stated that Deshpande (1978) "tried to derive the method from the Kac equation but his derivation is rather a kind of plausibility argument". It is difficult to know the basis of this statement. Unbiasedness and consistency of DSMC of Deshpande were proven in the report of Deshpande (1978). The analysis of the present paper is the

same as that of Deshpande (1982) and is much more transparent than the one given by Deshpande (1978) earlier. The actual calculations of low density flows past a cone at Knudsen number close to unity (see Deshpande *et al* 1978) show that the RCN strategy and the TC strategy of Bird require very nearly the same CPU time even though the RCN strategy requires an operation count that goes like N^2 instead of like N for the TC strategy. This is primarily because the number of operations required to advance the solution from one time level to the next is dominated by the convection operator O_{con} and *not* by the collision operator O_{col} for flows having $\text{Kn} = O(1)$.

The step (a) above requires the calculation of SUM given by (21), and SUM in turn depends on the intermolecular force law. For rigid sphere molecules

$$\int_0^{2\pi} \int_0^d gb \, db \, d\varepsilon = \pi d^2 g,$$

where d is the diameter of the molecules. The SUM then is given by

$$\text{SUM} = \pi d^2 \sum_{1 \leq i < j \leq N} g_{ij}. \quad (27)$$

For a molecular pair i, j retained for a collision the vector relative velocity \mathbf{g}_{ij} is known. The scattering angle θ and the azimuthal angle ε in (4) are drawn with uniform distributions from the intervals $[0, \pi]$ and $[0, 2\pi]$. For these values of g_{ij} , θ , and ε , the post-collision velocities v' , w' can then be determined from relations (2) and (4).

In case of molecules with soft potential having point-centres of repulsion we have,

$$F = \text{intermolecular force between two molecules separated by distance } r = a/r^s. \quad (28)$$

Defining the dimensionless impact parameter α by

$$\alpha = b[mg^2/2(s-1)a]^{1/(s-1)}$$

we obtain

$$gb \, db \, d\varepsilon = K_0 g^\omega \alpha \, d\alpha \, d\varepsilon, \quad (29a)$$

where

$$\omega = (s-5)/(s-1), \quad K_0 = [2(s-1)a/m]^{1/(s-1)}. \quad (29b)$$

For such molecules SUM reduces to

$$\text{SUM} = \pi \alpha_{\text{max}}^2 K_0 \sum_{1 \leq i < j \leq N} g_{ij}^\omega, \quad (30)$$

where α_{max} is the cut-off value of the dimensionless impact parameter. The scattering angle θ for molecules with soft potentials is no longer a uniformly distributed random variable. The scattering angle θ is a function of α given by

$$\theta = \pi - 2 \int_0^{\eta_1} d\eta \{1 - \eta^2 - [2/(s-1)](\eta/\alpha)^{s-1}\}^{-1/2}, \quad (31)$$

where η_1 is the positive real root of the equation

$$1 - \eta_1^2 - [2/(s-1)](\eta_1/\alpha)^{s-1} = 0. \quad (32)$$

The scattering angle is determined by drawing a random number α uniformly distributed between $[0, \alpha_{\max}]$, and then computing θ by the evaluation of the integral (31). This integral in general has to be computed numerically, but for some values of s closed form results are available, e.g. for a Maxwell molecule $s = 5$, and (31) reduces to

$$\theta = \pi - 2(1 - 2q^2)^{\frac{1}{2}} K(q), \quad (33)$$

where

$$q^2 = \frac{1}{2} \{1 - 1/[1 + (2/\alpha^4)]^{\frac{1}{2}}\},$$

and $K(q)$ is the complete elliptic integral of the first kind (Abramowitz & Stegun 1965). The above detailed algorithm about drawing random numbers g , α or θ , ε can be briefly summarized by the simplified expressions for $p(\Omega, g)$ given by

$$p(\Omega, g) = p(\theta, \varepsilon, g) = (g/\Sigma g), \text{ for rigid spheres, and}$$

$$p(\Omega, g) = p(\alpha, \varepsilon, g) = (g^\omega/\Sigma g^\omega) (\alpha/\pi\alpha_{\max}^2), \text{ for soft potentials.}$$

3.4 An efficient operator-split DSMC

We have now given methods for constructing operators $O_{\text{con}}(\Delta t)$ and $O_{\text{col}}(\Delta t)$ used in advancing the solution in time. The CPU time required depends on the number of arithmetic operations involved in $O_{\text{con}}(\Delta t)$ and $O_{\text{col}}(\Delta t)$. For advancing the solution through two time steps we have to use the sequence twice, that is,

$$f^{n+2} = [O_{\text{con}}(\Delta t) O_{\text{col}}(\Delta t)][O_{\text{con}}(\Delta t) O_{\text{col}}(\Delta t)] f^n, \quad (34)$$

which involves two convection and collision operators. On the other hand the equivalent sequence

$$f^{n+2} = O_{\text{col}}(\Delta t) O_{\text{con}}(2\Delta t) O_{\text{col}}(\Delta t) f^n, \quad (35)$$

involves only one convection and two collision operators. It has been found that the sequence (35) required about half as much time as required by the sequence (34). This time saving is due to the following reason. After the convection of molecules is done the computer code has to arrange the molecular list according to cell numbers. This arrangement is done by subroutine ARANG. Such an arrangement is necessary for calling subroutine COLSN which performs collisions cell by cell. The sequence (35) makes only one call to subroutine ARANG while the sequence (34) requires two calls. This is the reason for the saving in CPU time when sequence (35) is used instead of the sequence (34). Table 1 shows a comparison between the CPU times taken by the two sequences for advancing the solution through two time steps.

4. Extension of the Kac-Prigogine based DSMC to mixture of gases

Let us consider the binary mixture of two gases denoted by subscripts a and b . The

Table 1. Comparison of CPU[†] times

Method	Subroutines (s)		Complete cycle (s)
	CONV	ARANG	
Sequence (34)	17.8	165.9	195.8
Sequence (35)	15.5	70.9	95.9

[†] Computer used is CYBER 170/730 system at VSSC, Trivandrum. The RDP = rate of data processing defined by the CPU time required to advance the solution through $2\Delta t$ per molecule is a measure of the efficiency of the numerical method. The RDP for the sequence (34) is 0.032 s per molecule per $2\Delta t$, while it is 0.016 s for the sequence (35).

relevant Boltzmann equations for the one-particle probability density functions $\Phi_a(t, \mathbf{x}, \mathbf{v})$ and $\Phi_b(t, \mathbf{x}, \mathbf{v})$ are

$$\begin{aligned} (\partial\Phi_a/\partial t) + \mathbf{v}_{a1} \cdot (\partial\Phi_a/\partial \mathbf{x}) &= J(\Phi_a, \Phi_a) + J(\Phi_a, \Phi_b), \\ (\partial\Phi_b/\partial t) + \mathbf{v}_{b1} \cdot (\partial\Phi_b/\partial \mathbf{x}) &= J(\Phi_b, \Phi_a) + J(\Phi_b, \Phi_b). \end{aligned} \quad (36)$$

The collision terms J are defined by

$$\begin{aligned} J(\Phi_a, \Phi_a) \equiv n_a \int |\mathbf{v}_{a1} - \mathbf{w}| \sigma_{aa}(\Omega, |\mathbf{v}_{a1} - \mathbf{w}|) \times \\ [\Phi_a(\mathbf{v}'_{a1})\Phi_a(\mathbf{w}') - \Phi_a(\mathbf{v}_{a1})\Phi_a(\mathbf{w})] d\Omega d\mathbf{w}, \end{aligned} \quad (37a)$$

$$\begin{aligned} J(\Phi_a, \Phi_b) \equiv n_b \int |\mathbf{v}_{a1} - \mathbf{w}| \sigma_{ab}(\Omega, |\mathbf{v}_{a1} - \mathbf{w}|) \times \\ [\Phi_a(\mathbf{v}'_{a1})\Phi_b(\mathbf{w}') - \Phi_a(\mathbf{v}_{a1})\Phi_b(\mathbf{w})] d\Omega d\mathbf{w}, \end{aligned} \quad (37b)$$

$$\begin{aligned} J(\Phi_b, \Phi_a) \equiv n_a \int |\mathbf{v}_{b1} - \mathbf{w}| \sigma_{ab}(\Omega, |\mathbf{v}_{b1} - \mathbf{w}|) \times \\ [\Phi_b(\mathbf{v}'_{b1})\Phi_a(\mathbf{w}') - \Phi_b(\mathbf{v}_{b1})\Phi_a(\mathbf{w})] d\Omega d\mathbf{w}, \end{aligned} \quad (37c)$$

$$\begin{aligned} J(\Phi_b, \Phi_b) \equiv n_b \int |\mathbf{v}_{b1} - \mathbf{w}| \sigma_{bb}(\Omega, |\mathbf{v}_{b1} - \mathbf{w}|) \times \\ [\Phi_b(\mathbf{v}'_{b1})\Phi_b(\mathbf{w}') - \Phi_b(\mathbf{v}_{b1})\Phi_b(\mathbf{w})] d\Omega d\mathbf{w}, \end{aligned} \quad (37d)$$

Here n_a, n_b are the number densities of species a and b , σ_{aa}, σ_{ab} etc. are cross-sections for a - a , a - b etc. collisions, and dependence of Φ_a, Φ_b on t and \mathbf{x} is suppressed for brevity. The solution of (36) can be constructed in two steps by adopting the split scheme:

(i) *Convection step*

Integrate the equations

$$(\partial\Phi_a/\partial t) + \mathbf{v}_{a1} \cdot (\partial\Phi_a/\partial \mathbf{x}) = 0, \quad (\partial\Phi_b/\partial t) + \mathbf{v}_{b1} \cdot (\partial\Phi_b/\partial \mathbf{x}) = 0$$

over small time duration Δt by moving particles a and particles b with their respective velocities. This convection of the particles is exactly similar to the

convection step described earlier for monocomponent gases. We thus obtain the intermediate solution $\overline{\Phi_a^{n+1}}$, $\overline{\Phi_b^{n+1}}$, and the convection operator $O_{\text{con}}(\Delta t)$ corresponding to the solution is defined by

$$\begin{bmatrix} \overline{\Phi_a^{n+1}} \\ \overline{\Phi_b^{n+1}} \end{bmatrix} = O_{\text{con}}(\Delta t) \begin{bmatrix} \Phi_a^n \\ \Phi_b^n \end{bmatrix}. \quad (38)$$

(ii) *Collision step*

Next, construct the solution

$$\begin{bmatrix} \Phi_a^{n+1} \\ \Phi_b^{n+1} \end{bmatrix} = O_{\text{col}}(\Delta t) \begin{bmatrix} \overline{\Phi_a^{n+1}} \\ \overline{\Phi_b^{n+1}} \end{bmatrix}, \quad (39)$$

by integrating the homogenous Boltzmann equations

$$\begin{aligned} (\partial\Phi_a/\partial t) &= J(\Phi_a, \Phi_a) + J(\Phi_a, \Phi_b), \\ (\partial\Phi_b/\partial t) &= J(\Phi_b, \Phi_a) + J(\Phi_b, \Phi_b), \end{aligned} \quad (40)$$

over time duration Δt with $\overline{\Phi_a^{n+1}}$, $\overline{\Phi_b^{n+1}}$ as initial velocity distribution functions. The solution so obtained will be first-order accurate in time.

The collision operator $O_{\text{col}}(\Delta t)$ for solving (40) is constructed using the relationship between the Boltzmann equations (40) and the Kac-Prigogine master equation. We write the master equation for a binary mixture of gases in a box of volume "Vol" as

$$\begin{aligned} (\partial P_0/\partial t) &= J(P_0) \\ &= \frac{1}{\text{Vol}} \sum_{1 \leq j < k \leq N} \int |\mathbf{v}_{aj} - \mathbf{v}_{ak}| \sigma_{aa}(\Omega_{jk}, |\mathbf{v}_{aj} - \mathbf{v}_{ak}|) \times \\ &\quad [P_0(V'_{ajk}, V_b) - P_0(V)] d\Omega_{jk} \\ &\quad + \frac{1}{\text{Vol}} \sum_{j=1} \sum_{k=1} \int |\mathbf{v}_{aj} - \mathbf{v}_{bk}| \sigma_{ab}(\Omega_{jk}, |\mathbf{v}_{aj} - \mathbf{v}_{bk}|) \times \\ &\quad [P_0(V'_{abjk}) - P_0(V)] d\Omega_{jk} \\ &\quad + \frac{1}{\text{Vol}} \sum_{1 \leq j < k \leq M} \int |\mathbf{v}_{bj} - \mathbf{v}_{bk}| \sigma_{bb}(\Omega_{jk}, |\mathbf{v}_{bj} - \mathbf{v}_{bk}|) \times \\ &\quad [P_0(V_a, V'_{bjk}) - P_0(V)] d\Omega_{jk}, \end{aligned} \quad (41)$$

where

$$\begin{aligned} V &= \{V_a, V_b\}, \quad V_a = \{\mathbf{v}_{a1}, \mathbf{v}_{a2}, \dots, \mathbf{v}_{aN}\}, \\ V_b &= \{\mathbf{v}_{b1}, \mathbf{v}_{b2}, \dots, \mathbf{v}_{bM}\}, \\ V'_{ajk} &= \{\mathbf{v}_{a1}, \dots, \mathbf{v}'_{aj}, \dots, \mathbf{v}'_{ak}, \dots, \mathbf{v}_{aN}\}, \\ V'_{bjk} &= \{\mathbf{v}_{b1}, \dots, \mathbf{v}'_{bj}, \dots, \mathbf{v}'_{bk}, \dots, \mathbf{v}_{bM}\}, \\ V'_{abjk} &= \{\mathbf{v}_{a1}, \dots, \mathbf{v}'_{aj}, \dots, \mathbf{v}_{aN}, \mathbf{v}_{b1}, \dots, \mathbf{v}'_{bk}, \dots, \mathbf{v}_{bM}\}. \end{aligned}$$

Further, $\sigma_{aa}d\Omega_{jk}$ is the differential scattering cross-section for a - a collisions, $\sigma_{ab}d\Omega_{jk}$ for a - b collisions and so on. In (41) $P_0(t, V)$ is a joint probability density function. An interesting property of (41) is that it reduces to the homogenous Boltzmann equations (36) under the hypothesis of molecular chaos. For, we then have

$$P_0(t, V) = \Phi_a(t, \mathbf{v}_{a1})\Phi_a(t, \mathbf{v}_{a2}) \dots \Phi_a(t, \mathbf{v}_{aN})\Phi_b(t, \mathbf{v}_{b1}) \times \\ \Phi_b(t, \mathbf{v}_{b2}) \dots \Phi_b(t, \mathbf{v}_{bM}). \quad (42)$$

Integrating the master equation (41) with respect to all the velocity variables except \mathbf{v}_{a1} and observing that

$$\sum_{1 \leq j < k \leq M} \int d\Omega_{jk} |\mathbf{v}_{bj} - \mathbf{v}_{bk}| \sigma_{bb}(\Omega_{jk}, |\mathbf{v}_{bj} - \mathbf{v}_{bk}|) \times \\ [P_0(V_a, V'_{bjk}) - P_0(V)] D\mathbf{v}_{a2} \dots D\mathbf{v}_{bM} = 0,$$

we obtain the first of the homogenous Boltzmann equations (36). In establishing this result we have assumed that N and M are sufficiently large so that

$$n_a \simeq (N - 1)/\text{Vol}, \quad n_b \simeq (M - 1)/\text{Vol}.$$

Similarly, integrating the master equation (41) with respect to all velocity variables except \mathbf{v}_{b1} and invoking (42) we obtain the second of the homogenous Boltzmann equations (36). Thus, under the condition of molecular chaos, we obtain

$$J(\Phi_a, \Phi_a) + J(\Phi_a, \Phi_b) = \int J(P_0) D\mathbf{v}_{a2} \dots D\mathbf{v}_{aN} D\mathbf{v}_{b1} \dots D\mathbf{v}_{bM}, \quad (43)$$

$$J(\Phi_b, \Phi_a) + J(\Phi_b, \Phi_b) = \int J(P_0) D\mathbf{v}_{a1} \dots D\mathbf{v}_{aN} D\mathbf{v}_{b2} \dots D\mathbf{v}_{bM}. \quad (44)$$

These relations are very crucial to the present DSMC method for a binary mixture. These relations enable us to tackle the nonlinear Boltzmann equations through the linear Kac-Prigogine master equation. What is now required for the development of DSMC is the Monte Carlo game exactly simulating the Kac-Prigogine equation governing the time evolution of the $(N + M)$ -particle probability density function $P_0(t, V)$.

It may be observed that the equivalence between (40) and (41) requires the condition of molecular chaos and even though we can ensure its satisfaction at some initial time by properly sampling the $N + M$ velocity vectors, its validity thereafter is in general not guaranteed. As time proceeds correlations between velocity vectors will appear thus destroying the chaos. However, the molecular chaos has the self-preservation property in the limit of an infinite number of particles. It is therefore possible to reduce the distortion introduced in the numerical simulation by choosing sufficiently large N and M in a cell.

The development of the Markoff model for the simulation of the master equation (41) is very similar to the case of a monocomponent gas. The details of the Markoff model for a binary mixture are given in Deshpande (1983), only a brief description is given here.

5. Markoff model for a binary mixture

For the purpose of developing the Markoff model we introduce the following probability distributions

$$P_{aajk} = P_{aa}(\Omega_{jk}, |\mathbf{v}_{aj} - \mathbf{v}_{ak}|) = |\mathbf{v}_{aj} - \mathbf{v}_{ak}| \sigma_{aa}(\Omega_{jk}, |\mathbf{v}_{aj} - \mathbf{v}_{ak}|) / S_{aa},$$

$$S_{aa} = \sum_{1 \leq j < k \leq N} \int |\mathbf{v}_{aj} - \mathbf{v}_{ak}| \sigma_{aa}(\Omega_{jk}, |\mathbf{v}_{aj} - \mathbf{v}_{ak}|) d\Omega_{jk}, \quad (45)$$

$$P_{abjk} = P_{ab}(\Omega_{jk}, |\mathbf{v}_{aj} - \mathbf{v}_{bk}|) = |\mathbf{v}_{aj} - \mathbf{v}_{bk}| \sigma_{ab}(\Omega_{jk}, |\mathbf{v}_{aj} - \mathbf{v}_{bk}|) / S_{ab},$$

$$S_{ab} = \sum_{j=1}^N \sum_{k=1}^M \int |\mathbf{v}_{aj} - \mathbf{v}_{bk}| \sigma_{ab}(\Omega_{jk}, |\mathbf{v}_{aj} - \mathbf{v}_{bk}|) d\Omega_{jk}, \quad (46)$$

$$P_{bbjk} = P_{bb}(\Omega_{jk}, |\mathbf{v}_{bj} - \mathbf{v}_{bk}|) = |\mathbf{v}_{bj} - \mathbf{v}_{bk}| \sigma_{bb}(\Omega_{jk}, |\mathbf{v}_{bj} - \mathbf{v}_{bk}|) / S_{bb},$$

$$S_{bb} = \sum_{1 \leq j < k \leq M} \int |\mathbf{v}_{bj} - \mathbf{v}_{bk}| \sigma_{bb}(\Omega_{jk}, |\mathbf{v}_{bj} - \mathbf{v}_{bk}|) d\Omega_{jk}. \quad (47)$$

The probability distributions P_{aajk} , P_{abjk} , and P_{bbjk} are functions of discrete variables j, k and continuous variables θ, ε . The dependence on θ, ε is because of the dependence of the distributions on Ω_{jk} .

Define operators O_{aa} , O_{ab} and O_{bb} by

$$O_{aa} P_0(t, V) = \sum_{1 \leq j < k \leq N} \int P_{aajk}(\Omega_{jk}, |\mathbf{v}_{aj} - \mathbf{v}_{ak}|) \times P_0(t, V'_{ajk}) d\Omega_{jk}, \quad (48)$$

$$O_{ab} P_0(t, V) = \sum_{j=1}^N \sum_{k=1}^M \int P_{abjk}(\Omega_{jk}, |\mathbf{v}_{aj} - \mathbf{v}_{bk}|) \times P_0(t, V'_{abjk}) d\Omega_{jk}, \quad (49)$$

$$O_{bb} P_0(t, V) = \sum_{1 \leq j < k \leq M} \int P_{bbjk}(\Omega_{jk}, |\mathbf{v}_{bj} - \mathbf{v}_{bk}|) \times P_0(t, V'_{bbjk}) d\Omega_{jk}. \quad (50)$$

These operators give the $(N + M)$ -particle probability density function after one collision of the type a - a , a - b , and b - b . In terms of these operators (41) can be written in the compressed form

$$(\partial P_0 / \partial t) = (B_{aa} O_{aa} + B_{ab} O_{ab} + B_{bb} O_{bb} - BI) P_0(t, v), \quad (51)$$

where $B = B_{aa} + B_{ab} + B_{bb}$, $B_{aa} = S_{aa} / \text{Vol}$, $B_{ab} = S_{ab} / \text{Vol}$, $B_{bb} = S_{bb} / \text{Vol}$, and $I = \text{identity operator}$. Notice that as collisions are allowed the set of velocity vectors V changes which in turn causes changes in S_{aa} , S_{ab} and S_{bb} . The variables

B_{aa} , B_{ab} , B_{bb} and B therefore change with time. For small values of time duration Δt , the variables B , B_{aa} , B_{ab} and B_{bb} can be treated as constants and we can write the formal solution of (51) as

$$P_0(t + \Delta t, V) = \exp(-B\Delta t) \exp[\Delta t(B_{aa}O_{aa} + B_{ab}O_{ab} + B_{bb}O_{bb})] P_0(t, V). \quad (52)$$

The operators O_{aa} and O_{bb} do not commute with O_{ab} and consequently

$$\begin{aligned} & \exp[\Delta t(B_{aa}O_{aa} + B_{ab}O_{ab} + B_{bb}O_{bb})] \\ & \neq \exp(\Delta t B_{aa} O_{aa}) \exp(\Delta t B_{ab} O_{ab}) \exp(\Delta t B_{bb} O_{bb}). \end{aligned}$$

It is therefore not possible to develop a simulation in which b - b collisions are performed first, a - b collisions next and a - a collisions last, or for that matter any fixed sequence of collisions of various types. Expanding the exponential in (52) we obtain

$$P_0(t + \Delta t, V) = \exp(-B\Delta t) \times \sum_{r=0}^{\infty} [(\Delta t B_{aa} O_{aa} + \Delta t B_{ab} O_{ab} + \Delta t B_{bb} O_{bb})^r / r!] P_0(t, V).$$

It is now easy to construct a Monte Carlo estimator for $P_0(t + \Delta t, V)$. We first draw a Poissonly distributed random integer r with mean $B\Delta t$ and then draw r uniformly distributed random variables $Rf_1 \dots Rf_r$ lying in the interval $[0, 1]$. We then construct an operator O according to the following procedure. Define

$$O = O_1 O_2 \dots O_r, \quad (53)$$

where

$$\begin{aligned} O_k &= O_{aa}, \text{ if } 0 < Rf_k < B_{aa}/B, \\ O_k &= O_{ab}, \text{ if } B_{aa}/B < Rf_k < (B_{aa} + B_{ab})/B, \\ O_k &= O_{bb}, \text{ if } (B_{aa} + B_{ab})/B < Rf_k < 1. \end{aligned}$$

Evidently the expectation of O defined by (53) for fixed r is

$$E\{O\} = (B_{aa}O_{aa} + B_{ab}O_{ab} + B_{bb}O_{bb})^r / B^r$$

and hence $O_1 O_2 \dots O_r P_0(t, V)$ is an unbiased Monte Carlo estimator for $P_0(t + \Delta t, V)$ in the limit of $\Delta t \rightarrow 0$.

Now if we have a sample at time t of $N + M$ velocity vectors, which is a realization from the ensemble with probability density $P_0(t, V)$ then a realization from the ensemble with probability density $P_0(t + \Delta t, V)$ can be easily constructed using the operator sequence (53). We just let O operate on V . The operator O is an ordered product of O_1, \dots, O_r and each of these factors can be any one of the operators O_{aa} , O_{ab} , O_{bb} . Hence, it is enough for the purpose of letting O operate on V if we know how transformed samples $O_{aa}V$, $O_{ab}V$ can be obtained. The procedure for obtaining the transformed sample consists in drawing a pair j, k of molecules either of a - a type, a - b type, b - b type, and the azimuth ε and scattering angle θ are then sampled from the relevant distributions. A collision is then allowed between the molecules of the pair and precollision velocities replaced by the post-collision velocities using collision dynamics.

In operating O_1, O_2, \dots etc. on V the exact order of the various operators has to be preserved and a - a collisions, a - b collisions etc. cannot be performed in any way we please without introducing a bias in the estimator. No such ordering is present for monocomponent gases. The present Markoff model for a binary mixture can be easily extended to the mixture of several components.

6. Concluding remarks

A direct simulation Monte Carlo method based on the Kac-Prigogine master equation has been developed for the numerical simulation of the Boltzmann equation. This method requires the estimation of collision-rate per unit volume. The operation count required to determine the collision can be linearly related to the number of particles by resorting to sample mean Monte Carlo estimator. This fact has not been noticed by Nanbu (1986) in his critique of the method. A computationally efficient version of the present DSMC has been developed by employing a suitable sequence of convection and collision operators. Further, the DSMC has been extended to multicomponent mixtures of gases and it has been shown that it is necessary to perform the collisions in a certain sequence to obtain unbiased simulation.

A part of the work reported here was performed for a project supported by VSSC, Trivandrum. The remaining part was completed with support from ISRO through a new project sponsored through its RESPOND programme. The authors are grateful to ISRO for their continued financial support and in particular express their gratitude to Prof. S Dhawan who foresaw the need for the RESPOND programme. The authors thank Prof. R Narasimha for sustained encouragement, association and many suggestions made during the course of these projects.

References

- Abramowitz M, Stegun I A 1965 *Handbook of mathematical functions* (New York: Dover)
- Ananthasayanam M R, Narasimha R 1986 Proposed International Tropical Reference Atmosphere upto 1000 km in XXVI COSPAR meeting, Toulouse, France, June-July
- Belotserkovskii O M, Yanitskii V E 1975 *USSR Comput. Math. Math. Phys. (Engl. Transl.)* 15(5): 101-104
- Bird G A 1970 *Phys. Fluids* 13: 2676-2681
- Bird G A 1976 *Molecular gas dynamics* (Oxford: Clarendon Press)
- Bird G A 1986 Direct simulation of typical AOTV entry flows, AIAA Paper 86-1310
- Deshpande S M 1976 An unbiased and consistent Monte Carlo game simulating the Boltzmann equation, Report 76 FM 15, Dept. Aerosp. Eng., Indian Inst. Sci., Bangalore
- Deshpande S M 1978 An unbiased and consistent Monte Carlo game simulating the Boltzmann equation, Report 78 FM 4, Dept. Aerosp. Eng., Indian Inst. Sci., Bangalore
- Deshpande S M 1982 Monte Carlo simulation of low density flows, Proc. Workshop on Monte Carlo Methods, Bhabha Atomic Research Centre, Bombay
- Deshpande S M 1983 *USSR Comput. Math. Math. Phys. (Engl. Transl.)* 23: 117-122
- Deshpande S M, Subba Raju P V 1973 Calculation of free molecule drag and heat transfer parameters for the SLV-3 using Monte Carlo method, Report 73 FM 4, Dept. of Aerosp. Eng., Indian Inst. Sci., Bangalore

- Deshpande S M, Subba Raju P V 1981 The splitting technique and its application to problems in low density flows and combustion, Proc. Workshop-cum-Seminar on Computation Fluid Dynamics, Vikram Sarabhai Space Centre, Trivandrum
- Deshpande S M, Subba Raju P V, Narasimha R 1978 *Proc. Indian Acad. Sci.* C1: 441-458
- Deshpande S M, Subba Raju P V, Ramani N 1979 *Proc. 11th Int. Symp. on Rarefied Gas Dynamics*, Cannes (ed.) R Campargue (Paris: Commissariat a l'Energie Atomique)
- Deshpande S M, Subba Raju P V, Ramani N, Narasimha R 1977 Monte Carlo simulation of low density flows. Part I: Basic theory and results, Report 77 FM 4, Dept. Aerosp. Eng., Indian Inst. Sci., Bangalore
- Moss J N 1986 *Proc. 15th Int. Symp. on Rarefied Gas Dynamics, Grado* (Stuttgart: B G Teubner)
- Nanbu K 1986 *Proc. 15th Int. Symp. on Rarefied Gas Dynamics, Grado* (Stuttgart: B G Teubner)
- Pullin D 1974 Ph D thesis, Imperial College, London
- Yanenko N N 1971 *The method of fractional steps* (Berlin: Springer-Verlag)
- Yanitskii V E 1973 *Zh. Vychisl. Mat. Mat. Fiz.* 13: 505-510
- Yen S M 1985 *Annu. Rev. Fluid Mech.* 67-96

A profile of aerodynamic research in VSSC with application to satellite launch vehicles

T S PRAHLAD

Flight Dynamics Group, Vikram Sarabhai Space Centre (VSSC),
Trivandrum 695 022, India

Present address: Aeronautical Development Agency (ADA), NAL
Campus, Belur, Bangalore 560 037, India

Abstract. Some of the aerodynamic and fluid dynamic problems associated with the satellite launch vehicles of the Indian Space programme are discussed in this paper. Taking into account the aerodynamic flight profile of a launch vehicle and also the configurations of interest, the topics considered are vehicle lift-off fluid dynamics, strap-on aerodynamics, strap-on separation problem, stage separation aerodynamics, boat-tail aerodynamics, hypersonic flow problems and some special fluid dynamic problems of interest like nozzle flows and shock wave-boundary layer interaction. The topics are mostly related to external fluid dynamics though certain aspects of internal ballistics are also touched upon. More emphasis is placed on the results and their applications rather than on the methodology used. Also, the main features of two special wind tunnel facilities developed at the Vikram Sarabhai Space Centre (VSSC) – the hypersonic wind tunnel and the heat transfer facility – are discussed briefly.

It is hoped that this paper will give an idea of the profile of aerodynamic research being conducted in VSSC with application to satellite launch vehicles in view.

Keywords. Launch vehicles; space technology; strap-on configurations; boat-tailed bodies; shock wave/boundary layer interaction; wind tunnel facilities.

1. Introduction

Aerodynamics and fluid dynamics play a crucial role in many aspects of launch vehicle technology through the interaction of the ambient atmosphere with the external configuration of the moving vehicle and through the internal ballistics of the various propulsive devices used in the vehicle. Thus, a variety of theoretical,

computational and experimental techniques have been evolved for tackling fluid dynamic problems and the associated effects caused by high stagnation temperatures, chemical non-equilibrium, real gas properties, low densities, high Mach numbers, complex three-dimensional geometries, multiphase flows, turbulence etc. All the above subjects have been areas of continuing research. The advent of the Space Shuttle, and the wide range of aerothermal environments it has to go through during its ascent and flyback phases, has brought into sharper focus many of the complex three-dimensional fluid dynamic problems that need to be understood and tackled for an optimal design and performance evaluation of current and future launch vehicles.

In this paper, we would like to present a profile of some of the aerodynamic and fluid dynamic research that is currently in progress at the Vikram Sarabhai Space Centre (VSSC) in the context of the Indian space programme, so lovingly nurtured and shaped by Prof. S Dhawan for over a decade. Himself a specialist in fluid dynamics, he took a keen interest in its growth and its application to the practical problems posed by the Indian space programme. With his academic background he could clearly see the need for developing both the scientific and application aspects of a discipline like launch vehicle fluid dynamics, and this has been the guiding principle of most of the research and development programmes initiated in this area. Also, the development of certain facilities in VSSC, like the country's first blow-down Hypersonic Wind Tunnel and the unique Heat Transfer Facility with high temperature supersonic flow simulation, owe a lot to his support and encouragement. Thus, it is indeed a privilege to write this paper in honour of Prof. Dhawan.

The external configurations of the SLV-3 that was successfully flown in July 1980 and of the Augmented Satellite Launch Vehicle (ASLV) and the Polar Satellite Launch Vehicle (PSLV), currently under development in VSSC, are shown in figure 1. SLV-3 is a simple aerodynamic configuration with a blunt cone and a flared interstage between the first and the upper stages. It has four fins to provide aerodynamic stability as well as control with movable fin tips during the first stage flight. In ASLV, two strap-on boosters are added to SLV-3, but without the fins, to act as the first stage of a five-stage launch vehicle with 150 kg payload capability in low earth orbit. The payload shroud is increased in diameter from 800 to 1000 mm leading to a bulbous configuration. The PSLV is a vehicle that is being developed for launching a 1000 kg satellite in a 900 km sun-synchronous orbit. The basic vehicle is of 2.8 m diameter with 6 strap-on boosters of 1 m diameter which augment the thrust at take-off. Aerodynamically, complexity arises again because of the strap-on boosters and the bulbous payload shroud (also referred to as heat shield) necessary for accommodating the payload. The strap-on and bulbous shroud concepts are likely to be used in future launch vehicles also.

The topics covered in this paper are grouped under the following headings: (a) Vehicle lift-off fluid dynamics; (b) strap-on aerodynamics; (c) strap-on separation problem; (d) stage-separation aerodynamics; (e) boat-tail aerodynamics; (f) some hypersonic flow problems; (g) special fluid dynamic problems – three-dimensional nozzle flow, heat transfer effects on nozzle liners, three-dimensional boundary layers, shock wave-boundary layer interaction, drag estimation from flight etc; (h) special wind tunnel facilities of VSSC.

These topics are mostly related to external fluid dynamics with which the author

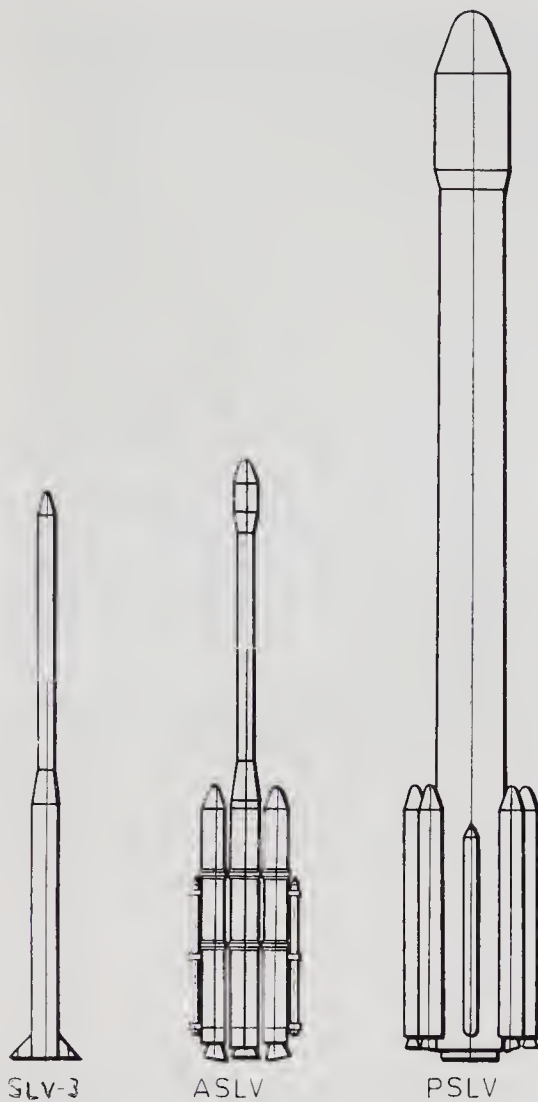


Figure 1. Aerodynamic configurations of Indian Satellite Launch Vehicles.

has been more directly involved, though certain aspects of internal ballistics are also touched upon. More emphasis is placed on results and their applications rather than on the details of the methodology used. The above list of the aerodynamic and fluid dynamic work being done in VSSC is by no means exhaustive. Also, some of the standard design calculation methods have not been covered here though they have been extensively and successfully used for many important project-related tasks.

2. Vehicle lift-off fluid dynamics

Jet interaction with the launch pad as well as with the vehicle itself, constitutes an important and complex fluid dynamic problem during the lift-off of a launch vehicle. The aspects to be considered are – diversion of jets away from the launch pad through a suitable jet deflector, pressure and thermal loads on the jet deflector and acoustic loading effects on the vehicle caused by jet reflection from the launch pad.

Different types of jet deflectors that can be used in practice and the corresponding increase in sound pressure levels are illustrated in figure 2. While flat plate deflectors are used for SLV-3 and ASLV (figure 3), a double wedge and an inclined plate type of deflector were considered for the larger PSLV. Figure 4 represents the fluid dynamic problem of the core jet impinging on a double wedge deflector as the vehicle lifts off and the problem becomes more complex in the presence of the strap-on jet, as seen in figures 5 & 6, with interactions between shocks, core and strap-on jets and boundary layer. These Schlieren pictures along with surface pressure distributions were obtained in laboratory cold flow simulation tests using a small open jet facility (Prasad & Kutty 1985). Typical pressure distributions along the centre line and across the span of a double wedge deflector are shown in figure 7 from which one can obtain an estimate of deflector foundation loads.

In order to design a suitable thermal protection system over the deflector for withstanding the heavy thermal loads during lift-off, recourse was again taken to subscale static tests using both double wedge and inclined plate types of deflectors (VSSC 1985). The test set-up is shown in figure 8; the jet deflector model had a 50 mm thick high temperature refractory coating on top of a steel plate with suitable anchorages. A typical erosion pattern can be seen in figure 9. Several tests were conducted on both types of deflectors with varying geometrical properties. The overall conclusion from these tests was that the erosion depth and the extent were roughly the same in both types of deflectors, though there were marginal

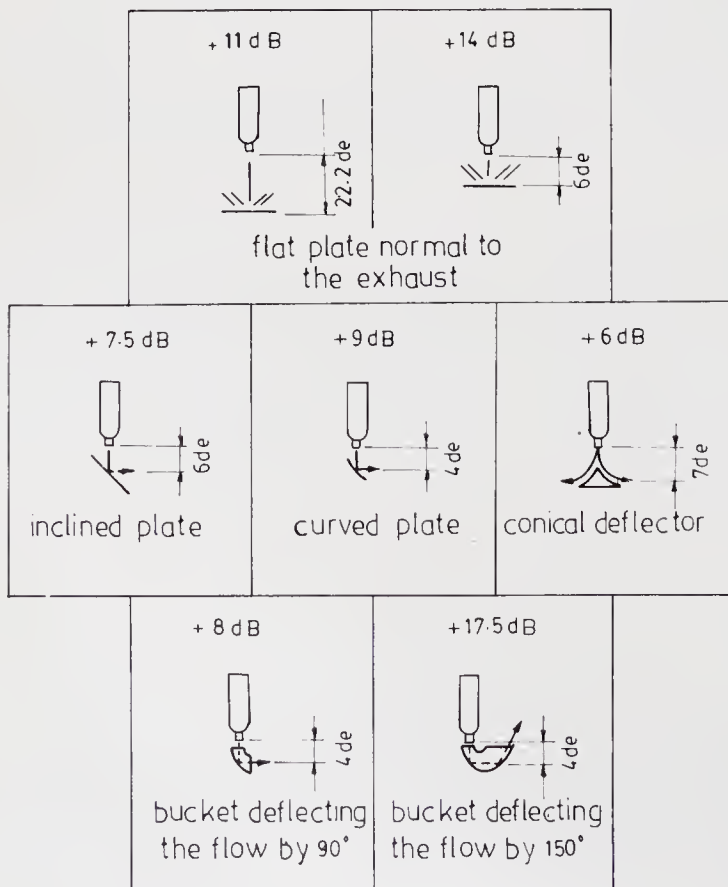


Figure 2. Increase in overall sound pressure level due to jet deflector over the undeflected jet.

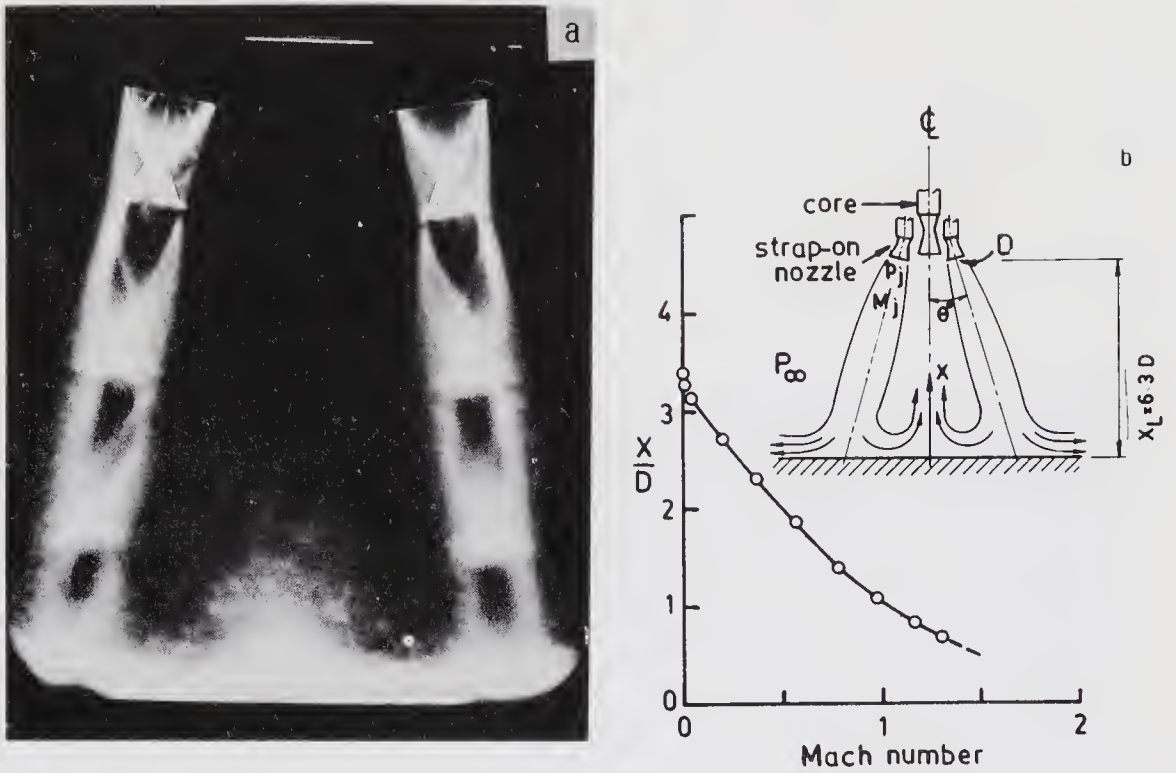


Figure 3. Lift-off fluid dynamic problem of ASLV; Two strap-on jets impinging on a flat surface (a) Schlieren view (b) Centre line velocity distribution in fountain jet: $M_j = 2.98$; $X_L/D = 6.3$; $p_j/p_\infty = 0.5$.

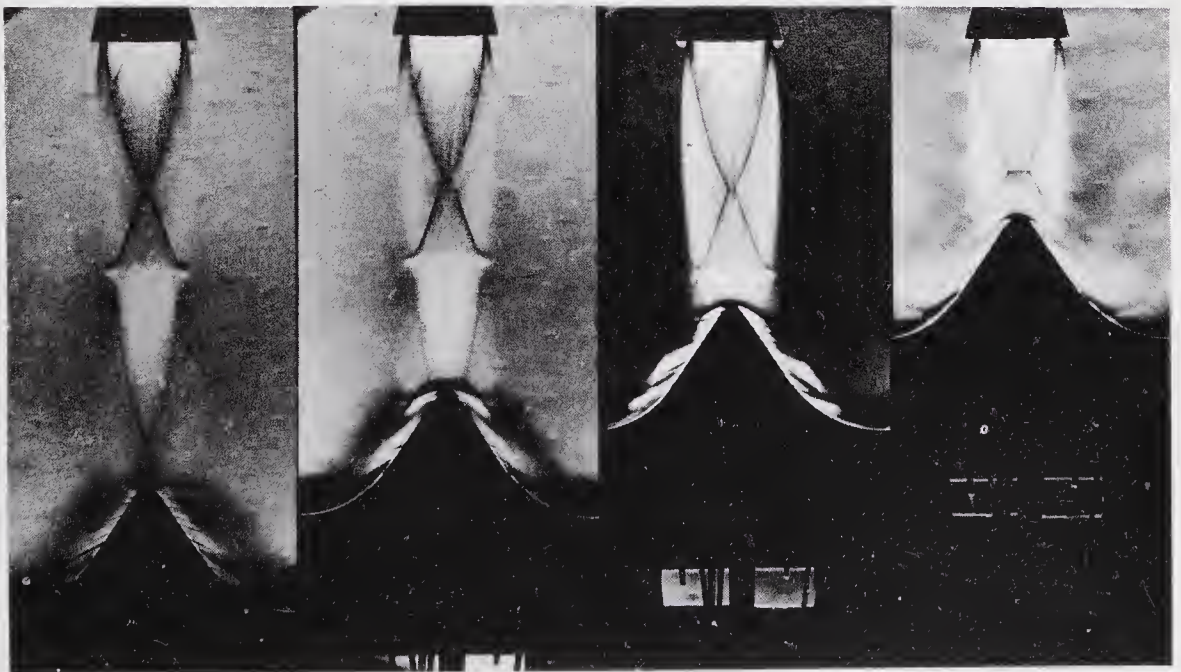


Figure 4. Flow field of core jet impinging on a double wedge deflector as the vehicle lifts off.

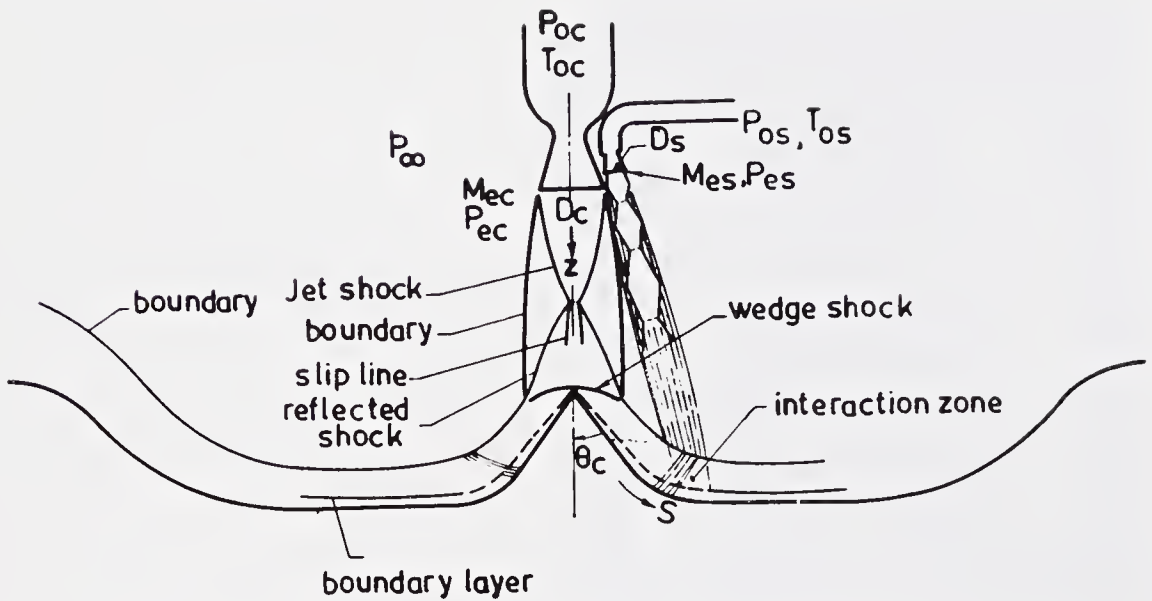


Figure 5. Schematic of the flow field due to core and strap-on jet impingement on double wedge deflector.

differences. The erosion was of acceptable extent and repair would be possible from one launch to the next.

Using approximate semi-empirical methods, the overall sound pressure distribution along the length of the vehicle was estimated for ASLV and PSLV as shown in figure 10 (M S Sastry 1986, private communication). There is need for subscale experiments in this area also for refining the above estimates.

Thus, there is considerable complexity in the fluid dynamic problem that arises during the lift-off of a launch vehicle. Though one can tackle specific design problems through a combination of suitably tailored subscale experiments and semi-empirical methods, there is clearly a need for obtaining a much better understanding of the fluid dynamic aspects involved and their effects on pressure loads, surface erosion, sound pressure levels etc. The newly emerging field of computational fluid dynamics can play a significant role in this along with carefully conducted subscale tests.

3. Strap-on aerodynamics

The aerodynamics of multibody configurations involving strap-on boosters has been receiving considerable attention in VSSC because of its relevance to current and future launch vehicle programmes. Methods are under development for subsonic, transonic and supersonic flow analyses involving two or more strap-on boosters. This section gives a brief account of these methods and the important results obtained.

3.1 Subsonic flows

The well-known panel method with surface singularity distribution and incompressible flow assumption is used for the multibody configurations of interest. For ASLV,

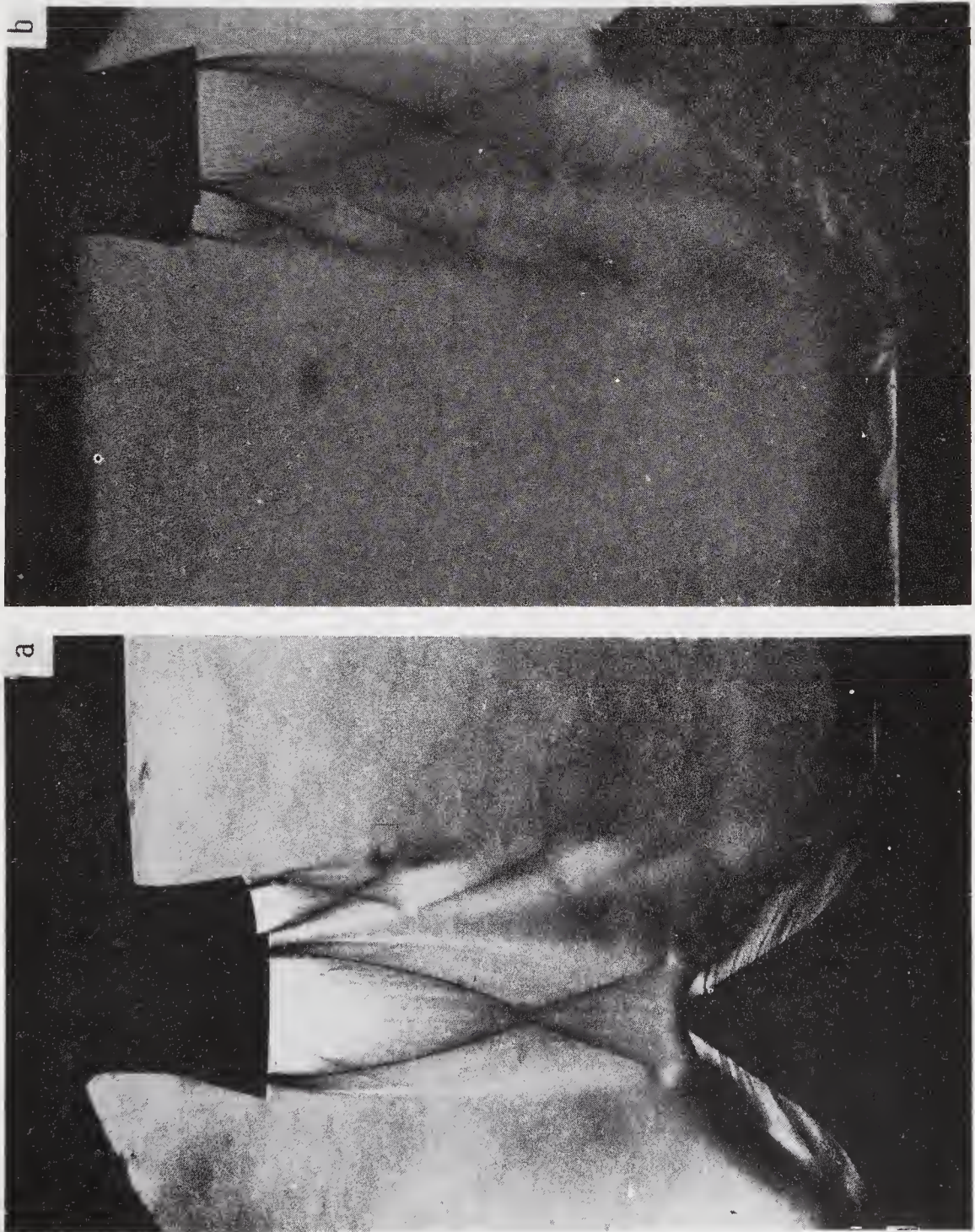


Figure 6. Schlieren pictures of core and strap-on jets impinging on (a) double wedge deflector, and (b) single inclined surface deflector.

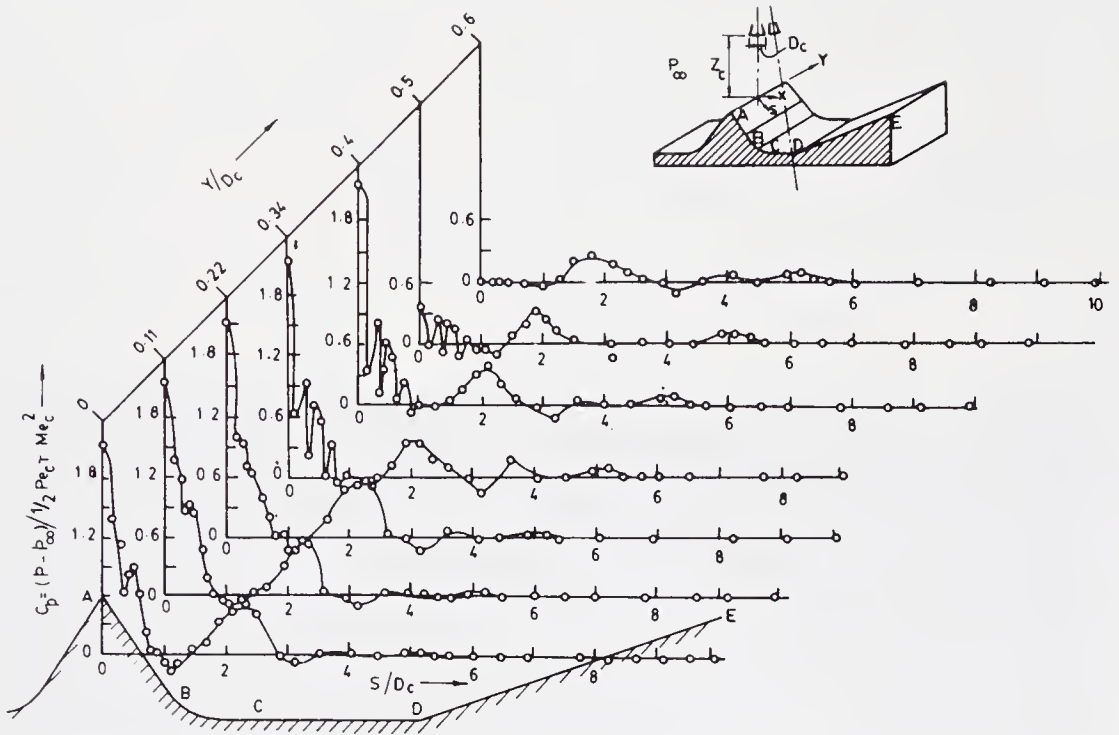


Figure 7. Typical pressure distribution along the centre line and across the span of a double wedge jet deflector, core jet Mach number $Me_c = 3.12$, strap-on jet Mach number $Me_s = 3.0$, core jet pressure ratio $Pe_c/P_\infty = 0.88$, strap-on jet pressure ratio $Pe_s/P_\infty = 0.7$, distance from exit plane of core nozzle $Z_c/D_c = 3.0$, p = local static pressure, C_p = pressure coefficient, γ = specific heat ratio.

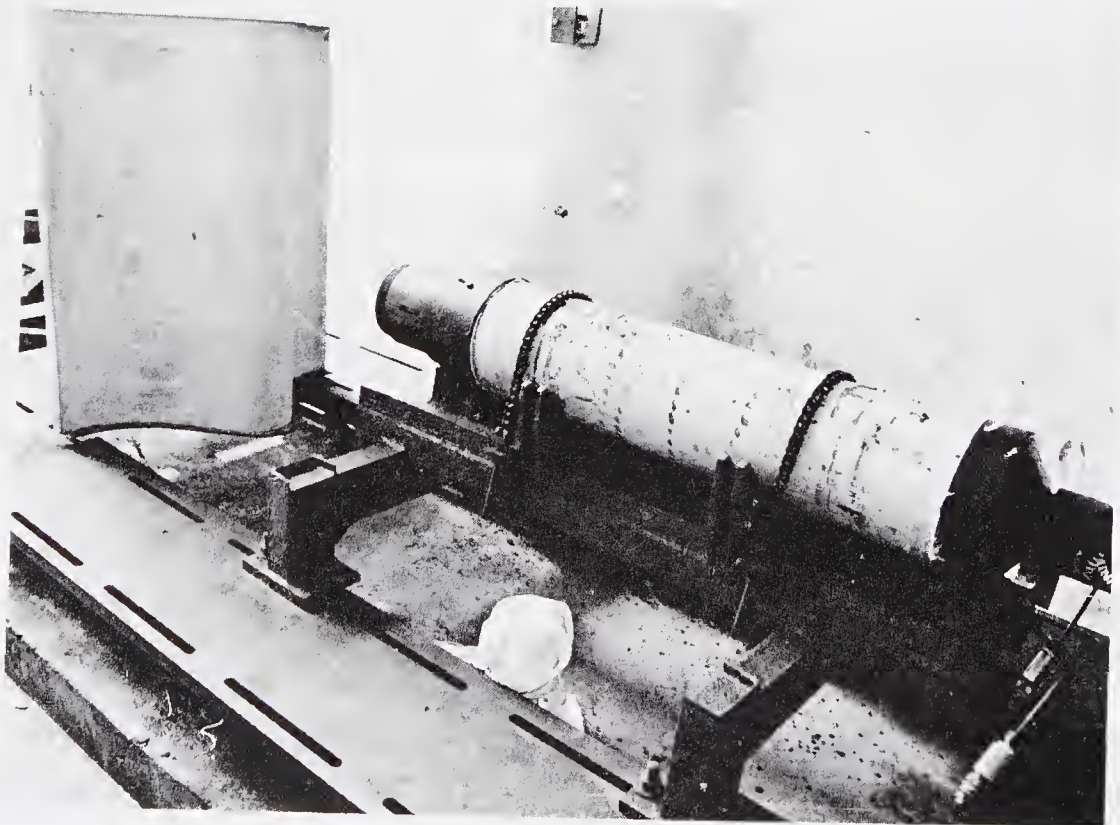


Figure 8. Static test set up with 200 mm diameter solid rocket motor and double wedge deflector with high temperature refractory lining.

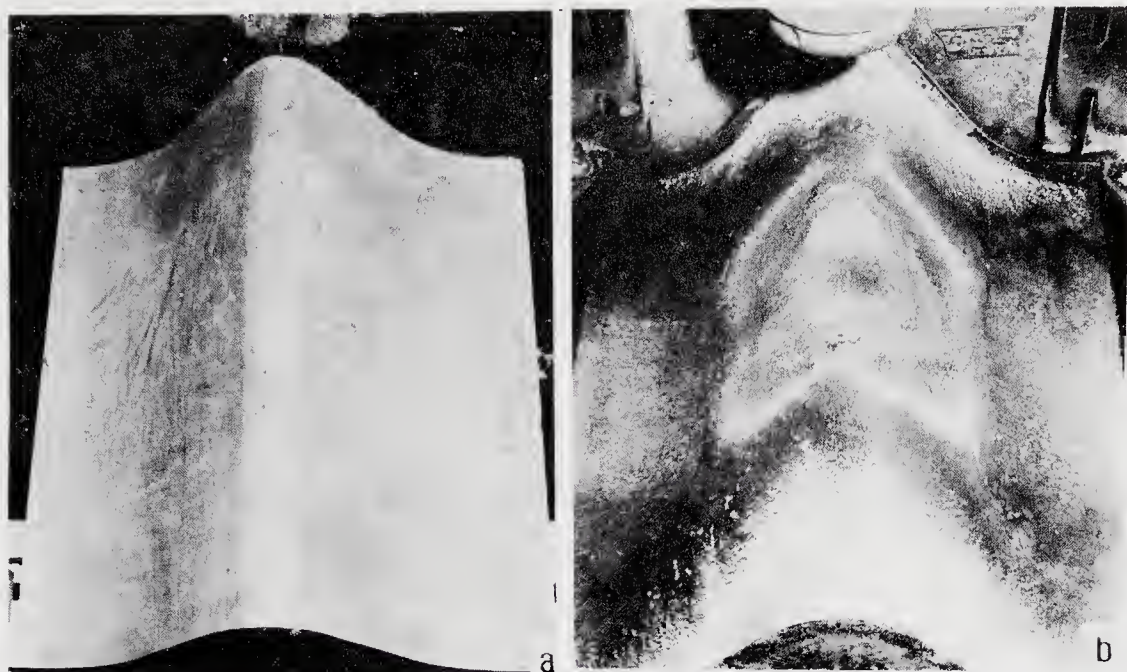


Figure 9. Double wedge deflector model (a) before and (b) after static test showing the erosion pattern.

800 panels have been used, along with symmetry considerations, and are distributed as shown in figure 11 (Devassia *et al* 1982, pp. 553–558). Computations were performed on the CDC CYBER 170/730 system of VSSC. Longitudinal pressure distributions along various generators for a given gap between the core and the strap-on as well as the circumferential pressure distribution are shown in figures 12 and 13 along with the experimentally measured static pressures. The conditions are not exactly identical as the test Mach number is around 0.5 whereas computation assumes $M = 0$. Also, the model has connectors between the core and the strap-on which are not taken into account in the computation. Further, the computational method does not correct for viscosity. Taking all these factors into account, the agreement can be considered quite reasonable for purposes of preliminary design.

Integrating such pressure distributions calculated at the angle of incidence, aerodynamic load distributions have been obtained along the vehicle length for purposes of structural design. A typical load distribution is shown in figure 14. Similar computations have also been performed for PSLV with a larger number of strap-on boosters.

3.2 Supersonic flows

The flow field arising out of a supersonic free stream past a strap-on multibody configuration is shown in figure 15 which indicates the complexity of the fluid dynamic problem involved here with multiple shock interactions and reflections. The inviscid supersonic flow field governed by Euler equations is solved (Singh *et al* 1987) by a shock-capturing scheme using MacCormack's (1969) second-order explicit predictor-corrector method. An 'overlap grid scheme' is used wherein the strap-ons and the core are wrapped in separate meshes such that there is an overlap region between the two grids (figure 16) where the core and the strap-on solutions

source collocation method; prediction error ± 5 dB

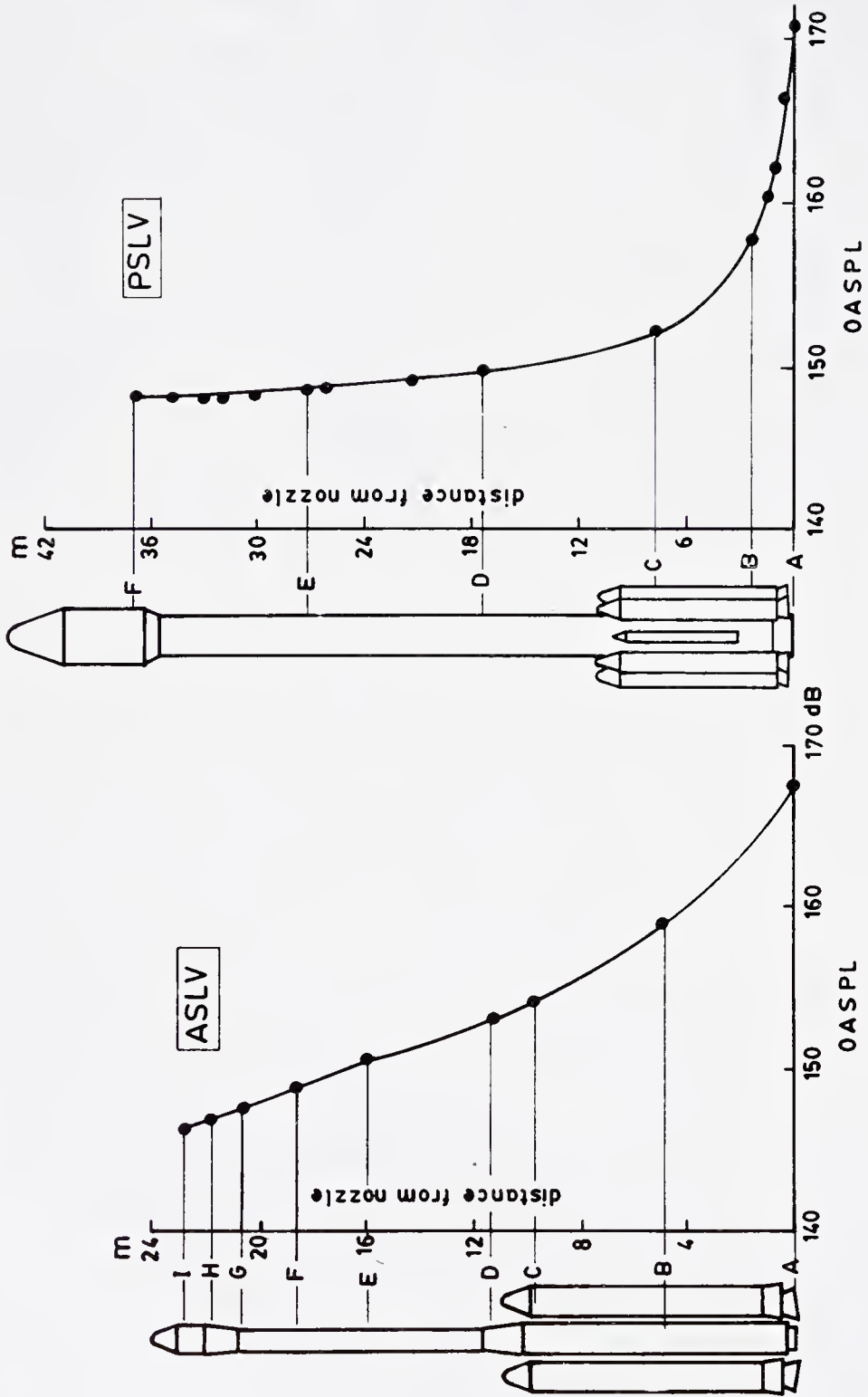


Figure 10. Overall sound pressure levels (OASPL) at various stations along the length of the vehicle during take-off.

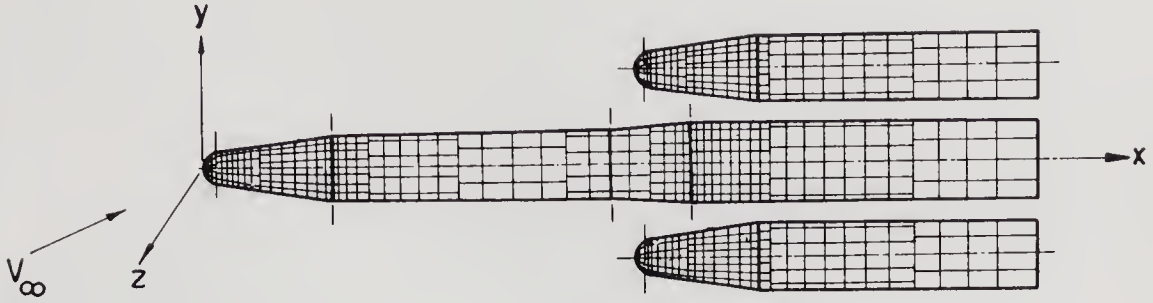


Figure 11. Distribution of panels for subsonic inviscid flow field calculation on a strap-on configuration. Note the various types of distributions at different longitudinal locations on the body. Circumferential distribution is adjusted to have elements of similar shape as far as possible.

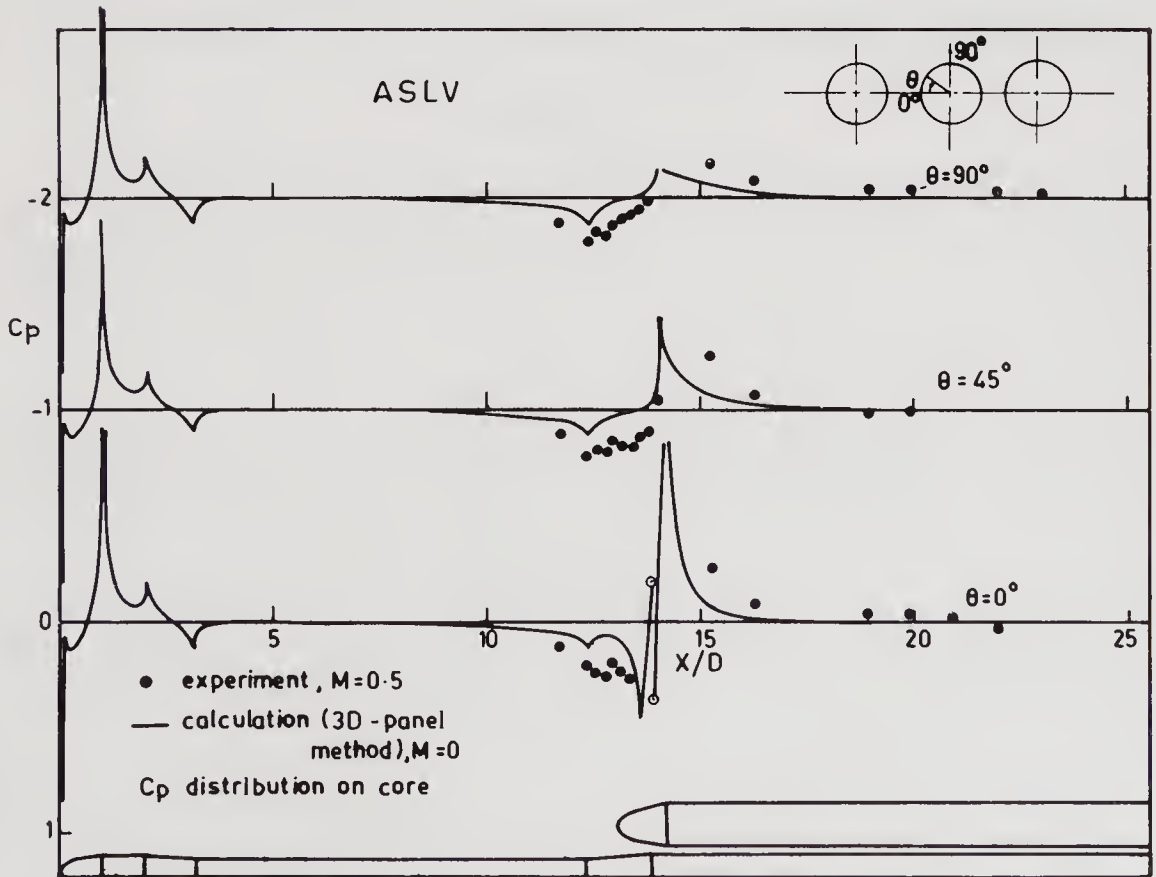


Figure 12. Pressure distribution along the length of the core vehicle; Comparison between computed and experimental results.

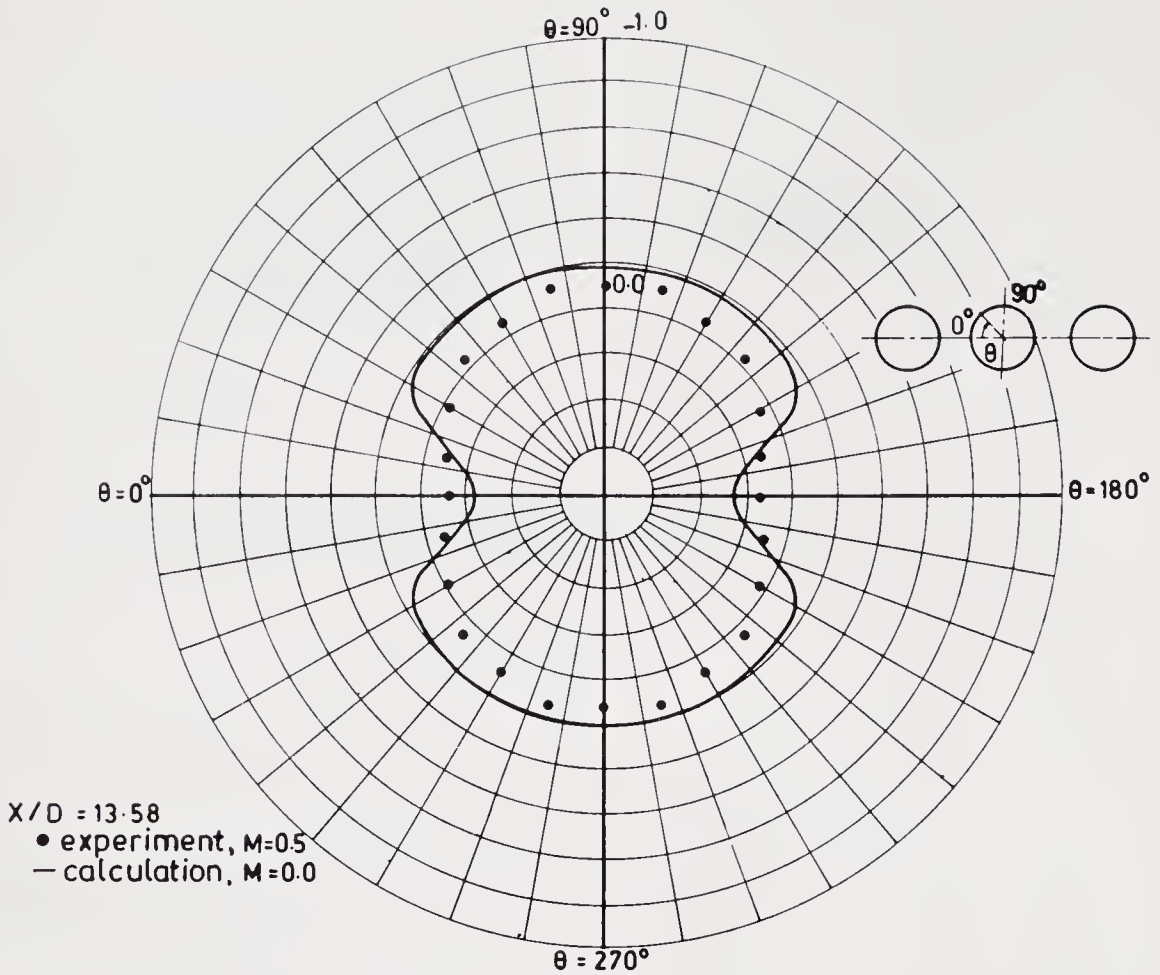


Figure 13. Typical circumferential pressure distribution on the core vehicle.

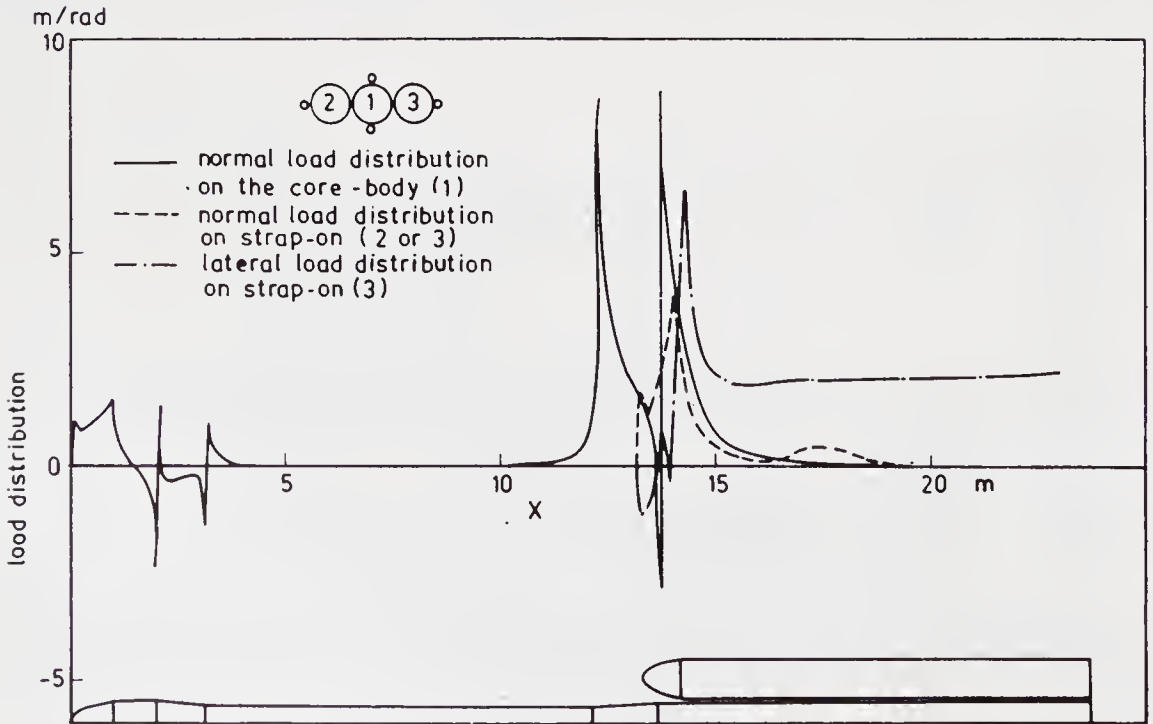


Figure 14. Typical aerodynamic load distributions on a strap-on configuration obtained by integration of surface pressure variation from the panel method.

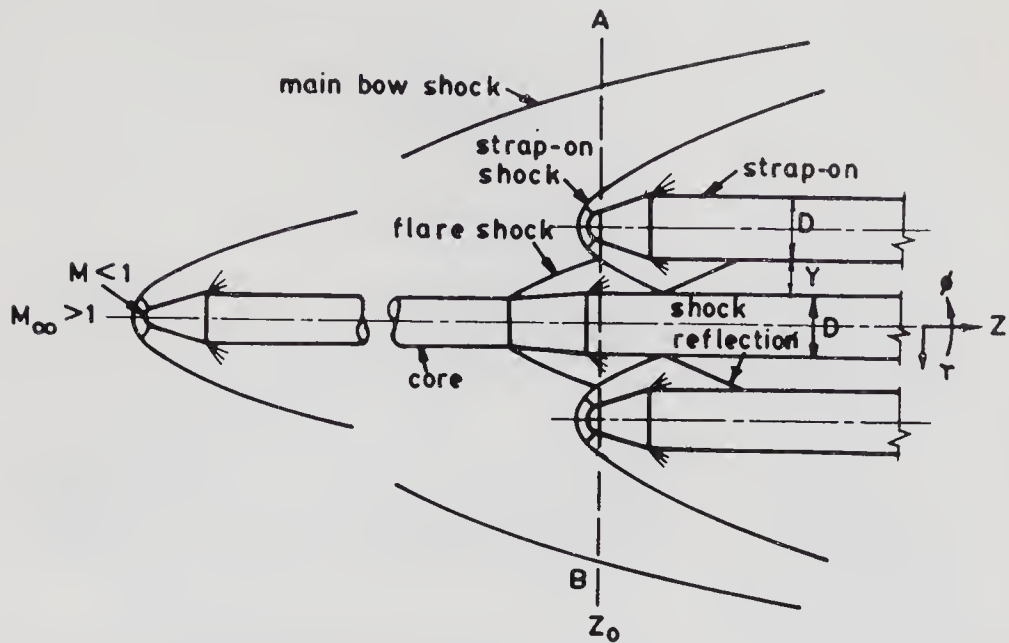


Figure 15. Schematic of supersonic flow field over launch vehicle with strap-on boosters.

can be interpolated. As there is no upstream influence in supersonic flows, the flow ahead of the strap-on upto plane AB (figure 15) is simulated about the core vehicle using a single grid scheme, while downstream of the plane AB, the computation is carried out with the overlap grid. To capture strap-on shock and its reflection accurately, clustering of the grids was found necessary in the strap-on region both in the radial and in the circumferential directions.

Figure 17 shows a typical pressure contour in the strap-on region obtained from the above computation and figure 18 represents a computer simulated Schlieren. Figure 19 gives the longitudinal pressure distribution and figure 20 the aerodynamic loading distribution on the strap-on, one of the primary parameters of design interest. The different regions of the load distribution can be correlated to the impingement and reflection of the shocks and expansions arising in this region in supersonic flow. Another important parameter of design interest is the variation in side force acting on the strap-on as a function of distance from the core and is indicated in figure 21 as obtained through integration of the pressure distribution. A comparison made with limited wind tunnel results is encouraging though more detailed generation of experimental data and comparisons are called for. The trend indicates that viscous effects, ignored in the present calculation, are not likely to be very dominant (except perhaps for a narrow circumferential band around the generator facing the core vehicle) as far as overall force levels are concerned. Similar work is in progress for the larger number of strap-ons in PSLV and the corresponding overlap grid scheme is indicated in figure 22.

While the above calculations are purely inviscid, viscous effects assume importance where the shock from the strap-on interacts with the core boundary layer. A typical shadowgraph picture of this interaction region is shown in figure 23, and boundary layer separation is indicated, as expected, for larger nose bluntness (Raja Kuperan 1982). The high overpressure observed in this region can also be seen in the figure.

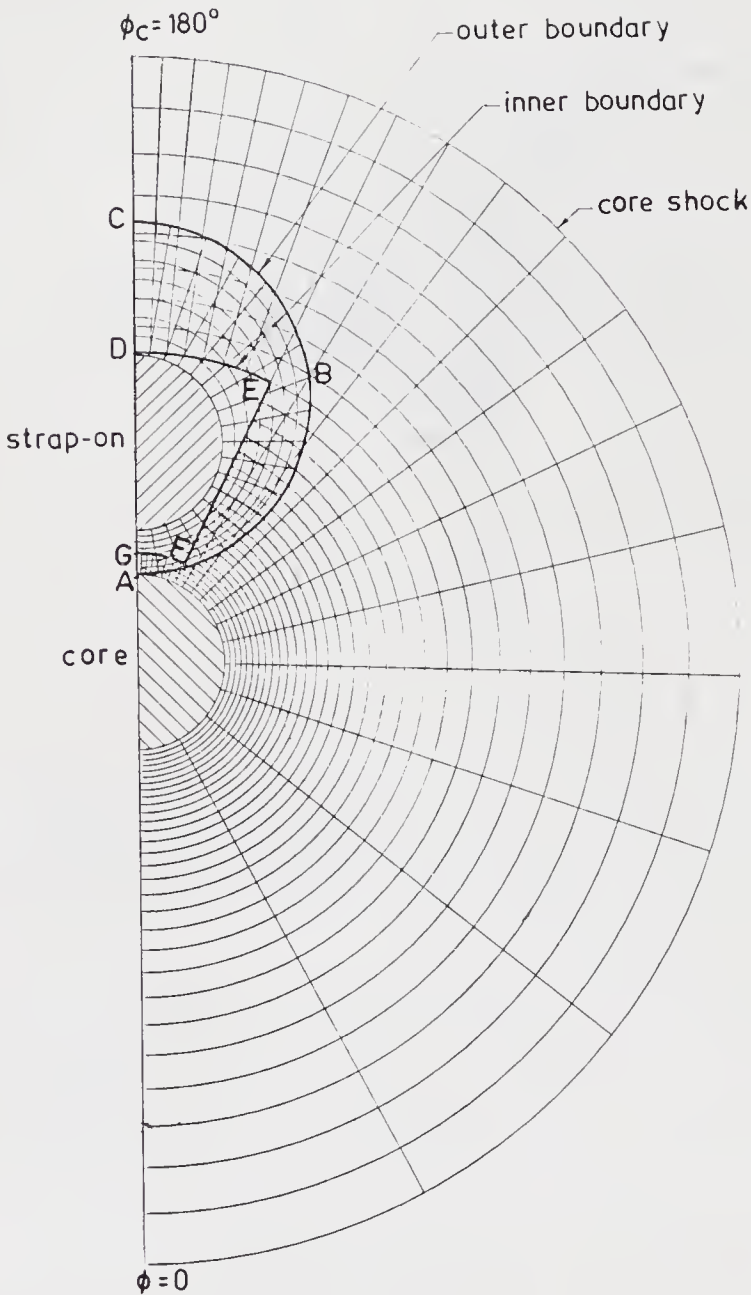


Figure 16. Grids for core and strap-on bodies with an overlap region ABCDEFG for interpolating the core and strap-on solutions.

3.3 Transonic flows

For tackling the transonic flow problem for a multibody configuration like a strap-on launch vehicle, an attempt is being made to solve the full potential equations in cylindrical polar coordinates through a component adaptive grid approach (Jai Mohan 1986, unpublished). The grid adopted for the core and the strap-on with an overlap region is shown in figure 24. Some preliminary results obtained for a low Mach number at zero incidence are compared with the incompressible panel method solution in figure 25 as a validation check for the code. Further work is in progress.

Efforts are also being made to extend the panel method to the solution of the full potential equation for transonic flow. This requires surface as well as field distribution of singularities and can involve large demands on computational time

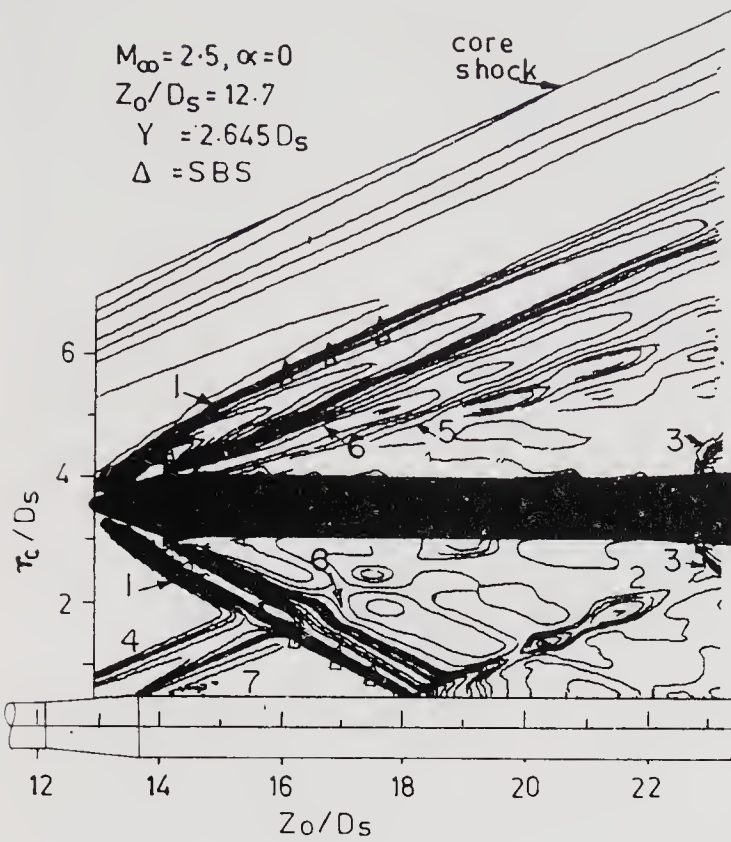


Figure 17. Pressure contours in the region of strap-on shock interference with the core; 1: Incident shock, 2: Reflected shock, 3: Strap-on flare shock, 4: Core flare shock, 5: Recompression shock, 6: Strap-on expansion fans, 7: Core expansion fans. SBS: Single body simulation method.

and memory for the three-dimensional case (K J Devassia 1986, private communication).

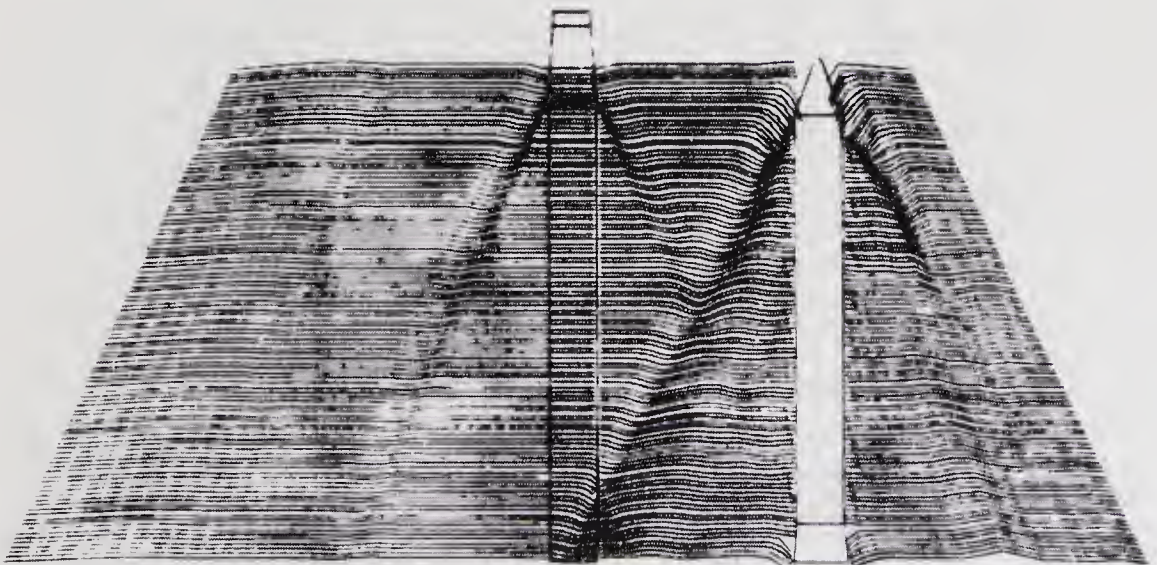


Figure 18. Typical computer simulated Schlieren for the interference region between core and strap-on: $M_\infty = 2.5, \alpha = 0, \text{Gap} = 4.145 D$.

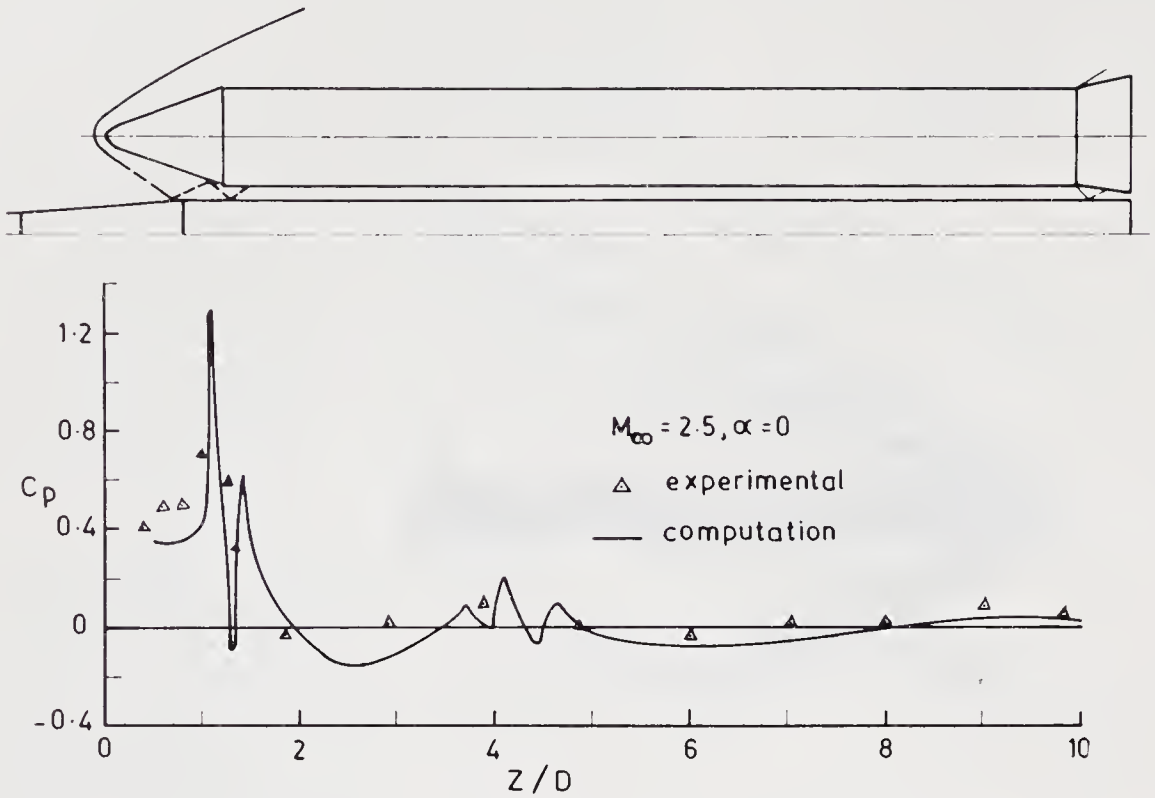


Figure 19. Longitudinal pressure distribution on the strap-on in comparison with experimental values M_{∞} = free stream Mach number, α = angle of incidence, C_p = pressure coefficient, z = axial distance, D = strap-on body diameter.

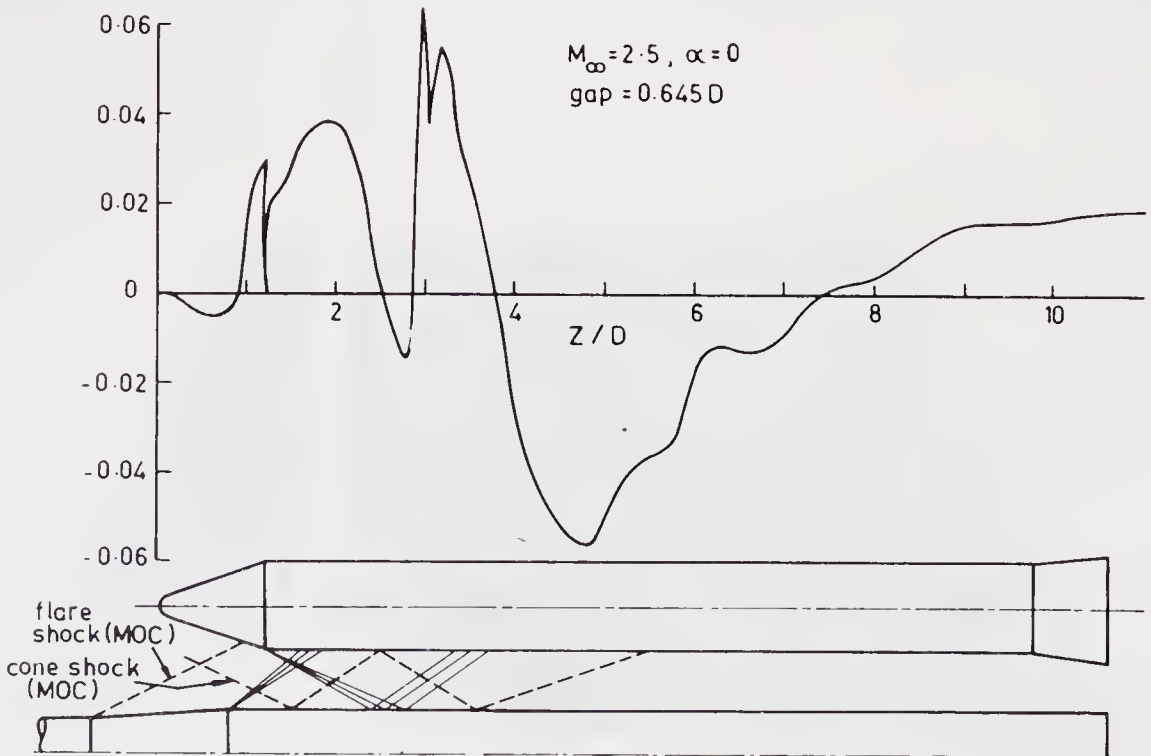


Figure 20. Aerodynamic load distribution on the strap-on; ordinate is $(S/D_s)(dC_s/dz)$ where S is base area, D_s is the strap-on diameter and C_s is the side force coefficient.

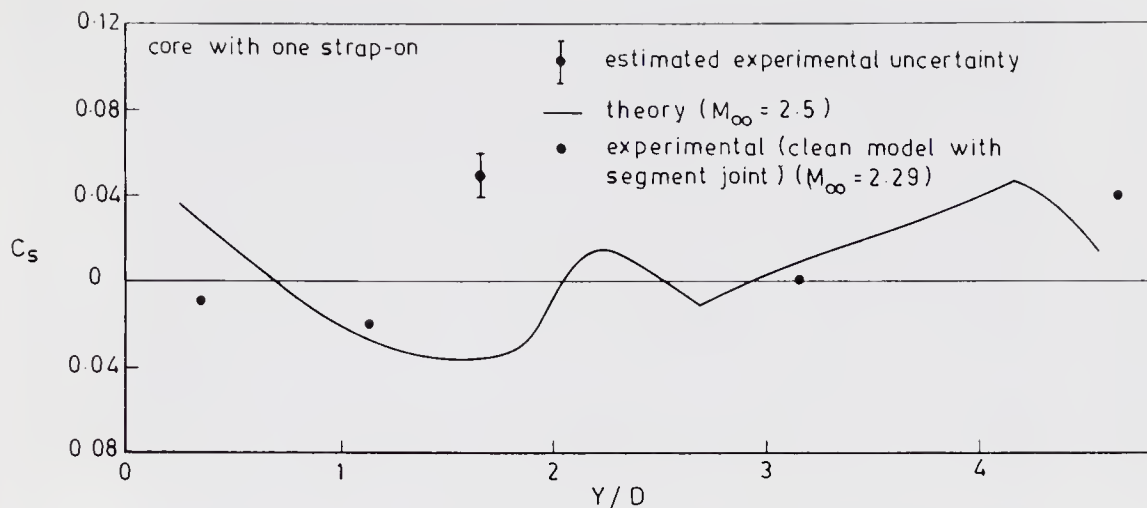


Figure 21. Variation of side force coefficient C_s of strap-on with lateral gap.

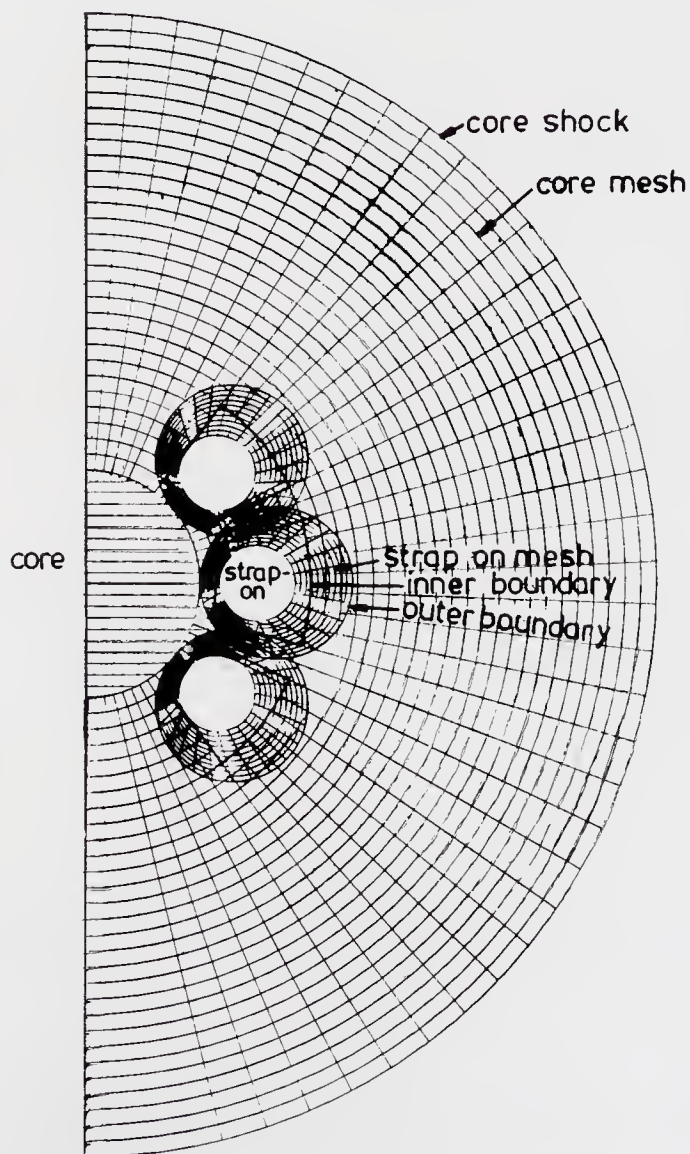


Figure 22. Overlap grid pattern for larger number of strap-ons as in PSLV.

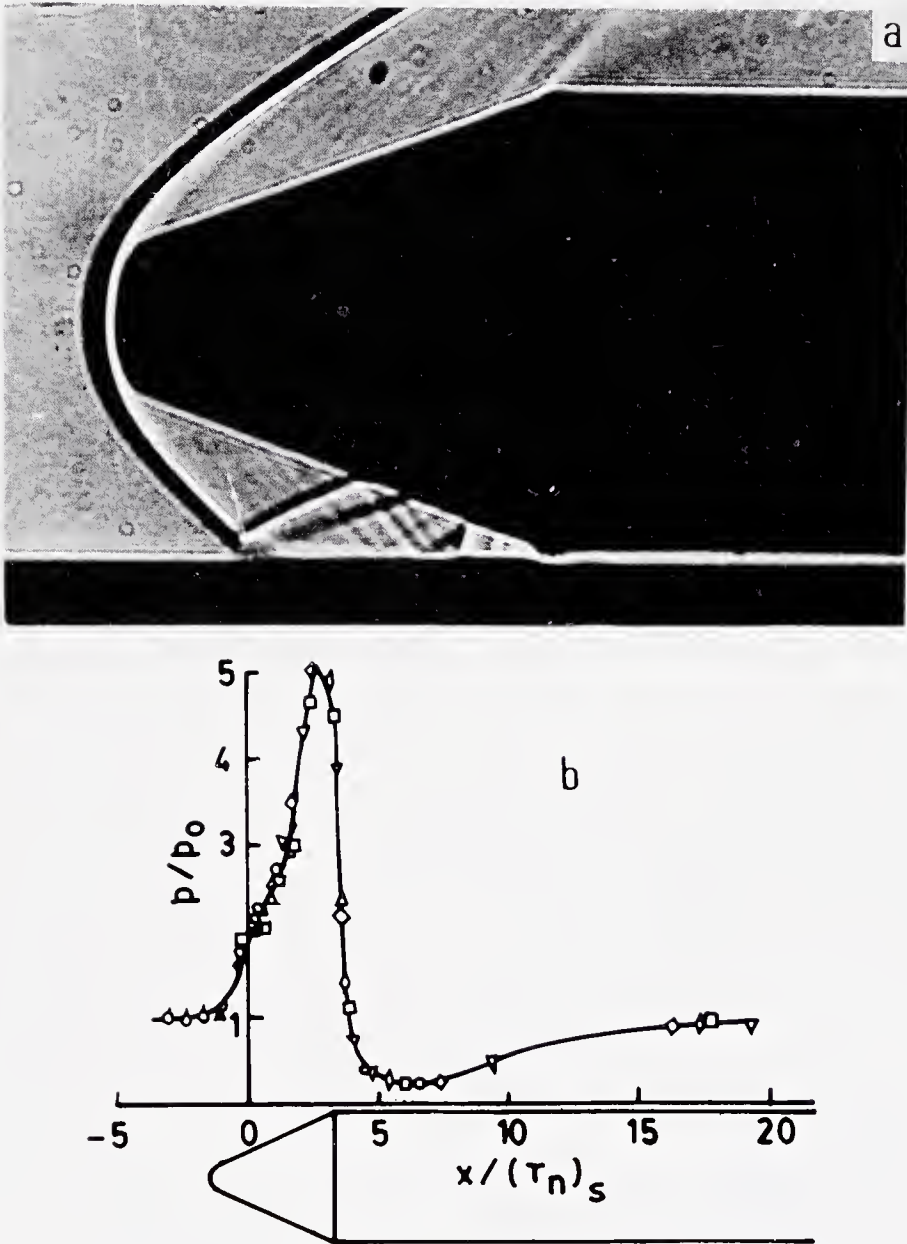


Figure 23. Strap-on shock interaction region; (a) Shadowgraph of shock reflections near strap-on booster nose. (b) Surface pressure distribution along the most windward generator of core-vehicle showing a region of high overpressure and the resultant high overpressure along the core body.

4. Strap-on separation

Laterally separating bodies pose a considerable challenge to analysis efforts when separation occurs during atmospheric flight, especially under supersonic Mach numbers and high dynamic pressure conditions (figure 26). Both ASLV and PSLV, one involving two strap-ons and the other involving six, have recently been considered.

While the initial separation force is imparted by an active system like a spring, the subsequent dynamics of the separating body is highly influenced by the complex aerodynamics involving both body interference and high incidence effects; an

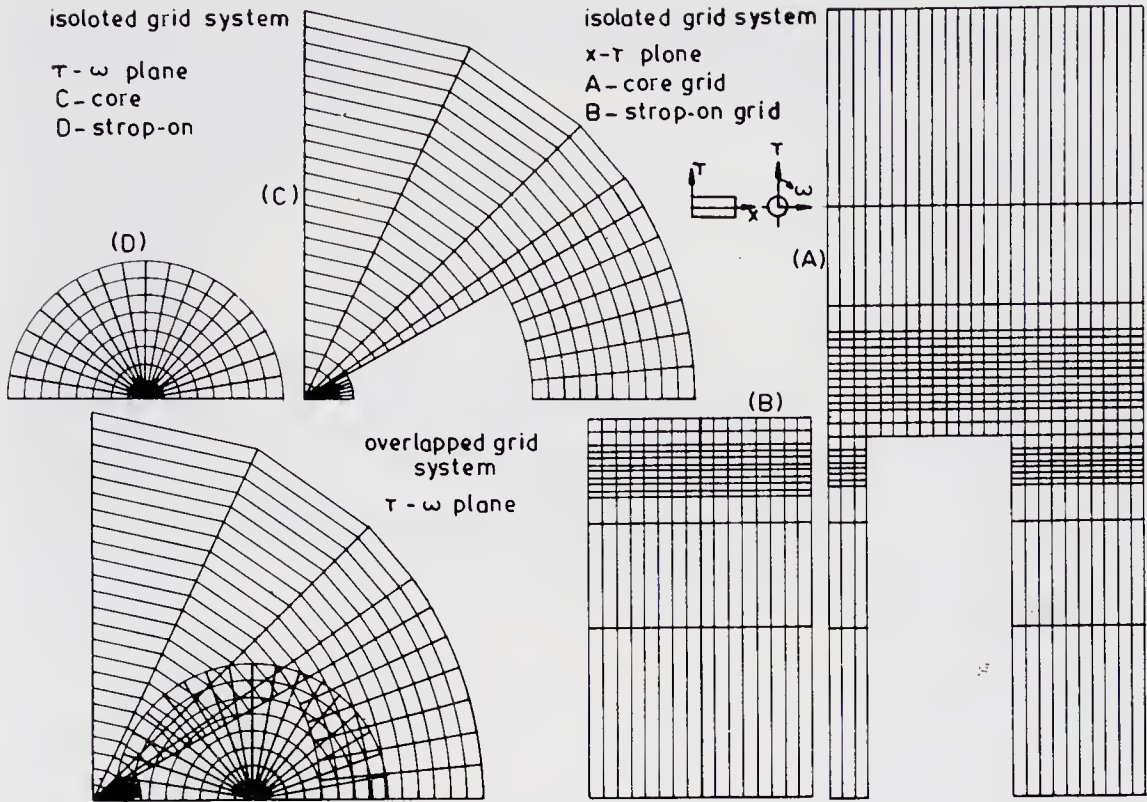


Figure 24. Component adaptive grid with overlap for core and strap-on for transonic full potential equation computation.

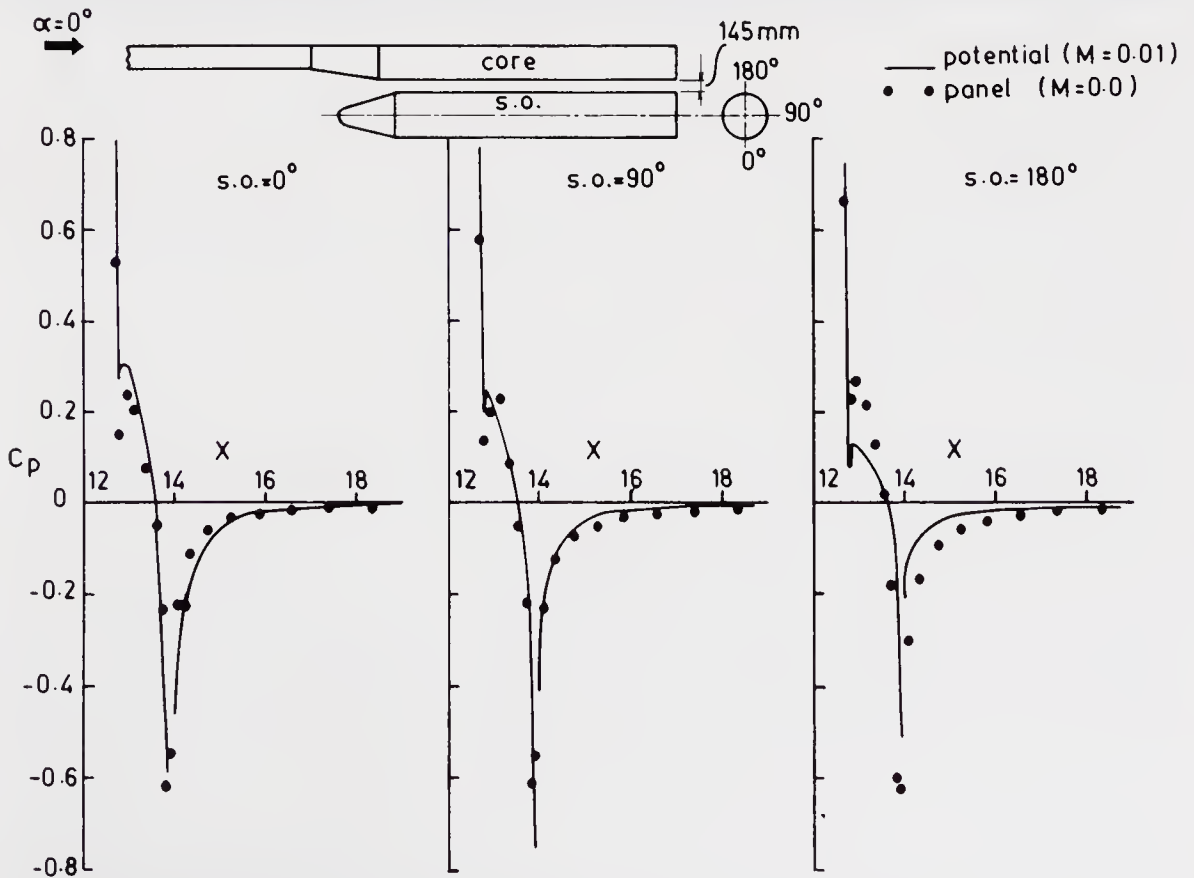


Figure 25. Preliminary results on pressure coefficient on strap-on using the full potential equation code in comparison with panel code results.

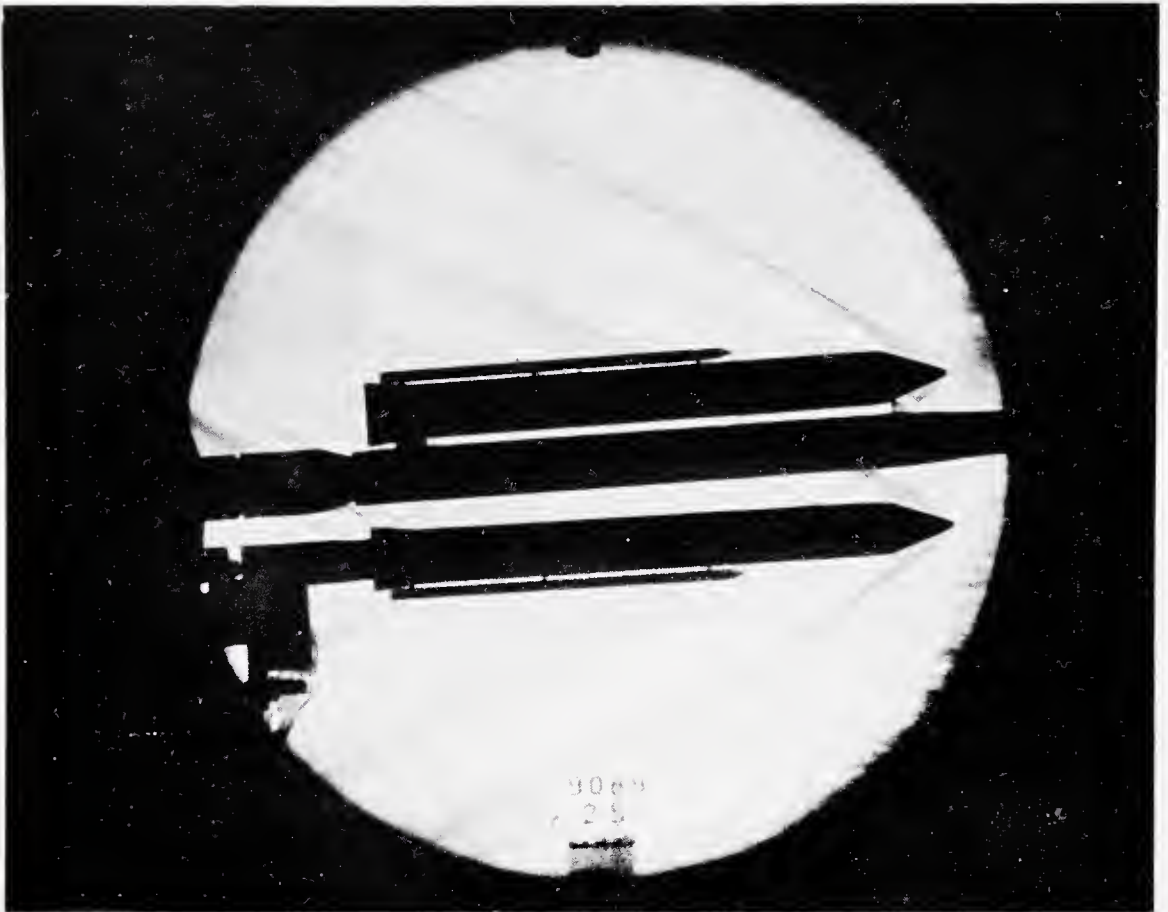


Figure 26. Schlieren picture indicating the flow field complexity during strap-on separation.

analytical solution is extremely difficult and the wind tunnel is pressed into service in a problem-solving mode.

The investigation was conducted through a two-step approach in the 1.2 m trisonic wind tunnel of the National Aeronautical Laboratory, Bangalore. At first, a coarse aerodynamic grid was generated using wind-tunnel measurements at fixed locations of the laterally separating body. The results were used for an approximate design of the separation system springs. This was followed by a more accurate time march analysis for the qualification of the design. Here the numerical simulation of the dynamics was done in an integrated fashion though off-line using wind tunnel results obtained at various steps of the separating trajectory for aerodynamic force and moment inputs (Sundara Murthy *et al.* 1986).

Figure 27 shows the different positions of the separating strap-on boosters of ASLV at various times when the vehicle is at zero incidence and figure 28 shows the effect of freestream incidence on the right and the left boosters. Figure 29 represents one of the extreme cases where the worst combination of parameters like angle of incidence, tail-off thrust etc. are considered. By an approximate analysis, it has been verified that entry of the separating body into the core jet will not pose a serious problem.

The irregular variation of aerodynamic forces is also shown in these figures highlighting the complexity of the interference effects between the core and the separating strap-on. An attempt is being made to extend the Euler solution approach of § 3.2 to the problem of the aerodynamics of separating strap-ons.

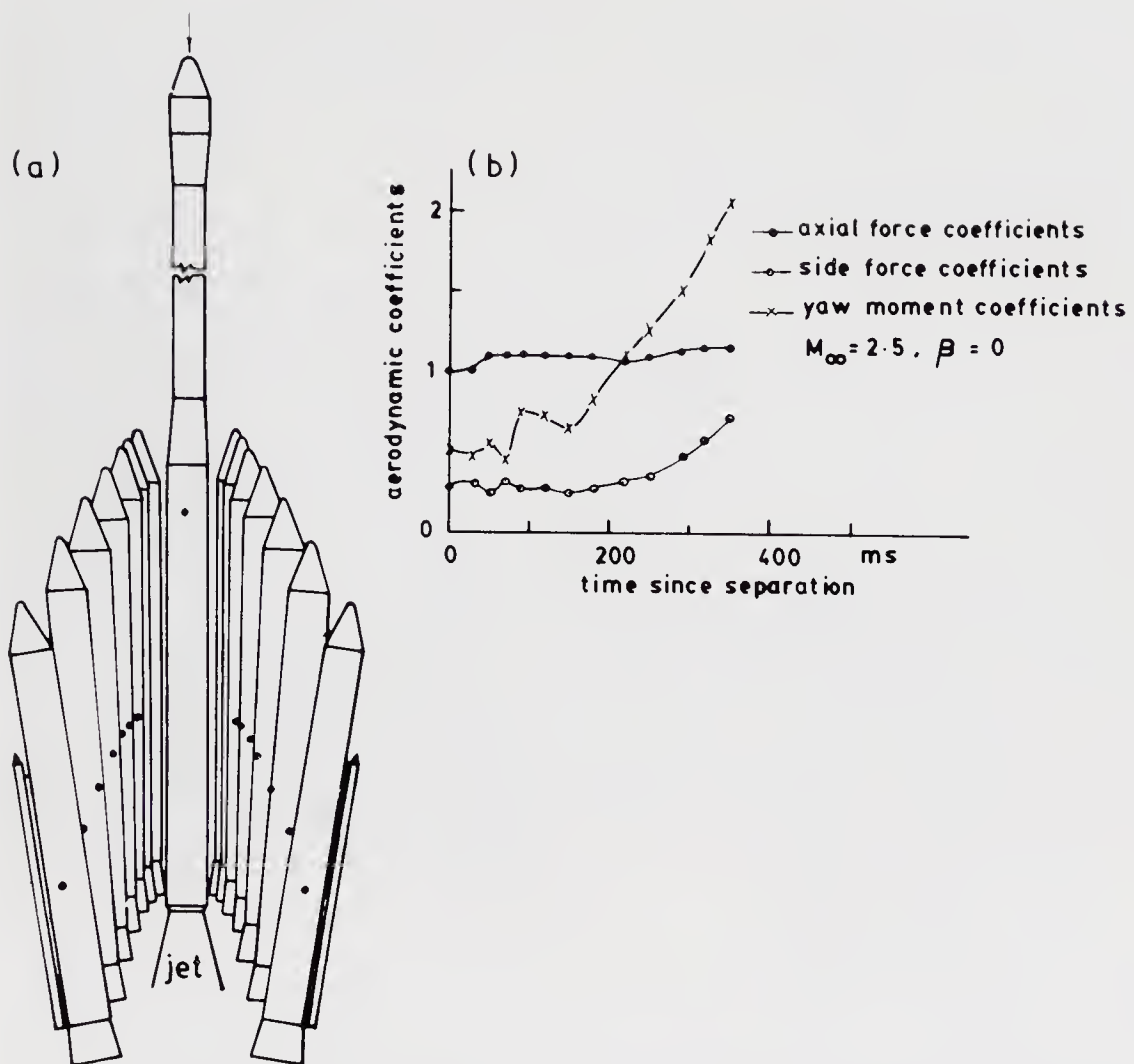


Figure 27. (a) Separation of strap-on booster at zero angle of incidence ($M_\infty = 2.5$, $\beta = 0$) and (b) the corresponding aerodynamic coefficients.

5. Stage-separation aerodynamics

The problem of stage-separation flow interactions that arises during the atmospheric flight of multistage rockets is quite complex as can be seen in the Schlieren picture shown in figure 30. Wind tunnel tests for this purpose can be quite expensive, time consuming and difficult to carry out.

In order to capture all the physical features, an attempt is being made to simulate the flow field numerically using the full Navier-Stokes equations in the region of interest shown in figure 31. In the first phase, the time-dependent problem has been tackled by employing the fluid in cell (FLIC) method (Saxena *et al* 1983, pp. 643–648). This has been applied to the simpler supersonic base flow problem as well as for the stage separation problem (laminar case), where the application of various boundary conditions, grids and convergence acceleration methods were tested out. Exponentially stretched grids and techniques of local time stepping and grid sequencing were found to result in a considerable saving in computational

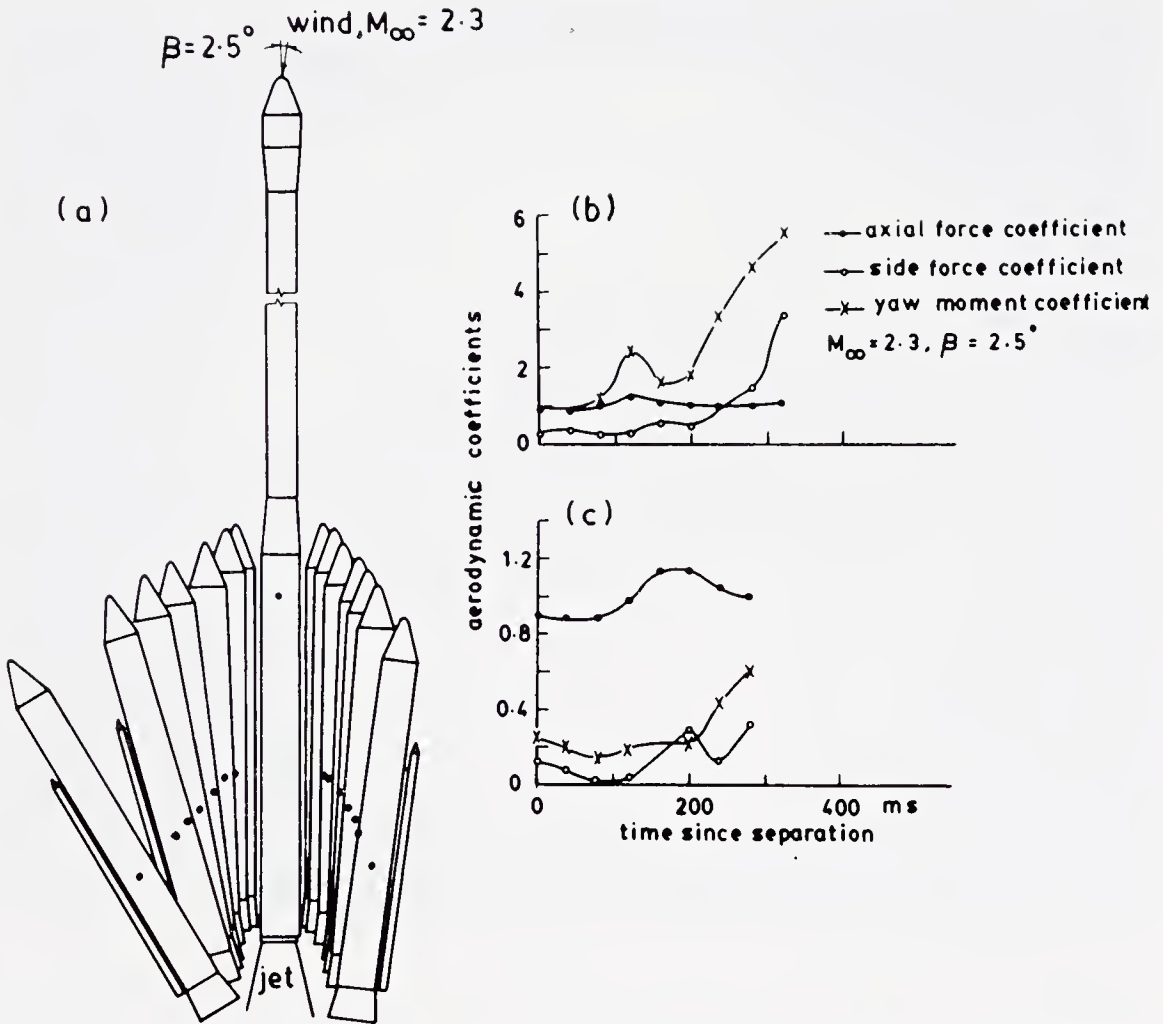


Figure 28. (a) Asymmetric separation of strap-on boosters at angle of incidence (yaw plane) ($M_\infty = 2.3$, $\beta = 2.5^\circ$). The corresponding aerodynamic coefficients, (b) leeward booster, (c) windward booster.

time. Figure 32 shows the FLIC solution for the base flow problem with supersonic jet and freestream.

However, this study brought out that even though qualitatively good results could be obtained through conventional FLIC, it could result – being first order accurate – in large numerical damping which competes with the physical viscosity in separated flow and viscous-inviscid interaction regions leading to highly smeared shocks.

To eliminate these limitations, the second-order accurate MacCormack's explicit scheme with operator splitting was tried in the second phase of the work. However, a final decision was taken to go for the state of art implicit techniques because of the very large CPU times that would be required on the VSSC CDC 170/730 computer system for the high Reynolds number Navier-Stokes solutions by the explicit method. Work also has been done in improving the conventional FLIC method and making it second-order accurate and thus competitive with the other methods mentioned above (S K Saxena, 1986 – Ph.D thesis, under preparation).

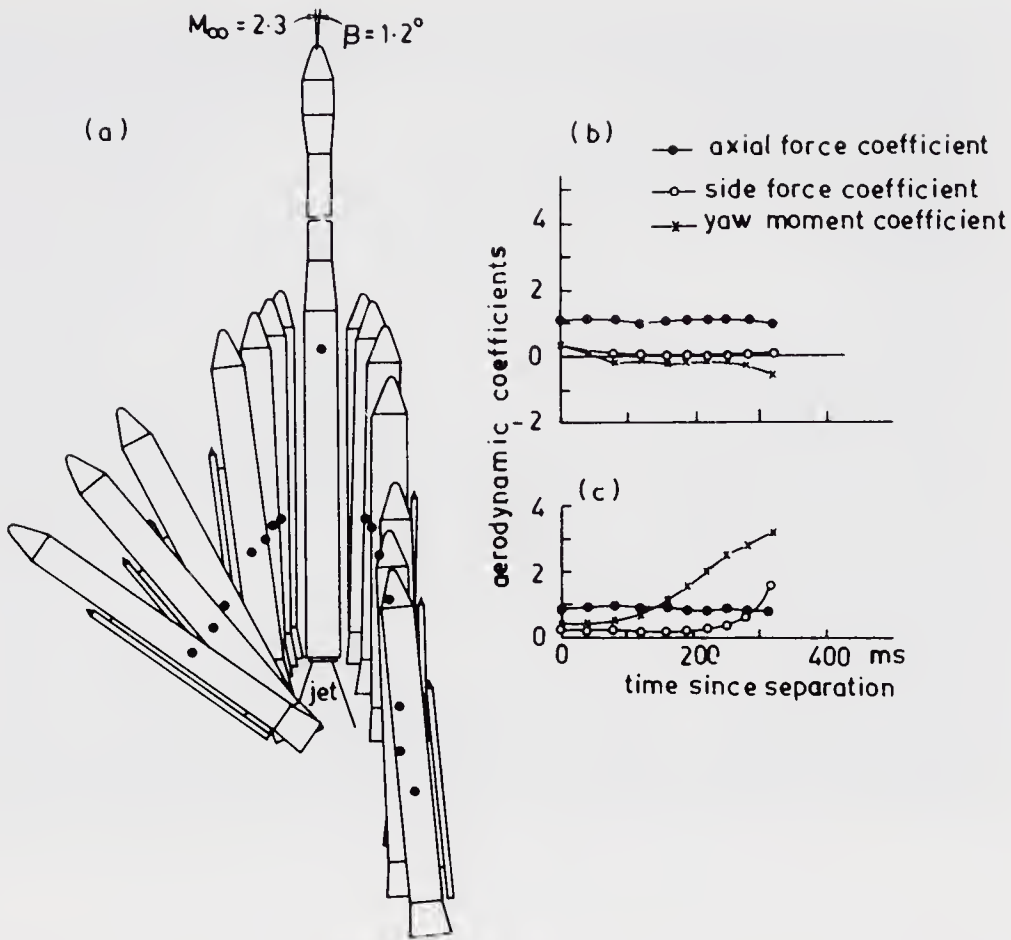


Figure 29. (a) Highly asymmetric separation of strap-on boosters under a severe off-nominal condition ($M_\infty = 2.3$, $\beta = 1.2^\circ$). The corresponding aerodynamic coefficients for (b) windward booster, (c) leeward booster.

6. Boat-tail aerodynamics

In many launch vehicles the payload shroud has to be larger in diameter as compared to the rest of the vehicle in order to accommodate payloads of larger volumes. This leads to bulbous (or hammerhead) configurations which are susceptible to problems like transonic buffet, shock wave-boundary layer interactions, local flow separations etc. Some of these problems of both steady and unsteady nature are under investigation at VSSC.

6.1 Supersonic flow

Aerodynamic loading distributions computed through a simple second-order shock expansion approach (Goyal 1981) are shown in figure 33 for PSLV and ASLV forebodies along with experimental results. An equivalent body concept is used wherein each meridian is defined by an equivalent axisymmetric body at zero incidence. Three-dimensional inviscid flow field solution on such bodies at angle of incidence is also obtained by the shock capturing finite difference Euler solver (Singh & Rajaram 1985) with grid clustering close to the body to resolve the entropy layer. A typical result is shown in figure 34.

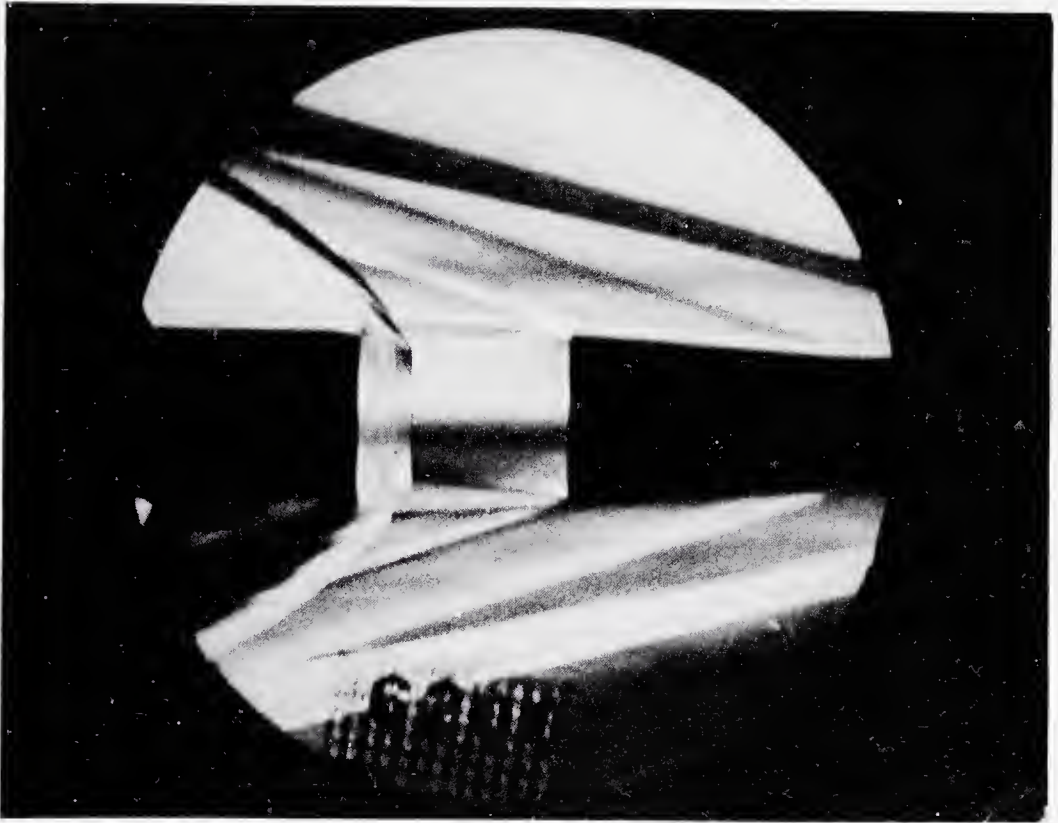


Figure 30. Schlieren picture of stage separation with separating booster (left) in the vicinity of sustainer (right) jet.

A supersonic flow field simulation has also been attempted for the boat-tailed payload shroud of PSLV through a time-dependent Reynolds-averaged Navier-Stokes code (Purohit 1986) using the Baldwin & Lomax (1978) turbulence model. Figure 35 shows a 1/80th scaled-down model (used for wind tunnel tests) and the grid system employed with clustering of grids near the surface and around the boat tail. Pressure distributions obtained at various Mach numbers 1.80, 2.47, 3.0 and 3.5 from the computational code are compared with experimental results at zero incidence in figure 36. Details of the velocity field near the boat tail and shock strengths for various Mach numbers are shown in figure 37. From this, it is seen that the flow is separated upto Mach number 2.47 beyond which it is attached. The observation is further substantiated by the skin friction plots along the boat tail shown in figure 38. At $M = 2.47$, the condition of incipient separation prevails.

6.2 Transonic flow

Transonic flow calculations have been performed for a boat-tailed body using the full potential equations (Jai Mohan 1985). In the boat-tailed region, where viscous effects are important, an axisymmetric viscous bump model is introduced at the shock foot in the inviscid calculation. This solves the integral boundary layer equations, using as initial conditions the local flow upstream of the shock and the total flow field is simulated in an interactive manner. A typical comparison with experimental results is shown in figure 39.

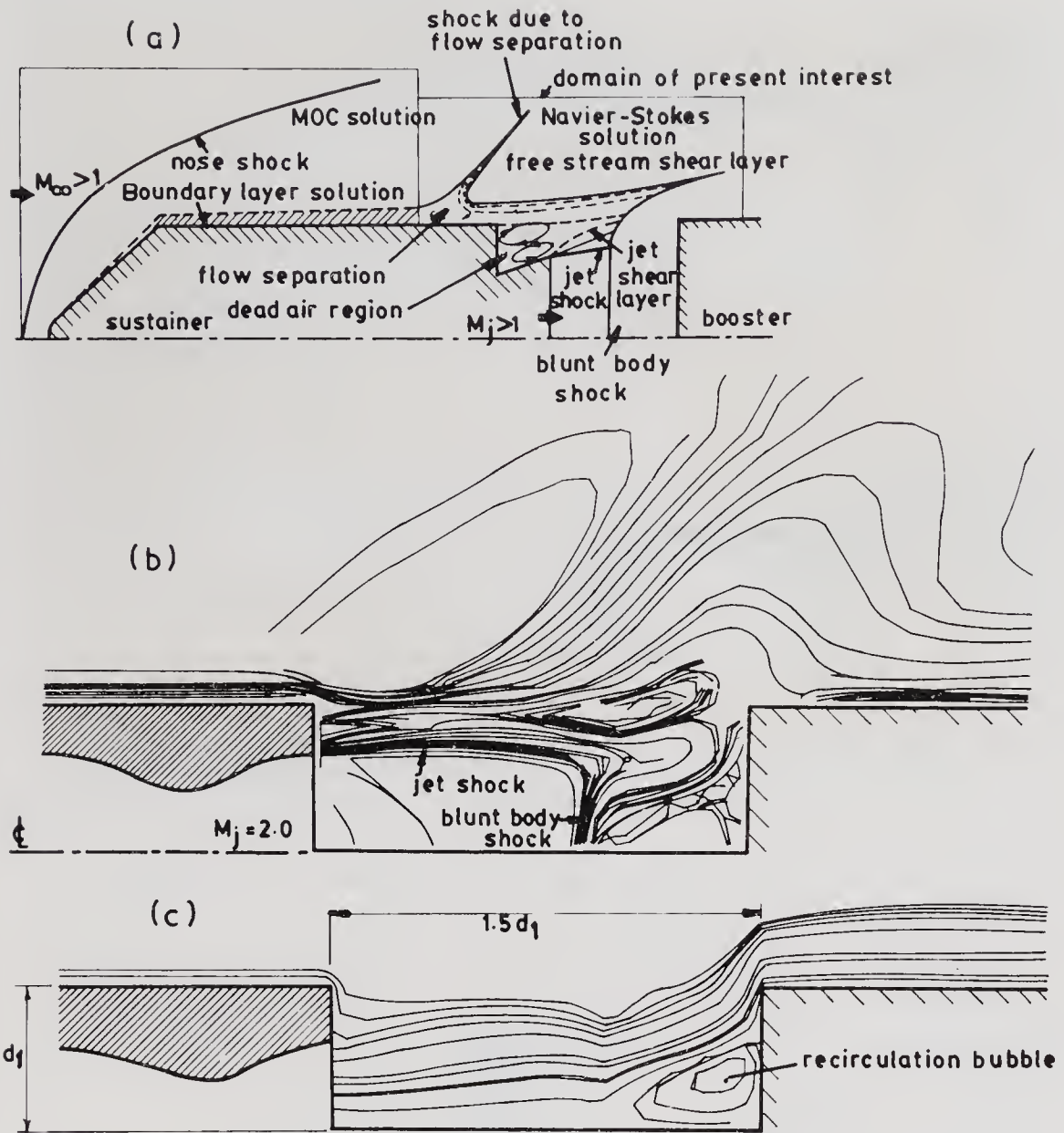


Figure 31. Numerical simulation of jet on-stage separation aerodynamics through FLIC (fluid in cell method); Free stream Mach number = 2.0, jet Mach number = 2.0, exit jet to base diameter = 0.6, Reynolds number based on length upto base = 0.4×10^6 , specific heat ratio = 1.4, (a) General configuration and domain of present interest, (b) Constant Mach number contours, (c) Streamline plot.

An attempt has been made to tackle the transonic unsteady flow problem over a boat-tailed configuration using the unsteady Reynolds-averaged Navier-Stokes code mentioned earlier (Purohit 1986). Figure 40 shows the body considered and the grid system used. It also shows a comparison of the steady-state results obtained from the computation with the experimentally obtained pressure coefficient C_p for a Mach number of 0.8 and a Reynolds number of $10^6/\text{metre}$. From the unsteady surface pressure data shown in figure 41, sound pressure levels (SPL) are evaluated at various locations on the payload shroud. As can be seen in the figure, a maximum SPL of 152 dB at a frequency of 300 Hz was resolved at $X/D = 1.08$. The

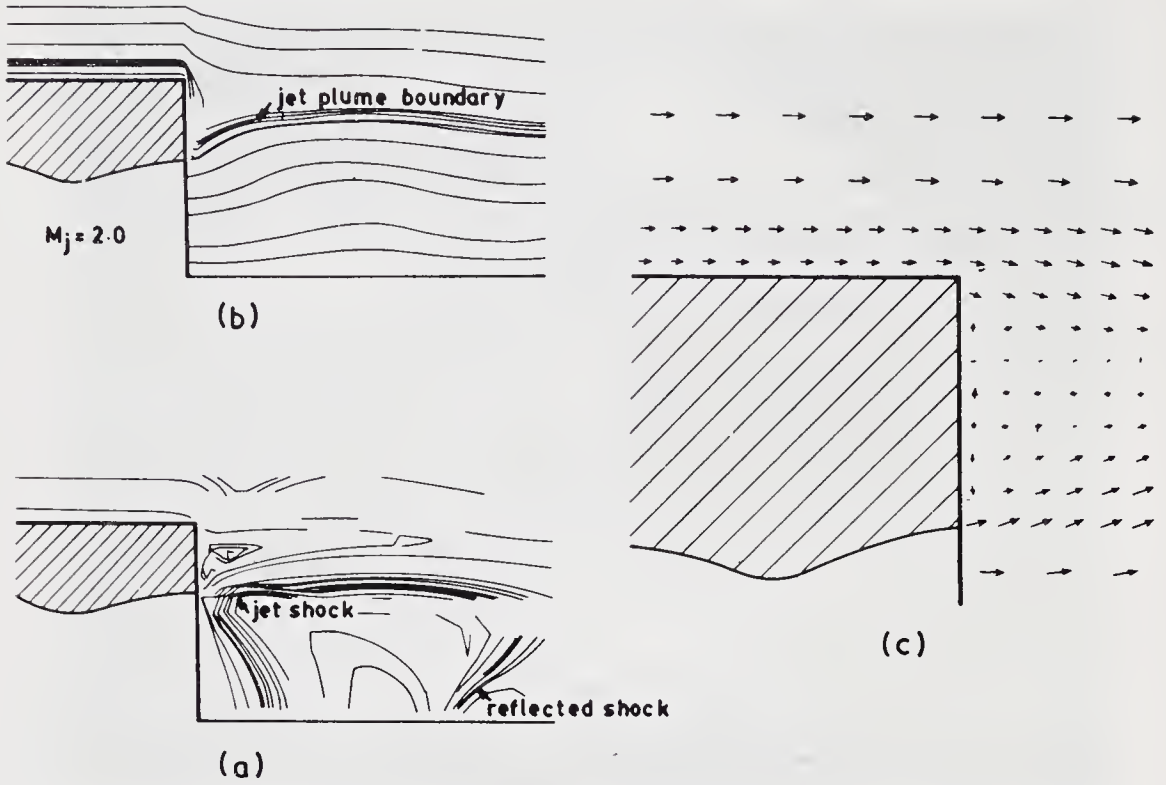


Figure 32. Numerical simulation of base flow with jet through FLIC (Fluid in cell method); Conditions same as in figure 31. (a) Constant Mach number contours. (b) Streamline plot. (c) Velocity plot.

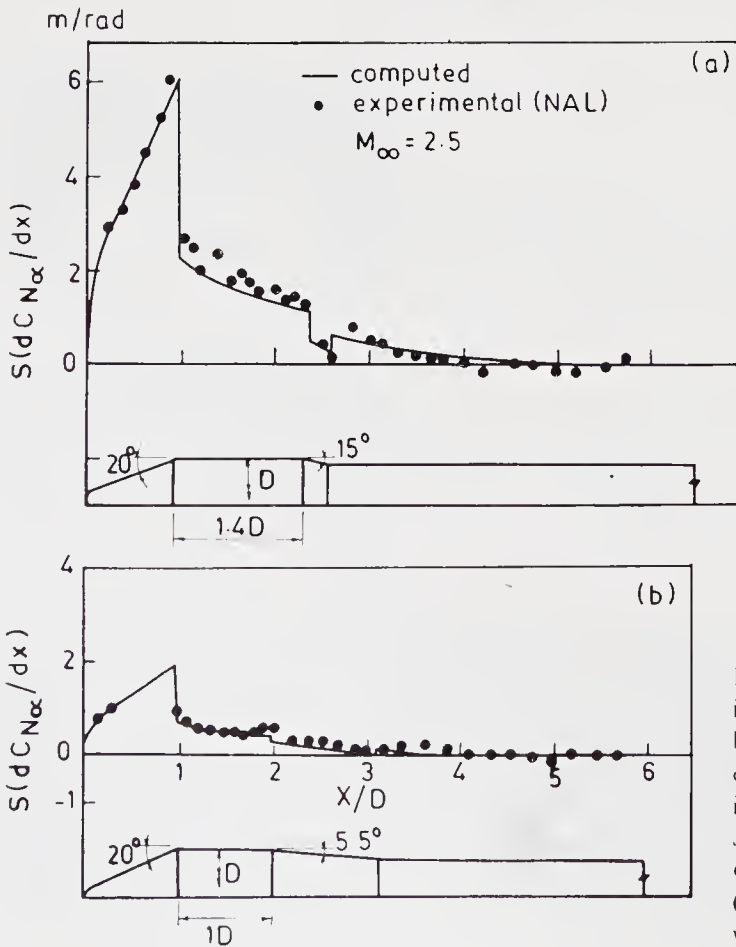


Figure 33. Aerodynamic loading distributions on boat-tailed bodies through second-order shock expansion approach in comparison with experimental results; S = reference area based on D , C_N = normal force derivative. (a) PSLV with $D = 3.2$ m. (b) ASLV with $D = 1$ m.

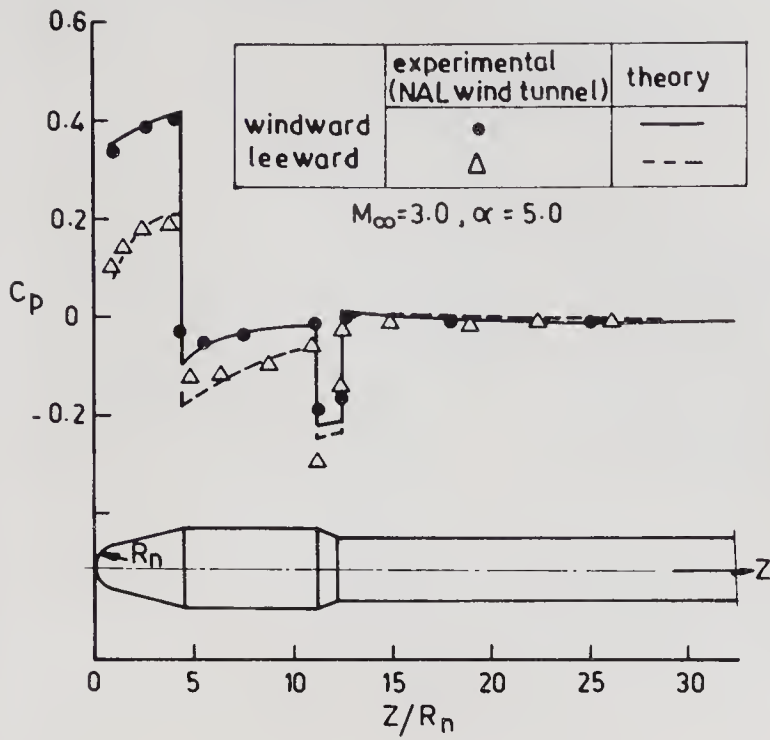


Figure 34. Pressure coefficient on a boat-tailed body in supersonic flow at incidence obtained from shock capturing finite difference Euler solver in comparison with experimental results.

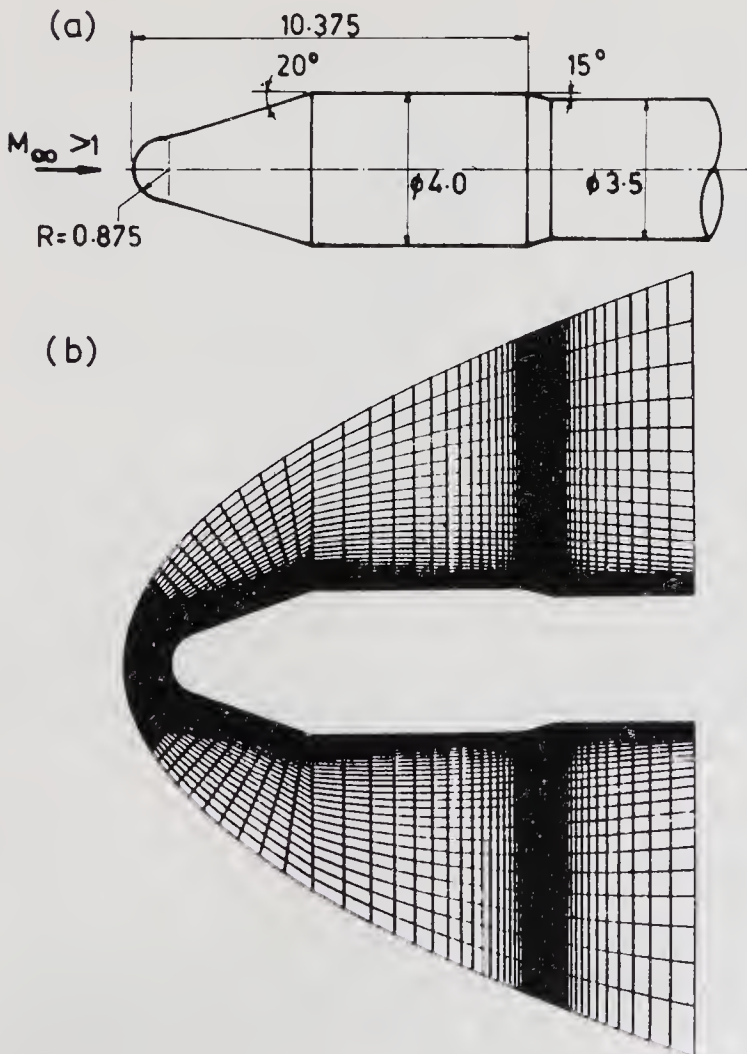


Figure 35. (a) The boat-tailed heat shield configuration and (b) the grid system used for the Reynolds-averaged Navier-Stokes solution.

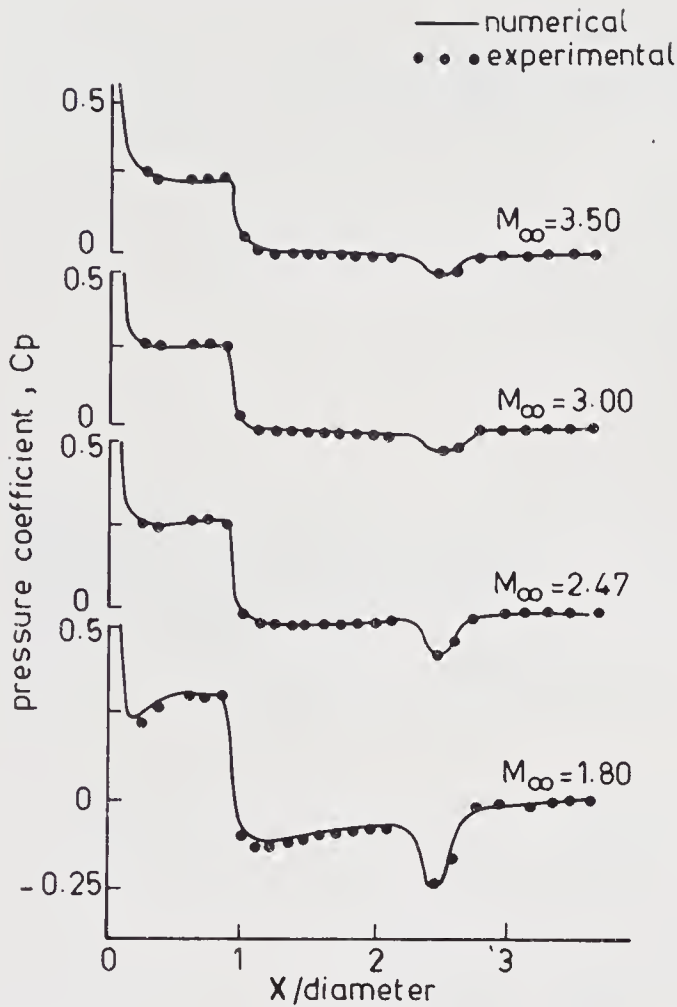


Figure 36. Pressure coefficient along the length of the body obtained through Navier-Stokes solver in comparison with experimental results.

highest credible frequency of the numerical analysis was 14.8 kHz which can be improved by considering a finer mesh. Also, the initiation and development of vertical motion caused by boundary layer separation at the boat-tail corner is captured by the time-dependent calculation as shown in figure 42.

Unfortunately, these unsteady flow computations had to be restricted to the zero incidence case because of computer limitations in considering the additional circumferential variation that occurs at the angle of incidence, even though the code is capable of handling the 3D problem. Further, an approach of this type which uses Reynolds averaged equations with a steady-state turbulence model is expected to capture relatively low frequency phenomena like shock oscillations during transonic buffet. Through this approach, it may not be possible, however, to capture accurately the high frequency content of aerodynamic noise.

7. Some hypersonic flow problems

Hypersonic flow simulation is important for an ascending launch vehicle in the upper regions of the atmosphere and assumes further significance if atmospheric reentry is involved as in the case of the Space Shuttle. In order to simulate the stagnation region flow, locally similar solutions incorporating the effect of the

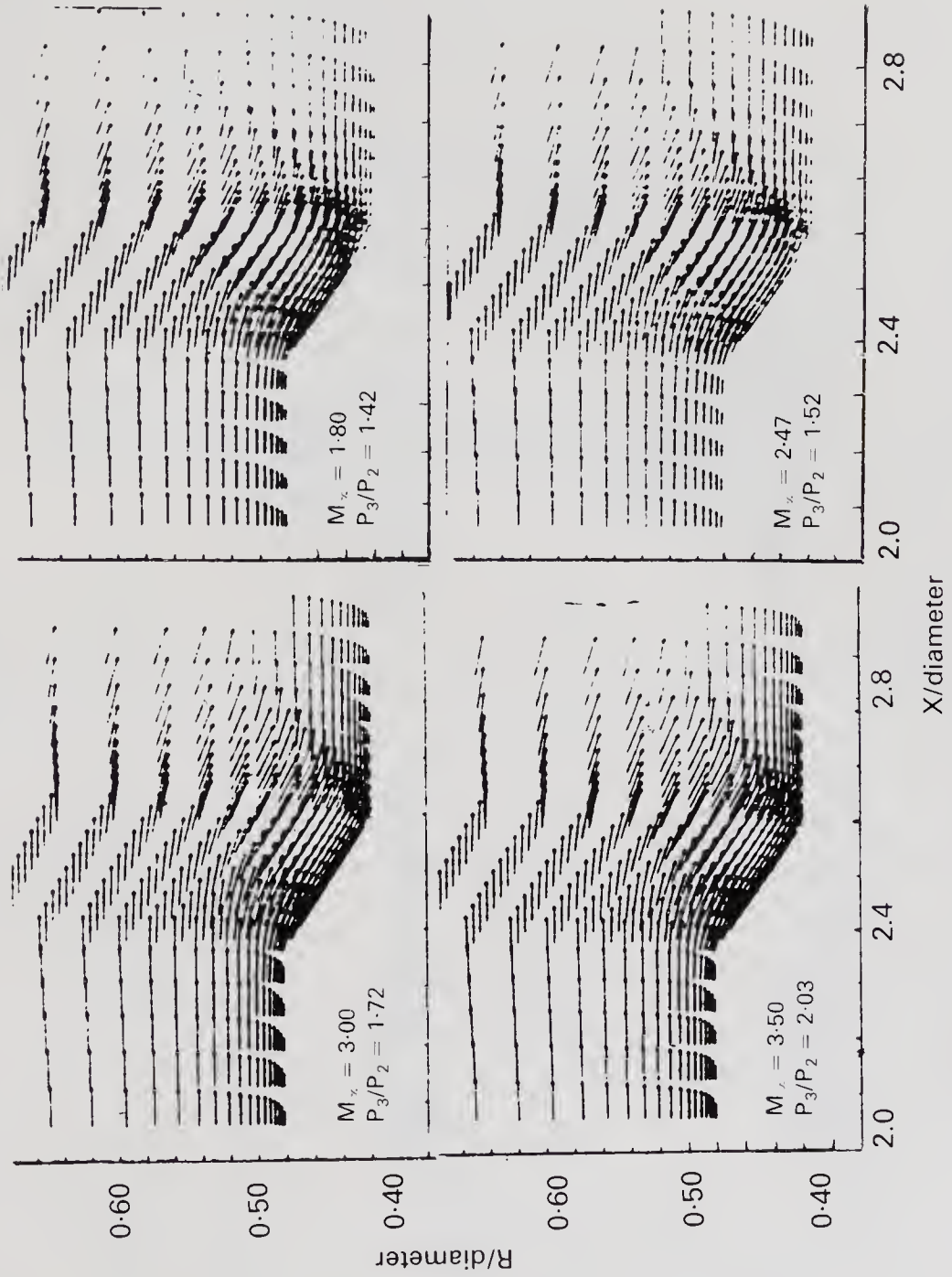


Figure 37(a). Flow field along boat-tail junction for various Mach numbers.

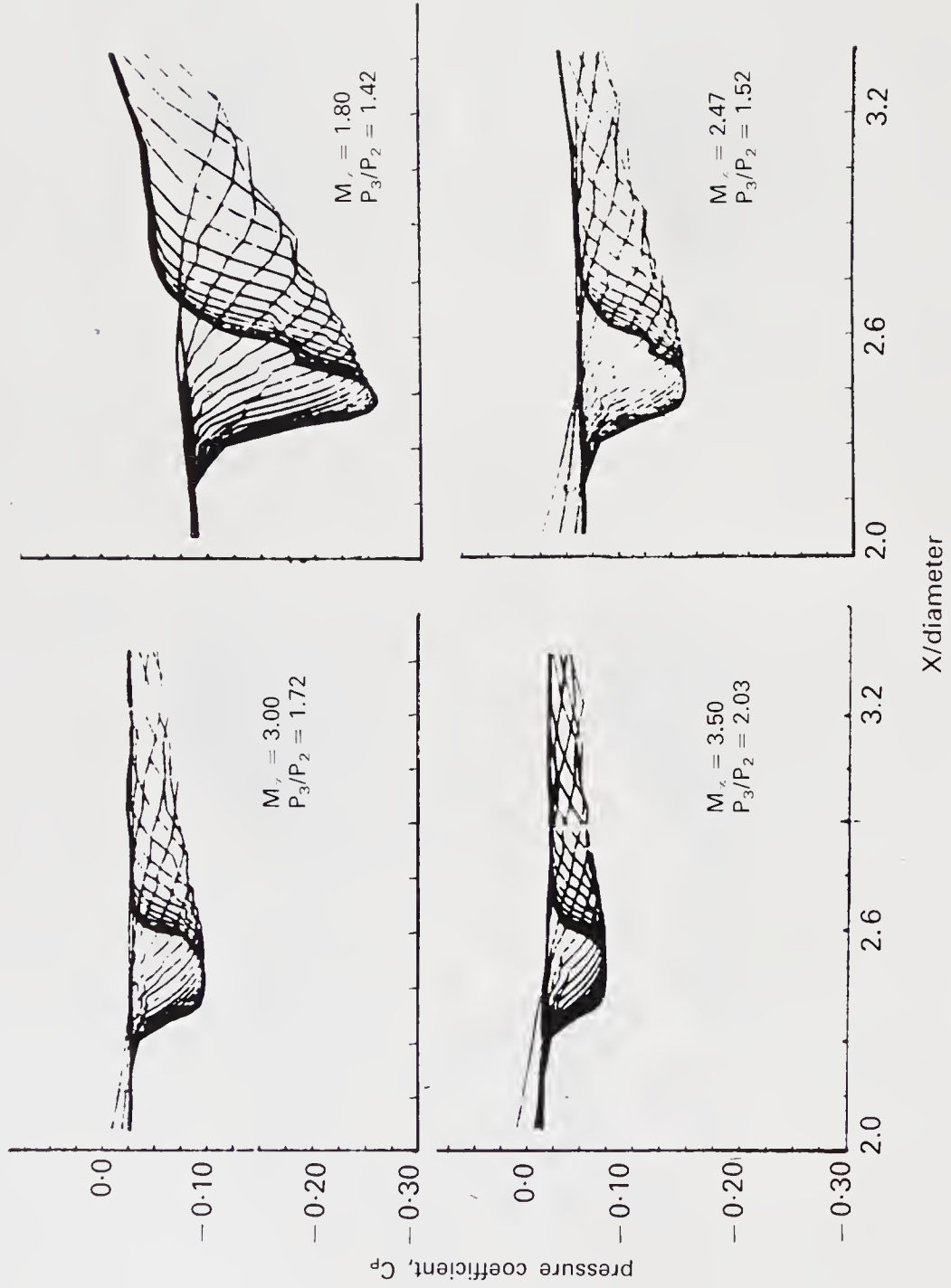


Figure 37(b). Shock strengths for Mach numbers corresponding to those of figure 37a.

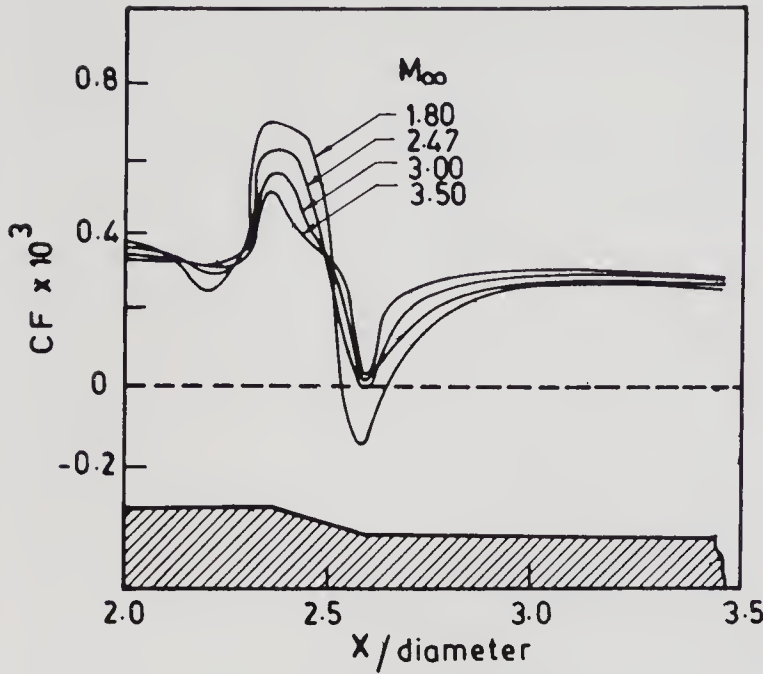


Figure 38. Skin friction coefficient along boat tail showing incipient separation condition at $M = 2.47$.

stagnation point shock curvature, which may be different from the body curvature, have been obtained on the basis of full steady-state Navier-Stokes equations. An improved series expansion of the flow variables is developed and the leading term of the series is evaluated with surface slip and shock slip boundary conditions (Pradeep Kumar 1986, unpublished). The variations of stagnation point impact

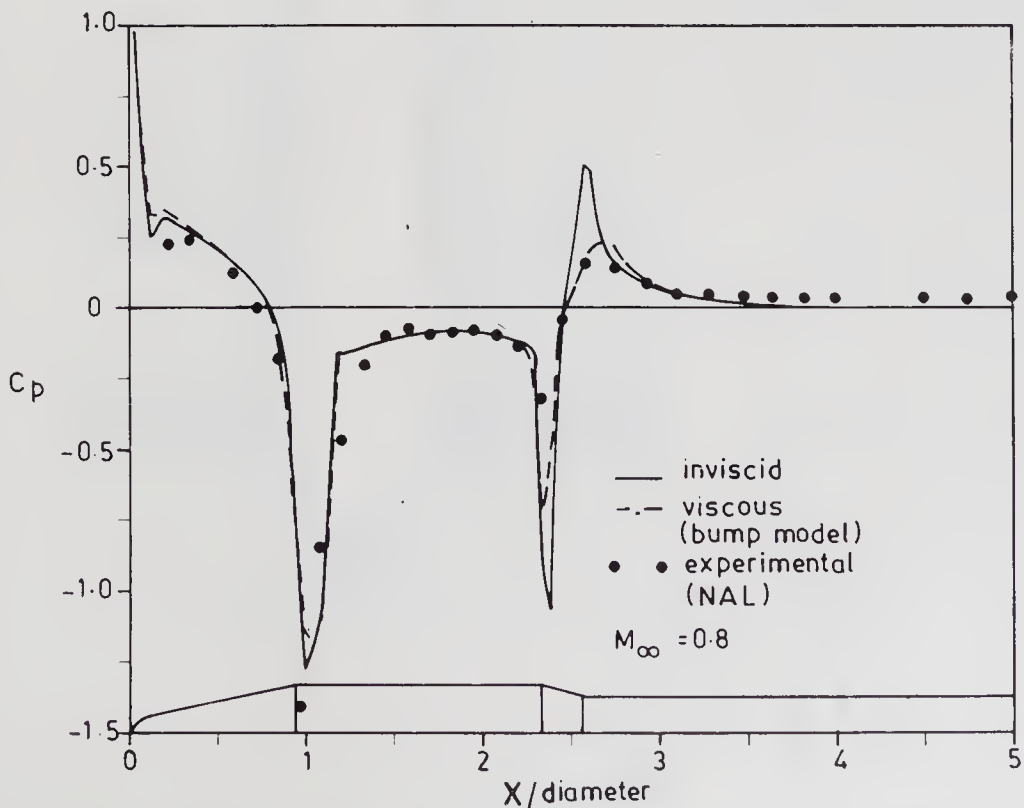


Figure 39. Transonic pressure distribution on a boat-tailed configuration with viscous correction through 'bump model'.

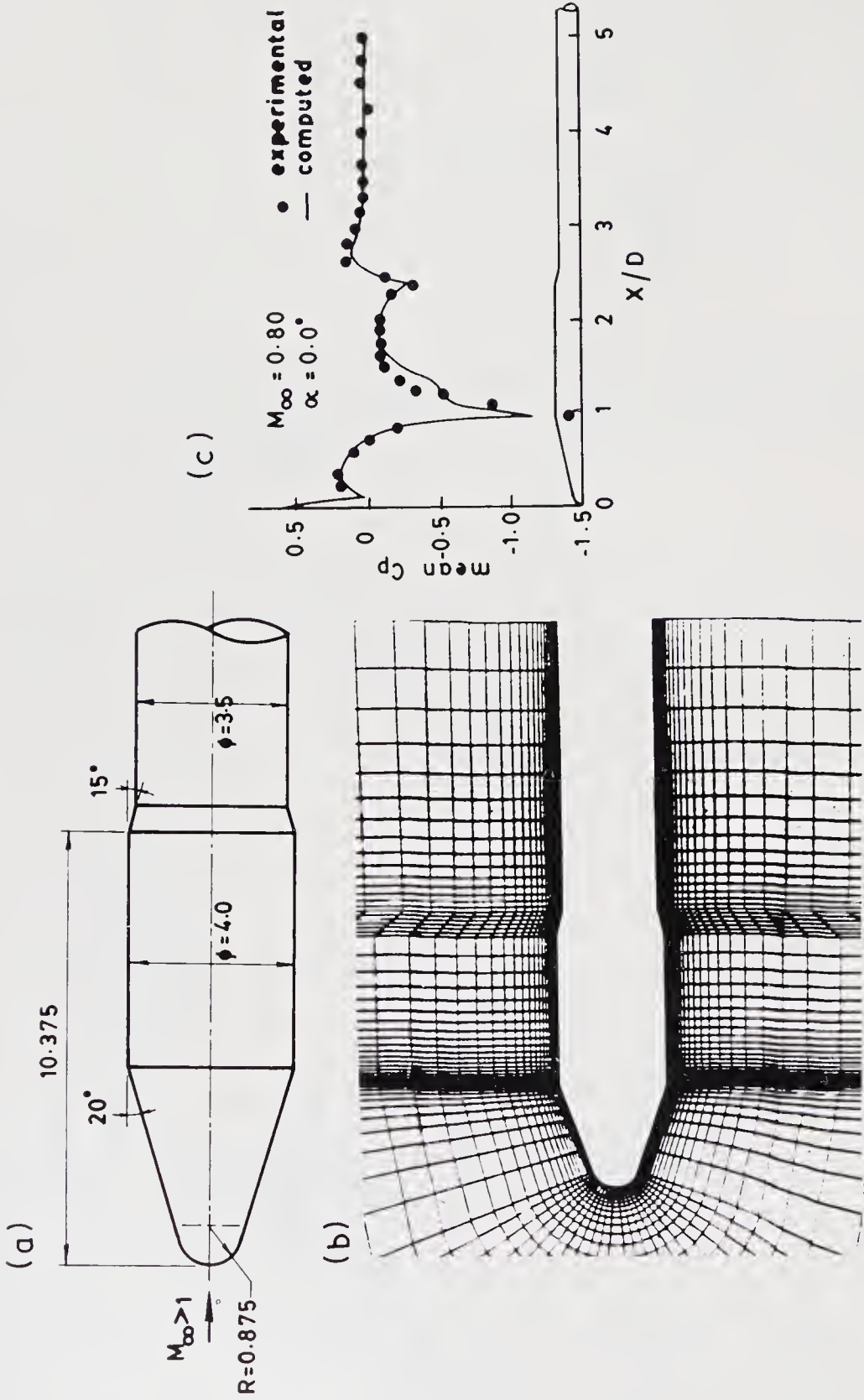


Figure 40. (a) Body and (b) grid system for a boat for transonic flow computation through unsteady Reynolds-averaged Navier-Stokes code; (c) comparison of steady state pressure distribution with experimental results

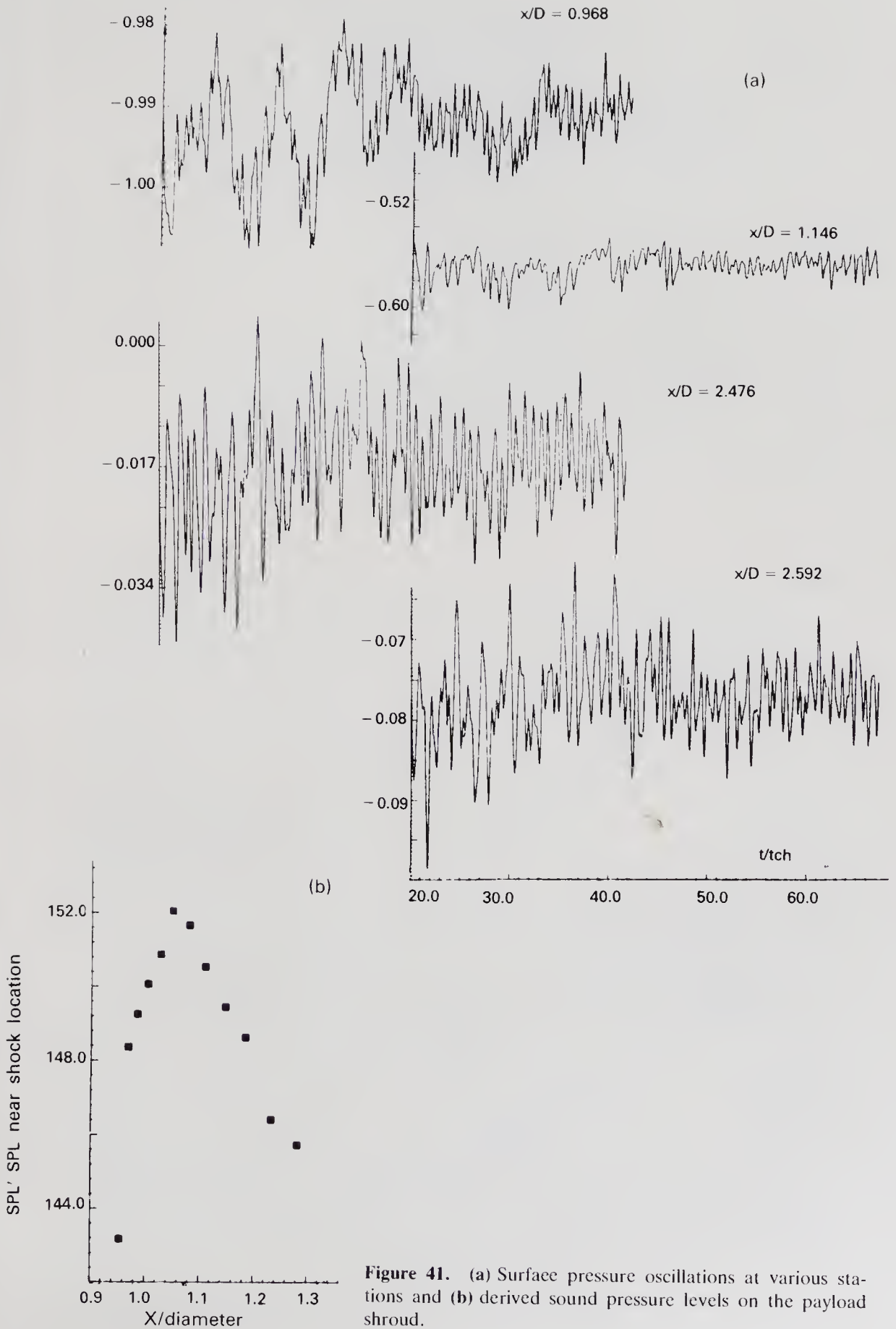


Figure 41. (a) Surface pressure oscillations at various stations and (b) derived sound pressure levels on the payload shroud.

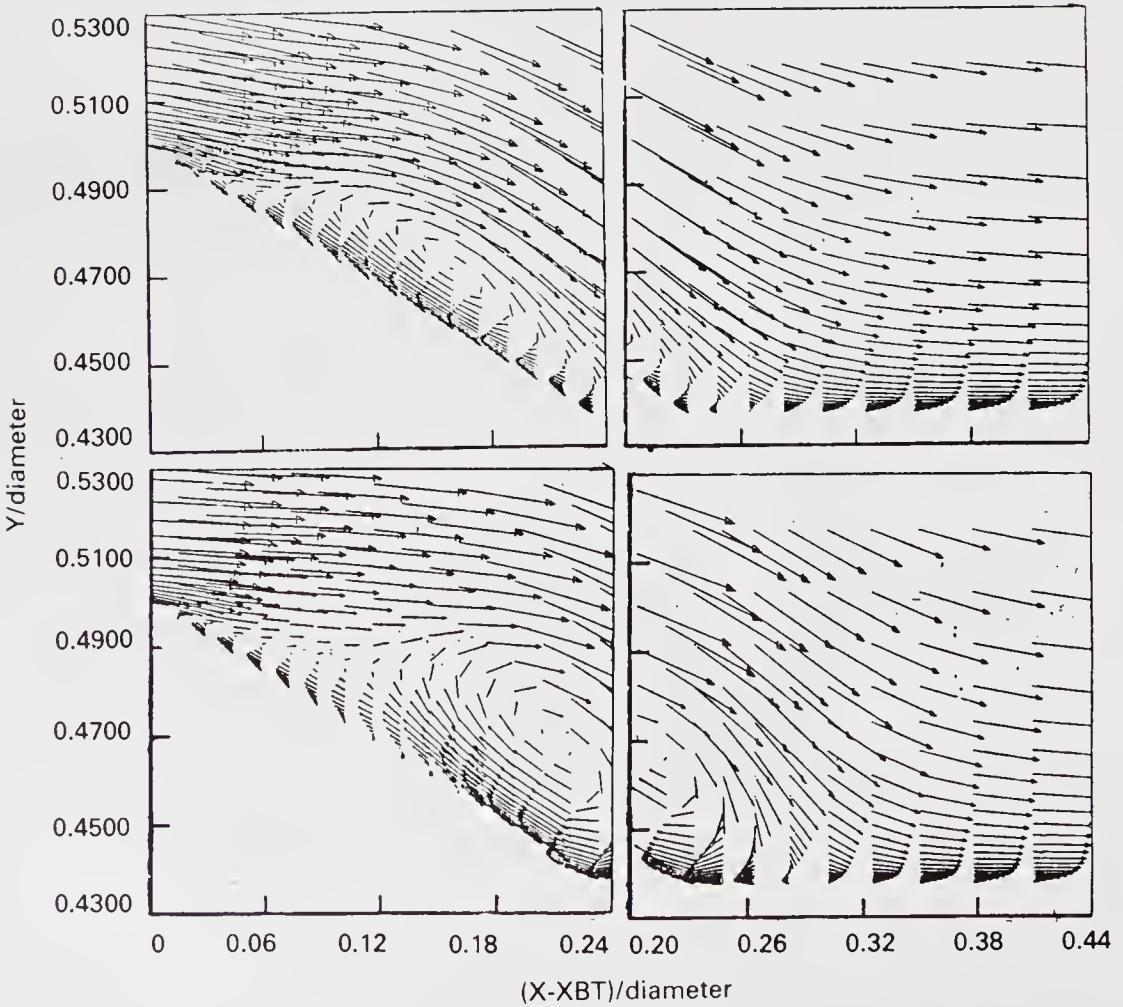
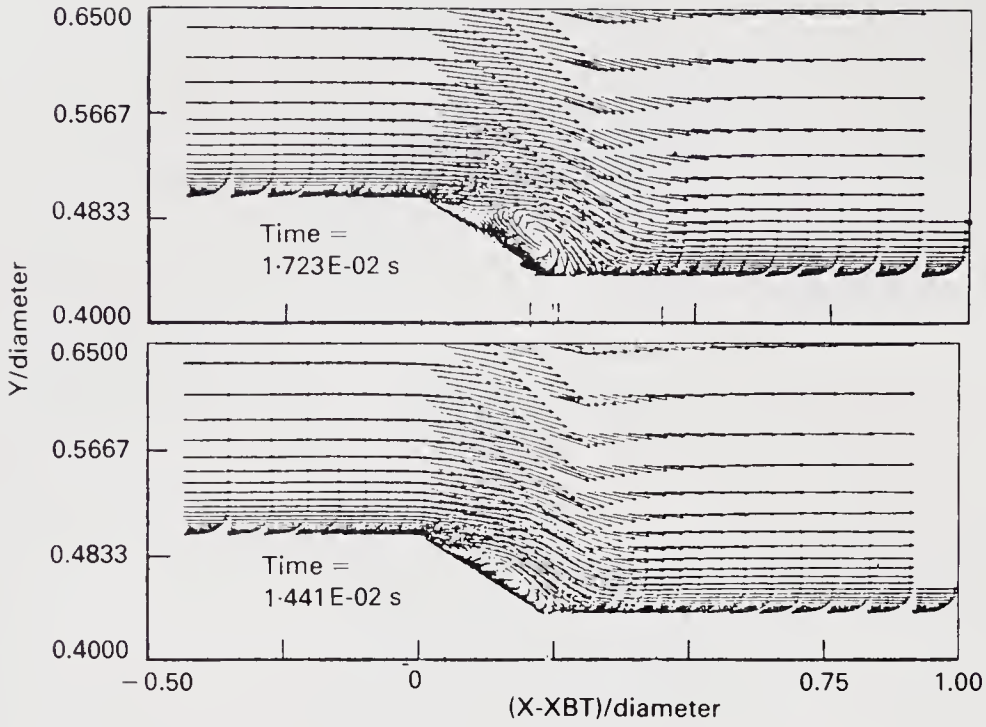


Figure 42. (See facing page for caption.)

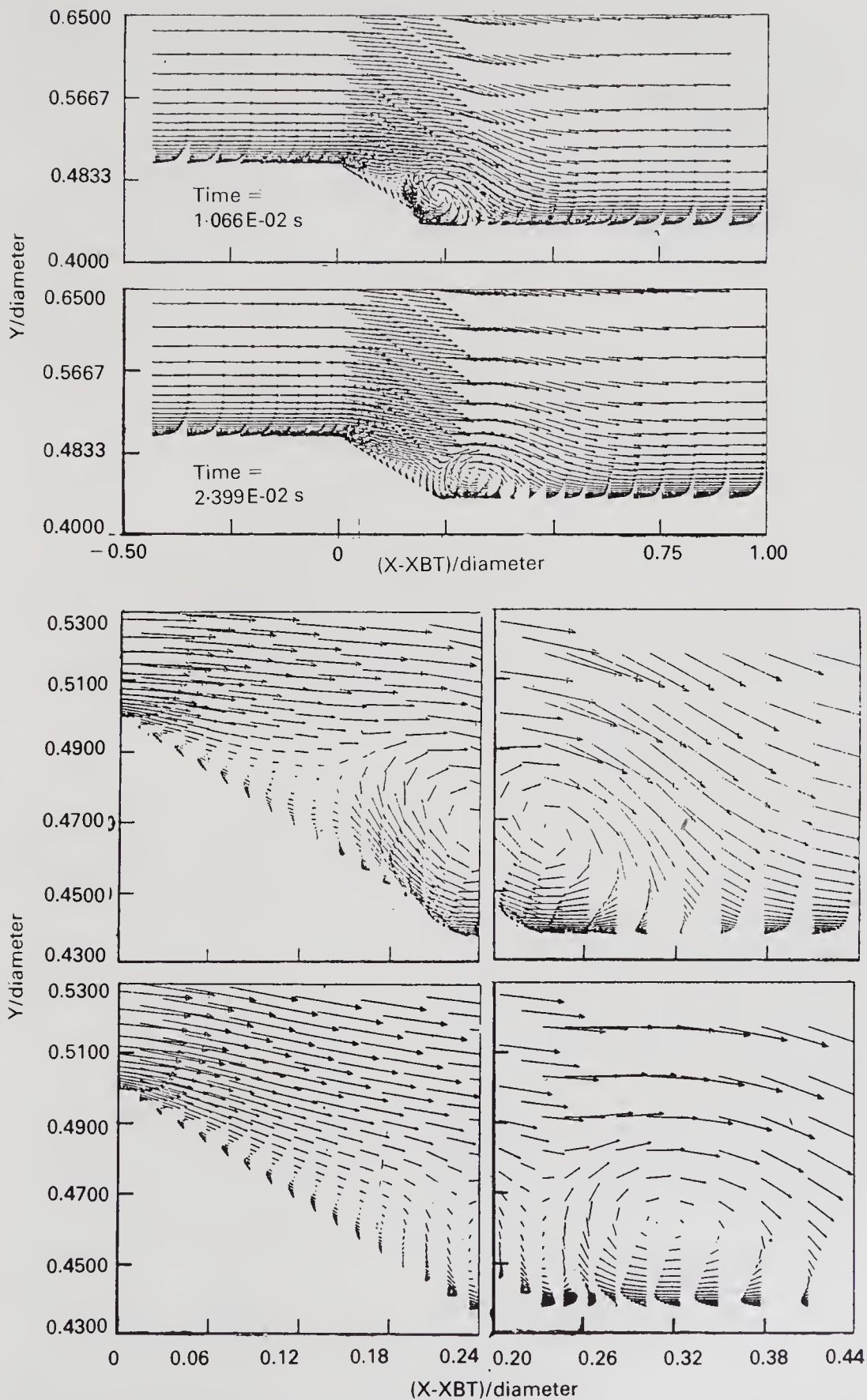


Figure 42. Capture of vortical motion in the boat-tailed region through Navier-Stokes code. The right hand portion is the flowfield in the boat-tailed region in enlarged scale.

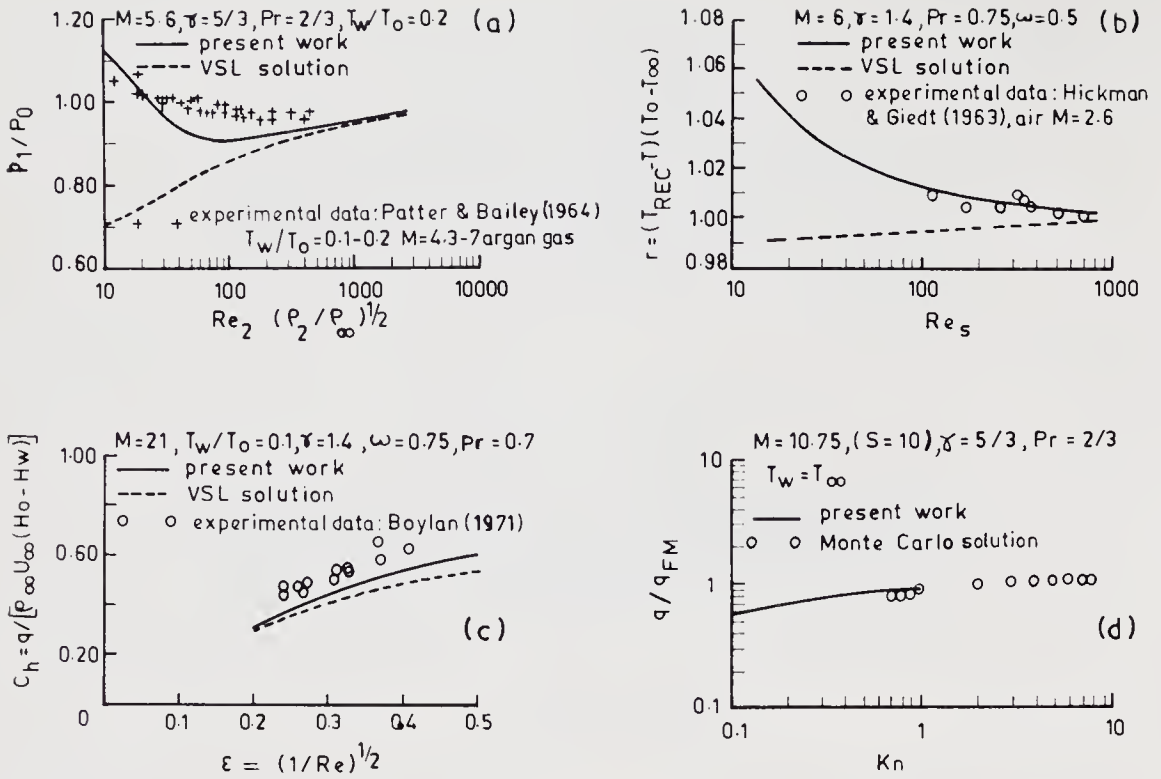


Figure 43. Stagnation point solution in hypersonic flow from steady state Navier-Stokes equations compared with experimental and other theoretical results. (a) Impact pressure comparison with experimental data, (b) variation of recovery factor, (c) heat transfer comparison with experimental data, (d) q/q_{FM} variation with Knudsen number (based on diameter). FM-free molecular.

pressure, heat transfer and recovery factor are compared in figure 43 with viscous shock layer/Monte Carlo solutions and experimental results available in the literature. With decreasing Reynolds number, the correct trend is seen in the present Navier-Stokes solution as compared to the viscous shock layer solution.

An alternating direction implicit scheme is being used to extend the solution of the Navier-Stokes equations downstream, using the stagnation solution as one of the boundary conditions. It will include the shock transition zone also so that correct post-shock conditions are obtained for the analysis of radiating/non-equilibrium flow. This investigation is under progress.

For situations like reentry, where Reynolds numbers are generally higher and the flow becomes more complex because of the three-dimensional effects induced by angle of incidence or geometry, a full Navier-Stokes solution may not be feasible. Simplified methods like the viscous shock layer approach may have to be used for such problems. A viscous shock layer computational scheme with the Baldwin-Lomax turbulence model is being developed for solving the three-dimensional hypersonic viscous flow field over a body of arbitrary cross-section at an angle of incidence (S Swaminathan 1986, unpublished) and is represented schematically in figure 44. This method solves, through a finite difference scheme, the three-dimensional viscous shock layer equations written in a non-orthogonal coordinate system with no slip boundary conditions at the wall and Rankine-Hugoniot jump conditions at the shock. Validation of the scheme is under progress.

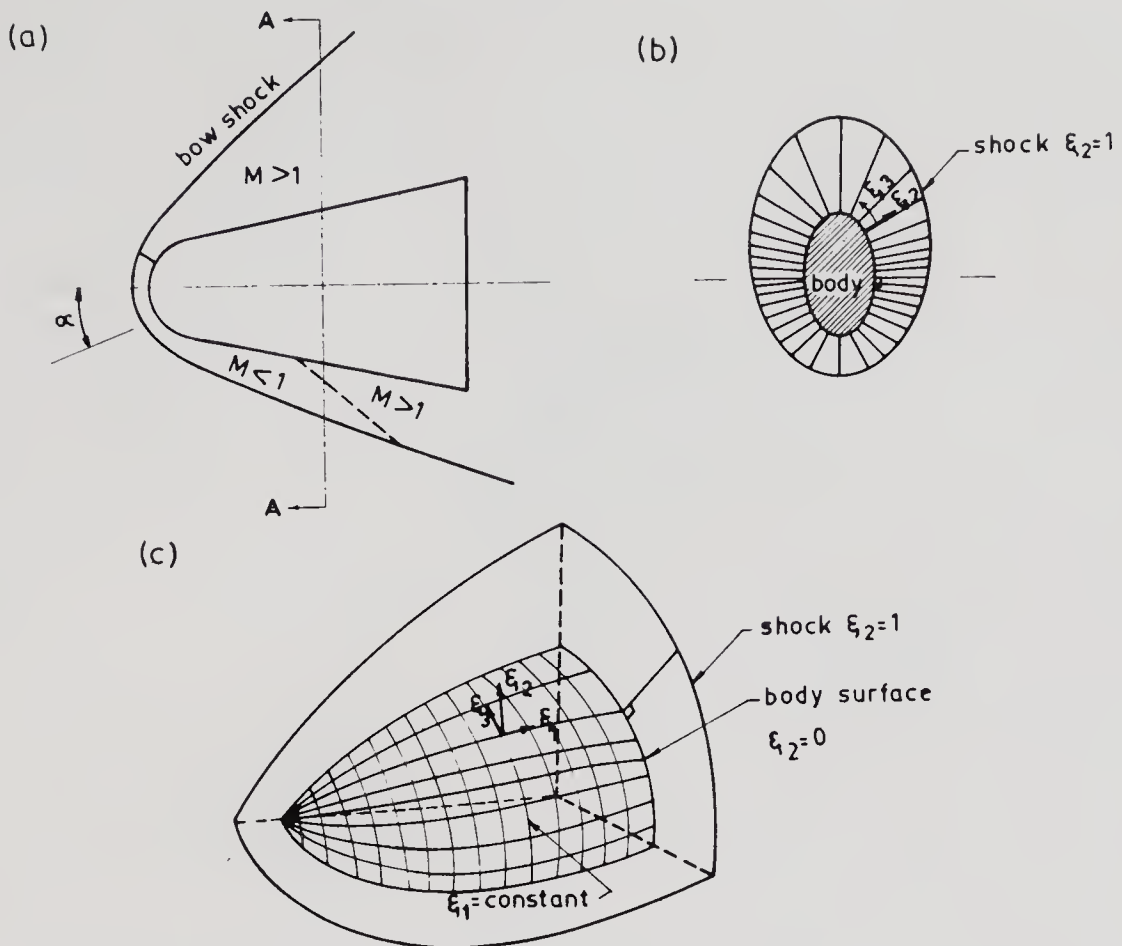


Figure 44. Schematic of three-dimensional viscous shock layer computational scheme. (a) Schematic of flow field, (b) section AA showing normal coordinate, (c) body coordinate system.

8. Special fluid dynamic problems

8.1 Three-dimensional nozzle flow

In many practical situations, either the nozzle geometry or conditions like fluid injection from the nozzle wall for thrust vector control render the flow field three-dimensional and simple one-dimensional analysis will not suffice. An attempt has been made (R Balu 1986, unpublished) to solve the three-dimensional Euler equations for such a flow field using a finite volume method with cells of general hexahedral shape using a cylindrical coordinate system as shown in figure 45. An explicit MacCormack predictor-corrector scheme is used to solve the discretised governing equations through an unsteady approach. Typical boundary conditions include fixed supersonic flow at the inlet and linear extrapolation of flow variables at the outlet. For subsonic flow, the boundary conditions are specified using characteristic variables.

Results obtained for the secondary injectant specific impulse as a function of the injectant mass flow rate are shown in figure 46 and are obtained through integration of the pressure distribution on the nozzle wall obtained from the above Euler solution. Comparison with test results is very encouraging considering the two-phase flow effects associated with liquid injection.

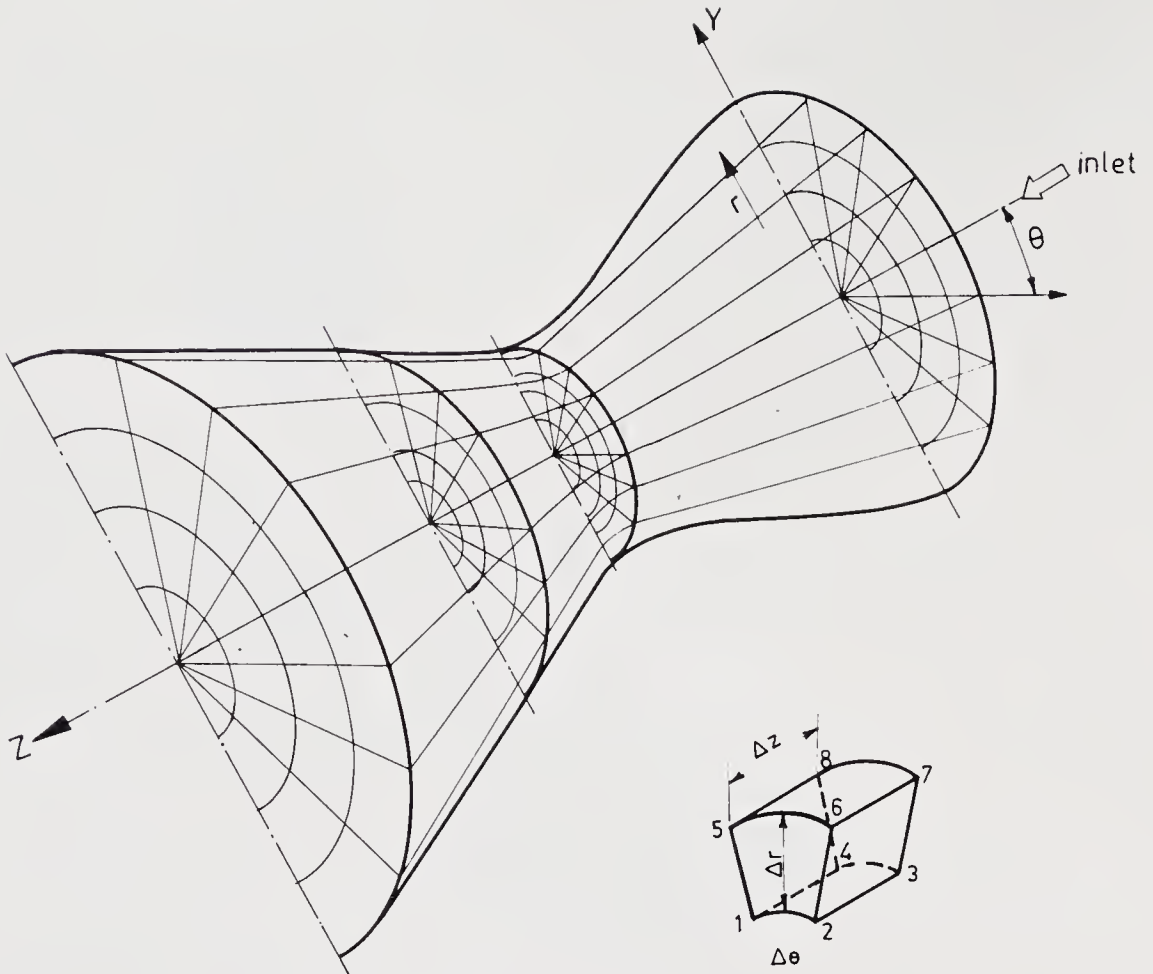


Figure 45. Finite volume discretisation of nozzle flow.

8.2 Heat transfer effects on nozzle liners

Solid rocket motor nozzles use charring ablative liners like carbon phenolic and silica phenolic in order to protect the back-up structure from adverse heat transfer effects due to high temperature gas flow. The phenomenon of charring ablation is quite complex and a number of parameters like convective heat transfer into the liner, the nozzle process parameters, mass transfer effects due to pyrolysis etc influence the thermal design and performance of the liner. Using data from six static tests on solid rocket motors, it is shown (Prahlad 1977) that a simple correlation of char depth against the major heat transfer parameters – the Fourier number and the Biot number – would be possible, provided the same material and the same process are used and the flame temperatures for the various test cases are roughly the same. Figure 47 shows such a correlation of char depth, non-dimensionalised against the original liner thickness, with Fourier number F_0 and Biot number B_i . Figure 48 represents the correlation functions graphically for carbon phenolic + silica phenolic liner and for silica phenolic liner alone (valid for the particular process employed in VSSC). The validity of these correlation functions is represented in figure 49 where measured char depth is plotted against char depth obtained from the correlation functions. For nozzles varying in throat diameter from 84 mm to 330 mm, the correlation functions are seen to be valid to within $\pm 15\%$.

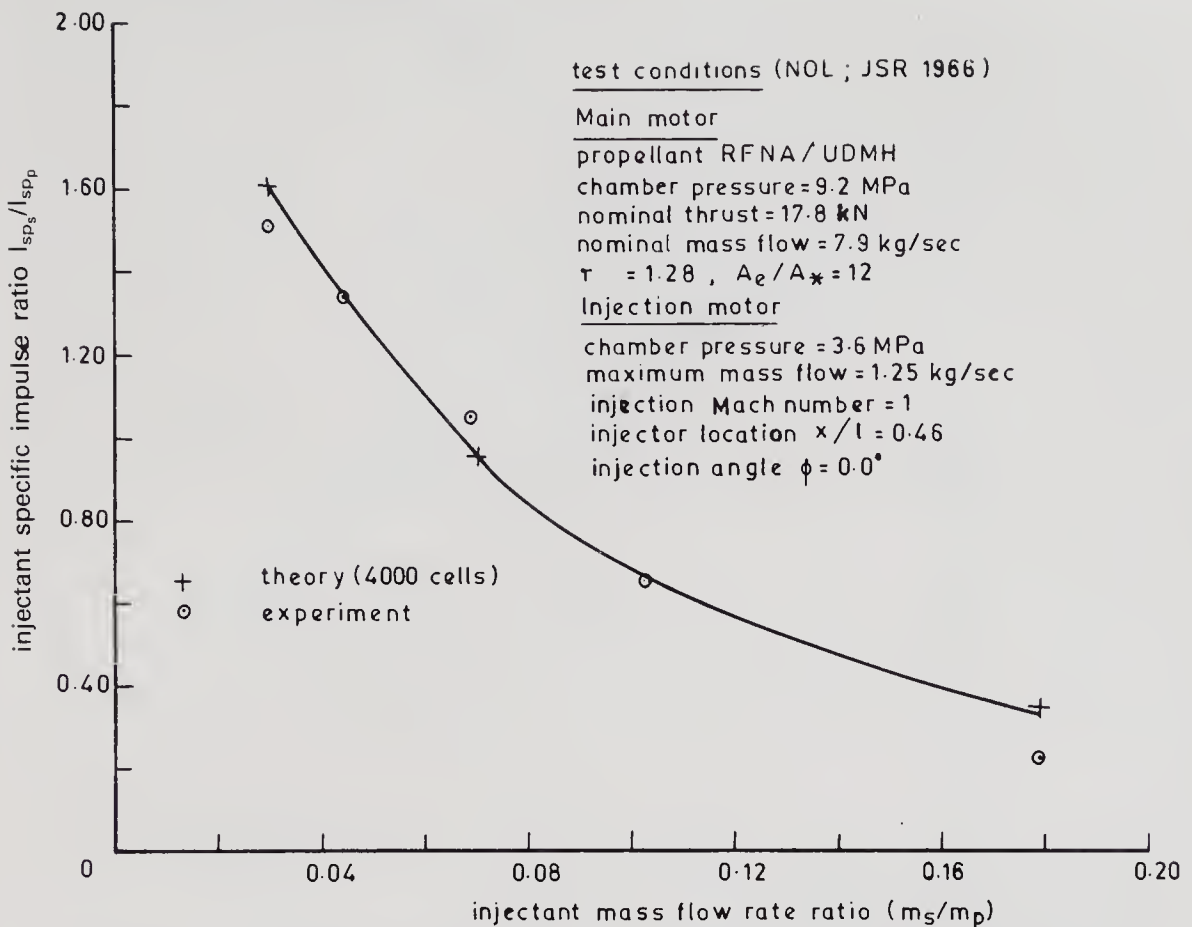


Figure 46. Computed injectant specific impulse for hot gas secondary injection compared with experimental results. I_{sp} —specific impulse, s—secondary, p—primary.

The chief merit of such a simple correlation as indicated above is that it can provide a handle for extrapolating the results of subscale tests to full-scale nozzles fabricated by the same procedure. It can also act as a simple method for the thermal design of a new nozzle that will employ the same materials and process.

8.3 Three-dimensional boundary layers

In order to analyse viscous effects in many practical situations, a good three-dimensional turbulent boundary layer code would be required which can use the inviscid solution obtained from the full potential or Euler equations as the outer boundary condition. A three-dimensional turbulent compressible boundary layer programme is written (R Swaminathan, 1986, unpublished) in an orthogonal curvilinear surface co-ordinate system proposed by Blottner & Ellis (1973) using the zig-zag Kellor box scheme suggested by Krause *et al* (1968) (figure 50). The code is applicable for both axisymmetric bodies at incidence and for swept wings. The skin friction obtained on a paraboloid of revolution in laminar incompressible flow at an angle of incidence of 10° is compared with Blottner's results in figure 51 for various circumferential locations. The wall-flow angle in the widely used infinite swept wing test case of Van den Berg & Elsennar (1972) is computed under various assumptions and is shown in figure 52. The comparison is similar to results obtained from many other codes used for simulating this test case and there have been

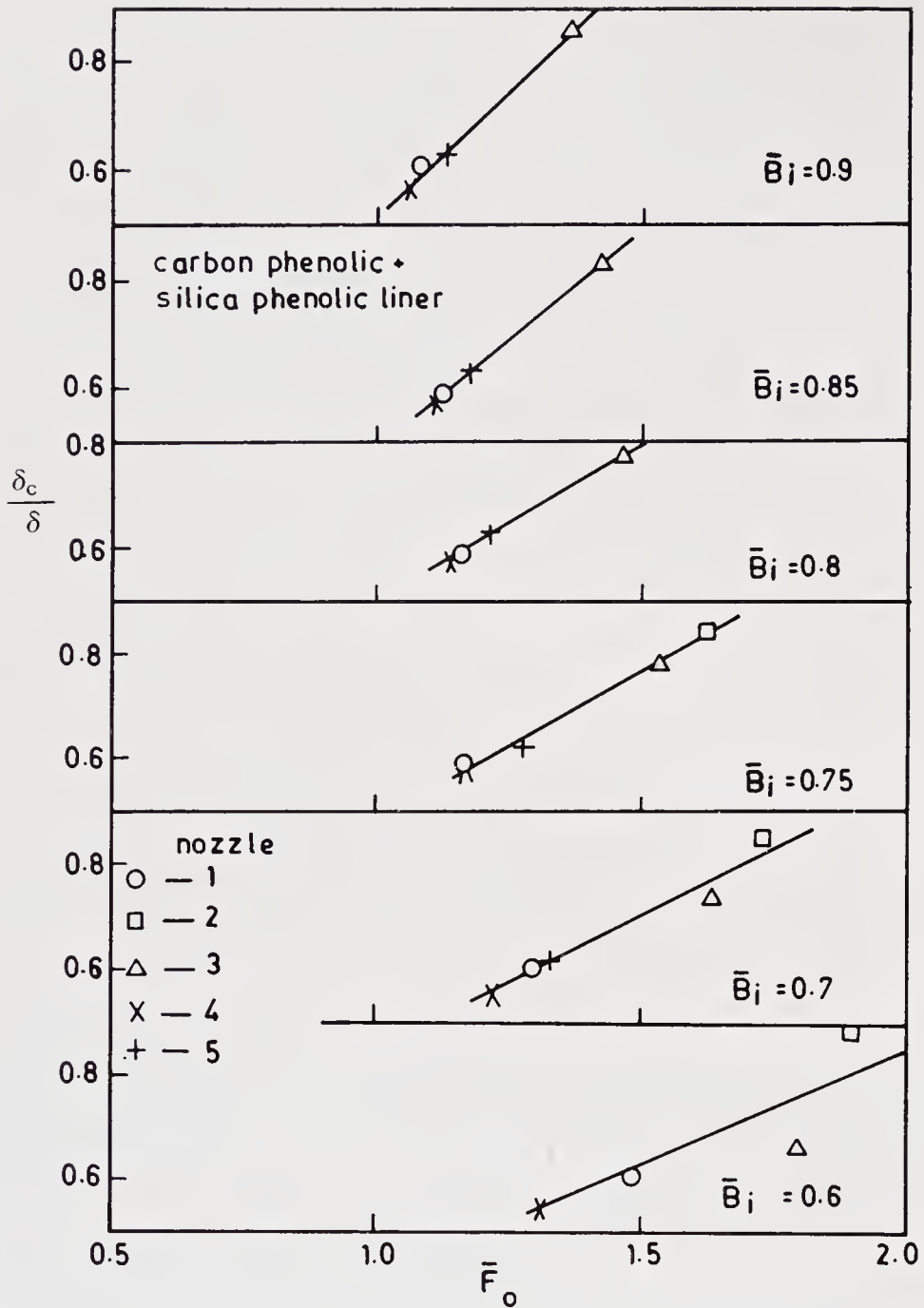


Figure 47. Char depth variation in rocket motor nozzle liner as a function of Fourier and Biot numbers.

questions raised about the applicability of the downstream test data (close to separation) for validating boundary layer codes. Further validation checks on the 3D boundary layer code are under progress. It is also planned to use this code for relative evaluation of various existing 3D turbulence closure schemes and for trying out new modelling ideas.

8.4 Shock wave-boundary layer interaction

The shock wave-boundary layer interaction is an important aerodynamic problem for launch vehicles in the boat-tail region, interstage flares, strap-on-core

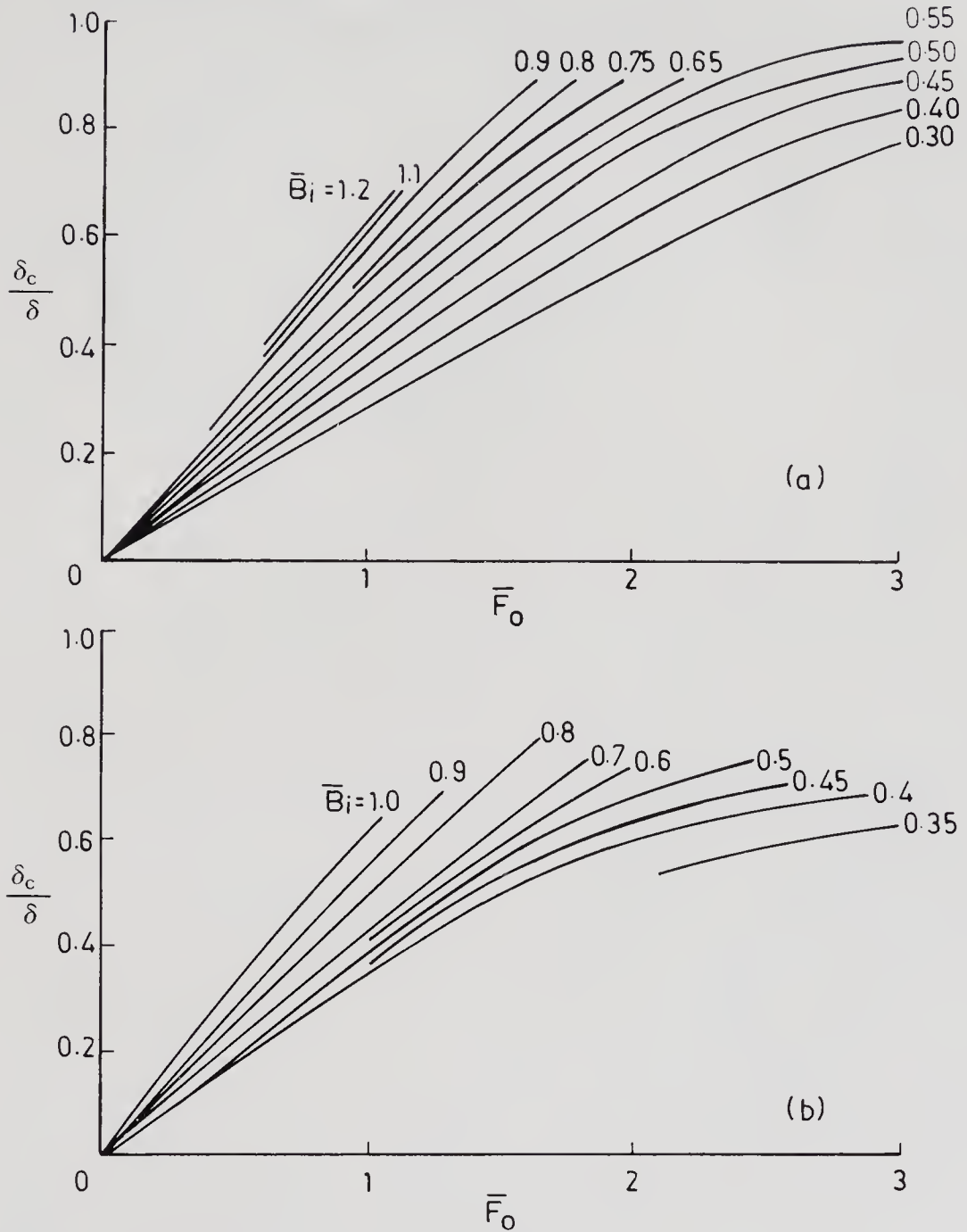


Figure 48. Graphical representation of char depth as a function of Fourier and Biot numbers for different nozzle liners, (a) carbon phenolic + silica phenolic liner, (b) silica phenolic liner alone.

interference region etc. from the point of view of flow unsteadiness, heat transfer, vehicle drag etc. Capability for analysing such problems through computational codes which solve the Reynolds-averaged Navier-Stokes equations are under development in VSSC using various numerical schemes like the second-order predictor-corrector numerical scheme of MacCormack, implicit time marching etc. (Madhavan & Swaminathan 1986a). An algebraic eddy viscosity model is used for turbulent flow calculations. Typical results obtained for a laminar flow calculation over an axisymmetric cylinder-flare (15 degrees) configuration at Mach number 2.8 and Reynolds number of 0.8×10^6 using the implicit code (Madhavan &

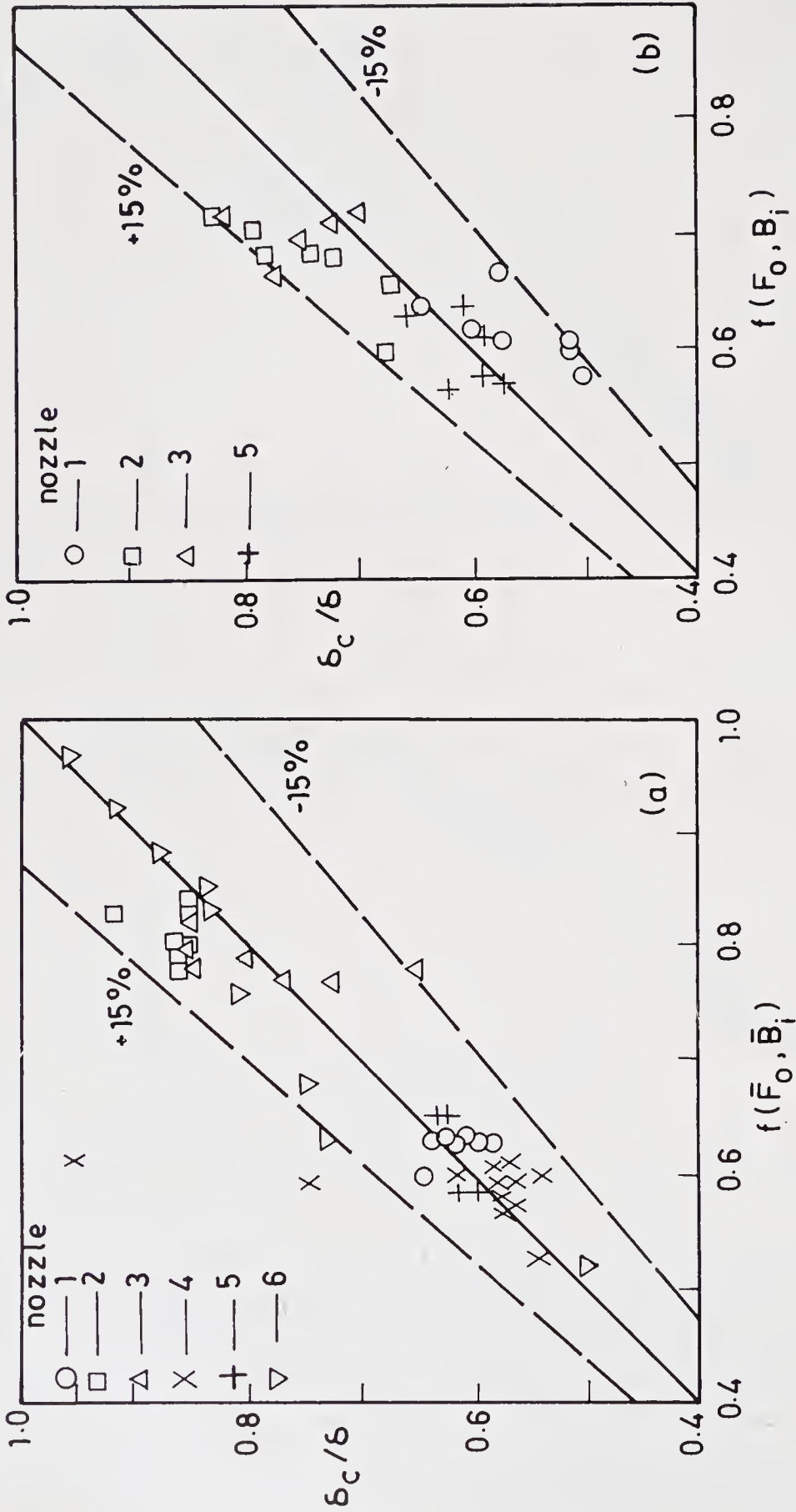


Figure 49. Comparison of measured char depth with functional representation of figure 48. (a) and (b) as in figure 48.

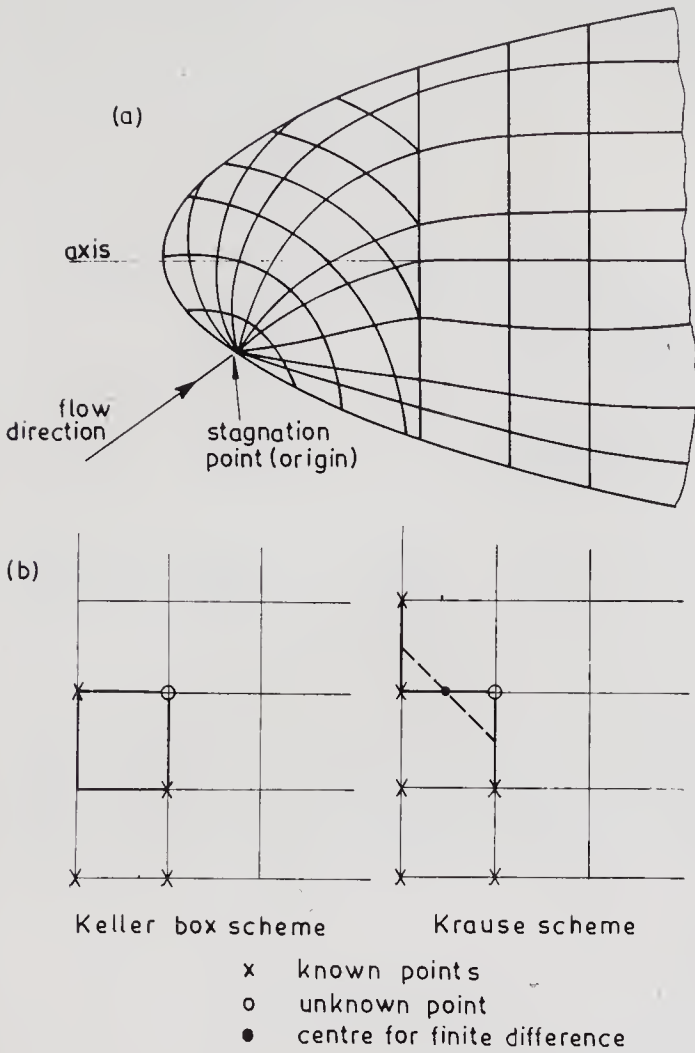


Figure 50. Co-ordinate system and zig-zag keller box scheme for computing three-dimensional boundary layers on axisymmetric bodies at incidence. (a) Curvilinear surface orthogonal coordinate system (Blottner & Ellis 1973) for a blunt body. (b) Different grid schemes.

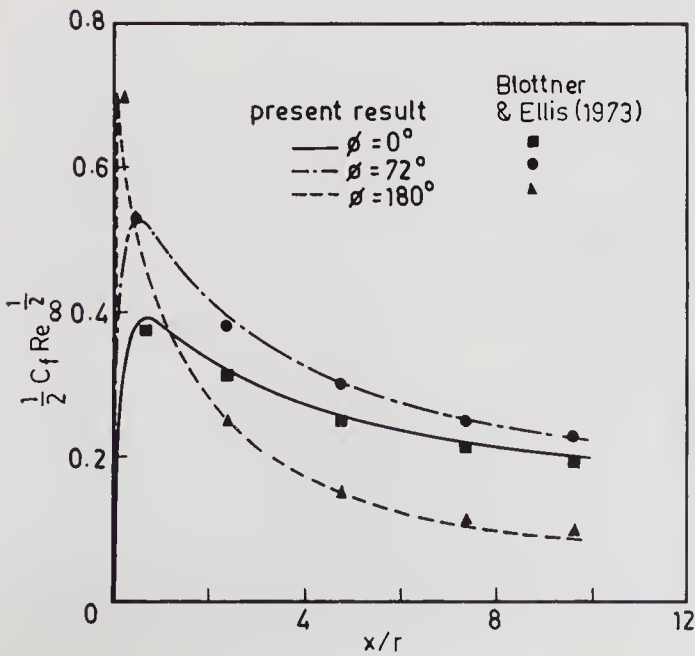


Figure 51. Laminar incompressible skin friction on a paraboloid of revolution at 10 degree angle of incidence compared with Blottner's results (for validating the code).

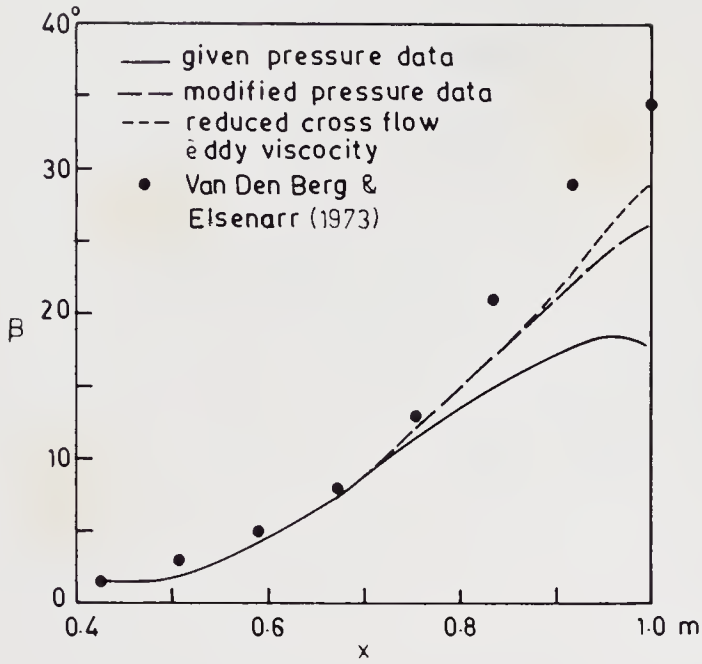


Figure 52. Computed wall flow angle for the infinite swept wing experiment of van den Berg & Elsenarr (1972).

Swaminathan 1986b) are shown in Figure 53 and are compared with computational and experimental results available in literature (Hung 1980). The variation of heat transfer coefficient on a flat plate due to shock impingement generated by a 10° wedge-shock generator at Mach number 6 is shown in figure 54 where the

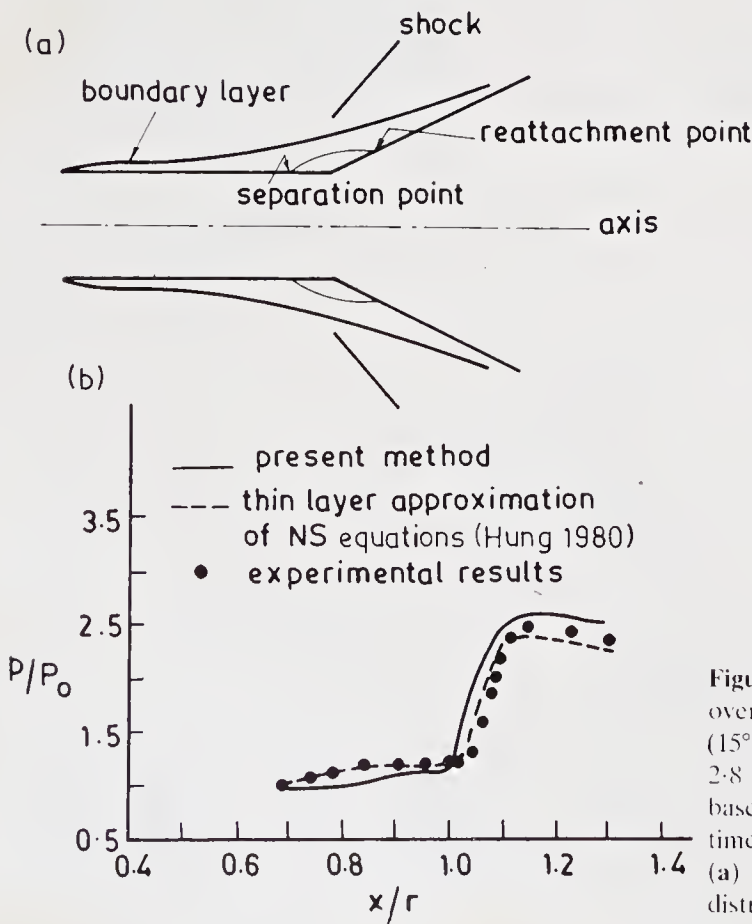


Figure 53. Surface pressure distribution over an axisymmetric cylinder flare (15°) at free stream Mach number of 2.8 and Reynolds number of 0.8×10^6 based on length, obtained by implicit time marching Navier-Stokes code. (a) Geometry of the flow, (b) pressure distribution.

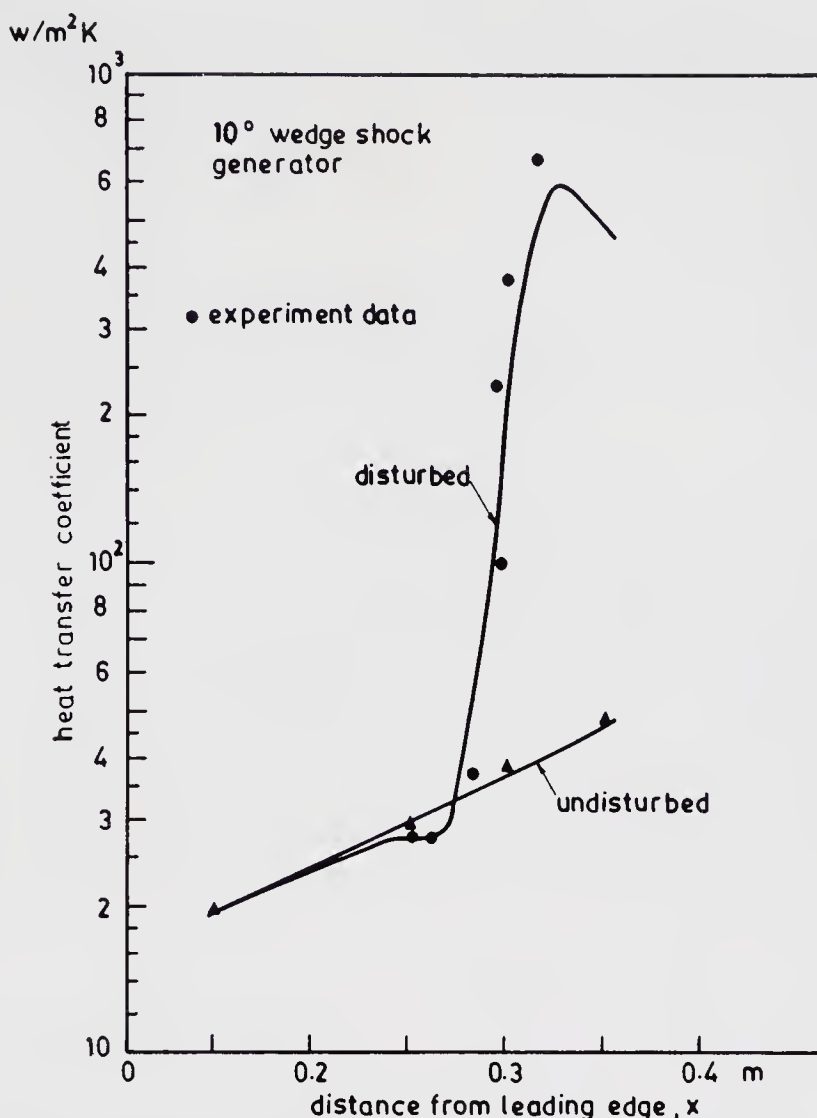


Figure 54. Computed variation of heat transfer coefficient on a flat plate due to shock impingement generated by a 10° wedge.

computations are again performed by an implicit code (R C Mehta, 1986, private communication). In order to achieve a significant saving in storage and computational time, a wall function approach has also been attempted in the solution of the Navier-Stokes equations in the shock wave-boundary layer interaction region where a pressure-gradient corrected wall law is used instead of doing the numerical integration right upto the wall. Results obtained at Mach number 2 and at Reynolds number of 0.3×10^6 are shown in figure 55 which indicates that this is a feasible approach when flow separation is not involved (Saxena & Mehta 1985, pp. 13–17).

However, from the point of view of flow field analysis in regions involving strap-on booster and core body, there is need to understand and solve the three-dimensional shock wave-boundary layer interaction problem. Initial results of an attempt to compute the flow field on a flat plate resulting from shock impingement of a spherical shock generator are shown in figure 56 and are obtained through MacCormack's explicit-implicit scheme (R C Mehta 1986, private communication). An experimental investigation of the interaction of an incident

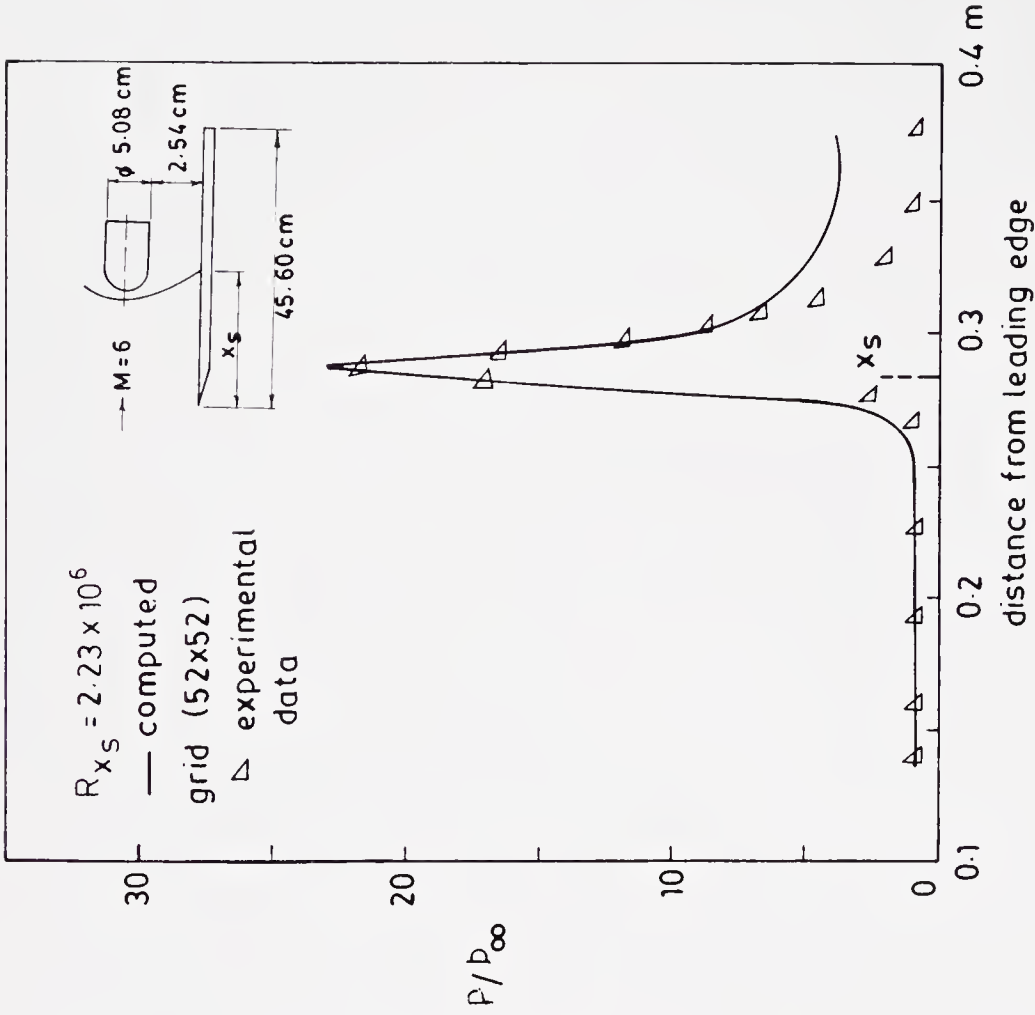


Figure 56. Distribution of interaction pressure ratio on flat plate due to a spherical shock generator.

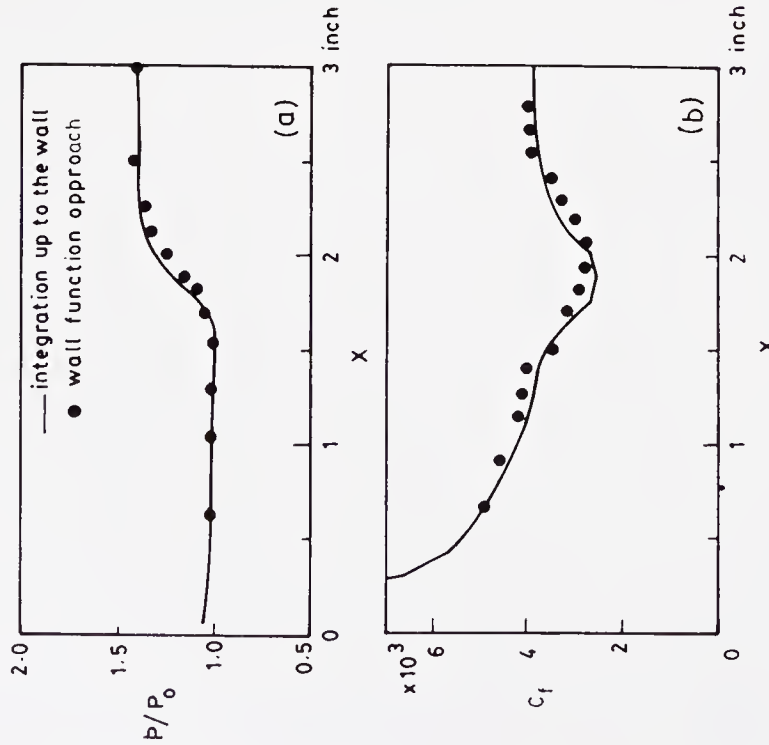


Figure 55. Surface pressure (a) and skin friction (b) distribution obtained by wall function approach in the shock wave-boundary layer interaction region at $M_\infty = 2.0$, Reynolds number based on length = 0.3×10^6 , incident shock angle = 32.6° .

oblique shock with a cylindrical afterbody has also been carried out to understand the complex three-dimensional shock wave-boundary layer interaction phenomenon (Raja Kuperan 1985). The tests were carried out at Mach number 2.9 and an undisturbed boundary layer thickness Reynolds number of 1.7×10^5 . The interaction flow features were studied through surface pressure measurements, oil flow and Schlieren visualisations. Some of the results are shown in figure 57. Salient features observed were the presence of severe cross flow over the cylinder, a larger upstream pressure influence on the leeward side as compared to the windward side etc. Further experimental investigations on 3D shock wave-boundary layer interactions are planned.

8.5 Drag estimation from flight

The analysis of flight data of aerospace vehicles to obtain aerodynamic parameters under actual flight conditions is an important activity. An attempt has been made to estimate the drag variation of the Satellite Launch Vehicle (SLV-3) in the supersonic region (Subbaraju *et al* 1986), using the longitudinal force equation. Reasonably good estimates of thrust, gravitational and other forces, radar data for altitude and measured accelerometer values form the inputs to the analysis. An extended Kalman filter with one-stage smoothing and iteration has been found to be appropriate for analysing the simulated data. The filter parameters have been found to drive the initial estimates towards the true value. The results obtained for a typical flight have been shown in figure 58. Further analysis using flight data from other vehicles is in progress.

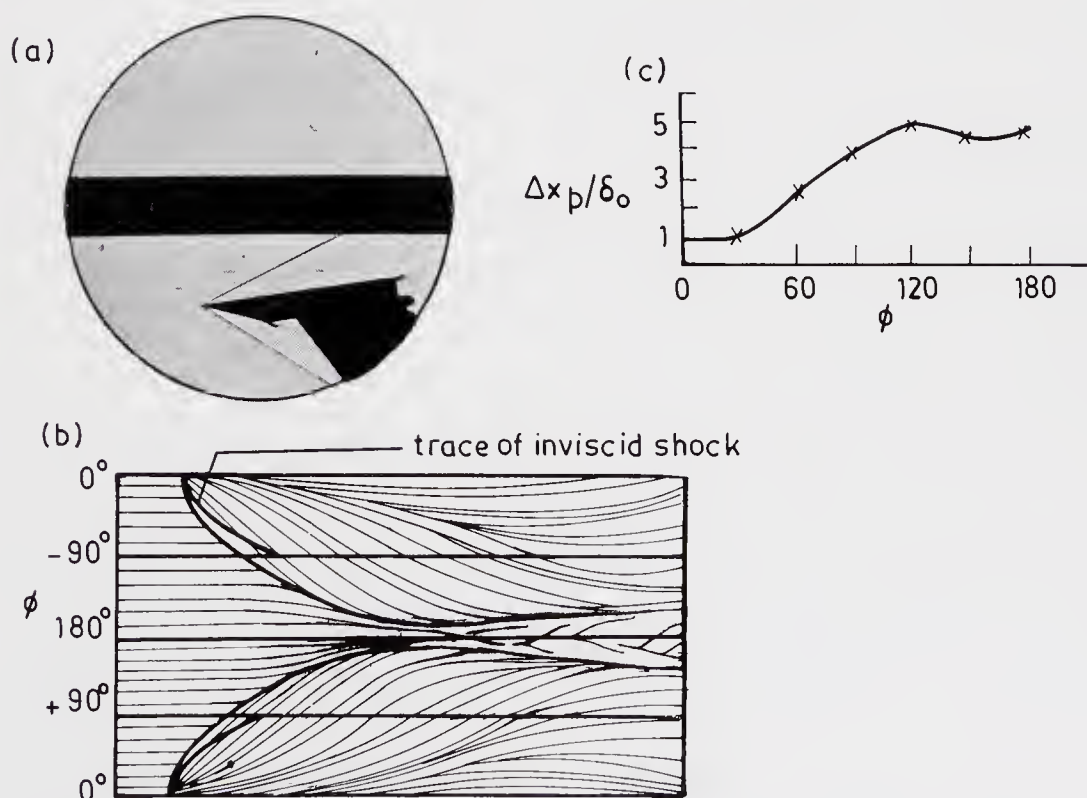


Figure 57. Interaction of an oblique plane shock with a cylindrical afterbody. (a) Shock pattern at the interaction, (b) surface flow pattern, (c) longitudinal location of pressure rise point around the circumference.

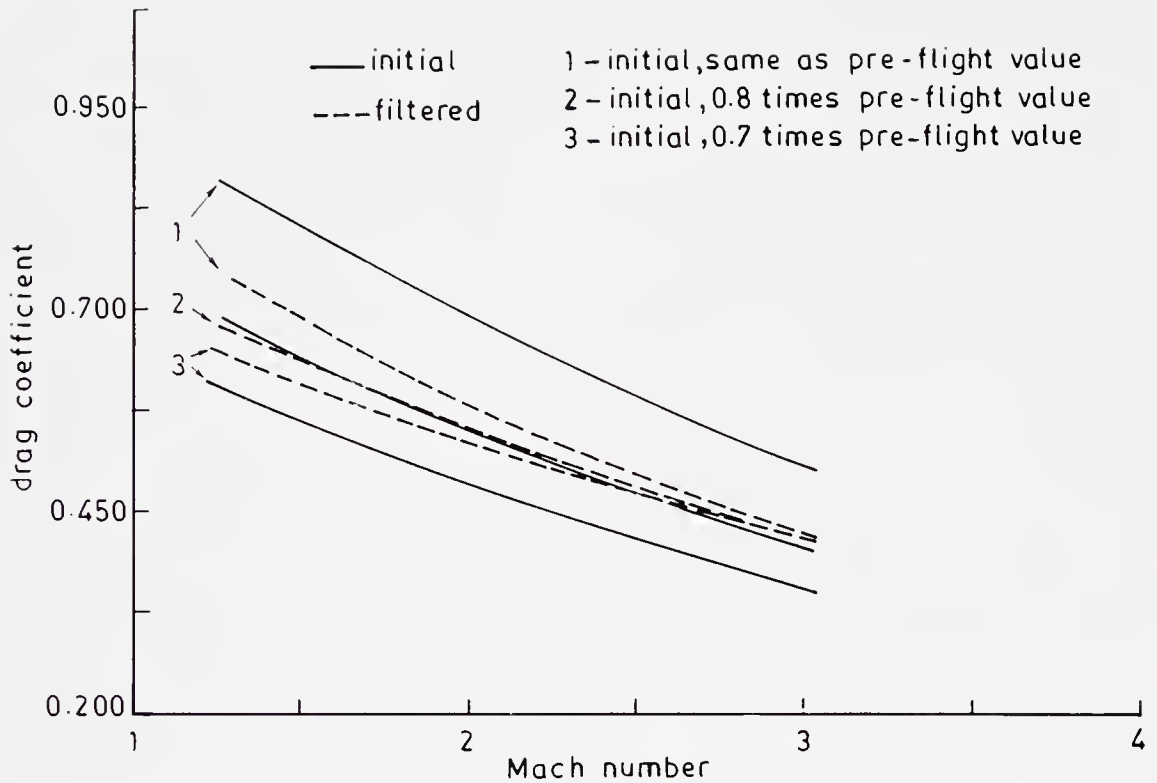


Figure 58. Estimation of drag coefficient in the supersonic region from satellite launch vehicle flight data.

9. Special wind tunnel facilities of VSSC

Over the years, VSSC has designed and developed the following wind tunnel facilities (VSSC, 1981):

- (a) Subsonic wind tunnel – 650 mm² cross-section and speeds upto 200 kmph.
- (b) Supersonic wind tunnel – 152.5 mm × 203 mm cross-section, 1.5 to 4 Mach number range, Reynolds number 19.5×10^6 to 195×10^6 per metre and run time upto 60 s.
- (c) Open jet facility – 50 mm diameter free jet, Mach number range of 1.5 to 4 and run time upto 200 s.
- (d) Hypersonic wind tunnel – 254 mm diameter free jet, 4 to 8 Mach number range, Reynolds number 1 to 18×10^6 , maximum stagnation temperature upto 1000 K, run time upto 35 s.
- (e) Heat transfer facility – 150 mm free jet diameter, Mach number range 1.5 to 4, stagnation temperature 1000 K (phase I) and 2000 K in phase II, Reynolds number upto 15×10^6 based on free jet diameter and run time upto 135 s.
- (f) Air driven shock tunnel – 100 mm diameter tube with 2.5 m driver length and 10 m channel length, maximum driver pressure of 140 atm, 320 mm jet diameter, Mach number 4 to 8, stagnation temperature 500–1800 K and 5 ms test duration.

All the high speed blowdown facilities are supported by a common high pressure system with a storage capacity of 42.7 m³ at 43 kg/cm² pressure.

Among these, the hypersonic wind tunnel is the first of its kind designed and developed in the country and the heat transfer facility is the only supersonic

blowdown tunnel in the country where a range of stagnation temperatures can be simulated. Salient features of only these two facilities are presented here.

9.1 VSSC hypersonic wind tunnel

A photograph of the VSSC hypersonic wind tunnel and a schematic of the facility indicating the major subsystems are shown in figure 59 (Kukillaya & Banerji 1978). The facility uses the common high pressure system mentioned above and, as the pressure drop during the operation of the tunnel is not large, a simple design for the pressure regulating system (upstream of the air heater) is used. This is shown schematically in figure 60 and comprises a 65 mm motorised globe valve driven by a variable speed direct current motor with two pneumatic feedback controlled secondary valves operating parallel to it.

Figure 61 shows a cross-section of the 40 kw electrically heated pebble bed type air heater, capable of heating up the air to a maximum temperature of 1000 K in the range of massflows handled by the tunnel. The initial heating time is around 4 hr and the cycle time is around 1 hr between successive tunnel operations.

A range of conical and contoured nozzles, as represented in figure 62, are designed and fabricated. The contoured nozzle profiles were generated by the method of characteristics with boundary layer displacement correction, with the thickness of the wall determined by thermal stress considerations. The test section which encloses the free jet is one metre in diameter with the main jet entering at one end and being collected by the scoop at the opposite end, a sliding arrangement being provided for the scoop for varying the free jet length from 1.5 to 2.5 diameters. The test section also houses an electromechanical model suspension system with provision to inject the model into the flow after stabilization, vary the angle of incidence, and obtain longitudinal movement.

The vacuum system consists of a series of pumps with suction rates varying from 200 m³/hr to 400 m³/hr at 1 torr vacuum level with a total vacuum capacity of 284 m³.

A typical calibration of the facility is shown in figure 63. The tunnel is being used for various tests and experimental studies in the hypersonic region like force measurements on PSLV, hypersonic flow interactions in the bulbous region of the payload shroud, flare effectiveness at hypersonic speeds, aerodynamic characteristics of separated boosters, stagnation point velocity gradients for satellite configurations etc. It is planned to build up a hypersonic data base for possible future programmes like lifting reentry.

9.2 VSSC Heat Transfer Facility

The VSSC Heat Transfer Facility is a special purpose supersonic blow-down tunnel where the incoming air can be preheated through a suitable combustor. The main motivation for developing this facility is the need for evaluating the thermal response of the candidate materials like cork, thermal paint etc. used as thermal protection systems over payload shrouds, composite motor cases, sounding rocket fins, vehicle bases and other subsystems of a satellite launch vehicle. In contrast to the Kinetic Heating Simulation facility (where infrared heating elements are used to simulate heat flux history with time), both the heat flux and the flow shear are simulated in the Heat Transfer Facility over sample specimens. However, because

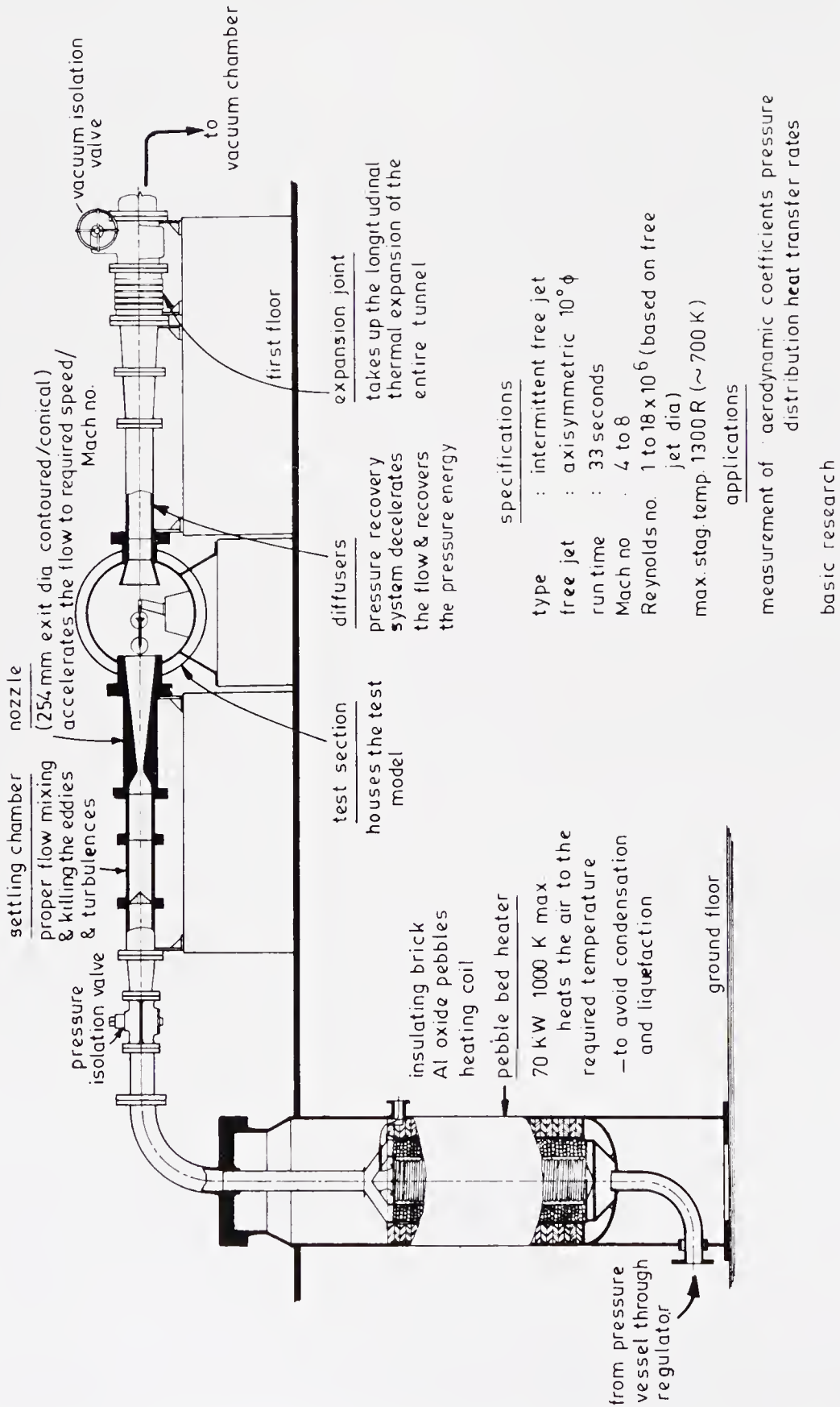


Figure 59. (a) Schematic of the VSSC hypersonic wind tunnel and its major subsystems.

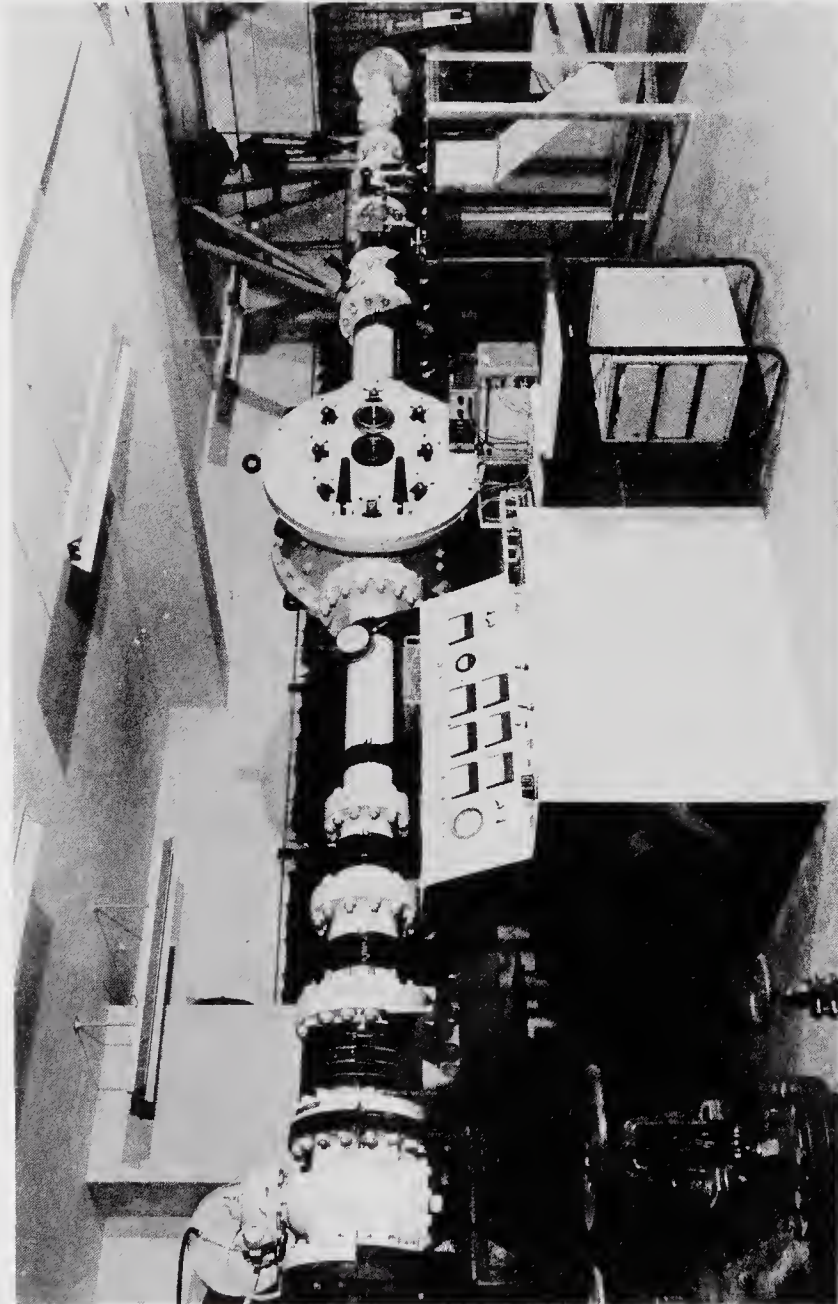


Figure 59. (b) Photograph of the VSSC hypersonic wind tunnel and its major subsystems.

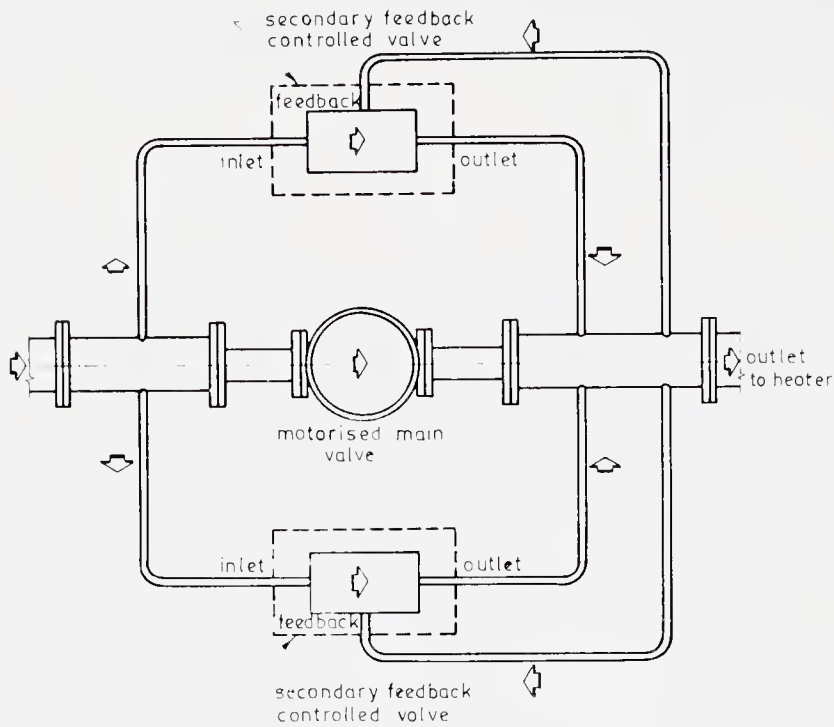


Figure 60. Schematic of the pressure regulating system of the VSSC hypersonic wind tunnel (type: electro-pneumatic feedback controlled; main valve drive: variable speed DC motor; maximum inlet pressure: 40 atm; regulated pressure range: 3–20 atm; accuracy $\pm 1\%$).

of the difficulty of varying flow conditions during a blow down, time variation of heat flux cannot be simulated and has to be replaced by a suitably defined constant value of heat flux and blow-down time.

A photograph of the Heat Transfer Facility and a schematic indicating the major subsystems is shown in figure 64 (Subhash *et al* 1981). The compressed air is drawn from the common air storage system. For the pressure regulating system the main problem is to maintain a constant stagnation pressure in the settling chamber (downstream of the combustor) for a desired set temperature as the reservoir storage pressure is continuously dropping, which makes it necessary for the inlet air pressure to the combustion system to be held constant. Based on the experience of the hypersonic wind tunnel, a system as shown in figure 65 is designed where the required mass flow rate at a desired regulated inlet pressure of the combustor is provided by the operation of a variable speed motorised main valve, 2 numbers of servo-controlled secondary valves and by a constant area bypass valve. Details can be found in the report by Subhash *et al* (1981).

The temperature augmentation of incoming air is achieved in two phases through air heaters where thermal energy release is obtained by combustion of kerosene in excess oxygen. The first phase heater has the capability of raising the temperature upto 1000 K and the second phase heater upto 2000 K. A standard gas turbine engine flame tube with slight modifications has been used in heater I (figure 66) and further augmentation of temperature upto 2000 K is achieved in heater II working on the principle of an afterburner in series with heater I. The air heaters were designed by the Propulsion Division of the National Aeronautical Laboratory, Bangalore (Rao 1979).

The downstream system consisting of the nozzle, test section, collector and diffuser is shown in figure 67. Because of the fairly long duration of blow-down

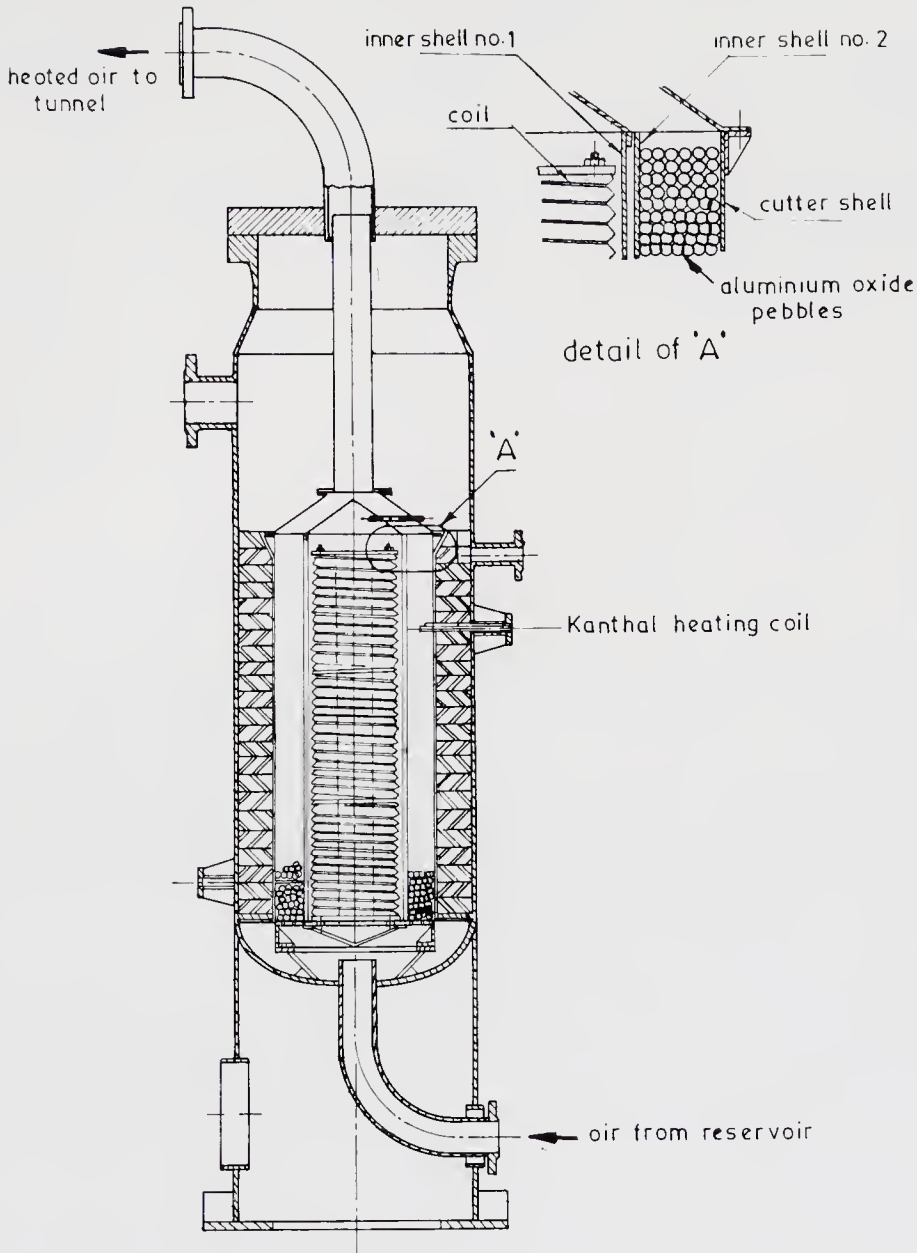
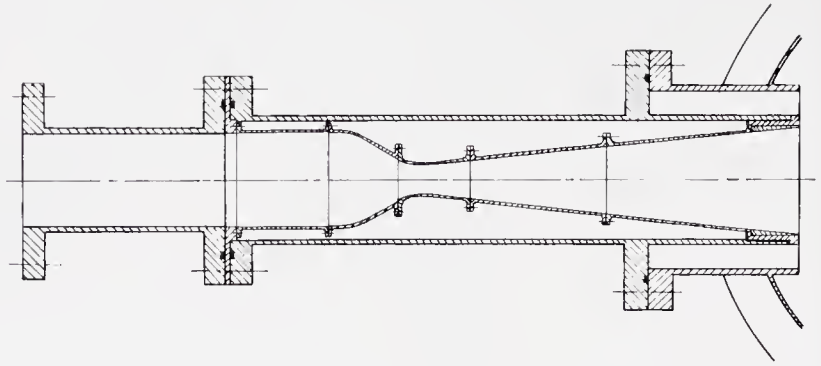


Figure 61. Cross-sectional view of the 40 kw pebble bed heater of the VSSC hypersonic wind tunnel.

time (55 to 135 s), the nozzle requires water-jacketing and is fabricated through an electrodeposition technique. The test section is provided with a model mounting-injection-incidence system, a quick door opening and closing mechanism and Schlieren windows. The flow collector in the form of a truncated cone has a high temperature nimonic liner and a thin ceramic paper sheet in between the liner and the collector for thermal protection. The air injector enables the start of the tunnel at a lower stagnation pressure by creating a low pressure zone downstream of the collector, and also protects the diffuser wall from the hot gases by creating a cooler annular zone. The water-cooler injects water under sufficient pressure in the form of fine small jets at a section downstream of the air injector and brings down the bulk gas temperature of the hot gases as well as lowering the exhaust noise. The

conical nozzle
 exit dia — 235 mm (~9.25°)
 expansion angle — 12°
 (included)
 Mach nos — 4,5,6,7 & 8
 common divergent section
 with replaceable throat section
 (water cooled for Mach no.8)
 material — SS



contoured nozzle
 exit dia. 254 mm (10°)
 Mach nos 4,5,6,7 & 8
 water cooled throat section
 for Mach no 8
 material throat : nickel
 divergent copper
 (electroformed)

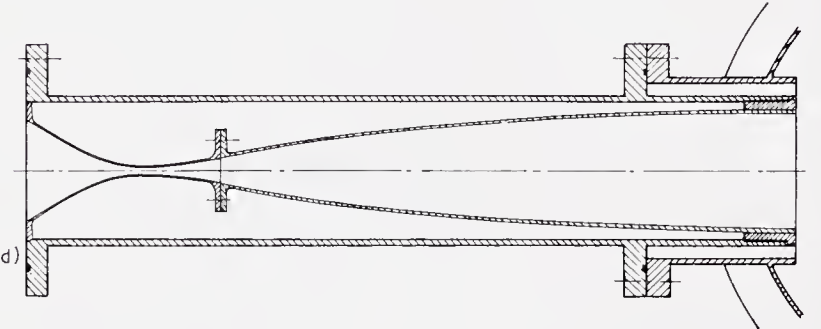


Figure 62. Details of the conical and contoured nozzles of the VSSC hypersonic wind tunnel.

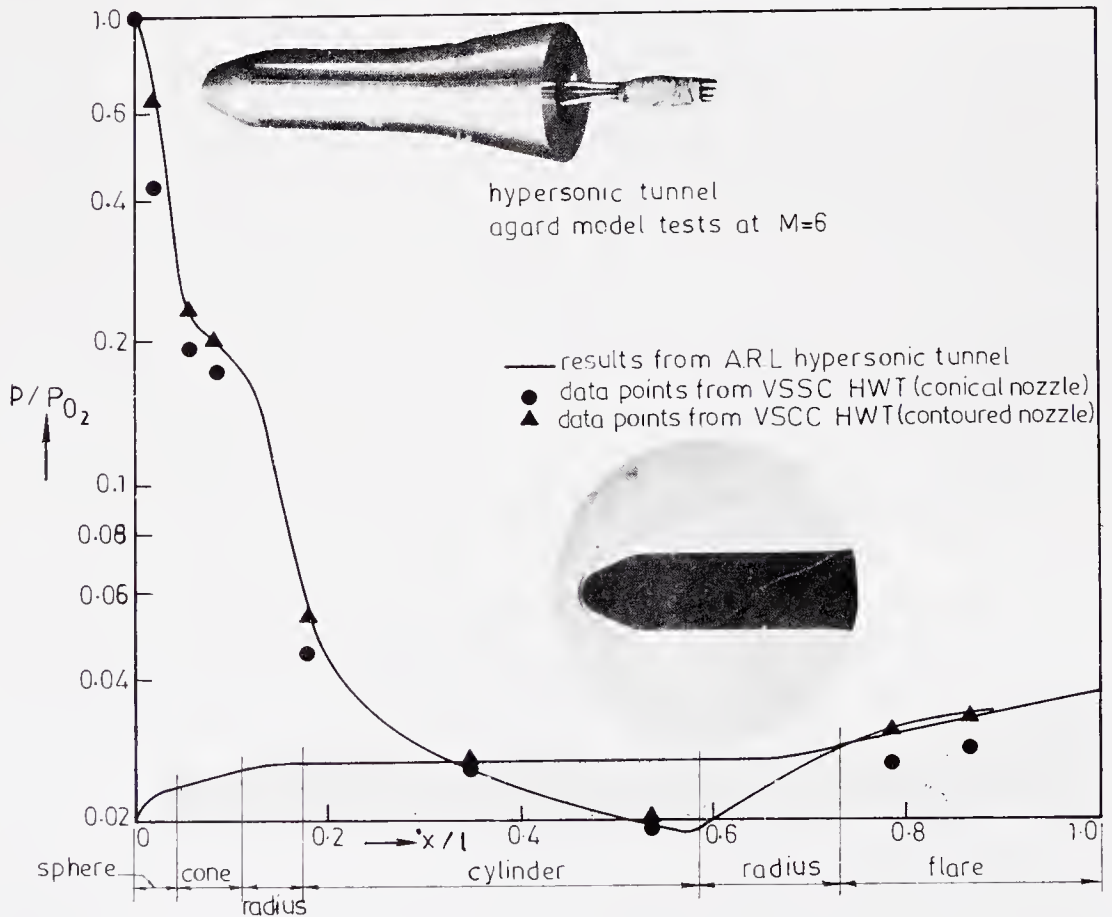


Figure 63. Typical calibration of VSSC hypersonic wind tunnel with conical and contoured nozzles, p —local pressure, P_{02} —total pressure behind the shock.

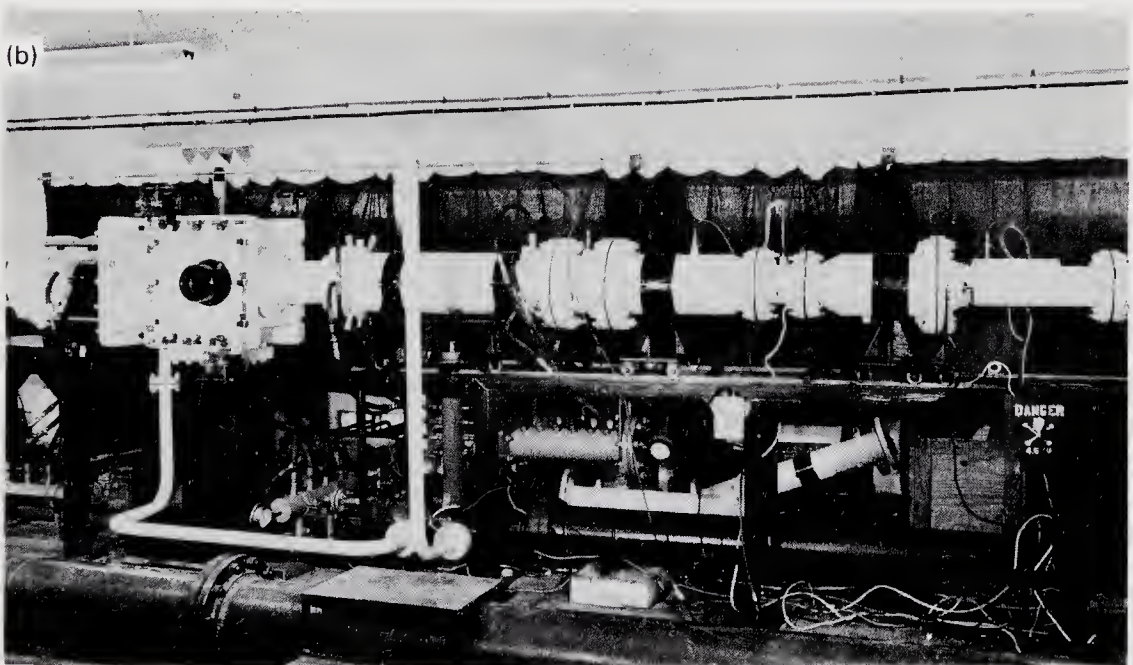
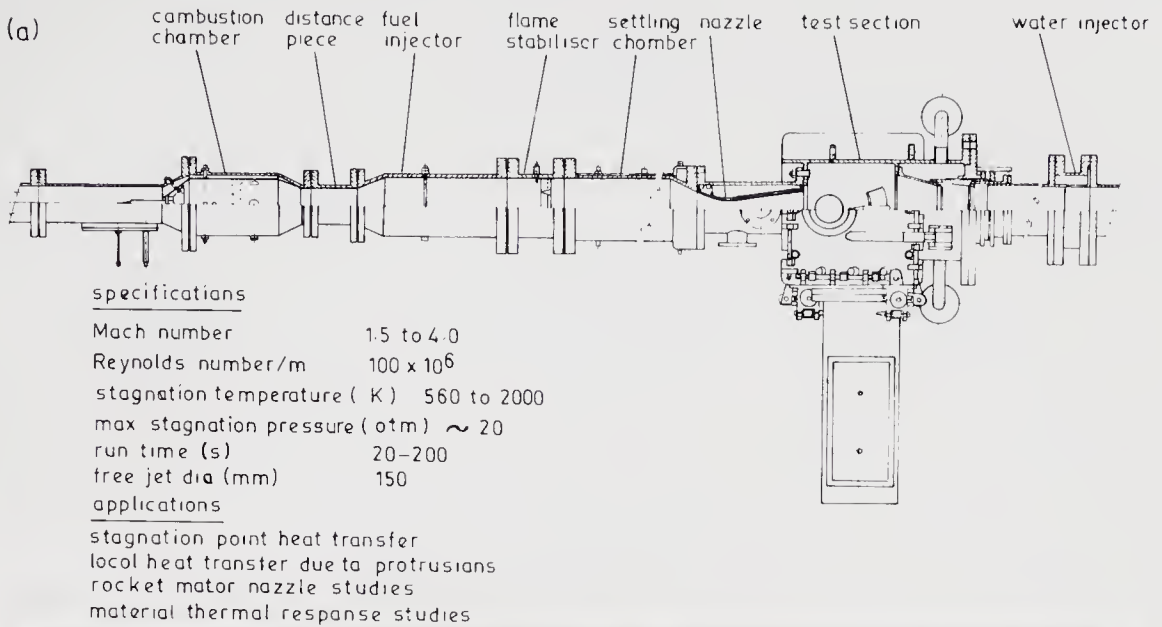


Figure 64. (a) Schematic, and (b) photograph, of the VSSC Heat transfer facility and its major subsystems.

diffuser system consists, as in a conventional supersonic tunnel, of a constant area supersonic diffuser followed by a subsonic diffuser in order to achieve the pressure recovery. Two metallic expansion bellows are provided to take care of thermal expansions during blowdown, and to act as longitudinal vibration/shock dampers for the tunnel components and high pressure piping.

The facility calls for a stringent safety system for control of temperature in the combustor and the resultant pressure increase. Thermocouples mounted on the combustors continuously monitor the temperature on temperature indicator-controllers (TIC). When the indicated temperature increases above the set temperature, the TIC energises a relay and enables the fuel pressurising pump to trip and simultaneously close the solenoid valve of the fuel injector.

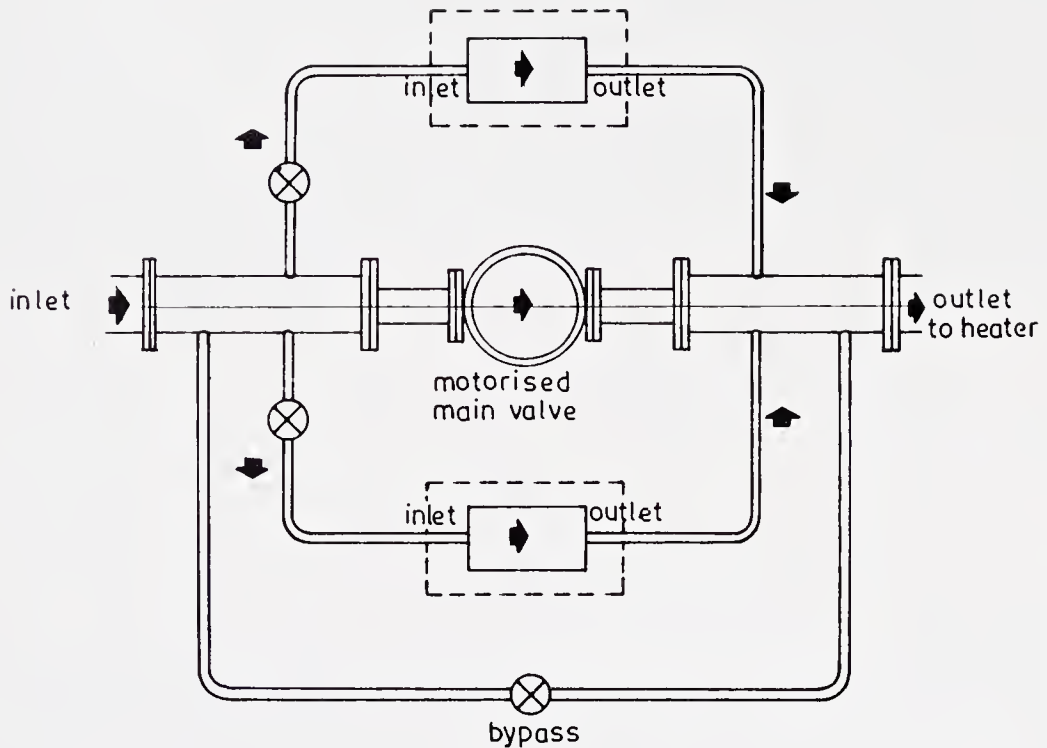


Figure 65. Schematic of the pressure regulating system of VSSC Heat Transfer Facility. Type: electro pneumatic; main valve drive: variable speed DC motor; maximum inlet pressure: 40 atm; regulated pressure: 3–20 atm; range accuracy: $\pm 1\%$.

The facility is now operational upto 1000 K (phase I) and the afterburner for increasing the stagnation temperature capability to 2000 K will be installed shortly. It has been extensively used for the thermal evaluation of cork used as the thermal protection material over the SLV-3 composite motor case and interstages, and over the ASLV payload shroud. Another programme that will be taken up shortly is the mapping of heat transfer fields in nozzle flows with secondary injection. It is also planned to use the facility to generate a data bank on the candidate thermal protection materials for future lifting reentry vehicles.

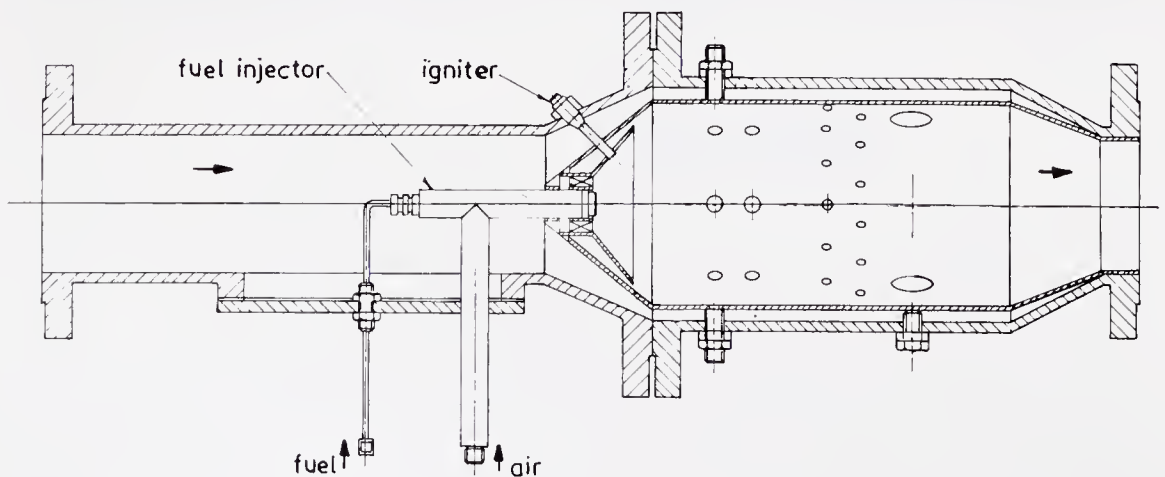


Figure 66. Combustion chamber assembly of heater I (upto 1000 K) of heat transfer facility.

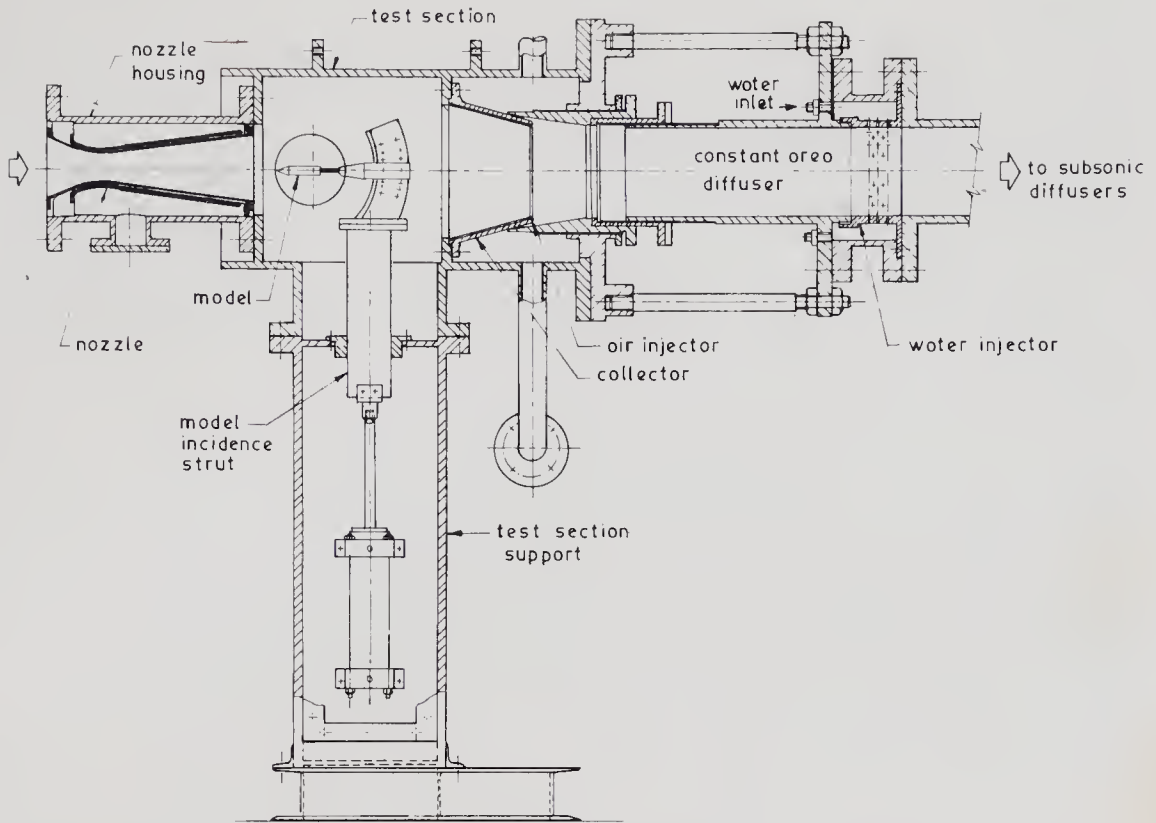


Figure 67. A cross-sectional view of test section, collector, air injector, water cooler and diffuser systems of VSSC heat transfer facility.

10. Concluding remarks

An attempt has been made in this paper to present a profile of the aerodynamic research and development activities being conducted at the Vikram Sarabhai Space Centre. The focus has been on application to satellite launch vehicle configurations of interest to the Indian space programme. Thus, greater emphasis is placed on results and applications rather than on the methodology used. Two special test facilities developed in VSSC – the hypersonic wind tunnel and the heat transfer facility – are also described briefly.

As in many other practical applications, the aerodynamic problems of launch vehicles are three-dimensional in nature involving complex geometry and complex flow interactions. It is expected that the rapidly emerging field of computational fluid dynamics (CFD) will play an increasingly significant role in analysing many of these problems. However, both because of the inherent limitations in our understanding and modelling of phenomena like transition and turbulence, and also because of non-availability at present of large computational resources, we will have to take an integrated approach involving analytical, computational and experimental methods for obtaining practical solutions to many of the aerodynamic problems of launch vehicles. It is hoped that, through such an integrated approach, VSSC will be able to meet successfully the aerodynamic challenges that will be posed by possible future programmes like lifting reentry.

References

- Baldwin B S, Lomax H 1978 Thin layer approximation and algebraic model for separated turbulent flows, AIAA Paper 78-257, January 1978
- Blottner F G, Ellis M A 1973 *Comput. Fluids* 1: 133-158
- Boylan D E 1971 *AIAA J.* 9: 1661-1663
- Devassia K J, Nair S R, Sheo Prakash 1982 *Proceedings of the Thirteenth International Symposium on Space Technology and Science* (Tokyo: AGNE Publishers)
- Goyal V K 1981 Cylinder effects on aerodynamic loading of following boat tail and cylinder combination at supersonic speed, VSSC:TN:02:045:81, Aerodynamics Division, VSSC, Trivandrum, October
- Hickman R S, Giedt W H 1963 *AIAA J.* 1: 665-672
- Hung C M 1980 *AIAA J.* 18: 921-928
- Jai Mohan 1985 Simulation of shock-boundary layer interaction effects in transonic potential flow, VSSC-ADDG-ARD-002, Aerodynamics Division, VSSC, Trivandrum, July
- Krause E, Hirschel E H, Bothmann Th 1968 *Zeit. Angew. Math. Mech.* 48: 205-208
- Kukillaya S P, Banerji A 1978 SSTC 10 inch Hypersonic Tunnel - Design details and description, SSTC-ARD-78, Space Science and Technology Centre, Aerodynamics Division, VSSC, Trivandrum
- MacCormack R W 1969 The effect of viscosity in hypervelocity impact catering, AIAA Paper No. 69-354
- Madhavan N S, Swaminathan V 1986a *Int. J. Numer. Methods Fluids* 6: 387-393
- Madhavan N S, Swaminathan V 1986b Numerical simulation of supersonic turbulent axisymmetric flows using an implicit time marching scheme, Thirty-first ISTAM Congress, Gwalior, October
- Potter J L, Bailey A B 1964 *AIAA J.* 2: 743-745
- Prahlad T S 1977 Correlation of char depth data from static tests on nozzles, SLV-NTHR-77-1, Vikram Sarabhai Space Centre, Trivandrum, May
- Prasad J K, Kutty C S 1985 Impingement on PSLV jet deflector: cold flow simulation test results, VSSC:ATTF:07:85, Aerothermal Test Facilities, VSSC, Trivandrum, October
- Purohit S 1986 Numerical simulation of transonic flow past bulbous heat shield. *Proceedings of the Third Asian Congress of Fluid Mechanics* (Tokyo: ACFM)
- Purohit S 1987 *Aeronaut. J.*: 183-189
- Raja Kuperan E 1982 Experimental investigation for strap-on launch vehicle at supersonic regime, VSSC:SSTC:ARD:Nov(3)/1982, Aerodynamics Division, VSSC, Trivandrum
- Raja Kuperan E 1985 Interaction of an incident oblique shock with a cylinder turbulent boundary layer, M Sc thesis, Birla Institute of Technology, Ranchi
- Rao K V L 1979 Air heaters for the heat transfer test facility, Consultancy report 1977-79, Propulsion Division, National Aeronautical Laboratory, Bangalore
- Saxena S K, Deshpande S M, Narasimha R, Prahlad T S 1983 *Proceedings of the Second Asian Congress of Fluid Mechanics, Beijing, China* (Beijing: ACFM)
- Saxena S K, Mehta R C 1985 *Proceedings of the First National Conference on Aerodynamics* (Madras: Indian Inst. Technol.)
- Singh K P, Rajaram U 1985 Numerical simulation of three-dimensional inviscid supersonic flow over launch vehicles, VSSC-ADDG-009/Dec, Aerodynamics Division, VSSC, Trivandrum
- Singh K P, Deshpande S M, Prahlad T S, Narasimha R 1987 Numerical simulation of inviscid supersonic flow over a launch vehicle with strap-on boosters, AIAA 25th Aerospace Sciences Meeting, Reno, Nevada, January
- VSSC 1981 Document prepared in connection with Review of Hypersonic and Heat Transfer Facilities of VSSC, Engineers, Aerodynamic Facilities, Aerodynamics Division, VSSC
- VSSC 1985 Configuration design of jet deflector for PSLV launch pad system, VSSC:ADDG:TR:1:85, Aerospace Dynamics and Design Group, Vikram Sarabhai Space Centre, Trivandrum, January
- Subbaraju P V, Ananthasayanam M R, Deshpande S M 1986 Post flight data analysis for drag estimation of a satellite launch vehicle using extended Kalman filter, VSSC-FDG-ARD-012/86 FM1, VSSC, Trivandrum, May
- Subhash A N, Alok Banerji, Kukillaya S P 1981 Heat transfer facility of Aerodynamics Division - design and development, VSSC:TR:34:226:81, Aerodynamics Division, VSSC, Trivandrum, February
- Sundara Murthy H, Narayan K Y, Suryanarayana G K, Rajeev Lochan, Sasidharan Nair K G, Varambally B S 1986 *J. Aeronaut. Soc. India* 38: 215-221
- Van den Berg B, Elsenaar A 1972 Measurements in a three-dimensional incompressible turbulent boundary layer in an adverse pressure gradient under infinite swept-wing conditions, NLR TR 72092 U National Aerospace Laboratory, Amsterdam

Dimensional analysis and equilibrium radiation

HANS W LIEPMANN

Graduate Aeronautical Laboratories, California Institute of Technology, Pasadena, CA 91125, USA

Professor Dhawan and I have been colleagues and friends for a very long time; to be more precise, for more than 35 years, ever since Dr. Dhawan came from Minnesota to Caltech as a graduate student. By now he has caught up with me in everything but age. Similarity and dimensional analysis have played an important role in his research as well as in mine. For some years now I have been playing with the application of dimensional analysis to statistical thermodynamics. This little study of radiation thermodynamics is offered as a tribute to Dr. Dhawan as a small token for a great scientist, engineer, administrator and, most of all, human being.

Keywords. Dimensional analysis; equilibrium radiation; radiation thermodynamics; cavity radiation.

1. Cavity radiation at rest

Dimensional analysis is so important in fluid dynamics, that we take its use for granted. In the physics curriculum dimensional analysis, DA for short, is usually omitted and the prejudice exists that one can only check known results. In classical and statistical mechanics DA is hardly ever even mentioned in spite of the fact that it can be used to great advantage in obtaining the essentials often very easily. In the following DA will be used to obtain a few results of the theory of cavity radiation both at rest and in motion. Assumed is a knowledge of the fundamentals of classical thermodynamics and, for the moving cavity, a few results of relativistic mechanics.

The complete thermodynamics of a system is contained in one of the canonical equations of state, i.e. in the functions $E(V, S, N)$, $H(p, S, N)$, $F(V, T, N)$, or $G(p, T, N)$, where E , H , F and G are the energy, enthalpy, free energy and free enthalpy, respectively. N is the number of particles and the rest of the variables have the usual meaning. Here $H(p, S, N)$ is chosen. H is the most important state variable for fluid systems, a fact which ultimately stems from the Lorentz invariance of the independent variables p , N and S . The thermodynamic identity for H is

$$dH = TdS + Vdp + \mu dN, \quad (\mu = \text{chemical potential}),$$

with H , S , V , N being extensive variables.

2. Equilibrium radiation

The photons making up the radiation field have zero rest mass and hence N is not an independent variable of state, the chemical potential is zero and consequently the canonical equation reduces to $H = H(p, S)$. Now besides p and S , H can depend only on the universal parameters k , the Boltzmann parameter, c , the velocity of light and \hbar , the Planck (or Dirac) parameter. These facts are sufficient to establish the equation of state except for an undetermined numerical constant A , say. First of all, S/k is obviously a non-dimensional product. From H , p , c and \hbar one can make up only one other dimensionless product and hence it follows that

$$H = (p c^3 \hbar^3)^{1/4} \phi(S/k)$$

with ϕ an undetermined function. But since only H and S are extensive variables H must be simply proportional to S , and hence

$$H = A (p c^3 \hbar^3)^{1/4} (S/k),$$

T , V , E etc. follow easily by differentiation. In particular,

$$pV = H/4 = E/3,$$

and the usual expressions for $E(T, V)$ and $S(T, V)$:

$$E/kT = 3(kT)^3 (V/A^4 \hbar^3 c^3); (S/k) = (H/kT) = 4(E/3kT).$$

Of course the number A cannot be determined from DA. One usually hopes that such a number is of order unity. In this case this is correct: Comparison with the standard statistical derivation of radiation thermodynamics shows that

$$A = [45/\pi^2]^{1/4} = 1.4613.$$

Note that for an ultrarelativistic material gas for which $kT \gg mc^2$, the rest mass m is unimportant and H is independent of m as well, but the chemical potential remains finite and hence H depends on N so that

$$H = N(p c^3 \hbar^3)^{1/4} \phi(S/kN).$$

Evidently,

$$pV = H/4 = E/3,$$

follows here as well, but the thermal and caloric equation of state depend now on the function ϕ .

3. Cavity radiation in motion

Moving cavity radiation was used already by Planck in 1908 as a model system to establish the appropriate relativistic transformation of the temperature. Using two results from relativistic mechanics, i.e. the transformation of V and the invariance of p one can easily extend the approach used above: For a moving system with velocity u and momentum J (considered parallel for simplicity) the thermodynamic identity now reads:

$$dH = Tds + Vdp + \mu dN + udJ,$$

with H a function of the extensive variables S , N and J and the intensive p . [H thus depends on the momentum and is the analogue of a Hamiltonian. F London remarks that the common use of the same letter to denote the enthalpy and the Hamiltonian shows a mystical foresight! (London 1964, p. 125)] For black body radiation the term in N is again missing and it is certainly possible to find from the other variables an additional non-dimensional product involving J but it is somewhat cumbersome and it is simpler to introduce a new potential (i.e., a "Lagrangian"),

$$\tilde{H} = H - uJ,$$

with the thermodynamic identity.

$$d\tilde{H} = T ds + V dp + \mu dN - J du,$$

and to find the appropriate $\tilde{H}(p, S, N, u)$. The new dimensionless parameter is now simply $(u/c) = \beta$.

Consequently the canonical equation for moving cavity radiation becomes

$$\tilde{H} = (pc^3 \hbar^3)^{1/4} (S/k) \phi(u/c),$$

with a still undetermined function ϕ . The transformation of V is simply related to the length contraction known from mechanics:

$$V = V_0(1 - \beta^2)^{1/2}$$

The invariance of S follows either from the fact that in statistical mechanics (S/k) is simply a number or else from the consideration that setting a system into motion is a reversible, adiabatic process. Since V is the derivative of H with respect to p at constant S and u ,

$$V = \frac{1}{4} [c(\hbar/p)]^{3/4} (S/k) \phi(\beta),$$

and hence,

$$\phi(\beta) = \text{const} (1 - \beta^2)^{1/2},$$

$$\tilde{H} = A (pc^3 \hbar^3)^{1/4} (S/k) (1 - \beta^2)^{1/2}.$$

Taking the partial derivative with respect to S yields the temperature, i.e.,

$$T = T_0 (1 - \beta^2)^{1/2}.$$

The momentum follows from the derivative with respect to u and thus

$$Ju = \tilde{H} \beta^2 / (1 - \beta^2).$$

Thus β is related to a dimensionless parameter α , say, by

$$(1 - \beta^2) (1 + \alpha^2) = 1,$$

with

$$\alpha = JK c / [AS (pc^3 \hbar^3)^{1/4}].$$

The transformation for the enthalpy H becomes

$$H = H_0 / (1 - \beta^2)^{1/2} = H_0 (1 + \alpha^2)^{1/2}.$$

The transformation for the energy is more complicated because of the additional dependency of V on β .

$$E = E_0 (1 + \beta^2/3)/(1 - \beta^2)^{1/2}.$$

Defining the mass M by J/u yields

$$H = Mc^2.$$

All the other known results can of course be obtained from the expression for \tilde{H} or H . Since thermodynamic equilibrium of any system with a radiation cavity persists independent of the motion, the appropriate transformation formulae apply to all systems.

The "total specific enthalpy", h_0 , of high speed aerodynamics is seen to follow as the first approximation for small β and normalizing the zero of specific enthalpy (or energy) to mc^2 . Thus

$$h_0 = h(p, s) + (u^2/2).$$

Reference

London F 1964 *Superfluids* (New York: Dover) vol 2

Limits and models in fluid mechanics*

KIRIT S YAJNIK

Fluid Mechanics Division, National Aeronautical Laboratory,
Bangalore 560 017, India

Abstract. A framework is presented for examining the effectiveness of limiting and modelling arguments used in the analysis of fluid flows. It consists of examining the consequences of the arguments on the flow problem as a whole and breaking down the limiting/modelling process into a sequence of steps and associated sequence of flow problems, termed here as 'lidels'. The notion of validity of lidels is given. Several examples are given to explain the present approach.

Keywords. Limit; flow model; modelling; fluid mechanics; asymptotic expansions.

1. Introduction

Limiting and modelling arguments are probably the most fascinating elements in the wizardry used in the analyses of flow problems. These flexible instruments enable fluid dynamicists to apply physical and mathematical ingenuity to highlight key features of the problem at hand and to strip it of essentially secondary features. The resulting simplification often facilitates analysis and computation and gives valuable insight into the nature of fluid flows. Occasionally, however, the results are intriguing and it may not be evident whether we can accept them as manifestations of real flows.

A typical limiting argument applied to a governing equation or initial or boundary condition seeks to obtain a statement that is exact in a chosen limit. The statement is also expected to be a good approximation when the parameters are close to the limiting values. The argument can in general be executed formally and systematically by using asymptotic expansions to indicate the conditions under which the resulting statement is a good approximation or to obtain improved approximations. A modelling argument, on the other hand, relies on physical or mathematical judgement, experimental information, and, in some cases, on analogies, and it leads to a statement that is taken as a part of the problem. Unlike limiting arguments, there is usually no indication of conditions under which it is exactly or approximately correct. Also, there are no general systematic ways of constructing improved models. Furthermore, some of the resulting statements may contain parameters or functions that are chosen subsequently depending on the

*Invited general lecture at 3rd ACFM, Tokyo, September 1986

particular class of problems one is dealing with. Thus there is generally much greater understanding and agreement about the limiting arguments* and the range over which they provide useful approximations, although there have been quite a few surprises when apparently straightforward limiting arguments have been applied to seemingly innocuous problems.

Although these arguments are qualitatively different, it is proposed to consider them together in this work for several reasons. First, they often alter the nature of the problem as a whole and their effectiveness is best judged by the information provided by the modified problem. Second, there are instances when we have to use both limiting and modelling arguments (e.g. turbulent boundary layer) and a common methodology of examining the consequences would be useful. Third, there seems to be enough scope for extending certain ideas such as validity, which have been fruitfully applied to limiting arguments, to the modelling arguments. The last reason is the main motivating factor of the present approach, which, one hopes, would lead to a sharpening of the acceptance standards of modelling arguments.

Let us recall a few classical examples. The low Reynolds number analysis of Stokes, based essentially on a limiting argument, led to the formula for the drag of a spherical particle that has been widely used. However, when a similar argument was applied to a circular cylinder, it led to nonexistence of a solution. This type of difficulty was resolved much later by using methods of singular perturbations inspired by boundary layer analysis.

The problem of steady attached flow past a streamlined body for an incompressible fluid at large Reynolds number was historically first attacked by solving the corresponding inviscid flow problem in two dimensions. An additional condition, known as the Kutta condition, has to be imposed to determine the circulation around the aerofoil. This could be interpreted as the application of limiting arguments coupled with a modelling argument. One could advance limiting arguments to obtain the Kutta condition as a conclusion, although such a systematic argument is not known to the author.

While the correctness of the Kutta condition has never been seriously questioned for the original class of problem for which it was proposed, it should be noted that neither is a higher order Kutta condition available nor is it clear what should be a similar argument or statement when the aerofoil is oscillating or when there is an oscillating flow about a stationary aerofoil. Flow visualisation studies seem to show that the stagnation point, under certain conditions, is not at the trailing edge, but near it. Yet inviscid analysis based on the Kutta condition has been immensely useful in aeronautics and indeed it has been widely applied to cases where the aerofoil has a small base or when there is a small separated region near the trailing edge.

The well-known analysis of von Karman for a vortex street deals with a model problem in which not only the viscous diffusion of vorticity is not considered, but also vorticity is taken to be concentrated, illustrating that not only governing equations but also initial or boundary conditions may be modified by these arguments.

* Limiting arguments are related to so-called rational approximations (Van Dyke 1964, p. 3) which can be distinguished from other, irrational, approximations. These approximations can be distinguished from 'models' in several ways as was done by Ojhi (1982, p. 105) for turbulent flows.

Free streamline models, beginning with the Kirchoff model, specify the displacement effect of the wake in a separated flow past a body usually in terms of a boundary condition on the separating streamline. This family of models illustrates another rather common feature of model problems, namely incompleteness, as one quantity, typically base pressure, has to be specified. This type of input is problem-specific. Of course, there are well-known cases of incompleteness, which call for general inputs. The problem of calculating mean flow and moments of low order in stationary turbulent flows is bedevilled by the absence of a physically sound and mathematically sufficiently general closure hypothesis, although several well-known closure hypotheses have been useful in practical applications and also in clarifying some features of the flow.

As explained above, we are concerned here with examining limiting arguments and model arguments together on the basis of their consequences on the problem as a whole. It is expedient to call the modified problem a *lidel* (a word coined by the combination of 'limit' and 'model') to distinguish the argument from the resulting problem and to emphasise a common framework for considering both types of arguments. The plan is to present first a general framework, which is followed by the notion of validity and a classification scheme to handle similarities of structures in a systematic way. The general methodology of examining the consequences of the arguments in several stages is finally illustrated by several examples.

2. Framework

The main idea is to consider arguments of limiting or modelling character together and to examine the resulting modified problem, which is termed as a 'lidel' or a 'lidel problem'. The arguments which make assumptions about solutions of the original problem are also included. For instance, if it is argued that the flow, which is subjected to time-independent boundary conditions, and which starts from a given initial condition, approaches a steady flow at large times, the resulting steady flow problem is considered a lidel for large time behaviour. One case study is given later to indicate several types of large time behaviour that can arise in flow problems. Similarly, if a boundary layer for given initial conditions and a suitable pressure distribution tends to become similar, the problem of obtaining a similarity solution is considered as a lidel for large downstream distances.

Classical hydrodynamic stability problems of boundary layers formulated for early stages of transition employ several ingredients such as undisturbed parallel flow, small disturbance of assumed form, modelling of spatial growth by temporal growth, which can be considered as limiting or modelling arguments; the stability problem is then regarded as a lidel for a certain class of disturbances and a certain range of downstream distance. When the analysis is applied to the flow resulting from a vibrating ribbon, an additional ingredient which changes a forced oscillation problem into a free oscillation problem is needed, which can also be regarded as a modelling argument.

Since the limiting modelling process frequently leads to incompleteness, hypotheses or statements of a general nature that are added to complete the problem are treated as parts of the lidel. On the other hand, information about numerical values of certain parameters, which are problem-specific, or which are not obtained by the

argument but by comparison of the results with experimental data or other solutions, is termed as auxiliary input. Some inputs are matters of convenience (e.g. wall functions in certain turbulent flow computations) and some are such that the final results are not supposed to be sensitive to the chosen values provided they are in certain ranges (c.g. velocity profiles in integral models of boundary layers). This type of information which is necessary but which is not central to the lidel problem is also treated as auxiliary input (see figure 1). Arguments used in replacing partial differential equations and the initial and the boundary conditions by finite difference statements are also considered here as limiting/modelling arguments. Grid size, coefficients of terms added for damping out certain effects (that is, numerical viscosity), and relaxation factor etc. are examples of auxiliary inputs.

A few points have to be noted about the present approach. First, there is no restriction on the mathematical form of the lidel problem. Second, the expected correspondence between the solutions of the lidel and the original problem can vary from being exact for certain conditions, certain values of parameters, or in certain limits, to mere qualitative similarity. Since this range of correspondence may appear too broad to some readers, the need for such flexibility is shown by an example. The problem of a two-dimensional inviscid layer of constant vorticity with a slip at the wall responding to a small initial disturbance at the surface of the rotational region was formulated (e.g. Pullin 1981) to simulate dominant features of a turbulent boundary layer at large Reynolds number. Clearly, the correspondence between the results of this problem and real boundary layers can at best be qualitative. We regard this problem as a lidel of real turbulent boundary layers for large Reynolds numbers. Third, a clear distinction is made between the statement of a lidel and a method for *its* solution. However, it should be pointed out that some arguments which change the nature of the problem are conventionally regarded as

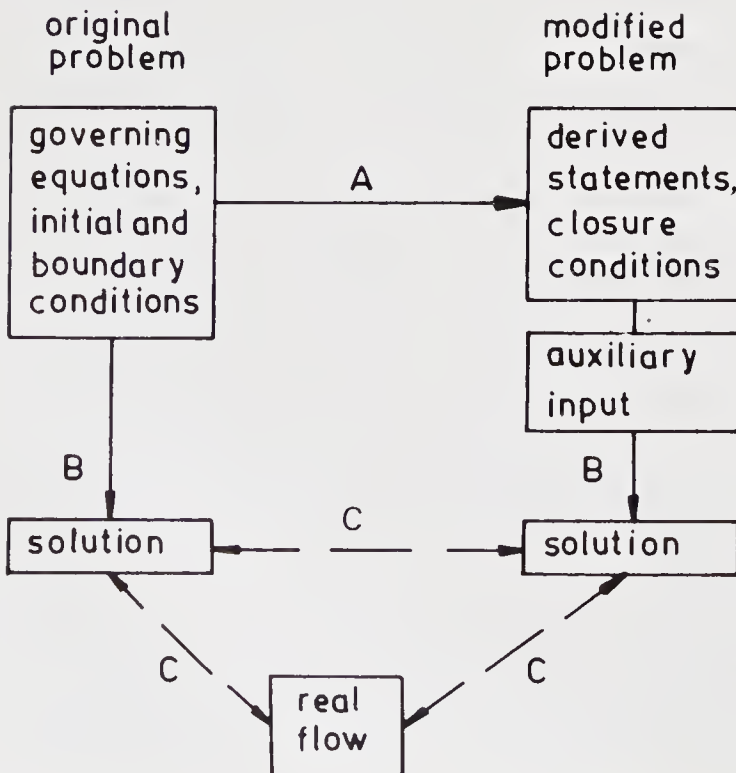


Figure 1. General framework for examining consequences of limiting and modelling arguments. A arguments, B analysis or computation, C correspondence.

a part of the method of solution of the *original* problem. For instance, there is a class of methods of obtaining approximate solutions of boundary layers in which the partial differential equations are first replaced by a few integral relations, then some additional statements are added and then one proceeds to solve ordinary differential equations. We first note that what is actually solved is a substitute problem and not the original problem. We regard the first two parts as not really part of the method of solution of the original problem governed by partial differential equations but as modelling arguments that replace the original problem by a substitute problem. It should be emphasised that the change in the mathematical structure is evidently accompanied by the change in the nature of information. For instance, Newton's laws and energy conservation would hold for the layer as a whole but not for its individual parts.

The next major idea is to split the limiting/modelling process into a sequence of steps or stages and to examine the solutions of problems before and after a step. Although such splitting may not always be possible, it can give useful understanding of the limiting/modelling process. In some instances, examination of the solution of the problem prior to a limiting/modelling stage reveals conditions when the model is likely to be valid. For instance, the problem of steady incompressible inviscid flow past an aerofoil can be obtained in two steps or stages. First, one considers the large-time behaviour for a viscous fluid initially at rest and takes a large-time limit. Second, one allows the viscosity to approach zero or the Reynolds number to approach infinity without stretching coordinates and one adds the Kutta condition. The problem obtained at the end of the first step is a *lidel* that is capable of describing viscous effects in the boundary layer and the wake in the absence of unsteadiness. The problem obtained at the end of the second step, that is, the inviscid flow problem, is also a *lidel* in the present context. In order to understand what the second step does, one can compare the problems at the end of the first and the second stage.

Consider the discrete potential vortex model classically used in the computational studies of the stability of a mixing layer. One can visualise three steps of the limiting/modelling process starting from an initial value problem of a viscous layer of finite thickness. First, viscosity is allowed to approach zero. Second, the thickness of the layer is allowed to approach zero, so that the thin layer is replaced by a velocity discontinuity, a vortex sheet. Third, the vortex sheet is replaced by a set of initially equidistant discrete (potential) vortices of equal strength. The problem at the end of the second step has no length scale, while a length scale, the initial distance between neighbouring discrete vortices, is introduced in the last step. Little wonder that the vortex sheet is unstable to disturbances of any wave length (Kelvin-Helmholtz instability) and the discrete vortex calculation, if performed without numerical fixes, shows that the layer crosses itself after some time.

In some instances, when the model is thought to be fully satisfactory, one learns from such examination about some features that the modelling process might have filtered out. One has to keep in mind that the order of steps may be important and that there might be more than one acceptable sequence. A few examples are given later to illustrate the possibilities.

There is another type of splitting that can be thought of. When the incompleteness of the *lidel* problem is remedied by closure conditions, one can, in some cases,

compare them with corresponding experimental results or results of problems that are upstream in the limiting/modelling process. Such direct comparison can tell us about the range of applicability of the closure conditions. One case study is given later to illustrate this type of comparison.

Before proceeding further, we need to examine the notion of the validity of a lidel.

3. Validity

In order to discuss conditions under which a lidel serves the intended purpose, it seems desirable to introduce the notion of the validity of a lidel. It is essentially a generalisation of the idea of validity of an asymptotic expansion. If a standard is specified for the solution of a lidel and a criterion is specified for the difference between the standard and the solution of the lidel, we can say that the lidel is valid if it meets the criterion on comparison with the standard. The standard can be the solution of the original problem or a problem that is upstream in the limiting/modelling process or the results of a carefully chosen experiment. If the correspondence is exact for some conditions or quantitative, but approximate in some sense, it is easy to see how the criterion can be specified. On the other hand, it is difficult to see how qualitative correspondence can be translated into a criterion. For example, it is difficult to specify when flow visualisation pictures have the desired correspondence with discrete vortex model prediction. However, it turns out that it is clear when the lidel solution differs qualitatively from the standard. For example, if a lidel consisting of closely spaced discrete vortices for a vortex sheet leads to the sheet crossing itself after a certain time, it is clear that the lidel cannot be valid for such large times.

We need to bear in mind that the validity of a lidel is usually restricted to a certain range of parameters or regions in space and time. Also, if the lidel needs auxiliary input, the validity is subject to the values of adjustable parameters being chosen in a certain range.

While limiting and modelling arguments might give some information on or indication of the range of validity, experience has shown it to be quite incomplete. Therefore, an a posteriori validation exercise is necessary if we do not wish to run the risk of being misled by some features of the lidel flows into believing that real flows have those features.

4. Classification of lidels

The lidels can be classified in several ways. For instance, one can differentiate them on the basis of the nature of correspondence expected, or on the nature of arguments used in formulating the lidel problems, or on the degrees of freedom of the lidels as indicated by the number of adjustable parameters. The scheme given here for flow problems is on the basis of the mathematical form of the lidel problem. Table 1 gives the classes with illustrative examples, which are largely self-explanatory.

Table 1. Classification of lidels

Class	Example
Differential	Attached potential flow with Kutta condition Free streamline models Karman vortex street Discrete vortex models Flows governed by Euler, boundary layer or parabolised Navier–Stokes equations Large Reynolds number approximations of internal/external separated flows Stokes flow Hydrodynamic stability problems Reynolds averaged equation models with closure hypotheses Lorenz convection model
Integral & integro-differential	Control volume analysis Integral models of laminar/turbulent boundary layers Integral relations for laminar boundary layer Contour dynamics analysis of flow with distributed vorticity
Numerical	Panel & vortex lattice models Finite difference models of potential flow, Euler equations, boundary layer equations, parabolised or full Navier–Stokes equations
Mapping	Poincare maps of certain flow problems
Hybrid	Viscous-inviscid interaction Chapman–Korst model Large eddy simulation models

5. Examples

A few case studies are given to illustrate and elaborate the ideas in the earlier sections.

5.1 *Vortex interactions*

The spatial organisation of rotational regions has been of intense interest since the early seventies. In nominally 2D mean flow fields, these regions, called “vortices” for brevity hereafter, undergo striking motions which have been termed pairing, merging etc. Several investigations model the motion as two-dimensional and inviscid, as some of the observed features of flows are believed to be governed by largely two-dimensional and inviscid processes.

The motion at a point in the interior of such a rotational region can be decomposed into two parts, one owing to vorticity in that region and the other to the rest. The second part essentially convects the region and imposes an irrotational straining velocity field.

The first basic model problem A consists of a single vortex, having uniform vorticity in a region of elliptic shape. The flow outside the region is irrotational. Also, there is a velocity field with uniform strain rate imposed by boundary conditions at large distances. The flow field is termed as an elliptic vortex in a

uniform straining field. Following the steady solution studied by Moore & Saffman (1975), Kida (1981) and Neu (1984) have obtained a class of exact solutions of Euler equations which are illuminating. We first describe certain features of solutions before taking up modelling issues.

As the boundary of the rotational region retains its shape and its area is constant, the velocity field at an instant is characterised by two quantities, namely, the ratio of the major to the minor axis of the elliptical boundary and the angle made by the major axis with one principal direction of the strain rate, the parameters of the problem being vorticity ω and the principal value of strain rate γ . The problem can be transformed into that of a Hamiltonian system and the phase space trajectory diagrams are given in figures 2a–e. The radial coordinate r and the angular coordinate θ of a point indicate the ratio of the major to the minor axis and the angle made by the major axis with the principal axis at any instant. An isolated point (nodal point) or an intersection of trajectories is a steady state, which may be stable or unstable depending on whether none or some of the neighbouring trajectories move away from it. A closed trajectory that goes to all quadrants indicates a periodic motion in which the major axis rotates around the vortex centre. A closed trajectory that does not go to all quadrants indicates that the vortex undergoes angular oscillations. A trajectory that moves indefinitely away from the origin indicates indefinite increase of the ratio of the major to the minor axis or flattening out of the ellipse. We thus see from the figures 2a–e that there are many different types of large-time behaviour that can arise depending on the value of strain rate to vorticity ratio and the initial condition. We summarise the ranges in which these types of behaviour can occur.

Steady vortex	$0 < \gamma/\omega < 0.15$
Oscillating vortex	$0 < \gamma/\omega < 0.15$
Rotating vortex	$0 \leq \gamma/\omega < 0.1227$
Indefinite flattening of vortex	$0 < \gamma/\omega$

Thus an elliptic vortex can undergo simple motions, only if the strain rate is sufficiently small. If the strain rate is sufficiently large, the vortex invariably flattens out.

The second basic model problem B consists of two interacting vortices, initially of circular cross-section and of uniform vorticity, both having equal circulation and area. Two models B1 and B2 obtained from B are based on the contour dynamics method (Zabusky *et al* 1979) and the discrete vortex model in which distributed vorticity is modelled by a cluster of concentrated vorticity. Figures 3a & b show that merging occurs if the initial distance between vortices to diameter ratio is less than a critical value and simple relative motions occur otherwise. The results of the two models B1 and B2 are qualitatively similar, and the critical values obtained by them are about 1.702 and 1.7.

One may link the problems A and B by arguing that one vortex influences the other vortex by imposing a rigid body translation and rotation, and a straining velocity field. In the simplest case, the strain rate can be taken to be uniform. So the problem A can be considered as a lidel having qualitative correspondence with the problem B. Then one expects a correspondence between the parameters of the two models. The initial strain rate (at the vortex centre) to vorticity ratio is

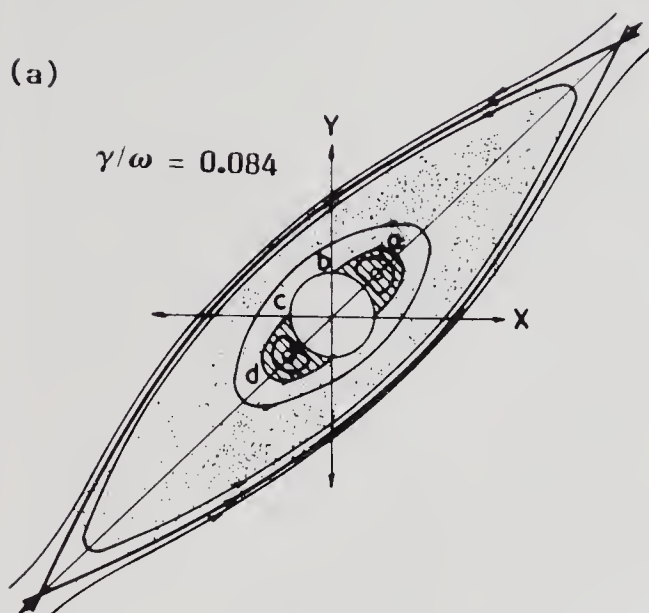
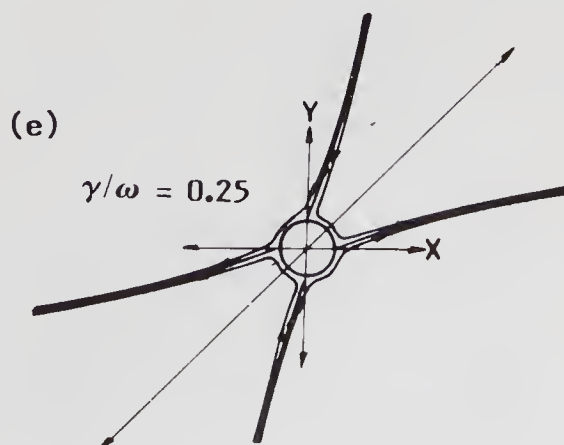
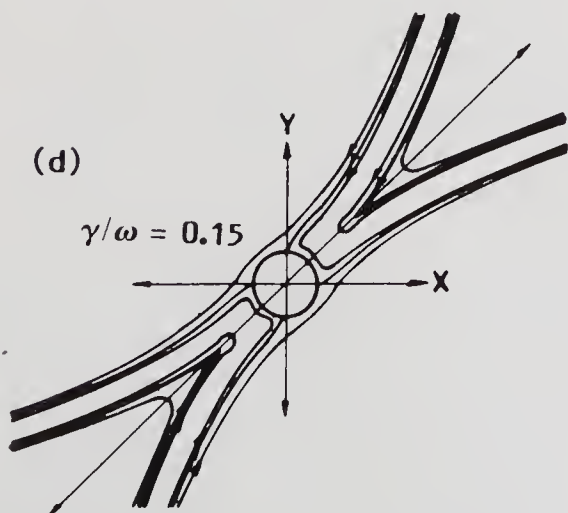
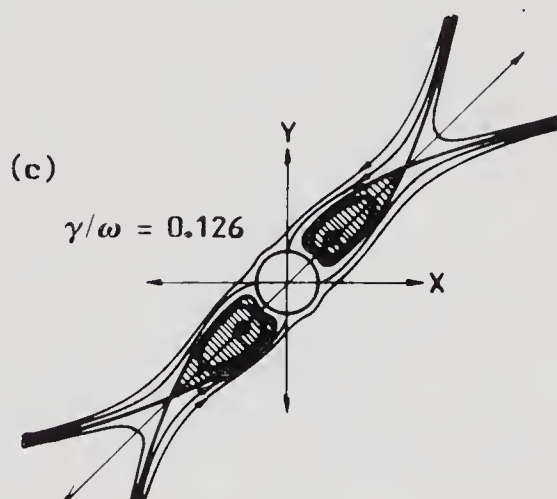
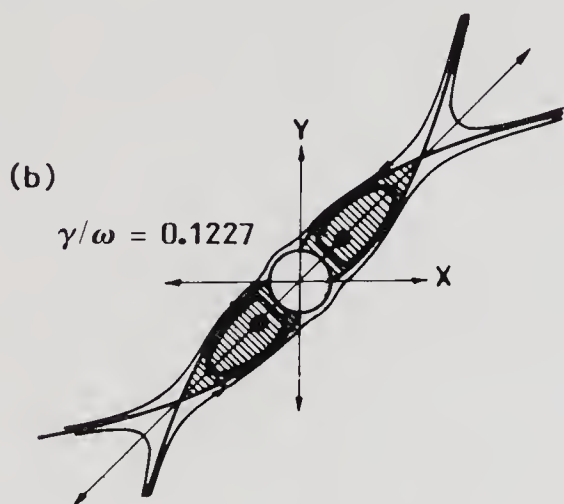


Figure 2. Phase space polar plot for elliptic vortex in a uniform strain rate field (Neu 1984). Radial and angular coordinates (r, θ) indicate ratio of major to minor axis and the angle made by the major axis to one principal direction of strain rate. Strain rate/vorticity (a) below the first critical value (0.1227); (b) equal to the first critical value (0.1227); (c) between the first and the second critical values (0.1227 and 0.15); (d) equal to the second critical value (0.15); (e) larger than the second critical value.



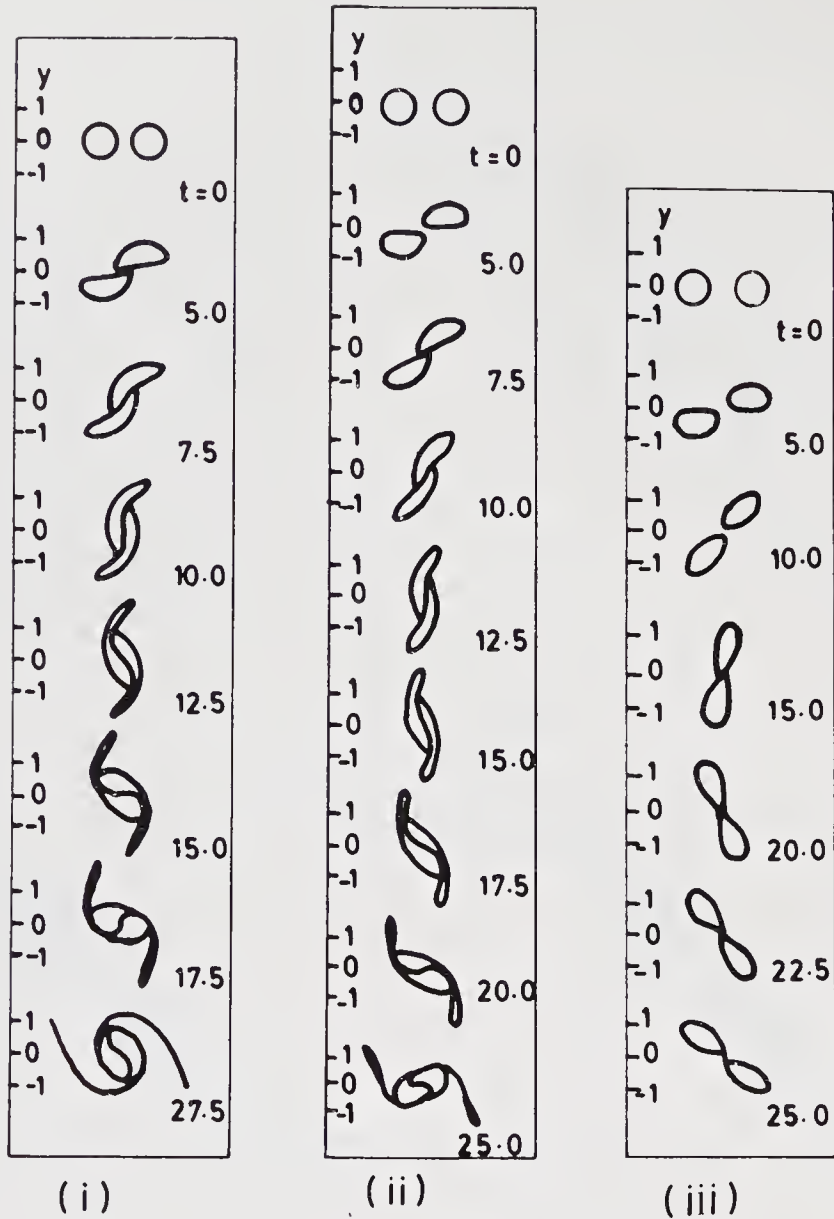


Figure 3(a). Interaction of two vortices of equal strength and of initial circular shape of equal diameter. Results of contour dynamics (Jacob & Pullin 1985). Initial distance between vortex centres/diameter has values 1.3293, 1.5066 and 1.7016 in cases (i), (ii) and (iii), respectively.

inversely proportional to the square of the distance to the diameter ratio. The critical value of strain rate/vorticity that allows the elliptic vortex to retain its shape and rotate is 1.227. This would correspond to the critical value of the initial distance between vortices to the diameter ratio of 1.01, which is much smaller than 1.7. There is a qualitative correspondence between the two models in the sense that when the strain rate is smaller than a certain critical fraction of vorticity, or when the distance between the two vortices is greater than a particular critical multiple of vortex diameter, each vortex is able to undergo simple motions with limited deformation. Limitations on the correspondence arise from non-uniform and time

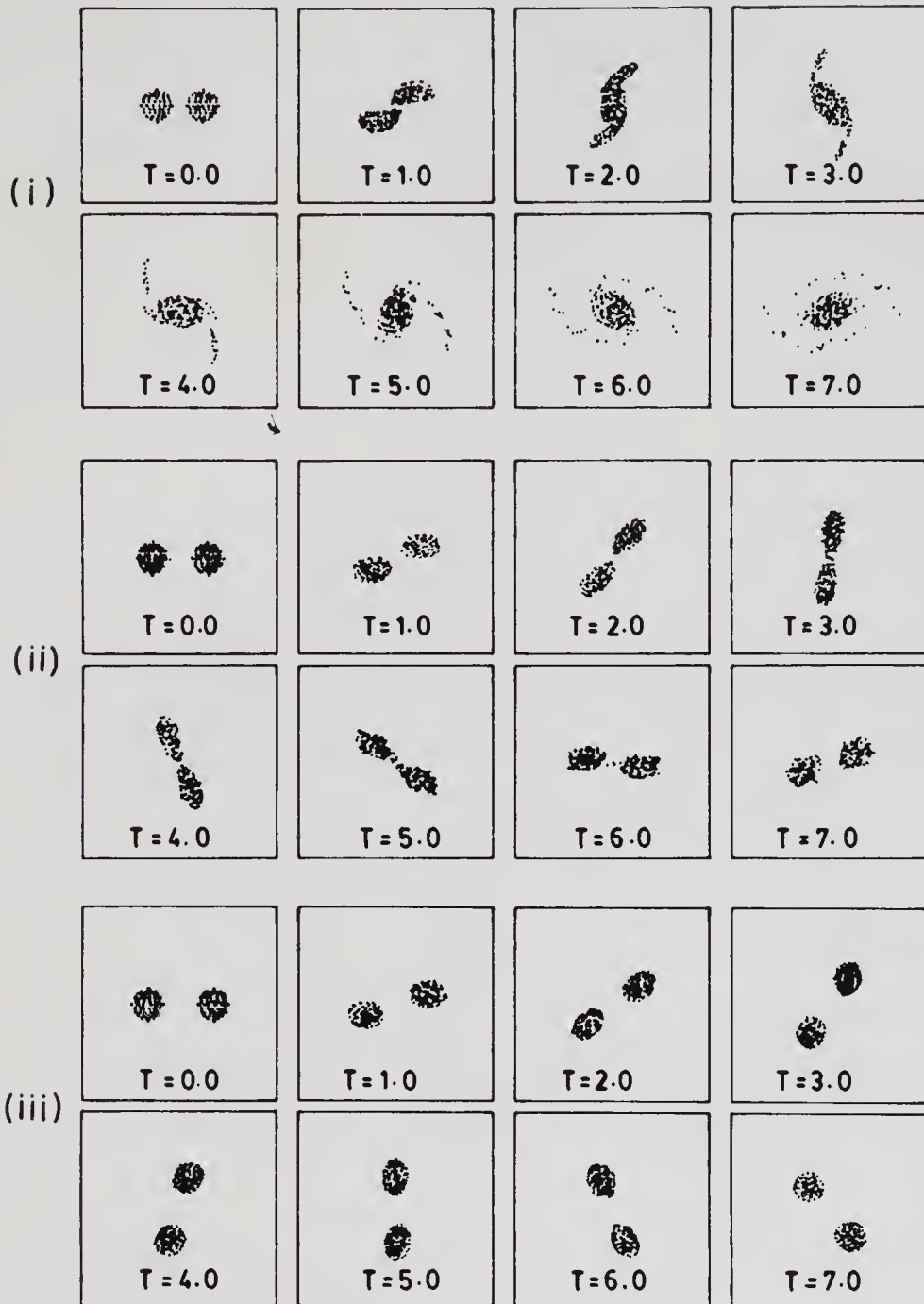


Figure 3(b). Results of discrete vortex model (Tsuboi & Oshima 1985). Distance/diameter has values 1.4, 1.7 and 2 in cases (i), (ii) and (iii), respectively.

dependent strain rate fields imposed by the neighbouring vortex and subsequent non-elliptic shapes in the model B.

There is another aspect of the results of model A which is of interest. The steady flow solution can be considered to be a candidate lidel for large-time behaviour for time-independent boundary conditions. Frequently one argues that, for time independent boundary conditions, the flow may be expected to approach a steady state or a similarity solution. Sometimes longitudinal distance plays a role similar to time and one seeks fully developed flow. In turbulent flow investigations, one

considers stationary flow, self-preserving flow, or equilibrium flow. The results of the model A show that if such large-time (or large-streamwise distance) lidels are used, the following possibilities could well arise.

- (a) The steady flow solution may exist only for a range of parameters.
- (b) In this range, there could be more than one steady flow solution (including stable and unstable cases).
- (c) If the parameter is within the range required for steady flow, initial conditions for the flow at large-time to approach the steady flow may be restricted to some range.

The above possibilities have to be kept in mind in interpreting results of simple large-time lidels, especially for flows with distributed vorticity.

5.2 *Attached flow past a body*

Attached steady inviscid flow with the Kutta condition as applied to air-flow past an aerofoil can be considered a lidel obtained in a sequence of three steps, namely (a) small compressibility effect, (b) large-time after start-up from rest, and (c) small viscosity. The Kutta condition is needed in the third step for 2D problems. Another acceptable sequence of steps would be (b) and (c) followed by (a). Several calculations of the upstream model using this sequence (that is, allowing for compressibility, with Euler equations) suggest that the problem of incompleteness does not appear at this stage. Even if the freestream speed is small, the flow near the body would need to pass through a supersonic pocket, and a shock, to go around the sharp trailing edge with accompanying drop in total pressure and the resulting pressure discontinuity near the rear stagnation point on the smooth surface. This is an example of how one learns about flows as well as the limiting/modelling processes by splitting into limiting/modelling steps.

5.3 *Integral lidels of laminar boundary layers*

A large family of methods were developed in the early stages of boundary layer theory, which model dynamics of the layer as a whole by using momentum, and in some cases, energy integrals, and additional inputs. The methods were intended to provide quick, reasonably good approximations. Despite their simplicity and gross nature of additional information, they ended up providing rather accurate information on integral parameters. Several variants for turbulent boundary layers have also enjoyed success and sustained use in applications.

From the present viewpoint, an integral model of a boundary layer consists of integral relations like momentum and energy integrals, additional inputs in the form of velocity profile families or relations amongst integral parameters and possibly auxiliary inputs.

One can visualise obtaining such a lidel in three steps. The first one would be to obtain an integral formulation of the boundary layer problem. There is an integral transform formulation of the boundary layer problem (Yajnik 1984) that is suitable for the present purpose. The second step would consist of expansion in the transform variable, which generates a sequence of integral relations. One truncates after a few terms. Hence, this second step is essentially based on limiting arguments. The third step consists of imposing additional conditions. This is viewed as a modelling step. Traditional integral methods employ the first relation, that is,

the momentum integral, and, at most, the second relation, which is the energy integral. There is a considerable variety of additional conditions that have been used (see, for example, Rosenhead 1963, pp. 292–317). Interestingly, if one retains a larger number of terms of the expansion, one needs additional conditions that can provide for such flexibility. The method of weighted residuals (e.g. Dorodnitsyn 1962, Abbott & Bethel 1968) provides for the use of certain polynomial expressions for this purpose. The above interpretation of integral methods provides improved understanding. The first step interestingly does not amount to any loss of information or involve any approximation, as it has been used to obtain a few exact solutions of the boundary layer problem. The transform formulations have some additional conceptual interest, as the basic nonlinear transform used in the formulation is a generalisation of boundary layer thickness and its expansion in the transform variable generates displacement, momentum and energy thickness, and similar ‘higher-order’ thicknesses! This example illustrates that examination of problems upstream in the limiting/modelling process tend to enhance our understanding.

5.4 *Modelling of turbulent boundary layers*

The classical modelling process consists of applying order of magnitude arguments to Reynolds averaged equations and introducing closure conditions of different kinds. If one carries out the process in two parts, namely, using limiting arguments of the boundary layer type, and subsequently invoking various closure hypotheses, there are some advantages (Yajnik 1970). First, the results of the first step are independent of any particular closure condition. Second, the results can be considered to be exact in the limit of large Reynolds numbers. Third, surprisingly asymptotic forms similar to well-known empirical laws can be obtained without making any closure hypotheses. This approach has been extended by many workers to account for heat transfer, compressibility, spectral domain, moderately large Reynolds number, non-stationary case etc. This example shows that it is advantageous to carry out limiting argument stages before modelling stages.

5.5 *Wake-boundary layer interaction*

Two Stanford conferences have shown how evaluation of calculation methods for turbulent shear flows needs highly coordinated exercises. The methodology of evaluating a method consisting of derived equations, closure hypotheses and an integration procedure certainly shows the effectiveness of the package. In some cases, however, a simpler exercise aimed at testing components of lidels can be quite instructive. For instance, in a recent study of the interaction of the turbulent wake of an aerofoil and a wall boundary layer by Sundaram & Yajnik (1986) one finds that experimental observations as far downstream as four chords have a trend similar to the Cebeci-Smith eddy viscosity hypothesis, but the scales are different (figure 4). The inference is that when simple closure conditions are applied to complex flows arising from the merging of flows of two different types, some modifications in the closure conditions are called for.

Although here we have split the model problem rather than the modelling process into components, the basic idea is to break down a complex structure into

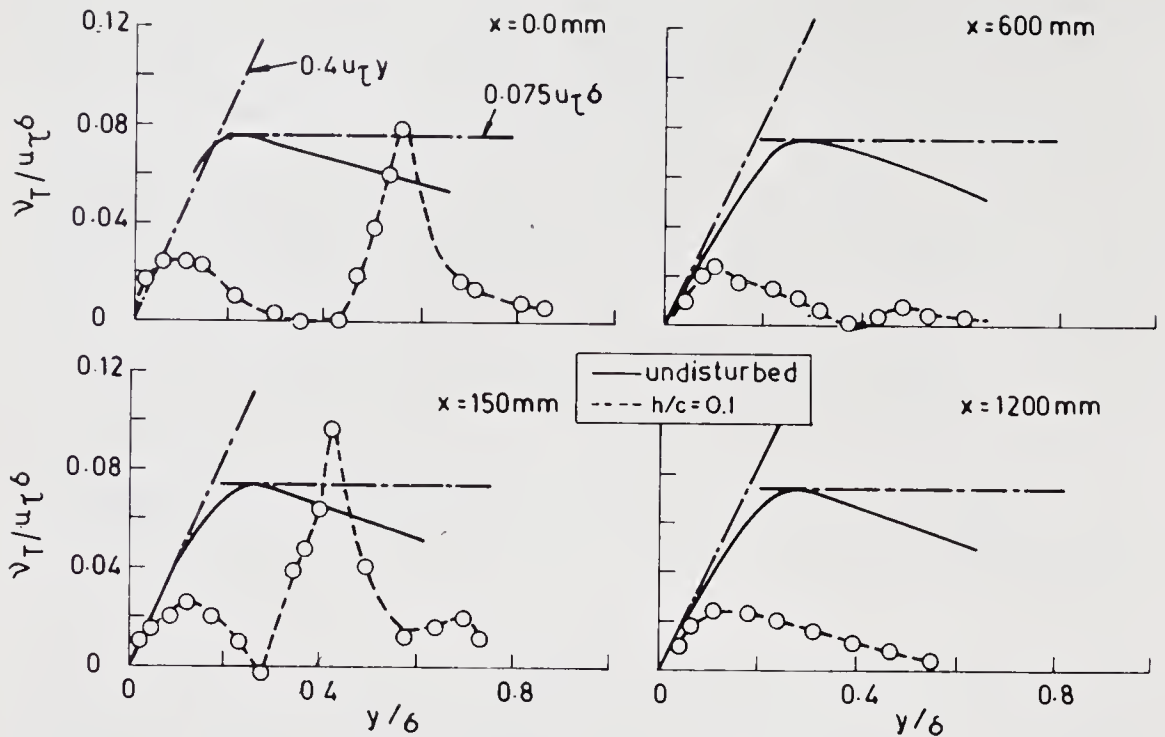


Figure 4. Eddy viscosity distribution in an undisturbed boundary layer in nominally zero pressure gradient (—), and in an aerofoil wake merging with a boundary layer (—○—) in experiments of Sundaram & Yajnik (1986); (---) Cebici-Smith model. h , height of aerofoil (NACA 0012) above wall, c , aerofoil chord, ν_T eddy viscosity, u_τ , skin friction velocity, δ , boundary layer thickness, x , longitudinal distance.

parts to facilitate investigation and to enhance our understanding of flows as well as the reasoning used in the analysis of flows.

References

- Abbott D E, Bethel H E 1968 *Ing.-Arch.* 37: 110–124
- Dorodnitsyn A A 1962 *Advances in aeronautical sciences* (ed.) Th von Karman (London: Pergamon) vol. 3, pp. 207–220
- Jacobs P A, Pullin D I 1985 *Phys. Fluids* 28: 1619–1625
- Kida S 1981 *J. Phys. Soc. Jpn.* 50: 3517–3520
- Moore D W, Saffman P G 1975 *J. Fluid Mech.* 69: 465–474
- Neu J C 1984 *Phys. Fluids* 27: 2397–2402
- Ohji M 1982 *Surveys in fluid mechanics* (eds) R Narasimha, S M Deshpande (Bangalore: Indian Acad. Sci.)
- Pullin D I 1981 *J. Fluid Mech.* 108: 401–421
- Rosenhead L (ed.) 1963 *Laminar boundary layers* (London: Oxford University Press)
- Sundaram S, Yajnik K S 1986 *Proceedings of the third Asian congress fluid mechanics* (ed.) T Matsui (Tokyo: ACFM) App. 2: 1–9
- Tsuboi K, Oshima Y 1985 *J. Phys. Soc. Jpn.* 54: 2137–2145
- Van Dyke M 1964 *Perturbation methods in fluid mechanics* (New York: Academic Press)
- Yajnik K S 1970 *J. Fluid Mech.* 42: 411–427
- Yajnik K S 1984 Integral transforms and boundary layers, NAL Tech. Memo. FM-TM-84-11, National Aeronautical Laboratory, Bangalore
- Zabusky N J, Hughes M H, Roberts K V 1979 *J. Comput. Phys.* 30: 96–106

Variable property analysis— is there anything to it?

H S MUKUNDA

Department of Aerospace Engineering, Indian Institute of Science,
Bangalore 560 012, India

Present address: NRC Research Associate, NASA Langley Research
Centre, Hampton, Virginia 23665, USA

Abstract. This paper discusses a few situations in combusting flows and attempts to demonstrate that including variable thermodynamic and transport properties in the analysis does more than simply improve the accuracy of predictions. The qualitative behaviour of the result itself is altered. Three examples are considered—single droplet combustion, forced convective turbulent boundary layer combustion, and free convective combustion.

The flame to droplet radius ratio is very well predicted by variable property theory and the improvement is a direct consequence of the property variation. In the case of turbulent boundary layer combustion of solid/liquid fuels it is shown that the fuel exerts a significant influence on regression rate as is found in the experiments. The constant property theory, however, shows relative independence of regression rate with regard to the nature of the fuel. The prediction of regression rate is improved substantially in the case of free convective combustion.

Keywords. Variable property analysis; single droplet combustion; forced convective turbulent boundary layer combustion; free convective combustion; regression rate.

1. Introduction

In many areas like fluid mechanics and aerothermochemistry the impression of a large number of workers is that the role of variable thermodynamic and transport properties is essentially cosmetic. Any reasonable choice of the constant property is adequate to describe the physics. The use of variable properties may improve the predictions. On the other hand, there is an impression amongst some that computer calculations including all effects is a sure cure for all bad comparisons between theory and experiments.

There is a middle path. It consists in making matters just as complex as is desirable to describe the behaviour appropriately. The same statement can be

expressed differently: Matters can be made as simple as nature would accept. Three situations where it has been necessary to do this are described herein.

2. The droplet combustion problem

The classical problem which has received attention for over forty years is as follows: An atomised spherical droplet of fuel is burning in an atmosphere of oxidant (like air). It could burn in a normal gravitational environment as it does in many applications. Basic experimental studies on the combustion of droplets in zero-g environments have also been conducted. The measured parameters are the instantaneous drop diameter vs. time, flame diameter vs. time and initial diameter vs. time of burn-out. Typical measurements of combustion show that the flame to drop diameter ratio rarely exceeds 8–10 for many hydrocarbon liquids like heptane, octane and so on. The mass burn rate is expressed in terms of an evaporation constant which is the slope of (drop diameter)² versus time plot.

The theory consists of the solution of conservation equations of mass, species and energy. The momentum equation is generally not considered as it leads to negligible variations in pressure and velocity of flow. If thermodynamic and transport properties are taken to be constant, one obtains from a simple quasi-steady theory (SQST)

$$\dot{m} = 4\pi(k/c_p)_{av} r_s \ln(1 + B), \quad (1)$$

\dot{m} = mass burn rate (kg/s), $(k/c_p)_{av}$ = ratio of conductivity to specific heat of gas at average conditions (kg/m·s), r_s = drop radius (m),

$$d_f/d_s = \ln(1 + B)/\ln(1 + \beta/s), \quad (2)$$

$$B = [c_p(T_\infty - T_s) + H\beta/s]/Q,$$

T_∞ , T_s = ambient and surface temperatures (K), β = oxidant mass fraction at infinity, s = stoichiometric ratio, H = heat of combustion per unit mass of fuel (MJ/kg) and flame temperature

$$T_f = [(c_p T_s - L + H)/s + c_p T_\infty]/[c_p(1 + \beta/s)]. \quad (3)$$

Values of \dot{m} (or K , which is burning constant), d_f/d_s (flame diameter/droplet diameter) and T_f have been calculated for a few cases and compared with measurements under various conditions as in table 1. Of the three measurables, \dot{m} (or K) is most successfully predicted by SQST. The success of SQST has been in isolating the final functional dependence of \dot{m} on r_s or equivalently, the d^2 -law which has been observed in the experiments. But the quantitative evaluation of \dot{m}/r_s (or K) involves the judicious choice of thermodynamic and transport properties. One should conclude from the correlation of SQST predictions with experimental results obtained under natural convection (which is larger than under zero-g) that the prediction of \dot{m} is an overestimation. In fact, if the value of (k/c_p) is evaluated at the mean temperature between the drop surface and the flame, the estimated burn rate will be significantly larger than is actually observed (Aldred & Williams 1966).

Similarly, the value of (d_f/d_s) assigned by SQST is also an example of gross overestimation (see table 1). Because of its logarithmic dependence on B , d_f/d_s has

Table 1. General comparison of experimental data with SQST (*n*-heptane).

Technique	Condition	d_0 (mm)	$k = 4\dot{m}/$		T_f (K)	Reference
			$\pi\rho_c d_s$ (mm ² /s)	d_f/d_s		
Stationary suspended drop	Unsteady natural convection	1.5	1.1	3.0	1800	Hedley <i>et al</i> (1971); Aldred & Williams (1966)
Porous burner	Steady natural convection	12.0	1.8	1.35	2000	Aldred & Williams (1966)
		1.5	1.04	1.8		
Drop in zero-g	Unsteady no convection	0.95	0.78	6–10		Isoda & Kumagai (1959)
Theory (SQST)	Quasi-steady no convection	Any size	1.1	29.0	2300	

negligible dependence on the chosen mean thermodynamic and transport properties, (2). Furthermore, d_f/d_s is considered to be independent of the diameter of the droplet in spite of the fact that the experimental observation has recorded that the initial movement of the flame is away from the droplet, followed by a gradual decrease in size as the drop continues to shrink steadily (Isoda & Kumagai 1959). These aspects deserve a careful reexamination.

Referring to table 1, the theoretically predicted values of T_f are again seen to be considerably larger than the experimental values (the free convection effect does not alter the flame temperature significantly). Although SQST predicts the adiabatic flame temperature, (3) predicts a strong dependence of T_f on c_p . While this ambiguity can be easily eliminated by considering the exact variation of c_p in the field, the inclusion of kinetics and unsteadiness becomes a necessary prerequisite for the realistic prediction of T_f .

Such discrepancies between the predictions of SQST and the experimental results have been attributed to various factors: finite kinetics, unsteadiness of the combustion process, variations of thermodynamic and transport properties, and natural convection. Of these, the effects of natural convection are not considered for the present due to the discrepancies which exist between SQST predictions and data from zero-g experiments. Lorell *et al* (1956) show through numerical calculation of the effect of single-step kinetics that for justifiable constants the effects of kinetics are small. It can therefore be concluded that the explanation for the above stated discrepancies must be in either the *nonsteady nature or variable properties*.

The analysis carried out by Raghunandan & Mukunda (1977) showed that the transient effects of drop-heating get completed in 20–25% of the burn time. Coupled transient heating and gas phase behaviour have confirmed that steady state results are recovered after this period of time. The variable property effects were investigated in some detail. The conservation equations were non-dimensionalised and transformed by

$$\eta = \exp \int (\dot{m}c_p)/(4\pi r^2 k) dr. \quad (4)$$

It is worth noting that the original equations are written in r and later transformed into η . The solutions are set out in terms of η and then, the reverse transformation,

$$1/r = (4\pi)/\dot{m} J(\eta). \quad (5)$$

$$J(\eta) = \int_{\eta}^1 (k/c_p) (d\eta/\eta),$$

was used to obtain (d_f/d_s) as

$$(d_f/d_s) = J(\eta_s)/J(\eta_f), \quad (6)$$

$$K_c = (\delta/\rho_c) J(\eta_s), \quad (7)$$

$$\begin{aligned} T_f = [T_\infty/I_2(1) + T_s/I_1(\eta_f) \exp P(\eta_s, \eta_f) + \\ + (a_1 h_{1f} + a_2 h_{2f} + a_3 h_{3f})/(\eta_f a_1)] \div \\ \div \{1/I_2(1) + [1/I_1(\eta_f)] \exp P(\eta_s, \eta_f)\}, \end{aligned} \quad (8)$$

where,

$$I_1(\eta) = \int_{\eta_s}^{\eta} \{(1/c_p) \exp [P(\eta_s, \eta)]\} d\eta,$$

$$I_2(\eta) = \int_{\eta_f}^{\eta} \{(1/c_p) \exp [P(\eta_f, \eta)]\} d\eta,$$

$$P(\eta_1, \eta_2) = - \int_{\eta_1}^{\eta_2} \sum_1^4 (c_{pi}/c_p) Le_i (dY_i/d\eta) d\eta.$$

The problem was solved for a single-step fast reaction with four species, fuel, oxidiser, product and inert. For n -heptane class of compounds, the products are CO_2 and H_2O . N_2 forms the inert. The species mass fractions in the product which is otherwise treated as a single species is assigned to the various product species in terms of stoichiometric mass proportions. The solution provides the distribution of mass fractions of various species and temperature. The transport properties are calculated with exact relations for these from Svehla (1962). The variation of properties is shown in figure 1. One can notice that (k/c_p) varies from 2×10^{-4} to 10×10^{-4} g/cm·s. Thus one would expect the results of variable properties not to be the same as those of constant properties.

The results of calculation and comparison are presented in table 2. In the case of constant property theory one has to choose a value of k and c_p . A value of $k = 1.2 \times 10^{-4}$ cal/cm·s·K is chosen to make predictions of K realistic. This corresponds to a temperature of 670–700 K for the mixture. This temperature is far below the mean of T_f and T_s . Table 2 also demonstrates that the improvement in the prediction of d_f/d_s is significant when variable c_p and k are employed. The value of $K = 0.72$ mm² agrees well with observations and the predicted flame temperature is the same as the adiabatic flame temperature. The values of d_f/d_s and T_f are still

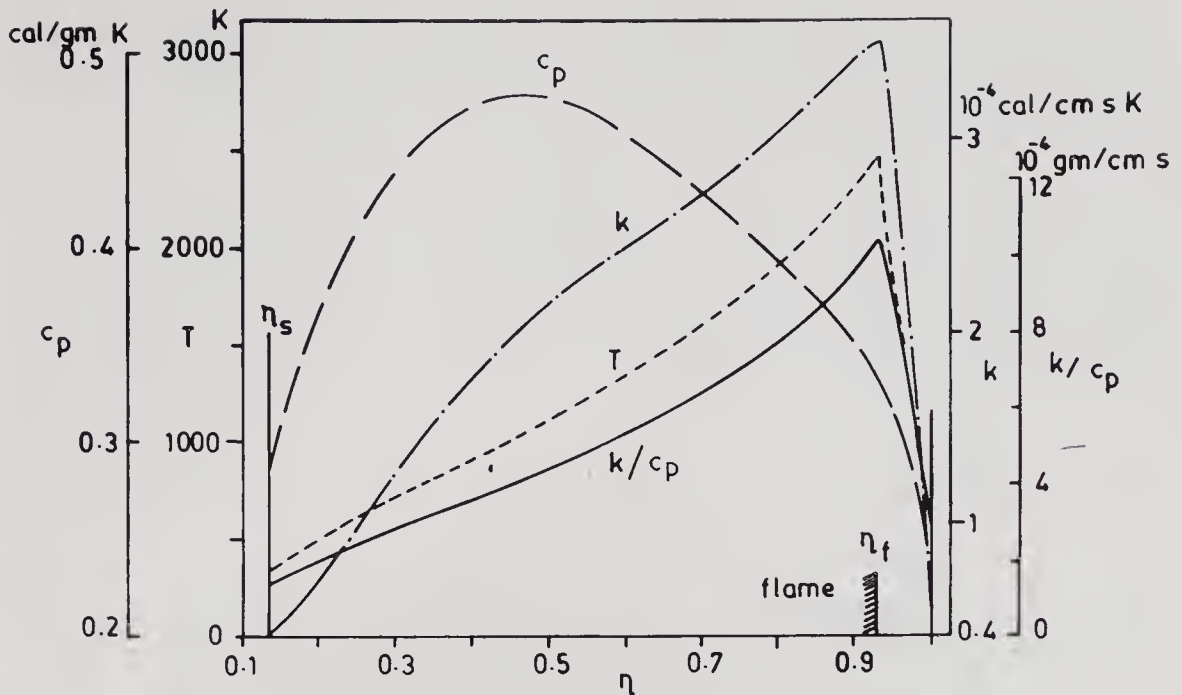


Figure 1. Variations of T , c_p , k & k/c_p with η -variable property analysis.

larger than observed (see table 1) and these are considered to be related to the treatment of finite kinetic calculations. These calculations of a meaningful nature are yet to be carried out. But the important feature is that the use of variable properties essentially entails computing integrals related to these in a rather straightforward manner and leads to improvement in result not related to any additional physical feature.

3. Forced convection turbulent boundary combustion

The physical flow field is simply a flat plate of solid fuel (could be liquid fuel as well) with gaseous oxidant flowing past. On ignition a flame will stabilize inside the boundary layer and fuel regression will take place. The question is to determine the dependence of the steady fuel regression rate on the thermochemical properties of the fuel-oxidant system. This geometry is of importance in hybrid rocket engine operation where oxidant flowing through the circular port of the fuel tube leads to combustion in the fuel-oxidiser interface region. A theory using turbulent boundary layer concepts was set out by Marxman and co-workers (Marxman &

Table 2. Comparison of results from various approximations

	k Constant c_p Constant	k Variable c_p Constant	k Constant c_p Variable	k Variable c_p Variable
$K(\text{mm}^2/\text{s})$	0.7193	1.11	0.543	0.723
d_f/d_s	28.3030	23.87	20.900	15.300
$T_f(\text{K})$	2548.0000	2548.00	2506.000	2506.000

$k = 1.2 \times 10^{-4}$ is chosen; $c_p = 0.304$ is chosen.

Gilbert 1963; Marxman *et al* 1964; Marxman 1965; Marxman & Wooldridge 1968). Invoking Reynolds analogy and using the results of skin friction for zero injection they obtained an expression for regression rate of hybrid fuels as

$$\rho_p \dot{r} = 0.03 \text{Re}_x^{-0.2} G(c_f/c_{f0}) \cdot B. \quad (9)$$

This result delineates the effects of fluid mechanics and chemistry. The effect of fluid mechanics is represented by the factor $\text{Re}_x^{-0.2} G$ and thermochemistry by $B(c_f/c_{f0})$. The ratio c_f/c_{f0} represents the reduction in skin friction or heat transfer due to injection (called the blocking effect). The term was evaluated by Lees (1958) from simple film theory as

$$(c_f/c_{f0}) = [\ln(1+B)]/B. \quad (10)$$

Marxman & Gilbert (1963) used (10) to obtain c_f as

$$c_f = 0.0225 [\ln(1+B)]/B \text{Re}_\delta^{-0.25}, \quad (11)$$

where Re_δ is the Reynolds number based on boundary layer thickness. Equation (11) is substituted in the momentum integral equation, when an expression for c_f/c_{f0} in a log-log plot leads approximately to

$$c_f/c_{f0} = 1.2B^{-0.77}. \quad (12)$$

To check this result Marxman (1965) compared it with the experimental results of Mickley & Davies (1957) and Pappas & Okuno (1960). The comparison between predictions of (12) and the results of the above workers was shown to be satisfactory.

Substitution of (12) into (9) leads to the final result

$$\rho_p \dot{r} = 0.036 G \text{Re}_x^{-0.2} B^{0.23}. \quad (13)$$

It is seen from this equation that $\rho_p \dot{r}$ is relatively insensitive to B due to the low exponent (0.23) on B . This constitutes one of the principal results of the theory stressed by Marxman and co-workers. The above theory was compared with the experimental results of the Plexiglas-oxygen system obtained at ambient pressure in two-dimensional burners and the comparison was claimed to be satisfactory. The estimates of B were made for essentially diffusion-limited combustion in the above comparison. The aspect of diffusion-limitedness does not affect the basic nature of (13) but only alters the value of B which is influenced by the wall oxidiser concentration. Wooldridge *et al* (1969) in an elaborate study, not often referred to in the open literature, have presented extensive and useful data on the regression rate at various pressures obtained for Plexiglas (PMMA)*, polyurethane (PU) and PBAN* in a cylindrical rocket engine. Two of these are presented as fuel weight loss vs. burn time data as shown in the figure 2. The authors claim good comparison between the theory and experimental results at high pressures (about 215–265 psi, 1 psi = 6.895×10^3 Pa). The fuel weight loss at low pressures (~ 45 psi) is substantially less than at 215 psi. It is to be recalled as noted earlier that good comparison between diffusion limited theory and near ambient pressure experiments were reported in Marxman & Gilbert (1963) and Marxman (1965). Thus one is led to the anomalous situation where the same theory for diffusion-limited conditions is said to have compared well with numerically widely different results.

PMMA—polymethylmethacrylonitrile; PBAN—polybutylacrylonitrile.

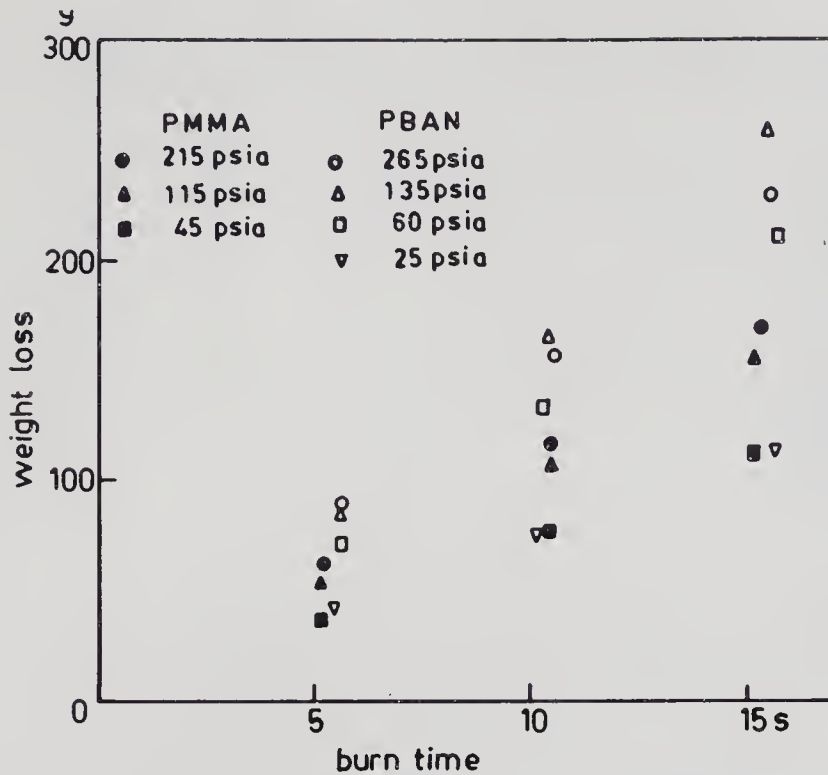


Figure 2. Results of Wooldridge *et al* (1969) on PBAN and PMMA-O₂ systems.

The situation has been carefully analysed by examining the work of Wooldridge *et al* (1969). It appears that the mass flux G used in the theoretical estimate goes up to 1.6 times the mean mass flux. The motivation for the use of increased flux comes from the fact that in the relation for $\rho_p r$ derived from boundary layer analysis, G is the free stream flux, and in an enclosed flow, by analogy the maximum flux rather than the average flux should be used. But it should be pointed out that the maximum flux in a fully developed pipe flow is only about 20% larger than the average flux. The factor used in the computer analysis of the data by Wooldridge *et al* (1969) increases to 60% in a distance of about 5 times the port diameter. This distance is based on the fact that the boundary layer growing on the wall will merge at about five times the port diameter. In actuality, the length for merger of boundary layers depends on the inlet Reynolds number. In view of the above, the claim of good comparison is not indeed justified. To further establish the lacuna of this theory it is worth examining the results of Wooldridge *et al* (1969) summarised in table 3. It can be observed that the predictions from Marxman's theory and the experimental results are widely different. Further, comparison of results for PBAN and PU with nearly identical B and at the same flux indicates a difference in mass regression rate of nearly 18%. Even if it is stated that the estimate of B needs modification to explain this variation in regression rate, the values of B for PBAN-O₂ and PU-O₂ would need to be different by a factor of two. This is too large a factor to be expected.

A further confirmation of the possible influence of B comes from the effect of pressure (figure 2). It is seen that the regression rate decreases by a factor of 0.7 for PMMA-O₂ and 0.5 for PBAN-O₂ when pressure is decreased from 215 to 45 psia and 265 to 25 psia respectively. Since pressure effects have to enter through

Table 3. Weight loss data of Wooldridge *et al* (1969) and theory

Fuel	<i>B</i>	G_{ox} Initial (g/cm ² ·s)	Observed fuel weight loss (g)	Fuel weight loss by Marxman's theory (g)	Molecular weight of gases near wall	Weight loss by present theory (g)
PMMA	9.3	7.03	160	130	90–100	180–190
PBAN	8.0	7.73	260	132	250–350	260–280
PU	8.0	7.73	220	132	150–250	220–250

Experiments with 1" ID, 12" long engine (Diffusion Limited) (1" = 2.54 cm)

kinetics—largely of a gas phase nature in these nonhypergolic systems—their influence should be felt through *B* only. Again one can estimate the variation in *B* needed to account for the reduction of regression rate of these magnitudes. They turn out to be 4.7 and 20. These factors are too large to be realistic. Thus the examination of the work of Marxman and co-workers suggests that the law needs strong corrections particularly with the thermochemical factor.

Further evidence about it can be obtained by examining the relative regression rates of several fuels by two other groups of investigators – Blazowski *et al* (1975) and Julain *et al* (1978). The ordering of the fuels in terms of regression rate with oxygen is shown below.

Blazowski *et al*: Delrin \geq PMMA \geq PP \geq PE \geq PSt

Julain *et al*: PSt \geq PMMA \geq Delrin \geq PP \geq PE

(PP: polypropylene, PSt: polystyrene, PE = polyethylene).

The experiments of Blazowski are in the stagnation point apparatus and that of Julain *et al* (1978) in a two-dimensional flat plate burner. But the nature of the apparatus should not matter since the thermochemical influence is similar in both cases. The point to be noticed in the above ordering is that even qualitatively, fuels are classed differently by different workers. The mass regression rate ratio between extreme fuels is 1.6 and 2 for the two sets of workers respectively. It appears from these that even though fuels with the same name have been used by different workers, they would be chemically different because of antioxidants or additives which could affect regression.

Thus there is enough of a case made to state that the fuel does matter as far as regression rates are concerned and Marxman's theory is inadequate in describing this. After careful consideration of various aspects, Paul *et al* (1982) reasoned that the effect of wall injection on heat transfer (or skin friction) as evaluated in Marxman's theory does not include variation of density and other properties through the boundary layer. The theoretical considerations essentially set out to handle this led to

$$(c_f/c_{f0})^{1/2} = \int_0^1 \{(\rho/\rho_\infty) (1/1 + B\zeta)\}^{1/2} d\zeta. \quad (14)$$

Using the similarity between momentum and mass transfer, the expression for density ratio was put down as

$$\rho/\rho_\infty = \{1 - [B\rho_{\infty i}/(1+B)](u/u_\infty) + (1+B\rho_{\infty i})/(1+B)\}^{-1}, \quad (15)$$

where $\rho_{\infty i}$ is the ratio of density of the free stream to that of injected species. Introducing (15) into (14) gives

$$(c_f/c_{f0})^{1/2} = 2\{(1+B)/B^2(1-\rho_{\infty i})\}^{1/2} \times \\ \times \ln\{(1+B)^{1/2}[1+(1-\rho_{\infty i})^{1/2}]/[(1+B\rho_i)^{1/2}+(1-\rho_{\infty i})^{1/2}]\} \quad (16)$$

The predictions from this expression were checked with the experimental results of Romanenko & Kharchenko (1963) on the injection of CO_2 and Freon into air and found to be in excellent agreement (Paul *et al* 1982). The theory was then modified to include combustion and this leads to

$$\rho_p \dot{r} = 0.056 G^{0.8} (x/\mu)^{-0.2} (\rho_f/\rho_\infty)^{0.71} (\rho_w/\rho_\infty)^{0.14} \times \\ \times B(1+B)^{-[0.73-0.002(\rho_w/\rho_\infty)]}. \quad (17)$$

This result shows that the dependence of \dot{r} on B is stronger than is given by Marxman's expression. It is also stronger than is simply apparent in (17) because (ρ_w/ρ_∞) depends on B as well. A comparison of the predictions from the present theory and the experimental results are shown in table 3 and figure 3. As can be seen from both these, the success of the present theory is glaringly evident. Thus, it

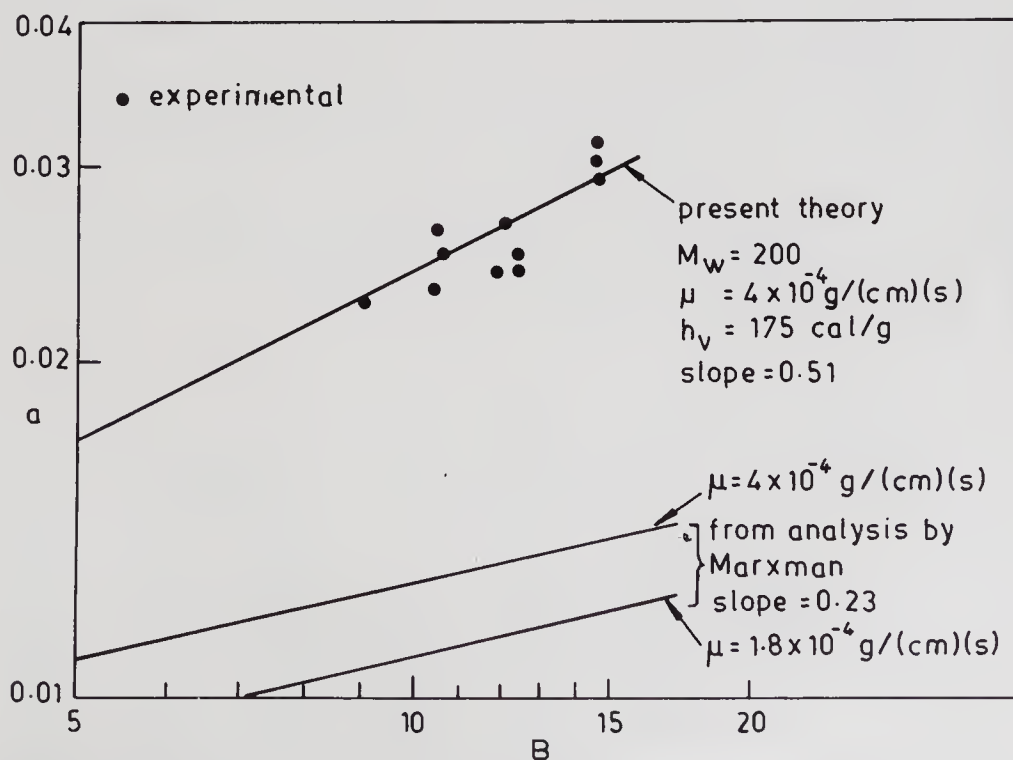


Figure 3. Results of a versus B from present experiments and theory as well as Marxman's theory.

is correct to summarize that the fuel exhibits a strong influence on the combustion rate and this feature is predicted by the theory which includes variable thermochemical properties.

4. Free convective combustion

A vertical flat fuel plate burning in a 1-g environment constitutes the free convective combustion situation. The evaluation of regression rate dependence on thermochemical properties is the central problem here. This subject has been treated by several workers. Kosdon *et al* (1969) solved the conservation equations for burning of vertical plates using similarity hypothesis. The predictions have been compared with experimental results on vertical cellulosic cylinders. While the flame stand-off is shown to behave qualitatively the same way ($y_f \sim x^{1/4}$) in both cases, quantitative comparison has called for adjustment of wall mixture properties suitably. The experimental stand-off behaves as

$$y_f \approx 0.0085 x^{1/4} \quad (x, y_f \text{ in m}),$$

and constant property theory gives

$$y_f \approx 0.0135 x^{1/4} \quad (x, y_f \text{ in m}).$$

The correct prediction of mass burn rate calls for the use of 700 cal/g for the effective heat of vaporisation (L) and this is asserted by them to be reasonable for α -cellulose. Consistent adjustment of transport properties to yield better comparison of flame stand-off will in turn affect the mass burn rate and in fact it is not possible to meaningfully choose any set of parameters which permit simultaneous correct prediction of mass burn rate and flame stand-off within the frame work of constant property analysis.

Subsequently, Kim *et al* (1971) formulated the problem in a similar manner and carried through the solutions as a function of various parameters by treating Lewis number, $\rho\mu$ and ρk as constants in the field. They also developed an expression for mass burn rate using a profile technique. By far this development has been accepted in the combustion literature. They also obtained similarity solutions for various cases and compared their results with experiments. Table 4 summarizes the comparisons drawn from Kim *et al* (1971).

Table 4. Comparison of results of earlier theories and experiments

Fuel \rightarrow	Benzene		Toluene		Methanol	
	Gr'	A	Gr'	A	Gr'	A
Experiment	4.8×10^8	167	8.5×10^8	150	10^8	100
Theory	4.8×10^8	244	8.5×10^8	271	10^8	120
Variation (%)	—	46	—	80	—	20

$$Gr' = g_0 \rho_w^2 x^3 / \mu_w^2; \quad A(x) = \left(1/\mu_w\right) \int_0^x \dot{m}'' dz.$$

As can be noticed, the predictions are different from theory by 45–80% in the case of benzene and toluene. In the case of methanol, the comparison is about satisfactory with a deviation of about 20%. In the case of PMMA-O₂ and α -cellulose-air, the theoretical predictions are coupled with experiments to determine the parameters B and L and to assess if these are reasonable. In the case of PMMA-O₂, B and L are obtained as 4.2 and 714.5 cal/g. In performing these calculations the authors (Kim *et al*) use a fuel surface temperature of 325°C and viscosity at wall equal to that of nitrogen at 395°C. This arbitrary choice of values is hard to justify. The parameters B and L from the literature (Krishnamurthy & Williams 1972) for Plexiglas are about 8 and 325 cal/g respectively. Thus the estimates of Kim *et al* (1971) are in substantial error. Stated differently, the predictions of burn rates for Plexiglas from its known properties would be in significant error [by a factor $\ln(1+8)/\ln(1+4.18) = 1.34$].

Kim *et al* (1971) argue that their markedly higher burn rate predictions for heavy fuels like benzene and toluene are related to low Lewis numbers in the fuel rich region. In the discussion of this point in the paper there are several statements which do not help resolution of the causes for the discrepancy. Thus, the two principal features of the experiments, namely the mass burn rate and flame stand-off, are inadequately explained by the current theories. Consequently, a theory based on free convection under diffusion limited conditions with thin flame approximation was evolved (Hegde *et al* 1986). A single-step reaction with possibility of four to five species (like in the earlier case of droplet combustion) was assumed. The governing partial differential equations were treated by similarly retaining the variation in thermodynamic and transport properties. The resulting differential equations are ordinary and of the ninth order. The boundary conditions are set out at the surface of the plate, at the thin flame location and at infinity. The three-point boundary value problem was solved by the quasilinearisation method. A comparison between the present theory, earlier theory and experiments is shown in table 5. It is noticed that the maximum error in the prediction of burn rate is about 15% and in most cases it is lower. The variable property theory predicts

Table 5. Comparison of results with experiments

Fuel	B	Constant properties		Variable properties		Experiment	% Error
		$y_f/x^{1/4}$ ($\times 10^3$)	\dot{m}_{av}'' ($\times 10^3$)	$y_f/x^{1/4}$ ($\times 10^3$)	\dot{m}_{av}'' ($\times 10^3$)	\dot{m}_{av}'' ($\times 10^3$)	Theory-experiment/experiment ($\times 100$)
Methanol	2.57	14.4	13.1	12.0	13.0	15.0	-13.3
Ethanol	2.73	16.9	15.3	12.1	13.0	15.0	-9.3
Acetone	4.61	18.7	20.2	12.8	15.6	15.9	-2.0
Benzene	5.58	21.4	24.4	13.9	16.7	16.5	1.2
Toluene	5.38	21.6	24.5	13.4	16.4	15.7	4.5
Xylene	5.10	21.7	23.5	13.6	15.4	14.3	7.7
Kerosene	3.15	21.2	20.1	11.6	14.1	16.5	-14.5
Cellulose	1.08	13.5	9.4	8.2	8.0	7.5	6.6
PMMA	1.69	15.6	12.1	10.2	11.2	10.4	7.9
PMMA-O ₂	7.79	20.1	29.0	10.3	23.1	24.0	3.8

Units for $y_f/x^{1/4}$, $m^{3/4}$, \dot{m}_{av}'' are kg/m²s. Oxidant in all cases is air (except the last one).

much lower stand-off distance compared to the constant property theory. The flame stand-off distance obtained experimentally is $Y_f/x^{1/4} = 0.0085 \text{ m}^{3/4}$ and the variable property theory gives $Y_f/x^{1/4} = 0.0082 \text{ m}^{3/4}$. The improvement in prediction from the constant property theory can be seen to be dramatic. The good comparison of both burn rate and flame stand-off is due not to a single factor like Lewis number, but the complete treatment of variable properties.

5. Concluding remarks

This paper started with the assertion that it would demonstrate that accounting for variable properties does more than just improve the comparison between theory and experimental observations over the theories using constant properties, and would make the qualitative character of the predictions physically meaningful.

The example of forced convection turbulent boundary layer analysis demonstrates this. The conclusion arrived at by the simple constant property theory that the regression rate of the fuel is nearly independent of the thermochemical features of the fuel for a fixed oxidant is shown to be incorrect. Experiments show significant dependence on fuel characteristics and the variable property theory demonstrates this. Incidentally, a correlation for the regression rate as a function of various parameters has been established. The cases of droplet combustion as well as free convective plate combustion are those in which dramatic improvements in the quality of comparisons between theoretical and experimental results are seen. The flame to droplet radius ratio and flame stand-off distance are predicted quite accurately with no assumptions on free parameters. The burn rate also is better predicted by the variable property theory.

Dr B N Raghunandan, Dr P J Paul & Mr M Hegde have contributed to the understanding seen in this paper.

References

- Aldred J W, Williams A 1966 *Combust. Flame* 10: 396–397
- Blazowski W S, McAlevy R F III, Cole R B 1975 An investigation of the combustion characteristics of some polymers using the diffusion flame technique, Stevens Inst. Technol., Tech. Report MERT 71004
- Hegde M, Paul P J, Mukunda H S 1986 *Twentyfirst Symp. (Int.) on Combustion* (Pittsburg: Combustion Inst.)
- Isoda H, Kumagai S 1959 *Seventh Symp. (Int.) on Combustion* (London: Butterworths) pp. 523–531
- Julain P, Most J M, Fusean Y, Sztal B 1978 *Seventeenth Symp. (Int.) on Combustion* (Pittsburg: Combustion Inst.) pp. 1041–1051
- Kim J S, DeRis J, Kroesser W F 1971 *Thirteenth Symp. (Int.) on Combustion* (Pittsburg: Combustion Inst.) pp. 949–961
- Kosdon F J, Williams F A, Buman C 1969 *Twelfth Symp. (Int.) on Combustion* (Pittsburg: Combustion Inst.) pp. 253–264
- Krishnamurthy L, Williams F A 1972 *Fourteenth Symp. (Int.) on Combustion* (Pittsburg: Combustion Inst.) pp. 1151–1164
- Lees L 1958 *Third AGARD Colloquium* (New York: Pergamon)
- Lorell J, Wise H, Carr R E 1956 *J. Chem. Phys.* 25: 325–331

- Marxman G A 1965 *Tenth Symp. (Int.) on Combustion* (Pittsburg: Combustion Inst.) pp. 1337-1349
- Marxman G A, Gilbert M 1963 *Ninth Symp (Int.) on Combustion* (Pittsburg: Combustion Inst.) p. 371
- Marxman G A, Muzzy R J, Wooldridge C E 1964 Heterogeneous combustion. *Prog. Astronaut. Aeronaut.* 15: 485-522
- Marxman G A, Wooldridge C E 1968 Advances in tactical rocket propulsion, *AGARD Conference Proceedings*, vol. 1, p. 421
- Mickley H S, Davis R S 1957 Momentum transfer for flow over flat plate with blowing, NACA TN-4017
- Pappas C C, Okuno A F 1960 *J. Aerosp. Sci.* 27: 321-333
- Paul P J, Mukunda H S, Jain V K 1982 *Nineteenth Symp. (Int.) on Combustion* (Pittsburg: Combustion Inst.) pp. 717-729
- Raghunandan B N, Mukunda H S 1977 *Combust. Flame* 30: 71-83
- Romanenko P N, Kharchenko V N 1963 *Int. J. Heat Mass Transfer* 6: 727-738
- Svehla R A 1962 Estimated viscosities and thermal conductivities of gases at high temperatures, NASA TRR 132
- Wooldridge C E, Kier R J, Marxman G A 1969 Investigation of combustion instability in hybrid rockets, NASA CR-66812
- Wooldridge C E, Muzzy R J 1965 *Tenth Symp. (Int.) on Combustion* (Pittsburg: Combustion Inst.) pp. 1351-1362

Integrated design approach for advanced aerospace vehicles

A P J ABDUL KALAM, B S SARMA and PRAHLADA

Defence Research & Development Laboratory, Kanchanbagh,
Hyderabad 500 258, India

Abstract. Advanced aerospace vehicle design requires special design features that should meet the mission requirements of high payload to weight ratio in the case of space launchers and low radar cross-section for specific missiles/aircraft. The conventional design packages used are discussed in relation to their constraints. An interactive integrated design approach to eliminate the constraints imposed by individual design modules through interface design modules is discussed. Typical examples of such interface design modules are given. Also, a computer network necessary for an interactive integrated design approach interfacing the mainframe with a computer-aided design and drafting system and parallel processing is presented.

Keywords. Integrated design approach; advanced aerospace vehicles; interface design module.

1. Aerospace vehicle system design

Recently, a review revealed that the design effort used for a launch vehicle system is about 300 man-years and for a missile system about 200 man-years. If the design has to be completed in two years' time, at least a 100 designers of various disciplines will have to be provided, and again for design of other similar aerospace systems, a number of designers have to be deployed. As can be seen from figure 1, for a launch vehicle system or missile or aircraft, technical specifications are generated by a team of specialists to meet the mission requirements. This leads to subsystem characteristics with different alternatives. After a detailed review and based on the experience gained, the subsystem options considered are evaluated in the kinematic system model for the performance. Estimation of reliability and cost would also be carried out. This will lead to total system specifications with subsystem configurations. Subsequently, detailed design of subsystems is carried out for aerodynamic configuration, airframe, guidance, control and propulsion. The design packages for these subsystems and previously generated data banks are utilized in arriving at detailed designs.

Once the subsystem hardware is realized and tested, critical design reviews are carried out with available test data. Guidance and control hardware and software

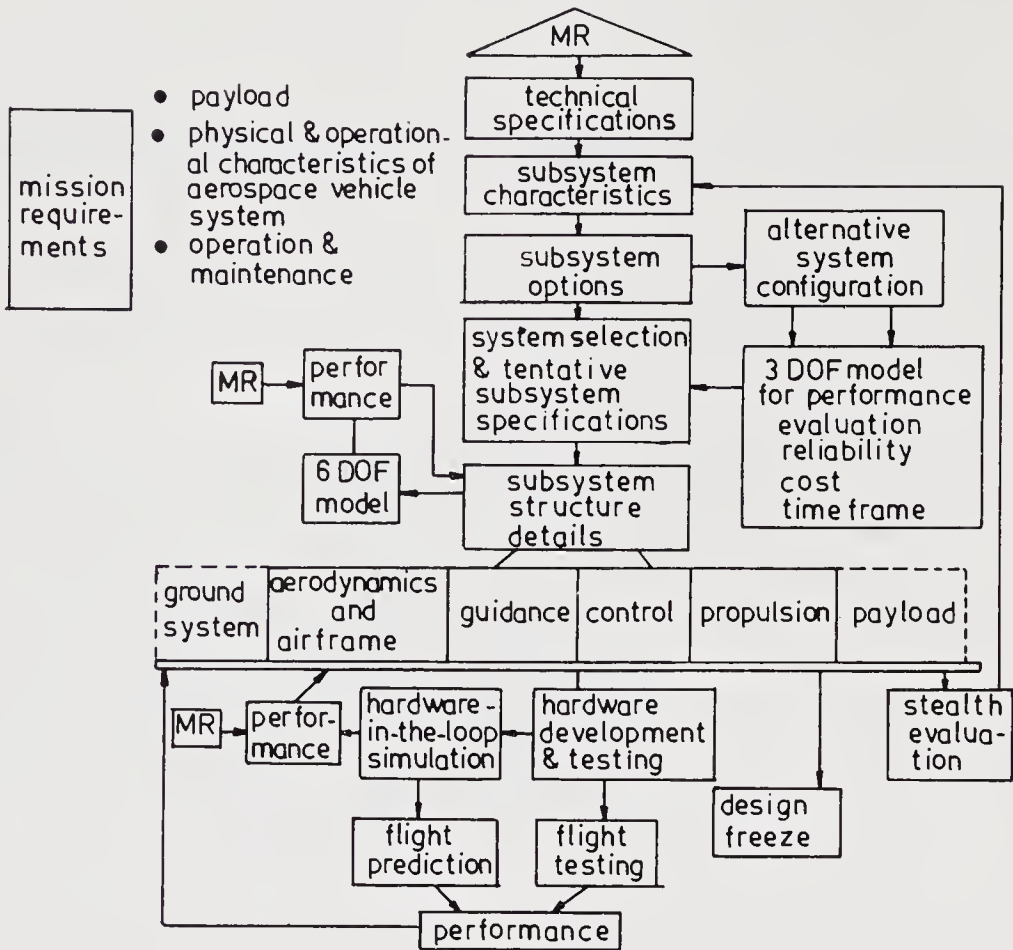


Figure 1. Aerospace vehicle system design – an outline.

like the inertial navigation system, on-board processor and autopilot go through hardware-in-loop simulation (HILS) for detailed performance evaluation. Various subsystems are integrated and checked out through the flight test. The flight test data are again fed back to the designers after post-flight analysis to further improve the designs. This completes the design cycle for which, based on missile and launch vehicle experience, about 200 to 300 man-years are required. How the various subsystem level design packages can be linked and integrated into a total system design package for the aerospace vehicle is the focus of our attention. The number of design man-years used has been high since the design of the subsystems is done through sequential rather than parallel operations. A 6-DOF* trajectory run for evaluation of a typical system having subsystem modules numbering about 200 takes about an hour of computer time on a third generation computer system. To reach a final design with failure module analysis incorporated, it may be essential to have 2000 simulated computer runs. Also each design package, e.g. aerodynamic design, starts with certain constraints followed by the subsequent design, like structural design. Hence these constraints are not seen together in a sequential design process. It is essential that these system constraints are seen in totality so that unrealistic constraints can be removed during the integrated design process.

* DOF – degrees of freedom.

2. Interface design modules

Based on the design efforts carried out, the three typical design packages or modules given below are considered for interfacing conventional design modules:

- i) aero-propulsion interaction for a ramjet;
- ii) structure-control interaction of a typical aerospace vehicle;
- iii) integrated electrical-structural design.

These examples focus on the subsystem level interactions to be taken care of in the integrated design approach.

2.1. Aero-propulsion interaction for a ramjet

The integrated design of an aero-propulsion system like a ramjet needs multi-design packages such as vehicle body flow field analysis, air-intake internal flow field analysis, analysis of interaction of multiple intakes, combustor flow field analysis and matching of combustor and intake operations.

For high performance axisymmetric intake of the ram rocket system operating upto a Mach number of 3 and angle of attack upto 5° , the typical critical pressure recovery for the intake alone will be of the order of 0.82 at starting, as shown in figure 2a. However, as can be seen from figure 2b, when the fuselage is integrated with the air intakes, the critical pressure recovery for the same Mach number and angle of attack reduces to 0.65 for a cruciform configuration of 4 air-intakes positioned at 45° from the vertical. Figure 2c gives the variation of fuel flow rate with time for matching of the intake to the combustor. In such a system, where the propulsion performance is matched with aerodynamic pressure recovery, the specific impulse obtained from figure 2d for the integrated ram rocket system with a pressure recovery of 0.6 is about 580 s. The specific impulse is therefore twice that of the conventional rocket propulsion system. The above example suggests how the propulsion, aerodynamic and combustion phenomena are all interlinked, and hence, the need for the designer to have an insight into the mechanism of the three subsystems.

2.2 Structure-control interaction of typical aerospace vehicle

Many of the guided and controlled aerospace vehicles have to be designed for flexibility of the airframe due to flight loads, engine deflections etc. In the case of aerospace vehicles, even though the vehicle is flexible, the control system designers normally use the rigid vehicle approximation to start with, and then by iterative process, consider the effect of vehicle flexibility on control system design after flexibility data of the airframe become available. The bending mode shape for a typical aerospace vehicle is given in figure 3a. For the control system designer, the first input is the type of structural frequency variation with respect to time of flight as shown in figure 3b. The possible design is normally based on 'moderate' joints at intersections. The structural frequency will be of the order of 30 Hz and this needs to be separated from the control frequency by a factor of at least 4 in order to make the compensator design possible. In figure 3c, the control system performance of a rigid vehicle, an uncompensated flexible vehicle and compensated flexible vehicle are shown. It is seen that if the vehicle is flexible, the control system gain margin is reduced. If the flexibility effects are not addressed during the design of the control

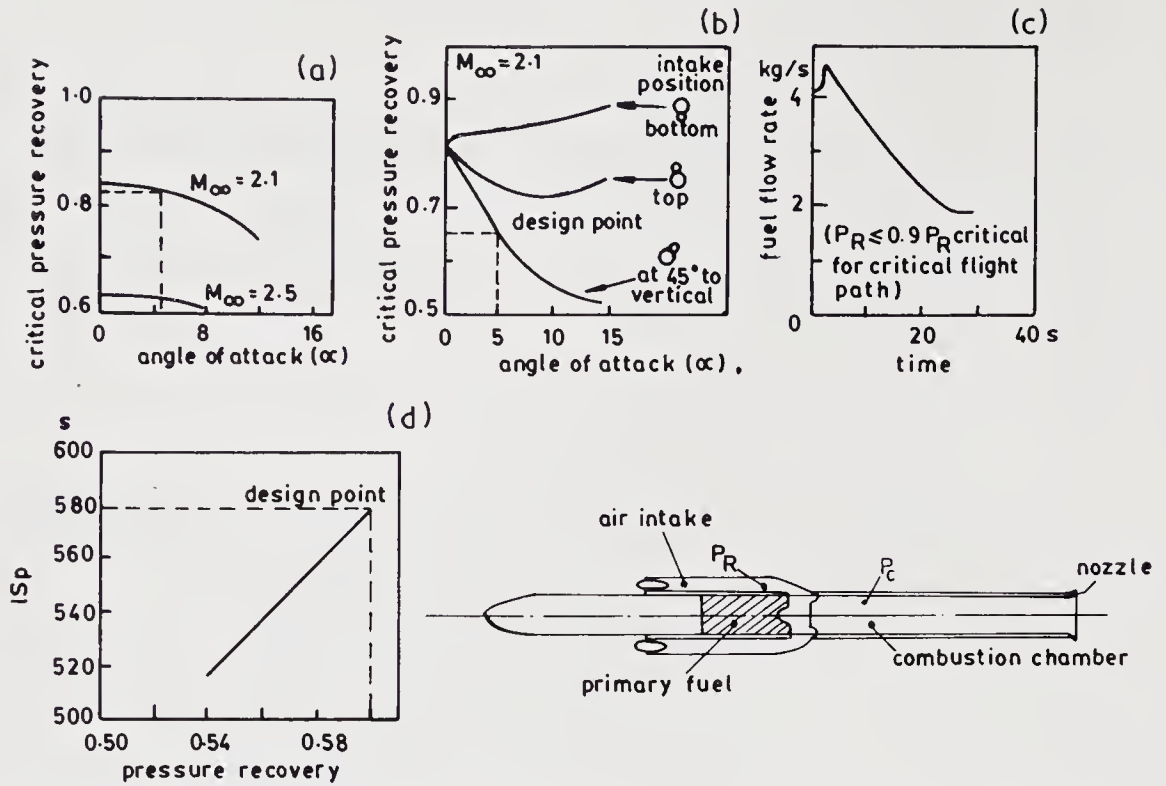


Figure 2. Aero-propulsion interaction for a ramjet. The interface packages required are (i) vehicle body flow field analysis; (ii) air-intake internal flow field analysis; (iii) analysis of interaction of multiple intakes; (iv) combustor flow field analysis; (v) matching of combustor and intake operation. (a) Stand-alone performance of axisymmetric intake. (b) Installed performance of axisymmetric intake. (c) Curve obtained by matching of intake to combustor. (d) Typical ISp vs. intake pressure recovery (intake operation supercritical).

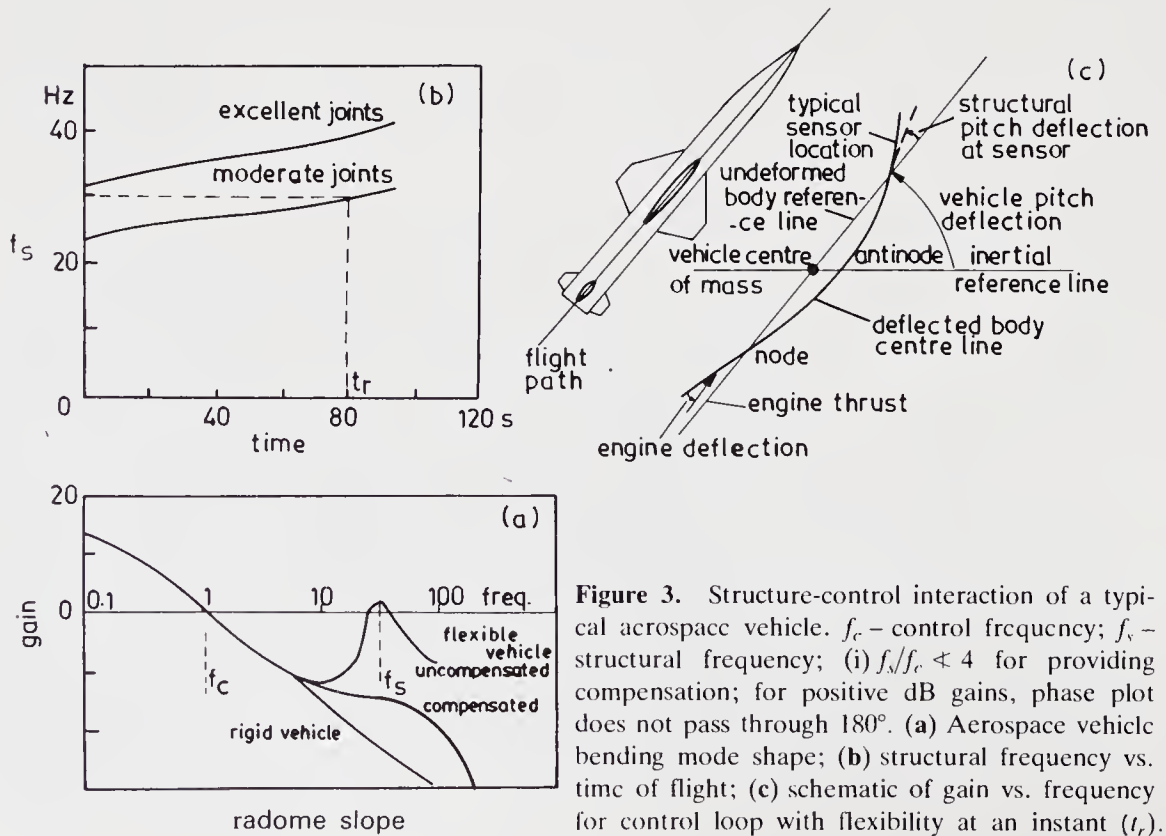


Figure 3. Structure-control interaction of a typical aerospace vehicle. f_c - control frequency; f_s - structural frequency; (i) $f_s/f_c \leq 4$ for providing compensation; for positive dB gains, phase plot does not pass through 180° . (a) Aerospace vehicle bending mode shape; (b) structural frequency vs. time of flight; (c) schematic of gain vs. frequency for control loop with flexibility at an instant (t_r).

system, the response of the control system in flight becomes oscillatory, leading to instability at certain flight conditions along the trajectory. Hence, it is essential to integrate the control system design package and the structural design so that a compensated control system is possible with sufficient gain margins.

2.3 Integrated electrical-structural design

The antenna system of the homing-seeker for a typical missile system is housed in a composite radome. While the radome has to meet the aerodynamic shape and structural requirements, the design of the radome structure is also driven by the acceptable near-field antenna pattern with minimum loss. In order to meet the above requirement, the thickness of the structure is obtained by taking into consideration the dielectric constant and loss tangent of the radome material. The shell thickness, established from the electrical considerations as shown in figure 4 is then analysed for buckling and bending behaviour. The typical shape of the radome is a tangent ogive with L/D ratio of 2.5 to 3 as shown in figure 5a. The designer has many choices for radome material from glass-polyester, glass-epoxy and glass-polyimide to ceramic for various Mach numbers and a temperature range of 100–600°C as shown in figure 5b. The designer can select the glass-epoxy radome or ceramic radome depending upon the loss tangent requirement for electrical design. As can be seen in figures 5c and d, for the glass epoxy, the loss tangent rapidly increases with temperature and the dielectric constant is also high, whereas for the ceramic radome, the rate of increase is much lower. Based on the mission requirement, weight and temperature constraints, a ceramic or a glass epoxy radome has to be selected as indicated in figure 6a. It can be seen from the radiation pattern of the antenna without the radome that the received power is about 20 dB and with the glass-epoxy radome it is about 21 dB. Another most important performance requirement is to minimize the side lobe of the radiation pattern. For a fused silica ceramic radome, the side lobe is lower compared to the glass-epoxy radome. The designers have to translate these factors into electro-mechanical design. This experience needs to be validated and built into the design package.

In the case of guidance, the guidance law has to be chosen suitably to keep the miss-distance to a minimum. For a typical surface-to-air missile, a 5 m miss-distance will result only from a radome slope of 0.07 as shown in figure 6b. For a

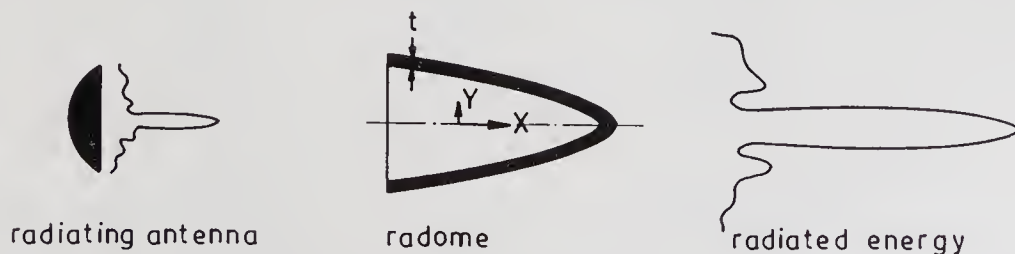


Figure 4. Integrated electrical-structural design. Field – $F_o(X, Y)$; near field – $F(X, Y)$; $T'(\theta)$ – transmission coefficient; Φ' – insertion phase.

$F(X, Y) = F_o(X, Y) |T'(\theta)| \exp(-j\Phi')$, where T' and Φ' are F_n of thickness t , dielectric constant ϵ , Loss tangent $\tan \delta$. The sequence of steps in the operation is (i) obtain t as F_n of X to get an acceptable near field pattern; (ii) check for buckling and bending strengths; (iii) finalise t .

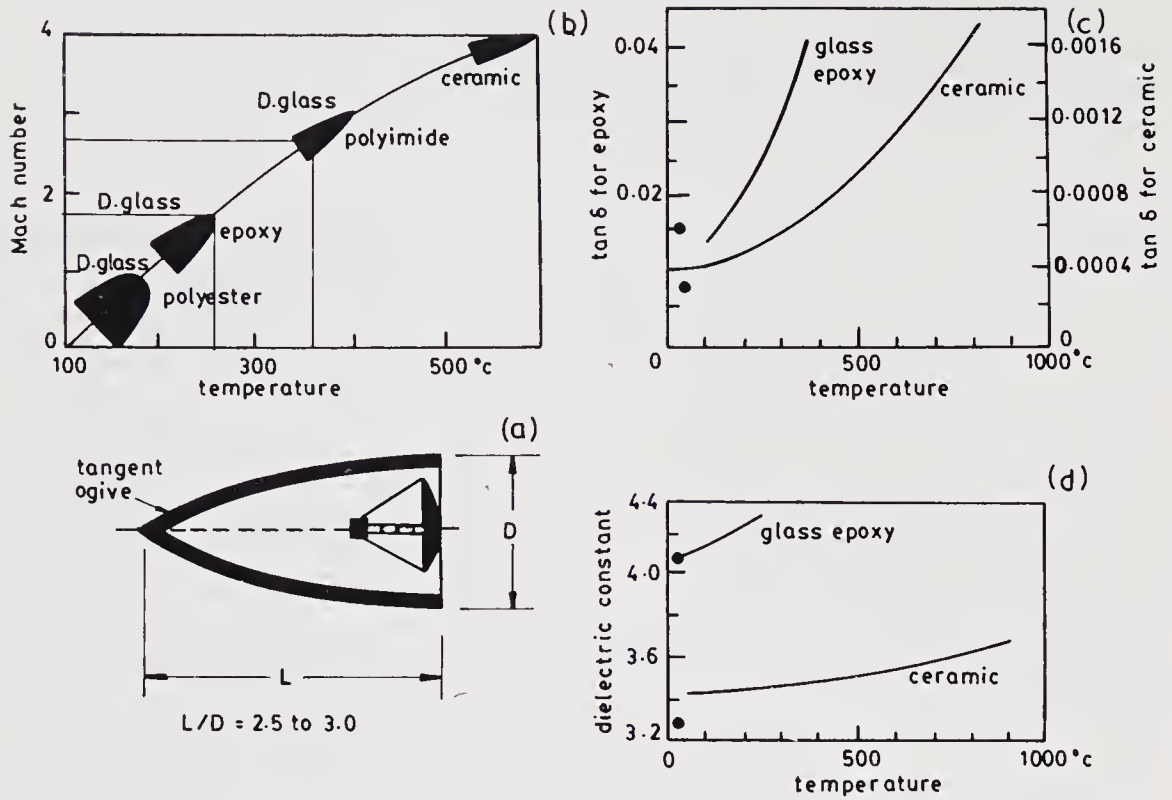


Figure 5. (a) Typical radome geometry; (b) choice of materials for the radome; (c) variation of Loss tangent with temperature; (d) variation of dielectric constant with temperature.

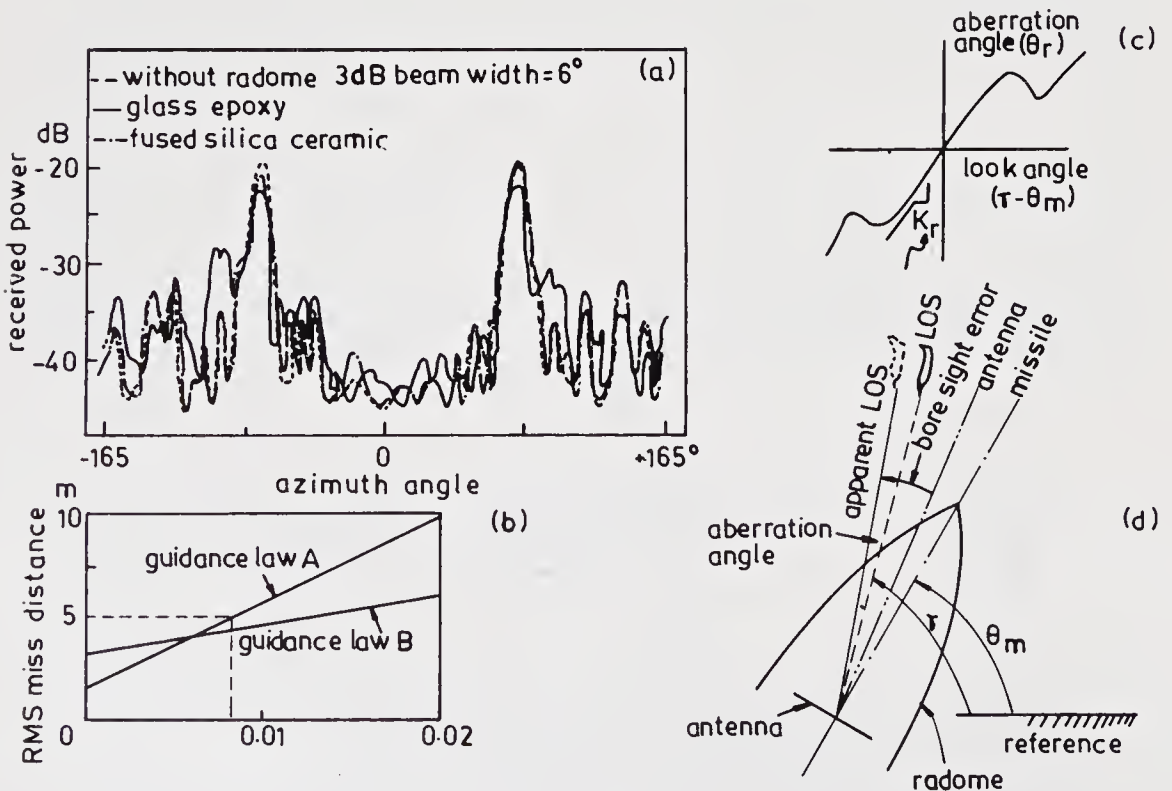


Figure 6. Radome guidance-performance. (a) Radiation patterns of the transmitting antenna with ceramic and epoxy radomes. (b) Effect of radome slope on miss distance. (c) Radome slope. (d) Boresight error and aberration angle.

given radome slope as defined in figures 6c and d, it is essential to get a minimum aberration angle, i.e., the angle between the line of sight (LOS) to the actual and the line of sight to the apparent target positions. To realize this, it is essential that the right choice of radome material, thickness profiling and antenna positioning be made. This is an example of how the electrical design drives the overall missile seeker head design.

3. Aerospace vehicle integrated design

In §2, the interaction of subsystem level design packages has been discussed for three design cases, viz., aero-propulsion, control-structure and electrical-structural design. In an integrated design approach for an advanced aerospace vehicle, 6 individual design modules with the system constraints as inputs along with the required data base have to be built, and as many as 6 interface design modules are to be integrated with the interactive integrated design (core) package in addition to the weight and cost modules. The most important additional links which have to come in are the designers' experience and expertise in design. Can they be converted into realistic algorithms? These need to be in the form of a design database so that individual design software packages can be made to communicate with each other through the interface design modules and the interactive integrated design module. The interactive integrated design module shown in figure 7 removes the constraints normally introduced by individual design modules like aerodynamics, structures, control and guidance systems through interface using major interface design modules. An interactive integrated design approach will

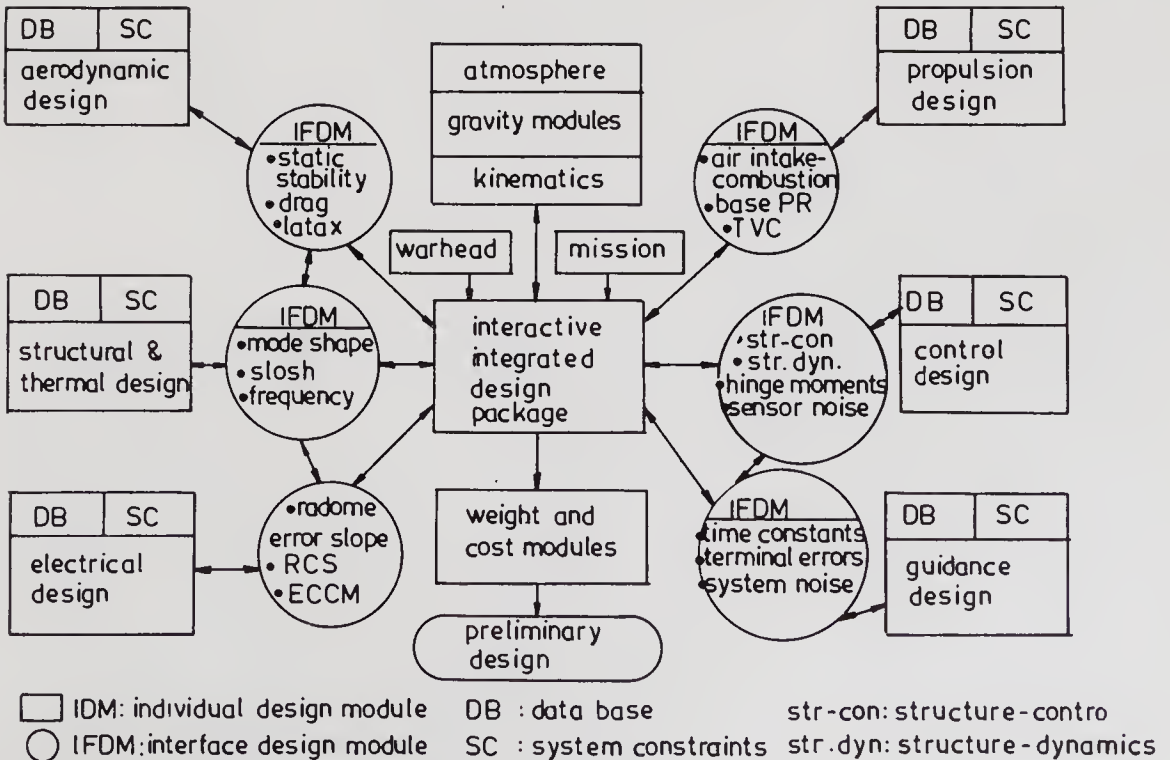


Figure 7. Aerospace vehicle integrated design – an outline.

bring out a reduction of design cycle time to one fifth its value, and at the same time, the design will be built on experience without losing any of it.

The interactive integrated design approach requires an extensive computational effort and sophisticated computer facilities covering the mainframe system, computer-aided design and drafting (CADD) system, parallel processors etc. The computer network for an integrated design approach is presented in figure 8. In this network, the mainframe system will have interactive terminals through a network processor. The kinematics and the interactive design interface modules are housed in this system. The network processor is interfaced with a CADD system with an ethernet for as many as 18 CADD servers. Each CADD server is provided with 4 disk packs of 500 MB storage space each and also with 8 user work-stations. The subsystem designs are generated in the CADD centre which has an interactive graphic display. Parallel processors are also interfaced with the network processor of the mainframe system through a front end processor and they are utilized for major number-crunching operations that are normally required for aerodynamic, combustion and structural analysis. Parallel processing of major individual design modules will help to bring down the computational delay on the mainframe system and also on the CADD system. Communication is also established between the parallel processor and the CADD system through the mainframe system. Such a computer network facility is an essential requirement for an integrated design approach. In the Defence Research and Development Laboratory/Defence Research and Development Organisation the methodology for an interactive integrated design approach has been evolved with a two-year programme for the integrated design package using the above scheme.

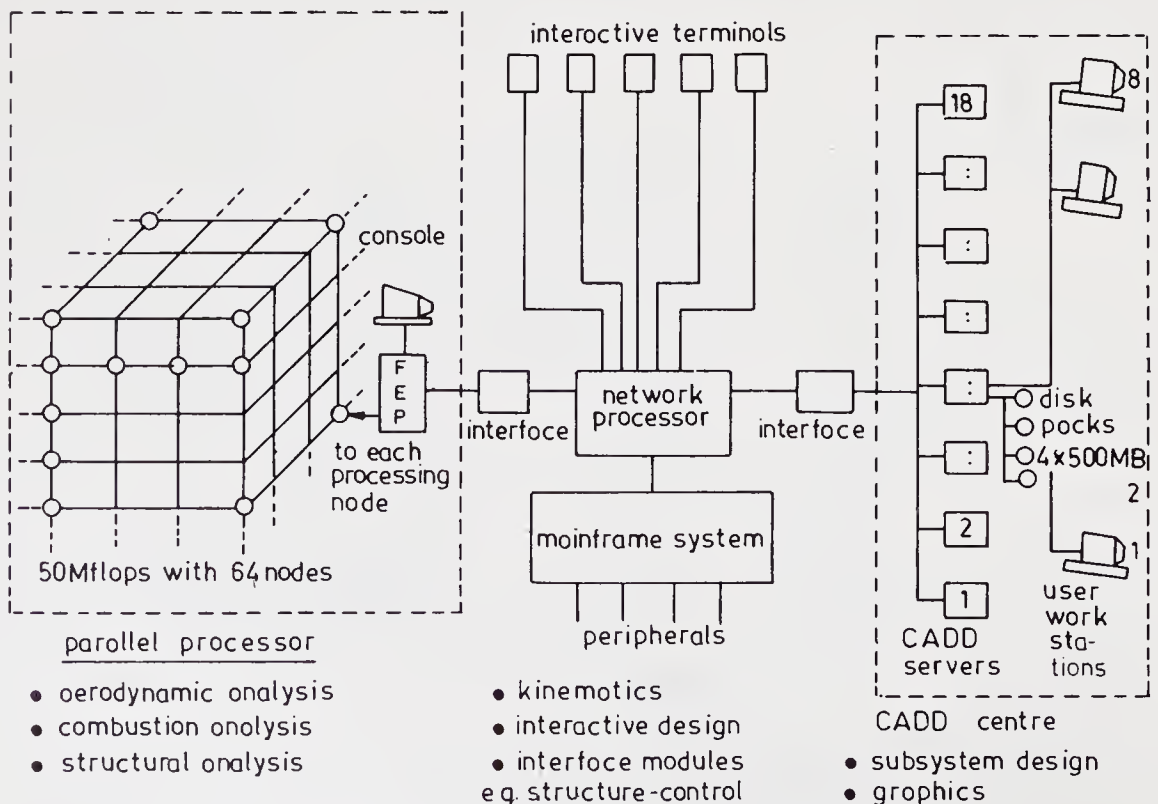


Figure 8. Schematic of a computer network for interactive design.

4. Conclusions

A conventional design approach for the subsystem of an aerospace vehicle results in a long design cycle time because of sequential and iterative design steps. Also, existing methods introduce constraints into the designs. Three examples project the need for an integrated design approach where interfacing of more than one subsystem is involved. An interactive integrated design approach is configured along with a computer network involving the available CADD Centre and mainframe system, and a proposed parallel processor computer.

This note has been prepared based on detailed discussions with designers in various areas of technology. We are particularly thankful to Dr Annapurna, Shri N R Iyer, Dr Subhash Chandran, Dr J Gowri Krishna, Dr K Neelakantan, Shri N V Kadam and Shri A Sivathanu Pillai for their assistance.

Development of solid propellant technology in India

M R KURUP, V N KRISHNAMOORTHY and M C UTTAM

Indian Space Research Organisation, Department of Space, SHAR Centre, Sriharikota 524 124, India

Abstract. Space research in India started in 1961 when a two-stage rocket was launched from Thumba on 21 November 1963. On the sudden passing away of Dr. Vikram Sarabhai, the originator of the Indian space programme, Prof. Satish Dhawan became the second chairman of ISRO. His stewardship saw it through its teething troubles on to launching of several R & D tasks and growth of several ISRO Centres. Major breakthrough in many hightech areas took place during this period. High energy composite solid propellants were developed, characterized and produced at the Vikram Sarabhai Space Centre and at the Sriharikota Centre. Exotic fuel binders such as HEF-20, Polyol and HTPB for these propellants were also developed in ISRO as part of the indigenisation programme. The Satellite Launch Vehicle-3 (SLV-3) conceived in the early seventies, was fitted with four stage motors filled with solid propellants made in ISRO's own plants. These facilities, including critical process equipment, have come up as a result of ISRO's indigenization efforts. The SHAR Plant known as SPROB has been further augmented to produce large propellant grains to meet the needs of the Polar Satellite Launch Vehicle (PSLV).

Keywords Solid propellant; HTPB-based propellant; rocket motor; propellant binder.

India took her first step into the space age in 1961, when the Government of India entrusted the study of the subject of space research and peaceful applications of outer space to the Department of Atomic Energy (DAE). Next year, DAE set up the Indian National Committee on Space Research (INCOSPAR) to organise the space programme. On 21 November 1963 a 2-stage Nike-Apache rocket was successfully launched from Thumba and the Thumba Equatorial Rocket Launching Station (TERLS) became operational, thereby heralding the dawn of the Indian Space Programme. The Indian Space Research Organisation (ISRO) came into being in 1969. In 1972 the Government of India set up the Space Commission and created the Department of Space with ISRO under its purview.

Dr. Vikram A Sarabhai, the visionary who was the originator of the Indian space programme passed away suddenly in 1971. Prof. Satish Dhawan, who was then Director IISc, became the second chairman of ISRO. His stewardship of the space programme from 1972 to 1984, saw it through its teething troubles on to launching of a wide variety of R & D tasks, growth of four ISRO centres, success of satellite and launch vehicle projects and finalization of a profile for the decade of the 1980s. Major breakthroughs in several high technology areas took place during this period. We will describe below the success achieved in the area of solid propellants.

With the acquisition of a limited technology transfer arrangement with France for sounding rockets, ISRO had started manufacturing composite propellants based on PVC resin from 1968 onwards. However, the 'Why' and 'How' had to be understood and more energetic propellants for satellite launch vehicles had to be developed. The Propellant Engineering Division (PED) and an R & D section in the Rocket Propellant Plant (RPP) were assigned the responsibilities.

Composite propellants contain a crystalline oxidiser, a polymeric fuel binder in a liquid state, a metallic fuel and a curative as the main ingredients. There are a number of minor additives to impart specific properties to the cured propellant. Ammonium perchlorate is the universally accepted oxidiser. Atomised aluminium powder is the metallic fuel generally employed. Polyurethane- and polybutadiene-based binder systems are the common ones used for a long time, but there are variants of each of these two systems: e.g., CTPB, PBAN and HTPB. These binders are not easily available and it became essential to develop them. ISRO's R & D efforts in this direction resulted in the development of high energy binders like Polyol and HEF-20. Later on for larger motors the choice fell on HTPB. This too has been successfully developed and know-how transferred to industries for large scale production.

As is usual a thorough literature survey preceded our efforts in the development of solid composite propellants. Since the field is a highly guarded one we had to analyse the published material carefully and accept them with caution. Ternary diagrams were drawn and computer programmes developed to arrive at theoretical compositions. With the large number of variables in materials and percentage compositions, adopting the above procedure helped in reducing the number for experimentation to a manageable level. The so-called test tube level trials then followed. During this phase some of the formulations had to be rejected based on processing problems, and safety considerations. The shortlisted compositions were then tried out in kg-levels in mixers having the same geometry as in industrial scale operations. Control parameters initially fixed were monitored. The slurry characteristics, viscosity build-up, curing pattern and mechanical properties were determined from propellants cast in cartons. Measurement of the ballistic properties was done in small motors which gave a good idea of the energetics of the system. This was followed by thorough characterization of the final propellant, for its rheological, mechanical, thermal and ageing properties, its performance, and the associated hazards.

The mechanical properties and failure behaviour of HTPB-based propellants have been studied in detail at ISRO. Figure 1 shows the uniaxial failure boundary plotted for one of our propellant systems currently in use. Here the maximum value of the strain at maximum stress (E_m) is found to be 45%. The limiting value of the strain

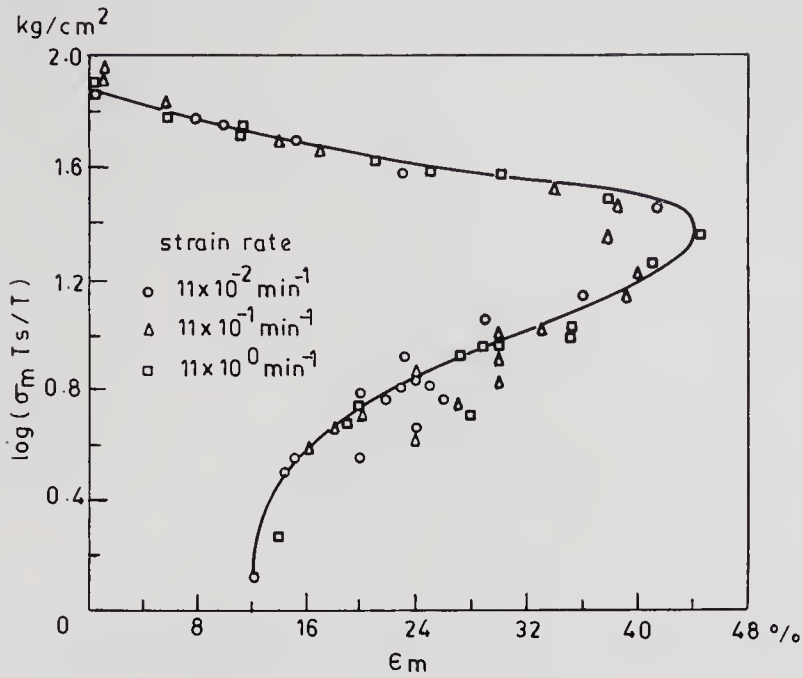


Figure 1. Uniaxial failure boundary.

beyond which the propellant will eventually fail either in relaxation or in creep is found to be 12%. Figure 2 is a master stress-relaxation modulus curve reduced to -15°C for the same propellant. Relaxation modulus values are deduced from the slope of the master stress-strain curve. The glassy modulus of propellant at very high strain rate or at very low temperature (E_g) and the equilibrium modulus of propellant at very low strain rate or very high temperature (E_e) can be found by extrapolation to very low and very large time scales, respectively. Variation of yield stress with temperature and time is shown in figure 3. As time elapses, the temperature at which the yield stress is minimum shifts to lower values. For example at 4 hours of time, 50°C is the temperature of minimum yield stress for this

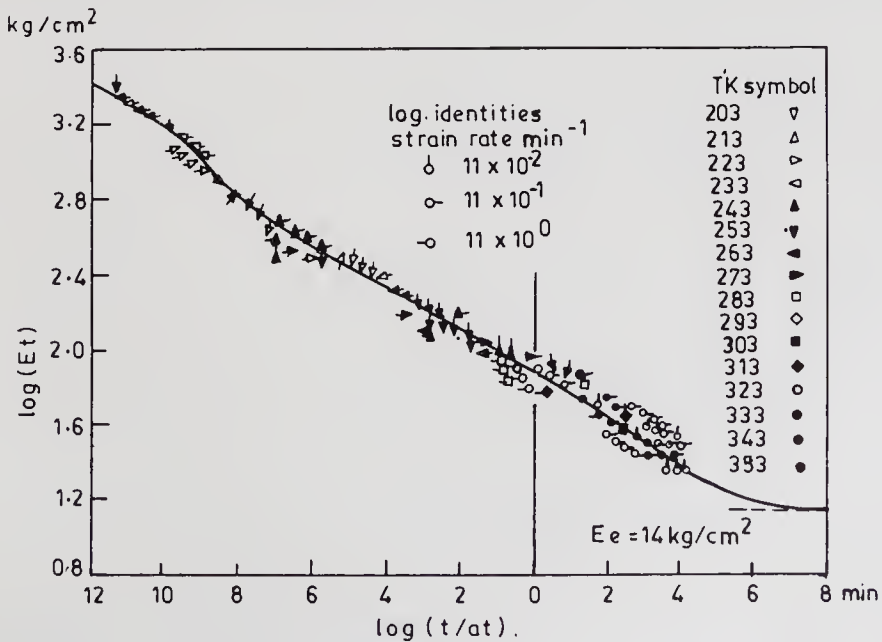


Figure 2. Master stress-relaxation modulus curve reduced to -15°C .

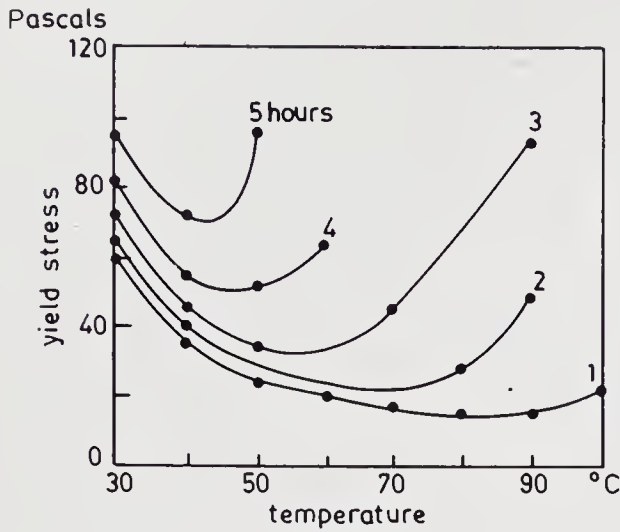


Figure 3. Variation of yield stress with temperature.

propellant. Similar is the case with the consistency index k , which is one of the parameters for describing the rheological property of slurry, plotted in figure 4. A minimum value of k is shown at a particular temperature which shifts to lower values with lapse of time. Auto ignition, spark, friction tests etc., characterize the propellant from the hazard angle. Ultimately the composition chosen must be feasible for industrial production with available equipment and known methods without causing extreme hazards to property and human life. Since most ISRO rocket motors are of the case-bonded type (i.e. the propellant is cast inside an insulated and lined rocket chamber and during curing the grain sticks to the wall), the thermal properties are also to be ascertained and process conditions suitably adjusted to ensure defect-free grains. Coefficient of linear expansion, thermal

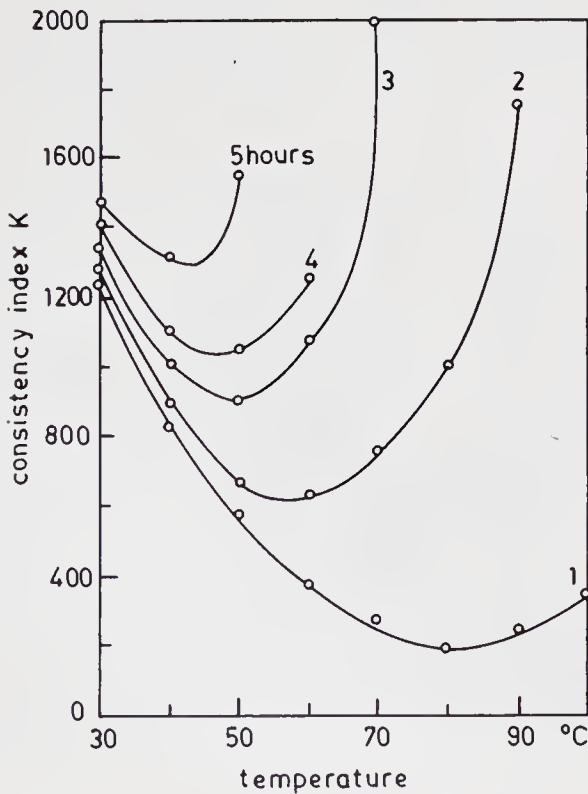


Figure 4. Variation of consistency with temperature.

Table 1. Dimensions and other parameters of the 4 stage motors of the SLV-3 configuration.

Parameter	Stage 1	Stage 2	Stage 3	Stage 4
Diameter (mm)	1000	800	800	650
Length (mm)	8700	4850	1620	860
Rocket case material	15 CDV6	15 CDV6	FRP	FRP
Propellant binder	PBAN	PBAN	HEF-20	HEF-20
Specific impulse (s)	254	268	278	284
Propellant weight (kg)	8600	3200	1080	320

conductivity/diffusivity, specific heat, and glass transition temperature are determined experimentally. Static tests with adequate instrumentation confirm the ballistic performance of the formulations.

It was decided in the early seventies that a satellite launch capability, though on a modest scale, must be acquired by ISRO. Looking at the existing technologies and also the immediate prospects of developing new technologies, it was very clear that the propulsion units will have to be solid motor based. The SLV-3 configuration with 4 stages of solid motors was thus born. The dimensions and other important parameters of these stage motors are given in table 1.

For those of us engaged in development of solid propellants this decision was a morale booster. We set about designing equipment and facilities both at RPP and a new and much bigger plant at SHAR. Both these facilities were realised in time for the SLV-3 programme and except for less than 15% of high tech equipment the entire scheme was conceived and implemented by ISRO engineers and scientists. The SHAR plant known as SPROB has been further augmented for PSLV demands and we have today the capability to produce single grains measuring 3 m in diameter and capable of carrying 25–30 tonnes of propellant. It compares well with similar facilities anywhere in the world. In terms of propellant properties such as specific impulse, burn rate, density and mechanical properties also ISRO is very close to the frontiers.

The 'deadly parallel'* approach promoted by Prof. Dhawan in the case of propellant R & D paid rich dividends and as a result we are today very close to the best in the world in this strategic item. His policies encouraged us to diversify, especially on the raw materials and in the indigenization of critical equipments. Engineering a production unit at Alwaye for ammonium perchlorate, building a Propellant Fuel Complex at Thumba, indigenizing equipment like perchlorate grinder and vertical mixer and development of a 4 MeV Linear Accelerator with assistance from the Tata Institute of Fundamental Research are some of the important contributions towards self-reliance in Solid Propellant Technology. ISRO

* This is a management term for taking up parallel activities to achieve the same objectives, deliberately initiated in the critical areas for healthy competition and assured outcome.

can today build a solid booster carrying hundreds of tonnes of high energy solid propellant.

The inspiration and guidance for this extraordinary effort have come mainly from Prof. Dhawan, and we are happy to dedicate this paper to him.

Development of navigation guidance and control technology for Indian launch vehicles

S C GUPTA and B N SURESH

Vikram Sarabhai Space Centre (VSSC), Trivandrum 695 022, India

Abstract. The orbital injection accuracy of any payload depends on the calibre of the inertial guidance system used on board the launch vehicle. This paper outlines the mission definition and the rationale for the selection of a proper guidance system to meet final mission objectives. The functions and the architecture of the navigation, guidance and control are discussed. The developmental aspects of the sophisticated inertial sensors, inertial systems, associated complex electronics, on-board computers, control actuators and systems are reported. The complexity of the on-board control and guidance software and the test and evaluation procedures used for their validation are included. The general scheme of the inertial guidance systems and the critical role played by them in the realization of Indian satellite launch vehicles SLV-3, ASLV and PSLV are presented in brief.

Keywords. Inertial guidance; navigation; vehicle flexibility; stabilized platform; strap-down system; control algorithm; hardware-in-loop simulation.

1. Introduction

Higher payload capacity and greater accuracy in orbital injection are the two primary demands on satellite launch vehicles. While the sizing of the multistage propulsion system determines the payload capacity, it is the calibre of the control and guidance system which determines the injection accuracy. Automatic inflight stabilizing of the attitude – angular orientation – of the vehicle and steering its path from launch pad to orbit injection constitute the functions of the control and guidance system. The autopilot carrying out the 3-axis stabilization function is a multivariable, interacting, non-linear feedback control system. It employs high precision angle and angular rate sensors, control function computation electronics, actuator electronics and control thrusters, each component requiring for its realization sophisticated technologies and intensive analytical modelling and simulation processes. The guidance system in its general form is also a multivariable feedback control system. While the autopilot aims at achieving the desired instantaneous values, the guidance system strives to achieve the desired

end-of-flight conditions. The guidance system employs the navigation system as its sensor to detect the instantaneous velocity and position of the vehicle and charts out the remaining path by continuously recalculating the vehicle attitude and main propulsor burn programs. The navigation system is generally based on high precision measurement of acceleration and on high speed, high accuracy computations. In the open-loop guidance case, the vehicle attitude and propulsor burn programs are decided before the flight and no correction to it is done during the flight; this amounts to removal of the feed-back in the guidance loop. As a result the navigation system even if provided in open-loop guided vehicles performs only a monitoring role. Thus navigation, guidance and control are among the most crucial and challenging fields in space engineering and technology.

Proper choice of a guidance system depends on the final mission objectives. The various aspects of the system are to be planned and studied in detail during the initial phase of the design of a launch vehicle. The mission definition in terms of orbit attitude, inclination and permissible dispersion dictates the selection of the suitable on-board guidance system configuration. If the dispersions in the launch vehicle subsystem's parameters are small such that they can still achieve the specified mission with open loop guidance (OLG) then the OLG scheme is chosen. Otherwise closed loop guidance is selected. This selection is based on detailed Monte Carlo simulation by considering various vehicle parameter dispersions.

The specifications of the sensors and subsystems are also to be so chosen as to meet the mission objectives. For example, where the orbital dispersions are large as in the case of open loop guided vehicles, an attitude reference system (ARS) will meet the requirements, whereas in closed loop guided vehicles a full-fledged inertial navigation system is inevitable. Similarly a control scheme in terms of bandwidth, gain, deadzone etc. can be chosen either to minimise flight loads or to minimise trajectory dispersions depending on the requirement of reduction in the structural loads or trajectory dispersions. Therefore it is essential to carry out detailed system engineering studies before finalising a suitable guidance scheme for a vehicle considering the various aspects of the mission, technology constraints and cost.

The functional configuration of an inertial guidance system for a launch vehicle is given in figure 1. The inertial guidance system will have a navigation system with rate-integrating gyros or dry-tuned gyros and servo accelerometers as inertial sensors to measure vehicle variables such as instantaneous vehicle attitude (θ , ψ , ϕ), acceleration (\ddot{x} , \ddot{y} , \ddot{z}), velocity (V_x , V_y , V_z), and position (x , y , z) with respect to an inertial frame. The guidance system makes use of the information provided by navigation and generates the necessary steering commands θ_c , ψ_c to the vehicle to achieve the final mission. The autopilot receives (θ_c , ψ_c) from guidance, vehicle attitudes (θ , ψ , ϕ) from navigation, body rates (p , q , r) from the rate-gyro, vehicle lateral accelerations (a_x , a_y and a_z) from the lateral accelerometer package and computes attitude error function commands e_x , e_y , e_z as per the control law to drive the actuators so as to generate the necessary control forces (F_x , F_y , F_z) and moments to stabilize and steer the vehicle. All the operations involving real-time processing on-board the vehicle for navigation, guidance & control functions are carried out by special purpose microprocessor-based on-board computers.

This paper outlines the mission definition and design methodologies for guidance systems. The developmental aspects of hardware and software elements to meet

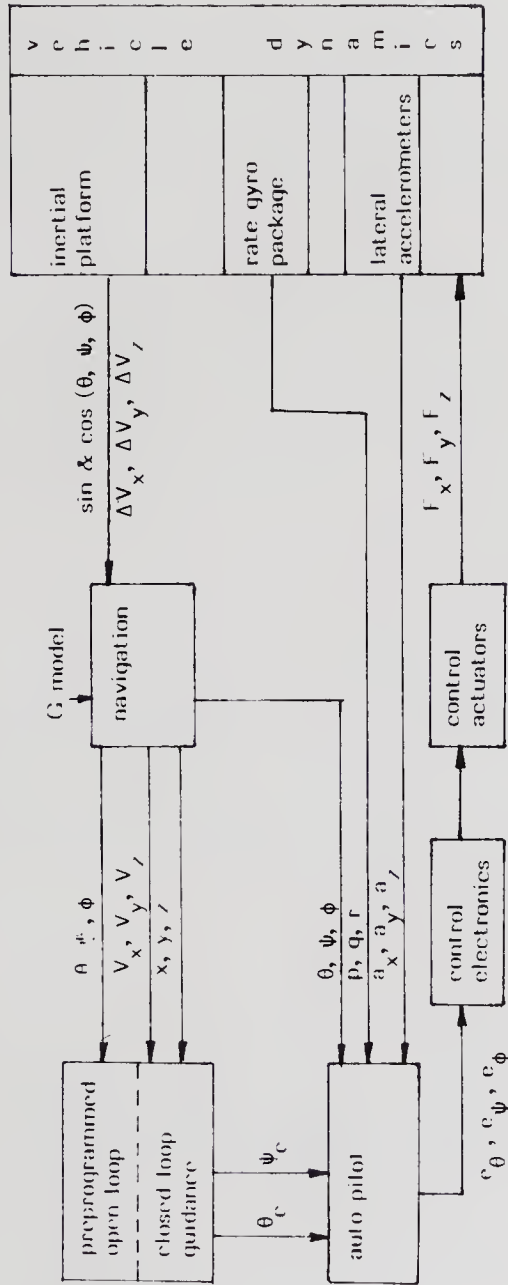


Figure 1. Functional configuration of a guidance system for a launch vehicle.

the guidance system requirements with respect to the mission are discussed. Test and evaluation procedures used for guidance system validation are included. The general scheme of guidance systems used in Indian Satellite Launch Vehicles, SLV-3, ASLV and PSLV are presented in brief.

2. Mission definition

Operational launch vehicles with polar- and geo-synchronous missions demand high accuracy injection of satellites with errors in altitude and inclination angles less than ± 10 km and $\pm 0.1^\circ$, respectively. The guidance system must ensure such high accuracy injection, otherwise satellite fuel will have to be used for orbit correction at the expense of its life-time. Consequently, closed-loop guidance is indispensable for such missions.

For low earth orbit (LEO) missions where wider dispersions on apogee and perigee are permissible open-loop guidance is adequate. In such open-loop guidance missions, trajectory dispersions are functions of the errors from (a) stage thrust variation, (b) wind disturbances, (c) pitch programme, (d) attitude control, (e) spin stabilization errors etc. For example, in the case of SLV-3 these errors were estimated, and their 3σ dispersions on apogee and perigee were calculated by Monte Carlo simulation. The corresponding values were 975 ± 230 km and 425 ± 65 km for a 41.5 kg satellite.

The Augmented Satellite Launch Vehicle (ASLV) has the capability to position 150 kg class satellites in LEO with orbital tolerances of ± 50 km in altitude and $\pm 0.5^\circ$ in the inclination. This can be achieved only by closed-loop guidance. The Polar Satellite Launch Vehicle (PSLV) has even more stringent orbital specifications since it has to position a 1000 kg Indian Remote Sensing Satellite (IRS) in a precise polar orbit of 900 km with an inclination of 99.1° . The orbital tolerances are ± 15 km in altitude and $\pm 0.1^\circ$ in inclination. These accuracies can be achieved only with closed-loop guidance upto the injection of satellite into orbit.

3. Design methodology

The major design considerations for the guidance system are (a) error analysis for estimating the terminal errors in altitude, velocity, flight path angle and the corresponding orbital dispersions, (b) selection of suitable inertial sensors and inertial navigation system meeting the navigation error budget, (c) selection of a suitable on-board guidance algorithm, and (d) on-board control scheme and stability analysis (Fernandez & Macombe 1962; Leondes 1963).

In closed-loop guided vehicles the guidance system errors such as (a) sensor random errors, (b) alignment errors, (c) computational algorithm errors and (d) final velocity cut-off errors are uncorrected. These cumulative errors upto the final injection point contribute to the orbital dispersions (McClure 1960). Hence, a detailed error analysis is carried out and the error budgets for the different elements of the inertial navigation system are specified.

The on-board guidance scheme is selected based on the accuracy, robustness, optimality, computation time, on-board memory and reliability. The scheme so

elected must steer the vehicle to the desired point over a wide range of off-flight conditions. For example in ASLV a terminal and explicit form of velocity-to-be-gained guidance scheme is chosen (Dasgupta & Ramakrishna 1984). This selection is based on the requirements of ASLV where all the stages are of the solid propellant type and no thrust cut-off is convenient. Also, the guidance terminates at the end of the third stage coast phase since the fourth stage, which is the last stage, is spin stabilized. With liquid propulsion systems where thrust cut-off is convenient, explicit guidance schemes are most suitable. Hence, an explicit guidance scheme is planned for PSLV, the last stage of which is a liquid propellant rocket.

Important design considerations for the launch vehicle control systems are (a) selection of control thrusters type and thrust sizing, (b) vehicle controllability, (c) effect of tracking error on the final mission, (d) aerodynamic and thrust misalignment loads on the vehicle, (e) control structure interaction and selection of suitable filters (Greensite 1970).

A typical diagram of a launch vehicle pitch control system considering the vehicle flexibility is given in figure 2 (Kadam 1976, 1977). The vehicle has highly non-linear-dynamic characteristics with time-varying parameters. The control thrusters are sized to overcome the net disturbance forces due to thrust misalignment, aerodynamic load, lateral CG offset etc. During the dense atmosphere region of the flight it is necessary to use a proportional control system, with a large enough saturation limit on the control force, in order to reduce the aero-structural loads. However, in the upper atmospheric region, where the disturbance loads are not widely varying and aero-structural loads are relatively small, the on-off reaction control type systems can be used.

Control system analysis is initially carried out using short period dynamics of the vehicles, where vehicle parameters are assumed constant over a short period of time. Subsequent to this, simulations are carried out using a 6-degree-of-freedom trajectory programme to check for trajectory dispersions, loads on the vehicle etc.

The overall vehicle control system bandwidth is quite low. For example, in SLV-3 and ASLV it is about 1 Hz. It is essential to keep enough separation between the cross-over frequencies of the autopilot and the structural bending frequencies. In order to study the control structure interaction, flexibility analysis is carried out considering 3 to 4 bending modes and 2 to 3 slosh modes of liquid stages. Suitable filters are to be designed to ensure enough stability margins. The inertial sensors are to be positioned in the vehicle such that local deformations of the vehicle are minimal. The best locations for sensors are the antinodes of the first bending mode.

The selection of forward and rate gains, control system dead zone and the thruster force levels is made to meet the design objectives of stable limit cycle, low tracking error and low control fuel consumption.

4. Guidance systems for Indian satellite launch vehicles

An overall diagram of the control and guidance system used in SLV-3 is given in figure 3. Since open-loop guidance is used here the pitch programme is stored on board in the vehicle attitude programmer (VAP). Only the attitude reference system is used to sense the actual attitude angles of the vehicle about pitch, yaw and roll. A 3-axes rate-gyro package is used to measure the angular rates of the vehicle.

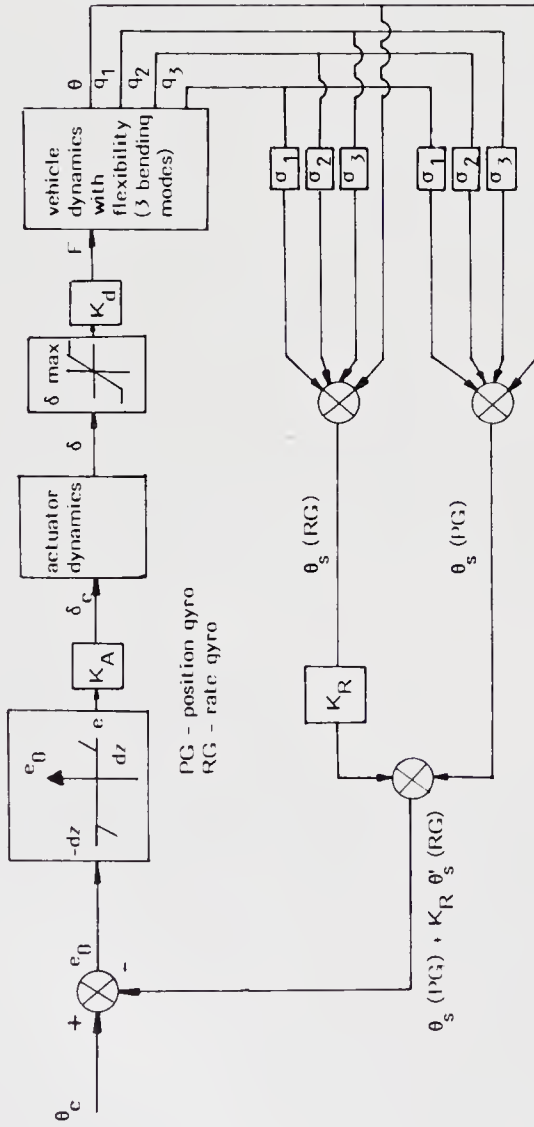


Figure 2. Block diagram of launch vehicle pitch control system.

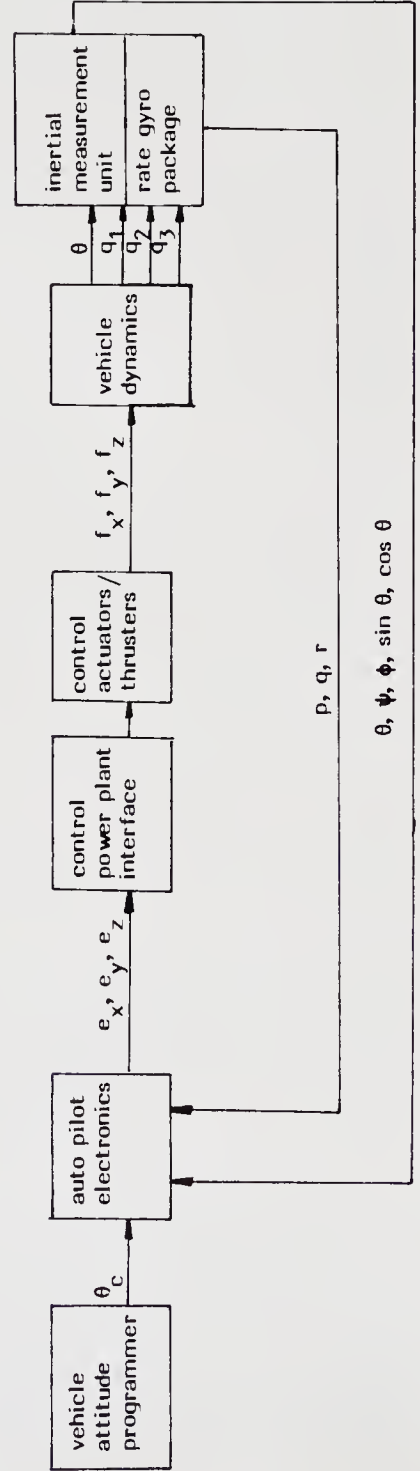


Figure 3. Guidance system used in SLV-3.

An analogue autopilot is used and the computations of attitude errors and attitude control commands are carried out using the analogue circuits.

The guidance system configuration for ASLV and PSLV is given in figure 4. The system comprises an Inertial Navigation System (INS), rate-gyro packages (RGP), an on-board computer (OBC), stage processor modules (SPM), selection logic (SL), and necessary control power plant interfaces (CPIF). The on-board computer carries out the navigation, guidance and control functions.

5. Development of guidance hardware

5.1 Inertial sensors

VSSC has developed various inertial grade sensors like rate gyros (RG), rate-integrating gyros (RIG), dynamically-tuned gyros (DTG) and servo accelerometers (SA). The specifications of the sensors are defined such that they meet the mission objectives of PSLV. Indigenous rate-gyros have already been used in SLV-3. Rate-integrating gyros with beryllium components have been qualified. The achieved specifications are as follows:

Random drift stability (1 sigma)	
fixed drift, °/hr	: 0.005,
mass unbalance, °/hr/g*	: 0.05.
Day-to-day drift coefficient stability (1 sigma)	
fixed drift, °/hr	: 0.03,
mass unbalance, °/hr/g	: 0.15.
Anisoelatic drift coefficient, °/hr/g ²	: 0.08.
Torque scale factor stability	: 0.1%.

Analyses have been carried out and it has been observed that these specifications meet PSLV mission requirements.

Dynamically-tuned gyros (DTG) have been qualified for the Indian Remote Sensing Satellite (IRS) application and the specifications achieved are as follows:

Drift stability (3 sigma)	
fixed drift, °/hr	: 0.15,
mass unbalance, °/hr/g	: 0.2.
Input axis alignment stability, arc second	: 10.

Error analysis indicates that with these specifications it is possible to meet PSLV mission requirements.

The pendulous type servo accelerometers meeting the following specifications have also been developed:

scale factor, ma/g	: 5,
scale factor stability (1 σ , 7 days), μ g	: < 100,
bias stability (1 σ , 7 days), μ g	: < 100,
nonlinearity, μ g/g ²	: < 20,
input axis misalignment, arc second	: < 600,

Excepting input axis misalignment, the rest of the specifications meet PSLV mission requirements. This parameter will be further improved progressively.

* g - acceleration due to gravity.

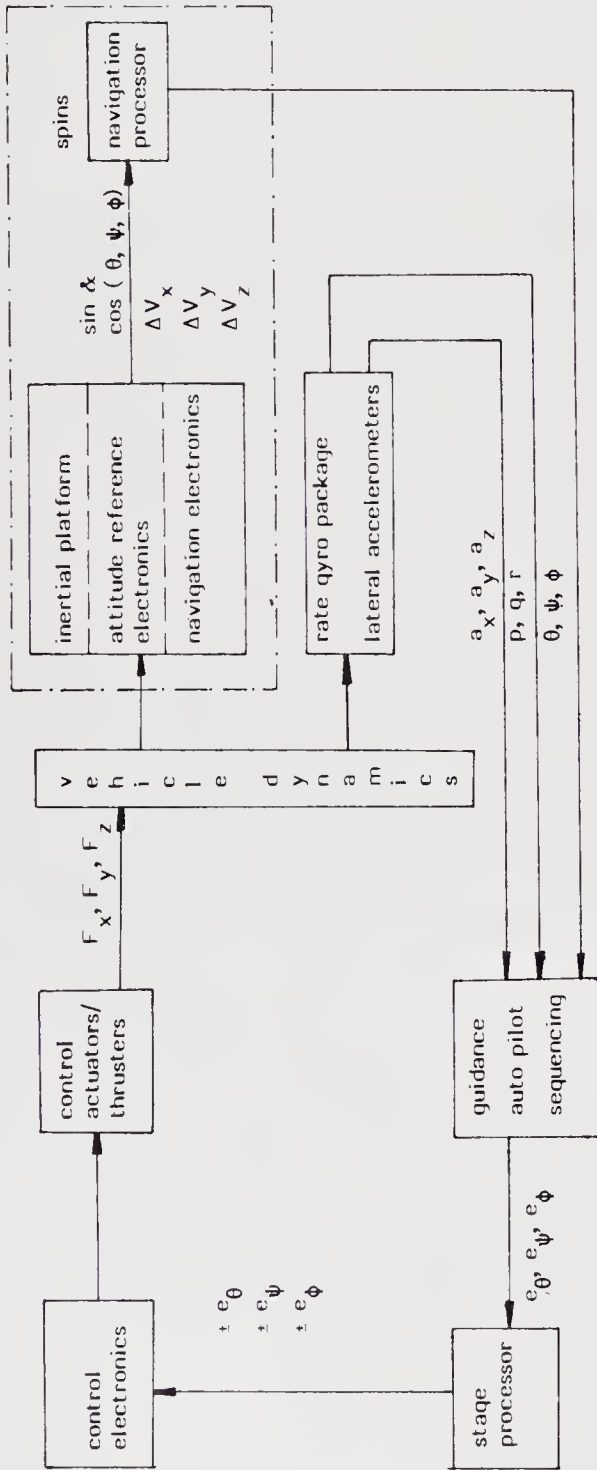


Figure 4. Guidance system configuration for ASLV/PSLV.

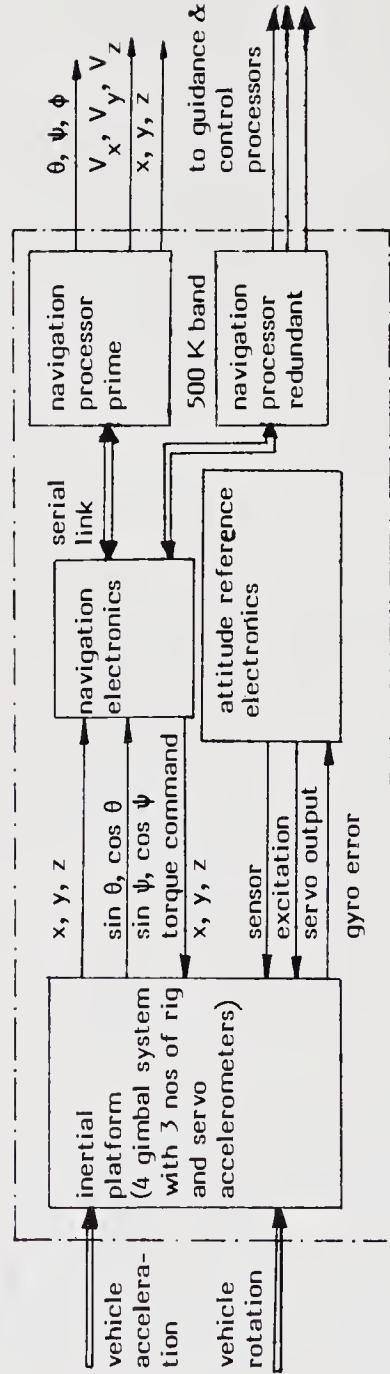


Figure 5. Schematic configuration of SPINS.

5.2 Inertial systems

The inertial measurement unit (IMU) used as an attitude reference system in SLV-3 is built indigenously using imported sensors and the system has performed satisfactorily in flights. The broad specifications are as follows:

configuration	: 4 gimbal, all attitude platform,
fixed drift, °/hr	: 0.2,
mass unbalance, °/hr/g	: 2,
resolver setting error, arc min	: 12,
servo slaving error, arc min	: 12.

The stabilized platform inertial navigation system (SPINS) for ASLV consisting of the inertial platform module (IPM), attitude reference & electronics module (AREM), navigation electronics module (NEM) and navigation processor (NP) has been indigenously developed and qualified. A schematic of the functional modules of (SPINS) is shown in figure 5 (Bose *et al* 1986). The platform in this system is a four-gimbal stabilized unit and contains three rate integrating gyros (RIG) and three servo accelerometers (SA). At present imported sensors are used in the system and subsequently they will be replaced with indigenous sensors. The gimbal servo components like resolvers, torquers etc. are indigenous. The platform senses the vehicle altitude and acceleration in the inertial frame. AREM provides the platform power supplies, gimbal servo electronics and interface electronics to telemetry. The navigation electronics module has velocity encoding electronics, interface electronics to navigation processor and telemetry. The broad specifications of SPINS are given below:

gyro bias drift, °/hr	: 0.06,
gyro unbalance, °/hr/g	: 0.75,
aniso elastic drift, °/hr/g ²	: 0.25,
accelerometer bias, μg	: 360,
accelerometer scale factor error, ppm	: 300,
accelerometer nonlinearity, $\mu\text{g/g}^2$: 42,
input axis misalignment, arc second	: 90,
alignment	
vertical, arc second	: 180,
azimuth, arc second	: 940,
gyro torquing stability, %	: ± 0.15 .

The redundant strap-down inertial navigation system (RESINS) is one of the candidate systems for PSLV. An engineering model using imported DTG has been realized and is undergoing tests. A schematic diagram of the system is shown in figure 6 (Puri *et al* 1983). The system consists of an inertial sensing unit (ISU) and an electronics unit including a navigation processor. The ISU comprises three DTG and four SA. One accelerometer is redundant along the thrust axis. The ISU is mounted on the vehicle with proper vibration isolators. The system electronics unit consists of sensors rebalance electronics, navigation processor, thermal control electronics and excitation, interface and power system electronics. The system provides the redundancy in that the operation of any two of the three gyros and three accelerometers is sufficient for mission success.

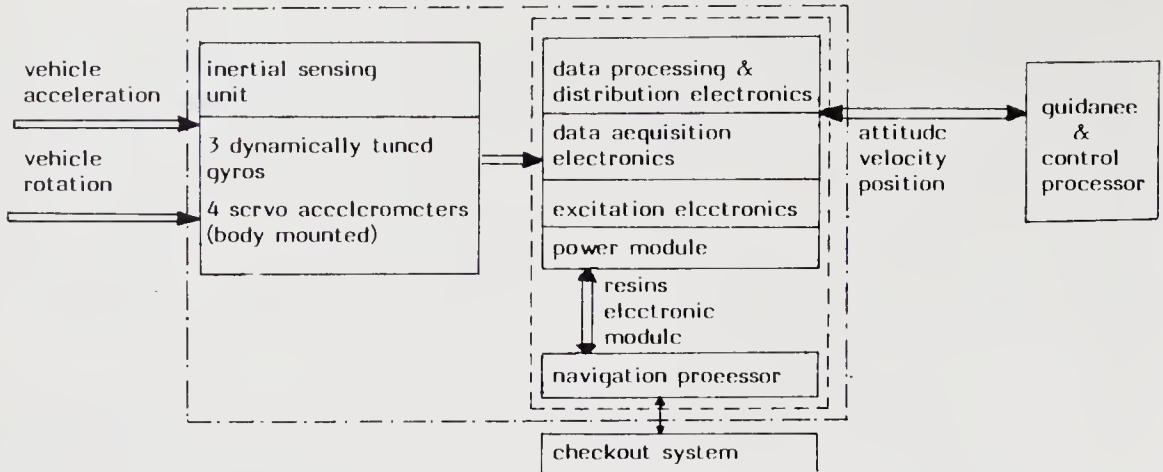


Figure 6. The schematic of the functional modules of redundant strap-down inertial navigation system (RESINS).

5.3 Control actuators and thrusters

The various types of stage control systems used in SLV-3 and ASLV are secondary injection thrust vector control, electro-hydraulic fin tip control, monopropellant and bipropellant reaction control systems. In addition to the actuators and control thrusters meeting different force levels, each system requires a fairly large number of control components like solenoid valves, pressure regulators, relief valves, accumulators, bipropellant valves etc. with a wide range of specifications. All these components have been developed indigenously and qualified. The systems have functioned satisfactorily in SLV. Electromechanical actuators with different torque levels have been developed and are in different phases of testing for PSLV applications.

5.4 On-board computers

An on-board computer (OBC) system based on the M6800 processor has been developed and qualified for ASLV. The system consists of three processor modules, navigation guidance & control processor (NGCP), stage processor module (SPM) and navigation electronic module (NEM) processor. The broad specifications of OBC are given below:

basic word length.	: 8 bits,
hardware multiply/divide	: 16 bits,
clock frequency	: 1 MHz,
hardware multiply/divide time	: 50,
memory global RAM	: 1 K Byte,
local RAM	: 3 K Bytes,
PROM	: 20 K Bytes,
number of serial ports	: 4,
C/O link	: 19.2 KBS,
stage processor	: 500 KBS,
navigation electronics	: 500 KBS,
power	: 20 Watts.

The general configuration of NGCP is given in figure 7. There are two Motorola 6800 processors, one termed navigation processor and the other guidance & control processor. Each of these processors has a hardware multiply/divide unit and its own local memory, both EPROM and RAM. The communications between the two processors is through a global memory of 1K byte capacity. The functions of the navigation processor are sensor data processing, velocity and position computation and telemetry posting. The guidance and control processor carries out guidance computations, autopilot calculations, vehicle sequencing functions and telemetry data generation. The SPM receives the sequencing and attitude control commands from GCP through the serial data link and, after the required checks, outputs the above commands to control electronics/sequencing relays etc.

The real-time executive (REX) resident in OBC is responsible for carrying out all real-time operations on-board by utilizing the self-check routines, task scheduler and error handling routines.

It is estimated that the computational load requirements are quite high in PSLV, compared to that of ASLV and hence the on-board computer based on MC 68000 processor will be used. An engineering model of OBC for PSLV is under realization.

6. Development of guidance system software

The on-board software for both ASLV and PSLV is quite complex and consists of navigation, guidance and autopilot software in addition to the sequencing function generation and error recovery procedures (Kurien & Bharati 1985). The OBC has its own system-executive software. Figure 8 gives an overview of the total guidance system software for ASLV.

The navigation software does the processing of velocity encoder data to perform the compensation of sensor errors and generates the vehicle attitude angles, inertial velocity and position vectors.

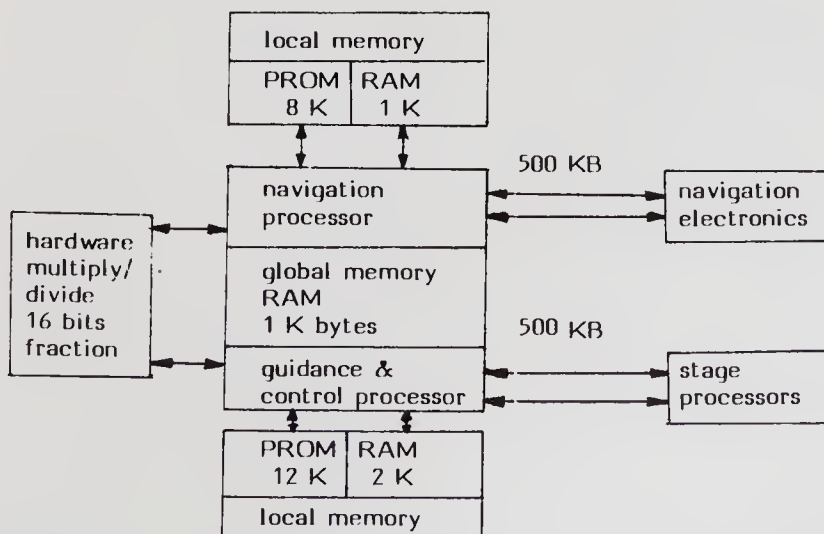


Figure 7. General configuration of navigation, guidance & control processor.

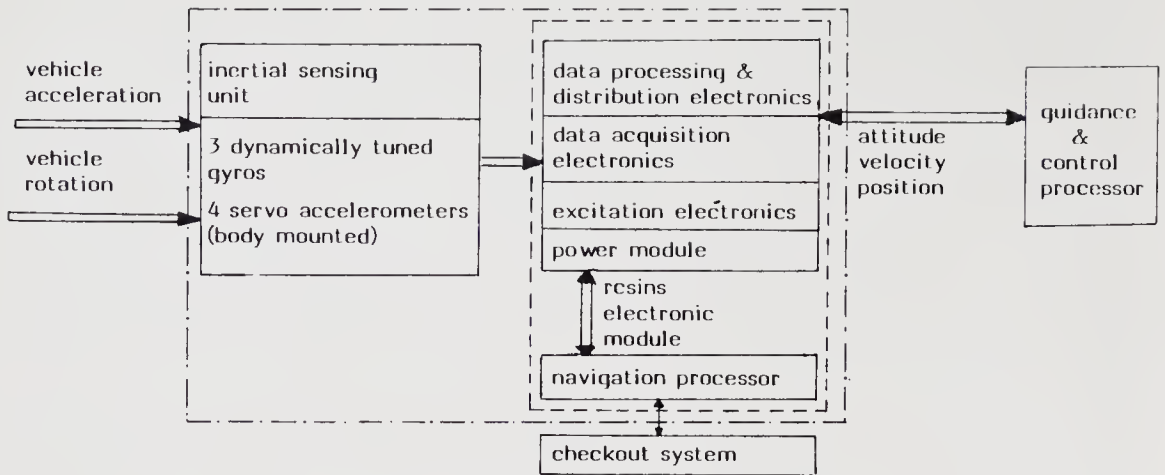


Figure 8. An overview of guidance system software.

The guidance software generates the predetermined attitude commands for open-loop guidance during atmospheric flight and computes pitch and yaw commands θ_c , ψ_c on-board during the closed-loop guidance phase. For example in ASLV, the terminal velocity-to-be-gained (VG) guidance algorithm is used for the thrust phase and a reorientation algorithm is used during the coast phase of the third stage to circularize the orbit based on the flight performance of the lower stages up to the end of the third stage burn-out and a nominal fourth-stage performance.

The autopilot software in ASLV compares the vehicle attitudes with the guidance commands, resolves them to vehicle axes and generates the attitude control commands by mixing the weighted body rates for necessary damping. The digital controller implements the gain selection and shapes the control commands by using a suitable filter to ensure vehicle stability and performance during flight.

The system software resident in the on-board computer essentially carries out the following functions:

- schedule execution of different tasks in real time;
- maintain the real-time clock and synchronize different tasks;
- establish communication between tasks and processors;
- execute the error recovery procedures;
- self-check and diagnostics;
- receive and process commands from the ground checkout computer during the pre-launch operations.

These functions are carried out by a set of system programmes termed the real-time executive (REX).

7. System validation

7.1 Test and evaluation of subsystems and the guidance system

The performance of various hardware and software elements of the guidance system is evaluated extensively by carrying out detailed performance tests initially at the subsystem level and then at the system level. Each individual subsystem is

subjected to extensive evaluation both under standard room and flight environment conditions. After qualification of these subsystems they are further integrated and tested for their functional links, communication protocols etc. Subsequent to this, a detailed system level performance is evaluated.

The on-board software is also subjected to thorough review and evaluation to ensure error-free software. The validation route followed for software is summarized in figure 9. Detailed evaluation tests of the integrated applications software are carried out initially using a digital simulation test bed with a six-degree-of-freedom vehicle trajectory. These tests are the first real indicators of software performance at various phases of flight. In the next phase digital simulation is carried out by integrating the coded level software with the vehicle trajectory programme using an OBC simulator.

The final evaluation of on-board software is done under dynamic flight conditions in the hybrid simulation. The entire software is mapped with the actual hardware memory of OBC. Under simulated dynamic inputs of acceleration and rotation of vehicle, trajectory simulation runs are taken with OBC performing all the tasks as in flight. These tests reveal the errors in sign conventions, data transfer under static and dynamic modes, scale factor mismatches, input/output mismatches, and tuning requirements of the coefficients used in the on-board software to achieve the required performance. The performance of the system executive under simulated flight environments (including failure modes) is evaluated and checked against specifications.

7.2 Hardware-in-loop simulation

Hardware-in-loop simulation (HLS) is the mandatory pre-flight test for the guidance chain to verify the overall design and integrated performance of all the hardware and software elements in the real-time environment for assessing their flight

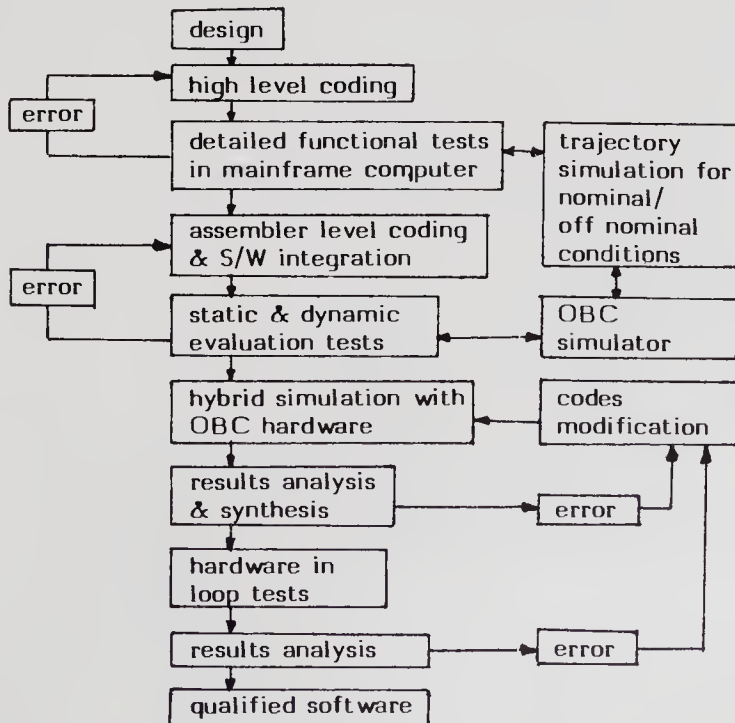


Figure 9. Validation of on-board software.

worthiness, to remove deficiencies, if any, in the subsystems, to ensure the compatibility of various subsystems, their interfaces with ground-based checkout systems and to examine system behaviour with respect to nominal and simulated failure-mode conditions. The hardware-in-loop configuration for evaluation of a guidance system is shown in figure 10 (Warrier 1984).

The interaction of the vehicle with the guidance system is through angular kinematics. In order to realize this interaction, inertial system units like the inertial platform and rate-gyro package are mounted on the angular motion simulator (AMS) which is a three-gimbal system to simulate the pitch, yaw and roll axes of the vehicle. The corresponding servos are slaved to the attitude signals generated in real-time by hybrid computer. The control thruster simulators are incorporated into the analogue segment of the hybrid computer. Detailed simulation tests are carried out for both nominal and off-nominal conditions corresponding to 3 sigma dispersions of the vehicle parameters as specified for evaluation of the performance of hardware and software elements of the guidance system. From these tests, the final orbital dispersions in terms of altitude and inclination errors are also verified.

8. Conclusion

A review of the functions and the architecture of the navigation, guidance and control system of satellite launch vehicles is presented. The rationale behind the choice of systems for different types of orbital missions is explained. Indigenization of the sophisticated inertial sensors, inertial systems, associated complex electronics, on-board computers, control-thruster components and systems is reported. Development of the navigation, autopilot and guidance algorithms, and their

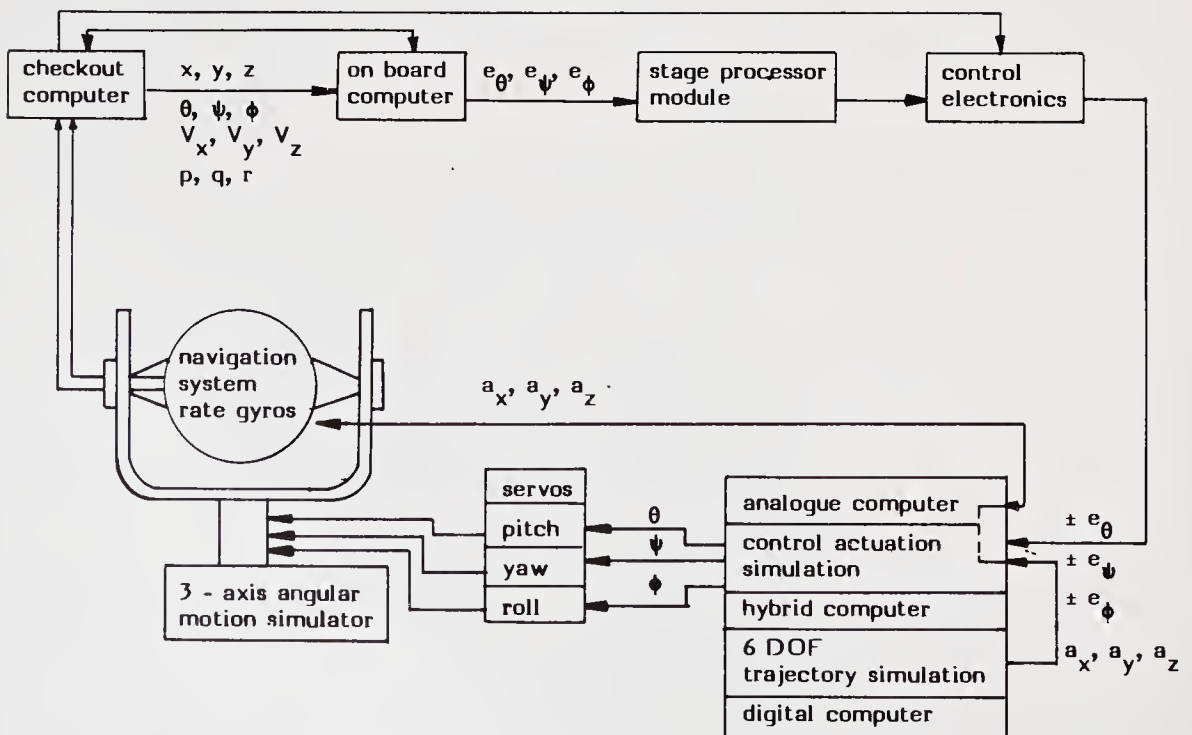


Figure 10. Block diagram for hardware-in-loop simulation for guidance system.

validation process, is described. The critical role played by this field in the realization of Indian satellite launch vehicle SLV-3, ASLV and PSLV is brought out.

References

- Bose A *et al* 1986 Critical design report on stabilised platform inertial navigation system (SPINS) for IGS-ASLV, VSSC-IGSP-TR-173, April
- Dasgupta S, Ramakrishna S 1984 Explicit VG guidance algorithm for a solid powered closed loop guided mission. *International symposium on space technology & science*, Tokyo
- Fernandez M, Macombe G R 1962 *Inertial guidance engineering* (Englewood Cliffs, NJ; Prentice Hall)
- Grecnsite A L 1970 *Control theory: Vol. 1. Elements of modern control theory* (East Lansing, MI: Spartan Books)
- Kadam N V 1976 Design of pitch & yaw control systems for SLV-3, Part 1, Rigid body dynamics, VSSC-TM 40016, May
- Kadam N V 1977 Design of pitch yaw control systems for SLV-3, Part II, Flexible body dynamics, VSSC-TM-18-025, September
- Kurien T, Bharati M 1985 Critical design review report for integrated software for on-board computer for ASLV; VSSC-IGSP-TR-155, September
- Leondes C T 1963 *Control and dynamics systems, advances in theory and applications* (London: Academic Press)
- McClure C L 1960 *Theory of inertial guidance* (Englewood Cliffs NJ: Prentice Hall)
- Puri S N *et al* 1983 Preliminary design report on redundant strapdown inertial navigation system for PSLV; VSSC-IGSP-TR-30(4)-83, February
- Warrier P V E 1984 IGS hardware-in-loop simulation master plan, VSSC-IGSP-TR-123, December

ISRO spacecraft technology evolution

K KASTURIRANGAN¹ and K R SRIDHARAMURTHY²

¹ ISRO Satellite Centre, Airport Road, Vimanapura P O, Bangalore 560 017, India

² ISRO Headquarters, Cauvery Bhavan, Kempegowda Road, Bangalore 560 009, India

Abstract. Evolutionary trends in the technologies related to Indian Space Research Organisation (ISRO) satellites, both past and present, are outlined. The issues related to the developmental complexities of different spacecraft subsystems are discussed in the context of the needs of the current generation operational spacecraft like the Indian Remote Sensing Satellite (IRS) and the Indian National Satellite (INSAT) II. Considerations pertinent to reliability and long-life requirements, crucial to operational satellites, are also highlighted.

Keywords. Indian space programme; satellites; operational systems; technology and development; remote sensing; communication.

1. Introduction

The growth and evolution of satellite technology in the Indian Space Research Organisation (ISRO) since the inception of related activities in the early seventies was a step-by-step process. During the initial step, which can be termed the learning phase, the basics of the technology were learnt in the process of actually designing, building and operating the satellite *Aryabhata* (Rao & Kasturirangan 1979). During the next step, which can be characterized as experimental, missions like *Bhaskara* (Kasturirangan 1985) and APPLE (Ariane Passenger Payload Experiment) (Vasagam & Shrivastava 1983) were conceived and executed to gain experience in the conduct of a space mission on an end-to-end basis, in respect of specific application goals in remote sensing, meteorology and communications. Essential methodologies like characterization and design of the remote sensing payloads and the associated definition of spacecraft platforms, three-axis stabilization as well as orbit-raising and on-orbit operations for geosynchronous missions were learnt during this phase. The third step involving the design and development of operational satellites is currently under way. The Indian Remote Sensing Satellite (IRS-1) represents the first in a series of remote sensing satellites (Navalgund & Kasturirangan 1983) capable of providing operational services for

resource survey and monitoring. IRS-1 is slated for launch towards the first quarter of 1988. In the case of communications and meteorology, the indigenously developed Indian National Satellite (INSAT) II (Rao & Ramachandran 1987; Rao *et al* 1987) represents the second generation INSAT satellites with augmented capacity and improved capabilities, vis-a-vis, the presently bought out INSAT I satellites (Dhawan *et al* 1979). INSAT II satellites are planned to replace the present INSAT I series in the 1990's. A series of 150 kg class satellites known as Stretched *Rohini* Satellite Series (SROSS) (Rao *et al* 1982) are also presently under development for the conduct of astronomy and aeronomy experiments as well as new and novel application-oriented missions.

In this paper, we propose to trace the evolution of the different technologies related to the ISRO satellite missions, in the context of increasing demands on the performance capabilities, sophistication and reliability of the current IRS-1 and INSAT II operational spacecraft under development.

2. Systemic aspects of spacecraft configuration

Central to the definition of a spacecraft is the specification of a mission goal or a set of mission goals related usually to the areas of science, applications or technology. Once the mission goal is laid down, it is possible to identify a set of interactive technical elements that include on one side a spacecraft carrying a payload or a set of payloads appropriate to the mission and a compatible launch vehicle system for placing the satellite in a pre-selected orbit, and on the other side, a network of ground-based telemetry, telecommand and tracking systems that serve to receive the data and exercise control over the spacecraft in its orbital phase. The mission normally concludes with a set of activities involving processing, analysis and interpretation of the data obtained from the experiments.

Once the orbit, the basic payload instrumentation, and the mission duration are defined, it is possible to assess the first level requirements of attitude/orbit control and electrical power needed for the payloads and the other supporting spacecraft subsystems. The attitude/orbit control enables the orientation of the payloads, and other elements having directional properties (such as the antenna), in the requisite directions and helps maintain the orbital parameters within allowable limits. The other important supporting subsystems of the satellite include the structure for providing mechanical support and rigidity to the different electronic and electro-mechanical elements, a thermal-control system for maintaining the temperature of different subsystems within allowable limits, downlink telemetry to process the data gathered by the satellite and transmit the same to the ground station and an uplink that performs the task of sending commands for exercising the satellite in different operating modes while in orbit.

The overall sizing of the spacecraft with respect to its weight and size is carried out at this juncture with due consideration to the constraints imposed by the launch vehicle and the environment. The constraints from the launch vehicle side include the extent of the available volume within the shroud and the total allowable weight for achieving the desired orbit. The environmental factors include the launch stresses, the micro-gravity, the ultra-high vacuum of space and the particulate and ultra-violet radiations.

The final configuration of a spacecraft is arrived at by a series of iterations that ensure compatibility between the spacecraft, the rocket and the ground systems on one hand and between the different subsystems of the spacecraft on the other. Some of the major elements of this iterative procedure leading to the spacecraft configuration definition are illustrated in figure 1.

The development and improvement of satellite technology has thus been a continuing endeavour dictated by increasing demands on the performance capability of the satellites in terms of their higher capacity and longer life times.

3. Evolution of technologies of subsystems

As mentioned earlier, a satellite is the product of a variety of engineering disciplines. Even though these disciplines have been brought to bear on the

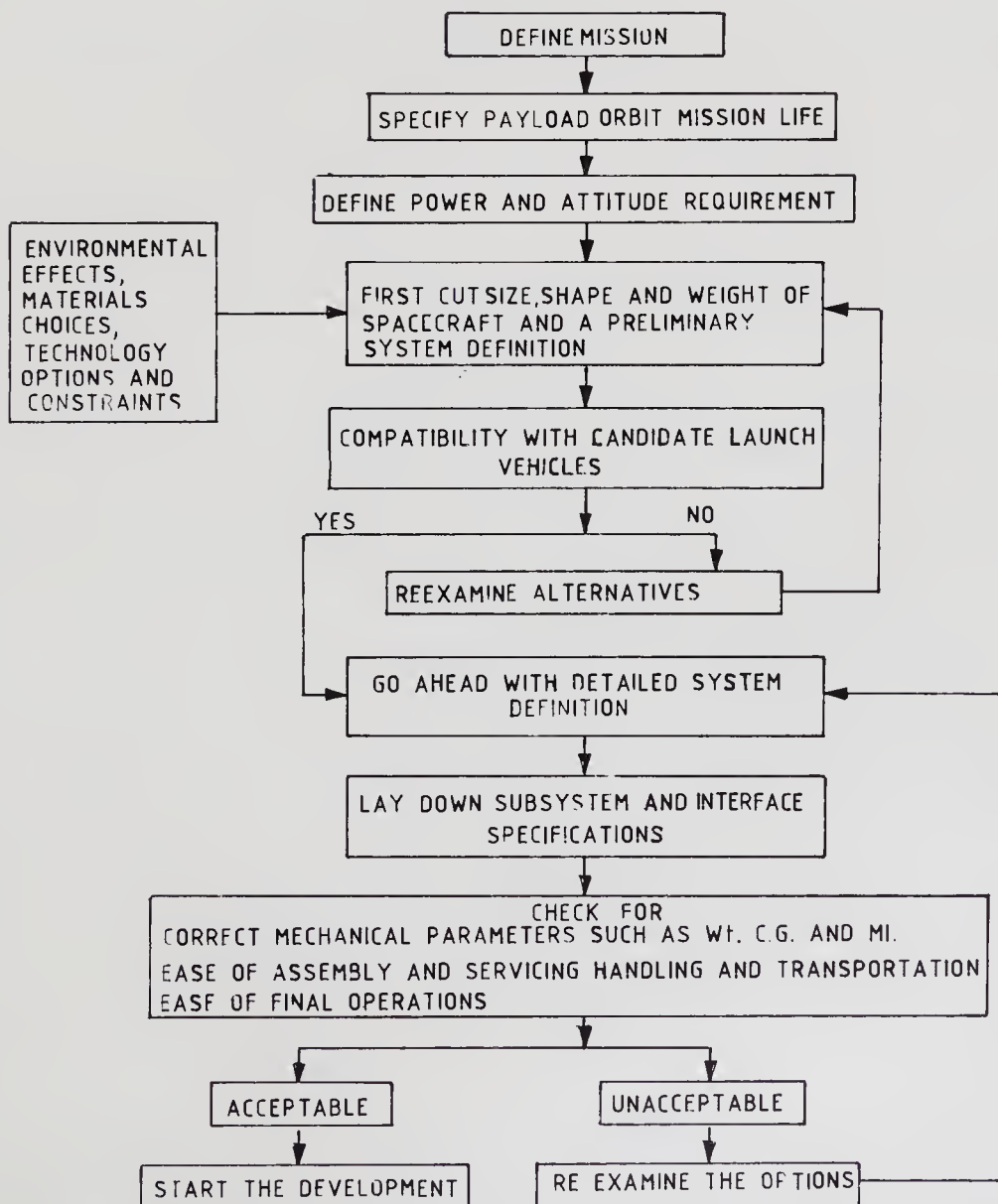


Figure 1. Iterative procedure leading to definition of spacecraft configuration.

realization of a number of conventional terrestrial systems, what distinguishes the application of these engineering principles to a space system is the need to realize systems that could operate unattended and with a high degree of reliability in the hostile environment of space. The other and equally important aspect is to make the systems lightweight, low-power consuming and miniature, calling for a high degree of design optimization. In the following few pages, the evolution of the technologies of different satellite subsystems towards a higher level of complexity and sophistication is dealt with keeping the above considerations in mind.

3.1 Structure

The main function of the structure is to safely house all the subsystems and provide adequate shielding against the hostile environment of space. It should have the ability to withstand environmental loads arising from ground handling, transportation, launch and orbit phases. Evolving an efficient and optimum structure (Adams 1966) encompasses three types of activities, viz., design, analysis and testing. There is a strong interaction among these three elements leading to the realization of a structure.

3.1a Design considerations: The criticality of flight and in-orbit loads for design, will vary depending on the needs like stiffness requirements, alignment needs and resistance to thermal distortions. For small spacecraft, the design is generally strength-based. In most of the medium and large spacecraft, stiffness requirements dominate as in the case of IRS where the fundamental frequencies in longitudinal and lateral directions should be kept around 30 and 15 Hz, respectively, to avoid strong coupling between launch vehicle and satellite dynamics. Similarly, an acoustic environment becomes important for structural elements like panels with large area to mass ratios like those in IRS and INSAT.

The design of a satellite structure becomes more complex as its size increases due to the interactions involved with other systems. Interaction between the satellite and the launch vehicle is one area of concern when the size of the satellite increases. The loads on a satellite cannot be determined precisely before a dynamic-coupled analysis of launch vehicle and satellite is carried out. This information is also necessary for generating realistic test specifications. Interaction of structural design with that of other subsystems of the satellite also becomes progressively more and more important as the size becomes larger, making increased demands on design complexity. Control system and structure interaction is an area that requires considerable attention. This interaction arises when structural and control frequencies overlap. For example, the INSAT satellite incorporates large panels, whose structural responses could result in some amount of such interaction and this has to be taken into account in control system design. Larger sizes of satellites would involve stronger interaction, and structure or control system design cannot be handled in isolation as is shown in figure 2. Another potential area of interaction is that between thermal and structural systems. Traditional approaches of thermal management as those employed in *Aryabhata* and *Bhaskara*, involve calculation of temperatures at various points in the satellite using inter-element radiation and conduction with external and internal loads. These do not suffice for larger systems and we need to integrate this with structural

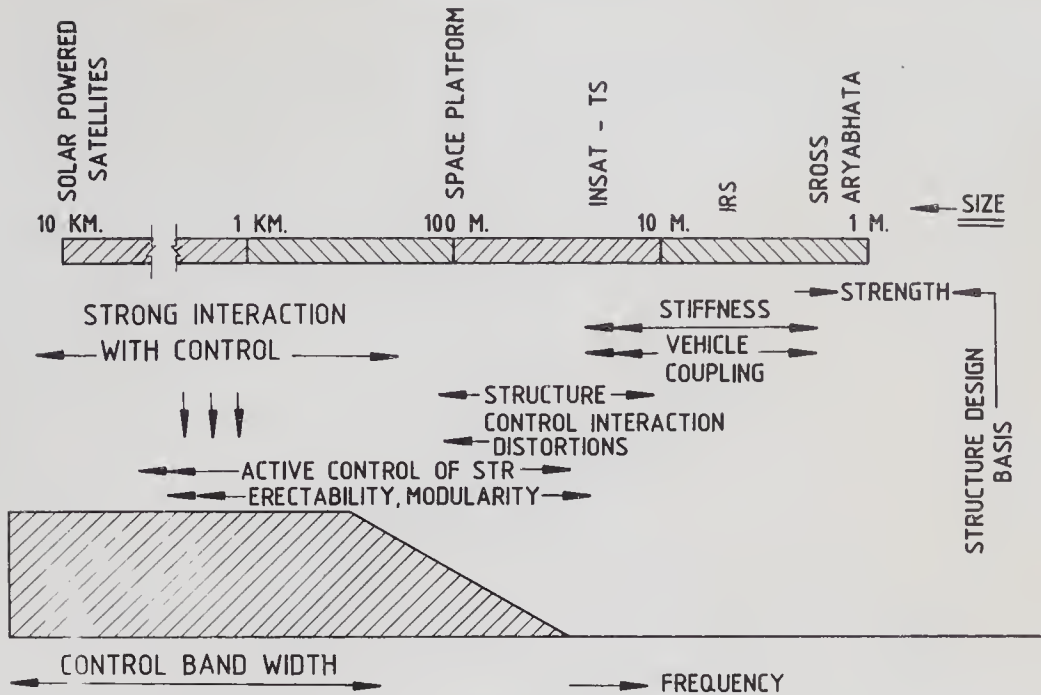


Figure 2. Design considerations of structure in relation to its size.

responses due to view factors affecting temperature distribution. All these factors contribute to making the satellite structural design a highly complex and iterative exercise.

Material selection and fabrication processes contribute primarily to realizing design goals. From *Aryabhata* with a structural mass of 30% of the total mass to INSAT II TS (TS—test satellite) with an estimated mass of 7.5%, there has been a steady decrease in the proportional structural mass of ISRO spacecraft. With the use of conventional metals like aluminium, mass reduction could not be continuously improved. The considerable weight reduction in the recent ISRO spacecraft like IRS has come about with the increasing substitution of metal honeycomb for structural elements in place of machined solid elements. This is reflected in figure 3.

Several process and fabrication related problems have to be solved in using honeycomb sandwiches. These include honeycomb-sandwich bonding technology, optimization of process parameters, quality control procedures including non-destructive testing (NDT) and use of lighter cores and adhesives with stricter fabrication tolerances. In addition, special attention has been paid to load transferring mechanisms in honeycomb sandwiches, namely, in insert design and in the use of adhesives of lighter weight. For instance, reduction of weight from 15 gm per insert in APPLE to 6.8 gm per insert in IRS, has been due to these efforts. In assuring the quality of honeycomb and composite components, appropriate NDT techniques such as ultrasonic bond testing, laser holography and acoustic emission have been pressed into service.

Concerted technology development efforts are presently under way for further savings in structural mass in a spacecraft through the use of materials like CFRP, magnesium alloys, aluminium-lithium alloys and beryllium for various structural components.

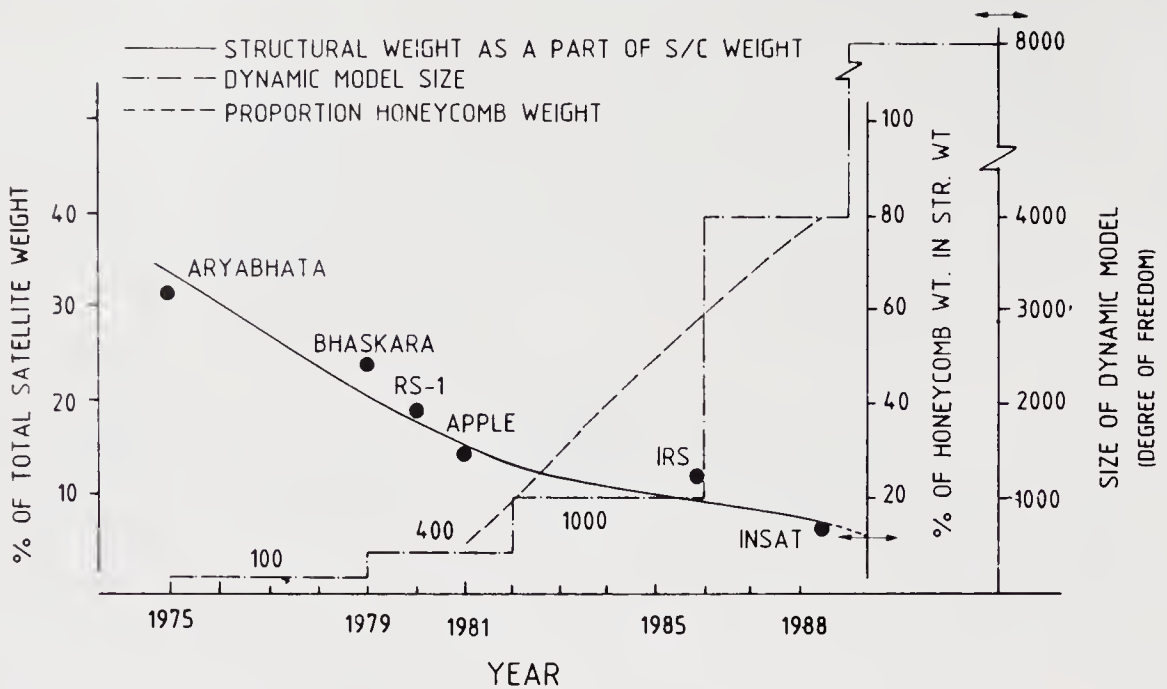


Figure 3. Optimization trends in structures of Indian spacecraft. (←→ indicates state of art).

3.1b *Structural testing*: A changing trend in testing of satellites is noticed in the efforts to simulate flight environment as closely as possible. For *Aryabhata*, only static and sinusoidal dynamic tests were carried out. With a sweep rate of a quarter octave per minute, the dynamic test programme had a high degree of conservatism built in. Whereas, some of the later satellites like APPLE were additionally subjected to random vibration levels, acoustic environment simulations were not carried out in the experimental satellites.

The essential features of a realistic flight simulation are the decreasing conservatism in testing and closer tolerances allowed in specifications. The challenges involved in simulation of simultaneous application of static loads in different directions have been met by development of automatic static loading set up with load checks and correction devices, notch or abort provisions, and multiple jacks for supplying loads.

With the setting up of a facility to perform modal analyses of large spacecraft for extracting modal parameters like mass, stiffness and damping, it is possible to update the analytical model for realizing optimum designs.

Another major element of spacecraft structural testing in ISRO was related to building of a 1100 m³ acoustic chamber at the National Aeronautical Laboratory. IRS and SROSS have been tested successfully in this facility. Acoustic testing will form an important component of the test program for all future ISRO satellites.

3.1c *Structural analysis*: The role of structural analysis is to develop mathematical models of structural behaviour and obtain solutions to support design and testing activities. Design validation and improvements to achieve minimum weight designs, providing inputs for testing and correlation of analytical models with test data, are the important functions of analysis.

The analysis tool is essentially centred around the finite element method which was developed over the last 30 years somewhat in parallel with the growth of computers. These two, in fact, contribute enormously towards fulfilling analysis needs. However, over the years, the increasing complexity of analysis can be seen from the over ten-fold increase in the sizes of idealisation of static and dynamic models from *Aryabhata* to INSAT II (see figure 3). Apart from the sheer increase in the size of problems, functionally there has been growth and diversification of activities. Static analysis and free vibration were considered sufficient in the earlier years of *Aryabhata* and *Bhaskara* due to lesser needs and paucity of resources. Presently, analysis encompasses in addition to the above, creation of low order dynamic models, subsystem modelling, analysis of accuracies in representing dynamic behaviour especially for large sizes, computer-aided design, optimization, correlation with test data and model improvements, creation of unified data bases, consideration of nonlinearities and so on.

The increasing complexity of satellites has been reflected in attempts at the development of extensive data-integrity checks, detailed subsystem modelling and development of computer-aided design packages for interactive design. Inherent difficulties in handling large-sized dynamic problems, often infeasible by direct methods, have necessitated work on dynamic substructuring which is also useful in providing inputs to testing of the units of a large structure, which cannot be tested as a whole. Emphasis on mass reduction needs optimization routines. Efforts on IRS and INSAT II reflect much of this higher level sophistication in analysis.

In a nutshell, the evolution of structural design, analysis, and testing methods have led to the realization of optimal structural hardware for satellites like IRS and INSAT II. Further, such improved and sophisticated approaches have also resulted in a reduced number of models to be built for design validation through testing in view of the higher degree of confidence in the design, analysis, and testing methods for the current satellites.

3.2 Thermal control system

The thermal control system of a spacecraft enables maintenance of the temperature of the different systems within specified limits while the spacecraft is in orbit. During its normal operations in space, a near-earth orbiting spacecraft receives heat input from the internal operation of the equipment, externally from the sun (140 mW/cm^2), in the form of reflected albedo radiation (48 mW/cm^2), and emission radiation (23 mW/cm^2) from earth. Further, the spacecraft radiates heat back into space, which is at a temperature of about 3 K. The objective of the thermal control design is to realize acceptable equilibrium temperatures for the different systems taking into account various heat inputs and outputs.

Realization of an effective thermal control system involves three major elements. They are design of suitable control system, thermal analysis and thermal testing.

3.2a Thermal design and analysis: The type of thermal control system to be used for a particular spacecraft depends on the geometry of the spacecraft, mission phases, stabilization, power dissipation inside the spacecraft and the temperature ranges specified for various systems which are housed in the spacecraft. Table 1 gives the thermal design trends from the first Indian spacecraft *Aryabhata* to IRS-1

Table 1. Thermal design trends from *Aryabhata* to IRS and INSAT

Aspect considered	<i>Aryabhata</i> / <i>Bhaskara</i> / <i>Rohini</i> missions	APPLE	IRS-1	INSAT II TS
Temperature control requirement	0–40°C for electronic packages, 0–35°C for TV camera and wider ranges for sensors and pneumatic systems	5–25°C for battery, 5–55°C for reaction control system and 0–40°C for electronic packages	0–10°C for battery, 10–20°C for payload, 5–55°C for RCS and 0–44°C for electronic packages	5–25°C for battery, 5–55°C for RCS, VHRR detector to be maintained at 105 ± 0.1 K in presence of solar sail and boom
Size of thermal mathematical model	Less than 20 nodes	154 nodes	450 nodes. Detailed model for critical systems like payload, battery, RCS etc.	500–1000 nodes. Detailed model for VHRR, communication payload, RCS, solar sail and boom etc.
Technology involved	Passive system, paints using selected optical properties and geometry, radiation shields and FRP insulation	System consisting of MLI blankets, optical tapes, surface property control, ground-commanded heaters	System consisting of MLI blankets, rigid OSR, proportional controllers and ground-commanded heaters.	System consisting of MLI blankets, rigid optical solar reflector, proportional and ground commanded heaters, passive cooler for VHRR, solar sail and boom
Test philosophy	Scale model tests with bonded heaters or no tests	Full-scale solar simulation test in 7 m chamber, and one acceptance test in 4 m chamber with bonded heaters	Full-scale test on structural/thermal model with bonded heaters. Solar simulation test on engineering/thermal model and IR acceptance test on flight model	Full-scale solar simulation test on engineering/thermal model in a 9 m dia thermovacuum chamber and one acceptance test on flight model

and INSAT II TS. The thermal control system in *Aryabhata* used passive techniques consisting of selected optical surfaces, radiation shields and insulation to control the subsystem electronics package temperature between 0 and 40°C during its one year design mission life. APPLE spacecraft needed multilayer insulation (MLI) blankets to insulate the spacecraft from sun irradiation and to minimize the power radiated into space during eclipse periods. In addition to selected optical surfaces, ground-commanded heaters were necessary to control the temperature of its reaction control system elements between 5 and 55°C. The current generation of spacecraft like IRS-1 and INSAT II call for the use of improved active and passive thermal control systems in view of the higher power loads, closer temperature ranges, cooling of detectors in payloads like those used in remote sensing, reduced thermal gradients etc. IRS-1 poses a much greater challenge than APPLE because of very narrow temperature ranges specified for power and chemical batteries. In addition to 0–10°C temperature range in case of the payload, the gradient within a camera has to be less than 2°C. The design approach is to minimize external thermal loads on the camera by providing two sets of shields and maintaining the

temperature using the proportional control heaters. A separate radiator has been provided for the battery so that the temperature excursion of the rest of the spacecraft does not affect the temperature control of the battery. Further, the temperature is controlled within the range by means of proportional controllers. In case of INSAT II TS in order to maintain the temperature of the Hg-Cd-Te infrared detector used in the Very High Resolution Radiometer (VHRR) payload around 105 ± 0.1 K, a passive radiation cooler is employed.

As the specified temperature range becomes narrower, it becomes essential to prepare detailed thermal mathematical models for the integrated spacecraft and for the critical systems housed in the spacecraft. The size of the thermal mathematical model has increased from 17 isothermal nodes in *Aryabhata* to 450 nodes in IRS-1. The size is higher for spacecraft like INSAT II TS. Another evolving feature is the detailed modelling at subsystem levels. A detailed mathematical model was prepared for Reaction Control System (RCS) of APPLE. In case of IRS-1, detailed mathematical models are prepared for payload, battery, RCS, solar panel and yoke. In INSAT II TS, separate analysis will be made for solar sail and boom, communication payload, VHRR payload, reflectors, solar panels and propulsion systems. The thermal control systems design and analysis work becomes more and more complex as the power dissipation of the payload increases and the specified temperature range narrows down as is expected in future satellites of the IRS and INSAT series.

3.2b Thermal testing: The thermal design as well as the performance of the thermal control system are verified on ground by testing the spacecraft in a thermovacuum chamber. The effect of the sun-load, can be simulated by means of a xenon-solar simulator or IR heaters. In case of IR heaters, only the absorbed load can be simulated. The planning and conduct of test activity is quite complex due to several reasons. The accuracy of simulation depends on various factors like size of satellite in relation to chamber size, the nature of various interfaces/fixtures used in the chamber and also the extent to which shapes, surface and orbital modes are simulated. However, error in heat exchange, in simulation of cold black space by a liquid nitrogen shroud, will be less than 1%. Further, in simulating solar beams by a xenon lamp, non-uniformities along the cross-section area and collimation errors cannot be avoided. One major issue involved is the very high cost of solar simulation. Hence, trade-off considerations are involved in the use of alternate methods like IR simulation, which have limitations in accuracy especially when there are large projections on the spacecraft surface which form shadows or exchange heat locally.

In the case of *Aryabhata* and *Bhaskara*, simple scaled-down models, with heaters simulating both the external and internal heat inputs were fabricated and tested in the thermovacuum chamber. The temperature accuracy in such tests was of the order of $\pm 5^\circ\text{C}$. In case of APPLE spacecraft, solar simulation tests were conducted in an external facility. A test was also carried out using IR heaters in a 4-meter diameter chamber in India, which does not have a solar simulator. A similar approach has been adopted for IRS. A large simulation chamber of about 9 m dia, with a 4 m solar beam is being planned in ISRO for testing future spacecraft like INSAT II and follow-on IRS series.

Figure 4 illustrates the trends in the usage of thermal control elements, the testing concepts and the analysis modelling for Indian satellites.

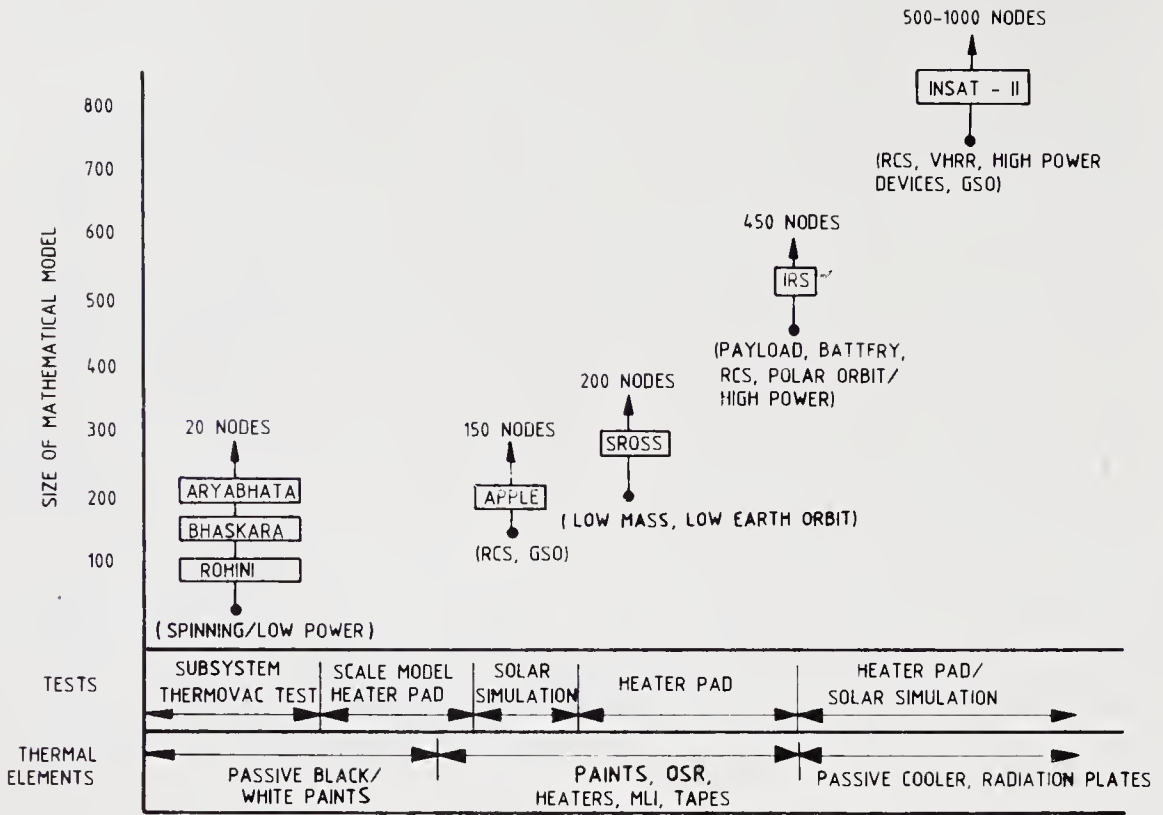


Figure 4. Trends in usage of thermal control elements, testing concepts and analysis modelling for Indian satellites. Details in paranthesis indicate the features/characteristics of the satellite systems or its orbit that have a bearing on thermal analysis and modelling.

The trend in thermal design and analysis is such as to meet the more stringent performance requirements (like smaller temperature excursions on specific subsystems, lower gradients etc) and evolving testing methodologies that result in closer simulation of actual orbital conditions and hence, more accurate evaluation of the thermal performance of spacecraft.

3.3 Spacecraft mechanisms

Spacecraft mechanisms are used to deploy systems like solar panels and antennae, which are stowed during the launch phase within the rocket heat shield and deployed subsequently in orbit. Other type of mechanisms used in spacecraft include booms which deploy instruments and unfurling mechanisms typically used for large antennae. *Aryabhata*, *Bhaskara* and *Rohini* satellites did not call for deployable elements as they had body-mounted solar panels and there were no other specific requirements. *APPLE* for the first time used a deployment system to deploy its two solar panels located symmetrically on either side.

Recently, ISRO has undertaken the design and development of deployment mechanisms for large solar panels used in its *IRS*, *SROSS* and *INSAT II* spacecraft. The mechanisms used in spacecraft like *INSAT II* carry out the total deployment of panels in a sequential manner. The *INSAT II* spacecraft also employs another

mechanism called coilable lattice boom, 14.95 m long when deployed, to correct the radiation imbalance torque generated by one-sided solar panels.

The notable challenges posed during the development of mechanisms include (i) simulation of thermal gradients at various parts of the mechanisms overcoming the difficulties involved in simulating exact boundary conditions at different places, and (ii) handling of the flexible mechanisms and conduct of zero-g simulated tests on them. On the analytical side also, these systems present complexities since the analytical models for zero-g conditions cannot be directly validated through zero-g tests, especially for mechanisms employing flexible structures. Hence, these are to be developed for 1-g conditions, validated through a test and then modified for zero-g conditions. Since most of these mechanisms are mission-critical items, they need to undergo elaborate testing to establish a high level of reliability within the constraints of simulating all space conditions.

3.4 Power system

The satellite power system has the function of generating the necessary power under different orbital and operating conditions of spacecraft as well as power conversion involving regulation and control of output to satisfy the requirements of satellite subsystems and payloads.

Power needs of Indian satellites have grown from a few Watts to the kiloWatt range. The technologies of power generation, storage and management, in response to these needs, have undergone significant improvements. While the *Rohini* series of satellites needed only 5 Watts, the INSAT II TS will call for the generation of a kiloWatt of power. Besides the magnitude of the power needed, mission-life requirements have grown from a few months to about 7 years. Varied requirements of power and mission, combined with high reliability, are the challenges to be met by the power system designer.

A satellite power system mainly comprises three major elements: power generation, storage and management. In the area of power generation, involving the use of panels with silicon solar cells, the thrust is to achieve high power per unit area, high power per unit weight, and the ability to withstand thermal, mechanical and radiation environments. Energy storage using chemical batteries to supply eclipse and peak requirements, need to have high energy storage density and long life. Power management using circuitry should achieve high system efficiency along with fault-tolerant interfaces to provide appropriate control over the generator and the storage elements.

3.4a Power generation: The basic device used for power generation in Indian spacecraft is the silicon *n/p* solar cells. In this area, efforts are directed towards improving the cell efficiency by way of development of back-surface reflector or back-surface field with reflector type cells, reliability and resistance to charged particle radiation. Technology of coverglass and cell interconnects (CIC) using indigenous solar cells have been developed in the country. Construction of a solar array involving thousands of cells is a complex process utilizing several advanced technologies. The design of solar panels has employed a rigid honeycomb structure with aluminium faceskin. Significant developments in interconnector design, solar cell welding and bonding, have been incorporated in the solar panel fabrication to

meet the stringent design goals of 24,000 thermal cycles (-100 to $+100^{\circ}\text{C}$) for spacecraft like IRS with the demand of a 3-year life. Figure 5 illustrates the evolutionary improvements in solar panel technology.

3.4b Energy storage: Presently, energy storage is achieved by secondary Ni-Cd batteries. Limited battery life constrains its design and application. Battery temperature control is very crucial for meeting the life-time requirements. This involves detailed study of the thermal behaviour of the battery under different charge/discharge conditions. It also calls for sophisticated battery charge control techniques. Another important area in battery technology is its structural design which has to be of minimum weight to meet the mechanical requirements and also to satisfy the thermal control requirements.

The design and technology for fabrication of batteries using Ni-Cd cells has been qualified for SROSS satellites. Further, simulation efforts, with much more stringent design goals for IRS and INSAT II spacecraft, are presently under way. Efforts to develop Ni-Cd cells indigenously have also been taken up in collaboration with Indian Industry.

3.4c Power management: Power management has a number of elements that include regulating the generated power, controlling the charge and discharge,

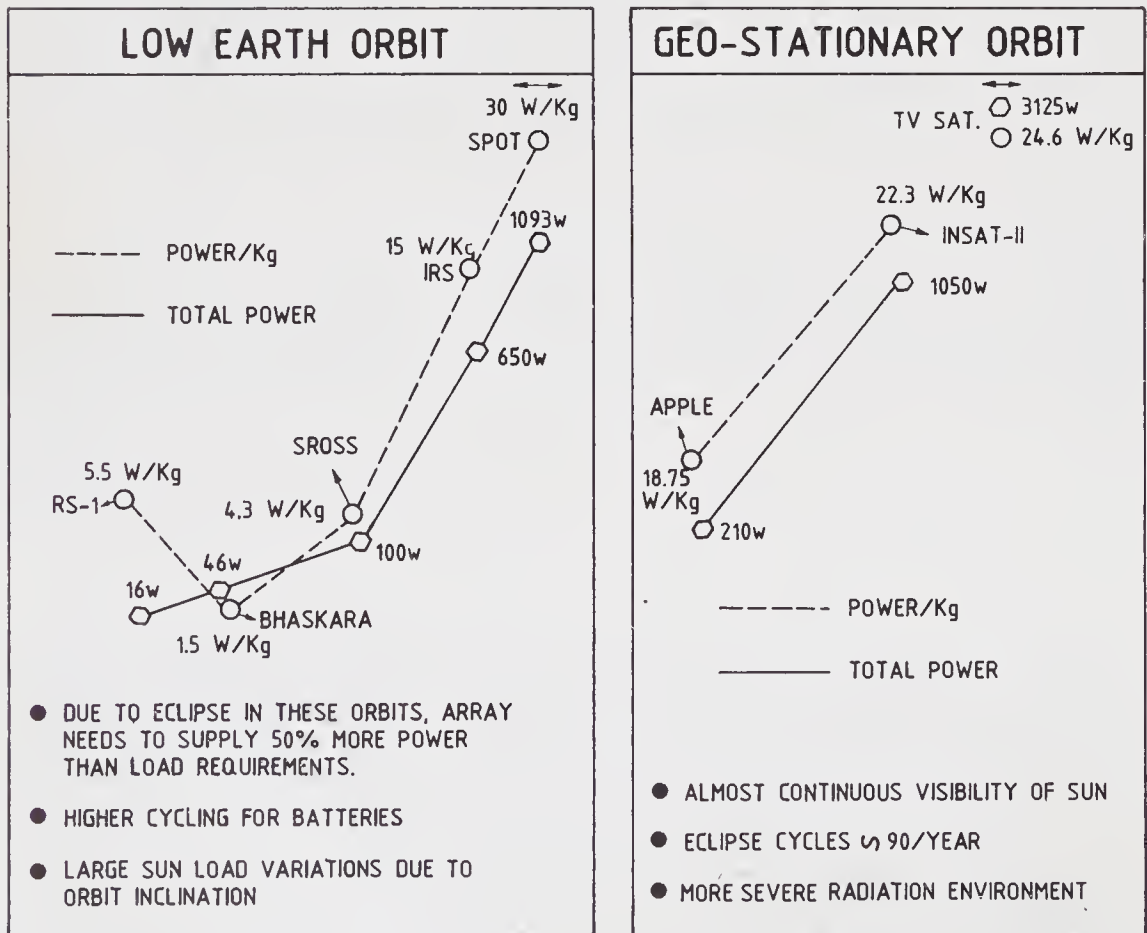


Figure 5. Evolutionary improvement in solar power systems of Indian satellites (\longleftrightarrow indicates state of art).

distributing power, meeting user requirement, providing fault tolerance and isolation against user malfunction, and monitoring of the generator and storage elements.

The modest power needs of earlier satellites like *Rohini* and *Bhaskara*, were met by a centralized system. Higher power requirements of the present generation spacecraft necessitate the development of distributed power systems employing novel techniques to achieve high efficiency, lower weight and volume, modular design and lower electro-magnetic interference. In order to perform the in-orbit battery management optimally, sophisticated battery control techniques have been developed including control of its thermal environment. For achieving battery efficiency and power density in power control, development of power inversion and AC distribution techniques at 50 Hz, 400 Hz and 20 kHz using computer-aided design techniques, is under way. Better design techniques incorporating series resonant power conversion and very low EMI, isolated CuK converter are being planned. Better packaging technologies using hybrid microcircuits have been undertaken. Modelling and analysis studies of nonlinear converters to achieve better frequency response, lower AC output impedance and higher audio susceptibility are also being taken up. Table 2 gives a summary of the trends in power systems growth for ISRO satellite missions.

On the whole, in the case of the power system, the drive is to realize highly reliable, efficient and long-life systems while keeping the increasing demands of power for satellites like INSAT II in view.

3.5 Attitude control system

Attitude control of a spacecraft (Scull 1966) is the orientation of its fixed axes with respect to a desired reference frame, thereby providing the necessary alignment for the operation of payloads, sensors, antenna and even solar panels. The relevant information about the attitude is generated by a system of sensors that sense the directions of certain well-known 'landmarks' in space such as the sun, the earth's magnetic field, the infrared horizon of the earth or some bright stars. There are at least four major elements to the design of a control system for a spacecraft. These include mission analysis, dynamic and reliability analysis, hardware implementation, and finally, testing and design evaluation.

Table 2. Power system growth for ISRO satellite missions

Spacecraft	Launch year(s)	Orbit*	Power level (W)		Solar array size (m ²)	Battery size (Amp hr)(cells) [†]	Design life (years)
			Raw	Regulated			
<i>Rohini</i> series	1980, 81, 83	LEO	16	5	0.97	1.6(12)	0.25
<i>Aryabhata</i>	1975	LEO	46	10	3.7	10(20)	0.5
<i>Bhaskara</i>	1979, 1981	LEO	47	15	3.7	10(20)	1
APPLE	1981	GEO	210	100	2.86	12(16)	2
SROSS-1	1987	LEO	100	30	7.2	12(12)	0.5-1
IRS-1	1988	LEO	650	250	8.5	2×40(16)	3
INSAT II TS	1989	GEO	1050	750	14	2×17(28 each)	7

* LEO—low earth orbit; GEO—geostationary earth orbit; [†] Values in parentheses are the number of cells in the battery.

In the mission-analysis phase, the overall mission profile, vis-a-vis, the attitude control requirements are examined. The availability of ground-support facilities and the interfaces between the on-board and the ground systems are additional considerations in mission analysis. Further, the activities include identification of failure modes, contingency procedures and the development of mission operations software compatible with the available computational facility.

Dynamics analysis is carried out for various control modes, ensuring stability for all possible mass distributions and flexibilities as well as disturbances such as gravity gradient, magnetic, solar radiation, aerodynamic, and those arising from the operation of the on-board hardware. Stability analysis is done for all possible modes including transition modes from one phase to another.

The implementation of an attitude control system has several approaches that can be broadly classified as passive, semi-passive, active and hybrid.

3.5a Earlier systems: Two of the common methods of attitude control are spin stabilization and three-axis control. Spin stabilization essentially involves spinning the satellite normally about the axis of the maximum moment of inertia and subsequent maintenance of the desired spin rate and spin-axis orientation. Three-axis control, on the other hand, involves a feedback loop for each of the axes wherein the attitude errors are sensed by sensors and the control electronics processes this information to implement the desired control laws and drives the torquing devices. Earlier Indian satellites like *Aryabhata*, *Bhaskara I* and *II*, *RS-D1* and *D2*, with body-mounted solar panels, were spin stabilized. However, as the payloads become more sophisticated, the demands on the specifications of attitude errors, body rates and jitter become more stringent. In addition, with the increase in the size and complexity of the spacecraft, the associated power requirements also increase. The natural solution to these requirements is found in the use of deployed solar panels and the 3-axis mode of attitude control. *APPLE* was India's first experimental geostationary communication satellite wherein our 3-axis control capability was first established.

3.5b Current systems: In respect of the current programmes, the 3-axis stabilization system for *IRS* is based on a 'zero-momentum' four reaction wheels configuration (with redundancy for any one wheel-failure) for the normal mode and *RCS* thrusters for acquisition and orbit control modes. Unlike the case of *APPLE*, *IRS* has a stringent specification on the platform stability of 3×10^{-4} deg s⁻¹ during the payload operation. This was perhaps the single most challenging feature in the *IRS* control system design and was eventually achieved with the implementation of a coarse compensation for the momentum coupling of the roll and yaw wheels and an extended Kalman filter which estimates the uncompensated coupling torques in addition to the attitude errors and rates. Another salient feature is the automatic detection and reconfiguration of the reaction wheel system in the event of a failure in one of the wheels, without any interruption in the control system performance.

The overall control system designed has to be fairly robust in the presence of parametric variations, noise and single-point failures, and yet has to be simple and reliable. Thus, the dynamics modelling and control system design has to be carried out with extreme care and has to be backed up by extensive computer and hardware-in-the-loop simulations, incorporating all the characteristics of the

hardware elements, nonlinearities, noise and scale factors. These simulations should embrace not only the normal mode performance but should comprehensively cover all the conceivable failure modes as well.

While the computer simulations form the heart of the overall control system design, an important concept in the design validation, particularly for high performance spacecraft like IRS entails the use of a 3-axis servotable. Here, the servotable reproduces the computer simulated motion with high accuracy. The various sensors are mounted on the servotable with earth and sun simulators and the other hardware such as the control electronics and actuators are kept in environmental chambers. The computer interfaces with these components in real time and collects all the relevant data which, in turn, are fed to the spacecraft dynamics model in the computer.

In the case of INSAT II, the control system design is a complex and innovative task. The use of a microprocessor-based system is inevitable, as it would facilitate the implementation of sophisticated control techniques as well as the safety features of automatic reconfiguration of wheels, RCS, sensors and automatic redundancy management at the subsystem level. An important constraint that has to be satisfied at all times, including during any of the complex control manoeuvres and also during any contingency operations, is that the sun should not be in the field of view of the Very High Resolution Radiometer (VHRR) cooler.

Two other major areas that have to be addressed additionally, are the effects of liquid sloshing and interaction of control with flexible structure. INSAT II during launch carries about 800 kg of liquid propellant. A detailed analysis has to be carried out to ensure that the presence of such a large amount of fluid does not introduce any adverse dynamic condition and the 'slosh' does not cause instability in any of the modes. Regarding the second aspect, with a solar sail on the north face for balancing the disturbance torques due to the action of the solar radiation pressure on the large array of solar panels on the south face, a detailed study on the control-flexible appendage interaction becomes indispensable as already stated earlier. This would essentially involve the modelling of the flexible body dynamics in terms of the frequencies and mode shapes for the flexibility modes and using this information together with the control torques to compute the reflected torques developed on the spacecraft body. The performance of the control system can then be evaluated through elaborate computer simulations.

Coming to the control electronics, the Attitude Control Electronics (ACE) does the on-board processing needed for spacecraft control and generates the control signals for driving the actuators. As the control system requirements become stringent, the ACE is required to carry out many functions involving a lot of high speed computations. Further, the system has to be versatile and flexible. Although some of the earlier spacecraft such as *Bhaskara I* and *II* and *APPLE* had entirely discrete IC-based hard-wired systems, partially microprocessor-based control electronics have been developed for *RS-D1* and *D2*, *SROSS* and *IRS* satellites. Microprocessor-based systems offer a lot of flexibility and multi-mission adaptability. "Remote programmability" feature is incorporated in the *SROSS* ACE to cope with unanticipated problems/failure modes. Microcomputer-based test systems have also been developed. To meet the large computational requirements of *INSAT II* and future satellites, bit-slice/multiprocessor-based systems incorporating fault tolerance and auto-reconfiguration features are under development.

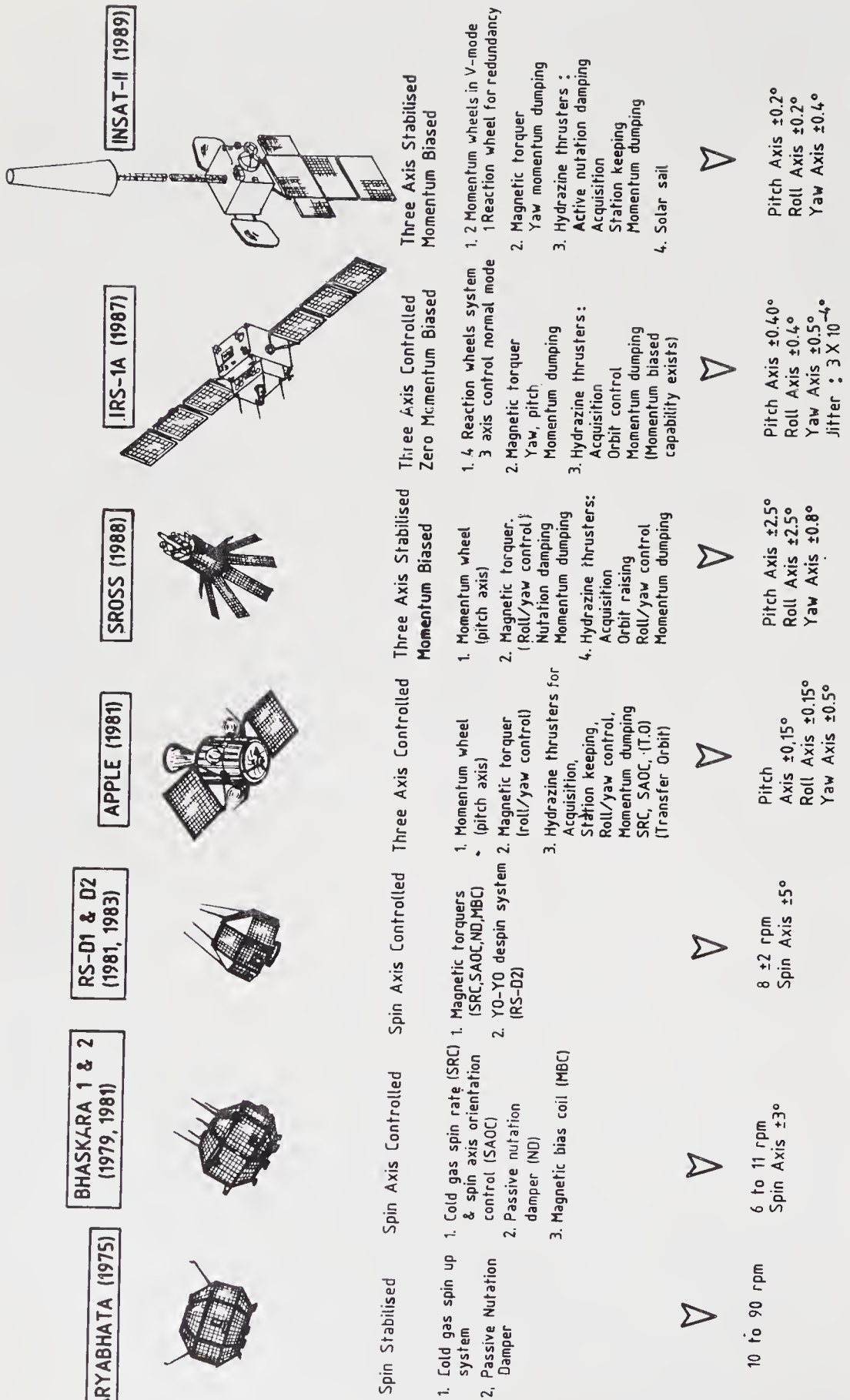


Figure 6. (a) Technology evolution of control systems for ISRO spacecraft

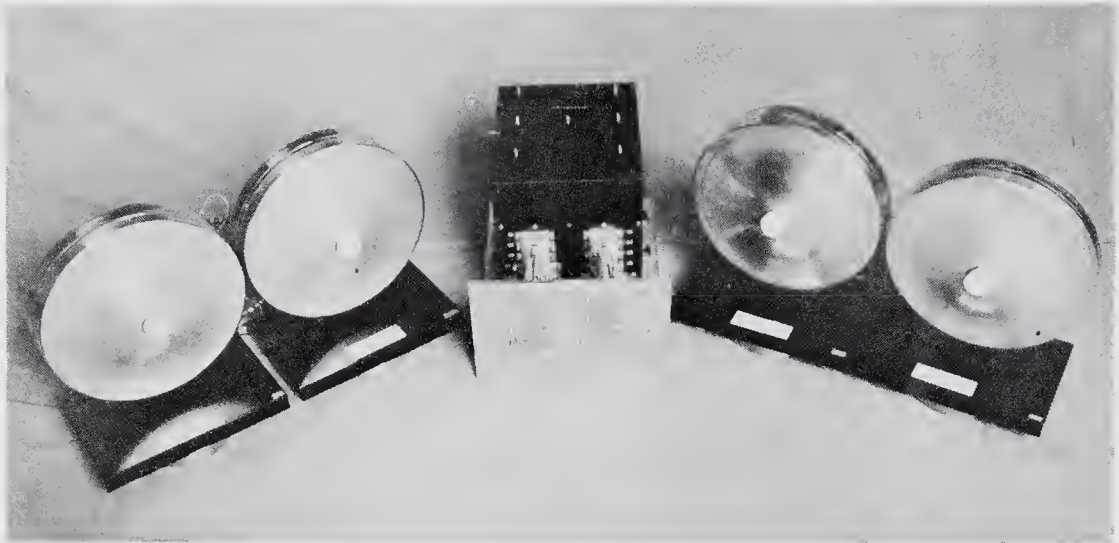


Figure 6. (b) Photograph of reaction wheels used in IRS.

Finally, mention should be made of the ISRO developments on some of the control system actuators like reaction wheels (RW), momentum wheels (MW), magnetic torquers, nutation dampers and reaction control systems (RCS). Magnetic torquers and nutation dampers were used in earlier satellites like *Bhaskara* and *Rohini*. APPLE additionally used a 20 Nm momentum wheel. IRS and INSAT II will employ reaction wheels. The technology of wheels involve those related to bearing, lubrication, high reliability motors etc. Studies on problems of cage instability, involving bearing assembly in a cage, form an important aspect of development as also those related to long life dictated by design and implementation strategies for bearing and lubrication. The reaction control system is separately dealt with elsewhere in this paper.

Figure 6a shows the technology evolution of the control systems for ISRO spacecraft. As is evident, the drive is towards a higher degree of pointing accuracies, low jitter and drift rates and long life systems.

3.6 Attitude sensors

Attitude sensors (Singer 1964) are used for deriving information on the orientation of the satellite axes in space for control purposes and also for interpreting the data from the scientific and application experiments on board. Attitude sensors can be electro-optical, magnetic, electromagnetic or inertial.

Figure 7a shows the progressive sophistication in the attitude measurement of ISRO spacecraft involving the use of more accurate and precise attitude sensors.

3.6a IR horizon sensors: The technology of the horizon crossing earth sensor, compatible with the state-of-art, is well-established in ISRO and such sensors were flown in *Bhaskara*, *Rohini* and APPLE missions. Another sensor, called a Conical Horizon Sensor, is derived from the horizon crossing sensor by incorporating a scanning mechanism so that in a non-spinning satellite such as a three-axis stabilized satellite, the sensor can sense the horizon crossing. The scanning mechanism is provided by a germanium wedge which is rotated by means of a

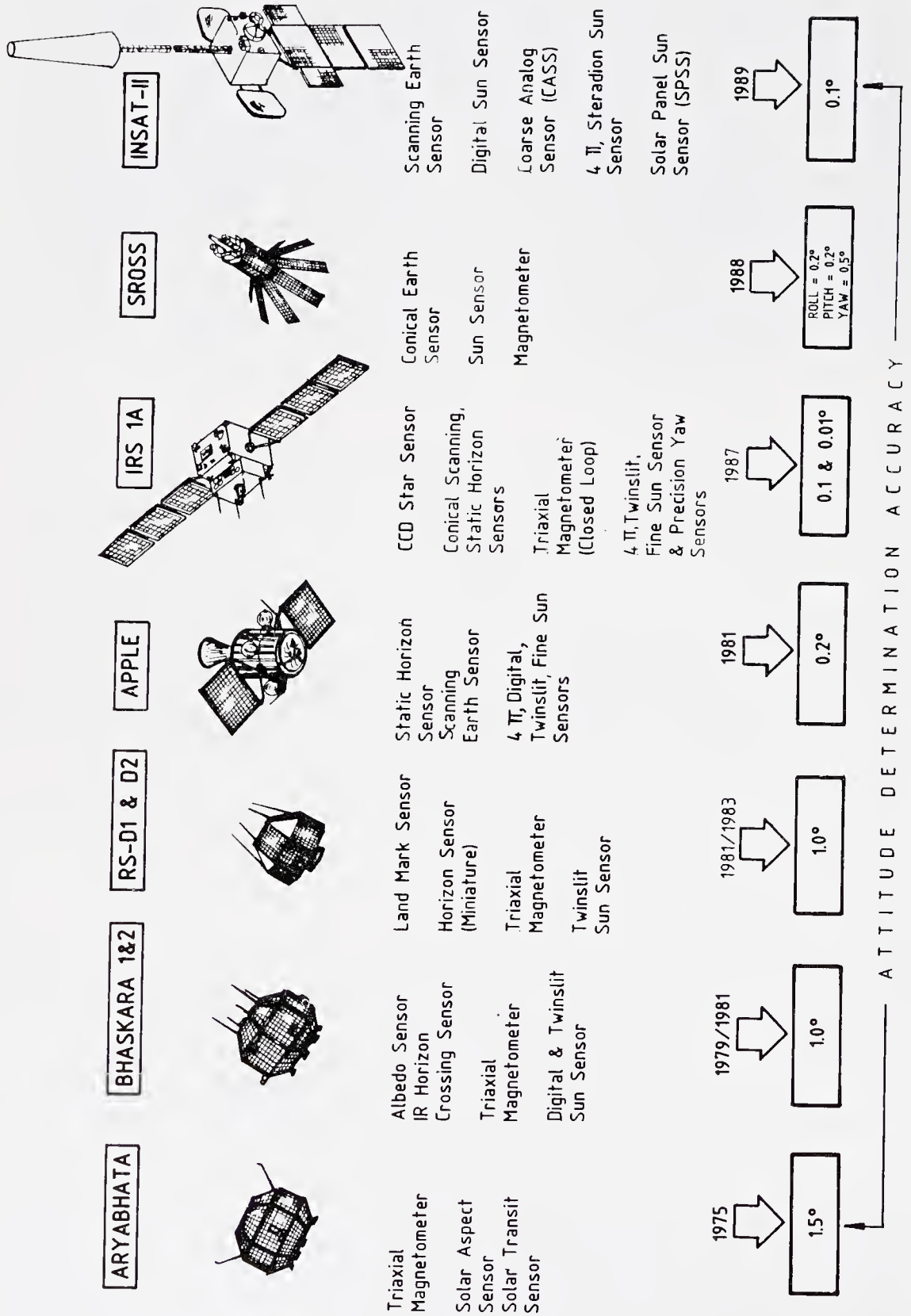


Figure 7. (a) Development trends of attitude sensors.

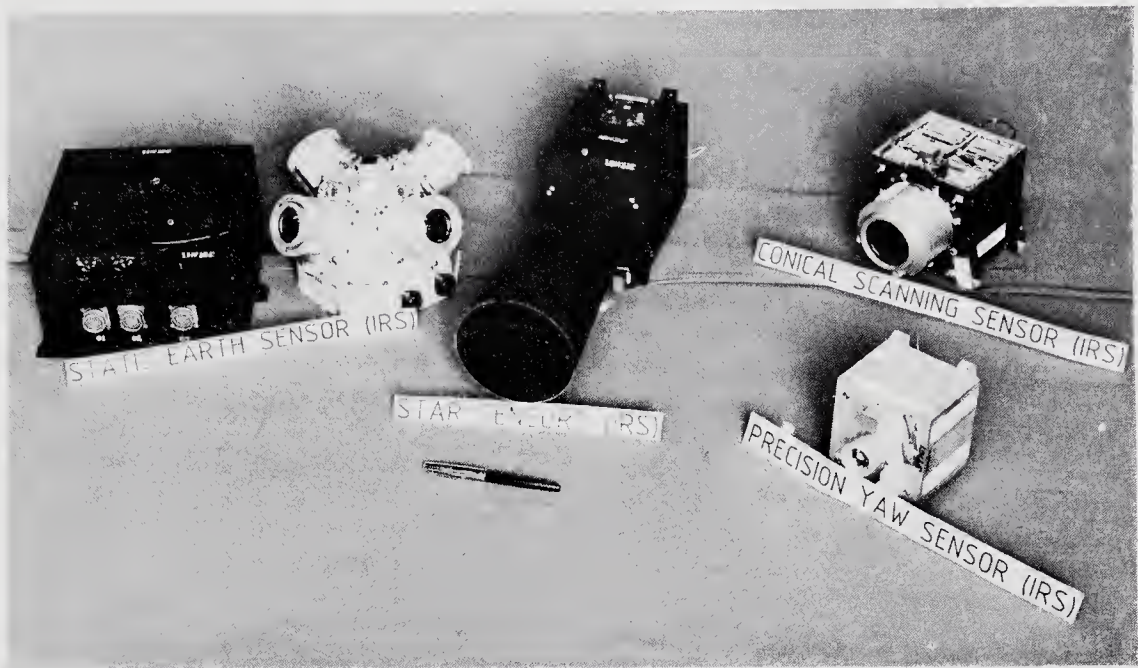


Figure 7. (b) Photograph of some of the ISRO-developed attitude sensors.

brushless d.c. motor. Sealed angular-contact duplex bearings are used in the system to ensure smooth uniform rotation with minimum oil vapour contamination on the optical elements. An angle encoder is incorporated to measure the earth pulse width to an accuracy of 0.01° . The sensor is hermetically sealed to avoid evaporation of bearing oil and special feedthroughs are used to carry the IR detector signal to the processing electronics. Such a sensor has been developed for IRS.

Problems of mechanical scan motion and its associated reliability concerns can be avoided by using an alternate type of sensor called the static horizon sensor which uses four infrared telescopes viewing four symmetrical points at the periphery of the earth. By radiometrical balancing, a null is established and deviations in this represent roll and pitch errors. Thermopile detectors of special geometry are used as the sensing devices. Since the energy of the earth signals is far less than that radiated from the telescopes to space an accurate thermal analysis is required to detect the earth signal. Precise thermal control is maintained on the sensor telescope and a division technique is used to cancel the effect of variation of radiation in the 14 to 16 micron band due to the seasons. Besides this, extremely low drift d.c. amplifiers and low noise processing electronics are used which give a very low noise output. The only disadvantage of such a sensor is its inability to cover a wide angular range and its susceptibility to extreme thermal transients. One such sensor was flown in APPLE and another has now been developed for IRS.

While for a low earth mission, a rotating wedge could be used to scan the earth as in a conical sensor, for a geostationary mission, it is not worthwhile to scan 360° since the earth subtends an angle of only 17° . Instead, it is preferable to scan more often using a scanning mirror and average the noise by collecting more samples. Such an approach is used in a scanning earth sensor which uses a metal scanning mirror in front of a horizon sensor. The scan motion is provided by means of a scan

drive and it is suspended on a torsion bar. A high precision angular encoder with corresponding optics generates pulses at 0.008° of the motion. The earth-pulse width is measured by using the pulses from the encoder. The encoder used in the sensor is based on the Moire fringe technique and is more complex since the scanner motion is sinusoidal unlike in a conical scanner where the speed is uniform. Also, the scanner views two chords of earth by two detectors in the image plane. This is carried out using specially fabricated small bolometers as detectors and low aberration aspheric germanium optics. Such a sensor is planned to be used in the INSAT II series of spacecraft.

3.6b *Star sensors*: High accuracy attitude determination requires a star sensor rather than an earth sensor due to the inherent limitation of edge sharpness of the IR radiation of earth. A star, being a point source, is very well-defined and serves as an accurate reference. IRS uses a star mapper which maps the sky in an 8° belt once in every orbital period of 103 minutes. Stars upto the 5th magnitude are detected and then the position information is passed on to ground which is used for precision attitude determination. The sensor uses catadioptric high speed optics and a 2048 element CCD detector. The CCD is cooled to -20°C by means of a thermo-electric cooler to reduce the dark current noise of the device. This sensor is novel in concept since it uses a linear array instead of an area array.

3.6c *Inertial sensors*: Highly accurate measurements of angular rate and angle of spacecraft call for the use of inertial sensors. The inertial sensor measures spacecraft attitude in the inertial frame of reference. It comprises a spinning wheel which maintains its inertial orientation in the absence of applied torques. Spacecraft motion about the gyro's input axes causes the gimbal supporting the spin axis to precess about the output axis. The measured value of the gimbal rotation about its output axis is proportional to the angular displacement of the gyro. A two-degree of freedom dry-tuned gyro has been developed for use in IRS. The gyro uses extremely high precision fabrication techniques and microprocessor-based temperature compensation and rebalancing techniques to avoid drift build-up. However, it needs correction once every few hours to reset the drift error to zero.

In a nutshell, a variety of attitude sensors with different characteristics and levels of accuracies have been developed for ISRO satellite missions.

3.7 Propulsion system

Propulsion (Berry 1984) is needed for the orientation (attitude control) and positioning (orbit control) of spacecraft after delivery into its nominal orbit by the launch vehicle.

ISRO has developed/under development four types of propulsion systems. The first one involves a simple cold gas system. The second uses a hybrid system of solid and liquid rockets. The third type employs monopropellant hydrazine, whereas the fourth is a unified propulsion system using fuel (monomethyl hydrazine) and oxidizer (N_2O_4). This is depicted in figure 8.

Aryabhata used a propulsion system that spun up the satellite to 90 r.p.m. by expelling dry air through two nozzles in a single shot blow-down mode by opening a single gas bottle containing 1 kg of dry air. Six gas bottles with a total fuel mass of

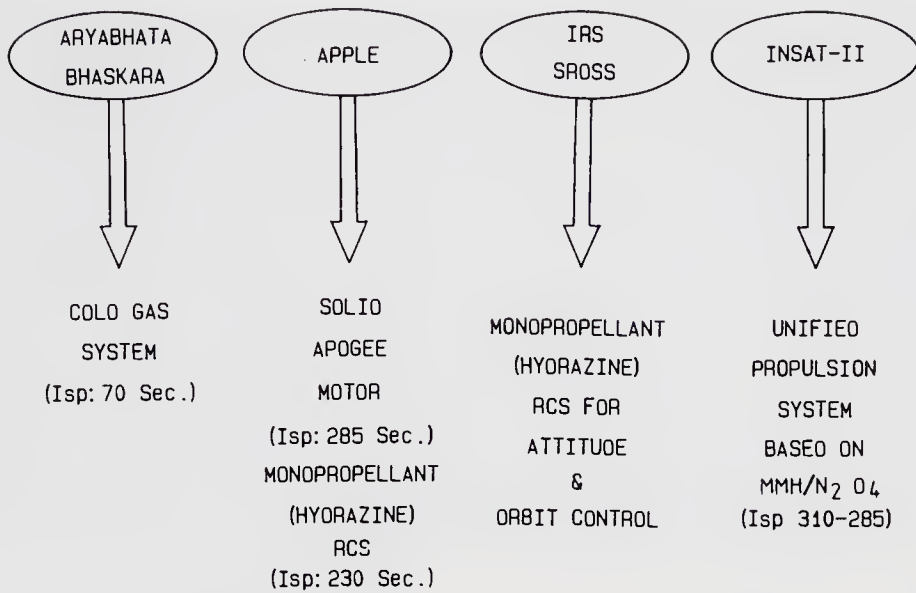


Figure 8. Propulsion technologies for ISRO spacecraft.

6 kg were provided. *Bhaskara* went for a higher level of sophistication using essentially the same hardware as *Aryabhata* but providing for intermittent spin-rate and spin-axis control. APPLE used two types of propulsion systems, a solid propellant motor for apogee boost operations and a hydrazine monopropellant RCS system for transfer orbit attitude control, 3-axis attitude acquisition, on-orbit roll/yaw control, momentum dumping and station keeping.

Figure 9a shows a schematic of the monopropellant hydrazine propulsion system used in IRS. Monopropellant hydrazine systems derive their energy (typically their fuel having a specific impulse of 230 s) from the thermal decomposition of hydrazine (N_2H_4), a liquid propellant. The decomposed hot gaseous products (nitrogen, and ammonia) can be expanded in the nozzle of a thruster to convert their thermal energy into the kinetic energy of the exhaust stream. N_2H_4 contained in tanks is fed under pressure to the engine through electrically operated, isolating, latching valves. A flow control valve allows propellant flow into the decomposition chamber where it is catalytically decomposed into hot gaseous products to be subsequently expanded through a nozzle. IRS carries 80 kg of hydrazine propellant for a 3-year operational life.

In the development of hydrazine-based RCS systems for IRS and SROSS, several elements were involved. These included a thruster engine, storage tanks, a feed system and flow control valves. All these employ a variety of materials like stainless steel (SS 304 series) and titanium alloys involving a variety of fabrication techniques including EDM, vacuum brazing, electron beam welding etc. In addition to these, development and use of propellants, special elastomers and catalysts posed quite a high degree of technological challenge. For example, techniques of loading the catalyst required special pre-conditioning to overcome the problems of reduction in specific surface as well as increase in pore volume and pore radius during extended operations beyond 500°C.

Further, in the case of development of engines with 1 Newton thrust, realization of injector configuration with the necessary splash plate and diffuser screens called for a high order of skill. The hardware has to successfully withstand repeated

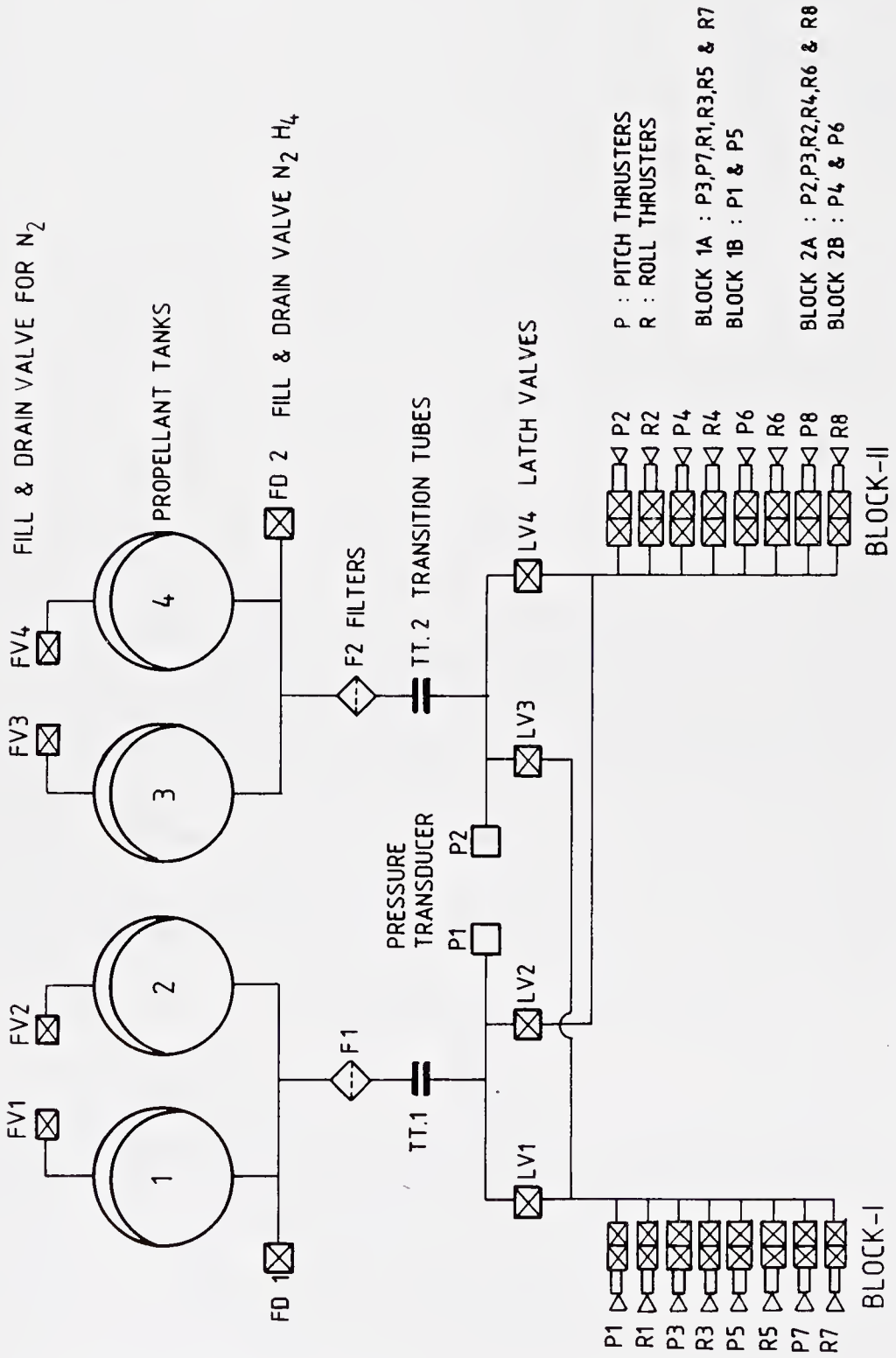


Figure 9. (a) Schematic of monopropellant hydrazine propulsion system used in IRS-1 satellite.

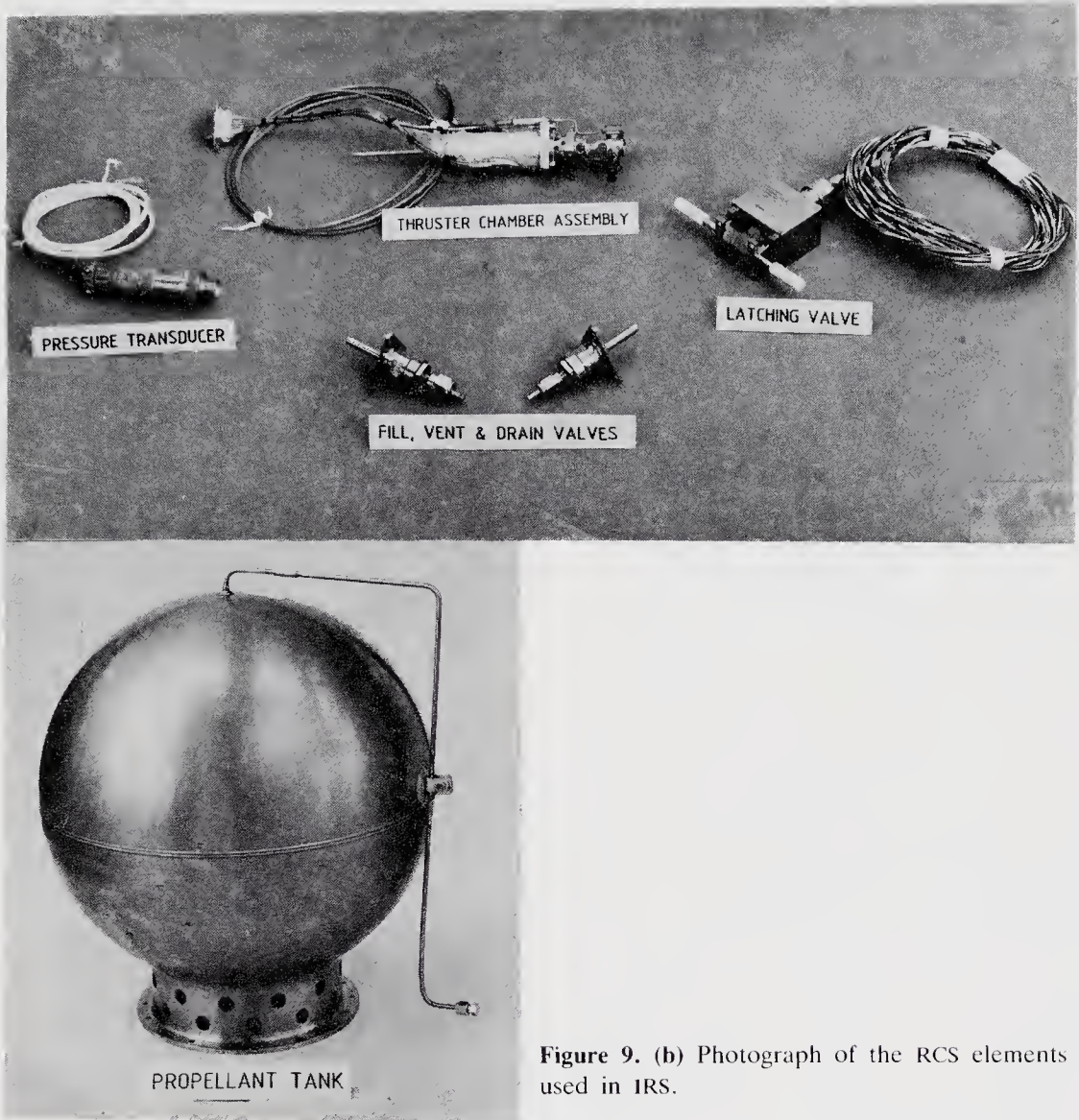


Figure 9. (b) Photograph of the RCS elements used in IRS.

thermal shocks from a number of firing operations that total half a million in a mission life of 3 years. Similarly, the flow control valve which accompanies the thruster calls for highly optimized designs with respect to the power, weight and capability to successfully withstand the corrosive environment of hydrazine over 10^6 operation cycles.

In the case of heavier satellites like the INSAT II series, the propellant requirements are in the range of 850–900 kg out of a total lift-off mass of around 1850 kg. To reduce the mass of the propulsion system for this class of heavy satellites, a more efficient system is required. It is in this context that N_2O_4 and monomethyl hydrazine (MMH) based bipropellant technology is being developed. Such a fuel-oxidizer combination can provide specific impulses in the range of 290–340 s depending on thrust level. This increase in performance over N_2H_4 (230 s) gives substantial mass reduction although it involves significantly increased system complexity. Figure 10 shows a schematic of the propulsion system of INSAT II.

The technology challenges involved in the development of this system are many and varied. Delivery of propellant under zero gravity conditions and against

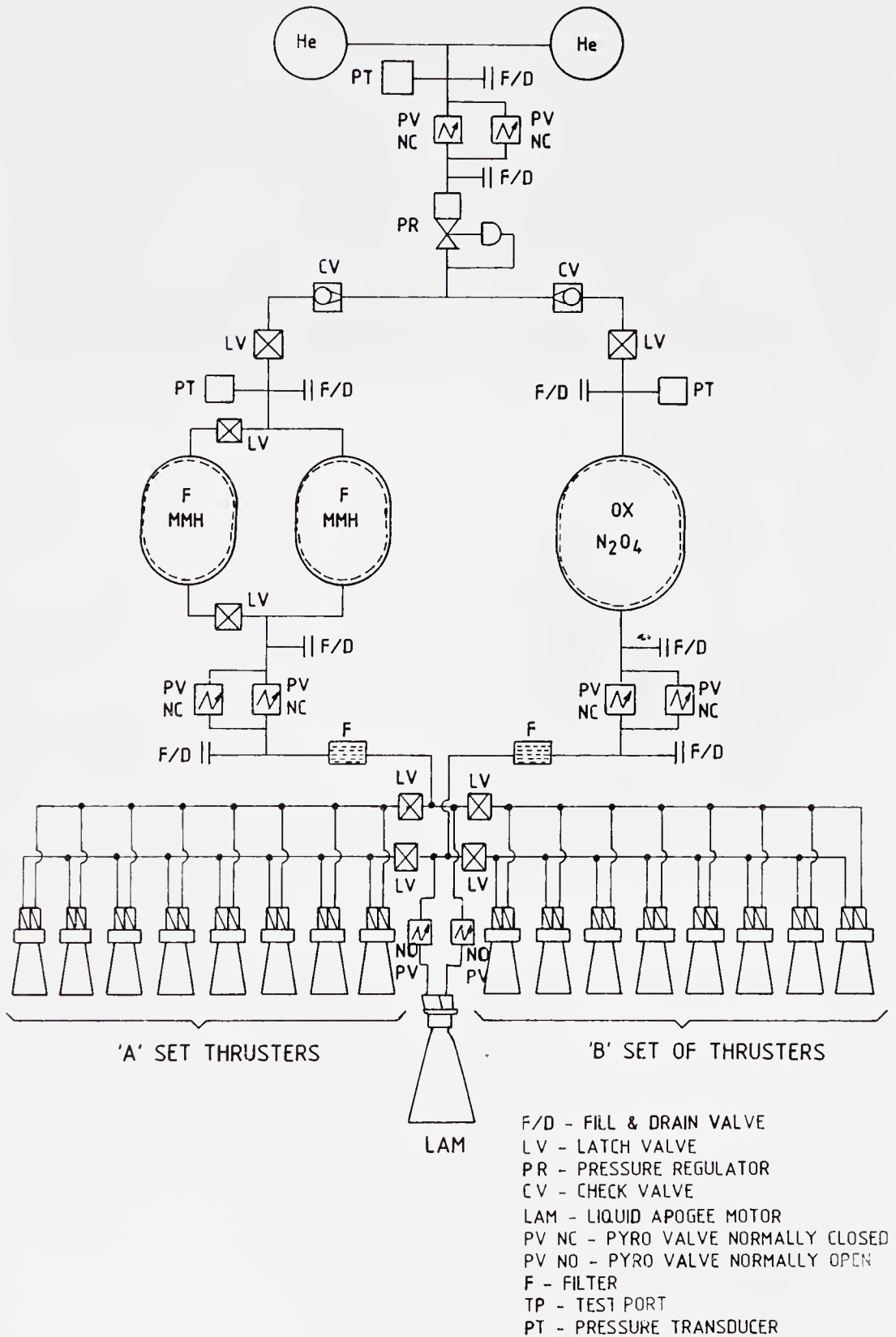


Figure 10. Schematic of unified propulsion system adopted for INSAT II.

micro-gravity induced by on-board thrusters is one example. Positive expulsion devices like bladders developed for the hydrazine system cannot be effectively utilized for long-life oxidizer systems because of material incompatibility issues. Passive devices for propellant acquisition by surface tension effects and for feeding it on demand, imply a new technology. Fabrication of thin walled Ti-tanks (of 1 mm wall thickness and 1000–1500 mm length) is a real challenge in terms of precision machining, vessel cleaning, welding and heat treatment. Storing of corrosive fluids over 7 to 10 years of life without contamination calls for good understanding of corrosion chemistry and the micro-structure of materials. Intense efforts are needed in many directions to (i) understand fluid dynamics behaviour under reduced gravity conditions, (ii) develop devices to acquire the propellant at the outlet, (iii) design systems that are weight-optimized and are easy to test, (iv) understand the propellant reaction on the materials chosen and develop the process accordingly, and (v) develop highly reliable and workable fabrication process and assembly techniques. Design, development and qualification of a 440 N engine for orbit-raising is another major effort for INSAT II.

Figure 11 shows a summary of the varied technological issues and challenges that are being currently addressed in the development of spacecraft propulsion systems in ISRO.

3.8 Spacecraft telemetry, tracking and command system

The telemetry, tracking and command (TTC) system in a space mission performs three primary functions, namely, telemetry, telecommand and tracking. The information gathered from the experiments, various auxiliary on-board instruments as well as from the spacecraft functioning itself is normally processed suitably and

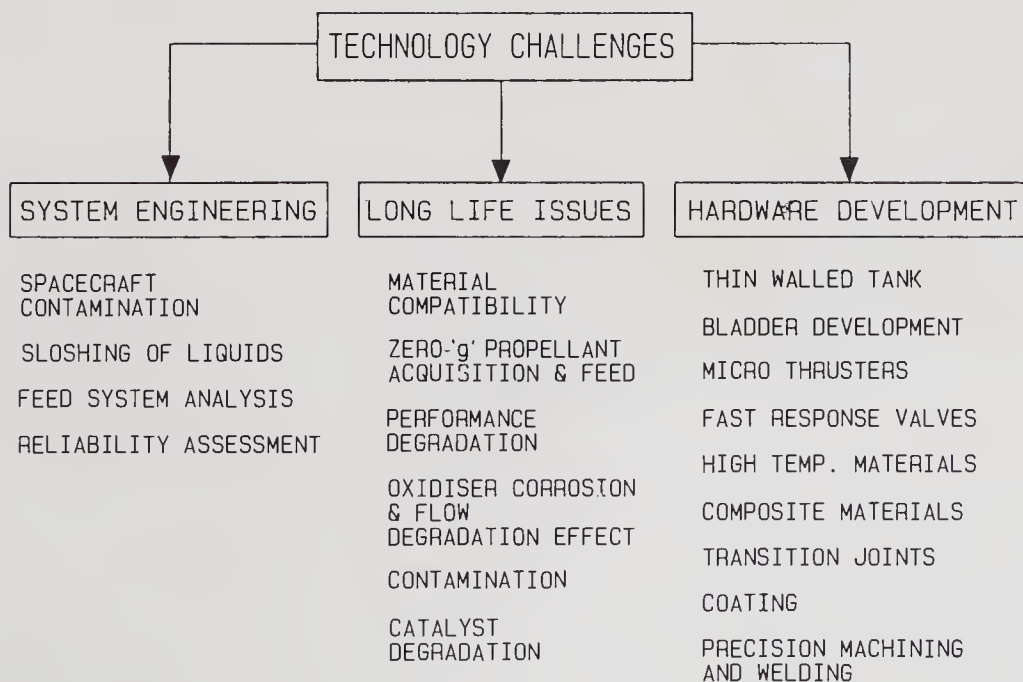


Figure 11. Technological issues and challenges being addressed in spacecraft propulsion systems development.

transmitted to a ground station via satellite telemetry. The telecommand system enables the exercise of control on the spacecraft from a ground station. Operations such as putting the spacecraft in different functional modes and correcting any in-orbit anomalies are carried out using this system. Determination of the location of the satellite at different times during its orbital motion is made possible by the tracking system. The TTC systems in ISRO spacecraft have evolved from the use of lower frequencies like VHF to those in the S band (1.55–5.2 GHz) to provide for higher accuracies, higher performance standards and for compatibility with international tracking networks. The current systems are also configured to provide for simultaneous commanding and ranging in uplink, and telemetry and ranging in downlink, by providing adequate transponder band-widths and by proper choice of telemetry, command bit rates and subcarrier frequencies to prevent mutual interference in the presence of ranging tones. The need for meeting higher tracking accuracies of about 10 m in range and 0.1 m/s in range rate is achieved through the design of a coherent S-band transponder and through the use of higher frequency tones in most recent satellites like the IRS. In order to achieve isotropic response for antenna, null filling antennae are provided in addition to the main antenna both for up and down links.

The telemetry systems used in ISRO spacecraft have evolved technologically in time to provide better reliability, flexibility and growth in performance. The number of channels monitored in spacecraft have risen from 90 in *Aryabhata* to around 600 in INSAT II (table 3). Current telemetry systems in ISRO spacecraft match the state-of-art through incorporation of multiple format capability to cater to the needs of different phases of the mission, like the satellite acquisition phase, normal operation phase etc., through the use of microprocessors. It also facilitates monitoring at higher sampling rates, any physical parameter on the satellite in the 'dwell' mode. The current systems also incorporate solid state memories in place of on-board tape-recorders to facilitate the recording of satellite health data when the satellite is in regions beyond the visibility of ground stations and to transmit them during subsequent visibility over a ground station.

With the advent of the operational era, ISRO has to develop data-handling systems for high-bit-rate data in the range of several megabits per second from its payloads, such as remote sensing cameras. The designer is faced with the challenge of incorporating appropriate synchronization codes and formatting provisions with the aim of minimizing the loss of data due to bit errors/slippages, and to facilitate identification and retrieval of data from different payload cameras along with auxiliary information to aid data processing. Communication systems in the X band (5.2–10.9 GHz) have been developed with quadri phase shift keying (QPSK) modulation schemes for transmitting high data rates (~ 25 million bits per second in the case of IRS-1) in remote sensing satellites like IRS.

The telecommand systems of ISRO spacecraft had to cope not only with growth in the capacity but also with diversity in services. *Aryabhata* had 35 ON/OFF commands. For IRS spacecraft the command system caters to 385 ON/OFF commands and 21 data commands which offer considerable flexibility in payload operations. The command system also generates commands for placing the spacecraft in the 'safe mode' in case of certain emergencies. Command systems have also been designed to perform certain automatic operations, for example, in the thermal control of the spacecraft.

Table 3. Growth and evolution of features of telemetry systems

Name of satellite	Total number of channels monitored	Salient features
<i>Aryabhata</i>	91	Multiplexer (MUX) – analog switches and counter controlled Analog-digital converter (ADC) – hard-wired Inputs – unipolar only Modulation – PCM/FM
<i>Bhaskara I and II</i>	422	MUX – 8-channel analog multiplexer devices and counter controlled ADC – hard-wired Inputs – unipolar Modulation – PCM/FM
APPLE	374	MUX – 8-channel analog MUX devices and counter controlled ADC – hard-wired Inputs – unipolar and bipolar Modulation – PCM/FM Dwell mode for selected channels
IRS	715	MUX – 8-channel analog and digital multiplexers and PROM controlled and distributed in panels Inputs – unipolar and bipolar ADC – bipolar module Modulation – PCM/PSK Multiple format and dwell mode for any channel
SROSS	325	MUX – 8-channel analog and digital multiplexers, controlled by (i) PROM, (ii) processor Inputs – unipolar and bipolar ADC – bipolar module Modulation – PCM/PSK Multiple format and dwell facility
INSAT II	Around 600	MUX – 8-channel analog and digital multiplexers and controlled by processor Inputs – unipolar and bipolar ADC – bipolar device Modulation – PCM/PSK Dwell of any selected channel

Some of the future directions for evolution of TTC systems include the development of high-bit-rate PSK modulated command systems, encrypted systems for higher security, internationally compatible packet telemetry and command systems, high gain coding systems incorporating convolutional coding, on-board data compression techniques and on-board fault-tolerant processor systems.

3.9 Assembly, integration and tests

The assembly, integration and test (AIT) operation involves integration of various systems in a satellite including its payload and ensuring of proper interfaces among them, both electrically and mechanically. The major tasks in achieving it call for a multi-disciplinary approach and include the design of an optimum layout for the subsystems of the satellite within the weight, volume and access constraints and development of an optimum electrical harness to interconnect the subsystems. Evolution of safe and reliable procedures for handling, assembly, and testing, as

well as development of hardware to meet the requirements of such procedures, are important functions associated with it. The AIT tasks demand special analytical and engineering skills for measuring and ensuring physical and electrical parameters like inertia, dynamic balance, alignment, electromagnetic compatibility and interface control. Many systems like dynamic balancing machines, centre of gravity and moment of inertia measurement systems have been designed and developed by ISRO to meet the specific requirements for satellites. Specific safety methods have also been evolved for handling and carrying out hazardous operations like fuel filling and pressurisation.

For building up operational grade spacecraft, the bulk of the experience gathered in the experimental *Bhaskara* and APPLE projects provide the infrastructural base. However, both IRS and INSAT II platforms are more complex and are designed for far more extensive tasks. The complex interplay between the platform subsystems and payloads (high resolution cameras in IRS and a large number of multifunction transponders and VHRR in INSAT II) demand a high degree of interactive design for the configuration layout and also rigorous test plans backed by analysis of in-orbit functional modes. Assembling of large spacecraft with tight control of contamination demand large professional-grade clean rooms and mechanical assembly halls. Simple manual assembly and spacecraft handling techniques cannot cope with the demands of large-sized spacecraft like IRS (950 kg) and INSAT II (1850 kg). Mechanisation, automation and built-in safety measures are to be incorporated in the design of handling and integration fixtures.

The second generation INSAT II satellite, for example, presents a higher degree of complexity for system integration. It carries 20 communication and broadcast transponders and a very high resolution radiometer operating in visible and IR bands, designed to serve for seven years. The three-axis stabilized platform fitted with deployable solar panels, solar sail and earth-viewing antennae, with a power generation and dissipation capacity of the order of 1 kW, presents a host of thermal and electromagnetic incompatibility problems. Coupled to this are the configuration constraints that restrict mounting area to 8.2 m² which is 8% less than that in INSAT I. Computer-aided approaches for subsystem layout design, electronic housing design, wire routing diagrams, and mass property estimates, become inevitable for handling integration-related problems. Interface data acquisition, control and dissemination also need to be computerised.

Detailed ground checkout procedures are drawn up and a dedicated and fully automated test set-up is configured for the conduct of error-free testing and logging of the results, logical sequencing, simulation of in-orbit functional modes and testing of transfer orbit/on-orbit control loops, during the process of AIT and prior to shipment of spacecraft. For transportation of the current generation spacecraft, a transportation system with a controlled environment is necessary for effective exercise of contamination control and to safeguard against hazards during transit. Similar procedural sequences and ground checkout test plans are drawn up for the operations during the integration of the spacecraft with the launcher as well as just prior to launch.

4. Reliability and life-time related issues

In the era of operational satellites, the realization of the highest planned reliability

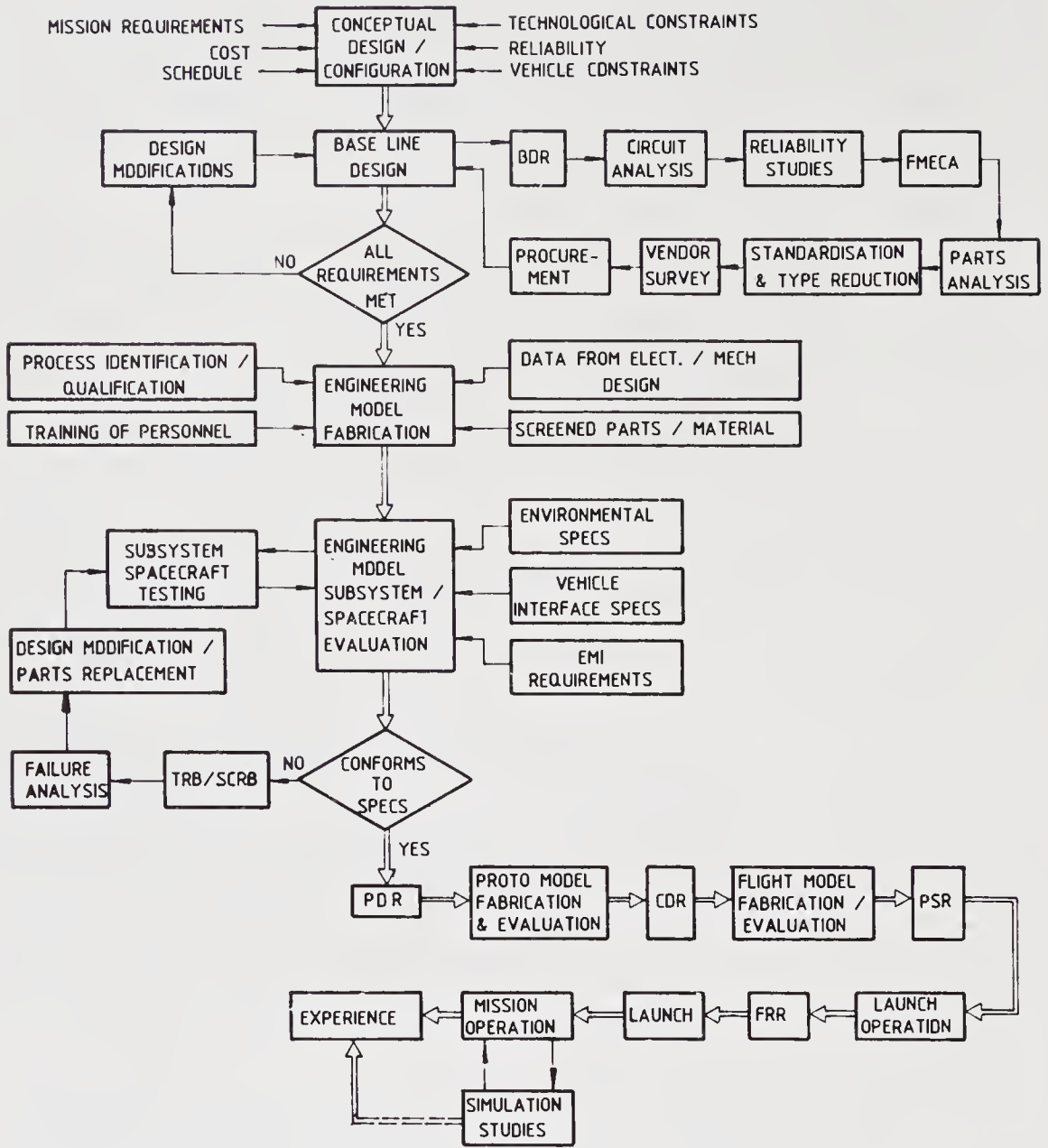
levels during the design life times of the satellites is the crucial factor determining the success of a mission. Planned life times for the IRS class of near-earth orbiting satellites are 2–3 years, whereas the corresponding value for the geosynchronous INSAT II class is 7 years. Contrast this with the earlier missions like *Aryabhata* or *Bhaskara*, that had planned life times of the order of 1 year and the APPLE communication satellite with its 2 yr life.

Reliability and quality aspects (R and QA) for ISRO satellites have undergone continuous evolution with the objective of realizing the state-of-art reliability levels. For example, the *Bhaskara* satellite had an estimated reliability of 0.55, whereas the reliability goal for INSAT II TS is 0.75 at the end of its 7 yr life. Quality and reliability aspects are brought to bear on several facets of satellite project activity that include choice of proper materials and components, well-defined fabrication methodologies, rigorous test and evaluation plans at subsystem and system levels, as well as carrying out analyses such as fault-free analysis, and failure-mode effect and criticality analysis (FMECA), that could provide valuable inputs to satellite design. Further, conduct of design reviews and instituting mechanisms for analysis, the review and the taking of appropriate corrective measures for problems and failures encountered during the various phases of the development of the satellite, form another important component of quality and reliability efforts.

In earlier experimental satellites like *Aryabhata* and *Bhaskara*, in view of the cost and time considerations, coupled with the fact that the goal was to gain experience in different methodologies for carrying out a satellite mission, MIL-STD-883 class of components were used, as also many other non-standard parts and materials. The tests were generally restricted to thermovacuum environments at subsystem and system levels and vibration only for sinusoidal specifications. In the case of APPLE, besides the use of class S radiation hardened components for the first time, solar simulation and thermal balance tests were carried out. Further, in these experimental programmes, FMECA and other reliability related analysis provided only limited inputs during design phase as the related methodologies had to be evolved as part of the programme.

In the current satellite programmes of IRS and INSAT II TS, based on previous experience and taking cognizance of the operational nature of the missions, comprehensive procedures in respect of R and QA have been drawn up. This is depicted in figure 12. Inputs from R- and QA-related aspects are ensured in all phases of the project, i.e., during the design, development and testing phases. Selection of high-reliability electronic components including screening and upgradation where necessary, use of approved standard materials, introduction of random tests to complement sinusoidal vibration tests at subsystem and system levels, doing acoustic tests at the system level and carrying out solar simulation tests to validate thermal balance aspects of the design at the engineering model level are some of the highlights of the current R and QA efforts in ISRO satellite projects. With the expected commissioning of the 9 m large space simulation chamber by 1988, solar simulation tests will be extended to flight models of all future IRS and INSAT II satellites.

Another major issue to be reckoned with in long-life satellite missions is the identification of factors that limit the life time, and the evolving of a suitable action plan to cope with the same, through possible solutions to improve the relevant



- BDR = BASELINE DESIGN REVIEW
- PDR = PRELIMINARY DESIGN REVIEW
- CDR = CRITICAL DESIGN REVIEW
- TRB = TEST REVIEW BOARD
- SCRB = SPACECRAFT REVIEW BOARD
- FRR = FLIGHT READINESS REVIEW
- PSR = PRE-SHIPMENT REVIEW

Figure 12. Reliability and quality assurance functions in a spacecraft programme.

critical elements. The main causes of limitations of the satellite life-time are depletion of consumables like the propellant in the RCS system, the slow performance decrease due to wear-out of susceptible parts like lubricated bearings, random or graceful degradation of components, the human error and obsolescence of the mission. Whereas, it is not possible to discuss all the related details in the paper, an idea of the pertinent aspects such as the limiting causes, the subsystems

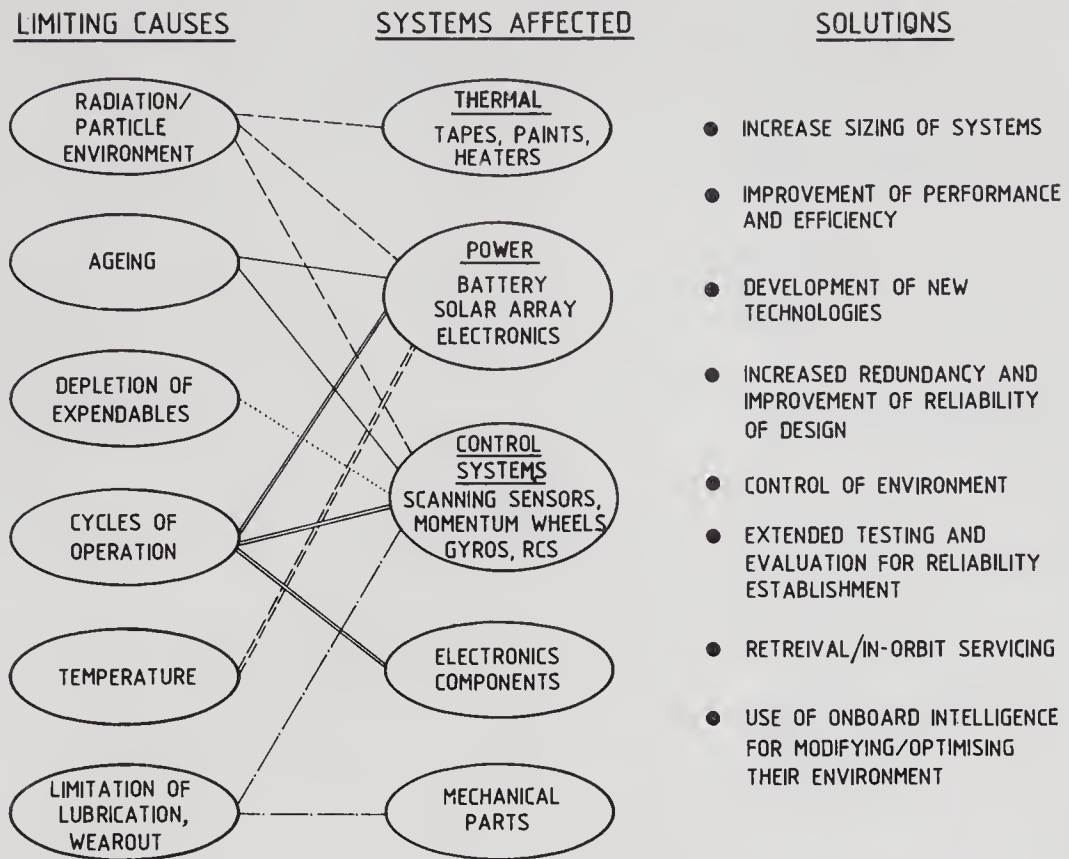


Figure 13. Impact of long life requirement of spacecraft on their technological and systemic aspects.

that get affected by such limiting causes and possible solutions, can be got from figure 13. Suffice it to say that in the developmental plans of IRS and INSAT II satellites, these factors have been carefully addressed and the related action plans have been carefully addressed and the related action plans have been integrated suitably into design, development, qualification and testing phases.

5. Mission planning and operations

A space mission as mentioned earlier, encompasses the space, ground, and operational segments. Detailed definition of the mission elements involves translation of the objectives of the mission into space, ground and operational requirements, and integrating them into an operational system to provide the required services to users. This is illustrated as a block schematic in figure 14 wherein the Indian remote sensing satellite mission is taken as an example. Starting from the mission objective of collecting and disseminating space imageries, mission analysis will be carried out to choose the orbit and identify attitude stabilization requirements, the type of launcher, as well as spacecraft power, thermal and control requirements, data transmission system and ground segment, inclusive of mission control and imagery processing. As the next step, the required hardware and software are developed and integrated. The planning includes elements of

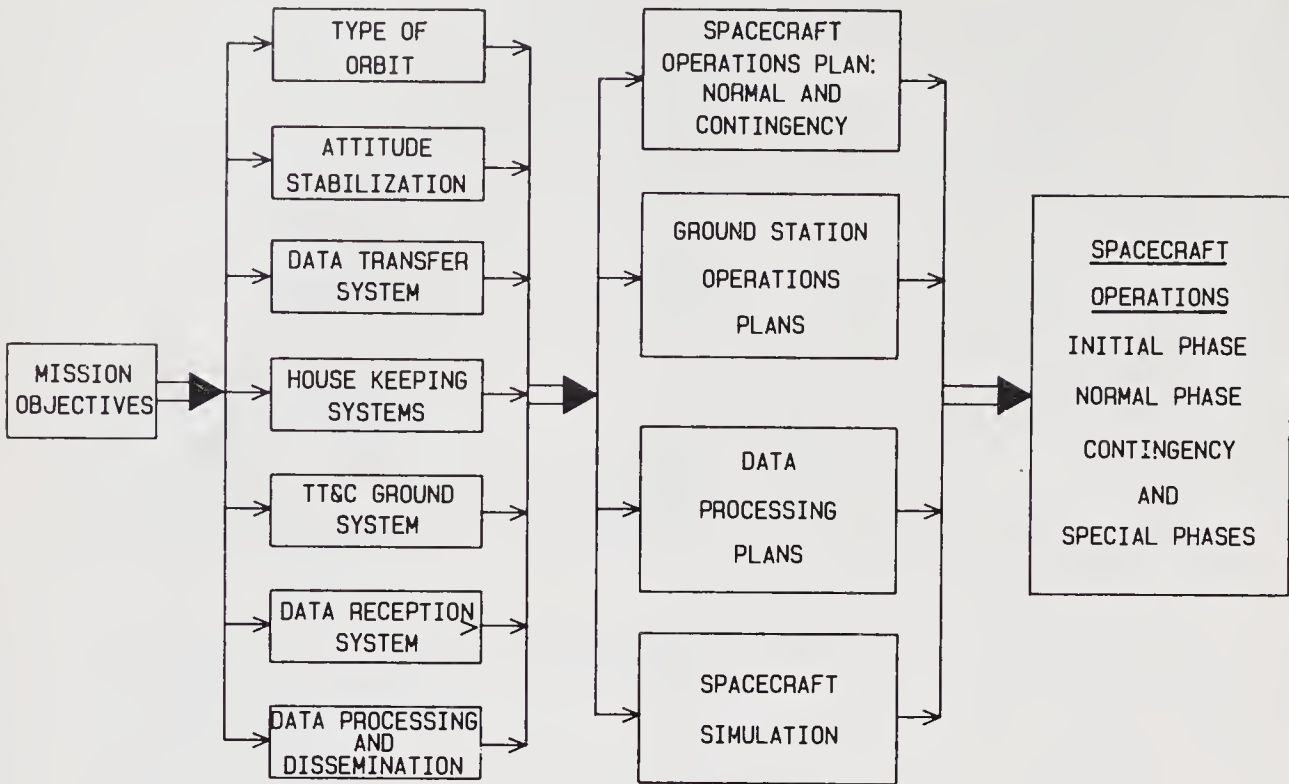


Figure 14. Mission planning and operations sequence.

space and ground systems, operations, data processing and spacecraft simulation. An important element in the link is the simulation. The spacecraft systems will be modelled and simulated on a computer which will be used for training the operators. Finally, all the efforts will culminate in the spacecraft operation once the launch leads to placing the spacecraft in orbit.

5.1 Earlier experience

Aryabhata provided ISRO first-hand experience of operating a satellite in orbit including managing contingency simulations. *Bhaskara* operations were more involved as the requirements included reception of television camera imagery and microwave radiometer data, their processing and dissemination to users. Further, the use of ground-based simulation for understanding in-orbit anomalies was successfully carried out during this mission. This helped in understanding the problem of corona in the TV camera and conclusions drawn from the simulation enabled switching-ON of one of the cameras successfully in *Bhaskara I*. APPLE provided for the first time, vital experience in the operations related to a geostationary mission. It involved operations in the transfer orbit phase like imparting high spin rates to the spacecraft, orbit-raising to near geosynchronous regime by firing the apogee boost motor, final orbit trimming, solar panel deployment, earth acquisition and three-axis stabilization, and finally normal on-orbit operations. This mission also provided some interesting experience in contingency manoeuvres that included pitch rotation for periodically overcoming the anomalies in thermal behaviour of the satellite.

5.2 Operational needs of current satellites

The operations of satellites like the IRS and INSAT II call for a high order of operational efficiency, and therefore, near-perfect planning to ensure routine user service. A few examples of spacecraft operations should highlight the complex nature of the task.

5.2a IRS operations: The short duration of visibility of near-earth satellites like the IRS, complicates the operations manifold. During the initial phase, a series of complex operations have to be performed on the satellite before it is brought into the safe operational state. Added to this, the satellite experiences eclipse in each orbit resulting in the non-availability of power from its major source, namely, the solar array. Also, the temperature control becomes critical. These operational problems are best illustrated by the example of IRS initial phase operations.

The IRS satellite is placed in orbit with the solar arrays folded, and the battery supplying power to the satellite. To reduce the load on the battery, it is essential to deploy the arrays at the earliest and orient them towards the sun. To achieve this, the satellite itself has to be placed in a fixed attitude mode, viz., the sun-pointing mode. These operations have to be carried out in the very first orbit and within 20 minutes of its injection.

In subsequent orbits, the satellite orientation has to be changed from the sun to the earth whereas the solar arrays continue to track the sun. All these manoeuvres call for extensive data analysis and command control of spacecraft in real-time. It is essential then that a significant part of the operations be automated. One of the most useful features that will be built into the IRS mission is the computerised data analysis, command generation and execution from remote ground stations, through a computer situated at the Mission Control Centre in Bangalore. The remote stations will be linked to the control centre through land/satellite links which will carry information back and forth. The computer at the Control Centre receives telemetry data, analyses it, and displays it on the terminals. It also prompts the spacecraft controller regarding the normal operations to be carried out in terms of command sequence and monitoring parameters. It also identifies abnormal situations and presents recovery procedures to be followed. Achieving such a high degree of sophistication, realizing and operating the system, is in itself a very challenging effort.

To illustrate the complexity of operating the IRS in the normal mode, the following example is useful. The IRS satellite images the earth in strips of 148 km width during its transit over a ground station in daylight. These strips progressively shift to the west every day and at the end of 22 days, the first strip is imaged again. This is an ideal situation, whereas in practice, the imagery taken on the first day and the 23rd day are slightly displaced due to orbit perturbation. This displacement goes on accumulating if left uncorrected. For the purpose of matching imageries taken on any 22-day cycle, it is specified that the total displacement should be within ± 14 kms. This calls for accurate determination of orbit, prediction of ground track, determination of required correction, execution of correction, and confirmation of its execution through another orbit determination.

The correction in the semi-major axis would be about 150–200 m needing a velocity increment of 0.1–0.3 m/s. Towards this, the semi-major axis has to be determined

to an accuracy of 20 m and the eccentricity to an accuracy of 10^{-4} degrees. This calls for very precise measurement of satellite range and accurate orbit determination. The range measurement has to be done from two globally separate stations. Finally, the corrections have to be executed at points in the orbit which may or may not be visible to our ground stations. In the latter case, the corrections are done in the programmed mode. Finally, all these operations should be carried out so as to cause no disturbance to normal data collection.

5.2b INSAT II operations: Let us now examine the complexity of INSAT II operations through an illustrative example. Normal communication satellites in geostationary orbit are maintained within $\pm 0.1^\circ$. The latest trend is to locate two or more satellites within $\pm 0.1^\circ$ in a cluster to increase the communication channel capacity at a single orbital slot. In the case of INSAT II, it is proposed to co-locate two satellites. This poses a number of complex problems which have to be solved. For example, frequency reuse through orthogonal polarization has to be employed to increase the communication capacity. Apart from other factors, the relative orientation of the on-board antennae on the two satellites affects the isolation between the two orthogonal channels. This depends upon the relative yaw errors of the two satellites which have to be kept as small as possible (less than 0.3°). As direct yaw measurement throughout the orbit is necessary, it is essential to depend upon gyros. This requires regular calibration and update of the gyros to achieve high accuracy yaw maintenance. Another problem is that when two satellites are co-located, if one of them loses its attitude stabilization, there exists a danger of RF interference in the two TTC channels which may be using at least one frequency in common. Additionally, the attitude-holding thruster firing may not impart pure rotational motion and this results in orbit drift. In such a case, the satellite may interfere with the normal co-located satellite. Careful data analysis and control operations are necessary to handle such delicate situations. The third and most important problem is station keeping. The position of a satellite in orbit is perturbed because of external forces. It experiences a north-south and east-west motion. The east-west motion has two components, one of them being due to eccentricity (this motion is diurnal). For effective co-location, the satellites have to be kept in station, and their daily motion kept in phase. For example, an eccentricity of 10^{-4} degree causes a diurnal oscillation of $\pm 0.36^\circ$. It is evident then that this motion has to be in phase for all satellites of the cluster. This requires that not only the magnitude but also the phase of the eccentricity vector has to be maintained. This is quite a complex challenge to be met by an operations engineer.

6. In-orbit anomalies and lessons learnt

During the in-orbit phase, many of the ISRO satellites experienced anomalies that were studied through suitable ground simulations, circumvented by appropriate contingency plans and the lessons learnt were incorporated into subsequent satellites.

In the case of *Aryabhata*, absence of redundancy to take care of single point failures in the power system resulted in the switch-OFF of the scientific experiments

on the third day in orbit when the +9 V supply failed. All the subsequent ISRO satellites are protected against single point failures of the mainframe systems.

TV camera systems on-board *Bhaskara-I* experienced anomalous behaviour in the early phase of the mission. The anomalies included premature shut-off of the TV heaters followed by large scale disturbances in the spacecraft status as monitored through telemetry parameters. A three-pronged approach was adopted to study this anomaly that included ground simulations using the simulation model of the spacecraft, evaluation of the payload performance in a thermovacuum environment over long durations and controlled experiments of the high voltage arcing phenomenon in the laboratory. These simulations strongly pointed to the possibility of a corona on-board resulting from high voltage DC/DC converters used for supplying 6 and 8 kV to the cathode and the grid, respectively, of the TV tube. Further, more detailed studies related to the corona occurrence under various pressure and temperature conditions led to the conclusion that such an arcing phenomenon will be most intense in the 250 to 100 torr region for high voltage in the regime of 6 to 8 kV. It was also concluded that a slow leakage of the trapped gases from the region of the corona in the payload, aided by thermal cycling effects could lead to a pressure regime below 100 torr when the payload can be switched ON safely. This conclusion was fully validated by the subsequent successful switch ON of one of the cameras a year after the launch. Studies in respect of these anomalies provided valuable inputs in respect of circuitry design involving the use of CMOS devices, material compatibility issues, especially in the presence of thermal cycling effects, and test philosophy for systems using high voltages.

In the case of APPLE, one of the major anomalies was the nondeployment of the north side solar panel. This anomaly, together with the constraints in thermal design that called for meeting the conflicting requirements of thermal control for transfer orbit and on-orbit phases, resulted in certain in-orbit thermal management problems for the satellite. The problem resulted in increased temperatures for systems such as the static horizon sensor or the battery thereby endangering their reliability. This problem was successfully overcome by a method called pitch rotation. It involved rotating the spacecraft around the pitch axis, at a slow rotation of about one rotation per hour, for a few hours around the period of anticipated peak temperature during the waning phase of the eclipse. The lessons learnt from APPLE aided in the generation of exhaustive qualification, testing, assembly and inspection procedures for the mechanisms that have been fully implemented in IRS and SROSS projects. Further, based on the experiences of APPLE, subsequent projects have taken note of possible failure modes, such as non-deployment of solar panels on one side of the spacecraft, by addressing the same at the design phase itself. For example, the IRS design provides for thermal and power management contingencies if solar panels on one side fail to deploy.

The above examples serve to illustrate how some of the in-orbit anomalies of the earlier ISRO satellites provided valuable inputs in the planning and implementation of the current satellites such as IRS and INSAT towards more reliable operation.

7. Cost and schedule performance

Any paper that deals with the evolution or assessment of technology development is not complete without touching upon the aspects related to cost and schedule

performance. The question seminal to such an evaluation is whether the development of a system/subsystem incorporating certain levels of new technology is accomplished in the most cost-effective way. This in turn calls for a reliable scientific method or a standard to compare with. Development of standards on a scientific basis for the evaluation of cost and schedule performance of a satellite project or its subsystem development activity is known to pose enormous limitations owing to uncertainties inherent in developmental activities and also the complex human resource interactions that are difficult to model. Even those few econometric and heuristic models that are developed in the US and in Europe, making use of considerable historical databases, do not yield results that are adequate for use as standards in their own countries. In the light of these, a reasonable method for such assessment could be through a comparison of cost and schedule performances between comparable systems developed in India and abroad. With reasonable assumptions relating to amortisation and development costs and accounting for all direct labour, material and infrastructure overheads including G&A overheads, the near-operational/operational class of the spacecraft developed in India are realized at a cost 10–20% lower than that of similar/same type of satellites abroad.

In terms of schedule management, the lead times for satellite development in ISRO is comparable to those abroad, taking into account the fact that a significant portion of lead time in the Indian case (about 20%) is in fact devoted to incremental infrastructure development for specific missions. Unlike the advanced countries, where the Industry has most of the infrastructure readily available, ISRO has to cope with development of specialized infrastructure through in-house activity as they are not readily available in Indian industry. Taking this into account, a normal lead time of 5 to 7 years for development of a new spacecraft bus is involved in ISRO. This is reduced to about 2 to 3 years depending upon payload complexity wherever an already proven bus is utilized. This situation is comparable to that achieved in other countries where significant advantage exists in terms of industrial R&D and production capability in aerospace products.

8. Concluding remarks

In this paper, we have essentially attempted to present spacecraft technology evolution in ISRO as traced through its different satellite missions, both past and current ones. The technology challenges faced in designing and building the current generation of operational satellites like IRS and INSAT II are specially highlighted. The paper is not meant to be a tutorial in satellite design and fabrication. As such, the related considerations in system and subsystem descriptions are limited only to those details that are pertinent to providing a cogent picture of the technology evolution and the associated challenges. Further, several additional aspects of a space mission like telemetry, tracking and command networks, spacecraft control centre, detailed methodologies for in-orbit management of satellites, data reception and processing related to ground systems for remote sensing satellites etc. have been dealt with, at best peripherally.

Other important elements not covered in this paper are the management systems set up for the execution of satellite missions. One of the greatest challenges faced in

the evolution of space activities in the country perhaps was in the development of suitable organization and management systems conducive for conduct of time-bound high technology projects. Many new organizational systems and methods have been conceived, experimented with and tested just like a host of technologies that were developed for space projects. Since a separate article (Rajan 1987) elsewhere in this issue deals with the management systems, the related details are not elaborated in this paper.

Establishment of a firm and durable base for indigenous capabilities in satellite technology is but one major aspect of a multi-faceted and multi-dimensional program relating to space that Prof. S Dhawan guided and nurtured over a period of twelve years. As part of his pioneering efforts in bringing the benefits of space for improving the basic quality of life of the people of India, a major thrust was given to space applications that included communications, natural resources survey, and meteorology. He also provided necessary support and encouragement to the space scientists so that they could undertake the planning and conduct of front ranking experiments in astronomy, aeronomy, and other areas of space sciences. To ensure the continuity of such efforts, he saw the need for establishing a strong indigenous base in space technology encompassing both launch vehicles and satellites. Before he relinquished the Chairmanship of ISRO, he saw to it that the necessary institutions for this purpose were built both inside and outside ISRO and their working culture was made conducive to the réalization of such high technology systems in a time-bound fashion.

It is a matter of great privilege for the authors to write an article on ISRO satellite technology for inclusion in this volume being brought out in honour of Prof. S Dhawan and we would like to thank Prof. R Narasimha and Dr A P J Abdul Kalam for it. The authors would like to record their indebtedness to Prof. U R Rao whose direction and encouragement were primarily responsible for the various developments reported in this paper. The interest shown by Col. N Pant while writing this paper is also gratefully acknowledged.

Several colleagues in ISRO assisted in the preparation of this article. While it is difficult to thank each one of them individually, we would like to make a special mention of M S S Prabhu, C V R Reddy, H Narayana Murthy, B L Agrawal, S Pal, Y K Singhal, P Kudva, P S Goel, Y K Jain, K Anantharam, K L Valliappan, V R Katti and Y N Bhushan.

References

- Adams J L 1966 Space Technology – spacecraft mechanical engineering, NASA SP-66
Berry W 1984 *ESA Bull.* 40: 6–24
Dhawan S, Singh J P, Kale P P 1979 *IEEE Trans. Broadcast.* BC-25: 121–127
Kasturirangan K 1985 *Int. J. Remote Sensing* 6: 387–400
Navalgund R R, Kasturirangan K 1983 *Proc. Indian Acad. Sci. (Eng. Sci.)* 6: 313–336
Rajan Y S 1987 this volume, pp. 397–413
Rao U R, Kasturirangan K 1979 *The Aryabhata Project* (Bangalore: Indian Acad. Sci.)
Rao U R, Kasturirangan K, Jayaraman V 1982 *J. Aeronaut Soc India* 34: 67–76
Rao U R, Pant N, Kale P P, Narayanan K, Singh J P 1987 The Indian National Satellite System, *Space Commun. Broadcast.* (accepted)

- Rao U R, Ramachandran P 1987 Second generation Indian National Satellite System Space Segment – INSAT II, International Astronautical Federation (IAF) Congress, Brighton, UK
- Scull J R 1966 Space Technology – spacecraft guidance and control, NASA SP-68
- Singer F (ed.) 1964 *Torques and attitude sensing in earth satellite* (New York: Academic Press)
- Vasagam R M, Shrivastava S K 1983 *J. Aeronaut. Soc. India* 35: 133–276

Management of the Indian space programme

Y S RAJAN

Indian Space Research Organization, ISRO Headquarters, F Block, Cauvery Bhavan, Kempegowda Road, Bangalore 560 009, India

Abstract. A brief survey of some salient aspects of the management of the Indian Space Programme is made, with special stress on the period 1972–1984. In view of the complexity of the subject matter, some major elements are addressed without necessarily offering conclusions on all the issues or the questions posed. Some major policy initiatives during the period 1972–1984 are also described.

Keywords. Indian space programme; national space programme management; space policy.

1. Introduction

The benefits from space activities have now become widely known in the country. In fact there is worldwide recognition of the importance of space activities not only for the developed nations but in particular for the developing countries. Such a recognition, even at well-informed levels, did not exist in the country when India formally organized its modest space effort through the establishment of the Indian National Committee for Space Research (INCOSPAR) in 1962. In November 1963 the first sounding rocket was launched from the Thumba Rocket Launching Station (TERLS) near Trivandrum. The founders of the Indian space programme recognized the potential for the immense benefits from space technology even in the early 1960s, when humanity was just ushering in the space era. Early ideas about possible space applications of relevance to India can be found in a number of writings and speeches by Dr Sarabhai, a selection of which have been brought out in a publication by the Indian Space Research Organization (ISRO) (ISRO 1979). The early ideas were mainly centred around the utilization of satellites for television and developmental education, meteorology, and remote sensing for natural resources management. The programme also included development and launch of sounding rockets for space science research. Though international cooperation dominated in the early years, careful stress was placed on self-reliance. Nucleii of trained manpower were formed at laboratories that were then part of INCOSPAR but were constituted into ISRO in 1969. It is not the purpose of this article

to dwell on these details. The beginnings, however, need to be noted to understand the management of the programme during the seventies and the early eighties.

Organisationally, the activities of ISRO were under the overall direction of the Physical Research Laboratory (PRL), Ahmedabad, till the sudden demise of Dr Sarabhai who was both Director, PRL and Chairman, ISRO. PRL was under the Department of Atomic Energy (DAE) which had considerable freedom from the “needlessly inelastic rules” of other Government Departments through the Atomic Energy Commission (AEC) structure. The elements of a profile for the decade 1970–1980 for the Indian space programme are elaborated in a document of the DAE (DAE 1970). The objectives and targets fixed in this profile had considerable impact on the activities of ISRO during the 1970s and 1980s.

The annual budget of ISRO grew to about Rs. 10 crores in 1972 and its manpower reached about 3000. Soon after Dr Sarabhai’s demise, after a brief period of interim arrangements, the Space Commission (SC) and the Department of Space (DOS) were formed in May 1972 essentially on the same lines as AEC and DAE. SC and DOS are responsible for all space activities in India. PRL was placed under DOS but with a separate director. Prof. S Dhawan became Chairman of the Space Commission, Secretary of DOS, and Chairman of ISRO, and remained so till the end of September 1984. The rapid growth of space activities and the implementation of major projects occurred around the mid-seventies. The trend continued subsequently. This article deals with some elements of the management of the Indian space programme during 1972–84.

2. Some major events

For a reasonable understanding of the activities and achievements of the programme during 1972 to 1984, the annual reports of DOS, placed in Parliament at the end of every financial year, can be consulted. Some major events are listed here.

1972: The Department of Space and the Space Commission set up by the Government of India to promote the development and application of space science and technology for identified national socioeconomic tasks. Prof. Dhawan takes charge.

1972–76: A number of airborne remote sensing experiments conducted for surveying earth resources.

Several indigenous sounding rockets were tested and flown for scientific experiments. A number of elements of solid propulsion, propellant and avionics systems developed on laboratory scale. Development of a launch range at Sriharikota begun. Tracking station experiments with liquid propulsion including a major technical know how arrangement with a French Company made.

1975: The first Indian satellite, *Aryabhata*, launched on 19 April 1975 from the Soviet Union.

1975–76: The first major space application programme, the Satellite Instructional Television Experiment (SITE), conducted during August 1975–July 1976 using the US Satellite, ATS-6.

1977: The satellite telecommunication experiments project (STEP) carried out from the middle of 1977 to 1979 using the Franco-German satellite, *Symphonie*.

1979: The second Indian satellite, a satellite for earth observations, *Bhaskara-1*, launched on 7 June 1979, from the Soviet Union.

1980: SLV-3, India's first satellite launch vehicle, puts the *Rohini* satellite into a near-earth elliptical orbit from Sriharikota on 18 July 1980.

1981: India's first experimental geo-stationary communication satellite, APPLE, successfully launched by the European Space Agency's (ESA) *Ariane* launch vehicle from Kourou, French Guyana, on 19 June 1981. India's second satellite for earth observation, *Bhaskara-II*, launched from the Soviet Union on 20 November 1981.

1983: The second developmental flight of SLV-3 successfully conducted from Sriharikota on 17 April 1983 and RS-D-2 satellite orbited. INSAT-1B, India's multipurpose domestic satellite, launched on board USA's space shuttle, *Challenger*, on 30 August 1983. A major national seminar to define National Natural Resources Management System conducted, arriving at a national consensus preparing ground for the Government decision on NNRMS made in early 1985.

1984: The first joint Indo-Soviet manned space mission launched on 3 April 1984. Prof. Dhawan retires in end-September 1984 and Prof. U R Rao who was Director, ISRO Satellite Centre, takes over the same unitary structure from 1 October 1984.

3. Description of some important managerial aspects

The annual budget of DOS which was around Rs. 10 crores during 1972 increased to about Rs. 100 crores during 1984. Manpower grew from about 3000 in 1972 to about 13,000 in 1982. A number of small units situated in and around Trivandrum were organised into a large Centre and called the Vikram Sarabhai Space Centre (VSSC) in 1972 and placed under a director. Similarly a number of smaller units located at Ahmedabad were brought under the Space Applications Centre (SAC). An ISRO Council consisting of centre directors, Director PRL and senior officers of the DOS secretariat was formed. This has provided a symbolic link as well as a forum for participative management between the Department which has the Government's powers and the centres which execute the jobs. It should be noted that in the normal parlance of traditional government departments, ISRO's centres and units would be 'subordinate' or 'attached offices', words which are not, however, prevalent in ISRO and DOS. Such participative management, jointly evolved between those who wield administrative powers and the executing agencies, is an important feature of the management of the Indian space programme.

A project for India's first launch vehicle SLV-3 was organized under VSSC during 1973, with a unified project team while retaining the elements of a matrix structure in the specialized divisions of VSSC. Some projects relating to launch vehicles were also organized at Sriharikota which later led to the formation of the SHAR Centre. Similarly a project for India's first satellite, which was subsequently named *Aryabhata* after launch, was formed at Bangalore under the overall direction of VSSC; the infrastructure built for the satellite projects led to the formation of the ISRO Satellite Centre (ISAC). The National Remote Sensing Agency (NRSA), an

autonomous society set up under the Department of Science & Technology (DST) in 1975, was transferred to DOS in December 1980, placing major remote sensing efforts under the single umbrella of DOS. In the eighties some smaller units were “spun off” from the major centres of ISRO.

Having core teams responsible for the major, well-identified projects, with tasks being executed by different centres/units of ISRO became an important factor in ISRO management from the late seventies. Partly for reasons of participative management and partly for reasons of technical complexities requiring a multi-disciplinary approach, various inter-centre management boards/councils were formed; some of these have executive functions, some have advisory roles. All the projects have a lead centre named for their execution. For example, VSSC is the lead centre for launch vehicle projects, ISAC for satellite projects. In addition, Indian industries execute major work packages as a matter of ISRO policy. This factor adds further complexities of contract management in addition to the internal technical and managerial coordination needed within the ISRO centres. The SLV-3 project had about 40 such industrial “work centres” and for the Polar Satellite Launch Vehicles (PSLV) the number has increased five- or six-fold.

In addition, the units of the space programme which started functioning in Ahmedabad and near Trivandrum in the early sixties, have now spread to a number of places in the country (see figure 1).

Yet another important feature in the management system, which emerged during the later half of the seventies and intensified in the early eighties, is the growth and coordination of joint programmes with the users of space applications. One important example is the operational multipurpose Indian National Satellite Project, INSAT-1. Such user interfaces add a newer dimension to the already complex management structures of the projects. Apex level user coordination bodies such as the INSAT Coordination Committee (ICC) and the Planning Committee for the National Natural Resources Management System (NNRMS) were also formed.

Coordination of efforts in space sciences took a newer shape through the Advisory Committee on Space Sciences (ADCOS) a brief report on which is given by ISRO (1987a).

The responsibility for the overall programme which is executed through a complex network of centres, projects, industries etc. still vested with a single person who held the positions of Chairman Space Commission/Secretary DOS and Chairman of ISRO. This is considered to be effective in combining various decision-making levels—technical, managerial, administrative and policy-making—thus cutting down delays. To assist the top decision maker, besides the usual secretariat of DOS, an ISRO Headquarters consisting of scientists and engineers was formed; these units also played a role in the overall programme management and in ensuring effective internal and external linkages. There are also a number of standing and transient Committees which assist in coordination. While it is difficult to describe these functional or hierarchical linkages even for one year or for one project because of the evolutionary and dynamic nature of these linkages, an extremely simplified organisational chart is shown in figure 2 (reproduced from one of the recent annual reports of DOS). Since the interrelationships and linkages are complex and time-varying, consensus management has been mostly resorted to in decision-making through Committees, Boards, Councils etc.

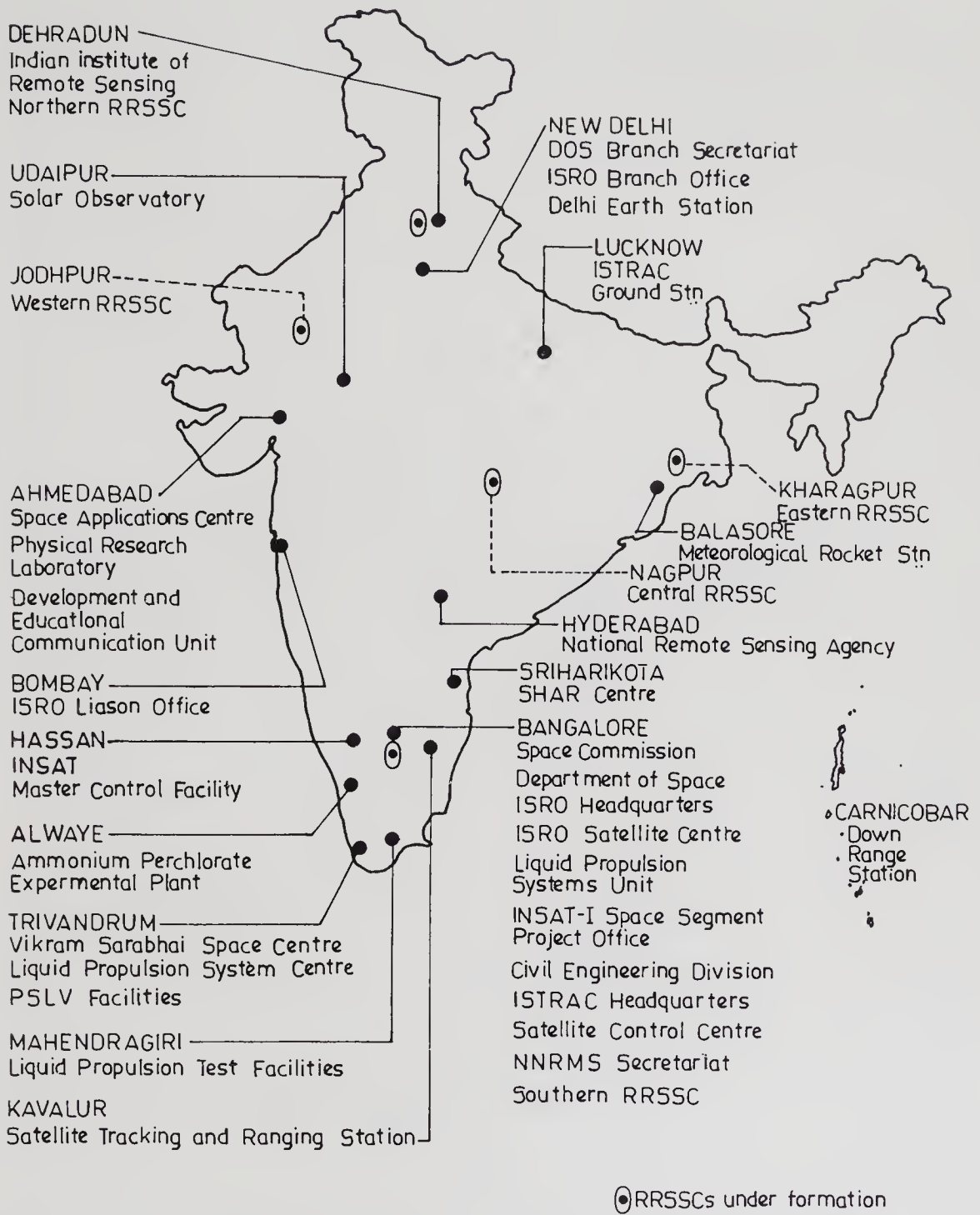


Figure 1. Establishments of the Department of Space.

The budget formulation within ISRO has since 1977 absorbed many features of zero-based budgeting. This approach has also been used as a tool for programme management. DOS has considerable freedom in financial management and has delegated substantial powers to the centres and projects.

Regarding the promotional avenues of scientific and technical personnel, which include technicians, ISRO/DOS has a merit promotion scheme broadly derived from DAE. Under this scheme a person after a prescribed number of years can be

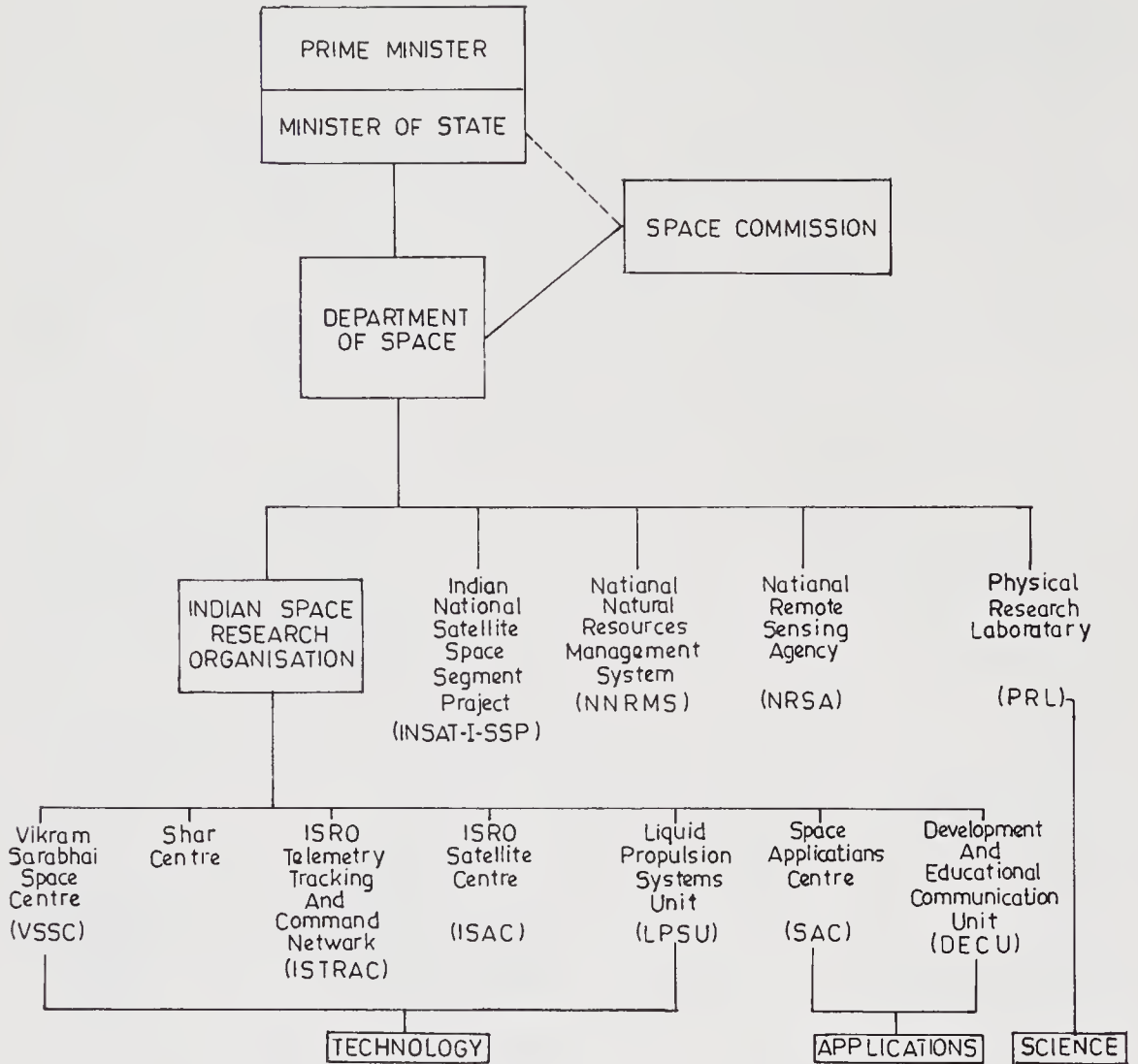


Figure 2. Organisation of the Department of Space, India.

reviewed for promotion and promoted irrespective of availability of vacancy. This system is nowadays called “flexible complementing”. The majority of ISRO scientists and engineers are still young and may average around 35 to 40 years. The age distribution however may have a sharp “bunching effect” because a large number of personnel were recruited during the 60s and early 70s after which the rate of induction has gone down.

The Indian space programme’s partnership with the Indian industrial sector is organized under four closely linked fronts, viz., technology transfer from the space programme to industry; consultancy by ISRO to industry; utilization of the industries’ own technology potential and expertise by ISRO; procurement of goods and services from industry for the space programme. From the mid-seventies the partnership with the industry on the above lines was stressed as a matter of policy and activities and projects of the space programme were accordingly oriented. While 3 technologies were licenced in 1977 by ISRO the cumulative total in 1984 was 88, with the figure in 1986 being 129. The annual flow of funds from the space programme to Indian industry was about Rs. 13 crores during 1977–78 and has

reached a level of about Rs. 119 crores in 86–87. Further details may be seen in the special publications by ISRO (1987b) and Sudarsan & Sridhara Murthy (1987).

Since 1974, ISRO has instituted a formal system for supporting extramural research funding in the academic system of the country under a programme called RESPOND. Some details can be found in an ISRO publication by Ananth (1985). The technical review systems in ISRO's projects also utilized the expertise of personnel from academic institutions.

4. Profile for the decade 1980–1990

A comparison of the 1970–80 decade profile for the space programme with actual achievements would indicate that the basic goals have remained the same. However, the details about the proposed projects were sparse in the original profile; it would appear that a few additional projects, not anticipated earlier, have been added during the execution of the profile. Funding for the profile period has been more than the figures projected earlier and the time-schedules have been different. The actual realization of events has taken place a few years after the milestones indicated earlier. But on the whole, targets have all been realized fully. During 1981, DOS also presented a profile for the period 1980–90 wherein the stress has been on transition to operational and semi-operational space systems to meet the country's requirements. The programme was graduating from minor projects to major ones; the projects are applications-driven; and the linkages between projects have become more complex. The integrated nature of the programme becomes more apparent. Further details can be seen in the article by Dhawan (1978), the decade profile 1980–90 given in the DOS (1981) document and the paper by Dhawan & Rao (1982).

5. Discussion on project and programme management systems

In a recent publication by Dhawan (1985) on "Application of space technology in India" a glimpse of the application of space technology in India is provided. The publication also addresses the choice of technology, the risks involved, and the necessity to sustain an Indian viewpoint throughout for larger socioeconomic purposes. It gives some clues to the policy formulation which has been marked by a distinct continuity in the objectives, goals and directions.

When Prof. Dhawan took charge of the programme about 10 years after its inception, he amplified on the basic goals and objectives set up already. He has evolved mechanisms and structures to implement the decade profile of 1970–80. Thus the organisational forms that evolved during the growth of the Indian space programme during his chairmanship contained some elements dictated by programmatic choices made earlier as well as elements which were needed to handle a growing, dynamic programme. To a certain extent it was influenced by the practices of DAE. To separate out these elements, if it were at all possible, would require considerable research. Research articles on the working of the detailed management systems of the Indian science and technology organisations or programmes are practically non-existent. The reasons are manifold: the organisations are perhaps busy with their programmes; there is a fear of disturbance of the

existing living systems; and the complexities of Indian public life add further inhibitions to data gathering and analyses. ISRO has not been an exception to this phenomenon. Therefore any attempt at description and analyses of the management system of the Indian space programme can contain many elements of the subjective biases of the author(s). This paper may also contain such biases. It is hoped that further studies suggested in this paper can be conducted in depth. Such studies could be good contributions to the Indian management literature.

In the early seventies, the implementation of larger projects like SITE, SLV-3 etc. have necessitated large multidisciplinary teams. This requirement has been met by integrating a number of existing smaller units into major centres located at Ahmedabad and Trivandrum and providing a fairly large project team. In case of the *Aryabhata* project, while some experienced personnel were drawn from the centres, a new geographical location was selected and an almost fully self-contained project team was formed at Bangalore. The management approach to these projects formed around the same period had significant differences, partly because of the nature of the then existing teams and their activities. Thus one sees in the management approach an ability to adopt new systems without being constrained by standard patterns. Such a trend continued even at later stages though the degree of uniformity in patterns of project management structures has increased considerably. With the approval of a number of projects like *Bhaskara*, APPLE, etc, the patterns adopted were in the nature of compact core teams, identified lead centres, multi-centre activities, matrix forms within centres to deliver sub-systems to the projects and so on. The multiplicity of such linkages and controls also tended to reduce the singular authority on the projects by the centre directors from the levels that existed in the early seventies. However the number of activities in the centres increased, making intra-centre coordination more complex and difficult. The conversion of ISRO into a government body in 1975 reduced certain flexibilities in procedures that existed earlier.

While from the sixties till 1972 the Chairman of ISRO was the main authority for decision-making, a number of subsidiary authorities for executing decision-making with fairly well-defined hierarchical structures emerged from 1972 onwards. Their number increased considerably thereafter with final organisational structures in the centres and projects. The dynamics of the programmes as they grew further especially with multi-centre projects being executed simultaneously during the seventies and the eighties exerted pressure on these authority structures. While consensus management helped a great deal in avoiding serious breaches, the need for conflict resolution in the speedy time-frame required for projects tended to raise the problems to the higher levels of authority, which in the ultimate rested with the Chairman, ISRO/Secretary, DOS. Since such a raising of the levels of decision-making can have negative effects on the managerial delegations given to the lower levels of the authority structures, formal and informal review systems of the projects and the programme activities by superior authorities especially by Chairman, ISRO, with the participation of a large number of technical teams drawn from different levels of ISRO systems and sometimes from outside ISRO provided an outlet for resolving conflicts in a speedier time-frame without seriously damaging consensus formation mechanisms and without making the lower levels of decision-making systems ineffective. The role of the Chairman, ISRO, in such a

process is both crucial and delicate. Characterization of specific elements of the chairman's role can be an interesting and important research topic. The fact that Prof. Dhawan has very successfully carried on these roles over a long period is borne out by the achievements of the programme and the momentum it gathered during his chairmanship.

The ISRO review systems during the seventies and eighties resulted in generation of formal documentation of systems engineering, design, quality assurance, test procedures etc. Presentations through audio-visual means were also used as a means of technical communications. Such a system of formal technical documentation and presentations has become a built-in part of the management processes of the Indian space programme. It has many useful features for the management of large systems.

Another important stress exerted by the major organized projects of the space programme has been on the R&D activities of ISRO and studies on future systems. Since the projects compete for ISRO resources for meeting their targets, activities which were not "visible" tended to be ignored. To minimize the effects of such pressures which affect the future of the space programme, some technology development projects (TDPS) were formulated. Reviews of some major R&D areas by Chairman, ISRO, were organized to get clarity and also to provide "visibility" to these activities. Study groups for defining future systems were formed drawing part-time personnel from ISRO centres/projects. The results of many of these efforts are mixed. A detailed study of these activities and their results with a view to get clues on the managerial strengths and weaknesses of ISRO in handling these R&D items and future studies, would be very valuable.

With respect to the interfaces with the user agencies relating to communications, television, meteorology, natural resources managements etc., right from the stages of formulation of approach up to the stages of actual joint execution, the systems evolved by ISRO since the mid-seventies have been unique and have many positive features. These systems and mechanisms evolved by Prof. Dhawan can be considered as one of the high points of his contribution to the national science and technology (ST) scene. The fact that these systems of linkages, coordination and implementation exist today, in operational forms for INSAT and in a semi-operational way for resources management, is worth noting. The evolution of these interfaces and their sustenance in the operational phase has important lessons applicable to a number of other areas in the country and perhaps a serious study would be useful.

Similarly Prof. Dhawan's efforts to develop a partnership between Indian industry and the Indian space programme are an example of his foresight regarding the needs of operational systems in the country, especially when the programme has to be self-reliant and viable based on indigenous efforts. While he might have derived his clues from the developed countries, a number of unique organisational linkages such as formal memoranda of understanding with major industries, formation of compact groups in ISRO to interface with industries etc., are his important contributions to the Indian scene. From the trend of increasing partnership with industry, it can be inferred that in the years to come the benefits to industries themselves will form one of the important justifications for the Indian space programme besides its direct applications. The managerial complexity

resulting from such a major role by the Indian industry will have considerable impact on the organisational forms of management adopted by ISRO/DOS so far.

As far as linkages with the educational system such as academic institutions, University Grants Commission (UGC) etc. are concerned, a number of managerial innovations have been tried since 1974 to promote university research in space technology and applications. It should be noted that as an educator himself, Prof. Dhawan has been keenly aware of the mutual benefits that can be derived from the Indian space programme and the educational system. While the participation of personnel from the academic system in the reviews of the technical activities and in the study groups of ISRO and for specific extramural research has increased considerably since 1974, the objective of creating major centres of excellence in research in space technology and applications in a number of places in the country has not been realized. This may be partly due to the fact that ISRO, as a matter of policy, refrained from opening new centres of education and has tried to draw upon systems from the existing institutions. It is also possible that ISRO R&D managers at the centres/units were too preoccupied with their immediate tasks to devote attention to nurturing these links. A few joint space technology cells formed recently with such a framework in view have started functioning. In the area of linkages with the academic systems, the Indian space programme would need to devote concerted attention in future to strengthening its R&D base which otherwise has begun to get eroded by the compulsions of the execution of multiple major projects and also due to the demands of running operational national space services.

Figure 3 shows some of the major features of and events in the management of space programmes described above as it evolved since the 1960s.

6. Discussion on personnel management and schedule management

While in an organisation, one has to deal with all personnel, in this article only ST personnel are addressed. The promotional policy has been described in an earlier section. By and large, ISRO has not adopted any formal training programme of the newly recruited or existing personnel. Induction of personnel to higher levels of managerial hierarchy, from outside ISRO, has been extremely limited since 1972 as also the “loss” of such personnel from ISRO to outside organisations. The efforts since 1972 have been the consolidation of the management systems around the existing personnel with suitable restructuring tailored to its needs. This may be partly conditioned by the fact that the organisation in 1972 was already about 3,000 strong and nuclei of managerial positions existed albeit in a rudimentary form. The recruitment of scientists and engineers is predominantly at the lowest level; young persons fresh from colleges and universities are recruited. They grow to fill the higher levels of hierarchy. The trend continues. Formally ISRO procedures allow for lateral entry at any level and also transfer of personnel between any centres/units of ISRO/DOS. In actual practice these are very limited probably due to the compulsions of the projects and also due to the growth of ISRO. There are some signs of slowing down of the growth rate in manpower since the 1980s. Given this slowing down and the ageing of the organisation, and also in view of the flexible complementing scheme of promotions, the hierarchical levels built up already are likely to be stressed further, calling for changes in the existing organisational structures. While

major changes have not taken place during 1972–1984, some smaller units were formed during the eighties. Some of these were necessitated partly by the needs of technical activities. Another important feature of personnel management in relation to programme management has been the maintenance of high morale in ISRO despite a number of initial failures or problems in the projects whether it is SLV-3, *Aryabhata*, *Bhaskara*, APPLE or INSAT-1A. A team of dedicated personnel have kept up their steady march towards the set goals and targets. It would be interesting to study the motivational factors behind this fact. Is it because of the challenge of space research, or the charm of the Chairman of ISRO and his long tenure, or due to the better programme management systems? Or the better promotion avenues for ST personnel in ISRO? Or due to availability of progressive and flexible administrative, financial and purchase rules in ISRO? Or, if a combination of these, in what proportion?

An analysis of the schedule management of the Indian space programme reveals many interesting features. While the time-targets projected in the decade profile of 1970–80 cannot be taken as specific items for comparison with actual events, by and large achievements of targets for satellites and launch vehicles have been well within the overall profile targets and subsequently stated time-schedules. It is difficult to assess specific slippages in project-schedules because the detailed milestones were evolved from 1972 onwards through specific projectisation. An impressive feature of the actual events from 1975 to 1984 will indicate that each year has at least a major milestone and no year is without a major event. This could not have been a mere accident but only an indicator of a carefully planned and executed programme which has aimed at optimal utilization of human, financial and other resources. In addition such events helped in sustaining the overall morale of the organisation and also in generating a feeling of oneness. A detailed analysis of utilisation of major rocket test facilities, propellant production plants etc, would further prove the fact of such careful planning; long periods of idling as well as heavy overcrowding in a few months have been avoided. This speaks well for the management system which was able to orchestrate various levels of the system in planning and execution, in the midst of technical and other uncertainties including a number of initial failures.

7. International cooperation

The Indian space programme has drawn upon, since its inception, benefits from the cooperative programmes offered by the developed countries to build up its trained manpower pool and to conduct a number of experiments in space sciences and applications. In some limited cases, 'licenced production' has been resorted to. In some cases technical know-how has been obtained, mostly paid for through the services of expert ISRO manpower and the supply of certain finished products to the supplier of the know-how. Since the late seventies, the international cooperation has increasingly acquired the level of "equal partnership". This has been mainly due to the fact that the Indian space programme has been steadily moving towards the goal of self-reliance and has also grown in size. The Indian space programme is in the unique position of having active and continuing cooperative links with a number of major space agencies in USSR, USA, Europe, France, West Germany etc.

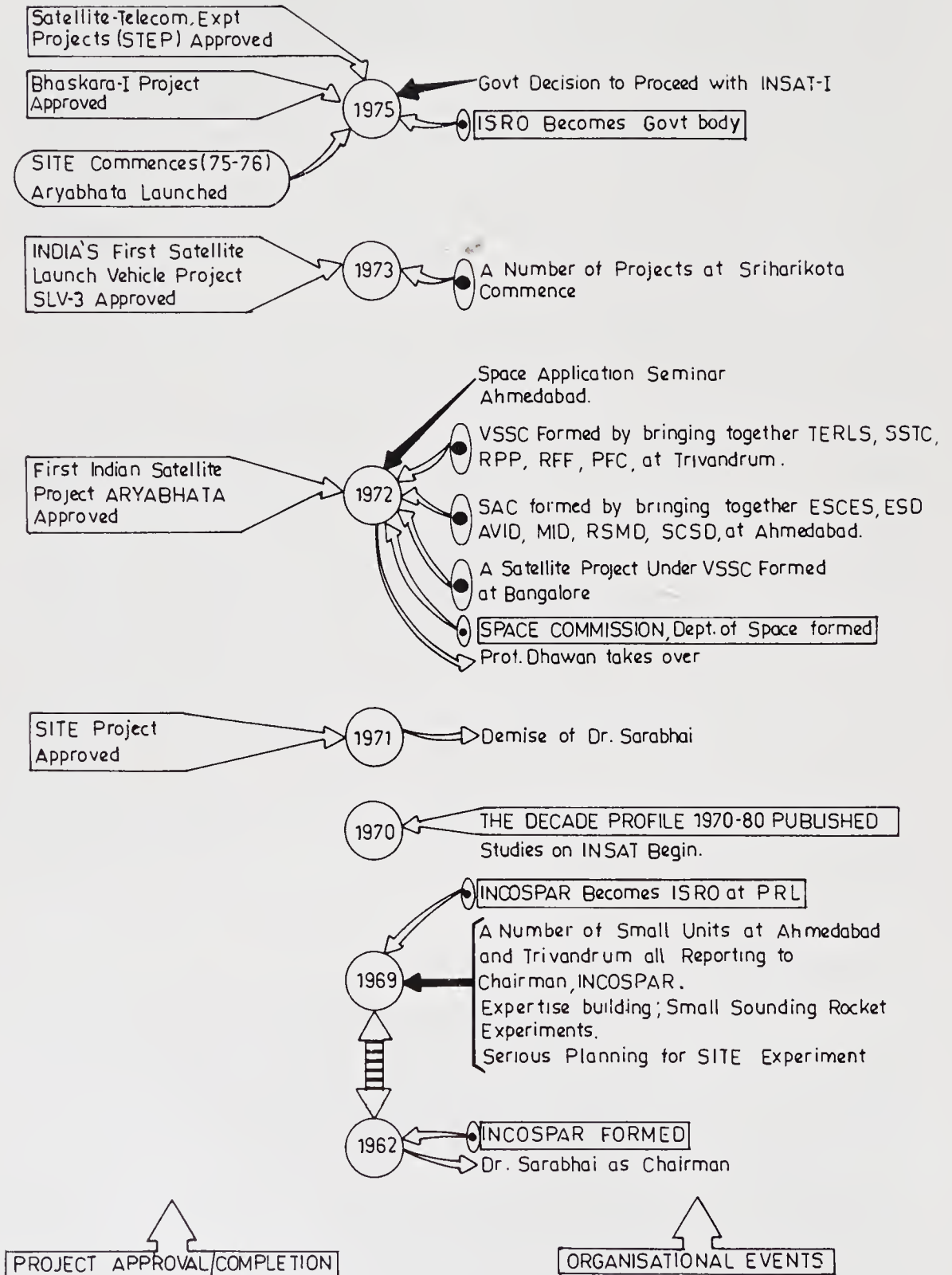


Figure 3. (See facing page for caption.)

FIG:3(contd)

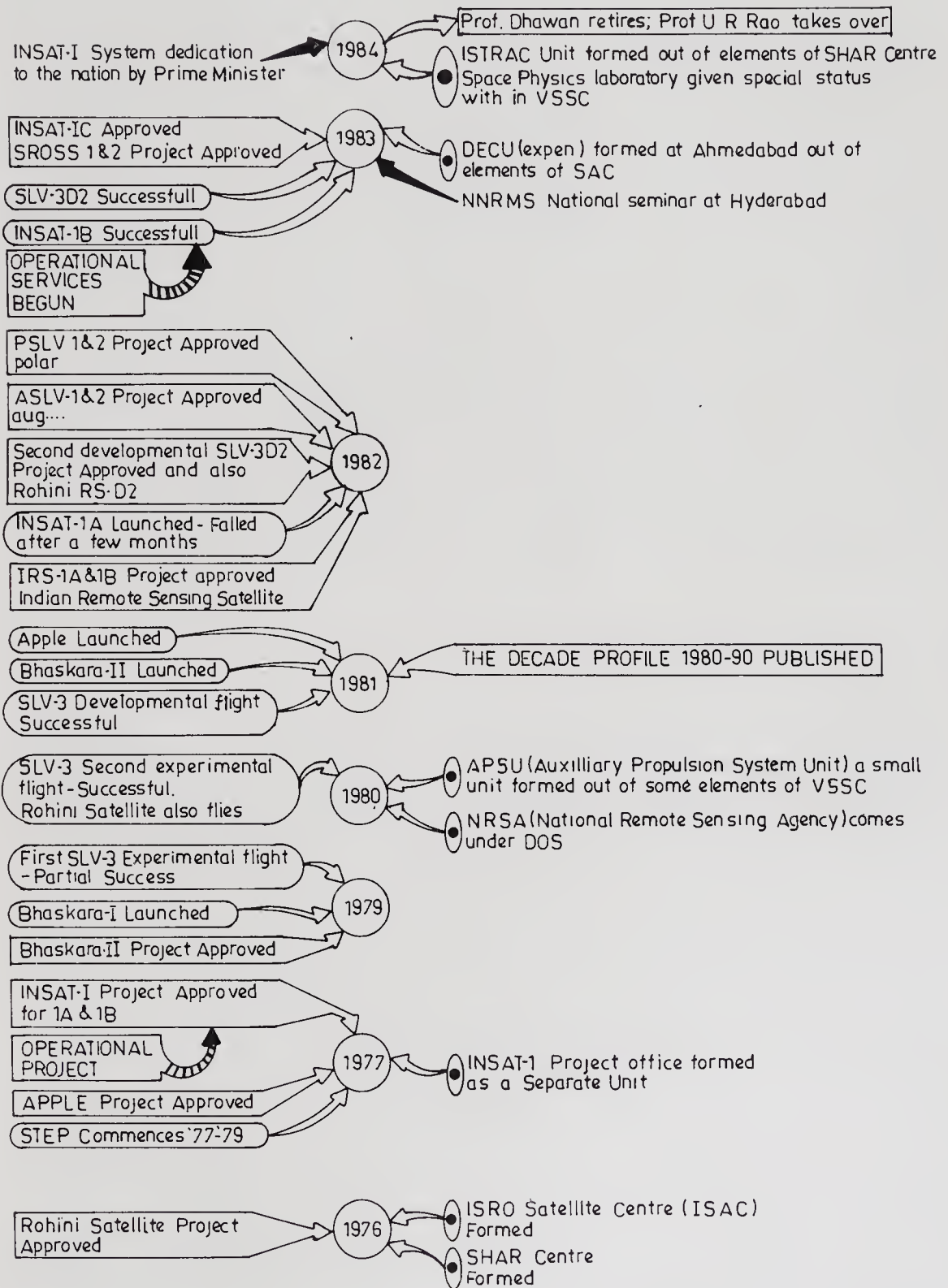


Figure 3. Some major organisational features and project events of the Indian space programme.

On the commercial front, a number of selected subsystems and equipment required for the Indian space programme have been purchased from abroad. Efforts have been made to reduce, as far as possible, the import component. The foreign exchange component of the budget of the space programme has ranged between 25 and 30%, approximately.

In the case of the INSAT-1 system, procurement of the space segment has been from abroad. The launches of the bigger ISRO satellites have been made with the help of foreign launch vehicles from spaceports abroad.

The pressures from the national operational services, the increasing commercial trends of the space services of many developed countries, and the competition between them for world markets can have an impact on the Indian space programme and therefore its management. On the other hand, the growth of the Indian space programme in size, its move towards operational systems, and the growing role of Indian industry as a major partner in the space programme can lead to India entering world markets through commercial channels as well as through cooperation channels especially because of its stated goal of sharing its experience with other developing countries. Some aspects of Indian views on self-reliance are given in an article by Rajan (1984).

The impact of these developments on the management systems of the Indian space programme could be considerable. Presently one can only speculate on possible impacts since the actual experience is limited.

8. A comparison with the management structures of other countries

It is not possible to address such a comparison in any depth. The management of the Indian space programme in an overall structural sense has a number of similarities to the evolution of the structure in the National Aeronautics and Space Administration (NASA) of USA and in the European Space Agency (ESA). But one should also note that ESA and NASA are also undergoing major structural changes. Placing all activities relating to the space programme, such as policy formulation, R&D, product development, project execution and the responsibility for operational space services to the users, under one single organisation led by a single person with unitary authority, is unique to India. While it has helped in the evolution of an integrated programme in a rapid manner with limited resources, it should be noted that the impact of the Indian space programme on various walks of life in the country, has just begun to consolidate, thanks to the major achievements of the programme during the seventies and the eighties. The space applications and therefore operational services in the country are likely to grow very rapidly during the late eighties and in the nineties. It is difficult to forecast the type of systems most suited under such circumstances. With the participation of major user agencies in the country in the operational applications of space activities and the growing partnership of the Indian space programme with industry and other institutions, one can envisage the emergence of some new forms of structures in India, similar to those which exist in the USSR or Japan for their space activities, with specialized institutes and industries dealing with specific standardized subsystems or components and the integration taking place through project and

programme structures; R & D may be carried out to a large extent in the university system or in special laboratories.

9. Concluding observations

Some questions on the future

Any management system is conditioned by its past, and has its impact on the future. Some of the possible dynamics that may be imparted by the management of the Indian space programme during 1972–1984 on future systems, can be a topic for detailed study in itself. Some pointers and also some questions posed are presented here.

By absorbing the objectives set forth in the 1970–80 decade profile and by organizing well-structured projects and activities to realize the objectives set forth earlier without being needlessly rigid about the details, Prof. Dhawan demonstrated the strength of continuity of *policy* in the execution of the Indian space programme. By building the management structures mostly around existing personnel and units, he again stressed the continuity aspect. However, during the period of his chairmanship, there were a number of newer units established in different places in India. Integration of existing smaller structures took place during the early seventies, building out of them major structures called centres/projects, with authority structures being more unitary than those that existed before. Such a process also led to the reduction of direct executive decision-making by the Chairman, ISRO. Simultaneously the newer units/projects which were established grew in a few years to form new centres, reducing the dominance of the centres established earlier. The projects placed under the centres also grew in complexity and were of an inter-centre nature drawing from all the ISRO centres as against the earlier ones which were predominantly executed in a single geographic location. Such inter-centre projects blurred the unitary authority of the centres over their projects. Industrial contracts added additional dimensions necessitating the involvement of contract/finance managers, such as senior officers of the DOS Secretariat, in the programme management structures. Though the delegation of financial and administrative powers to the centres and projects was considerable, the multiplicity of ISRO/DOS centres and units, and the magnitude of inter-centre projects executed by ISRO, led to complex and fast-changing functional and hierarchical relations, causing confusion in the earlier simpler forms of locally placed unitary authorities such as Centre Director/Project Director etc. This factor contributed to the increase of the mediatory role of Chairman, ISRO and therefore the headquarters.

While many facets of such roles of Chairman, ISRO and the subordinate authorities have been successfully adjusted from 1972 onwards to meet the requirements of the Indian space programme so far, it should be noted that the programme is growing at a rapid pace especially with respect to the delivery of operational services. Considerable increase in the decision-making authority at the lower levels of the management structures without affecting the overall integrated coordination between various elements of the programme will therefore become increasingly necessary to avoid stresses in the higher levels and to speed up

decision-making. The challenge to the space programme in the coming years will be to strike a judicious balance. How many useful clues will be available from the earlier experience of the flux of “change and continuity” is a matter for detailed study.

The user coordination systems built up since the mid-seventies as described earlier are remarkable, and could perhaps continue for some years with necessary changes required by new operational services. A constant review would be required especially because of the rapid growth of the applications, and the possibilities of introduction of newer services. Another challenge in the future would be to maintain an “openness” with regard to the introduction of newer patterns and newer systems. The successful ‘marriage’ of the R&D culture of ISRO with the rigours of operational services could come under strain unless watched carefully during the rapidly growing phase of the operational sector.

It would be an understatement to conclude that the management of the Indian space programme during the period 1972–1984 by Prof. Dhawan has been a unique and successful one, with very few parallel records in the world, and has a number of lessons in it for the future of the Indian space programme as well as many other sectors of Indian science and technology. It is, therefore, an excellent “field” for management researchers.

Regarding what can be in store for the future, an extract from an article by Dhawan (1985) will be in order:

“One has however to contend with change. Over the 25 years a new generation has grown up in India. Those who made the selection of space technology and provided the inspiration, initial momentum and enlightened political support have passed into history. How will the new generation of scientists, political leadership and the people at large see the social goals and the role that should be assigned to space technology?”

As the experimental phase transitions into space operations and the lives of millions of Indians can be influenced and affected, people are bound to ask, ‘Is this for our good?’ The tools have been built, how will they be used? Will TV, now that it can reach the millions, help them? Centrally beamed programmes reach every nook and corner but they are one way—what is the feed back? Don’t the teachers want to listen to the students? Can we not devise a two-way system? Will the resource managers’ decisions, armed with good and timely information, help the farmer, the urban elite or the stock exchanges? A million questions! These cannot be answered by space technology. Only people who care, can.”

Some of the answers to these questions will have tremendous impact on the future management of the programme.

The author is grateful to Prof. R Narasimha and Dr A P J Abdul Kalam for providing him with the opportunity of writing this article and to Dr K Kasturirangan for a number of useful discussions on the subject. The author has benefited considerably from the constructive criticism of A Chandran. The author, in his association with Prof. Dhawan, has been particularly fortunate in having the unique opportunity provided by Prof. Dhawan for sharing some of the excitement as well as the rigours of experience in the management of the Indian space

programme. This article would not be complete without mentioning the great contributions of the numerous ISRO personnel—scientific, technical, and administrative—to the Indian space programme, without whose dedicated efforts it would not be what it is today.

References

- Ananth 1985 A ISRO sponsored Research Programme (RESPOND), ISRO special publication ISRO-RESPOND-SP-13-85
- DAE 1970 Atomic Energy and Space Research, A Profile for the decade 1970–80, Atomic Energy Commission, DAE, Government of India
- Dhawan S 1978 *Proc. Indian Acad. Sci.*, C1:1–26
- Dhawan S 1985 Application of Space Technology in India, *Aryabhata* Lecture, Indian National Science Academy, August 2, 1985, Publication Indian Space Research Organisation, Bangalore
- Dhawan S, Rao U R 1982 The Indian Space Programme, 13th International Symposium on Space Technology & Science (ISTS), Tokyo, June–July 1982
- DOS 1981 Space Research and Development: Profile for the decade 1980–1990, Department of Space, Government of India
- ISRO 1979 Sarabhai on Space—A selection of writings and speeches, September 1979, Indian Space Research Organisation, Bangalore
- ISRO 1987a ADCOS, Advisory Committee for Space Sciences, Report of Activities 1980–86, ISRO special publication, ISRO-ADCOS-SP-28-87, March 1987, ISRO, Bangalore
- ISRO 1987b Space-Industry Programme—1986, A partnership in progress, Technology Transfer Group ISRO HQ, ISRO special publication ISRO-TTG-SP-27-87, March 1987
- Rajan Y S 1984 Self-reliance in the Indian Space Programme and sharing of experience, Proc. of Workshop V, Promotion of Space Research in Developing Countries, COSPAR XXV Plenary meeting 25 June–7th July 1984, Graz, Austria
- Sudarsan P, Sridhara Murthy K R 1987 India's Space Programme & Indian Industry—a partnership in progress, ISRO special publication, ISRO-TTG-SP-26-87, March 1987

A survey of wind engineering studies in India

G N V RAO

Department of Aerospace Engineering, Indian Institute of Science,
Bangalore 560 012, India

Abstract. In this paper, the work that has been done in several laboratories and academic institutions in India in the area of wind engineering in the past 20–30 years has been reviewed. Studies on extreme and mean hourly winds, philosophies adopted in model studies in wind tunnels and some of the important results that have been obtained are described. Suggestions for future studies are indicated.

Keywords. Extreme wind; industrial structures; aerodynamic loads.

1. Introduction

Wind engineering studies, which used to be called industrial aerodynamics at one time, may be said to mean the study of the effects of winds on non-flying structures and vehicles. It includes not only the study of winds in the atmosphere, but also that of wind loads on such earth-fixed structures as chimneys and cooling towers, land transportation vehicles like automobiles, ships and trains, and study of disasters due to wind; it is generally not considered at present to include windmills, pollution, ventilation problems etc., although one may expect in course of time that they may also become part of what is now called wind engineering. It may be said that such studies began in India in 1958, when the Railways requested the Department of Aerospace Engineering, Indian Institute of Science (abbreviated hereafter as IISc), Bangalore, to measure the wind loads on a platform shelter (figure 1) of the type widely used in smaller railway stations in India. The request apparently arose out of the observation that a significant number of them, designed on the basis of existing foreign codes, were failing although the specified dynamic pressure was quite high. By hindsight, one now knows that this observation was justified since recent studies (Davenport *et al* 1977) have clearly shown that wind loads at the corners and awnings on low-rise buildings are much higher than was originally estimated. The IISc measurements of pressure distribution on a model were made in smooth flow without simulating atmospheric turbulence, which is known to have a very significant effect on the pressure distribution on such structures. Nevertheless, the data proved to be helpful as testified by the very few, if any, reports of failures of redesigned shelters in recent times. There was a decade-long period of inactivity after this study before the investigation of the

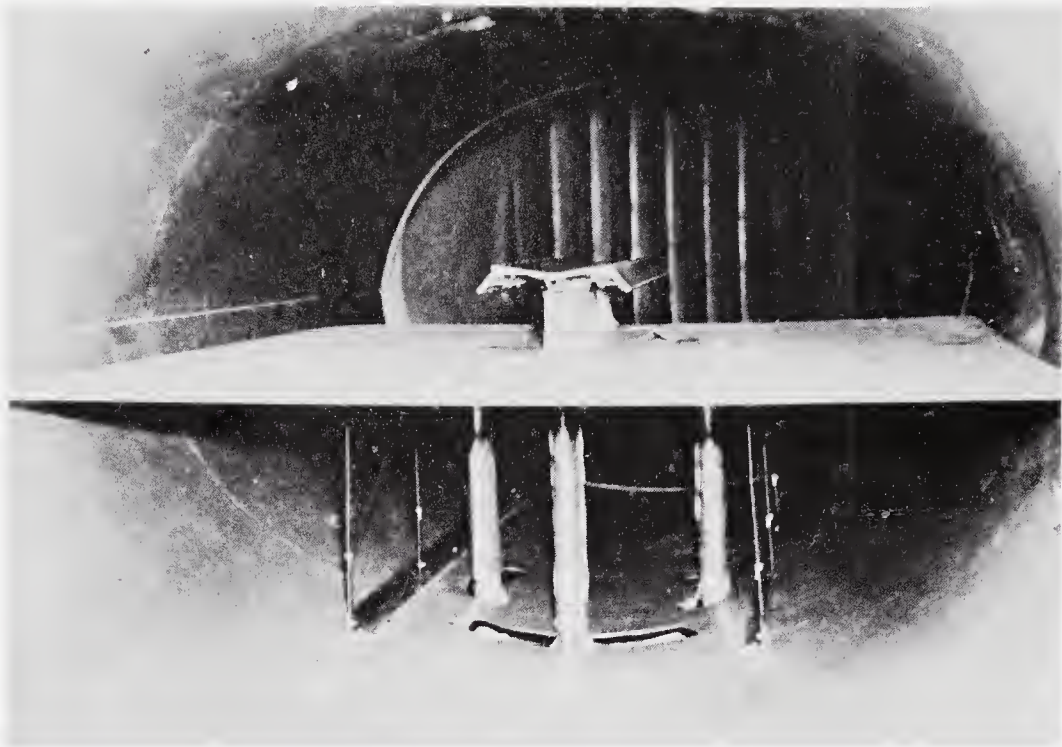


Figure 1. Model of railway platform shelter in the 2.25 m × 1.5 m elliptic wind tunnel.

aerodynamic stability of the proposed 150 m high RCC chimney for the Badarpur Thermal Power Station (Rao *et al* 1970) was taken up, also at IISc. Since that time more than 50 projects have been handled at the IISc (table 1).

The availability of wind tunnels of reasonable size after 1970 stimulated studies in wind engineering at the Indian Institutes of Technology (IIT), at Kanpur, Delhi, Bombay and Madras, as well as at Roorkee and Anna Universities (table 2). However, more than 80% of wind engineering studies in India have been carried out at the IISc. The experimental programmes have covered almost all aspects of wind engineering, comprising tests on models of chimneys, cooling towers, TV towers, land transportation vehicles like automobiles and ships, dispersion of

Table 1. Types of model studies conducted in India.

Chimneys: Single and multiflue chimneys as well as several identical chimneys in a line
Cooling towers: Single and upto six in various types of clusters
Cable-stayed suspension bridges: Sectional models of both erection and completed sections, tower legs
TV towers: Force and aero-elastic models
Antenna dish: Pressure distribution and aero-elastic models.
Land transportation vehicles: Railway carriages, railway engines, automobiles, trucks and ships
Buildings: Low and high-rise buildings including effect of aerodynamic interference
Miscellaneous: Windmills, helmets, mountains etc

Table 2. Major low speed wind tunnel facilities in India.

Facility	Location
4.25 m × 2.75 m Open circuit	IISc, Bangalore
2.5 m × 7.5 m Closed circuit elliptic cross-section	IISc, Bangalore
2.75 m × 1.8 m Closed circuit	HAL [†] , Bangalore
0.91 m dia Open circuit	NAL, Bangalore
0.9 m × 0.6 m Closed circuit	IIT, Kanpur
1.5 m dia Closed circuit	IIT, Madras
2.0 m × 2.0 m Open circuit	Roorkee University
1.25 m × 1.5 m Open circuit	DGCA, [‡] Technical Centre, Delhi

* NAL – National Aeronautical Laboratory; [‡] DGCA – Directorate General of Civil Aviation; [†] HAL – Hindustan Aeronautics Ltd.

pollutants etc. These studies and the experience of practising engineers indicated not only a need to revise some of the relevant Indian standards like IS-875 (1964) but also to study the nature of the Indian atmosphere in order to evolve more realistic wind speed specifications (Narasimha & Shrinivasa 1984; Seetharamulu *et al* 1985, pp. 47–51; Rao 1985b, pp. 11–19; Sharma 1985). Coinciding with the increase in the general awareness of problems in wind engineering in India, a number of seminars and workshops have been held, whose proceedings have been published (Seminar 1980; Workshop 1984; Asia-Pacific Symposium 1985; Indo-US Workshop 1985) and the Department of Science and Technology (DST) formed a Committee to identify problem areas and suggest the support required to study them (DST 1983). It is appropriate at this stage to review the work that has gone on and identify possible areas for further study. We begin by a consideration of the Indian atmosphere insofar as wind loads on structures are concerned.

2. Peculiarities of the Indian atmosphere in respect of wind loading analysis

Historically, wind loading on a structure was viewed in the early days as simply one of estimating the 'dynamic pressure' of the wind at the site of the structure and multiplying it by the 'shape factor' (or drag coefficient) and the characteristic area of the structure to obtain the wind force. This was the view taken in the Indian Standard Specification IS-875 (1964). However, as the number of tall and slender structures increased, it became clear that not only the dynamic action of wind for 'along-wind' or drag-direction load has to be computed, taking into account the unsteady nature of the wind load, but also that other dynamic responses like vortex excitation, galloping, flutter and ovalling have to be examined. It then became necessary also to know the characteristics of the Indian atmosphere in greater detail than had been done earlier. The starting point for this study was to put the extreme wind and mean hourly wind data on a more scientific basis.

A number of extreme wind analyses have been made using both the Fischer-Tippett type I (FT1) method or its variants (Rao 1985b, pp. 11–19), and the Fischer-Tippett type II (FT2) method. It is now recognised that five mechanisms operate to create high winds in India (Rao 1985b, pp. 11–19), namely, tropical cyclones, extra-tropical cyclones, monsoons, local thunderstorms such as *kal-baisakis* in

West Bengal and the pressure system. In most parts of India, there is a mix of the above population which is reflected in the curved line that one obtains when the reduced variate is plotted against the wind speed. It is well-known (Mayne 1979) that a linear regression will be obtained only if the mechanism is of a single type and will then correspond to the FT1 type. For example, the extreme winds in Western Europe and Canada are caused by the fully developed pressure systems which result in a linear regression of reduced variate against wind speed. At present, available theories for calculating the loads on a structure (Davenport 1967; Vickery & Basu 1984) implicitly assume the wind to be 'well-behaved', i.e., caused by a pressure system. In view of the fact that extreme winds at most of the locations in India are apparently caused by different mechanisms, it appears that a prediction based on FT2 is to be preferred (although it cannot be theoretically justified, but is simply a 'good fit' curve) than FT1. Nevertheless, a combination of FT1 analyses, local judgement and orography of India has yielded what is believed to be a more realistic extreme wind map for India (Sharma 1985).

Since a knowledge of existing probabilistic loading theories (Vickery & Basu 1984) requires mean hourly wind (MHW) speed, an attempt was made by Seetharamulu *et al* (1985, pp. 47–51) to generate such data from information supplied by the India Meteorological Department (IMD). They observed the surprising result that the ratios of peak gust (PG) to MHW for practically all the stations in India were higher than the values quoted for regions with winds due to the pressure system (Davenport 1967). Their observation appears to have borne out a somewhat similar observation of Narasimha & Shrinivasa (1984) that the ratio of peak gust to yearly average wind is higher in India than in the United States.

However, it is necessary to examine more closely not only the manner in which MHW is derived in India and many other countries but its definition as well. 'Mean hourly wind' of the India Meteorological Department is the mean wind during the last ten minutes of every hour and not the average during the entire hour. This is derived from an eye judgement of continuous wind data of the Dyne pressure tube anemograph in which the contribution of very short duration high winds cannot be given adequate importance in the integrated value. On the other hand, in those countries where the MHW is derived from some kind of integrating instruments such as a propeller or vane anemometer allowed to run continuously through the short duration peaks, one may expect a more realistic mean. Mani & Mooley (1983) have reported examining the true full hour mean and the mean of the last ten minutes and find a 5% difference between them, but the basis of the two means is not indicated. More recently, Rao *et al* (1985b) have examined the effect of various averaging times in moderate winds at Balasore and concluded that a much larger time interval of 15–20 min is required to obtain nearly steady values. However, the observations of Narasimha & Shrinivasa (1984) regarding the larger ratio of peak gust to yearly mean in India does suggest that the peak gusts are due to a different mix of populations than in the US since yearly means in IMD are obtained from the integrated values of the number of revolutions of the cup anemometer, and may therefore be taken as a true mean, in the sense that the contribution of the short duration gusts are properly counted.

Recently, Rao (1987) has found that the peak MHW for Madras does follow FT1 distribution but that the peak gust is significantly convex in the FT1 plot (figure 2).

Measurements of turbulence characteristics in the Indian atmosphere was

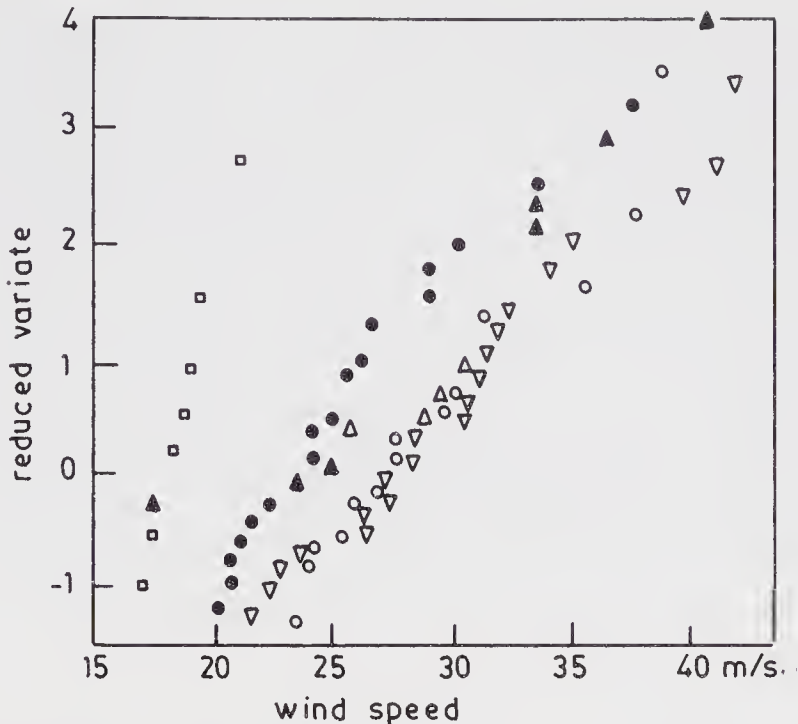


Figure 2. FT1 plot of reduced variate vs. wind speed for PG and MHW. (□ – MHW; the rest of the symbols represent peak gusts.)

initially attempted using an instrumented Canberra aircraft (DRDO 1975). More recently boundary layer measurements in the first 30 m have been made (Rao *et al* 1985b). The earlier measurements suggested that the frequency of atmospheric gusts in India of a certain duration are more than that in European countries. The latter boundary layer measurements have been made in pressure system winds of fairly low magnitude and one hopes that data during the high winds and cyclones (or near cyclonic regions) will become available in course of time.

To sum up, one may state that the foundations for a rational study of wind characteristics in India of the nature that is useful for structural design are now being laid.

3. Facilities

Table 2 gives the major facilities in the form of wind tunnels that are available in India. Smaller wind tunnels are available in a few other places. The most extensively used facility has been the 4.25 m × 2.75 m open circuit wind tunnel of the Department of Aerospace Engineering, IISc, Bangalore.

A major deficiency in most of the major facilities has been that they were not originally designed for wind engineering studies and as such it is quite difficult to reproduce the turbulence characteristics of the atmospheric boundary layer. The exception is the 2 m × 2 m wind tunnel at Roorkee University in which, however, the maximum wind speed is limited at present to 20 m/s with the tunnel empty.

Theoretical studies

Much of the attention in theoretical studies has been directed towards the interpretation of model studies to full scale. It appears that the effect of Reynolds

and Strouhal numbers is generally to reduce the amplitude of response of most structures subjected to vortex-excited oscillations (Rao 1975). A linear analysis of the response of simplified models of structures, such as sectional models of suspension bridges or cantilever structures mounted as linear mode models, enables the prediction of the full scale response more accurately (Rao, 1972).

4. Model studies

4.1 Modelling considerations

By far the greatest effort has been in the area of model studies. Table 1 gives a list of these studies. It is well-known that a number of non-dimensional parameters have to be satisfied to ensure that model results are a replication of the response of the full-scale structure. These are:

- (a) geometric similarity;
- (b) Reynolds number ($U_0 l / \nu$);
- (c) stiffness parameter ($EI / \rho U_0^2 l^4$);
- (d) density ratio (ρ_s / ρ_a);
- (e) structural damping (δ);
- (f) ratio of velocity of exit gases to free stream velocity;
- (g) ratio of wall thickness to diameter;
- (h) characteristics of the atmosphere: All the average and fluctuating components, and length scales, suitably scaled down. If the above non-dimensional parameters are satisfied, then the relation between the following model response parameters and that of the full-scale structure can be shown to be as follows:
 - (i) equality of Strouhal number: nl / U_0 ;
 - (ii) equality of non-dimensional amplitude response, both static and dynamic;
 - (iii) stress at any point, static and dynamic at the same free stream velocity.

It is well-known that it is practically impossible to satisfy all the requirements of dynamic similitude, in particular the Reynolds number (Re), and it is usual to develop or follow certain practices to extrapolate model results to full scale taking into consideration the deviations from strict similarity considerations. The practice adopted at the IISc is described later insofar as Re effect corrections are concerned. Although mean velocity profiles have been simulated, using Cowdrey's (1967) method (figure 3 shows the grid rods), simulation of atmospheric turbulence has not yet been done due to the short upstream fetch in most of the existing wind tunnels. The issue of both the mean velocity profile and turbulence structure is complicated by the knowledge that available information refers to well-behaved winds or winds due to pressure system while extreme winds in practically all parts of India are, as explained earlier, due to some kind of cyclone or thunderstorm.

4.2 Modelling practices

Depending on the nature of the problem to be studied, models are categorised as (1) rigid models, (ii) aeroelastic models, (iii) linear mode models, (iv) sectional models, and (v) distorted models (Rao 1985a). The practices adopted in the case of models of some of the important structures are described below.

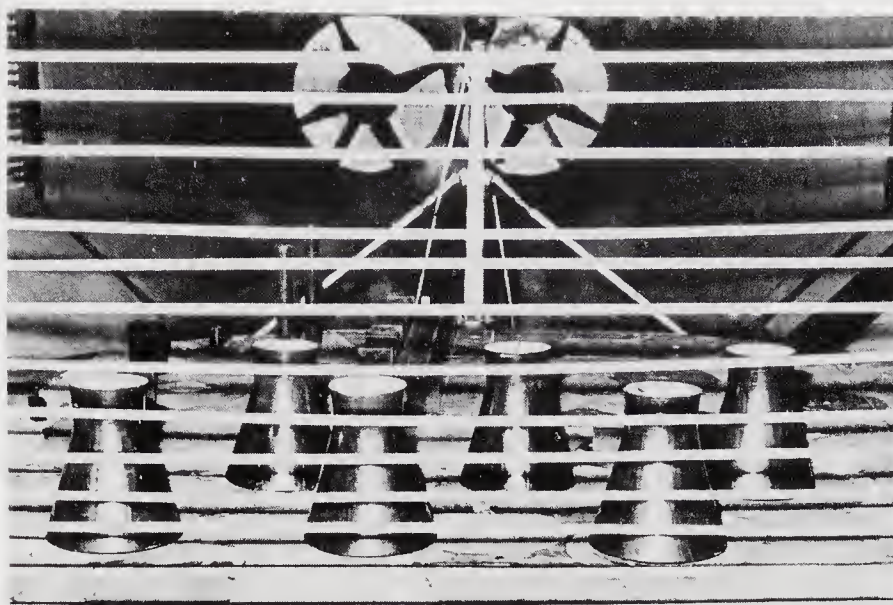


Figure 3. Parallel rods for generating mean velocity profile in a wind tunnel.

4.3 Chimney models

The usual practice in making chimney models is to make them as slightly distorted aeroelastic models. The models are made in aluminium by accurately boring on the inside and machining on the outside but the thickness is also geometrically scaled. This means that the models are not exactly replicated full scale chimneys but it is not difficult to work out the relation between a truly replicated model and an aluminium model, in the case of RCC and steel chimneys. Table 3 gives the relation between such models and full scale structures. The model is deliberately made smooth for reasons which will be explained later. Figure 4 shows a number of these aluminium models.

Table 3. Relation between geometrically similar and fully aeroelastic models.*

Property	Full-scale value
Frequency	$(n_m/N)(E_f/E_m)(\rho_m/\rho_f)^{1/2}$
Critical wind speed for vortex excited oscillation (velocity U_f)	$U_m(E_f/E_m)(\rho_m/\rho_f)^{1/2}$
Oscillatory amplitude	$N(\rho_m/\rho_f)^{1/2}$
Streamwise deflection, W_f , at the same dynamic pressure	$N(E_m/E_f)W_m$
Oscillatory moment at resonance at any point, M_{of}	$N^3(\rho_m/\rho_f)$
Along-wind moment at any point at the same dynamic pressure [†]	$M_{dm}N^3(0.8/1.2)$

* Subscript 'f' denotes full scale value and subscript 'm' the model value.
 N = model scale, more than 1.0.

[†] Full scale C_D is taken as 0.8 and that of model 1.2.

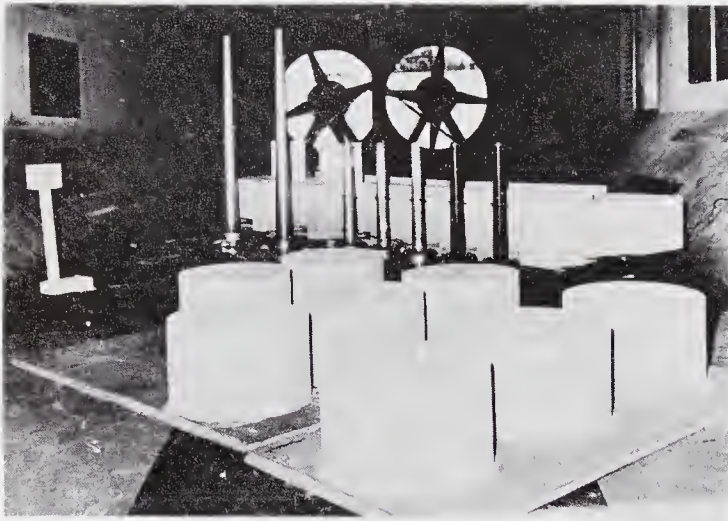


Figure 4. Cluster of aluminium chimney models.

4.4 Natural draught cooling tower models

Aluminium has also been used to make aeroelastic models of natural draught cooling towers. A particularly strong wood known as *Irumbuli* which is said to have a specific gravity of almost 1.5, is used as the former to spin thin aluminium sheets. By taking a sheet which is slightly thicker than the scaled-down value (or choosing the scale to suit a slightly thicker commercially available aluminium sheet), it was possible to obtain models which were accurate to within 5% in thickness and better than 1% in other dimensions. Figure 5 shows a group of such models.

4.5 Models of framed structures

Models of framed steel structures were made by choosing or getting rolled sheets of geometrically scaled-down thicknesses and bending them to the shape of the angle etc. Soldered joints were found to be unsatisfactory and hence all joints were silver-brazed. The same procedure is used in the case of aeroelastic models of antennae.

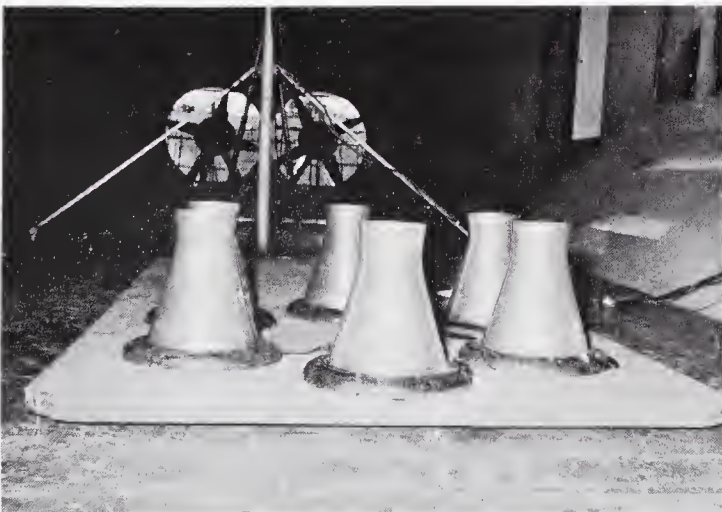


Figure 5. Aluminium aeroelastic models of natural draft cooling towers.

4.6 Sectional models of suspension bridges

Sectional models of suspension bridges are made by using both wood and steel sheets. A similar procedure is adopted in the case of linear mode models, such as those of the service towers for satellite launch vehicles (figure 6).

4.7 Damping of models

It is necessary during a test programme to vary the structural damping of models to overlap the expected value of the full-scale structure. This is done in the case of earth-fixed models like chimneys and linear mode models of satellite launch vehicles by mounting them on neoprene rubber pads of different thicknesses. In all other cases, oil dashpots are used.

5. Examples of model studies

5.1 Chimneys and towers

A number of studies (exceeding 30) of chimneys and towers have been carried out and these studies have yielded many useful results. It has been found that in the case of chimneys, it is more economical to use aerodynamic remedial measures when the dynamic moments due to a vortex or other modes of excitation at their natural frequency, exceed the direct wind (or 'along-wind') moment by more than about 10% (Krishnaswamy *et al* 1975, pp. 209–215; Rao *et al* 1985a; Rao 1985c, pp. Iiii–Ixiv). A very effective remedial measure has been the development of discrete strakes (figures 7 & 8) which has been incorporated in more than 20 chimneys in India and abroad. It is observed that the additive drag penalty of discrete strakes is much less than that of continuous strakes (figure 9).

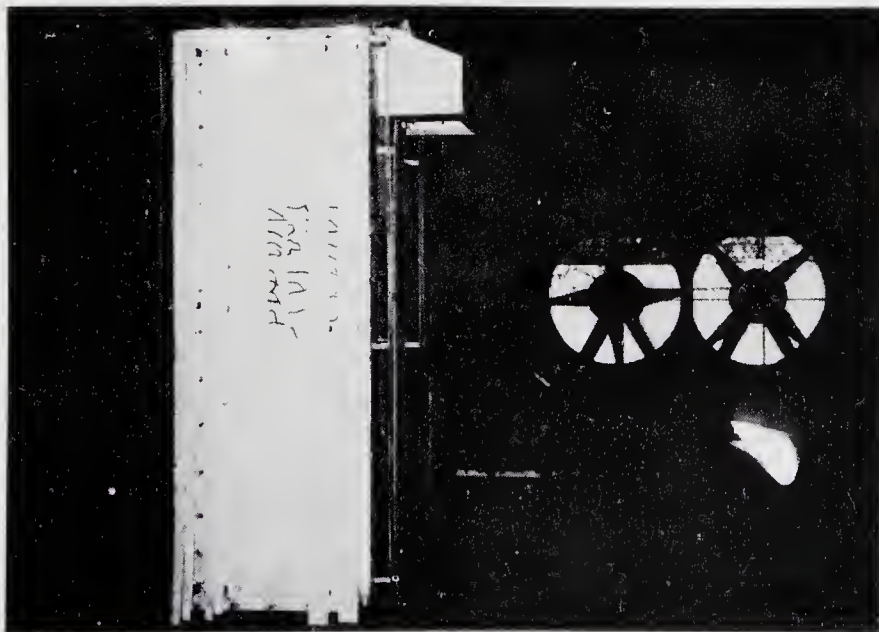


Figure 6. Linear mode model of service tower of satellite launch vehicle.

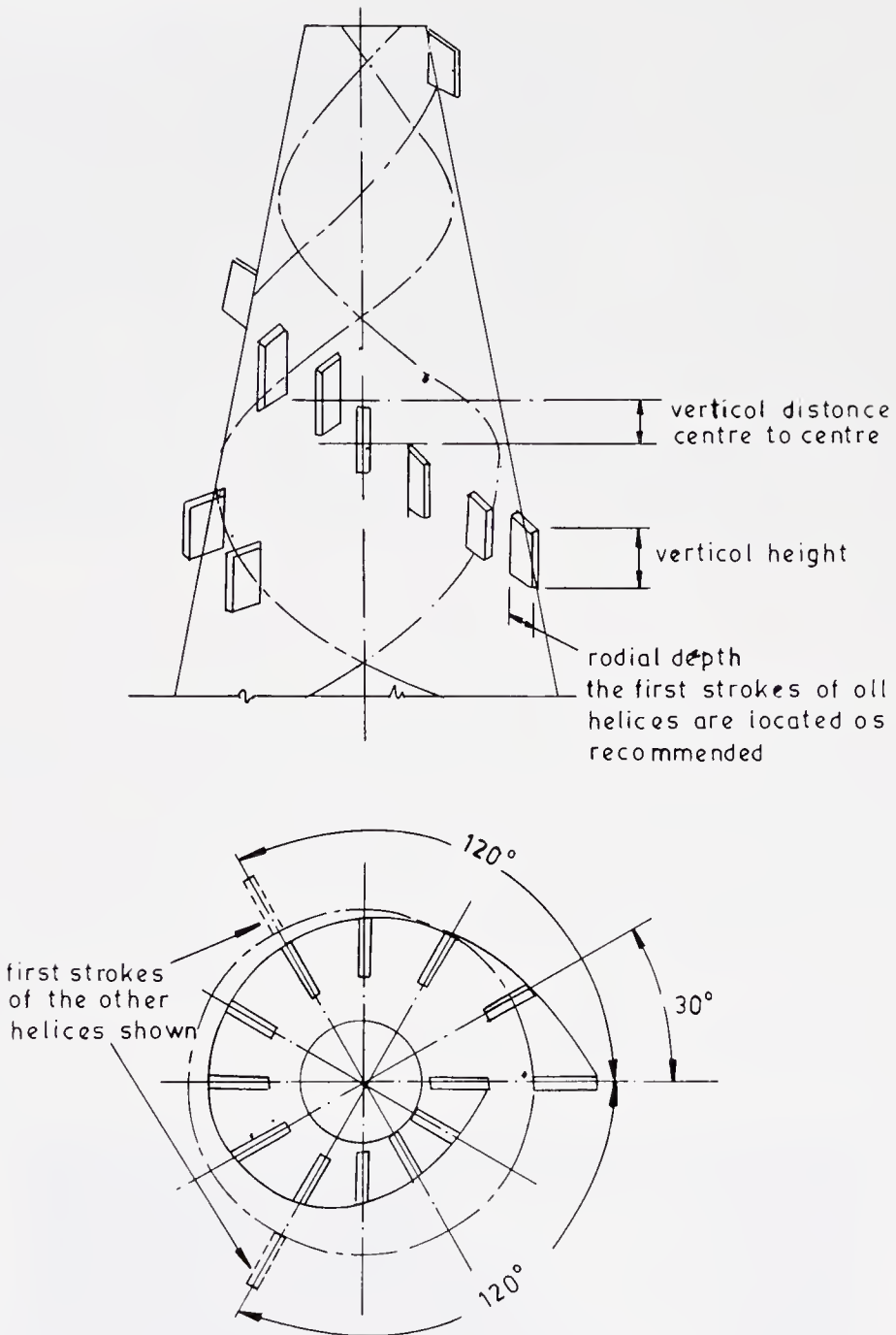


Figure 7. Geometric configuration of discrete strakes.

The study of the effect of aerodynamic interference between chimneys continues to attract worldwide attention (Price & Paidoussis 1984; Vickery 1981; Krishnaswamy *et al* 1975, pp. 209–215; Lakshmana Gowda & Prabhu 1987) but it must be stated that the exact nature of the enhanced oscillatory loading* and the effect of Reynolds number are not yet fully understood. There is however no dispute over the fact that aerodynamic interference between chimneys does lead to increased oscillatory response. Figure 10 shows the result of one such study at IISc which suggests that the enhancement can be as much as 10 times in subcritical Re flow. The remedial measures described earlier in the form of discrete strakes work equally well in substantially alleviating increased oscillatory amplitude. The effect

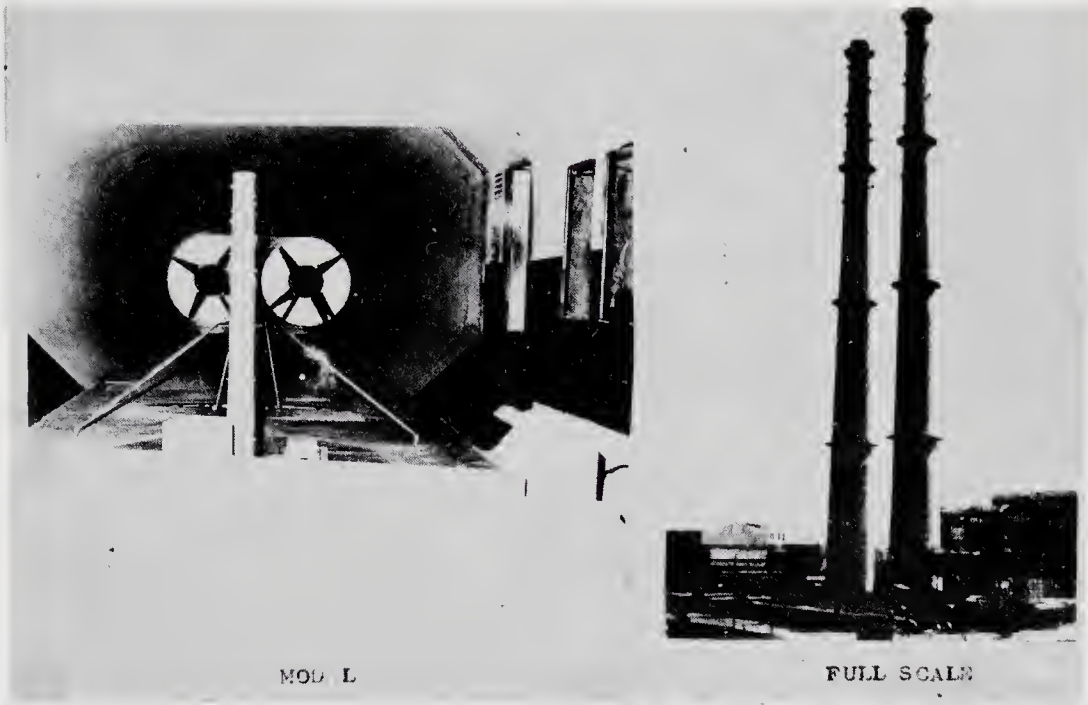


Figure 8. Discrete strakes on wind tunnel models and full scale chimneys.

of wind direction on a cluster of five chimneys is shown in figure 11. It is seen that a wind which is slightly inclined to the line of chimneys (by about 15°) gives rise to maximum load enhancement due to oscillation and the most severely affected one is the second one in the windward direction. In a study of the effect of the surrounding structures in a thermal power station, Swamy & Lakshmana Gowda (1983) found that they tended to reduce the wind load on chimneys. Prem Krishna *et al* (1983) found that aerodynamic damping of the chimney increases with increased wind speed even in subcritical flow.

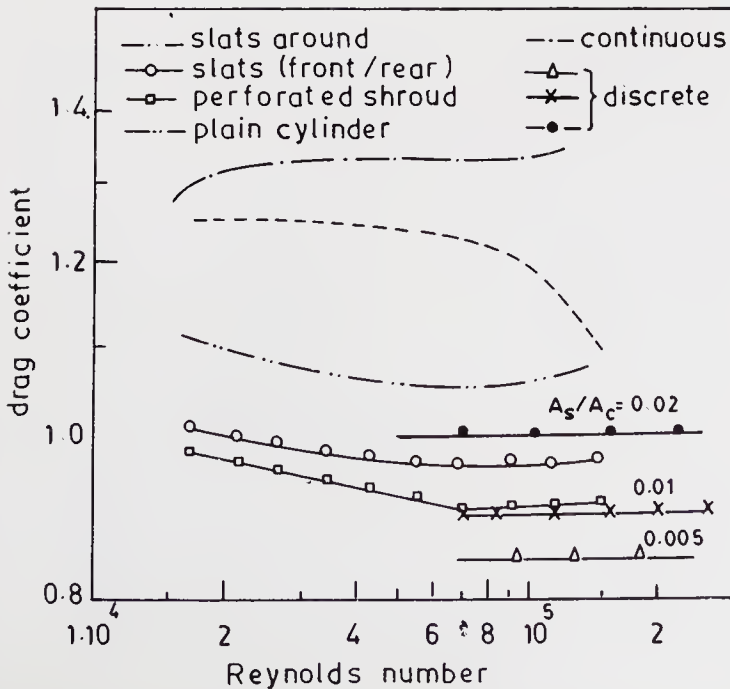


Figure 9. Total drag of chimney cross-section with aerodynamic remedial measures including continuous and discrete strakes.

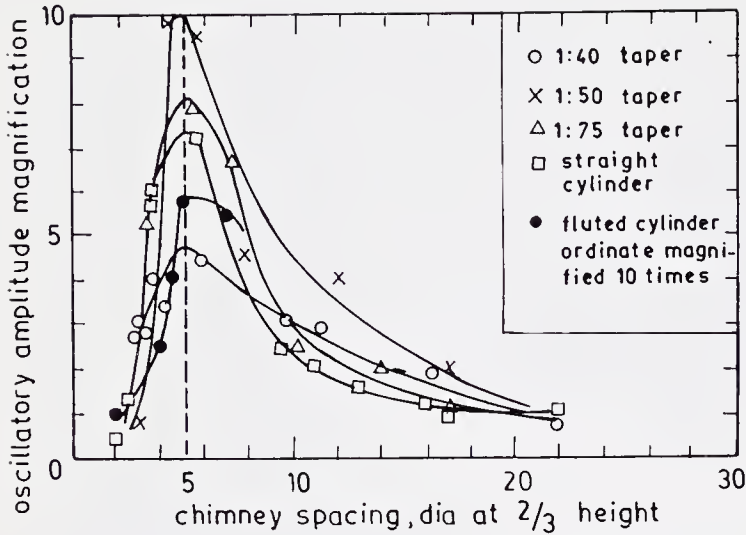


Figure 10. Effect of aerodynamic interference on oscillatory amplitude of leeward chimney.

Experimental and theoretical estimates of the gust factor for an unsymmetrical tower were carried out by Nigam *et al* (1981) who found that the gust factors in two perpendicular directions were substantially different, being 2.2 and 3.2.

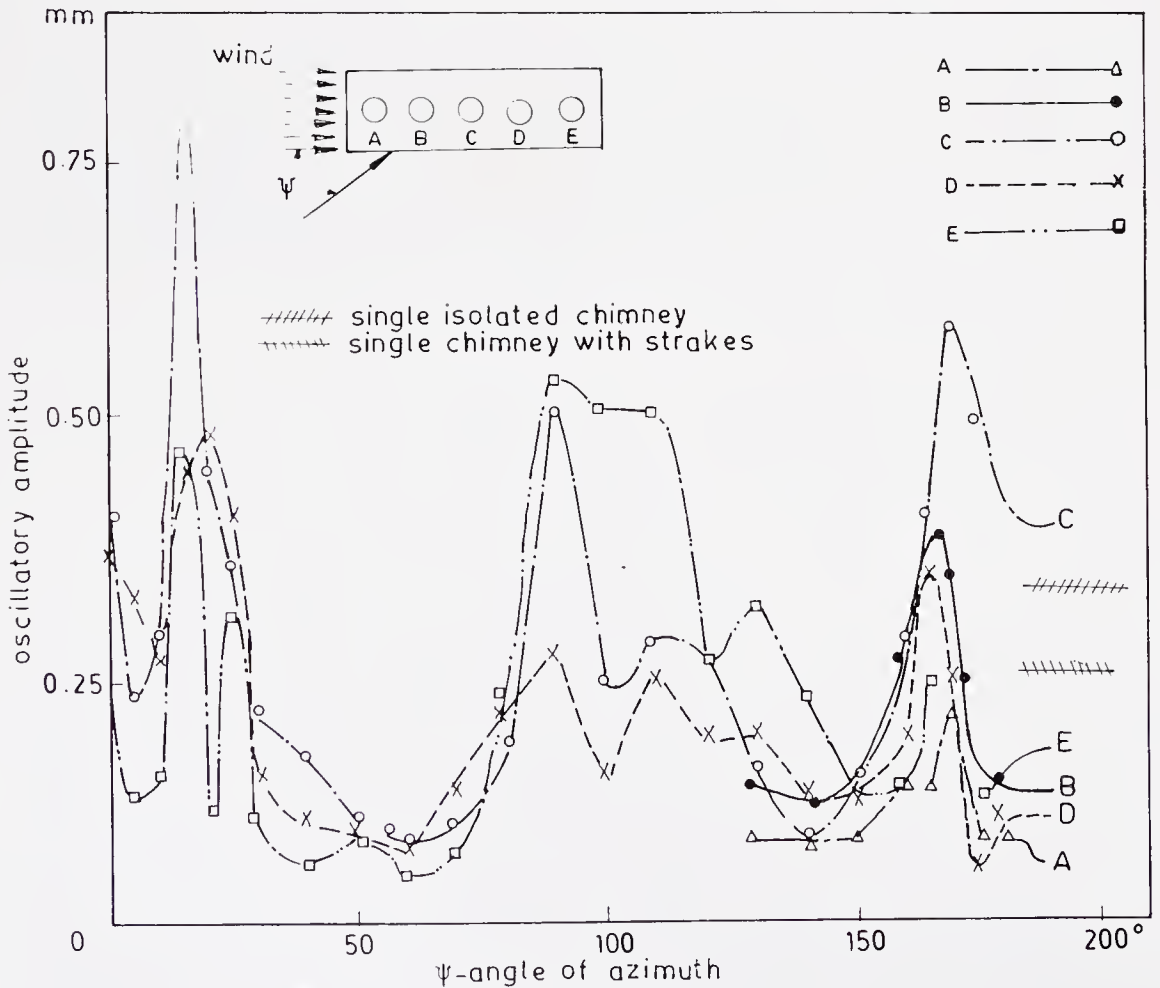


Figure 11. Effect of wind direction on amplitude enhancement.

5.2 Cooling towers

Tests on various planform configurations of cooling towers have been carried out on pressure distribution models to assess the effect of planform geometry (Rao & Reddy 1980). The load enhancement was found to vary from 1.4 to 2.0. Aeroelastic models of cooling towers have also been tested to determine tendencies for ovaling oscillations. It is found that critical loading due to aerodynamic interference takes place when the wind is inclined at an angle of about 45° to the line of cooling towers.

5.3 Cable-stayed suspension bridges

Sectional models of cable-stayed suspension bridges have been tested (Krishnaswamy *et al* 1971, pp. 678–698; Krishnaswamy 1981). Tests on linear mode models of the towers in their free standing mode have been made to assess galloping tendencies. When the cross-sectional shape was rectangular, with the bottom open, a set of discrete strakes was found to be very effective in suppressing model oscillations (figure 12) and increasing the critical wind speed for the onset of flutter (Krishnaswamy *et al* 1971, pp. 678–698). But this device did not work when the bridge had a nosing. So far, no aerodynamic remedial measure in the form of some flow-spoiling device has been found which will suppress galloping instability of square cross-sections.

5.4 Low-rise structures

A few studies of wind effects on low-rise structures have been made in simulated mean winds (Krishnaswamy *et al* 1971, pp. 678–698, 1982; Gupchup & Agashe 1981). The aim was to obtain mean pressure data.

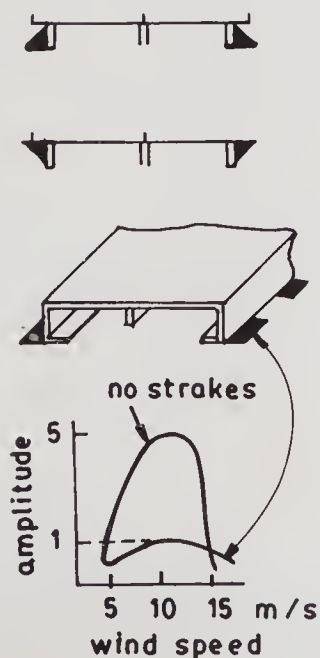


Figure 12. Effect of discrete strakes on oscillations of cable-stayed bridges.

5.5 Extrapolation of model results to full scale conditions

Considerable thought has been applied to clarify the extrapolation of model results to full-scale conditions both for along-wind load and across-wind load. The extrapolation obviously depends on the type of body and the approach adopted in the case of some typical bodies is given below. The dominant scaling parameter is the Reynolds number.

5.5a Sharp edged bodies: If the test Reynolds number exceeds 25,000, the model values are taken to be valid at full scale Re. This requirement is achieved in all test programmes so far.

5.5b Along-wind force-rounded bodies: Along-wind force on rounded bodies such as circular cylinders are estimated by conducting model studies with either known laminar boundary layer separation or by fixing transition with a trip wire (Swamy & Lakshmana Gowda 1983). Every effort is made in both cases to ensure that conditions corresponding to a region in the 'drag bucket' do not exist and the model surface is therefore made smooth. A 'proportionality factor' is then used to obtain full-scale value as follows:

$$\frac{\text{full-scale force coefficient}}{\text{model force coefficient}} = \frac{\text{full-scale circular cylinder force coefficient}}{\text{full-scale circular cylinder force coefficient at transcritical Re}}$$

The RHS terms are obtained from handbooks such as ESDU (1978). This procedure is believed to be more logical than the ESDU procedure of 'difference techniques', namely full-scale force coefficient = model force coefficient - (full-scale circular cylinder force coefficient at full-scale Re - circular cylinder force coefficient at model Re).

5.5c Dynamic response - rounded bodies: The estimation of full-scale dynamic conditions from model results is more complicated. Corrections have to be applied for differences both in Strouhal number (St) and Reynolds number (Re). Here, the known trends in Re vs. St and Re vs. oscillatory lift coefficient for circular cylinders are used (figures 13 & 14). As may be observed, there is no significant variation in oscillatory lift coefficient with Re, if care is taken to ensure that there is no 'lift bucket'. Hence, if tests are carried out on a smooth rounded body at an Re lying to the left of the oscillatory lift and drag buckets, one may expect the full-scale

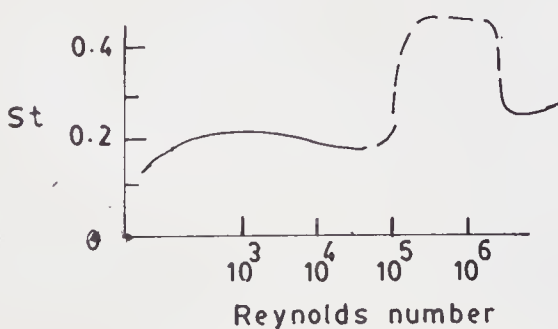


Figure 13. Strouhal number-Reynolds number relation for circular cylinder.

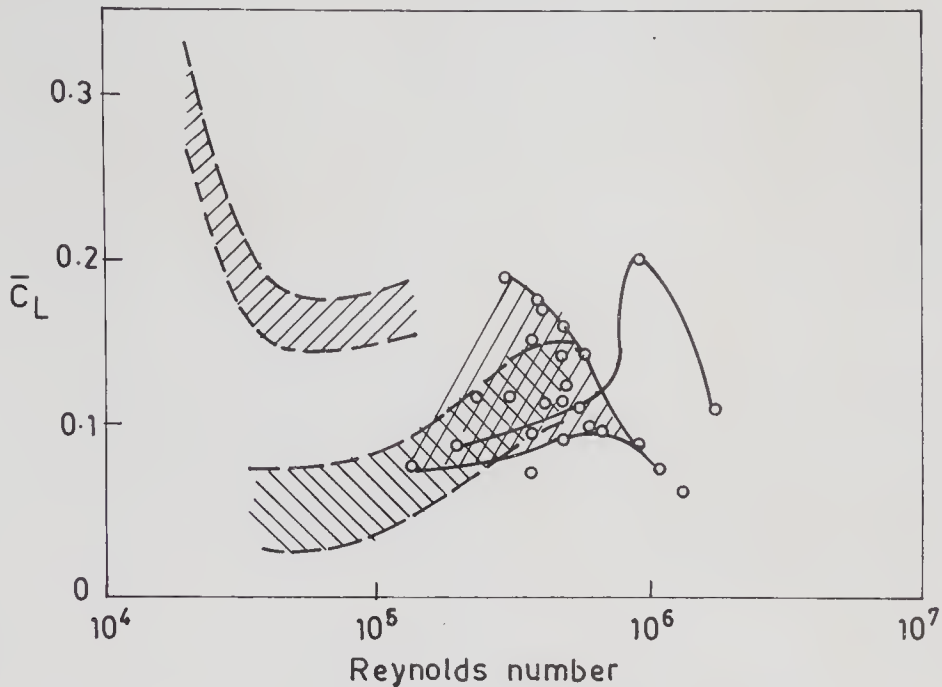


Figure 14. Oscillatory lift coefficient of circular cylinder.

oscillatory lift coefficient to be perhaps the same as that of the model value. Together with the known gradual and practically linear rise of St vs. Re from subcritical to transcritical Re (again excluding the 'inverted bucket region' of Re from 2×10^5 to 2×10^6), one arrives at the following simple rules of extrapolation of model results to full scale.

$$\frac{\text{Full scale } St}{\text{Model } St} = \frac{\text{St of circular cylinder at full scale } Re}{\text{St of circular cylinder at model } Re}$$

and

$$\text{non-dimensional model transverse oscillatory response} = \text{nondimensional full-scale transverse oscillatory response.}$$

6. Full-scale measurements

It is unfortunate that no systematic full-scale measurements were made on any structure in India till about 1986. The unusual lighting towers of the Jawaharlal Nehru Stadium at New Delhi have now been instrumented (figure 15) and plans are under way to instrument a few chimneys and cooling towers. One hopes that these measurements will not only throw light on those properties of the wind relevant to wind engineering but also lead to better methods of wind-loading analysis.

7. Conclusions

As stated earlier, it is believed that foundations for serious studies on wind engineering have been laid in India. A great deal more still needs to be done of

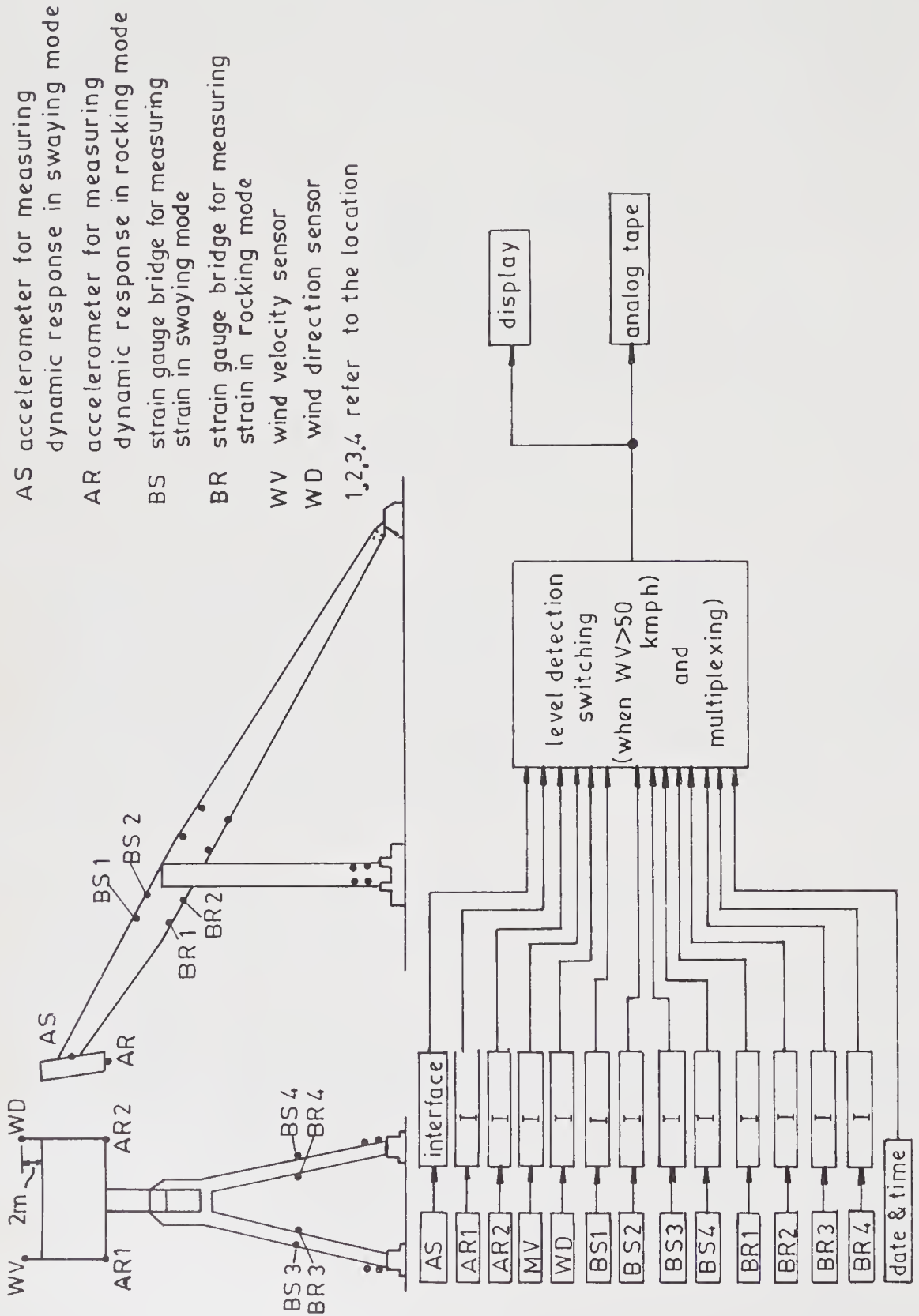


Figure 15. Instrumentation of lighting towers of Jawaharlal Nehru Stadium, New Delhi.

which the following appear to be most important in the foreseeable future.

- (i) Increase the number of Dyne pressure tube anemograph stations to at least 150, develop and install microprocessor-based wind speed and direction sensors with sufficient memory for storing the more important peak and average data.
- (ii) A larger number of wind engineering wind tunnels are required; this includes facilities for creating cyclonic conditions.
- (iii) More full-scale measurements on both tall- and low-rise structures have to be made. In particular, greater emphasis on the study of aerodynamic interference should be made.
- (iv) It is necessary to strengthen theoretical studies of both the meteorological data on wind loads and the dynamic action of the wind.

The foundations that have been laid have already demonstrated visibly the returns in terms of more economical designs and creation of more reliable databases. The future must build on these.

References

- Asia-Pacific Symposium 1985 *Asia-Pacific Symposium on wind engineering* (Meerut: Sarita Prakasan)
- Cowdrey C F 1967 A simple method for the design of wind tunnel velocity profile grids, NPL Aero note 1055, England
- Davenport A G 1967 *J. Struct. Div., Am. Soc. Civ. Eng.* 93: ST3
- Davenport A G, Surrey D, Stathopoulos T 1977 Wind loads and low-rise buildings:— Final report of phases I and II, BLWT-SS8, University of Toronto, Western Ontario
- DRDO 1975 Report on the measurement of atmospheric turbulence in India using an instrumented Canberra aircraft, Report of the Defence Research and Development Organisation, New Delhi
- DST 1983 Report of the Committee on wind engineering, Department of Science and Technology, New Delhi
- ESDU 1978 *Fluid mechanics* (London: ESDU) vol. 1–3
- Gupehup V N, Agashe S N 1981 *J. Inst. Eng. (India)* (Spec. Issue) 61: 94–97
- IS-875 1964 *Indian Standards Specification* (New Delhi: Indian Stand. Inst.)
- Indo-US Workshop 1985 Indo-US workshop on wind disaster mitigation, Proceedings, Structural Engineering Research Centre, Taramani, Madras
- Krishnaswamy T N 1981 *J. Inst. Eng. (India)* (Spec. Issue) ND2 61: 43–50
- Krishnaswamy T N, Rao A K, Rao G N V, Durvasula S, Reddy K R 1971 *Proc. III Int. Conf. on wind effects on buildings and structures* (Tokyo: University Press)
- Krishnaswamy T N, Rao G N V, Durvasula S, Reddy K R 1975 *Proc. IV Int. Conf. on wind effects on buildings and structures, Heathrow* (London: Pergamon Press)
- Krishnaswamy T N, Rao G N V, Durvasula S, Reddy K R 1982 Wind tunnel model study of 14 m dia parabolic antenna dish of the Space Application Centre, IWTR 164, Department of Aerospace Engineering, Indian Inst. Sci., Bangalore
- Lakshmana Gowda B H, Prabhu D R 1987 *J. Sound Vibr.* 112: 487–502
- Mani A, Mooley D A 1983 *Wind energy data for India* (New Delhi: Allied Publishers)
- Mayne J R 1979 *J. Ind. Aerodyn.* 5: 109–137
- Narasimha R, Shrinivasa U 1984 *Sadhana* 7: 259–274
- Nigam N C, Gupta A K, Mathur S P 1981 *J. Inst. Eng. (India)* (Spec. Issue) ND2 61: 69–76
- Prem Krishna, Badruddin Ahmed, Pande P K 1983 *Proc. 6th Int. Conf. on wind engineering* vol. 3
- Preece S J, Paidoussis M P 1984 *J. Wind Eng. Ind. Aerodyn.* 3: 329–348
- Rao G N V 1972 *J. Aeronaut. Soc. India* 24: 242–245
- Rao G N V 1975 *II US Natl. Conf. on wind engineering research* (University of Colorado Press) paper JV-8-1
- Rao G N V 1985a *J. Inst. Eng. (India)* AE 1&2 65: 11–18
- Rao G N V 1985b *Proc. Asia-Pacific Symp. on wind engineering* (Meerut: Sarita Prakashan)
- Rao G N V 1985c *Proc. Asia-Pacific Symp. on wind engineering* (Meerut: Sarita Prakashan)

- Rao G N V 1987 *Proc. US-Asia Conf. on EMNHD, Bangkok, Thailand* (Bangkok: Asian Inst. Technol.) pp. A12-1-A12-8
- Rao G N V, Durvasula S, Reddy K R 1985a *Natl. Sem. on Tall RCC chimneys*. (New Delhi: Natl. Thermal Power Corp.)
- Rao G N V, Durvasula S, Reddy K R, Palaniswamy S 1970 Final report on model tests of 15 m high smoke stack for Badarpur Thermal Power Station, IWTR 84, Dept. of Aerospace Engineering, Indian Inst. Sci., Bangalore
- Rao G N V, Reddy K R 1980 *Proc. I Asian Cong. Fluid Mechanics* (Bangalore: Asian Cong. Fluid Mechanics) vol. C, Paper B36
- Rao K N, Prabhu A, Narasimha R 1985b Averaging time for atmospheric turbulence data, Report 85 ASE, Centre for Atmospheric Studies, Indian Inst. Sci., Bangalore
- Scetharamulu K, Swamy B L P, Chaudhry K K 1985 *Proc. Asia-Pacific Symp. on wind engineering* (Meerut: Sarita Prakashan)
- Seminar 1980 Seminar on Industrial Aeronautics, Proceedings, Published by Institute of Engineers, India, ND2, vol. 61
- Sharma M C 1985 Indo-US Workshop on Wind disaster mitigation, Proceedings, Structural Engineering Research Centre, Taramani, Madras
- Sharma N C 1985 Indo-US Workshop on Wind disaster mitigation, Proceedings, Structural Engineering Research Centre, Taramani, Madras
- Swamy N V C, Lakshmana Gowda B H 1983 Wind Tunnel Studies on the Model of the RCC chimneys for Korba West Bank Thermal Power Station, Madhya Pradesh, Report 117, Department of Applied Mechanics, Indian Inst. Technol., Madras
- Vickery B J 1981 *J. Wind Eng. Ind. Aerodyn.* 1: 177-193
- Vickery B J, Basu R I 1984 *Eng. Struct.* 6: 324-330
- Workshop 1984 Workshop on wind effects on structures, organised by Inst. of Engineers (India), Selected papers published in vol. 65-66 of Aero Eng. Div., *J. Inst. Eng. (India)*

Hydrodynamic numerical modelling of storm surges – Application to the Bay of Bengal

P C SINHA

Centre for Atmospheric Sciences, Indian Institute of Technology,
New Delhi 110 016, India

Abstract. A hydrodynamic numerical model and a tide-surge interaction model are described for the evaluation of storm surges and their interaction with the tides in the Bay of Bengal. Numerical experiments are performed with the help of these models to simulate the surges generated by three recent severe cyclonic storms which struck the east coast of India and Bangladesh. The predicted peak sea-surface elevations compare well with the limited observed values.

Keywords. Storm surges; bottom stress; friction coefficient; idealized wind field; radiation condition; tide-surge interaction.

1. Introduction

Storm surges are the outcome of cyclonic winds blowing over a large surface of water, which is bounded by a shallow basin. The driving force of winds leads to accumulation of water on the shoreline which, in turn, results in a sudden and substantial rise in sea level. Every year tropical cyclones strike certain exposed coastlines in several parts of the world causing heavy loss of life and property. In fact, most of the world's greatest human disasters associated with tropical cyclones have been directly attributed to storm surges.

There can be little doubt that the number of casualties would be considerably lower if the surges could be predicted, say 24 hours in advance, thus allowing effective warnings in the threatened areas. The prediction must, of course, be accurate enough that one can distinguish between dangerous surges and surges that cause little harm, as people cannot be evacuated from exposed areas for every approaching storm. Some success in predicting storm surges has been achieved by computer oriented mathematical models.

Most of the work on numerical modelling of storm surges associated with tropical cyclones has been done for the Atlantic and the Pacific regions (e.g., Jelesnianski 1965, 1972, 1976; Jelesnianski & Chen 1982; Overland 1975; Reid *et al* 1977; Miyazaki *et al* 1961, 1962; Ueno 1964). There are many other models for the North Sea and the Northwest European Continental Shelf (Heaps 1976; Flather 1976, 1981; Heaps & Jones 1979; Nihoul 1982). Attempts have also been made to develop numerical models for simulating storm surges associated with tropical

cyclones over the Bay of Bengal (Das 1972; Flierl & Robinson 1972; Das *et al* 1974; Johns & Ali 1980; Johns *et al* 1981, 1985; Dube *et al* 1985; Sinha *et al* 1986).

The purpose of the present article is to give a brief description and the results of a depth-averaged model and a nonlinear tide-surge interaction model for the Bay of Bengal. The surges associated with the 1970 Chittagong cyclone, 1977 Andhra cyclone and more recent 1982 Orissa cyclone have been simulated with the help of the above models. A comparison of the model results with the observed values is found to be satisfactory.

2. Depth-averaged model

2.1 Description of the model

The curvature of the earth's surface is neglected and all conditions are referred to a system of Cartesian coordinates. The origin, O , is within the equilibrium level of the sea-surface, Ox points towards the east, Oy towards the north and Oz is directed vertically upwards. The displaced position of the sea-surface is given by $z = \zeta(x, y, t)$ and the position of the sea-floor by $z = -h(x, y)$. An open-sea boundary at $y = 0$ corresponds approximately to latitude 6°N . A northern coastal boundary is situated at $y = L$ (taken as 1800 km) and western and eastern coastlines correspond respectively to $x = b_1(y)$ and $x = b_2(y)$. This configuration is shown in figure 1.

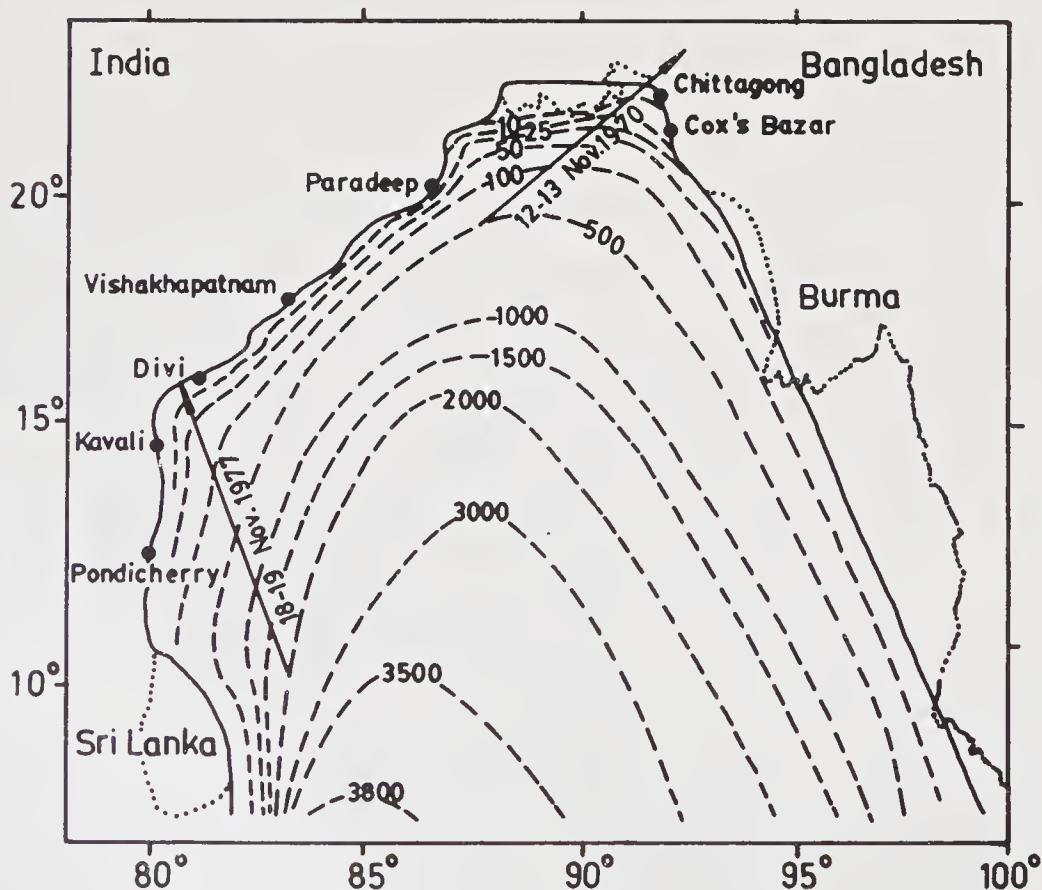


Figure 1. The coastal configuration in model A and the idealized tracks of the Andhra and Chittagong cyclones. Isobaths of the model bathymetry are also shown. The numbers refer to depths in metres.

The depth-averaged components of velocity, u and v , satisfy

$$\frac{\partial u}{\partial t} + u \frac{\partial u}{\partial x} + v \frac{\partial u}{\partial y} - fv = -g \frac{\partial \zeta}{\partial x} + \frac{\tau_x^\xi}{H\rho} - \frac{Ku}{H}(u^2 + v^2)^{1/2}, \quad (1)$$

$$\frac{\partial v}{\partial t} + u \frac{\partial v}{\partial x} + v \frac{\partial v}{\partial y} + fu = -g \frac{\partial \zeta}{\partial y} + \frac{\tau_y^\xi}{H\rho} - \frac{Kv}{H}(u^2 + v^2)^{1/2}. \quad (2)$$

The equation of continuity in vertically integrated form is

$$\frac{\partial \zeta}{\partial t} + \frac{\partial}{\partial x} (Hu) + \frac{\partial}{\partial y} (Hv) = 0. \quad (3)$$

In (1)–(3), f denotes the Coriolis parameter, the pressure is taken as hydrostatic, and H is the total depth $\zeta + h$. (τ_x^ξ, τ_y^ξ) denote the applied surface wind stress and the bottom stress is parameterized in terms of a quadratic law. ρ denotes the water density and the friction coefficient, K , is taken as 0.0026.

Applying the condition of zero normal velocity at the coastal boundary and a radiation type of condition at the open-sea boundary leads to

$$u - vb'_1(y) = 0, \quad \text{at } x = b_1(y), \quad (4)$$

$$u - vb'_2(y) = 0, \quad \text{at } x = b_2(y), \quad (5)$$

$$v = 0, \quad \text{at } y = L, \quad (6)$$

$$\text{and } v + (g/h)^{1/2} \zeta = 0, \quad \text{at } y = 0. \quad (7)$$

Further, it is assumed that the motion in the sea is generated from an initial state of rest, so that

$$\zeta = u = v = 0, \quad \text{everywhere for } t \leq 0. \quad (8)$$

2.2 Coordinate transformation for boundary representation

In most storm surge models the coastal boundary is represented by stair-steps. However, a more accurate representation is desirable and in order to facilitate the numerical treatment of an irregular coastal configuration we introduce a coordinate transformation given by

$$\xi = [x - b_1(y)]/[b(y)], \quad b(y) = b_2(y) - b_1(y). \quad (9)$$

The equations of continuity and momentum are transformed into

$$\frac{\partial}{\partial t} (b\zeta) + \frac{\partial}{\partial \xi} (bHU) + \frac{\partial \bar{v}}{\partial y} = 0, \quad (10)$$

$$\frac{\partial \bar{u}}{\partial t} + \frac{\partial}{\partial \xi} (U\bar{u}) + \frac{\partial}{\partial y} (v\bar{u}) - f\bar{v} = -gH \frac{\partial \zeta}{\partial y} + \frac{b\tau_x^\xi}{\rho} - \frac{K\bar{u}}{H}(u^2 + v^2)^{1/2}, \quad (11)$$

$$\frac{\partial \bar{v}}{\partial t} + \frac{\partial}{\partial \xi} (U\bar{v}) + \frac{\partial}{\partial y} (v\bar{v}) + f\bar{u} = -gH \left[b \frac{\partial \zeta}{\partial y} - \left(\frac{\partial b_1}{\partial y} + \xi \frac{\partial b}{\partial y} \right) \frac{\partial \zeta}{\partial \xi} \right] +$$

$$+ \frac{b\tau_y^\xi}{\rho} - \frac{K\bar{v}}{H}(u^2 + v^2)^{1/2}, \quad (12)$$

where,

$$bU = u - \left(\frac{\partial b_1}{\partial y} + \xi \frac{\partial b}{\partial y} \right),$$

$$(\bar{u}, \bar{v}) = bH(u, v).$$

Consequently the boundary conditions take the form

$$U = 0 \text{ at } \xi = 0 \text{ and } \xi = 1,$$

while (5) transforms into

$$bU - \left(\frac{g}{h} \right)^{1/2} \zeta = 0, \text{ at } \xi = 1.$$

Equations (10)–(12) form the basic set for the numerical solution process. These are solved on a staggered grid by using a conditionally stable semi-explicit finite difference scheme. The stability is only conditional upon the time step being limited by the space increment and the gravity wave speed.

Numerical experiments are performed with the help of this model to simulate the surge generated by the 1977 Andhra cyclone. An idealized wind field associated with this cyclone is described by an empirically based formula suggested by Jelesnianski (1965):

$$V = \begin{cases} V_0 \left(\frac{r}{R} \right)^{3/2}, & \text{for } r \leq R, \\ V_0 \left(\frac{R}{r} \right)^{1/2}, & \text{for } r > R, \end{cases} \quad (13)$$

where V_0 is the maximum sustained wind, R the radius of maximum wind, and r is the distance from the centre of the cyclone. We prescribe that the cyclone moves along the idealized straight-line track with uniform speed of translation. Based on the reports from the India Meteorological Department, we take $V_0 = 70 \text{ ms}^{-1}$ and $R = 80 \text{ km}$.

2.3 Results and discussions

Figure 2 shows the time variation of the sea-surface elevation at four coastal stations. The maximum peak surge of about 5.3 m is predicted at Kavali at $t = 50 \text{ hr}$. A maximum surge of 4.8 m is predicted at Divi Island at $t = 55 \text{ hr}$. Heavy inland flooding in this region, with an estimated peak elevation of 5 m, was reported to occur during the afternoon of 19 November 1977. The predicted and estimated maximum elevations are in good agreement although the model appears to produce the peak elevation some hours in advance of the reported time of flooding. Since the model has vertical side walls, the flood wave would presumably

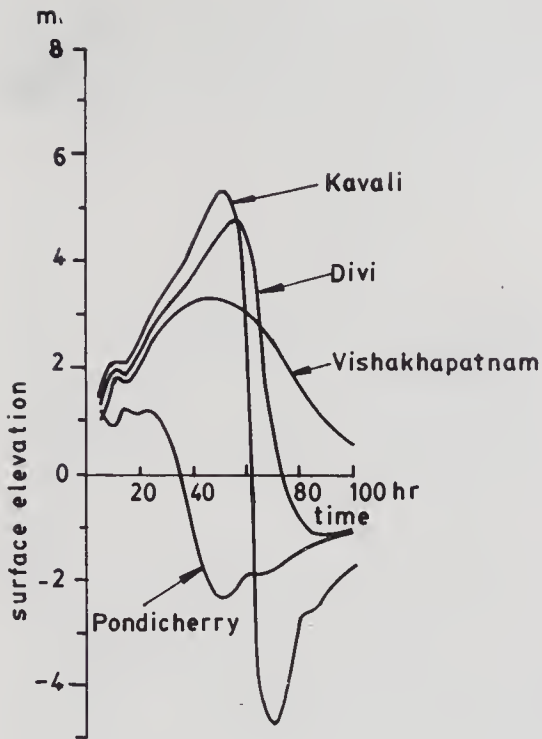


Figure 2. Time variation of surface elevation at four coastal stations along the Indian coast.

take an additional period of time to spread over the entire area of Divi where flooding was reported.

The time variation of the predicted sea-surface elevation at four coastal stations along the Bangladesh coast for the 1970 Chittagong cyclone is depicted in figure 3. A maximum surge of 5.5 m is predicted at Maijdi which occurred at 0245 hr BST

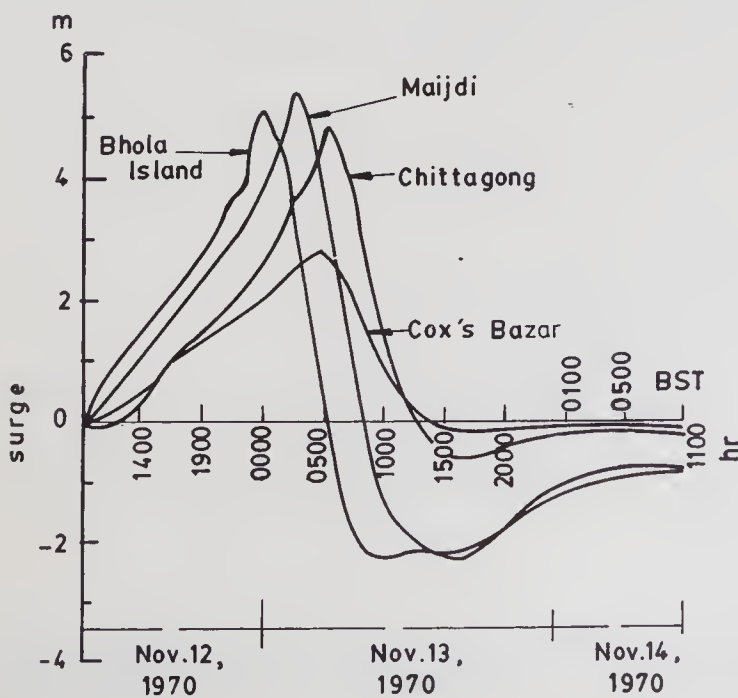


Figure 3. Time variation of the surface elevation at four coastal stations along the Bangladesh coast.

on 13 November. At Chittagong a maximum elevation of 4.9 m is predicted at 0520 hr which is in close agreement with the time of landfall. This value of 4.9 m is in good agreement with the observed range of maximum surge (4.2–7.2 m) at Chittagong.

3. Tide-surge interaction model

3.1 Formulation

The general procedure followed in the modelling of tide-surge interaction is to begin by generating the co-oscillating tide in a semi-enclosed basin by prescribing the sea-surface elevation along the open-sea boundary. The pure tidal solution developed in the basin then provides the initial dynamical conditions for the storm surge simulation with tidal forcing along the open-sea boundary continuing during the integration.

The basic model (model A) used is that described in § 2 which has a single open-sea boundary at 6°N. In order to represent the coastal orographical detail and the complex river system in the headbay, a high resolution stair-step model (model B) is nested within model A. The open-sea boundary of model B lies at 19° 33'N. For linking the parent model A with the nested model B, appropriate boundary conditions are needed through which the response in the model B is driven by that in the model A. This is done by using the prescribed elevations from the parent model and applying these as input conditions along the open-sea boundary of the nested model.

At the southern open-sea boundary of model A we use a generalization of the linearized radiation condition given by

$$v + (g/h)^{1/2}\zeta = 2a (g/h)^{1/2} \sin [(2\pi t/T) + \phi], \text{ at } y = 0, \quad (14)$$

where a and ϕ denote the prescribed amplitude and phase of the tidal forcing, respectively, and T is the period of the tidal constituent under consideration. Such a condition allows the outward radiation of an internally generated response from the analysis area and it also communicates the tides of the northern Indian Ocean into the Bay of Bengal.

In each of the rivers entering the headbay (figure 4) the following equations are satisfied.

$$\frac{\partial v}{\partial t} + v \frac{\partial v}{\partial y} = -g \frac{\partial \zeta}{\partial y} - \frac{Kv|v|}{H}, \quad (15)$$

$$b \frac{\partial \zeta}{\partial t} + \frac{\partial}{\partial y}(bHv) = 0. \quad (16)$$

At the point of entry into model B, the elevation and momentum flux are made continuous.

3.2 Generation of tides

The model equations (10)–(12) without the wind stress terms are integrated ahead in time subject to the prescribed forcing (14) along $y=0$. The computed tidal

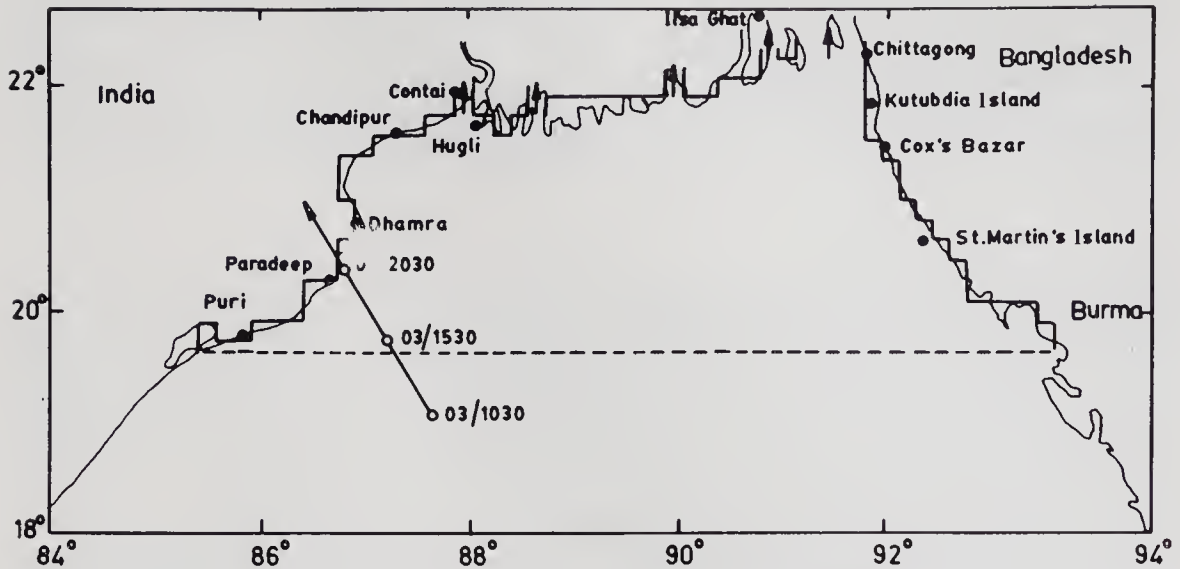


Figure 4. The coastal configuration in model B and the idealized track of the Orissa cyclone.

response becomes oscillatory after ten tidal cycles of integration. The amplitude and phase of the local M_2 constituent is obtained during the eleventh cycle by analysing the response using Fourier decomposition. With $a=0.3$ m and $\phi=0$, there is general agreement between the computed values of the amplitude and phase of the M_2 constituent and the corresponding observed data.

3.3 The surge response along the Orissa coast

The Orissa coast of India was affected by a surge-induced increase in the sea-surface level on 3 June 1982. The surge response is computed from the model by using pure wind-stress forcing of the June 1982 cyclone in the Bay of Bengal. Any contribution resulting from the barometrically generated component of the response is excluded from the simulation under the assumption that its effect is equivalent to a simple statistical correction.

3.4 Tide-surge interaction

Essentially the exercise consists of using the tidal solution to provide the initial sea-state condition for the surge calculation. The only procedural requirement is that of adjusting the phase of the tidal solution so that the initially prescribed dynamical state corresponds to the actual tidal conditions at the model time $t = 0$. It is observed that high tide occurred at Dhamra on 3 June at 2020 hr (IST). This is 9.8 hr after the time of commencement of the wind-stress forcing in the model simulation. Accordingly, when $t = 9.8$ hr in the model, it must be high tide at Dhamra.

The semidiurnal component of the tidal response in the model is given by

$$\zeta = a_1 \cos[(2\pi t/T) - \phi_1 + \phi] \quad (17)$$

where a_1 , ϕ_1 are known from pure tidal solutions. High tide at Dhamra must occur at $t = 9.8$ hr and (17) then leads to $\phi = 0.307$ radians. This value of ϕ is used

subsequently in the forcing of the tidal component of the solution during the tide-surge interaction experiment.

The pure tidal solution after 124.61 hr of integration, which gives the initial dynamical conditions in the basin is joined with the surge model in which the tidal forcing is prescribed by (14) with $a = 0.3$ m and $\phi = 0.307$ rad.

3.5 Results and discussion

The results of the simulations may be presented in several different ways, each illustrating a different aspect of the tide-surge interaction. From the point of view of the potential flooding risk, the crucially important parameter is the maximum total elevation of the sea surface predicted at points along the coastline. The elevation will partly be of tidal origin and partly of surge origin, the two combining in an essentially nonlinear way, and is referred to as $\zeta_{s+t+lst}$.

The computed envelope of the maximum elevation along the Orissa coast and the computed times of their occurrence is shown in figure 5. The observational estimates at Dhamra and Paradeep are seen to agree well with the corresponding computed times. An inference to be drawn here is that the maximum surge response appears to progress along the Orissa coast. On moving northeast from Paradeep, the time of occurrence of the peak elevation becomes progressively later, suggesting that the response has the form of a solitary elevation wave propagating along the coast.

It is informative to determine the computed elevation along the coast at the time of occurrence of the absolute peak elevation, which occurs about 50 km along the

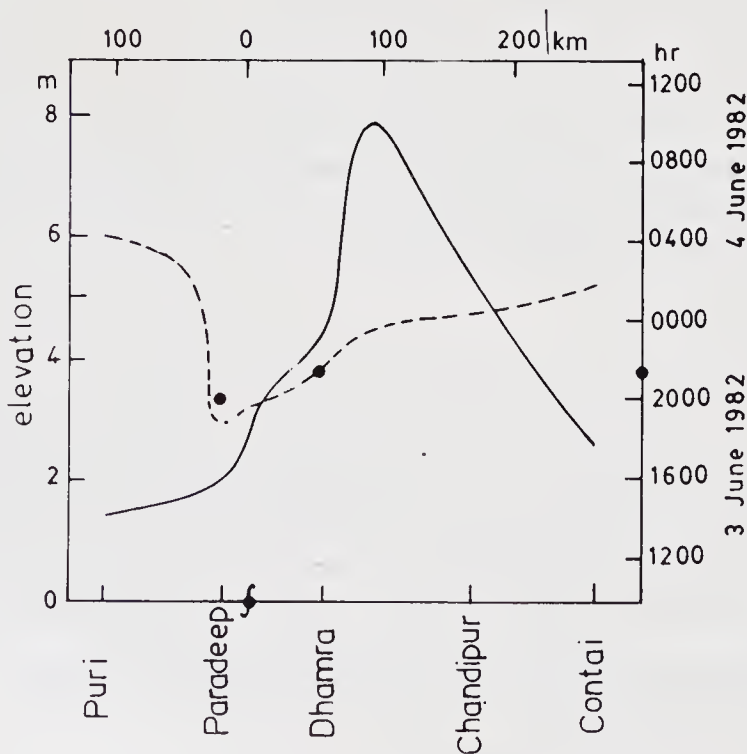


Figure 5. The computed envelope of the maximum elevation along the Orissa coast and the computed times of occurrence; — maximum value of $\zeta_{s+t+lst}$, - - - times of occurrence of maximum values; § denotes the position of landfall, ● denotes the time of landfall.

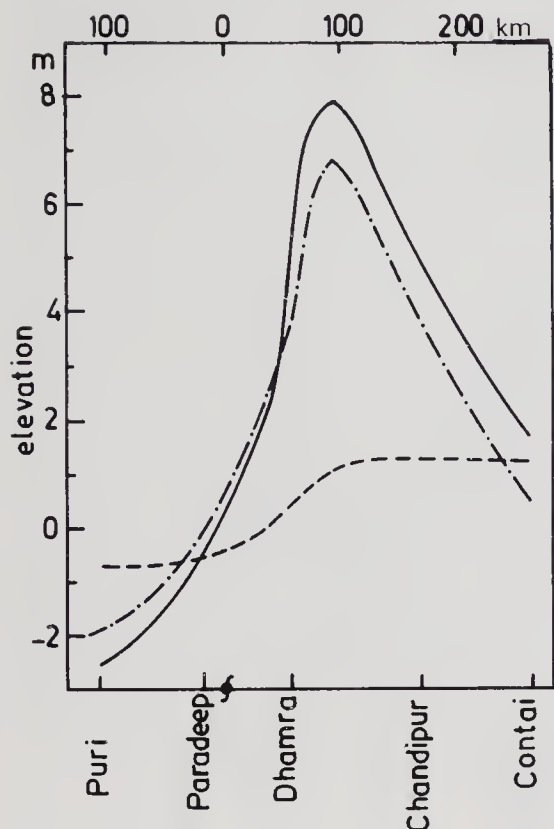


Figure 6. The computed elevation along the Orissa coast at the time of occurrence of absolute peak elevation; — $\zeta_{s+t+Ist}$; - - - ζ_t ; - · - · - ζ_{s+Ist} ; ‡ denotes the position of landfall.

coast from Dhamra. A plot of the sea-surface elevation along the Orissa coast at the time of occurrence of the absolute peak elevation is given in figure 6. Also shown is the component due to the pure tide, ζ_t , and the implied surge residual, ζ_{s+Ist} ($= \zeta_{s+t+Ist} - \zeta_t$). Thus, an absolute peak surge residual of approximately 7.76 m is predicted to occur about 95 km to the right of the landfall position. At the time of its occurrence, a surge residual of more than 1 m is predicted to affect a 240 km length of the coast. Unfortunately, there are no observations to substantiate the predicted results.

The dynamical consequences of the tide-surge interaction process are not effectively illustrated in a plot showing the spatial variation of $\zeta_{s+t+Ist}$ at a fixed position. This quantity is shown in figure 7 for Dhamra during the period 3–4 June 1982. Also shown is the temporal variation of ζ_t as well as that of the linear superposition of the pure surge and the pure tide defined by $\zeta_{s+t} = \zeta_s + \zeta_t$. Incorporation of the interactive effect is seen to advance the time of occurrence of the peak total elevation to 2120 hr compared to 2030 hr when based on an elevation of ζ_{s+t} . This difference of 50 min brings the predicted time of occurrence of the peak elevation into closer accord with the observational estimate of 2200 hr. A further consequence of the interaction is a reduction in the peak value of $\zeta_{s+t+Ist}$ to 4.33 m compared to 4.51 m of ζ_{s+t} . Near the time of maximum response, the interaction leads to a reduction in the total elevation on the rising tide and an increase on the falling tide. Such results have been noted previously by Banks (1974) and Johns & Ali (1980).

Finally, it is of interest to examine the combined tide and surge response at the port of Contai, which is located in the most westerly of the rivers (the Hugli) included in model B. In figure 8, the temporal variation of $\zeta_{s+t+Ist}$ is plotted

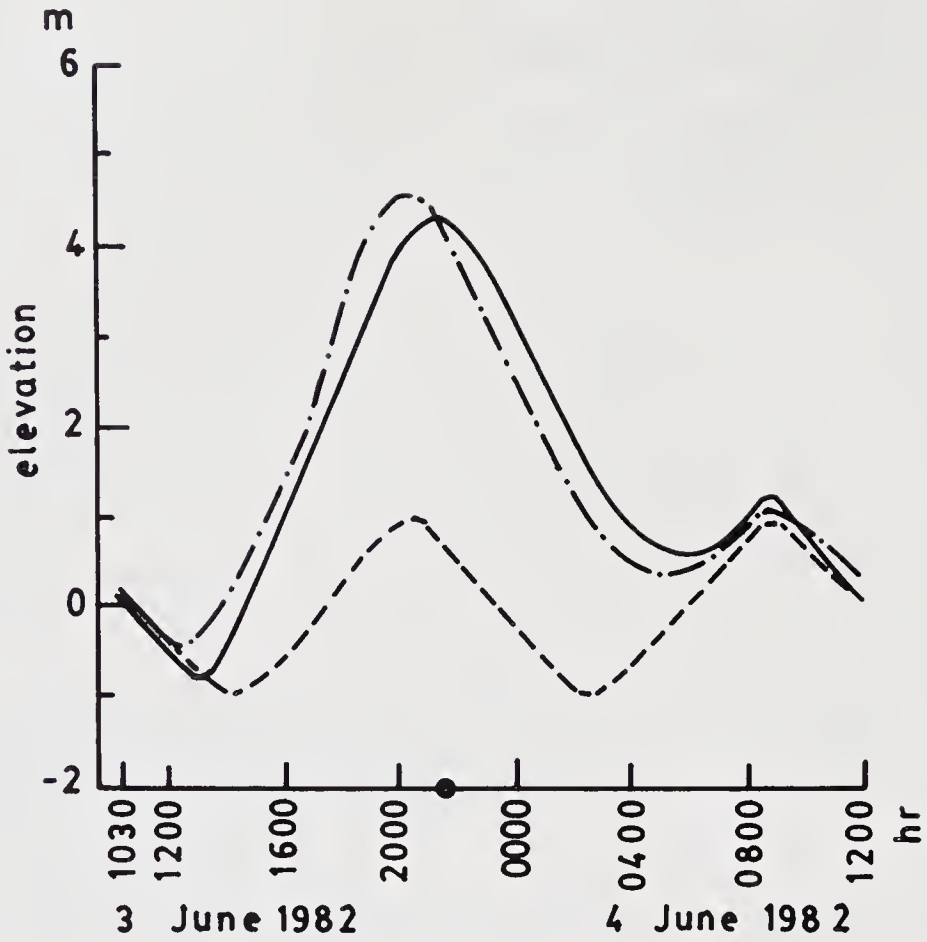


Figure 7. The computed variation of the elevation with time at Dhamra; — ζ_{s+t+1s} ; ---- ζ_i ; - · - · ζ_{s+i} ; ● denotes the time of landfall.

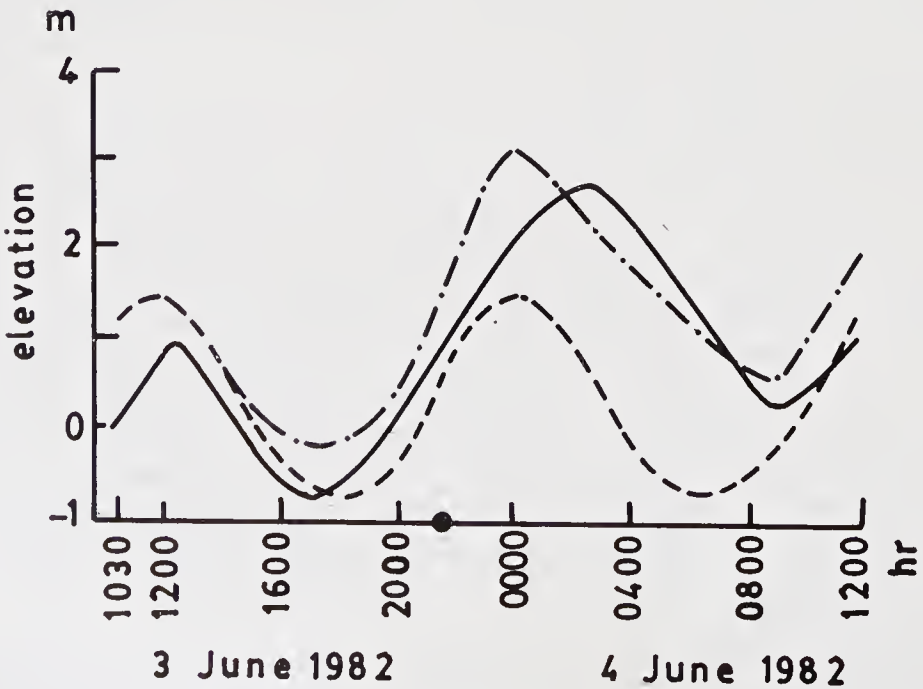


Figure 8. The computed variation of the elevation with time at Contai; — ζ_{s+t+1s} ; ---- ζ_i ; - · - · ζ_{s+i} ; ● denotes the time of landfall.

together with that of ζ_t and ζ_{s+t} . The maximum response is predicted at about 0240 hr on 4 June which is some 5.3 hr after the maximum response at Dhamra. The two stations are about 220 km apart so that the implied speed of propagation of the elevation wave is approximately 11.5 ms^{-1} .

A simple, theoretically based, estimate may be made for the phase speed if it is assumed that the response progresses along the coast in the form of a freely propagating shallow water gravity wave. The phase speed is given approximately by $(gh)^{1/2}$ where h is the mean depth. Bathymetry shows that in the region north of Paradeep, h lies between 10 and 20 m. Accordingly, the phase speed lies between 10 and 14 ms^{-1} . Hence the speed deduced from the numerical model lies between these values and thus provides further evidence concerning the dynamical character of the response after landfall of the cyclone.

At Contai, the relatively shallow water has the effect of increasing the amplitude of the semidiurnal tide and strengthening the contribution of nonlinearity. The maximum elevation occurs about 2.7 hr after the time suggested by an elevation of ζ_{s+t} . The maximum elevation is almost 0.45 m below the value derived from ζ_{s+t} . This difference is about 21% of the predicted elevation above the mean tidal level. This is a significant difference and must be incorporated into any effective predictive scheme.

References

- Banks J E 1974 *Philos. Trans. R. Soc. Lond. A* 275: 567–609
- Das P K 1972 *Nature (London)* 239: 211–213
- Das P K, Sinha M C, Balasubramanyam V 1974 *Q.J.R. Meteorol. Soc.* 100: 437–449
- Dube S K, Sinha P C, Roy G D 1985 *Dyn. Atmos. Oceans* 9: 121–133
- Flather R A 1976 Results from a storm surge prediction model of the northwest European continental shelf for April, November–December 1973, IOS Report no. 24, Inst. of Oceanogr. Sci., England
- Flather R A 1981 in *Floods due to high winds and tides* (ed.) D H Peregrine (London: Academic Press)
- Flierl G R, Robinson A R 1972 *Nature (London)* 239: 213–215
- Heaps N S 1976 in *Computing methods in applied sciences* (eds) R Glowinski, J L Lions (Berlin: Springer-Verlag)
- Heaps N S, Jones J E 1979 in *Marine forecasting* (ed.) J C J Nihoul (Amsterdam: Elsevier)
- Jelesnianski C P 1965 *Mon. Weather Rev.* 93: 343–358
- Jelesnianski C P 1972 *SPLASH* (Special programme to list amplitudes of surges from hurricanes) I. Landfall storm. NOAA Tech. Memo. NWS/TDL-46, Techniques Development Lab, Silver Spring, Md
- Jelesnianski C P 1976 A sheared coordinate system for storm surge equations of motion with a mildly curved coast, NOAA Tech. Memo. NWS/TDL-61, Techniques Development Lab, Silver Spring, Md
- Jelesnianski C P, Chen J 1982 *SLOSH* (Sea, lake and overland surges from hurricanes) Techniques Development Laboratory, NOAA, Silver Spring, Md (unpublished manuscript)
- Johns B, Ali A 1980 *Q.J.R. Meteorol. Soc.* 106: 1–18
- Johns B, Dube S K, Mohanty U C, Sinha P C 1981 *Q.J.R. Meteorol. Soc.* 107: 919–934
- Johns B, Rao A D, Dube S K, Sinha P C 1985 *Philos. Trans. R. Soc. Lond. A* 313: 507–535
- Miyazaki M, Ueno T, Unoki S 1961 *Oceanogr. Mag.* 13: 51–75
- Miyazaki M, Ueno T, Unoki S 1962 *Oceanogr. Mag.* 14: 103–117
- Nihoul J C J 1982 Hydrodynamic models of shallow continental seas—application to the North Sea, Neupre 11-B-4108, Etienne RIGA, La Salle
- Overland J E 1975 Estimation of hurricane storm surge in Apalachicola Bay, Florida, NOAA Tech. Rep., National Weather Service, U.S. Dept of Commerce

- Reid R O, Vastano A C, Whitaker R E, Wansrath J J 1977 in *The sea* (eds) E D Goldberg, I N McCave, J J O'Brien, J H Steele (New York: Wiley-Interscience)
- Sinha P C, Dube S, K, Roy G D 1986 *Int. J. Numer. Methods Fluids* 6: 305-311
- Ueno T 1964 *Oceanogr. Mag.* 16: 53-124

Author Index

Abbott D E	311	Benney D J	1, 2, 9
Abramowitz M	228	Bernal L	130
Acharya M	119	Bernard P S	80
Ackeret J	61, 62, 143	Berry W	378
Adams J L	362	Bethe H E	311
Adamson T C	144, 172, 173	Bevilaqua P M	130
Agashe S N	427	Bharati M	353
Aldred J W	314	Billings D F	
Ali A	434, 441	<i>see</i> Blumen W	64
Ananth A	403	Bird G A	219, 222
Ananthasayanam M R	217	Blackwelder R F	76, 78
<i>see</i> Subbaraju P V	283	Blaise D	176, 179–181, 183
Anders J B		Blazowski W S	320
<i>see</i> Hefner J N	122, 127	Blottner F G	275, 279
Antar B N	2	Blumen W	64
Anyiwo J C	166	Bogdanoff D W	62, 65, 68
Aref H	83	<i>see</i> Oskam P	197
Asaka S	83	<i>see</i> Settles G S	148, 149, 153, 156–158, 197
Asia-Pacific Symposium	417	Bogdonoff S M	156
Atwell N P		Bose A	351
<i>see</i> Bradshaw P	178	Bothmann Th	
Axford W I	84	<i>see</i> Krause E	275
		Bower T L	
Bachalo W D	162	<i>see</i> Demetriades A	58
Badri Narayanan M A	129, 131, 132, 134, 135, 139	Boylan D E	272
<i>see</i> Rao K N	114	Braden R P	130, 139
Badruddin Ahmed		Bradshaw P	178
<i>see</i> Prem Krishna	425	Briley W R	176
Bahi L	197	Brown G L	57, 58, 65, 67, 147
Bailey A B	272	Brusseleers M	144
Balasubramanyam V		Buman C	
<i>see</i> Das P K	434	<i>see</i> Kosdon F J	322
Baldwin B S	260	Burggarf O R	172, 173, 176
Ball K O W	194–196	<i>see</i> Rizetta D P	173, 176
Balu R	273	Bushnell D M	115, 166
Banerji A	285	<i>see</i> Hefner J N	122, 127
<i>see</i> Subhash A N	288		
Bangert L H	191	Cantwell B J	71, 114
Banks J E	441	Carr R E	
Barr P W		<i>see</i> Lorell J	315
<i>see</i> Simpson R L	147	Carter J E	176, 177
Basu R I	418	Cebeci T	176, 178
Batchelor G K	85	Cervantes de Gortari	137
Bauer F	204	Champagne F H	129
Beam R M	177	Chang P K	186
Belotserkovskii O M	223	Chapmann D R	151–153
Bennett J C	103	Charwat A F	144

- Chaudhry K K
see Seetharamulu K 417, 418
- Chen J 433
- Chen Shi-Yi 97, 104
- Childs M E
see Seebaugh W R 196
- Childs M E 192–194, 196
- Chinneck A 186, 189
- Chou (Zhou) Pci-yuan 98–100, 102–104, 110
- Chyu W J
see Coe C F 169
- Clark A R 129
- Clauser F H 114, 117
- Coe C F 169
- Cole R B
see Blazowski W S 320
- Coles D 58, 61, 114
- Collins D J 131
- Collins F G 2
- Corke T C 115, 121–123, 127
- Corrsin S 103
- Cowdrey C F 420
- Craik A D D 6
- Crawford D H 194
- Croeco L 176
- Crow S C 83, 129
- DAE 398
- DOS 403
- DRDO 419
- DST 417
- Das P K 434
- Dasgupta S 347
- Davenport A G 415, 418
- Davies R S 318
- DeRis J
see Kim J S 322, 323
- Deiwert G S
see McDevitt J B 182
- Delery J M 144, 147, 161–165, 186, 195
see Sirieix M 166–168
- Demetriades A 58
- Deshpande S M 217, 221–224, 226, 227, 231
see Saxena S K 257
see Singh K P 245
see Subbaraju P V 283
- Devassia K J 245, 251
- Dhawan S 360, 403, 412
see Liepmann H W 143
- Diehl Z W 115
- Dimotakis P E 65, 67
- Dods J B
see Coe C F 169
- Dolling D S 168–170, 184, 198
- Don Gray J 196
- Dorodnitsyn A A 311
- Drazin P G
see Blumen W 64
- Driver D M 168
- Dube S K 434
see Johns B 434
see Sinha P C 434
- Dumas R
see Favre A 58
- Durvasula S
see Krishnaswamy T N 423, 424, 427
see Rao G N V 416, 423
- Dziomba B
see Wagnanski I 135
- ESDU 428
- East L F
see Sawyer W G 159
- Eaton J K 168
- Elfstrom G M 149, 175
- Ellis M A 275, 279
- Elsennar A 275
- Erdos J 152, 153
- Eskinazi S 118
- Fabris G 105
- Fasel H
see Williams D R 3, 14, 17
- Favre A 58
- Feldman F
see Ackeret J 143
- Feo A 173
- Fernandez M 346
- Ferris D H
see Bradshaw P 178
- Ffowes Williams J E 84
- Fiedler H 129, 131
see Wagnanski I 135
- Finke K 171
- Flather R A 433
- Flierl G R 434
- Fohl T 83
- Fox J A
see Lessen M 68
- Fukuda M K 192, 193
- Fung K Y
see Sobieczky H 204
- Fuscan Y
see Joulain P 320
- Gadd G E 175
- Gai S L 192, 194, 195
- Garabedian P
see Bauer F 204
- Gartshore J S 191
- Gaviglio J
see Favre A 58
- Gerrard J H 29

Giedt W H	272	Jacobs P A	308
Gilbert M	318	Jacocks J L	
Glusko G S	178	<i>see</i> Whitefield J L	177
Goldschmidt V M	137	Jai Mohan	250, 260
Goldsmith E L	171	Jain V K	
Goldstein M E	93	<i>see</i> Paul P J	320
Goyal V K	259	Jameson A	
Grande E	169	<i>see</i> Bauer F	204
Green J E	144, 158, 172	Jayaraman V	
Greensite A L	347	<i>see</i> Rao U R	360
Grin V T	187	Jclesnianski C P	433, 436
Gropengiesser H	64, 67	Jensen R	
Grossman B	161, 173, 174	<i>see</i> Burggarf O R	173
Guezennec Y	125, 127	<i>see</i> Rizetta D P	176
<i>see</i> Corke T C	115, 121–123, 127	Johns B	434, 441
Gupchup V N	427	Johnson D A	154, 162
Gupta A K		Johnston J P	71, 168
<i>see</i> Nigam N C	426	Jones G C A	
Gupta S C	343	<i>see</i> Chinneck A	186, 189
		Jones J E	433
Hall G R	186, 187	Jones W P	178
Hama F R	1, 2, 12, 83	Julain P	320
<i>see</i> Williams D R	3, 14, 17		
Hankey W L	184, 185	Kachanov Yu S	2
<i>see</i> Shang J S	184	Kacker S C	116
Harch W H		Kadam N V	347
<i>see</i> Collins D J	131	Kailas Nath P	
Haritonidis J H	76, 78	<i>see</i> Prabhu A	122
Heaps N S	433	Kailas S	114
Hedley A B	315	Kalam A P J Abdul	327
Hefner J N	122, 127	Kalc P P	
Hegde M	323	<i>see</i> Dhawan S	360
Henderson L F	146	<i>see</i> Rao U R	360
Herbert T	2	Kambe T	83
Hickman R S	272	Kasturirangan K	359
Hingst W R		<i>see</i> Rao U R	360
<i>see</i> Fukuda M K	192, 193	Kempton A J	84
Hinze J O	129	Kharchenko V N	321
Hirschel E H		Kibens V	84, 95
<i>see</i> Krause E	275	Kida S	306
Horstman C C	170, 171, 175, 178, 180, 181, 183, 198	Kier R J	
	103, 108	<i>see</i> Wooldridge C E	318, 319
Huang Yong-nian	191	Kim J S	322, 323
Hubbart J E		Kiřtler A L	168
Hughes M H		Klebanoff P S	1, 9, 12, 115
<i>see</i> Zabusky N J	306	Kleiser L	3
Hung C M	198, 280	Kline S J	114, 147
Hussain A K M F	83, 84, 95, 129	Klineberg J M	176
		Knapp C F	2
IS-875	417	Komoda H	
ISRO	397, 400, 403	<i>see</i> Kovasznay L S G	12
Indo-US Workshop	417	Konzelmann U	1
Inger G R	161, 175, 179	Kooi J W	158, 167, 168
<i>see</i> Stanewsky E	179	Kordulla W	198
Isoda H	315	Korkegi R H	194, 195
		Korn D	
		<i>see</i> Bauer F	204

- | | | | |
|--------------------------|-------------------------|---------------------------|---------------|
| Korschelt D | 131 | MacCormack R W | 245 |
| Kosdon F J | 322 | Mack L M | 4 |
| Kovaszny L S G | 12 | Macombe G R | 346 |
| Krause E | 275 | Madhavan N S | 277 |
| Krishnamoorthy V N | 337 | Mangus J S | 123 |
| Krishnamurthy L | 323 | Mani A | 95, 418 |
| Krishnamurthy V | 188, 189 | Manjunath A R | 188, 189 |
| Krishnaswamy T N | 423, 424, 427 | Martin G F | |
| Kroesser W F | | <i>see</i> Hedley A B | 315 |
| <i>see</i> Kim J S | 322, 323 | Marumo E | 115, 118 |
| Krogmann P | 197 | Marvin J G | 178 |
| Kubota T | | <i>see</i> Driver D M | 168 |
| <i>see</i> Lewis J E | 173 | Marxman G A | 317, 318 |
| Kuehn D M | 148 | <i>see</i> Wooldridge C E | 318, 319 |
| <i>see</i> Chapmann D R | 151–153 | Mason W H | 175, 179 |
| Kukillaya S P | 285 | Mathews D C | 192, 193 |
| <i>see</i> Subhash A N | 288 | Mathur S P | |
| Kulkarni R S | | <i>see</i> Nigam N C | 426 |
| <i>see</i> Prabhu A | 122 | Maus J R | 196 |
| Kumagai S | 315 | Maxworthy T | 93 |
| Kumar S K | 125 | Mayne J R | 418 |
| Kurien T | 353 | McAlevy R F III | |
| Kurup M R | 337 | <i>see</i> Blazowski W S | 320 |
| Kutty C S | 240 | McClure C L | 346 |
| | | McCormack R W | 177 |
| La Balleur J C | 176, 177, 179–181, 183 | McDevitt J B | 160, 182 |
| Lai J C S | 131 | McDonald H | 176 |
| Lakshman Gowda B H | 424, 425, 428 | Mehta R C | 281 |
| Lakshmikantha H | 187 | Mehta U | 177 |
| Larson H K | | Meier G E A | 171 |
| <i>see</i> Chapmann D R | 151–153 | Meier H U | 178 |
| Launder B E | 98, 178 | Mellor G L | 77 |
| Laurien E | 1, 3, 14 | Melnik R E | 161, 173, 174 |
| Law C H | 148, 156 | Messiter A F | 144, 172 |
| <i>see</i> Shang J S | 184 | Meyer F | 1 |
| Lee Seegmiller H | | Mickley H S | 318 |
| <i>see</i> Driver D M | 168 | Miles J W | 61, 62 |
| Lees L | 176, 196, 318 | Miyazaki M | 433 |
| <i>see</i> Lewis J E | 173 | Mohanty U C | |
| Leondes C T | 346 | <i>see</i> Johns B | 434 |
| Lessen M | 68 | Mooley D A | 418 |
| Levchenko V Ya | 2 | Moore D W | 306 |
| Levy L L | 182 | Moss J N | 219 |
| <i>see</i> McDevitt J B | 182 | Most J M | |
| Lewis J E | 153, 173 | <i>see</i> Julain P | 320 |
| Li-Sung-nian | | Mukunda H S | 313, 315 |
| <i>see</i> Chou Pei-yuan | 103 | <i>see</i> Hegde M | 323 |
| Liepman H W | 114, 143, 171, 295 | <i>see</i> Paul P J | 320 |
| Lighthill M J | 90, 172, 175 | Mumford J C | 120, 127 |
| Lilley G M | 79 | Murphy M T | 168–170 |
| Lin C C | 1, 9 | Muzzy R J | |
| Lock R C | 177 | <i>see</i> Marxman G A | 318 |
| Lomax H | 177, 260 | | |
| London F | 297 | Nagamatsu H T | |
| Lorell J | 315 | <i>see</i> Bahi L | 197 |
| Lush P A | 94 | Nagaraja K S | |
| Lynn T B | 119, 122, 123, 126, 127 | <i>see</i> Braden R P | 130, 139 |

Nagib H M	123, 125, 127	Paul P J	320
<i>see</i> Corke T C	115, 121–123, 127	<i>see</i> Hegde M	323
Nair S R		Paynter G C	
<i>see</i> Devassia K J	245	<i>see</i> Seebaugh W R	196
Nanbu K	223, 226, 234	Peake D J	186, 188
Nandan M	203	Pearcey H H	143
<i>see</i> Stanewsky E	179	Perkins J J	
Narasimha R	113, 114, 125, 126, 166, 184, 191, 197, 217, 417, 418	<i>see</i> Settles G S	197
<i>see</i> Deshpande S M	223, 224, 226, 227	Platzer M F	131, 132, 135, 139
<i>see</i> Prabhu A	122	<i>see</i> Collins D J	131
<i>see</i> Rao K N	114, 418, 419	Plesniak M W	123, 125, 127
<i>see</i> Saxena S K	257	Plotkin K J	169
<i>see</i> Singh K P	245	Potter J L	272
<i>see</i> Viswanath P R	186, 188–191	Powell A	90
Narayan K Y		Prabhu A	14, 122, 166, 197
<i>see</i> Sundara Murthy H	256	<i>see</i> Rao K N	418, 419
Narayanan K		<i>see</i> Viswanath P R	188–191
<i>see</i> Rao U R	360	Prabhu D R	424
Nash C R		Pradeep Kumar	267
<i>see</i> Sawyer W G	159	Prahlad T S	237, 274
Navalgund R R	359	<i>see</i> Saxena S K	257
Neiland V	172	<i>see</i> Singh K P	245
Neu J C	306	Prahlada	327
Newman B G	191	Prasad J K	240
Niccolls W O	130	Prem Krishna	425
Nigam N C	426	Price S J	424
Nihoul J C J	433	Pullin D	222, 302, 308
Nosenchuck D M	114	Puri S N	351
Nuruzzaman A S M		Purohit S C	183, 196, 260, 261
<i>see</i> Hedley A B	315		
Nutant J	12	Raghu S	131
		Raghunandan B N	315
Oates G C	169	Raja Kuperan E	249, 283
Oertel H	58, 62	Rajan Y S	395, 397, 410
Ohji M	300	Rajaram U	259
Okuno A F	318	Rajeev Lochan	
Or C T	169, 184	<i>see</i> Sundara Murthy G K	256
Ortwerth P J	58	Ramachandran P	360
Oshima Y	83, 309	Ramakrishna S	347
Oskam B	197	Ramani N	
Oster D		<i>see</i> Deshpande S M	223, 224, 226
<i>see</i> Wygnanski I	135	Ramaswamy M A	203
Overland J E	433	Rao A D	
Owen F K	170, 171	<i>see</i> Johns B	434
		Rao A K	
Paidoussis M P	424	<i>see</i> Krishnaswamy T N	427
Palaniswamy S		Rao G N V	415–420, 423, 427
<i>see</i> Rao G N V	416	<i>see</i> Krishnaswamy T N	423, 424, 427
Pallone A	152, 153	Rao K N	114, 418, 419
Pande P K		Rao K V L	288
<i>see</i> Prem Krishna	425	Rao U R	359, 360, 403
Pant N		Reddy K R	427
<i>see</i> Rao U R	360	<i>see</i> Krishnaswamy T N	423, 424, 427
Papamoschou D	57	<i>see</i> Rao G N V	416, 423
Pappas C C	318	Reeves B L	196
Pate S R	192	Reid R O	433

- Reshotko E
see Fukuda M K 192, 193
- Reynolds W C
see Kline S 114
- Rist U 1
- Rizetta D 173, 176
see Burggarf O R 172, 173, 176
- Roache P J 2
- Roberts K V
see Zabusky N J 306
- Robinson A R 434
- Rockwell D O 130
- Romanenko P N 321
- Rose W C 154
- Rosenhead L 311
- Roshko A 57, 58, 65, 114, 148, 149, 155, 156, 175
see Liepmann H W 143
- Ross J M
see Bahi L 197
- Rott N
see Ackeret J 143
- Rotta J C 98, 179
- Roy G D
see Das P K 434
see Dube S K 434
see Sinha P C 434
- Rubesin M W 178
- Rundstadler P W
see Kline S J 114
- Saffman P G 84, 306
- Sagdeo P M 188
see Viswanath P R 186, 188–191
- Sandborn V A 147
- Sanders B W 186
- Sanderson R J 58
- Sankar N L 196
- Sankaran L
see Viswanath P R 186, 188–191
- Sargent L M
see Klebanoff P S 1, 9, 12
- Sarma B S 327
- Sarohia V 130
- Sasidharan Nair K G
see Sundara Murthy H 256
- Sastry M S 242
- Sato T
see Marumo E 115, 118
- Savill A M 120, 127
- Sawyer W G 158
- Saxena S K 257, 258, 281
- Schraub F A
see Kline S J 114
- Schubauer G B 1
- Schwendemann M F 186
- Scull J R 371
- Seddon J 158, 159, 171
- Seebass A R
see Sobieczky H 204
- Seebaugh W R 192–194, 196
- Seetharamulu K 417, 418
- Seminar 417
- Settles G S 148, 149, 153, 156–158, 197
- Shang J S 184, 185
- Sharma M C 417, 418
- Sheo Prakash
see Devassia K J 245
- Shih Hsun-kang
see Chou Pei-yuang 103
- Shine A J 58
- Shrinivasa U 417, 418
- Shrivastava S K 359
- Simmons J M 131
- Simpson R L 147
- Singer F 375
- Singh J P
see Dhawan S 360
- Singh K P 245, 259
see Rao U R 360
- Sinha M C
see Das P K 434
- Sinha P C 433, 434
see Dube S K 434
see Johns B 434
- Sirieix M 144, 166–168
- So R M C 77
- Sobieczky H 204
- Squire H B 1
- Sreenivasan K R 113, 114, 118, 122, 123, 126, 127, 166, 184, 359, 403
- Sridhara Murthy K R 359, 403
- Srinivasan G
see Lakshmikantha H 187
- Stanewsky E 144, 172, 179
see Krogmann P 197
see Sirieix M 166–168
- Stathopoulos T
see Davenport A G 415
- Steel P C 58
- Steger J L 176
- Stegun I A 228
- Stewartson K 172, 173
see Cebeci T 176
- Strickland J H
see Simpson R L 147
- Strykowski 114
- Subba Raju P V 217, 221, 223, 283
see Deshpande S M 223, 224, 226, 227
- Subhash A N 288
- Sudarsan P 403
- Sun C C 196
- Sundara Murthy H 256
- Sundaram S 311

Suresh B N	343	Vatsa V N	
Surrey D		<i>see</i> Burggarf O R	172, 173, 176
<i>see</i> Davenport A G	415	Veldman A E P	177
Suryanarayana G K		Vickery B J	418, 424
<i>see</i> Sundara Murthy H	256	Viegas J R	175, 178, 180, 181, 183
Suzuki K		Viswanath P R	143, 147, 186, 188–191
<i>see</i> Marumo E	115, 118	Von Ohain H J F	
Svehla R A	316	<i>see</i> Braden R P	130, 139
Swafford T W			
<i>see</i> Whitefield D L	177		
Swaminathan R	275	Wang Xilin	71
Swaminathan S	272	Wansrath J J	
Swaminathan V	277, 280	<i>see</i> Reid R O	433
Swamy B L P		Warming R F	177
<i>see</i> Seetharamulu K	417, 418	Warrier P V E	356
Swamy N V C	425, 428	Werle M J	
Ształ B		<i>see</i> Burggarf O R	172, 173, 176
<i>see</i> Julain P	320	Whitaker R E	
		<i>see</i> Reid R O	433
Takaki Ryuji	83	Whitefield D L	177
Takao T	83	Whitelaw J H	116
Taneda S	29, 30, 32, 34, 36, 37, 39	<i>see</i> Cebeci T	176
Tanner L H	192, 194, 195	Widnall S	92
Tassa Y	196	Wilcox D C	178
Thiede P		Williams A	314, 315
<i>see</i> Krogmann P	197	Williams D R	3, 14, 17
Thomas A S W	114	Williams F A	323
Thomke G J	148, 149, 155, 156, 175	<i>see</i> Kosdon F J	322
Tidstrom K D		Williams P G	172, 173
<i>see</i> Klebanoff P S	1, 9, 12	Winoto S H	71, 78
Townsend A A	129	Wise H	
Tracey C M		<i>see</i> Lorell J	315
<i>see</i> Chinneck A	186, 189	Wong W F	186, 187, 189, 192, 194
Tsai Shu-tang	103	Wooldridge C E	318, 319
Tsuboi K	309	<i>see</i> Marxman G A	318
Turner J S	83	Workshop	417
		Wortmann F X	71
Ueno T	433	Wu Zhong	99
<i>see</i> Miyazaki M	433	Wyganski I	129, 135
Unoki S			
<i>see</i> Miyazaki M	433	Yajnik K S	119, 299, 310, 311
Usher J R	6	Yanenko N N	223
Uttam M C	337	Yanitskii V E	222, 223
		Yegna Narayan K	191
VSSC	240	<i>see</i> Lakshmikantha H	187
Van Dyke M	29, 36, 38, 300	Yeh T	84
Van den Berg B	275	Yen S M	223
Vas I E		Yu N J	
<i>see</i> Oskam V	197	<i>see</i> Sobieczky H	204
<i>see</i> Settles G S	148, 149, 153, 156–158		
Vasagam R M	359	Zabusky N J	306
Vastano A C		Zaman K B M Q	95
<i>see</i> Reid R O	433	Zhang Z	71, 79
Vasudeva B R		Zhou (Chou) Pei-yuan	97–99, 101, 103, 104, 110
<i>see</i> Kovasznay L S G	12		
Vasudevan B		Zien H M	
<i>see</i> Prabhu A	122	<i>see</i> Lessen M	68

SUBJECT INDEX

- Advanced aerospace vehicles
 Integrated design approach for advanced aerospace vehicles 327
- Aerodynamic characteristics
 Characteristics of a typical lifting symmetric supercritical airfoil 203
- Aerodynamic loads
 A survey of wind engineering studies in India 415
- Asymptotic expansions
 Limits and models in fluid mechanics 299
- Blades
 Flat plate drag reduction by turbulence manipulation 113
- Boat-tailed bodies
 A profile of aerodynamic research in VSSC with application to satellite launch vehicles 237
- Boltzmann equation
 Monte Carlo simulation for molecular gas dynamics 217
- Bottom stress
 Hydrodynamic numerical modelling of storm surges—Application to the Bay of Bengal 433
- Boundary layer control
 Shock-wave-turbulent-boundary-layer interaction and its control: A survey of recent developments 143
- Cavity radiation
 Dimensional analysis and equilibrium radiation 295
- Collision dynamics
 Monte Carlo simulation for molecular gas dynamics 217
- Communication
 ISRO spacecraft technology evolution 359
- Control algorithm
 Development of navigation guidance and control technology for Indian launch vehicles 343
- Convective Mach number
 Observations of supersonic free shear layers 57
- Dimensional analysis
 Dimensional analysis and equilibrium radiation 295
- Drag reduction
 Flat plate drag reduction by turbulence manipulation 113
- Equilibrium radiation
 Dimensional analysis and equilibrium radiation 295
- Extreme wind
 A survey of wind engineering studies in India 415
- Flow model
 Limits and models in fluid mechanics 299
- Flow visualization
 Irregular flows 29
 Visualization and analysis of longitudinal vortices at curved walls of 2D laminar and turbulent channel flows 71
- Fluid mechanics
 Limits and models in fluid mechanics 299
- Forced convective turbulent boundary layer combustion
 Variable property analysis—is there anything to it? 313
- Free convective combustion
 Variable property analysis—is there anything to it? 313
- Friction coefficient
 Hydrodynamic numerical modelling of storm surges—Application to the Bay of Bengal 433
- HTPB-based propellant
 Development of solid propellant technology in India 337
- Hardware-in-loop simulation
 Development of navigation guidance and control technology for Indian launch vehicles 343
- Hot-wire measurements
 Irregular flows 29
- Idealized wind field
 Hydrodynamic numerical modelling of storm surges—Application to the Bay of Bengal 433
- Indian space programme
 ISRO spacecraft technology evolution 359
 Management of the Indian space programme 397

- Industrial structures
 A survey of wind engineering studies in India 415
- Inertial guidance
 Development of navigation guidance and control technology for Indian launch vehicles 343
- Integrated design approach
 Integrated design approach for advanced aerospace vehicles 327
- Interface design module
 Integrated design approach for advanced aerospace vehicles 327
- Irregular flows
 Irregular flows 29
- Jet
 The behaviour of excited plane jets 129
- Jet excitation
 The behaviour of excited plane jets 129
- Jet noise
 Recombination of two vortex filaments and jet noise 83
- Kac-Prigogine master equation
 Monte Carlo simulation for molecular gas dynamics 217
- Laminar-turbulent transition
 Vorticity field structure associated with the 3D Tollmien-Schlichting waves 1
- Launch vehicles
 A profile of aerodynamic research in VSSC with application to satellite launch vehicles 237
- Limit
 Limits and models in fluid mechanics 299
- Longitudinal vorticity
 Vorticity field structure associated with the 3D Tollmien-Schlichting waves 1
- Low density flow
 Monte Carlo simulation for molecular gas dynamics 217
- Modelling
 Limits and models in fluid mechanics 299
- Monte Carlo method
 Monte Carlo simulation for molecular gas dynamics 217
- National space programme management
 Management of the Indian space programme 397
- Navigation
 Development of navigation guidance and control technology for Indian launch vehicles 343
- Operational systems
 ISRO spacecraft technology evolution 359
- Poiseuille flow
 Vorticity field structure associated with the 3D Tollmien-Schlichting waves 1
- Power spectra
 Irregular flows 29
- Propellant binder
 Development of solid propellant technology in India 337
- Pseudo-similarity
 On the theory of turbulence for incompressible fluids 97
- Radiation condition
 Hydrodynamic numerical modelling of storm surges—Application to the Bay of Bengal 433
- Radiation thermodynamics
 Dimensional analysis and equilibrium radiation 295
- Recombination
 Recombination of two vortex filaments and jet noise 83
- Regression rate
 Variable property analysis—is there anything to it? 313
- Remote sensing
 ISRO spacecraft technology evolution 359
- Reynolds equations
 On the theory of turbulence in incompressible fluids 97
- Rocket motor
 Development of solid propellant technology in India 337
- Satellites
 ISRO spacecraft technology evolution 359
- Shock wave/boundary layer interaction
 A profile of aerodynamic research in VSSC with application to satellite launch vehicles 237
- Shock-wave-boundary-layer interaction
 Shock-wave-turbulent-boundary-layer interaction and its control. A survey of recent developments 143
- Single droplet combustion
 Variable property analysis—is there anything to it? 313
- Skin friction
 Flat plate drag reduction by turbulence manipulation 113
- Solid propellant
 Development of solid propellant technology in India 337
- Space policy
 Management of the Indian space programme 397

- Space technology
 A profile of aerodynamic research in VSSC with application to satellite launch vehicles 237
- Spreading rate
 Observations of supersonic free shear layers 57
- Stabilized platform
 Development of navigation guidance and control technology for Indian launch vehicles 343
- Storm surges
 Hydrodynamic numerical modelling of storm surges—Application to the Bay of Bengal 433
- Strap-down system
 Development of navigation guidance and control technology for Indian launch vehicles 343
- Strap-on configurations
 A profile of aerodynamic research in VSSC with application to satellite launch vehicles 237
- Successive approximation
 On the theory of turbulence for incompressible fluids 97
- Supercritical airfoil
 Characteristics of a typical lifting symmetric supercritical airfoil 203
- Supersonic free shear layers
 Observations of supersonic free shear layers 57
- Technology and development
 ISRO spacecraft technology evolution 359
- Tide-surge interaction
 Hydrodynamic numerical modelling of storm surges—Application to the Bay of Bengal 433
- 3D Tollmien-Schlichting waves
 Vorticity field structure associated with the 3D Tollmien-Schlichting waves 1
- Transonic flow
 Characteristics of a typical lifting symmetric supercritical airfoil 203
- Turbulence manipulation
 Flat plate drag reduction by turbulence manipulation 113
- Turbulent shear flow
 Visualization and analysis of longitudinal vortices at curved walls of 2D laminar and turbulent channel flows 71
- Turbulent shear layers
 Observations of supersonic free shear layers 57
- Turbulent structure
 Visualization and analysis of longitudinal vortices at curved walls of 2D laminar and turbulent channel flows 71
- Turbulent velocity fluctuation
 On the theory of turbulence for incompressible fluids 97
- Unbiased and consistent estimator
 Monte Carlo simulation for molecular gas dynamics 217
- Unsteady flows
 The behaviour of excited plane jets 129
- Variable property analysis
 Variable property analysis—is there anything to it? 313
- Vehicle flexibility
 Development of navigation guidance and control technology for Indian launch vehicles 343
- Viscous dissipation
 On the theory of turbulence for incompressible fluids 97
- Viscous effect
 Recombination of two vortex filaments and jet noise 83
- Viscous-inviscid interaction
 Shock-wave-turbulent-boundary-layer interaction and its control: A survey of recent developments 143
- Vortex
 Visualization and analysis of longitudinal vortices at curved walls of 2D laminar and turbulent channel flows 71
- Vortex dynamics
 The behaviour of excited plane jets 129
- Vortex filament
 Recombination of two vortex filaments and jet noise 83
- Vorticity field structure
 Vorticity field structure associated with the 3D Tollmien-Schlichting waves 1
- Wall wakes
 Flat plate drag reduction by turbulence manipulation 113
- Wind tunnel facilities
 A profile of aerodynamic research in VSSC with application to satellite launch vehicles 237

ACADEMY PUBLICATIONS IN ENGINEERING SCIENCES

General Editor: R Narasimha

Volume 1. The Aryabhata Project (eds U R Rao, K Kasturjangan)

Volume 2. Computer Simulation (eds N Seshagiri, R Narasimha)

Volume 3. Rural Technology (ed. A K N Reddy)

Volume 4. Alloy Design (eds S Ranganathan, V S Arunachalam, R W Cahn)

... attempt in bringing together a series of articles, written by eminent scientists of India and abroad... Academy deserves all praise in bringing out these two timely issues.

Powder Metall. Assoc. India, Newslett.

Volume 5. Surveys in Fluid Mechanics (eds R Narasimha, S M Deshpande)

An informal and stimulating publication... (provides) a survey of many important topics in Fluid Mechanics... All the papers are of excellent technical content and most are very well written. Many include lengthy reference lists, which are as useful as the body of the paper... The publishing quality is very good...

IEEE Journal of Ocean Engineering

... The general level (of papers) is high... Several are likely to have wide appeal... Judging by the invited lectures the Asian Congresses of Fluid Mechanics are off to a good start.

Journal of Fluid Mechanics

Volume 6. Wood Heat for Cooking (eds K Krishna Prasad, P Verhaart)

... interesting and stimulating account of technical thinking on the wood stove problem up to date... excellent collection of valuable and thought-provoking investigations on the subject.

Rev. Projector (India)

Volume 7. Remote Sensing (eds B L Deekshatulu, Y S Rajan)

... Several contributions are specifically addressing topics of national interest, however, the majority of the papers is of general interest for a wide community. The book can serve not only as an inventory of the Indian activities, but also as a textbook on techniques and applications of remote sensing.

Photogrammetria

... particularly refreshing...

Int. J. Remote Sensing

Volume 8. Water Resources Systems Planning (eds M C Chaturvedi, P Rogers)

... It is well got up and very well printed and forms a valuable addition to our limited literature on Water Resources of India.

Curr. Sci.

Volume 9. Reactions and Reaction Engineering (eds R A Mashelkar, R Kumar)

Volume 10. Reliability and Fault-Tolerance Issues in Real-Time Systems
(ed. N Viswanadham)

Volume 11. Composite Materials and Structures (ed. K A V Pandala)